

T.N. Krishnamurti  
Lydia Stefanova  
Vasubandhu Misra

# Tropical Meteorology

An Introduction

# Springer Atmospheric Sciences

For further volumes:  
<http://www.springer.com/series/10176>



T.N. Krishnamurti • Lydia Stefanova  
Vasubandhu Misra

# Tropical Meteorology

An Introduction



Springer

T.N. Krishnamurti  
Florida State University  
Tallahassee, FL, USA

Lydia Stefanova  
Florida State University  
Center for Ocean-Atmospheric Prediction  
Tallahassee, FL, USA

Vasubandhu Misra  
Florida State University  
Center for Ocean-Atmospheric Prediction  
Tallahassee, FL, USA

ISSN 2194-5217  
ISBN 978-1-4614-7408-1  
DOI 10.1007/978-1-4614-7409-8  
Springer New York Heidelberg Dordrecht London

ISSN 2194-5225 (electronic)  
ISBN 978-1-4614-7409-8 (eBook)

Library of Congress Control Number: 2013938488

© Springer Science+Business Media New York 2013

This work is subject to copyright. All rights are reserved by the Publisher, whether the whole or part of the material is concerned, specifically the rights of translation, reprinting, reuse of illustrations, recitation, broadcasting, reproduction on microfilms or in any other physical way, and transmission or information storage and retrieval, electronic adaptation, computer software, or by similar or dissimilar methodology now known or hereafter developed. Exempted from this legal reservation are brief excerpts in connection with reviews or scholarly analysis or material supplied specifically for the purpose of being entered and executed on a computer system, for exclusive use by the purchaser of the work. Duplication of this publication or parts thereof is permitted only under the provisions of the Copyright Law of the Publisher's location, in its current version, and permission for use must always be obtained from Springer. Permissions for use may be obtained through RightsLink at the Copyright Clearance Center. Violations are liable to prosecution under the respective Copyright Law.

The use of general descriptive names, registered names, trademarks, service marks, etc. in this publication does not imply, even in the absence of a specific statement, that such names are exempt from the relevant protective laws and regulations and therefore free for general use.

While the advice and information in this book are believed to be true and accurate at the date of publication, neither the authors nor the editors nor the publisher can accept any legal responsibility for any errors or omissions that may be made. The publisher makes no warranty, express or implied, with respect to the material contained herein.

Printed on acid-free paper

Springer is part of Springer Science+Business Media ([www.springer.com](http://www.springer.com))

# Preface

In the 1950s, Professors Herbert Riehl and Clarence Palmer laid the foundations for *Tropical Meteorology*. They recognized the importance of numerous phenomena such as trades, monsoons and tropical cyclones. They were the early teachers for whole generations of students to follow. Dr Joanne Simpson was also a pioneer in bringing out the importance of tropical clouds as a distinctly different entity from the middle latitude stratiform layers. Various meteorological centers in many parts of the tropical world started research and operations going back nearly 100 years. The India Meteorological Department was one of such earliest weather centers. The early history of the monsoon was regularly reported in the memoirs of the India Meteorological Department. The US Weather Service was initiated in 1870 and became the Weather Bureau in 1890. Even that far back tracking hurricanes and providing surface observations had begun. The scientific progress of tropical meteorology has been quite large in the last 50 years. Contributions to this area of science came not only from the tropical countries but also from many scientists at higher latitudes. Field experiments to collect tropical data sets for specific scientific phenomenon of the tropics have been a very active component of research in the last 50 years. This has furthered our knowledge of the structure and processes of the tropical latitudes. The area of numerical weather prediction for the low latitudes also made much progress in recent years. Models have improved with the inclusion of clouds explicitly, and diverse scales and scale interactions have been studied. Low-frequency modes of the tropics have also drawn a lot of attention in recent years with many scientific publications on the Madden Julian and the El Niño Southern Oscillation time scales. This text book recognizes these areas of science, and various chapters are developed by the authors to provide a sequential understanding for these important areas.

Tallahassee, FL, USA

T.N. Krishnamurti  
Lydia Stefanova  
Vasubandhu Misra



## Acknowledgements

This book came from years of teaching by the senior author. We wish to acknowledge the research and contributions of many colleagues and friends and former Ph.D. students, Drs. Naomi Surgi, Masao Kanamitsu, Hua Lu Pan, John Molinari, Fred Carr, Richard Pasch, Chia Bo Chang, K.S. Yap, Lahouri Bounoua, Zhan Zhang, Arun Kumar, Vince Wong, Loren White, and Jack Beven. The senior author would also like to express his thanks to numerous postdoctoral candidates who visited his laboratory, over a long period of years, including Jay Fein, Kenichi Kuma, M Kitade, Tadashi Tsuyuki, Masato Sugi, T. Yasunari, Ji Shan Xue, Arindam Chakraborty, Sulochana Gadgil, D.R. Sikka, Woo Jin Lee, H.S. Bhalme, Swati Basu, Ashish K. Mitra, Akiyo Yatagai, Wan Tun Yun, D.R. Chakraborty, William Heckley, Dave Pedgley, Noel Davidson, Philippe Bougeault, and many others. Their visits clarified and contributed to many ideas expressed in this book.



# Contents

<b>1 The Zonally Averaged Tropical Circulation . . . . .</b>	1
1.1 Introduction . . . . .	1
1.2 Zonally Averaged Time Mean Fields . . . . .	2
1.2.1 Zonal Velocity . . . . .	2
1.2.2 Mean Meridional Circulation . . . . .	3
1.2.3 Temperature Field . . . . .	5
1.2.4 Moisture Field . . . . .	6
1.3 Meridional Transports by the Zonally Symmetric Circulation . . . . .	6
1.4 Theory of the Hadley Cell . . . . .	9
1.4.1 Derivation of the Kuo-Eliassen Equation . . . . .	10
1.4.2 Interpretation of the Kuo-Eliassen Equation . . . . .	13
References . . . . .	15
<b>2 Zonally Asymmetric Features of the Tropics . . . . .</b>	17
2.1 Introduction . . . . .	17
2.2 Tropospheric Winds at 850 and 200 mb Levels . . . . .	17
2.3 The Motion Field in the Upper Troposphere . . . . .	20
2.4 The Temperature Field . . . . .	22
2.5 The East/West Circulations in the Tropics . . . . .	24
2.6 The Moisture Field . . . . .	25
2.7 The Sea Level Pressure Field . . . . .	27
2.8 Precipitation Field . . . . .	28
2.9 Other Parameters . . . . .	32
References . . . . .	32
<b>3 The Intertropical Convergence Zone . . . . .</b>	35
3.1 Observational Aspects of the ITCZ . . . . .	35
3.2 ITCZ Theory . . . . .	39
3.3 Regulation of the Warm Pool SST . . . . .	43
References . . . . .	46

<b>4 Heat Induced Circulation .....</b>	47
4.1 Adrian Gill's Atmospheric Model .....	47
4.1.1 Solutions to the Gill Model .....	50
4.2 Desert Heat Lows .....	59
4.2.1 Diurnal Change Over the Heat Lows .....	61
4.2.2 Vertical Motion and Divergence Structure of Heat Lows .....	62
4.2.3 Vertical Profiles of Radiative Transfer Over the Heat Low .....	68
4.2.4 Descent Above the Heat Low and Lateral Teleconnections .....	71
4.3 Heat Budget of the Heat Low .....	72
References .....	74
<b>5 Monsoons .....</b>	75
5.1 Definition .....	75
5.2 Monsoon Domain .....	75
5.3 Differential Heating and the Monsoon .....	76
5.4 A Principal Axis of the Asian Monsoon .....	78
5.5 Key Elements of the Asian Summer and Winter Monsoon .....	78
5.6 Monsoon Onset and Withdrawal Isochrones .....	81
5.7 Features of the Monsoon Onset .....	83
5.8 Onset of Monsoon and the Wall of Moisture from the South .....	84
5.9 Cooling of the Arabian Sea Following the Onset of Monsoon .....	87
5.10 Some Onset-Related Dynamical Fields .....	92
5.11 $\psi$ - $\chi$ Interactions .....	94
5.12 The Heaviest Rainfall of the Summer Monsoon .....	102
5.13 Breaks in the Indian Monsoon .....	103
5.14 Active, Break and Withdrawal Phases of Indian Monsoons .....	106
5.15 The Somali Jet .....	109
5.16 Boundary Layer Dynamics of the Somali Jet .....	113
5.17 Upwelling in the Somali Jet Region .....	117
References .....	118
<b>6 Tropical Waves and Tropical Depressions .....</b>	121
6.1 Introduction .....	121
6.2 Barotropic Instability .....	124
6.2.1 Necessary Conditions for the Existence of Barotropic Instability .....	124
6.2.2 Finite Difference Methods for Studying Barotropic Instability in the Tropics .....	127

6.3	Combined Barotropic-Baroclinic Instability . . . . .	128
6.3.1	Necessary Conditions for the Existence of Combined Barotropic-Baroclinic Instability . . . . .	128
6.3.2	Initial Value Approach to the Combined Instability . . . . .	130
6.4	Dual Parts of African Waves . . . . .	137
	References . . . . .	141
<b>7</b>	<b>Madden Julian Oscillation . . . . .</b>	<b>143</b>
7.1	Observational Aspects . . . . .	143
7.2	Theory of the MJO . . . . .	151
7.3	Westerly Wind Bursts in the MJO . . . . .	157
7.4	The MJO Connection During the Birth and Demise of ENSO . . . . .	158
7.5	Wave Energy Flux Across the Tropics . . . . .	158
7.6	Real Data Forecasts of ISO . . . . .	162
	References . . . . .	168
<b>8</b>	<b>Scale Interactions . . . . .</b>	<b>169</b>
8.1	Introduction . . . . .	169
8.2	Wave-Number Domain . . . . .	170
8.3	Frequency Domain . . . . .	173
8.4	Frequency Domain Examples . . . . .	174
8.5	Wave-Number Domain Examples . . . . .	177
8.5.1	Global Tropics . . . . .	177
8.5.2	Hurricanes . . . . .	180
	Appendix 1: Derivation of Equations in Wave-Number Domain . . . . .	185
	Appendix 2: A Simple Example . . . . .	193
	References . . . . .	196
<b>9</b>	<b>El Niño and Southern Oscillation . . . . .</b>	<b>197</b>
9.1	Introduction . . . . .	197
9.2	Observational Aspects . . . . .	197
9.3	The ENSO Scenario . . . . .	200
9.3.1	Arrival of a Sea Level Pressure Anomaly at the Near-Equatorial Latitudes . . . . .	200
9.3.2	Trade Winds . . . . .	202
9.3.3	Piling of Water Over the Western Pacific Ocean . . . . .	203
9.3.4	Thermocline Transitions . . . . .	204
9.3.5	Typical SST Anomalies, Normal and El Niño Years . . . . .	206
9.3.6	The Pacific North American Pattern (PNA) . . . . .	208
9.3.7	A River of Westerlies That Nearly Encircles the Globe Emanating from the El Niño Region . . . . .	208
9.4	Coupled Modeling of ENSO . . . . .	209
9.4.1	Zebiak-Cane Ocean Model . . . . .	210
9.4.2	Results from the Zebiak-Cane Model . . . . .	215
9.5	ENSO Theory . . . . .	218
	References . . . . .	219

<b>10 Diabatic Potential Vorticity Over the Global Tropics . . . . .</b>	221
10.1 Introduction . . . . .	221
10.2 Diabatic Potential Vorticity Equation . . . . .	222
10.3 Application of the Diabatic Potential Vorticity Equation to the Global Tropics . . . . .	223
10.3.1 Potential Vorticity . . . . .	223
10.3.2 Horizontal Advection of Potential Vorticity . . . . .	224
10.3.3 Vertical Advection of Potential Vorticity . . . . .	224
10.3.4 Vertical Differential Heating . . . . .	224
10.3.5 Horizontal Differential Heating . . . . .	227
10.3.6 Frictional Contribution . . . . .	228
10.4 Application of the Diabatic Potential Vorticity Equation to Hurricanes . . . . .	229
References . . . . .	231
<b>11 Tropical Cloud Ensembles . . . . .</b>	233
11.1 Introduction . . . . .	233
11.2 Understanding Simple Buoyancy-Driven Dry Convection . . . . .	235
11.3 Understanding Simple Buoyancy-Driven Shallow Moist Convection . . . . .	237
11.3.1 A Simple Cloud Model . . . . .	237
11.3.2 Initial and Boundary Conditions and Domain Definition . . . . .	241
11.3.3 Numerical Model Results . . . . .	242
11.4 A Cloud Ensemble Model . . . . .	244
11.4.1 Kinematics and Thermodynamics . . . . .	244
11.4.2 Cloud Microphysics . . . . .	247
11.4.3 Conversion Processes . . . . .	250
11.4.4 Modeling Results . . . . .	254
References . . . . .	258
<b>12 Tropical Boundary Layer . . . . .</b>	261
12.1 Empirical Concepts . . . . .	261
12.1.1 The Mixing-Length Concept . . . . .	261
12.1.2 The Wind Profile and Surface Drag . . . . .	262
12.1.3 Bulk Aerodynamic Method . . . . .	264
12.2 Observational Aspects of the Boundary Layer . . . . .	265
12.3 A Simple Model of the Tropical Boundary Layer . . . . .	270
12.4 Surface Similarity Theory . . . . .	272
12.5 Scale Analysis of the Large-Scale Tropical Boundary Layer . . . . .	275
12.6 Cross-Equatorial Flows and Planetary Boundary Layer Dynamics . . . . .	277
References . . . . .	279

<b>13 Radiative Forcing</b> . . . . .	281
13.1 Radiative Processes in the Tropics . . . . .	281
13.2 Shallow Stratocumulus Clouds and Radiative Transfer . . . . .	282
13.3 Surface Energy Balance . . . . .	283
13.3.1 Ground Temperature $T_g$ . . . . .	285
13.3.2 Evaluating Moisture Fluxes for Hydrological Budgets and Water Cycle Studies . . . . .	285
13.3.3 The Surface Sensible and Latent Heat Fluxes . . . . .	286
13.3.4 Net Solar (Shortwave) Radiation at the Earth Surface . . . . .	286
13.3.5 Net Thermal (Longwave) Radiation at the Earth Surface . . . . .	286
13.3.6 Surface Sensible Heat Flux . . . . .	288
13.3.7 Surface Latent Heat flux . . . . .	290
13.4 Top of the Atmosphere Net Radiation Fluxes . . . . .	291
13.4.1 The Net Solar Radiation at the Top of the Atmosphere . . . . .	291
13.4.2 The Net Thermal Radiation at the Top of the Atmosphere . . . . .	293
13.5 Radiative Forcing for the Hadley and East–West Circulation . . . . .	293
13.6 Life Cycle of the Monsoon . . . . .	295
References . . . . .	297
<b>14 Dry and Moist Static Stability</b> . . . . .	299
14.1 Introduction . . . . .	299
14.2 Some Useful Definitions . . . . .	300
14.3 Dry and Moist Static Energy . . . . .	300
14.3.1 Dry Static Energy . . . . .	300
14.3.2 Moist Static Energy . . . . .	302
14.4 Dry and Moist Static Stability . . . . .	302
14.4.1 The Dry Static Stability Equation . . . . .	303
14.4.2 The Moist Static Stability Equation . . . . .	306
14.5 Observational Aspects of the Trade Wind Inversion . . . . .	308
Reference . . . . .	315
<b>15 Hurricane Observations</b> . . . . .	317
15.1 Introduction . . . . .	317
15.2 Conventional Observations . . . . .	322
15.2.1 Observations of the Inner Core . . . . .	323
15.3 Tropical Cyclones Over the Indian Ocean Basin . . . . .	325
References . . . . .	330
<b>16 Genesis, Tracks, and Intensification of Hurricanes</b> . . . . .	331
16.1 Introduction . . . . .	331
16.2 Genesis . . . . .	332

16.2.1	Horizontal Shear Flow Instability . . . . .	332
16.2.2	Conservation of Potential Vorticity (PV) . . . . .	333
16.2.3	Diabatic Effects . . . . .	334
16.2.4	Order of Magnitudes for the Terms of the PV Equation in a Hurricane . . . . .	335
16.3	Tracks . . . . .	336
16.3.1	The $\beta$ Effect . . . . .	336
16.3.2	The Fujiwhara Effect . . . . .	337
16.3.3	The Extratropical Transition of Tropical Cyclones . . . . .	337
16.4	Intensity . . . . .	342
16.4.1	The Angular Momentum Principle . . . . .	342
16.4.2	Local Cylindrical Coordinates . . . . .	343
16.4.3	The Torques . . . . .	345
16.4.4	What Does the Angular Momentum Field in a Hurricane Look Like? . . . . .	345
16.4.5	Cloud Torques . . . . .	347
16.4.6	Surface Frictional Torques . . . . .	348
16.4.7	What Is a Constant Angular Momentum Profile . . . . .	349
16.4.8	Pressure Torques . . . . .	350
16.4.9	Inner Versus Outer Forcing . . . . .	352
16.4.10	Vortical Hot Towers . . . . .	355
16.4.11	Vortex Rossby Waves . . . . .	356
	Appendix 1: Transformation of shear to Curvature Vorticity . . . . .	357
	References . . . . .	358
17	<b>Modeling and Forecasting of Hurricanes</b> . . . . .	361
17.1	Introduction . . . . .	361
17.2	The Axisymmetric Hurricane Model . . . . .	362
17.3	Current Suite of Operational Models . . . . .	366
17.4	Multimodel Superensemble for Atlantic Hurricanes . . . . .	368
17.5	Multimodel Superensemble for Pacific Typhoons . . . . .	371
17.6	Ensemble Forecasts from a Suite of Mesoscale Models and Combination of Mesoscale and Large Scale Models for Atlantic Hurricanes . . . . .	373
	References . . . . .	375
18	<b>Sea Breeze and Diurnal Change Over the Tropics</b> . . . . .	377
18.1	Introduction . . . . .	377
18.2	Sea Breeze Models . . . . .	378
18.3	Some Observational Aspects of Diurnal Changes . . . . .	383
18.4	Diurnal Variation in the Monsoon Belt . . . . .	386
18.4.1	Diurnal Variation in Rainfall Over India . . . . .	390
18.4.2	Diurnal Change Transitions Between the Himalayan Foothills and the Eastern Tibetan Plateau . . . . .	391

18.4.3	The Arritt Nomogram .....	392
18.4.4	Monsoonal Scale Diurnal Oscillation of the Monsoon .....	395
	References .....	397
<b>19</b>	<b>Tropical Squall Lines and Mesoscale Convective Systems .....</b>	<b>399</b>
19.1	Introduction .....	399
19.2	West African Disturbance Lines .....	400
19.2.1	Squall Lines “An Integral Part of the African Wave” .....	401
19.2.2	Squall Lines Are Located Between Two Easterly Jet Streams .....	402
19.2.3	Other Squall Line Models .....	402
19.2.4	Squall and Non-squall Systems .....	405
19.3	Mesoscale Convective Systems .....	407
19.4	Organization of Convection .....	409
	References .....	413
	<b>Index .....</b>	<b>415</b>

# Chapter 1

## The Zonally Averaged Tropical Circulation

### 1.1 Introduction

We shall begin this text with a zonal-time averaged representation of the tropical atmosphere. These are height (or pressure)-time diagrams that illustrate several simplified climatological features of the tropical atmosphere such as the zonal wind, temperature, moisture (specific humidity) and the mean meridional circulation, i.e., the Hadley cell.

A long-term averaging, over a season or a month, is usually carried out to portray the zonally symmetric distributions of the atmospheric variables. Let  $Q$  be any variable that is a function of latitude ( $\varphi$ ), longitude ( $\lambda$ ), pressure ( $p$ ) and time ( $t$ ). We shall use the notation

$$[Q] = \frac{1}{2\pi} \int_0^{2\pi} Q d\lambda \quad (1.1)$$

to denote the zonal average of  $Q$  around a latitude circle, and the notation

$$\bar{Q} = \frac{1}{T} \int_0^T Q dt \quad (1.2)$$

to denote the time average of  $Q$  over a period  $T$ . The zonally averaged and time averaged quantity  $[\bar{Q}]$  is a function of latitude and pressure, i.e., it varies in the meridional-vertical plane.

In this chapter we shall first examine the geometry of the isopleths of the following quantities in the meridional-vertical plane –

- (i) Zonal velocity  $[\bar{u}]$ ,
- (ii) Mean meridional circulation  $[\bar{\psi}]$ ,
- (iii) Temperature  $[\bar{T}]$ ,
- (iv) Moisture  $[\bar{q}]$ .

One of the main purposes of this depiction is to take a quick look at the vertical structure of the tropical atmosphere as a function of latitude. In the next chapter we shall examine the important question of the zonal asymmetry of the tropical atmosphere.

## 1.2 Zonally Averaged Time Mean Fields

### 1.2.1 Zonal Velocity

The distribution of the zonal velocity for the four seasons is illustrated in Fig. 1.1. Over the Equator, easterlies prevail throughout the troposphere. The climatological westerly jet can be seen, strongest near 200 mb in the winter hemisphere. The latitude

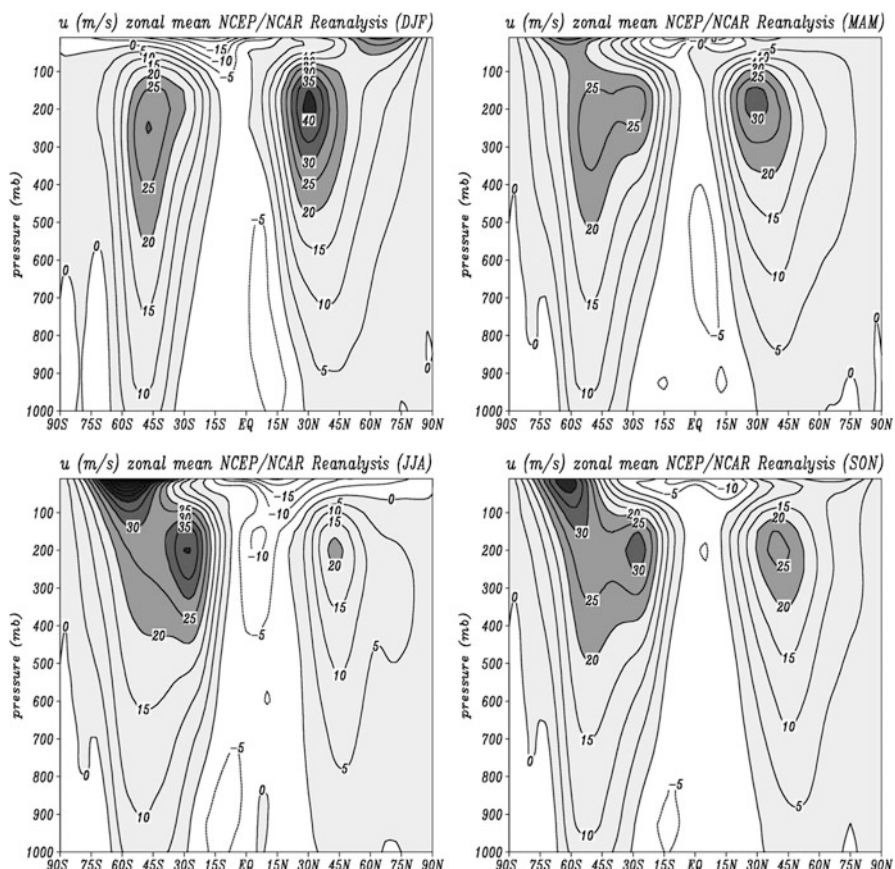


**Fig. 1.1** Zonal mean zonal wind component for winter (DJF), spring (MAM), summer (JJA) and fall (SON) seasons for the period 1970–2000. Units are in  $\text{m s}^{-1}$ ; the contour interval is  $5 \text{ m s}^{-1}$  (Computed from the NCEP-NCAR reanalysis)

of strongest westerlies defining the jet shifts from roughly 30°N during the northern winter to roughly 45°N during the northern summer season. Another interesting aspect of the zonally averaged seasonal mean flows is the vertical shear distribution. During the northern summer over the belt 0–20°N, the easterlies increase with height. In the same belt, during the northern winter, the easterlies increase in strength between the surface and 850 mb, and weaken with further increase in altitude. The easterly-westerly shears at different latitudes have important dynamical implications. During autumn, the tropical easterlies are strongest near the 300 mb surface, whilst during spring the strongest easterlies are found near the 700 mb level.

### 1.2.2 Mean Meridional Circulation

The mean meridional circulation is usually depicted via the use of the streamfunction. The mass continuity equation for zonally symmetric motions can be written as

$$\frac{1}{r} \frac{\partial[\bar{v}]}{\partial\varphi} + \frac{\partial[\bar{\omega}]}{\partial p} - \frac{\tan\varphi}{r} [\bar{v}] = 0 \quad (1.3)$$

or

$$\frac{1}{r} \frac{\partial[\bar{v}]\cos\varphi}{\partial\varphi} + \frac{\partial[\bar{\omega}]}{\partial p} = 0, \quad (1.4)$$

where  $\bar{v}$  is the meridional velocity,  $\bar{\omega}$  is the pressure vertical velocity, and  $r$  is the Earth's radius.

It is convenient to define a streamfunction  $\psi$  for the mean meridional circulation that satisfies the zonally averaged continuity equation, i.e.,

$$\frac{\partial[\bar{\psi}]}{\partial p} = [\bar{v}] \frac{2\pi r \cos\varphi}{g} \quad (1.5)$$

$$\frac{1}{r} \frac{\partial[\bar{\psi}]}{\partial\varphi} = -[\bar{\omega}] \frac{2\pi r \cos\varphi}{g} \quad (1.6)$$

Note that the choice of sign of  $\psi$  is arbitrary, as is the multiplicative constant  $2\pi r/g$ , which is introduced here so that the units of  $\psi$  are in kg s<sup>-1</sup>. With this choice of sign, a positive streamfunction corresponds to a clockwise circulation in the meridional-vertical plane. This is discussed in more detail in Sect. 1.4.

Construction of  $[\bar{\psi}]$  from observation is generally accomplished as follows. First, using a long record of monthly wind observations, the mean (seasonal or monthly) zonally averaged meridional wind  $[\bar{v}]$  is calculated as a function of

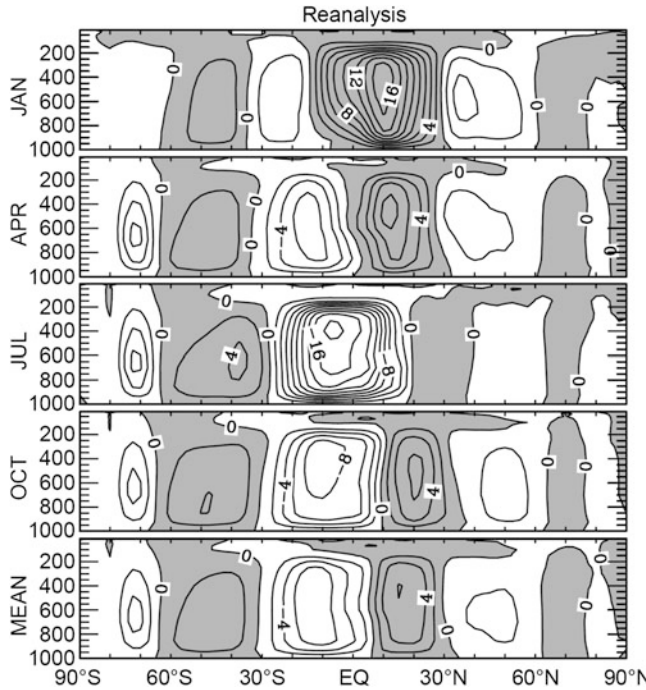


**Fig. 1.2** Mean zonal stream function for January, April, July, October, and annual mean for the period 1968–89. Units are in  $10^{10} \text{ kg s}^{-1}$ ; the contour interval is  $2 \times 10^{10} \text{ kg s}^{-1}$  (From Waliser et al. 1999)

latitude and pressure. Next, the vertical mean zonally averaged vertical velocity  $[\bar{\omega}]$  is calculated by solving the continuity (1.3). Finally, the mean zonally averaged streamfunction  $[\bar{\psi}]$  is calculated by solving the system of (1.5) and (1.6). The streamfunction field is a convenient way of looking at the circulation since it simultaneously conveys information about the meridional and the vertical motion.

Figure 1.2 shows the seasonal values of the mean meridional circulation. The interval between adjacent isopleths of  $[\bar{\psi}]$  indicates the amount of mass ( $2 \times 10^{10} \text{ kg s}^{-1}$ ) circulating in these channels. These are the kind of diagrams that are used to illustrate the so-called Hadley, Ferrel and Polar cells – the three cells of the mean meridional circulation. From the point of view of the tropics, the Hadley cell is the one of most interest. The ascending and descending branches of the cell are easy to identify in Fig. 1.2. The winter and summer Hadley cells are more intense than those during the other two seasons. This diagram is based on studies of Newell et al. (1972). There is an interesting seasonal shift of the latitude of the ascending branch of the Hadley cell, near  $10^\circ\text{N}$  during northern summer, near  $5^\circ\text{S}$  during northern winter, and near the Equator during the spring. In the ascending branch of the Hadley cell, the intensity of rising motion is of the order of  $0.4 \text{ cm s}^{-1}$ , while the north-south component attains a magnitude of the order of  $1\text{--}2 \text{ m s}^{-1}$ . We shall note from the distribution of temperature  $[\bar{T}]$  that these Hadley circulations

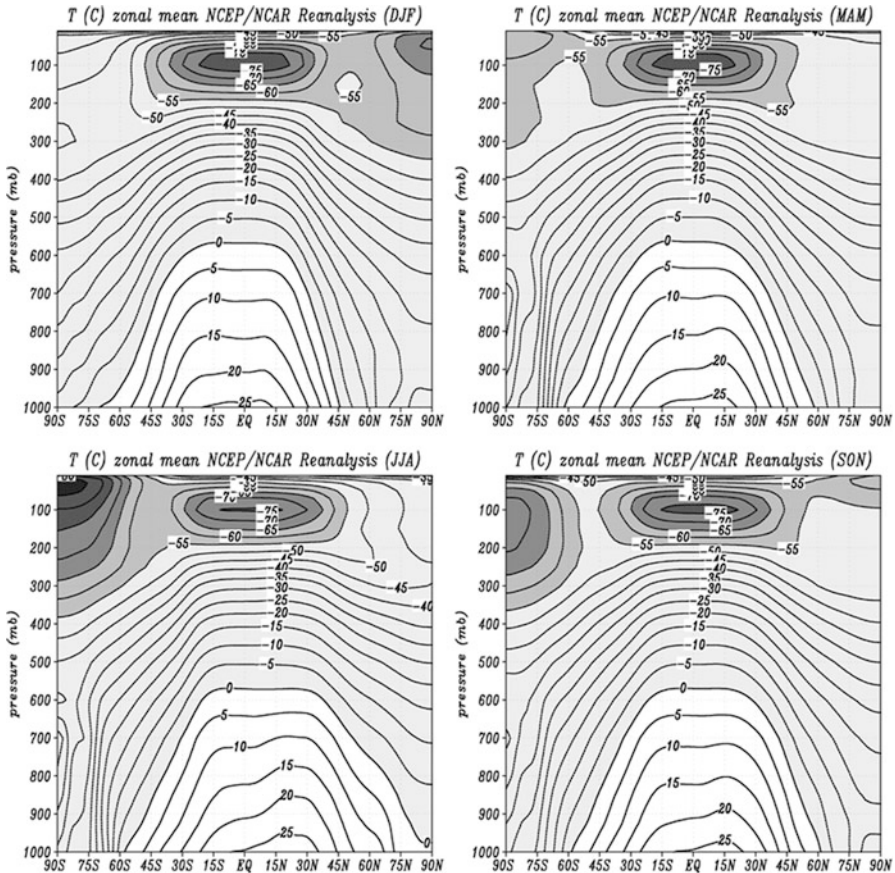


**Fig. 1.3** Zonal mean temperature for winter (DJF), spring (MAM), summer (JJA) and fall (SON) seasons for the period 1970–2000. Units are in  $^{\circ}\text{C}$ ; the contour interval is  $5\text{ }^{\circ}\text{C}$  (Computed from the NCEP-NCAR reanalysis)

are thermally direct, i.e. they transport heat along the temperature gradient. This has important implications for the generation of zonal kinetic energy from the zonally available potential energy.

Interannual variability of features seen in Fig. 1.2 is an important global change issue. It is also of great interest to examine regional local Hadley cell contribution and their variability.

### 1.2.3 Temperature Field

The field of zonally averaged seasonal mean temperature [ $\bar{T}$ ] is presented in Fig. 1.3. The thermal field illustrates the strong meridional gradient in the middle latitudes, and the lack of it over the tropics. Other features, such as the annual cold

tropical tropopause and warm subtropical lower tropospheric temperatures during the northern summer are worth noting. It should be pointed out that the zonal average smoothes out the land-ocean contrasts, and thus it is representative of neither land nor ocean. This is especially significant during the northern summer when the zonal asymmetries are quite large and the symmetric component, such as shown in Fig. 1.3, is not representative of the meridional variation, except perhaps in the context of the generation of zonal kinetic energy by the Hadley cell. Another important feature of these climatological zonal mean maps is the reversal of the temperature gradient (both in the vertical and in the horizontal) at and around the tropopause level (100 mb). This feature of strong temperature gradients at the tropopause forces the subtropical jet streams to maximize around 200 mb.

#### 1.2.4 *Moisture Field*

The field of specific humidity [ $\bar{q}$ ] is illustrated in Fig. 1.4. The largest values, around  $18 \text{ g kg}^{-1}$ , are found near the Equator. These should be compared with values of about  $6 \text{ g kg}^{-1}$  in the middle latitudes near  $45^\circ\text{N}$ . Such large magnitudes of moisture as found in the low latitudes have a strong effect on the virtual temperature correction. For a surface temperature of  $20^\circ\text{C}$ , the corresponding correction can be up to  $3^\circ\text{C}$ , which is quite substantial in thermodynamical calculations. The large meridional gradient of moisture in the tropics (see Fig. 1.4) gives rise to a considerable meridional gradient of the virtual temperature, even though the meridional gradient of temperature itself (Fig. 1.3) is small. The zonally symmetric component of moisture is again quite smooth and the land-ocean contrasts are not represented. It may be desired to illustrate anomalies of the temperature and specific humidity fields with respect to the latitudinal mean structures.

### 1.3 Meridional Transports by the Zonally Symmetric Circulation

It is well known that the Hadley cell plays an important role in poleward fluxes, and we shall illustrate this here. In this context, using the notation of Lorenz (1967), we consider a variable  $Q$ . Let  $Q = \bar{Q} + Q'$ , where  $\bar{Q}$  is a time average and  $Q'$  is the departure from that time average. We may also write  $Q = [Q] + Q^*$ , where  $[Q]$  is a zonal average, and  $Q^*$  is the departure from that zonal average. Using the above two relations, the total meridional transport of  $Q$  can be written in the form

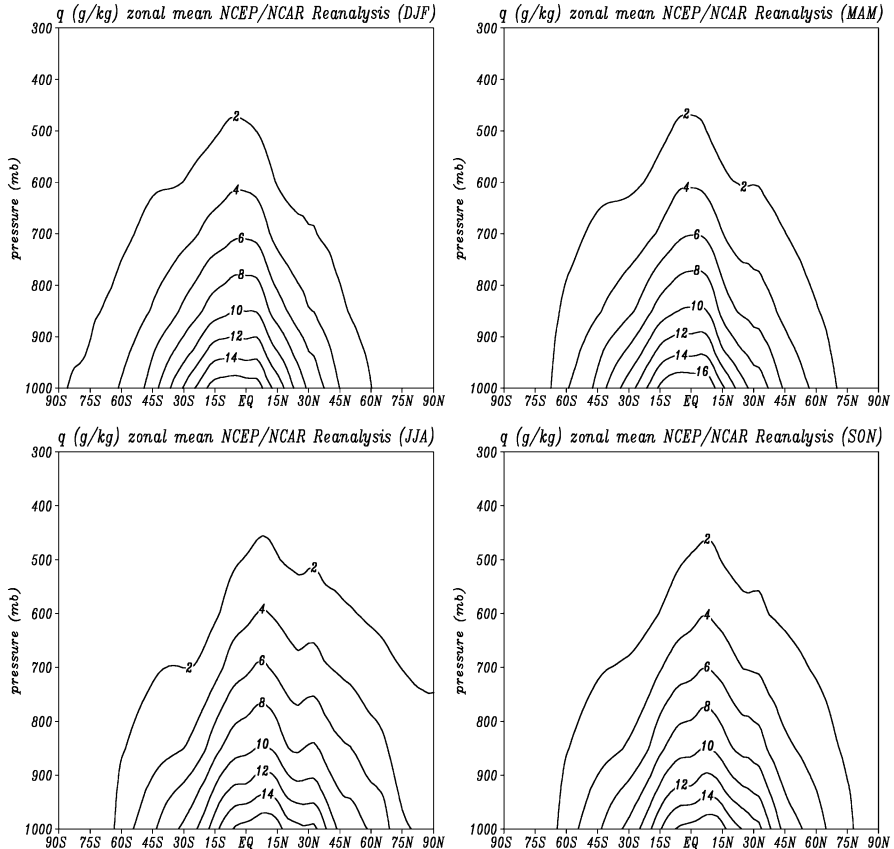


**Fig. 1.4** Zonal mean specific humidity for winter (DJF), spring (MAM), summer (JJA) and fall (SON) seasons for the period 1970–2000. Units are in  $^{\circ}\text{C g kg}^{-1}$ ; the contour interval is 2  $\text{g kg}^{-1}$  (Computed from the NCAR-NCEP reanalysis)

$$\begin{aligned}
 [Qv] &= [\bar{Q}] [\bar{v}] + \overline{[Q'] [v']} + \overline{[Q^* v^*]} \\
 \text{Total Transport} &= \text{Transport by the Mean Meridional Circulation (MMC)} + \text{Transport by Transient Eddies (TE)} + \text{Transport by Standing Eddies (SE)} \\
 (TT) &= \text{Mean Meridional Circulation (MMC)} + \text{Transient Eddies (TE)} + \text{Standing Eddies (SE)}
 \end{aligned}$$

Tables 1.1 through 1.3 show the following meridional transports for January and July, from Oort and Ramussen (1970):

- (i) Momentum
- (ii) Sensible heat
- (iii) Potential energy

**Table 1.1** Meridional transport of momentum<sup>a</sup>.  
The units are in  $\text{m}^2 \text{s}^{-2}$

	Equator	15N	30N	45N	60N
<b>January</b>					
TE	-0.1	3.4	13.3	11.2	2.8
SE	-0.7	0.1	4.6	0.9	-11.8
MMC	-0.8	4.9	-1.7	-2.3	0.5
<b>July</b>					
TE	1.4	1.1	4.4	7.2	-0.4
SE	0.7	2.5	3.1	0.3	-0.4
MMC	2.4	-0.2	-0.0	-0.9	-0.1

<sup>a</sup>Numbers represent averages for the layer between 1012.5 and 75 mb. For conversion to units of energy transfer, multiply by  $(2\pi r \cos \varphi)(p_0 - p)/g$

**Table 1.2** Meridional transport of sensible heat<sup>a</sup>.  
Units in  $^{\circ}\text{C m s}^{-1}$

	Equator	15N	30N	45N	60N
<b>January</b>					
TE	-0.4	-0.8	4.7	6.9	8.6
SE	-0.0	0.0	2.2	10.3	7.8
MMC	-27.0	-23.0	4.0	7.0	-3.0
<b>July</b>					
TE	0.1	-0.3	0.3	4.1	4.8
SE	0.1	0.1	0.2	0.7	-0.6
MMC	26.0	-1.0	2.0	4.0	1.0

<sup>a</sup>Numbers represent averages for the layer between 1012.5 and 75 mb. For conversion to units of energy transfer, multiply by  $(2\pi r \cos \varphi)(p_0 - p)/g$

**Table 1.3** Meridional transport of potential energy<sup>a</sup>. Units in  $10^3 \text{ m}^3 \text{s}^{-2}$

	Equator	15N	30N	45N	60N
<b>January</b>					
TE	-0.0	-0.1	-0.2	-0.4	0.2
SE	-0.0	-0.0	-0.1	0.1	0.2
MMC	40.0	37.0	-6.0	-14.0	6.0
<b>July</b>					
TE	0.0	-0.0	-0.0	-0.2	-0.0
SE	0.0	-0.1	-0.0	0.0	0.1
MMC	-40	2.0	-4.0	-7.0	-1.0

<sup>a</sup>Numbers represent averages for the layer between 1012.5 and 75 mb. For conversion to units of energy transfer, multiply by  $(2\pi r \cos \varphi)(p_0 - p)/g$

The transports by the three processes are identified by the following letters:

TE	Transient eddies
SE	Standing eddies, and
MMC	Mean meridional circulation

The calculations shown here are only for the northern hemisphere. Of interest for the tropical atmosphere are the entries at the Equator, 15°N and 30°N. During the northern winter the mean meridional circulation is fairly intense between the Equator and 30°N. Note that at the Equator and 15°N the mean meridional circulation is responsible for a large proportion of the transport. This proportion is particularly large in the case of sensible heat, and potential energy transports. The transport of momentum fluxes by the transient eddies become comparable and larger than the mean meridional circulation at 15°N and polewards. During the summer season the mean meridional circulation dominates the transport of the fluxes at the equator with comparatively much weaker transports at 15°N and polewards.

A clear message that emerges from these tables is that the inter-hemispheric cross-equatorial fluxes are largely carried out by the Hadley cell (a point deduced from the dominance of the Hadley cell transport at the equator). In the near-equatorial belt of 15°S–15°N the fluxes by standing and transient eddies are small compared to those by the Hadley cell. Next, we shall discuss some interesting aspects of the total (vertically integrated) Hadley cell transport.

Kinetic energy is a positive-definite quantity and its transport is simply dictated by the direction in which the Hadley cell transports it. Knowing the fact that the largest kinetic energy resides in the upper troposphere, i.e., near the 200 mb level, it is apparent that the transport of kinetic energy goes from the summer to the winter hemisphere following the upper branch of the Hadley cell.

Momentum, on the other hand, has a sign. In the Equatorial tropics, the largest easterly (negative) momentum again resides near 200 mb level and the negative momentum is transported from the summer to the winter hemisphere. This is equivalent to a transport of westerly (positive) momentum from the winter to the summer hemisphere.

Most of the moisture (specific humidity) resides in the lower troposphere. Thus it is the lower branch of the Hadley cell that is important for the cross-equatorial transport of latent heat, which therefore is being transported from the winter to the summer hemisphere.

The sensible heat ( $C_p T$ ) has large positive values near the Earth's surface and decreases with altitude. Therefore the net cross-equatorial transport of  $C_p T$  is dominated by the lower troposphere. This calls for a net cross equatorial transport of sensible heat from the winter to the summer hemisphere.

The potential energy ( $gz$ ) increases with altitude. As a consequence, the upper branch of the Hadley cell dominates the cross-equatorial transport of potential energy. Therefore the flux of potential energy is directed from the summer to the winter hemisphere.

## 1.4 Theory of the Hadley Cell

In this section we shall present a simple theory of the Hadley cell. This theory leads to a simple elliptic second order partial differential equation for the Hadley cell stream function in the latitude/pressure frame. This differential equation is quite

analogous to the quasi-geostrophic omega equation. The omega equation has a Laplacian-type operator on the left hand side that operates on omega, the unknown of that problem. On its right hand side are two forcing functions; one of these is the differential vorticity advection (an upper level advection minus an adjacent lower level advection). If the upper level advection is positive and larger than that of the adjacent lower level this forcing function is positive and locally contributes to rising motion. The second forcing function denotes the negative Laplacian of thermal advection, generally large where local thermal advection is at a maximum. This also contributes to a positive forcing function over regions of strong warm advection and rising motion. The Kuo-Eliassen equation for the Hadley cell stream function on the zonal-vertical plane is somewhat analogous. It contains two forcing functions that can be interpreted as:

- (i) External vertical differential of the meridional eddy flux of westerly momentum, and
- (ii) Internal meridional differential heating within the tropics.

These forcing functions determine the strength and geometry of the Hadley cell circulation.

#### 1.4.1 *Derivation of the Kuo-Eliassen Equation*

For the derivation of the Kuo-Eliassen diagnostic equation, we start from the following form of the primitive equations on a sphere in pressure coordinates –

- (i) The zonal equation of motion:

$$\begin{aligned} \frac{\partial u}{\partial t} + \frac{1}{r \cos \varphi} \frac{\partial(uu)}{\partial \lambda} + \frac{1}{r} \frac{\partial(uv)}{\partial \varphi} + \frac{\partial(u\omega)}{\partial p} - \frac{\tan \varphi}{r} uv \\ - \left( f + 2 \frac{\tan \varphi}{r} u \right) v - \frac{g}{r \cos \varphi} \frac{\partial z}{\partial \lambda} + F_u = 0 \end{aligned} \quad (1.7)$$

- (ii) The geostrophic balance in the meridional direction:

$$fu + \frac{g}{r} \frac{\partial z}{\partial \varphi} = 0 \quad (1.8)$$

- (iii) The hydrostatic equation:

$$\left( \frac{RT}{p\theta} \right) \theta + g \frac{\partial z}{\partial p} = 0 \quad (1.9)$$

(iv) The mass continuity equation:

$$\frac{1}{r \cos \varphi} \frac{\partial u}{\partial \lambda} + \frac{1}{r} \frac{\partial v}{\partial \varphi} + \frac{\partial \omega}{\partial p} - \frac{\tan \varphi}{r} v = 0 \quad (1.10)$$

(v) The first law of thermodynamics:

$$\frac{\partial \theta}{\partial t} + \frac{1}{r \cos \varphi} \frac{\partial(\theta u)}{\partial \lambda} + \frac{1}{r} \frac{\partial(\theta v)}{\partial \varphi} + \frac{\partial(\theta \omega)}{\partial p} - \frac{\tan \varphi}{r} \theta v - \frac{\theta}{C_p T} Q = 0, \quad (1.11)$$

where  $\varphi$  is the latitude,  $\lambda$  is the longitude,  $p$  is the pressure,  $u$  is the zonal wind,  $v$  is the meridional wind,  $\omega$  is the vertical velocity in pressure coordinates,  $f$  is the Coriolis parameter,  $r$  is the Earth's radius,  $g$  is the gravitational acceleration,  $z$  is the geopotential height,  $F_u$  is the zonal friction,  $T$  is the temperature,  $\theta$  is the potential temperature,  $R$  is the ideal gas constant,  $C_p$  is the specific heat at constant pressure, and  $Q$  is the diabatic heating.

The zonal average of any quantity  $q$  is given by  $[q] = \frac{1}{2\pi} \int_0^{2\pi} q d\lambda$ , and the departure from the zonal average is given by  $q' = q - [q]$ . Zonally averaging (1.7) through (1.11), and taking into account that  $[q_1 q_2] = [q_1] [q_2] + [q'_1 q'_2]$  and  $\frac{\partial}{\partial \lambda} [q] = 0$  yields

$$\frac{\partial [u]}{\partial t} + \frac{1}{r} \frac{\partial([u] [v])}{\partial \varphi} + \frac{\partial([u] [\omega])}{\partial p} - \frac{\tan \varphi}{r} [u] [v] - \left( f + \frac{\tan \varphi}{r} [u] \right) [v] - M = 0 \quad (1.12)$$

$$f[u] + \frac{g}{r} \frac{\partial[z]}{\partial \varphi} = 0 \quad (1.13)$$

$$\left( \frac{RT}{p\theta} \right) [\theta] + g \frac{\partial[z]}{\partial p} = 0 \quad (1.14)$$

$$\frac{1}{r} \frac{\partial[v]}{\partial \varphi} + \frac{\partial[\omega]}{\partial p} - \frac{\tan \varphi}{r} [v] = 0 \quad (1.15)$$

$$\frac{\partial[\theta]}{\partial t} + \frac{1}{r} \frac{\partial([\theta] [v])}{\partial \varphi} + \frac{\partial([\theta] [\omega])}{\partial p} - \frac{\tan \varphi}{r} [\theta] [v] - \frac{fp\theta}{RT} H = 0 \quad (1.16)$$

where

$$M = -\frac{1}{r} \frac{\partial[u'v']}{\partial \varphi} - \frac{\partial[u'\omega']}{\partial p} + \frac{2 \tan \varphi}{r} [u'v'] - [F_u] \quad (1.17)$$

$$H = \frac{RT}{fp\theta} \left( -\frac{1}{r} \frac{\partial[\theta'v']}{\partial\varphi} - \frac{\partial[\theta'\omega']}{\partial p} + \frac{\tan\varphi}{r} [\theta'v'] + \frac{\theta}{C_p T} [\mathcal{Q}] \right). \quad (1.18)$$

By making use of the zonally averaged continuity (1.9) in (1.6) and (1.10), we obtain:

$$\frac{\partial[u]}{\partial t} + \frac{[v]}{r} \frac{\partial[u]}{\partial\varphi} + [\omega] \frac{\partial[u]}{\partial p} - \left( f + \frac{\tan\varphi}{r} [u] \right) [v] - M = 0 \quad (1.19)$$

$$\frac{\partial[\theta]}{\partial t} + \frac{[v]}{r} \frac{\partial[\theta]}{\partial\varphi} + [\omega] \frac{\partial[\theta]}{\partial p} - \frac{fp\theta}{RT} H = 0 \quad (1.20)$$

The zonally averaged geostrophic (1.13) and the zonally averaged hydrostatic (1.14) may be combined to yield the zonally averaged thermal wind balance equation

$$f \frac{\partial[u]}{\partial p} = -\frac{g}{r} \frac{\partial^2[z]}{\partial\varphi\partial p} = \frac{RT}{p\theta} \frac{1}{r} \frac{\partial[\theta]}{\partial\varphi} \quad (1.21)$$

If we take  $\frac{\partial}{\partial t}$  of both sides of (1.21),  $\frac{\partial}{\partial p}$  of (1.19) and  $\frac{\partial}{\partial\varphi}$  of (1.18) and combine the result, we obtain

$$f \frac{\partial}{\partial p} \left\{ \frac{[v]}{r} \frac{\partial[u]}{\partial\varphi} + [\omega] \frac{\partial[u]}{\partial p} - \left( f + \frac{\tan\varphi}{r} [u] \right) [v] - M \right\} = \frac{RT}{p\theta} \frac{1}{r} \frac{\partial}{\partial\varphi} \left\{ \frac{[v]}{r} \frac{\partial[\theta]}{\partial p} + [\omega] \frac{\partial[\theta]}{\partial p} - \frac{fp\theta}{RT} H \right\}$$

After expanding and applying (1.21) again, this becomes

$$\begin{aligned} & \frac{\partial[u]}{\partial p} \left( \frac{\partial[\omega]}{\partial p} - \frac{1}{r} \frac{\partial[v]}{\partial\varphi} - \frac{\tan\varphi}{r} [v] \right) - \frac{\partial[v]}{\partial p} \left( f - \frac{1}{r} \frac{\partial[u]}{\partial\varphi} + \frac{\tan\varphi}{r} [u] \right) \\ & - \frac{RT}{fp\theta} \frac{\partial[\theta]}{\partial p} \frac{1}{r} \frac{\partial[\omega]}{\partial\varphi} = \frac{\partial M}{\partial p} - \frac{1}{r} \frac{\partial H}{\partial\varphi} \end{aligned} \quad (1.22)$$

Next, we introduce a streamfunction  $\psi$  that satisfies the zonally averaged continuity equation, i.e.,

$$[v] = \frac{1}{\cos\varphi} \frac{\partial\psi}{\partial p}, \quad [\omega] = -\frac{1}{r^2} \frac{\partial\psi}{\partial\varphi} \quad (1.23)$$

The stream function defined by (1.23) is the Hadley cell stream function. The choice of sign is arbitrary – the definition used here leads to a positive stream function corresponding to a clockwise circulation, and a negative stream function corresponding to a counterclockwise circulation. This is easy to see if we visualize rising motion in the south, northward motion aloft, sinking in the north, and

southward motion at low levels. For such a cell,  $\frac{\partial\omega}{\partial\varphi} > 0$  (rising  $\omega < 0$  in the south, sinking  $\omega > 0$  in the north) and  $\frac{\partial v}{\partial p} < 0$  ( $v > 0$  aloft,  $v < 0$  at low levels). It follows then that  $\frac{\partial^2\psi}{\partial p^2} < 0$  and  $\frac{\partial^2\psi}{\partial\varphi^2} < 0$ , i.e.,  $\psi$  is positive since  $\text{sgn}\left(\frac{\partial^2\psi}{\partial\varphi^2}\right) = -\text{sgn}(\psi)$ . Thus a positive  $\psi$  corresponds to clockwise circulation. Substituting (1.23) into (1.22), we obtain the Kuo-Eliassen equation in the form

$$A \frac{\partial^2\psi}{\partial p^2} + \frac{2B}{r} \frac{\partial^2\psi}{\partial\varphi\partial p} + \frac{C}{r^2} \frac{\partial^2\psi}{\partial\varphi^2} + 2B \frac{\tan\varphi}{r} \frac{\partial\psi}{\partial p} + C \frac{\tan\varphi}{r^2} \frac{\partial\psi}{\partial\varphi} = \cos\varphi \left( \frac{\partial M}{\partial p} - \frac{1}{r} \frac{\partial H}{\partial\varphi} \right) \quad (1.24)$$

where

$$A = -f + \frac{1}{r} \frac{\partial[u]}{\partial\varphi} - \frac{\tan\varphi}{r}[u], \quad B = -\frac{\partial[u]}{\partial p}, \quad \text{and} \quad C = \frac{RT}{fp\theta} \frac{\partial[\theta]}{\partial p} \quad (1.25)$$

Equation 1.24 is a diagnostic second order partial differential equation in the  $\varphi$ - $p$  plane, with  $\psi$  being the unknown. Provided the equation is elliptic (i.e.  $AC - B^2 > 0$ ), which generally is the case, (1.24) can be solved numerically as a boundary value problem to obtain the structure of the zonal mean circulation defined by  $\psi$ . The zonal mean circulation given by the left hand side is driven by the sources and sinks in the right hand side – the meridional gradient of diabatic heating, the vertical gradient of zonal friction, and the meridional and vertical fluxes of eddy heat and momentum.

The key to understanding the implications of (1.24) lies in understanding the impact of the forcing functions,  $F_1 = \cos\varphi \frac{\partial M}{\partial p}$ , and  $F_2 = -\frac{\cos\varphi}{r} \frac{\partial H}{\partial\varphi}$ .  $F_1$  is the external (to the tropics) forcing, containing the eddy flux of momentum terms.  $F_2$  is the internal forcing, containing the eddy convergence of heat flux terms and heating. Of the terms in  $F_2$ , the most important ones turn out to be the deep cumulus convection heating and the radiative heating and cooling, while the eddy terms are of secondary importance.

### 1.4.2 Interpretation of the Kuo-Eliassen Equation

We shall next discuss the solutions of (1.24). Generally, one takes the reanalysis data, such as those provided by NCEP and ECMWF to calculate each of the terms on the right hand side of (1.24). This requires the calculation of each term within  $H$  and  $M$ , which can be done using finite differences. The final values of  $H$  and  $M$ , averaged over a month or a season, are used to calculate the forcing functions  $F_1$  and  $F_2$ .

The momentum forcing ( $F_1$ ) is largely contributed by the first term in  $M$ , i.e.,  $\frac{\partial M}{\partial p} \approx -\frac{\partial}{\partial p} \frac{1}{r} \frac{\partial [u'v']}{\partial \varphi}$ . Since the order of the partial pressure and latitude derivatives does not matter, this term can be written as  $\frac{\partial M}{\partial p} \approx -\frac{1}{r} \frac{\partial}{\partial \varphi} \frac{\partial [u'v']}{\partial p}$ . Since the values of momentum flux are larger in the upper troposphere, we can write this term qualitatively as  $\frac{\partial M}{\partial p} \approx -\frac{1}{r} \frac{\partial}{\partial \varphi} \frac{[u'v']_{1000mb} - [u'v']_{200mb}}{800mb} \approx \frac{1}{r} \frac{\partial}{\partial \varphi} \frac{[u'v']_{200mb}}{800mb}$ . Upon integration over the entire tropical domain, this term becomes a boundary flux of westerly momentum. Thus the net eddy flux of westerly momentum at the mid-latitude boundaries of the tropics provides a positive forcing function to the driving of a Hadley cell.

The second term in the analysis of the Hadley cell theory is the tropical differential heating contained in  $F_2$ . This forcing function requires a calculation from all components of diabatic heating, such as convective and non-convective heating, radiative heating (including cloud effects), air-sea and land-air heat fluxes, and boundary layer-based convergence of eddy fluxes of heating. Convective heating within the ITCZ rain belt and radiative cooling over the subtropical highs (near 30°N) turn out to be the predominant sources of this differential heating. If the ITCZ is located near 5°S, as is the case during the northern winter season, and the subtropical highs are located near 30°N, then  $\frac{\partial H}{\partial \varphi}$  would be negative, leading to a positive forcing function  $F_2$ .

What fraction of the intensity of the Hadley cell is due to the external forcing from the boundary fluxes, and what fraction is due to the internal forcing stemming from the differential heating? The answer to this question is obtained through the following procedure.

The left hand side of (1.24) carries the unknown variable  $\psi$ , the Hadley cell streamfunction. The differential operator contains some non-constant coefficients ( $A$ ,  $B$ , and  $C$ , given by (1.25)) that vary in the  $\varphi$ - $p$  plane. These are calculated based on zonal and time averaged data sets. For a solution to be possible, the ellipticity condition  $AC-B^2 > 0$  needs to be assured. This condition may not always be satisfied by the reanalysis data, although such problem arises only at very few locations. In such case, one generally slightly adjusts the zonal wind  $[u]$  at different  $\varphi$  and  $p$  to assure the ellipticity of (1.24). The second order elliptic partial differential equation is then solved numerically. Several numerical methods, generally available in numerical analysis libraries, are available for such computation, such as matrix inversion and relaxation techniques. Given the forcing functions on the  $\varphi$ - $p$  plane and a solution procedure, one next solves for  $\psi$  using  $\psi = 0$  at the bottom and top boundaries. This provides the solution  $\psi(\varphi, p)$ , i.e., the Hadley cell. Because of the linearity of the differential equation and the use of homogeneous boundary conditions ( $\psi = 0$ ), it is possible to solve the problem separately for the two forcing functions. The separate solutions tell us the importance of the boundary eddy momentum forcing versus that of the internal differential heating.

Such calculations generally reveal that most – almost 75 % – of the drive of the Hadley cell comes from the internal differential heating over the tropics. The boundary forcing by the eddy flux of westerly momentum accounts for the remainder. There still remains an unanswered question as to whether the latter might still be needed in order to initiate the organization of convection in the tropics, which then becomes the dominant forcing. Such an interdependence of the two forcing functions can only be addressed via an initial value approach. There are yet other questions, such as the role of the sea surface temperatures and of the ITCZ in the definition of the Hadley cell. These will be addressed in the chapter on ITCZ.

## References

- Lorenz, E.N.: The Nature and Theory of the General Circulation in the Atmosphere, vol. 218. WMO, Geneva (1967)
- Newell, R.E., Kidson, J.W., Vincent, D.G., Boer, G.J.: The General Circulation of the Tropical Atmosphere, Vol 1, 2. The MIT press, Cambridge (1972)
- Oort, A.H., Rasmusson, E.M.: On the annual variation of the monthly mean meridional circulation. Mon. Weather Rev. **98**, 423–442 (1970)
- Waliser, D.E., Shi, Z., Lanzante, J.R., Oort, A.H.: The Hadley circulation: assessing NCEP/NCAR reanalysis and sparse in-situ estimates. Clim. Dynam. **15**, 719–735 (1999)

# **Chapter 2**

## **Zonally Asymmetric Features of the Tropics**

### **2.1 Introduction**

This chapter covers the zonally asymmetric climatology of the tropics. Seasonal or monthly mean weather maps are particularly important in the tropics. The following example illustrates this point. Over the North American continent, the January mean sea level isobar map consists of a large continental anticyclone extending southwards from the Arctic and Canada towards the southern United States. This monthly mean pattern does not reveal any of the migrating polar front cyclones that cause much of the weather there during the winter season. The reason for this is that climatological charts in middle latitudes do not display the transient disturbances. A similar exercise carried out over the global tropical belt shows that daily as well as monthly mean charts both carry much the same information. The subtropical highs, the equatorial troughs, the monsoon troughs, the trades of the two hemispheres are common in both the daily and the monthly mean charts. Another way of expressing this is that climatological means carry much of the variance of the total motion field in the tropics. Thus an understanding of the maintenance of the time averaged zonally asymmetric features of the tropics is important.

A detailed description of the time-averaged zonally asymmetric features of the tropics entails knowledge of a number of variables, such as the motion, temperature, pressure and moisture, at a large number of levels in the atmosphere. Much of the information on the time-averaged state of the tropical atmosphere is still not properly documented. Some salient features of the zonal asymmetries of the tropics are presented here.

### **2.2 Tropospheric Winds at 850 and 200 mb Levels**

One of the best sources of reference for time averaged low level flows over the tropics are the reanalysis data sets provided by NCEP and ECMWF. These can provide the mean flow field at 200 and 850 mb levels as shown in Figs. 2.1 and 2.2.

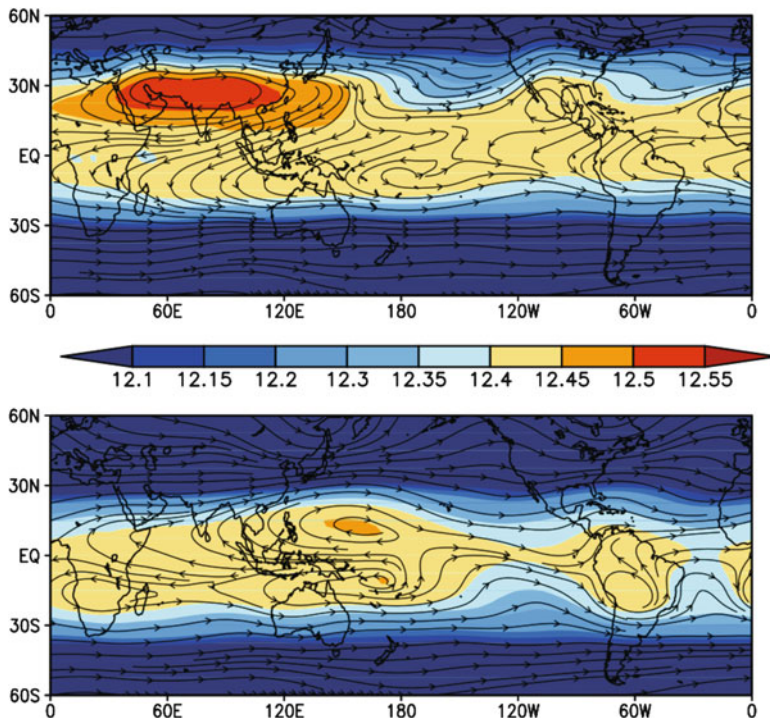


**Fig. 2.1** The climatological 200 mb circulation superposed over the corresponding geopotential heights (in km) for boreal summer season (JJA, *top*) and boreal winter season (DJF, *bottom*) (From the NCEP-NCAR reanalysis)

It is clear from these charts that the tropical flows are quite asymmetric in the zonal and meridional directions. The principal asymmetric features at the 200 mb (Fig. 2.1) are:

- (i) The Tibetan anticyclone in JJA;
- (ii) The strong tropical easterlies emanating from the Tibetan high in JJA;
- (iii) The Mexican high in JJA over Central America;
- (iv) The pronounced mid-oceanic troughs in the summer hemispheres of the Pacific and Atlantic Oceans;
- (v) The West Pacific high in DJF;
- (vi) The Bolivian high over continental South America in DJF.

Similarly, the principal asymmetric features at the 850 mb (Fig. 2.2) are

- (a) The subtropical highs over the oceans;
- (b) The tropical convergence zones;
- (c) The cross-equatorial monsoon flows of both the summer and winter Asian monsoons;
- (d) The heat lows over the deserts;
- (e) The Somali Jet along east Africa.

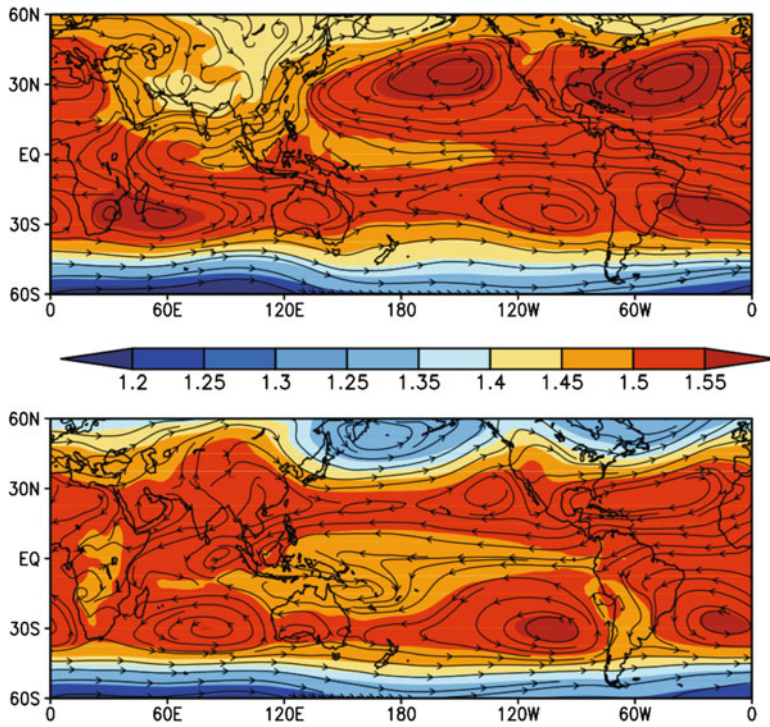


**Fig. 2.2** The climatological 850 mb circulation superposed over the corresponding geopotential heights (in km) for boreal summer season (JJA, *top*) and boreal winter season (DJF, *bottom*) (From the NCEP-NCAR reanalysis)

In Fig. 2.2 the reversal of winds in the lower troposphere from southwesterly to northeasterly between summer and winter monsoonal flows is apparent. The upper troposphere carries a monsoonal upper anticyclone complex that proceeds north from the general region of southern Indonesia and northeastern Australia (in January) to the eastern foothills of the Himalayas (by June). By its nature this anticyclone is a thermal high. Below this traversing high resides the low-level monsoon convection and associated heavy rain. The monsoon rain along the upper anticyclone path can be as large as 200 in. per month. The tropospheric averaged temperatures over this region are warmer than the surroundings due to the large latent heat release of the precipitating systems. The northward propagating anticyclone of the upper troposphere temporarily loses its identity as it approaches and traverses across the equatorial latitudes. At these very low latitudes the monsoon convection cannot sustain an upper level high because of the very low value of the Coriolis force. As a result, what we see at these latitudes is a radial outflow above the rain areas.

The 200 mb monthly mean climatology exhibits one other notable feature, namely, the largest clockwise flow system of the global northern winter climatology. This is the West Pacific high that is located south of Japan. The axis of this high

is oriented from west-northwest towards east-southeast. The lower extremity of this axis extends into the southern hemisphere over the eastern Pacific. This climatological clockwise flow entity spans almost the entire length of the Pacific Ocean. An interesting aspect of this high is that this clockwise flow carries an anticyclone (i.e., high pressure) over the western Pacific Ocean. The same axis, as it crosses the equator over the eastern Pacific Ocean, still carries clockwise flows, but here they are associated with low pressure. Although the winds do not change their polarity (they remain clockwise), the pressure does change polarity (between high and low) as it crosses the equator. This largest climatological system of the tropics deserves further studies. All of these features exhibit seasonal changes.

### 2.3 The Motion Field in the Upper Troposphere

The mean motion field at 200 mb has received far more attention in recent years because of the availability of high level cloud motion vectors and commercial aircraft wind reports.

Figures 2.3 and 2.4 illustrate two typical winter and summer maps respectively over the global tropical belt. The salient features of the winter season (Krishnamurti 1961; Sadler 1965) are summarized as follows. The subtropical westerly jet stream

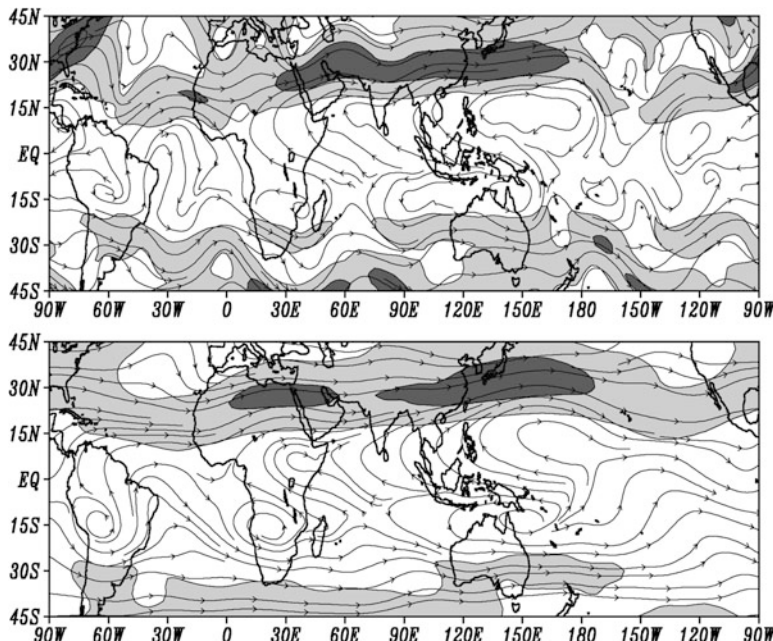


**Fig. 2.3** An example of northern winter 200 mb daily (top) and seasonal (bottom) streamlines and isotachs. The shading interval is  $25 \text{ m s}^{-1}$  (Computed from the NCEP-NCAR reanalysis)

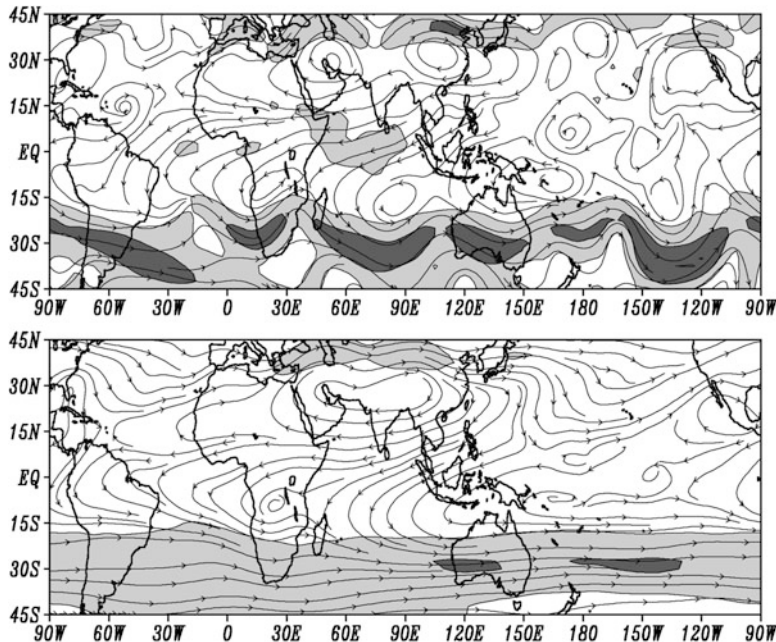


**Fig. 2.4** An example of northern summer 200 mb daily (*top*) and seasonal (*bottom*) streamlines and isotachs. The shading interval is  $25 \text{ m s}^{-1}$  (Computed from the NCEP-NCAR reanalysis)

exhibits a quasi-stationary three-wave pattern with maximum velocity off the southeastern United States, the Mediterranean Sea and the coast of Japan. The strongest winds are found in the latter region. The quasi-stationary geometry of the wind-speed field is an unexplained phenomenon. Although there is some evidence of its relation to intense convection over three continental regions of the equatorial tropics, i.e. the northwestern part of South America, central Africa and the Indonesia/Borneo area, these relationships have not been adequately explored.

The latitude of the subtropical jet streams during the northern winter is roughly 27°N (Krishnamurti 1961). During this period the flows over the southern tropical oceans, at 200 mb, exhibit mid-oceanic troughs in the motion field. These quasi-stationary troughs are found in the middle of the Atlantic and in the Indian and the Pacific Oceans (Krishnamurti et al. 1973). Their analogous counterparts are found over the northern tropical oceans during the northern summer, see Fig. 2.4.

The zonal asymmetry of the 200 mb flows during the northern summer has been discussed at some length in the literature (Krishnamurti 1971a, 1971b; Krishnamurti et al. 1973, 1974). The salient climatological features of these flows are: The Tibetan and West African high pressure areas, the mid-Pacific trough, the mid-Atlantic trough, the tropical easterly jet over Asia and equatorial Africa, and the Mexican high. The zonal expanse of the Tibetan High Complex is noteworthy. In the mean it extends for roughly 30W to 150E longitudes. The transients often occupy a larger size.

These large amplitude features of the time-averaged motion field carry about 50 % of the total variance of the total horizontal motion field. Thus one would see most of the above-mentioned features on daily upper-level maps during the northern summer (Krishnamurti et al. 1970, 1975). As stated earlier, it is important to appreciate and obtain a good understanding of the time-averaged large scale zonal asymmetry of the flows.

## 2.4 The Temperature Field

The most conspicuous aspect of the thermal field is the zonal asymmetry evidently related to the land-ocean distributions. Over the summer hemisphere the air over the land areas is generally warmer than that over the oceanic tropics, the converse being the case over the winter hemisphere. The most pronounced zonal asymmetry is found near the Earth's surface and near the 300 mb surface.

In the boreal summer season, the continental Asian monsoon releases a tremendous amount of latent heating from deep convection over a large fraction of the area. There is also associated subsidence warming in the adjacent Arabian and West African deserts (Rodwell and Hoskins 2001). Figure 2.5 illustrates the point of this zonal asymmetry from the climatological temperature distribution at 300 mb for boreal summer and winter seasons. The former is related to the sensible heat flux from the land areas and the latter to deep convective and subsidence warming.

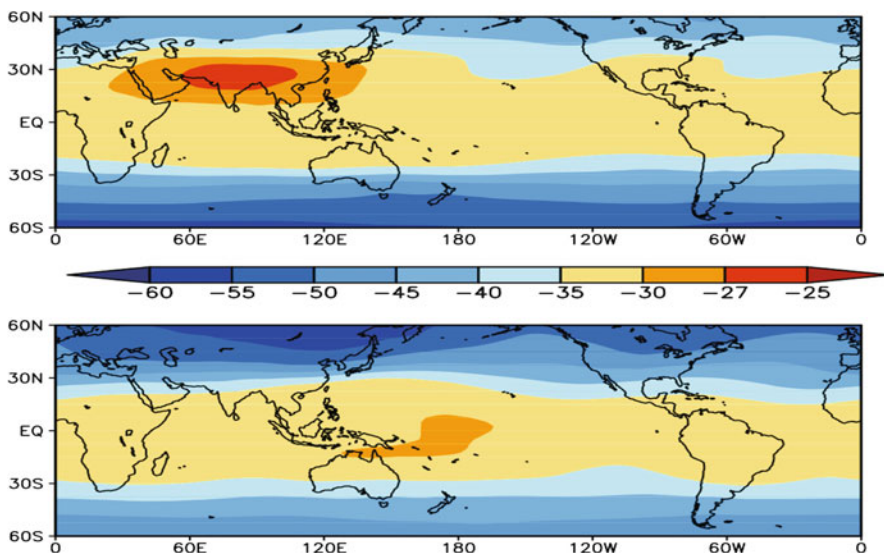


**Fig. 2.5** Climatological mean temperature at 300 mb for northern hemisphere summer (JJA, top) and northern hemisphere winter (DJF, bottom) (From NCEP-NCAR reanalysis. Units of °C)

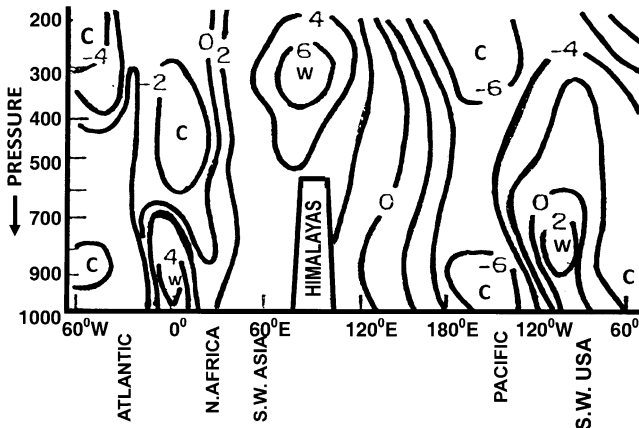


**Fig. 2.6** The vertical structure of the temperature anomaly field in boreal summer season at 32°N (After Flohn 1968)

The most pronounced zonal asymmetry occurs during the northern summer (Fig. 2.5, top). In addition to the latent heat release from deep convection, sensible heat from the elevated heat source of the Tibetan plateau is also contributing to this zonal contrast. The highest temperatures are found over the Tibetan Plateau. The mid-oceanic troughs are comparatively cold (Fig. 2.5 top). During the northern winter, the 300 mb zonal temperature gradient is relatively weaker (Fig. 2.5 bottom).

The absence in the southern hemisphere of a vast region of high altitude land mass like the Tibetan plateau, and the relatively smaller spatial extent and consequent reduced release of deep convective heating from the northern Australian and the maritime monsoons are some of the contributing factors for a weaker zonal asymmetry at 300 mb in the boreal winter. During this period the middle oceanic troughs (Fig. 2.5, bottom) over the southern oceans are colder and the anticyclonic circulations near the land areas of the southern hemisphere are relatively warm.

An interesting illustration of the zonal asymmetry of the thermal field comes from Flohn (1968). Figure 2.6 shows a vertical structure of the temperature anomaly field at 32°N where the zonal average is removed from the temperature distribution at each pressure level. The high temperature region over the Tibetan Plateau and relatively colder regions over the oceanic tropics are clearly evident. These time-averaged zonal asymmetries should be viewed along with the geometry of the divergent east–west circulation (presented in the next section) since they have important dynamical implications.

In contrast to the upper air temperatures, the surface air temperatures show a much larger zonal asymmetry between land and ocean in the boreal winter than in boreal summer (Fig. 2.7). This is because of the pronounced radiative heat loss from land and higher heat capacity of the oceans that result in smaller seasonal changes of the ocean temperatures. During the boreal summer season the Asian monsoon rains cool the land-surface thereby reducing the zonal temperature contrast between ocean and land.

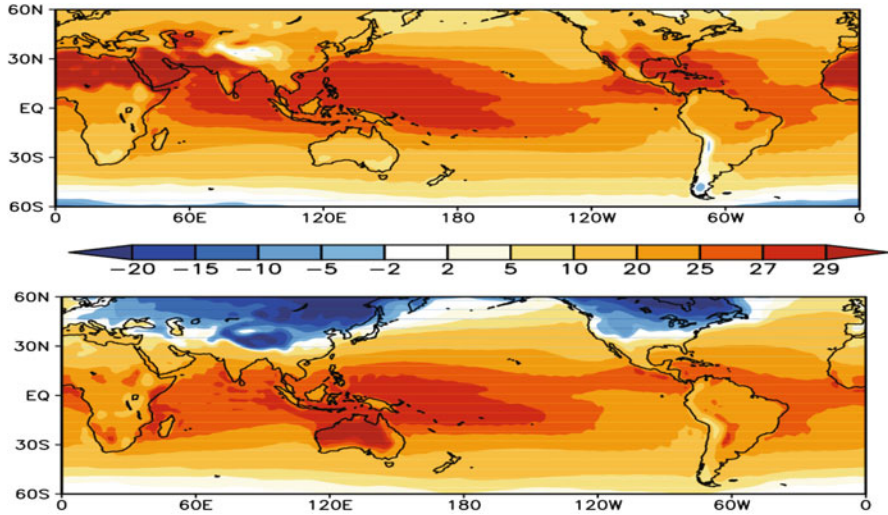


**Fig. 2.7** The climatological mean surface air temperature for northern hemisphere summer (JJA, top) and northern hemisphere winter (DJF, bottom) (From NCEP-NCAR reanalysis)

## 2.5 The East/West Circulations in the Tropics

The time-averaged east/west circulations are essentially divergent motions and are quite analogous to the Hadley type vertical overturnings described in Chap. 1. Here we decompose a horizontal velocity vector  $\mathbf{V}$  into a rotational part,  $\mathbf{V}_\psi$ , and a divergent part,  $\mathbf{V}_\chi$ , i.e.,

$$\mathbf{V} = \mathbf{V}_\psi + \mathbf{V}_\chi. \quad (2.1)$$

A time mean velocity potential  $\bar{\chi}$  is defined by

$$\bar{\mathbf{V}}_\chi = \nabla \bar{\chi} \quad (2.2)$$

We define the intensity of the Hadley and east/west circulations by the respective relations:

$$I_H = \frac{1}{2\pi} \int_0^{2\pi} \frac{\partial \bar{\chi}}{\partial \varphi} d\lambda \quad (2.3)$$

$$I_E = \frac{1}{\varphi_2 - \varphi_1} \int_{\varphi_1}^{\varphi_2} \frac{\partial \bar{\chi}}{\partial \lambda} d\varphi, \quad (2.4)$$

where  $\varphi_1$  and  $\varphi_2$  are the southern and northern limits of a tropical channel of interest. Note that  $I_H$  varies along  $\varphi$  (latitude), while  $I_E$  varies along  $\lambda$  (longitude). A proper geometrical depiction of the Hadley cell can be presented on a meridional vertical plane while that for the east/west circulation would be a zonal plane. The velocity potential for a seasonal mean is obtained as a solution of the equation

$$\nabla^2 \bar{\chi} = \nabla \cdot \bar{\mathbf{V}}, \quad (2.5)$$

where  $\bar{\mathbf{V}}$  is a seasonal mean horizontal velocity vector and is assumed to be known. In this discussion there are no east/west boundaries as the latitude band of interest encompasses the globe, and  $\bar{\chi}$  is set to zero at the north and south boundaries.

It is important to recognize that most of the variance (about 80 %) of the motion field in the tropics is described by the rotational part (Krishnamurti 1971a). However all circulations in the vertical planes, such as the Hadley and east/west type circulations, are divergent circulations and are not explicitly described by the rotational part of the wind. These divergent circulations are extremely important for the understanding of the time-averaged motion field of the tropics.

The geometry of the climatological velocity potential  $\bar{\chi}$  and the corresponding divergent motion field is illustrated in Fig. 2.8 for the boreal summer and winter seasons. The velocity potential isolopleths are shaded in blue for the outflow center and in red for the inflow center. Arrows indicate the divergent winds. It is quite clear from Fig. 2.8 that the divergent circulations are present in the zonal as well as the meridional planes. The major center of the east/west circulations during the northern summer season (Fig. 2.8 top) is found on the northern part of the Bay of Bengal, southeast Asia and south China Sea. During the northern winter season, this center of upper level outflow shifts towards Indonesia-Borneo. The streamlines of the divergent part of the flows converge to the mid-oceanic troughs in the summer and winter seasons. During the northern summer the other region of divergent outflow is the Pacific coast of southern Mexico. In the northern winter season, besides the region over Indonesia, the northwestern part of South America, and central Africa also exhibit upper level outflow. These three regions of high-level divergent outflow coincide roughly with the three intense rainfall belts of the northern winter. This geometry may have some important bearing on the wave number three in the quasi-stationary subtropical jet stream of winter discussed earlier.

## 2.6 The Moisture Field

This is by far the most important scalar field in the tropics. The distribution of the moisture, although to a large extent dynamically controlled, still determines the evolution of many smaller scale disturbances. The presence of desert and oceanic areas makes this field zonally asymmetric. The climatology of the moisture field is very important for the general circulation of the atmosphere. Scientists have asked

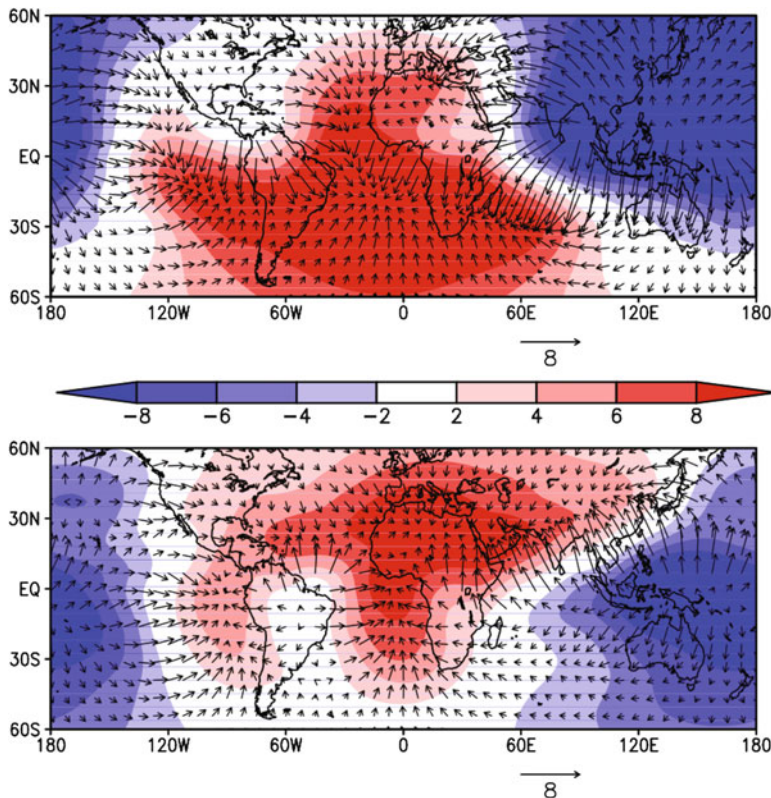


**Fig. 2.8** The climatological mean 200 hPa velocity potential ( $10^6 \text{ m}^2 \text{s}^{-1}$ ) and divergent wind ( $\text{ms}^{-1}$ ) for JJA (top) and DJF (bottom) (From the NCEP-NCAR reanalysis). The sample vector represents a divergent wind with magnitude of  $8 \text{ ms}^{-1}$

how important the definition of the detailed moisture field is. Some feel that a simple zonally symmetric geometry of the moisture field would adjust to a reasonable geometry in a matter of a few days of numerical integration in global general circulation models. This was, in fact, demonstrated by Mintz in some early runs with a two-level general circulation model. It seems from these studies that the spatial distribution of the time-averaged planetary scale moisture distribution can be explained from simple formulations of sources and sinks and a reasonable simulation of the advection. However, the assumption that the moisture variable is passive and its details somewhat dynamically redundant could be a disastrous one for studying the short-range evolution of tropical weather systems. It is felt that the climatology of the global moisture is an important topic and hence we present here, in Fig. 2.9, the moisture fields for July and January at 850 mb, i.e. the isopleths of specific humidity ( $\text{g kg}^{-1}$  units).

During the northern winter, three regions of large specific humidity ( $12 \text{ g kg}^{-1}$ ) – over the northwestern part of South America, equatorial Africa and over

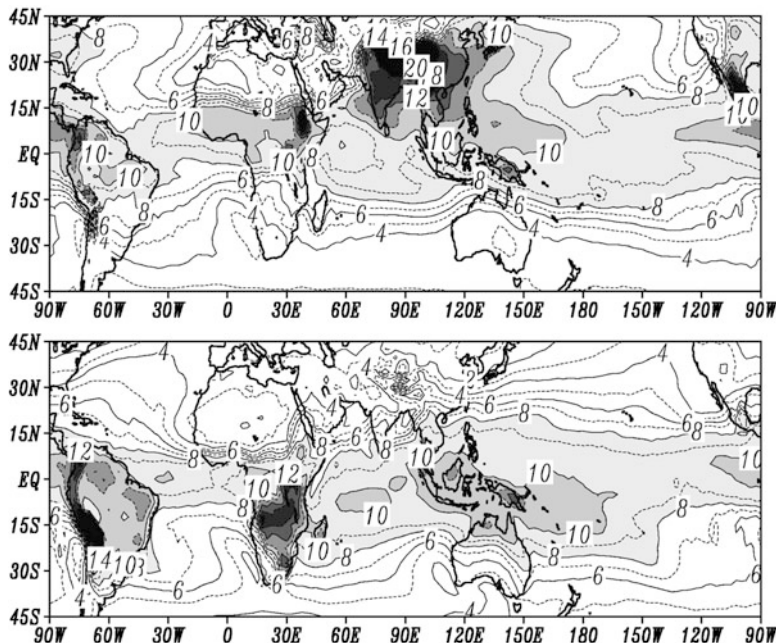


**Fig. 2.9** Mean July (top) and January (bottom) specific humidity. Units are  $\text{g kg}^{-1}$ , contour interval  $1 \text{ g kg}^{-1}$  (Computed from NCEP-NCAR reanalysis)

Indonesia – may be noted. These regions were earlier emphasized in the discussion of the northern winter east/west circulation and tropical rainfall belts. During the northern summer the regions of high moisture are found over the monsoon belts near the foothills of the Himalayas ( $14 \text{ g kg}^{-1}$ ) and over the equatorial eastern Pacific, again closely related to the location of the divergent outflows shown in Fig. 2.8. Large zonal asymmetries of the moisture field are found during the northern summer near  $20^\circ\text{N}$ . Because of the dynamical influences of the motion systems, the specific humidity distribution over the tropical oceans is not uniform. Gradients in the east/west and north/south directions over the oceans are primarily associated with weather systems with ascending and descending motions. The seasonal changes in the distribution of specific humidity are large. The largest values of specific humidity are found over the land areas and not over the oceanic tropics. This is related to larger temperatures of land areas that can hold large amounts of moisture prior to saturation, which makes the monsoon belts very moist.

## 2.7 The Sea Level Pressure Field

Here we shall present sea-level isobars for January and July (Fig. 2.10). The January features are dominated by the strong pressure gradient near  $100^\circ\text{W}$  over Asia, i.e. south of the Siberian surface anticyclone. The subtropical highs are better

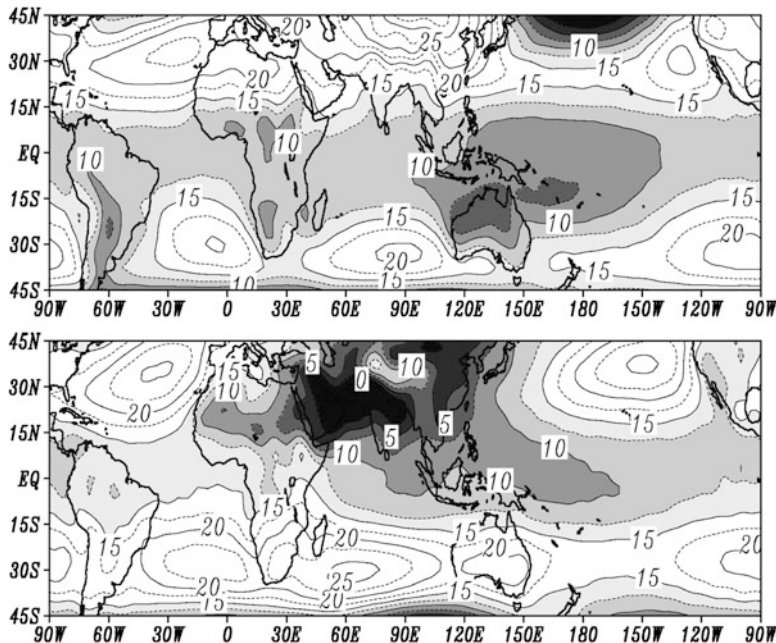


**Fig. 2.10** Mean January (top) and July (bottom) sea level pressure. Units are in mb, contour interval 2.5 mb (Computed from NCEP-NCAR reanalysis)

organized over the northern oceans during the northern summer and less so during the northern winter. The descending branch of the Hadley Cell is more intense near 30°N during northern winter compared to the northern summer (Fig. 2.10). The subtropical highs have intense descending motion towards the eastern part of the anticyclonic circulations. The descent is in part contributed by the east/west circulations of the northern summer (Figs. 2.8 and 2.10), which would account for the intensity of the subtropical high during the northern summer. The equatorial trough (low pressure belt near the Equator) is found as far as 20°N during the summer monsoon season over the Asiatic land mass. The tropical pressure field has frequently been described in the meteorological literature. It should, of course, be said that the various references show some differences in the distribution of pressure for the same month in different years. The zonal asymmetries of the pressure field are consistent with the asymmetries of the other time-averaged fields discussed in the previous sections.

## 2.8 Precipitation Field

Here we shall present the seasonal rainfall climatology for the Tropics (40°S–40°N). This is based on TRMM (Tropical Rainfall Measurement Mission), a NASA satellite program. The use of satellite data is necessary since large parts of

the tropics are covered by oceans where there are no rain gauge- or radar-based estimates of rainfall. The TRMM-based seasonal rainfall climatology is illustrated in Fig. 2.11a-d (Zipser et al. 2006). Here the units are inches per season. This estimate of precipitation comes from microwave radiometers that are carried by the TRMM satellite. The TRMM satellite carries microwave radiation-receiving channels that are located at the following frequencies: 10.65, 19.35, 37.0, 85.5 GHz dual polarization, 22.235 GHz vertical polarization.

For completion of such analyses, data from another suite of satellites, called the US Airforce DMSP (Defense Meteorology Satellite Program), is also added to the TRMM data base. These DMSP satellites carry microwave instruments (SSM-I, special sensor microwave instrument). There are normally four such DMSP satellites available at any one time. Thus TRMM together with DMSP provide coverage from a total of five satellites that measure microwave radiances at a number of frequencies. In order to translate the microwave radiances to rainfall rates, ground truth estimates of rainfall from rain gauge and radar are required. Such ground truth data are available in many land areas, and with a particularly high density in highly-populated places such as Japan, United States, Brazil and China. It is possible to use simple multiple regression techniques to relate these directly observed estimates of rain (from rain gauges and radar) to the brightness temperatures derived from microwave radiances measured at the different channels. Under assumptions of linear dependence between the brightness temperatures  $TB_i$  at the  $i$ th channel and the rainfall  $R$ , the regression

equation has the form  $R = a_0 + \sum_{i=1}^N a_i TB_i$ . If a more realistic non-linear relationship is assumed, the regression relationship is usually sought in the form  $R = \exp\left(a_0 + \sum_{i=1}^N a_i TB_i\right) - c$  (Berg et al. 1998). Here the left hand side denotes

the observed rain and the right hand side carries a number of terms each denoting a microwave channel. The multipliers  $a_i$  are the regression coefficients that are determined by a least square minimization technique. The reason this type of procedure works is that the microwave radiances which determine the corresponding brightness temperatures are emitted by the hydrometeors of the precipitating clouds. The cloud water, rain water, snow, ice and graupel all contribute to the radiances at different wavelengths. The regression procedure statistically infers the most likely rainfall rates corresponding to a given set of brightness temperatures. It must be also noted that a large sampling problem exists here. A cumulonimbus slowly passing over a rain gauge site may result in an inch of rain. A satellite, on the other hand, passes over that cloud in less than a second and cannot see all that the rain gauge does. However the premise is that over a season enough satellite passages may see a seasonal mean that may be close enough to what the rain gauge sees. Furthermore, the statistical regression is meant to push the satellite estimate of rain towards the observed estimates. Generally, the error in climatology over target areas is of the order of 15 %.

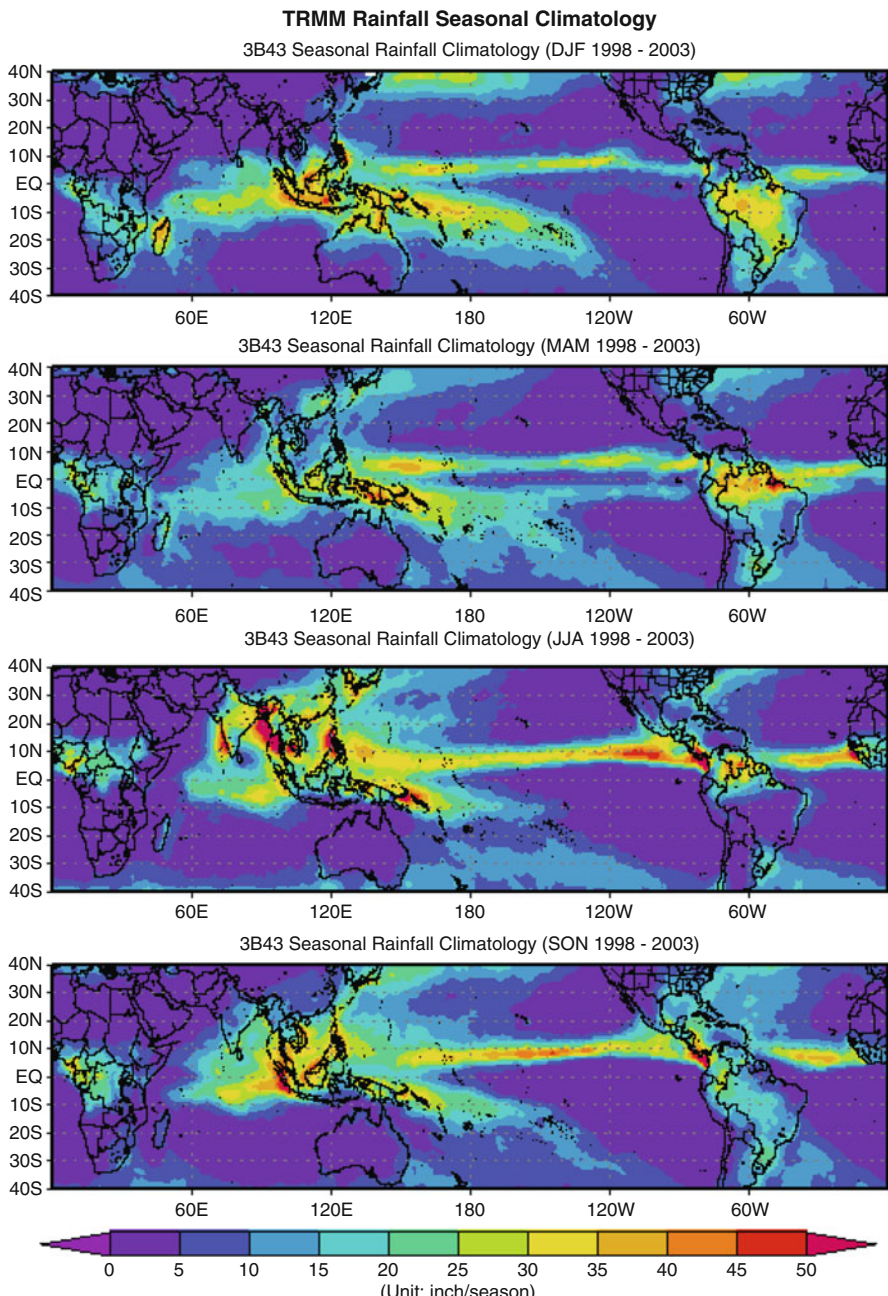


**Fig. 2.11** The seasonal rainfall climatology from Tropical Rainfall Measuring Mission (TRMM) (Obtained from NASA)

The salient features seen in Fig. 2.11a–d are the following:

- (i) The ITCZ over the Pacific Ocean is very well defined by a rainfall maximum. Those maximum rainfall amounts are on the order of 50 in./season.
- (ii) The ITCZ rainfall maximum stays north of the equator over the Pacific and Atlantic Ocean near  $5^{\circ}$ – $7^{\circ}$ N over all seasons.
- (iii) A double ITCZ in the Pacific Ocean during the spring season (March, April, and May) can be noted. This includes a second belt of weaker rains 10–15 in./season near  $5^{\circ}$ S latitude over the Pacific Ocean.
- (iv) The Pacific Ocean also carries a climatological rainfall feature called the South Pacific Convergence Zone (SPCZ). This feature starts at the Western Pacific near New Guinea and slants south-eastwards towards  $120^{\circ}$ W and  $40^{\circ}$ S. This feature is known to contain a considerable amounts of non convective rain whereas the ITCZ is known to contain much larger proportions of convective rain.
- (v) Over the Indian Ocean the northern winter season sees a rainfall maximum near  $5^{\circ}$ – $7^{\circ}$ S. The heaviest northern winter rains are over Northern Australia, Southern Indonesia, Borneo, and New Guinea. The maximum rainfall is of the order of 50–100 in./season. In general, satellite estimates do not resolve extreme rainfall very well. Rain gauge estimates of heavy seasonal rainfall during northern winter can be as large as 150 in./season. This implies a roughly 50 % underestimate of the rainfall climatology by satellite estimates.
- (vi) The most interesting feature of the tropical rainfall climatology is the annual march of heavy rains from Southern Indonesia in northern winter to the eastern foothills of the Himalayas in northern summer and a reverse traverse of this rainfall belt over the rest of the year. Along this line maximum monsoon rain of 100–300 in./season of rain progress north and south during most years. This axis of heavy rains is also called the Principal Axis of the Monsoon. This rainfall belt moves to Malaysia and Myanmar in the northern spring season towards the eastern foothills of the Himalayas by the months of July and August. The retreat brings fall season rains over Southern Malaysia and Northern Borneo. This cycle is completed by January.
- (vii) Other prominent features are the summer monsoon rains over large areas of India, Indochina, and China. Over China this belt of rain goes as far North as  $35^{\circ}$ N by August. There is a considerable interannual variability of seasonal rain. Those are best seen through monthly mean data sets over several years.
- (viii) The seasonal northward/southward march of rainfall is also a prominent feature over Africa. This migration from roughly  $10^{\circ}$ S in northern winter to roughly  $10^{\circ}$ N during northern summer can be clearly seen in this illustration.
- (ix) Other prominent features of the seasonal rainfall worth noting are the three main land area centers of rainfall over Borneo, Congo, and Brazil during the northern winter season.
- (x) Tropical rainfall exhibits large orographic maxima. Those are prominently seen over the Burmese Mountains in the northern spring season. Over the west coast of India during the northern summer season seasonal heavy rains are encountered along the Western Ghats.

- (xi) Winter season rains, especially during November and December, over south eastern India arise from the fetch of northeasterly monsoon surface winds accumulating moisture over the Bay of Bengal.
- (xii) Most tropical islands, such as Taiwan, Hawaii, Sri Lanka, Jamaica, Cuba, Madagascar, Borneo, Haiti-Dominican Republic and Puerto Rico exhibit seasonal rainfall maxima from an interaction of the tropical surface winds with local orography.

## 2.9 Other Parameters

The tropical climatologist should have a ready source of reference on the zonal asymmetries of several other observed and derived variables that cannot be easily presented in this kind of text. Among these, one of the most important fields is that of sea-surface temperature. One of the best sources of reference on this is a data set compiled by the Rand Corporation in Santa Monica, California (Alexander and Mobley 1974). This compilation contains a global ocean temperature distribution for a one degree latitude by one degree longitude mesh of grid points. Values of monthly averages for all 12 months are available. The following is a list of some other useful parameters:

- (i) Height of base and of the top of the trade wind inversion (Riehl 1945; Neiburger and Chien 1957)
- (ii) Monthly mean cloud amounts (Sadler 1970)
- (iii) Satellite digital cloud brightness charts (Taylor and Winston 1968)
- (iv) Orography, mountain heights (Gates 1973)
- (v) Albedo of the Earth's surface (Katayama 1967a)
- (vi) Tropical monthly rainfall (Wernstedt 1972)
- (vii) Monthly mean total solar radiation reaching the Earth's surface (Katayama 1966, 1967a, b)
- (viii) Net outgoing longwave radiation (Winston 1967)
- (ix) Monthly mean net solar radiation absorbed by the troposphere (Katayama 1966, 1967a, b)

There are, furthermore, charts of dynamical parameters such as energy, momentum, and moisture transports and fields of convergence of fluxes, etc. These again exhibit large zonal asymmetries in the tropical atmosphere. We shall refer to these in the discussions of transient motions of the atmosphere.

## References

Alexander, R.C., Mobley, R.L.: Monthly average sea surface temperature and ice pack limits on a 1 degree global grid. Rand Corporation Report, Santa Monica, pp. 1–30 (1974)

- Berg, W., Olson, W., Ferraro, R., Goodman, S.J., LaFontaine, F.J.: An assessment of the first- and second-generation navy operational precipitation retrieval algorithms. *J. Atmos. Sci.* **55**, 1558–1575 (1998)
- Flohn, H.: Contributions to a meteorology of the Tibetan Highlands. Rept. No. 130, Colorado State University, Fort Collins, 120pp (1968)
- Gates, W.L.: Analysis of the mean forcing fields simulated by the two-level, Mintz-Arakawa atmospheric model. *Mon. Weather Rev.* **101**, 412–425 (1973)
- Katayama, A.: On the radiation budget of the troposphere over the northern hemisphere (I). *J. Meteor. Soc. Jpn.* **44**, 381–401 (1966)
- Katayama, A.: On the radiation budget of the troposphere over the northern hemisphere (II). *J. Meteor. Soc. Jpn.* **45**, 1–25 (1967a)
- Katayama, A.: On the radiation budget of the troposphere over the northern hemisphere (III). *J. Meteor. Soc. Jpn.* **45**, 26–39 (1967b)
- Krishnamurti, T.N.: The subtropical jet stream of winter. *J. Meteor.* **18**, 172–191 (1961)
- Krishnamurti, T.N., et al.: 200 millibar wind field June, July, August 1967 by T.N. Krishnamurti, Edward B. Rodgers, Series: Report, Department of Meteorology, Florida State University, No. 70-2, 130 pp (1970)
- Krishnamurti, T.N.: Tropical east–west circulations during the northern summer. *J. Atmos. Sci.* **28**, 1342–1347 (1971a)
- Krishnamurti, T.N.: Observational study of the tropical upper tropospheric motion field during the northern hemisphere summer. *J. Appl. Meteor.* **10**, 1066–1096 (1971b)
- Krishnamurti, T.N., Kanamitsu, M., Koss, W.J., Lee, J.D.: Tropical east–west circulations during the northern winter. *J. Atmos. Sci.* **30**, 780–787 (1973)
- Krishnamurti, T.N.: Lectures on tropical meteorology in the dynamics of the tropical atmosphere. Published as colloquium notes. NCAR, Boulder, 105pp (1974)
- Krishnamurti, T.N., Astling, E., Kanamitsu, M.: 200mb wind field June, July, August 1972: Atlas published by Department of Meteorology, Florida State University, Tallahassee, Florida (1975). 116p
- Neiburger, M., Chien, D.: The inversion of the North Pacific Ocean Tech. Rept. No. 1, Dept. of Meteorology, University of California, Los Angeles, 74pp (1957)
- Rielh, H.: Tropical meteorology. McGraw-Hill Book company, New York, 392pp (1945)
- Rodwell, M.J., Hoskins, B.J.: Subtropical anticyclones and summer monsoon. *J. Climate* **14**, 3192–3211 (2001)
- Sadler, J.C.: The feasibility of global tropical analysis. *Bull. Amer. Meteor. Soc.* **46**, 118–130 (1965)
- Sadler, J.C.: Mean Cloudiness and gradient level wind chart over the tropics. Air weather services technical report 215, Vol. II, 60 pp (1970)
- Taylor, V.R., Winston, J.S.: Monthly and seasonal mean global charts of brightness from ESSA 3 and ESSA 5 digitized pictures, February 1967–1968. ESSA Technical report NESCR 46, National Environmental Satellite Center, Washington DC, 9pp, and 17 charts (1968)
- Wernstedt, F.L.: World Climatic Data. Climatic Data Press, Lemont (1972). 523pp
- Winston, J.S.: Planetary-scale characteristics of monthly mean long-wave radiation and albedo and some year-to-year variations. *Mon. Weather Rev.* **95**, 235–256 (1967)
- Zipser, E.J., Cecil, D.J., Liu, C., Nesbitt, S.W., Yorty, D.P.: Where are the most intense thunderstorms on earth? *Bull. Am. Meteor. Soc.* **87**, 1057–1071 (2006)

# Chapter 3

## The Intertropical Convergence Zone

### 3.1 Observational Aspects of the ITCZ

The Intertropical Convergence Zone, or ITCZ, is a belt of wind convergence and associated convection encircling the globe in the near-equatorial region. In a zonally averaged view, it is located at the equatorward edge – the rising branch – of the Hadley cell. The ITCZ is characterized by the low-level wind convergence, low sea level pressure, intense convection and associated cloudiness. The zonally averaged ITCZ is not stationary, but slowly migrates from south of the equator during the northern hemisphere winter to north of the equator during the northern hemisphere summer, following the Sun.

Figure 3.1 shows the seasonal climatology of the outgoing longwave radiation for winter (DJF), spring (MAM), summer (JJA) and fall (SON) over the global tropics. OLR is a satellite-derived measure of the Earth's long-wave radiation returned back to space. It is a function of the temperature of the radiating surface. Extremely high values (above  $280 \text{ W m}^{-2}$ ) are associated with clear skies and warm land surface, and are found over the tropical deserts. Low values of OLR (below  $220 \text{ W m}^{-2}$ ), on the other hand, are associated with either deep cumulus convection (high and cold cloud tops), such as over the equatorial landmasses and most of the equatorial oceans, or with cold land surfaces, such as the high-elevation Himalayas. Figure 3.2 shows the seasonal climatology of precipitation and 925 mb streamlines. Not surprisingly, the seasonal climatology of precipitation is well correlated with the seasonal climatology of OLR.

The precipitation maxima during the winter season (DJF) are mostly in the summer hemisphere. The largest amounts of precipitation are associated with the Asian winter monsoon. The rainfall is spread in a broad southwest to northeast oriented band over the Indian Ocean and a broad northeast to southwest oriented band in the western South Pacific. Over land, the precipitation maxima extend over the entire tropical South American continent and southern Equatorial Africa. In the northern hemisphere, there is a thin belt of precipitation spanning the entire breadth of the Pacific and Atlantic Oceans just north of the equator. During spring, the ITCZ

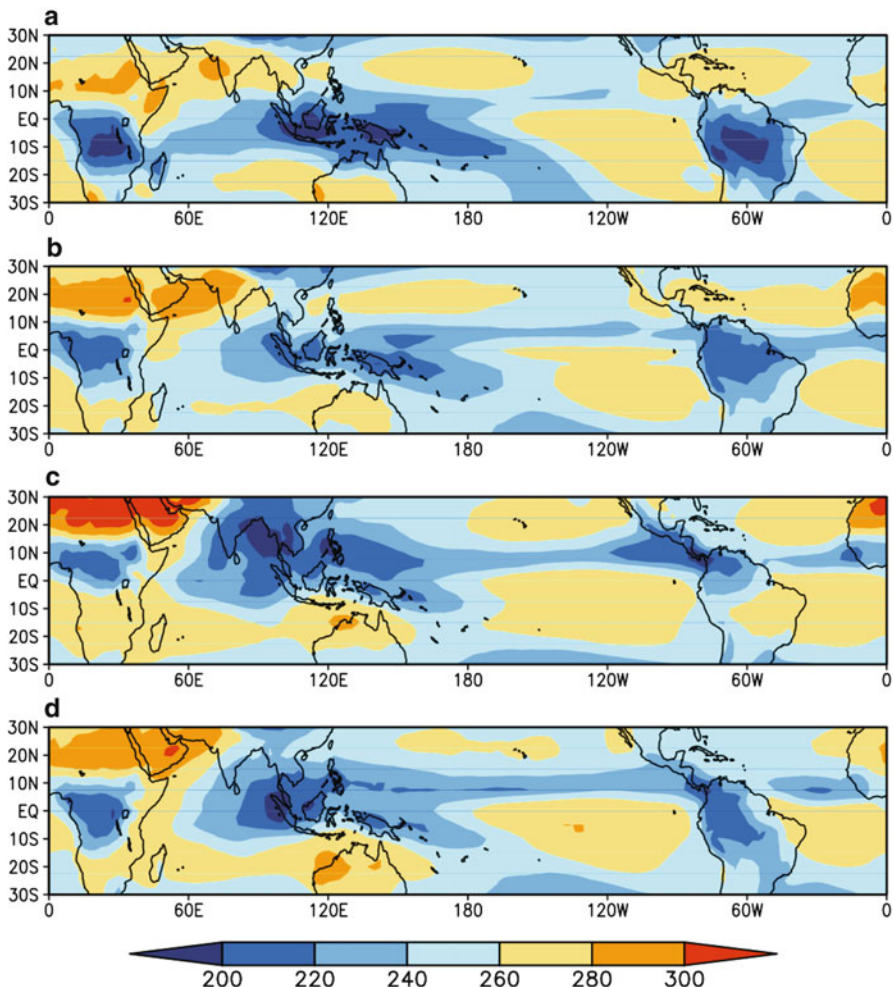


**Fig. 3.1** Tropical outgoing longwave radiation (OLR; Liebmann and Smith 1996) climatology for (a) winter (DJF), (b) spring (MAM), (c) summer (JJA), and (d) fall (SON) seasons. Units are  $\text{W m}^{-2}$

starts its northward migration. The Indian Ocean and the western South Pacific Ocean experience a reduction in precipitation. The thin bands of precipitation spanning the Pacific and the Atlantic Oceans strengthen and move further north. The precipitation over Equatorial Africa and South America shifts northward as well. This trend continues into the summer season. The summer Asian Monsoon now deposits large amounts of precipitation over southern Asia and the western equatorial Pacific. The precipitation bands spanning the Pacific and Atlantic Ocean are even stronger and further to the north of the equator, at about 7°N. In the fall, the ITCZ structure is quite similar to that of summer, but the beginning of a slow retreat to the south is evident.

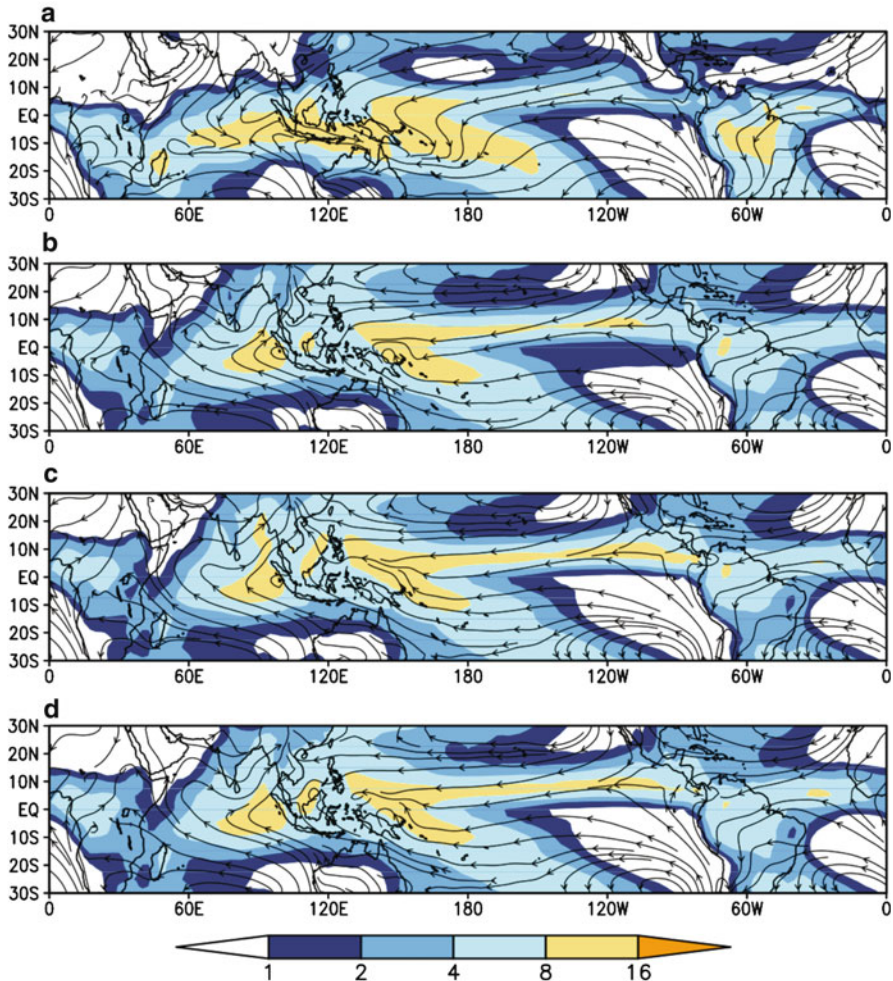


**Fig. 3.2** Tropical 925 mb streamlines (from NCEP-NCAR reanalysis) and precipitation climatology (Xie and Arkin 1996) for (a) winter (DJF), (b) spring (MAM), (c) summer (JJA), and (d) fall (SON) seasons. The units of precipitation are in mm day<sup>-1</sup>

Obviously, as illustrated by Figs. 3.1 through 3.3, a zonally averaged view is not fully adequate for the description of the ITCZ. Its position is affected by the landmass positions, the local circulation patterns and the ocean thermocline structure. In the eastern Pacific and the Atlantic the ITCZ lies north of the equator during all seasons, but over South America, Africa, the Indian Ocean and the western Pacific it undergoes significant displacements between summer and winter (see Figs. 3.1 and 3.2). Roughly speaking, the ITCZ remains north of the equator over the oceans east of the dateline, shifting by only a few degrees of latitude between summer and winter. West of the dateline, the shift between the summer and winter position of the ITCZ can be upwards of 40° of latitude.

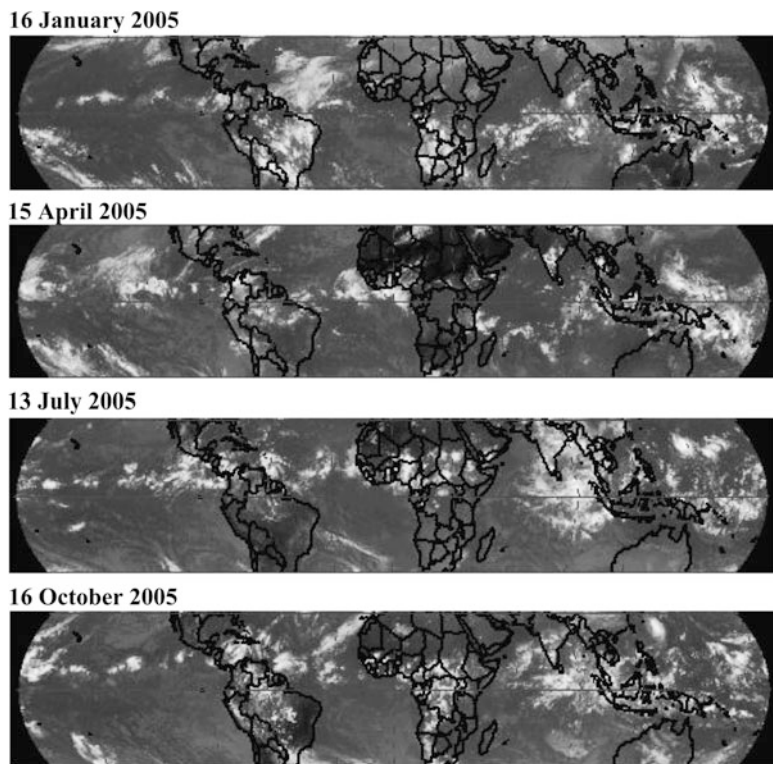


**Fig. 3.3** Daily examples of winter, spring, summer and fall composite infrared (IR) image obtained from US polar orbiting Satellite (AQUA) data set. The bands of *white* clouds near the equator illustrate the daily position of the ITCZ

The ITCZ also undergoes diurnal variation, with the maximum of convective activity occurring in the late morning and early afternoon, since this is the period of maximum solar heating and associated convection. There is also inter-diurnal variation due to changes in the large scale or local circulations, solar heating, tropical disturbances etc. Some daily examples of a winter, spring, summer and winter infrared images over the global tropics are shown in Fig. 3.3. The band of clouds encircling the earth in these images indicates the ITCZ location on a given day.

Additionally, the ITCZ location experiences interannual variations, such as those associated with the phase of El Niño or with the strength of the Asian Monsoon.

The horizontal convergence forming the ITCZ is the result of the meeting of the northeasterly trades in the northern hemisphere and the southeasterly trades of the southern hemisphere (see the low-level streamlines in Fig. 3.2). When there is only a very small cross-equatorial flow component, the ITCZ tends to be narrow, weak, and located close to the equator. When there is a cross-equatorial flow, the crossing

trades acquire a westerly component due to the change of the sign of the Coriolis force between the two hemispheres. The convergence is then between the easterly trades and the resulting near-equatorial westerlies. In such cases the ITCZ tends to be more spread out and located further away from the equator.

An interesting feature of the ITCZ is its avoidance of the geographical equator. Pike (1971) proposed the following explanation for this phenomenon. The warmest sea surface temperatures give rise to the strongest atmospheric convergence, rising motion, convection and, consequently, precipitation. The fact that the warmest sea surface temperatures are found away from the Equator is responsible for the asymmetric position of the ITCZ. Figure 3.4 shows the global tropical SSTs for the four seasons. The most striking feature of the SST distribution is the local temperature minimum at the Equator. For any season, the equatorial SSTs in the Pacific Ocean are cooler than the SSTs either to the south or the north of the equator. Numerical model integrations show that the cold equatorial SSTs develop spontaneously when a model is initialized with uniform SSTs between 10°S and 10°N as a result of upwelling and vertical mixing of the subsurface colder water. In such a model, the ITCZ is initially over the equator, but as the equator cools, the precipitation band moves away from the equator.

## 3.2 ITCZ Theory

The Conditional Instability of the Second Kind (CISK; Charney et al. 1971) was the earliest theory of ITCZ. According to this theory, boundary layer frictional convergence leads to the growth of the tropical disturbance through increased moisture convergence. The growth of this disturbance in turn promotes further strengthening of the boundary layer convergence leading to a positive feedback. From this theory, the latitudinal location of the ITCZ is determined by the balance of two forces: the rotation of the Earth and the abundance of moisture in the boundary layer. The former, in this case the Earth's rotation leads to converging boundary layer winds to move in a spiraling path owing to Coriolis force. This in turn causes higher winds from the presence of tangential winds (shown in Fig. 3.5). In the absence of the Earth's rotation, the converging winds would be weaker radial winds as illustrated in Fig. 3.5.

Therefore, the presence of the Coriolis force in the CISK would favor ITCZ over the poles. But abundance of moisture in the boundary layer at the equatorial latitudes will favor the ITCZ at the equator. The balance of these contrasting forces would then determine the latitudinal location of the ITCZ.

An alternative paradigm for the ITCZ was sought after finding from aqua planet model integrations (where all land points are replaced with ocean) and in the absence of equator-to-pole gradient of radiative-convective equilibrium temperature that the ITCZ was still located near the equatorial latitudes (Pike 1971; Sumi 1992; Kirtman and Schneider 2000). This model result was in conflict with the CISK theory. As the moisture in the boundary layer was nearly uniform in the aqua

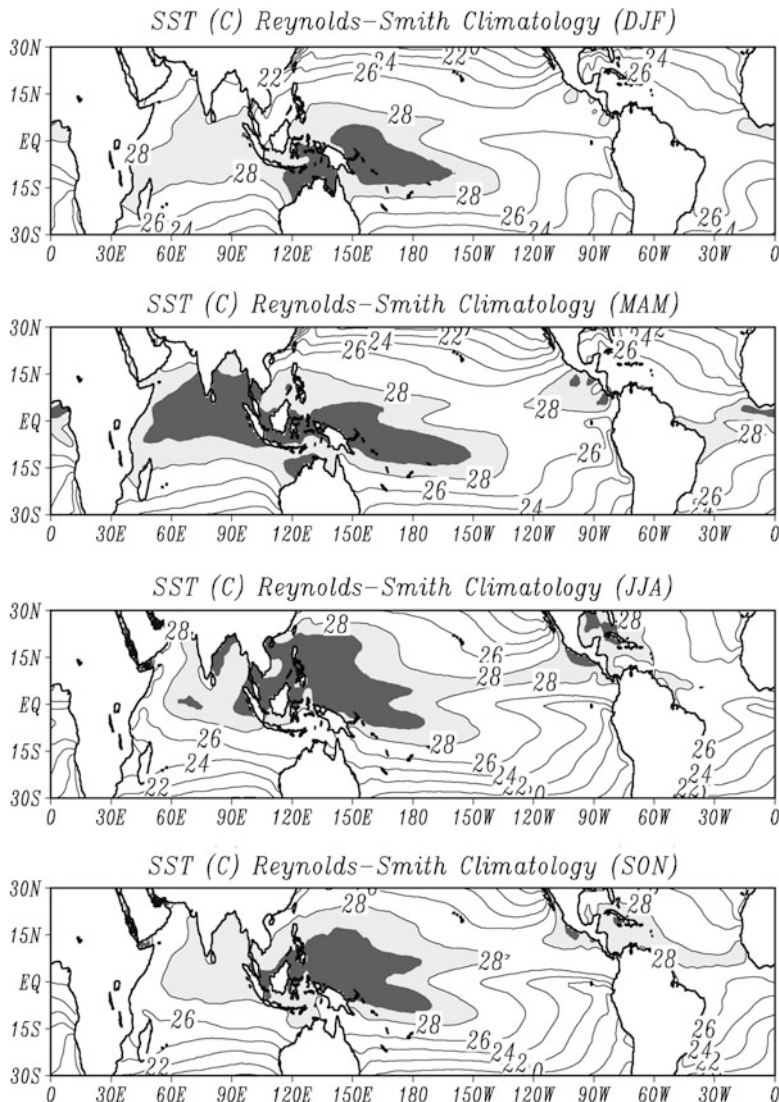
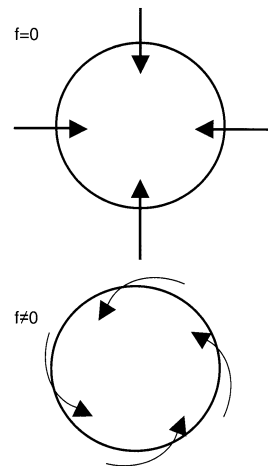


**Fig. 3.4** Tropical sea surface temperatures (SST) climatology for winter (DJF), spring (MAM), summer (JJA) and fall (SON) seasons. Units of °C. Values above 28°C are light shaded, values above 29°C are dark shaded (Computed from NCEP-NCAR reanalysis)

planet integration, it was intriguing that the ITCZ continued to remain in the equatorial latitudes, when the CISK theory would have predicted it to be located over the poles.

Despite these early aqua planet integrations, the significance of these results has been recently realized (Chao and Chen 2004; Chao and Chen 2001). In an aqua planet integration with spatially and temporally uniform SST and solar angle, Chao

**Fig. 3.5** A schematic rendition of the effect of rotation on boundary layer flow for  $f = 0$  (top) and  $f \neq 0$  (bottom) (After Chao and Chen 2004)



and Chen (2004) show that the latitudinal location of the ITCZ is the latitude where a balance is reached between two types of forces, both resulting from the Earth's rotation. The first force is related to the effect of the earth's rotation being equivalent to vertical stratification. This is explained in the following manner. If we combine the divergence equation given below, and ignoring the terms on the right hand side that don't have the Coriolis parameter, we have

$$\frac{\partial D}{\partial t} \approx f\zeta. \quad (3.1)$$

where,  $D$  is divergence,  $\zeta$  is vorticity, with the vorticity equation shown below

$$\frac{\partial \zeta}{\partial t} = -fD. \quad (3.2)$$

under an  $f$ -plane assumption, it gives

$$\frac{\partial^2 D}{\partial t^2} \approx -f^2 D. \quad (3.3)$$

This equation, excluding other terms on the right-hand side of the equation (that do not contain  $f$ ) represents the governing equation of a simple spring. Therefore, just as a spring resists compression and divergence, Chao and Chen (2004) gather that the Coriolis parameter resists convergence or divergence, which is what vertical stratification implies. Thus if the “spring” force of the Coriolis effect were acting alone, the equator (where  $f = 0$ ) would be the preferred location of the ITCZ as there would be no resistance to convergence or divergence.

The other effect of rotation is its influence on converging boundary layer winds that take a spiraling path, producing stronger tangential wind. These higher wind

speeds increase evaporation, which further fuels the convection. Thus if this force were acting alone, the poles would be the preferred location of the ITCZ. This latter effect of rotation is found to depend on the choice of the physical parameterization schemes of radiation, boundary layer and radiation.

Chao and Chen (2004) conducted a series of aqua planet integrations with the Goddard Earth Observing System Atmospheric General Circulation Model (GEOS-version 2; Takacs et al. 1994). They specified a uniform SST of 29°C. The resolution of the model was 4°(latitude)  $\times$  5°(longitude) grid model with 21 vertical levels. It uses the Relaxed Arakawa Schubert (RAS) scheme (Moorthi and Suarez 1992).

Like Sumi (1992), Chao and Chen (2004) also showed the formation of a single ITCZ in the equatorial latitudes in their aqua planet integration. These aqua planet experiments suggest that the inertial stability effect of the earth's rotation is a dominating factor. Furthermore, it was found that this ITCZ was more prominent when interactions between convection and surface fluxes were allowed in comparison to the experiment where surface fluxes were prescribed. The interaction between convection and surface fluxes was seen as a recipe to generate more vigorous convection. However, when radiation interaction is allowed without interaction of clouds (in lieu of prescribing globally uniform radiative cooling vertical profile) in these aqua planet integrations, the ITCZ moves off the equator ( $\sim 7^{\circ}\text{N}$ ). In this case the radiative cooling outside of the ITCZ responds to a low-level humidity gradient, with greater cooling outside of the ITCZ than the inside. This gradient in radiative cooling then warrants stronger downward vertical motion causing adiabatic warming to compensate for the stronger cooling outside of the ITCZ. The Hadley cell consequently becomes stronger raising the surface winds with resulting increase in surface evaporation. The second effect of rotation becomes stronger, moving the ITCZ away from the equator. Chao and Chen (2004) dwell further on the sensitivity of the ITCZ location to the choice of the convection parameterization scheme for which the readers can refer to their paper.

In the tropical eastern Pacific and the eastern Atlantic Ocean the ITCZ largely remains north of the equator. Over the tropical Indian Ocean however, the ITCZ migrates to the summer hemisphere. In a seminal work Philander et al. (1996) conducted idealized modeling studies to show that these features of ITCZ are a result of the global distribution of the continents and the land-sea geometry (or orientation). It is rather intriguing that despite the time averaged solar insolation being largest at the equator, the ITCZ with the warmest surface waters and heaviest rainfall are several hundreds of kilometers off the equator, especially in the eastern Atlantic and Pacific Oceans.

Philander et al. (1996) observed that in areas where the oceanic ITCZ is north of the equator, the meridional component of the equatorial Ocean's surface winds is southwesterly. This causes upwelling and shoaling of the thermocline at and south of the equator, while causing downwelling and deepening of the thermocline north of the equator. A shallow thermocline (a few tens of meters deep from the surface) in the eastern equatorial Pacific and Atlantic Oceans provides an ideal setting for robust air-sea interaction manifesting as a positive feedback between the SST and the surface winds, sustaining the cold equatorial tongue over the eastern Atlantic and Pacific Oceans.

The spatial variations in the depth of the thermocline result from the prevailing wind systems over the Oceans. The near absence of the easterly winds in the equatorial Indian Ocean that prevail in the other equatorial Oceans can be explained by the strong influence of the cross-equatorial winds of the continental Asian monsoons. In the Pacific and in the Atlantic Oceans the prevailing easterly trade winds drive the warm surface waters westwards, causing a zonal tilt of the thermocline. Therefore from the above argument one can appreciate the role of the continents, especially over the Indian Ocean in explaining the asymmetries over the equatorial Oceans. The inadequacy of the aqua planet integrations, especially in explaining the ITCZ location over the equatorial Indian Ocean where the prevailing winds appear erroneously easterly is quite apparent.

In idealized modeling studies, Philander et al. (1996) used an AGCM forced with symmetrical SST's about the equator to understand how the continental geometries can affect the surface winds. In these experiments, it was quite apparent that the West African bulge was critical for the asymmetries of the ITCZ in the Atlantic Ocean. The land north of 50°N over West Africa attains such high temperatures, that the land-sea type breeze of the West-African monsoon develops. These south-easterly cross-equatorial winds of the West-African monsoon promote coastal upwelling along southwestern Africa, which further accentuates the north-south temperature gradient and wind asymmetries through coupled feedbacks.

On the other hand, the effects of the coastal geometry of the North and South American continents are subtler. Philander et al. (1996) indicate that it is the inclination of the western coast of the Americas with respect to the meridians that generates the ITCZ asymmetries in the Pacific Ocean. Although the western coastal geometry of the Americas has an insignificant effect on the surface winds, it has critical implications for the ocean currents. Because of the particular coastal geometry the trade winds are perpendicular to the shore north of the equator, and parallel to the shore south of the equator. This induces along-shore ocean currents that are stronger south of the equator, causing stronger upwelling and sustaining north-south asymmetries in SST. Philander et al. (1996) claim that the presence of stratus clouds in the southeast Pacific is a secondary mechanism that further accentuates this asymmetry. The cold SSTs off the west coast of South America increase the static stability of the atmosphere, thereby promoting the formation of stratus clouds. The stratus clouds in turn reduce the downwelling shortwave flux thus cooling the SST further.

### 3.3 Regulation of the Warm Pool SST

In Fig. 3.4 besides the appearance of the cold equatorial tongue in the Pacific Ocean, the warm pool of SST in the equatorial western Pacific Ocean is also apparent. These warm pools are characterized by SST's of over 28°C. It has been observed however that the tropical SST is rather homogenous. This is depicted by the frequency distribution of the SST over global tropics in Fig. 3.6 (Clement et al. 2005).

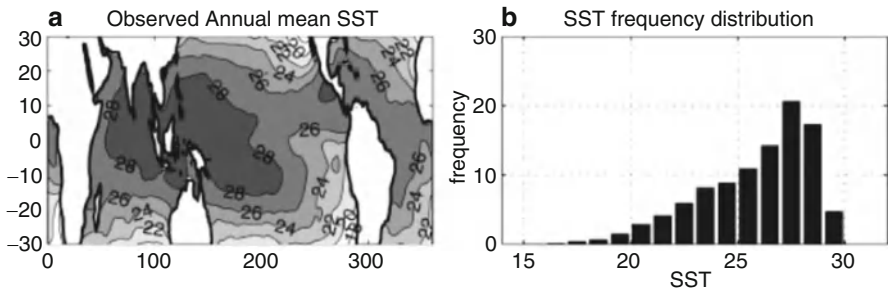


**Fig. 3.6** (a) Annual mean SST ( $^{\circ}\text{C}$ ). (b) Frequency distribution for the SST shown in (a) as a percent area (From Clement et al. 2005)

The distribution in Fig. 3.6 shows a negative skewness with over 50 % of the global tropical oceans having SST's in the range of  $28^{\circ} \pm 1^{\circ}\text{C}$ . Furthermore the peak frequency of the SST in Fig. 3.6 is at  $2^{\circ}\text{C}$  below the maximum SST at  $28^{\circ}\text{C}$ . These features of the tropical SST are persistent throughout the year (Sobel et al. 2002). In a series of idealized modeling studies Clement et al. (2005) show that the maintenance of the warm pool and the observed tropical SST distribution occurs from a combination of ocean dynamics, cloud feedbacks, and non-local atmospheric processes.

The SST distribution from a one-dimensional radiative convective equilibrium model that also neglects atmospheric and oceanic transports in addition to cloud feedbacks shows a very skewed SST distribution with the peak frequency occurring at the maximum SST contrary to observations. In fact it is found that the latitudinal structure of SST is similar to that of the downwelling shortwave flux with similar skewness, suggesting that local radiative-convective processes do as much in homogenizing the SST as the solar radiation.

The atmospheric circulation, through its impact on heat transport, clouds, water vapor and surface wind can have both a homogenizing and a heterogenizing influence on the SSTs: The heat transport preferentially removes heat from the warmest regions through the Hadley cell thus attempting to homogenize the SST. The drying over the subtropics from the subsidence of the Hadley cell, on the other hand, tends to heterogenize the SST from the reduced greenhouse trapping effects, which effectively cools the SST. Likewise the surface wind gradients, which are stronger in the subtropics than in the equatorial region, also tend to heterogenize the SST. The higher wind speeds in the subtropics bring the thermodynamic state of the atmosphere closer to the ocean making it more moist and warm. Consequently the subtropical SST cools in an equilibrium response to warmer and moist atmosphere that radiatively cools.

Through idealized ocean modeling experiments, Clement et al. (2005) explain the role of ocean dynamics in SST distribution. It is shown that for reasonable depth

of the equatorial thermocline and its zonal tilt from the imposed easterly wind stress, the resulting SST distribution is nearly uniform. This result is explained by the role of the Sverdrup dynamics, which upwells cold water and influences the SST in forming the cold equatorial tongue in the eastern Pacific. While Ekman dynamics moves the water poleward, homogenizing the SST at all longitudes. It may be mentioned that the Sverdrup dynamics has an influence on tropical SST where the thermocline is shallow. Otherwise it upwells warm water. It is for this reason Clement et al. (2005) suggest that Sverdrup circulations play a critical role in the geographical distribution of the warm pool. For example, in the tropical Indian Ocean where the thermocline is deep at all longitudes the region of homogenized SST extends through the basin. Conversely, in the Atlantic, where the thermocline is shallower, the warm pool is mainly observed in the western and off-equatorial regions of the basin.

Historically, clouds have been portrayed to be the most significant factor in regulating tropical SSTs. Ramanathan and Collins (1991) proposed the “cloud thermostat” theory, which points to the presence of highly reflective high level cirrus anvil clouds associated with deep convection overlying the warmest SSTs in the western Pacific Ocean, that reduce the incident solar radiation. They suggested that this negative feedback of high clouds act as a limiting factor on the western tropical Pacific Ocean warm pool SST and prevent it from exceeding a threshold value of around 32°C. Subsequent studies have however refuted the cloud thermostat theory to suggest the non-local influences of atmospheric circulation and spatial gradients of SST being important limiting factors for the warm pool SST (Wallace 1992; Hartmann and Michelsen 1993; Lau et al. 1994; Waliser 1996). Waliser (1996) illustrate this conflict in the following manner: Suppose a warm large-scale temperature anomaly is inserted in ocean surface mixed layer. The system will initially respond through enhanced surface latent and sensible heat fluxes. As a consequence of the enhanced fluxes low level atmospheric convergence over the region of the positive SST anomaly is initiated (Lindzen and Nigam 1987). This atmospheric convergence over the warm SST anomaly then gives rise to: (1) in-situ strong upward motion and compensatory sinking motion elsewhere, (2) reduction of surface wind speed, and (3) transport of low-level moisture. In the process, 1 and 3 enhances the short-wave cloud forcing while 2 and 3 reduces evaporation from the ocean surface. In essence, local shortwave cloud forcing is enhanced compared to the negative evaporation feedback over the region of the warm SST anomaly. But to arrive at this conclusion it was necessary to consider changes in the atmospheric circulation that occur over a much longer length scale compared to the initial SST anomaly that was introduced. This argument forms much of the basis for contending the cloud thermostat theory. The inherent local negative cloud feedback over the warm SST anomaly is coupled to the large-scale atmospheric circulation, which plays a critical role in determining the strength of the local feedbacks (Hartmann and Michelsen 1993).

## References

- Chao, W.C., Chen, B.: Multiple quasi-equilibria of the ITCZ and the origin of monsoon onset. Part II. Rotational ITCZ attractors. *J. Atmos. Sci.* **58**, 2820–2831 (2001)
- Chao, W., Chen, B.: Single and double ITCZ in an aqua planet model with constant sea surface temperature and solar angle. *Clim. Dynam.* **22**, 447–459 (2004). doi:[10.1007/s00382-003-0387-4](https://doi.org/10.1007/s00382-003-0387-4)
- Charney, J.G.: Tropical cyclogenesis and the formation of the ITCZ. In: Reid, W.H. (ed.) Mathematical problems of geophysical fluid dynamics. Lectures in applied mathematics. Am. Math. Soc. **13**, 355–368 (1971)
- Clement, A.C., Seager, R., Murtugudde, R.: Why are there tropical warm pools? *J. Climate* **18**, 5294–5311 (2005)
- Hartmann, D.L., Michelsen, M.: Large-scale effects on the regulation of tropical sea surface temperature. *J. Climate* **6**, 2049–2062 (1993)
- Kirtman, B.P., Schneider, E.: A spontaneously generated tropical atmospheric general circulation. *J. Atmos. Sci.* **57**, 2080–2093 (2000)
- Lau, K.M., Sui, C.H., Chou, M.D., Tao, W.K.: An inquiry into the Cirrus cloud thermostat effect on tropical sea surface temperature. *Geophys. Res. Lett.* **21**, 1157–1160 (1994)
- Liebmann, B., Smith, C.A.: Description of a complete (interpolated) outgoing longwave radiation dataset. *Bull. Amer. Meteor. Soc.* **77**, 1275–1277 (1996)
- Lindzen, D., Nigam, S.: On the role of sea surface temperature gradients in forcing low-level winds and convergence in the tropics. *J. Atmos. Sci.* **44**, 2418–2436 (1987)
- Moorthi, S., Suarez, M.J.: Relaxed Arakawa-Schubert: a parameterization of moist convection for general circulation models. *Mon. Weather Rev.* **120**, 978–1002 (1992)
- Philander, S.G.H., Gu, D., Halpern, D., Lambert, G., Lau, N.-C., Li, T., Pacanowski, R.C.: Why the ITCZ is mostly north of the equator. *J. Climate* **9**, 2958–2972 (1996)
- Pike, A.C.: The inter-tropical convergence zone studied with an interactive atmosphere and ocean model. *Mon. Weather Rev.* **99**, 469–477 (1971)
- Ramanathan, V., Collins, W.: Thermodynamic regulation of ocean warming by cirrus clouds deduced from observations of the 1987 El Niño. *Nature* **351**, 27–32 (1991)
- Sobel, A.H., Held, I.M., Bretherton, C.S.: The ENSO signal in tropical tropospheric temperature. *J. Climate* **15**, 2702–2706 (2002)
- Sumi, A.: Pattern formation of convective activity over the aqua planet with globally uniform sea surface temperature. *J. Meteorol. Soc. Jpn.* **70**, 855–876 (1992)
- Tackacs, L.L., Molod, A., Wang, T.: Documentations of the Goddard earth observing system (GEOS) general circulation model-Version 1. NASA Technical Memorandum 104606, vol. 1, Goddard Space Flight Center, Greenbelt, p. 97 (1994)
- Waliser, D.: Some considerations on the thermostat hypothesis. *Bull. Am. Meteor. Soc.* **77**, 357–360 (1996)
- Wallace, J.M.: Effect of deep convection on the regulation of tropical sea surface temperature. *Nature* **357**, 230–231 (1992)
- Xie, P., Arkin, P.A.: Analyses of global monthly precipitation using gauge observations, satellite estimates, and numerical model predictions. *J. Climate* **9**, 840–858 (1996)

# Chapter 4

## Heat Induced Circulation

This chapter dwells on the importance of diabatic heating in the deep tropics that acts as a forcing on some of the large-scale circulation features in the tropical and sub-tropical latitudes. First, we begin with the analytical solutions of a simple linearized shallow water model equations following Gill (1980). This work although an idealized modeling study, is highly instructive in understanding the circulation features such as the east–west (Walker) circulation, meridional (Hadley) circulation and easterlies associated with the trade winds. This idealized atmospheric modeling study is often referred as the “Gill” atmosphere.

### 4.1 Adrian Gill’s Atmospheric Model

A simple linear model solution representing the heat-induced tropical circulation was proposed by Gill (1980). This model shows the circulation that develops in response to diabatic heating. It shows how a localized heating over the equatorial region near Indonesia can generate Kelvin waves that produce a low-level easterly flow over the Pacific.

The following assumptions are made in deriving the analytical solution for the Gill atmosphere.

1. A steady state motion in a resting basic state forced by a given heating  $\tilde{Q}$ .
2. The forced motion is sufficiently weak that it can be treated by linear dynamics.
3. The friction takes the form of Rayleigh friction damping (linear drag is proportional to wind speed).
4. Thermal damping takes the form of Newtonian cooling (heating rate proportional to temperature perturbation).
5. Thermal and frictional damping rates are assumed to have the same time scale everywhere.
6. The solutions are for long-wave approximation, neglecting the high-frequency inertio-gravity waves, Rossby-gravity waves, and short Rossby waves.

Starting with the shallow water equations, namely:

- The x-momentum equation:

$$\frac{\partial u}{\partial t} + u \frac{\partial u}{\partial x} + v \frac{\partial u}{\partial y} - fv = -\frac{1}{\rho_0} \frac{\partial p}{\partial x} - F_x \quad (4.1)$$

- The y-momentum equation:

$$\frac{\partial v}{\partial t} + u \frac{\partial v}{\partial x} + v \frac{\partial v}{\partial y} + fu = -\frac{1}{\rho_0} \frac{\partial p}{\partial y} - F_y \quad (4.2)$$

- The continuity equation in the form

$$\frac{\partial p}{\partial t} + u \frac{\partial p}{\partial x} + v \frac{\partial p}{\partial y} = -p \left( \frac{\partial u}{\partial x} + \frac{\partial v}{\partial y} \right) - \tilde{Q} - F_p. \quad (4.3)$$

Here  $u$  and  $v$  are the zonal and meridional winds,  $p$  is the pressure,  $f$  is the Coriolis parameter,  $\rho_0$  is the mean air density,  $F_x$ ,  $F_y$  and  $F_p$  are frictional terms for the zonal and meridional momentum and pressure, and  $\tilde{Q}$  represents the heating.

In order to linearize this system, we express the dependent variables as a mean value plus some small perturbation, i.e.,  $u = \bar{u} + u'$ ,  $v = \bar{v} + v'$ ,  $p = \bar{p} + p'$ . For an atmospheric basic state at rest,  $\bar{u} = \bar{v} = 0$ . Substituting the expansions for  $u$ ,  $v$  and  $p$  into (4.1), (4.2), and (4.3),

$$\frac{\partial u'}{\partial t} + u' \frac{\partial u'}{\partial x} + v' \frac{\partial u'}{\partial y} - fv' = -\frac{1}{\rho_0} \frac{\partial p'}{\partial x} - F_x \quad (4.4)$$

$$\frac{\partial v'}{\partial t} + u' \frac{\partial v'}{\partial x} + v' \frac{\partial v'}{\partial y} + fu' = -\frac{1}{\rho_0} \frac{\partial p'}{\partial y} - F_y \quad (4.5)$$

$$\frac{\partial p'}{\partial t} + u' \frac{\partial(\bar{p} + p')}{\partial x} + v' \frac{\partial(\bar{p} + p')}{\partial y} = -(\bar{p} + p') \left( \frac{\partial u'}{\partial x} + \frac{\partial v'}{\partial y} \right) - \tilde{Q} - F_p \quad (4.6)$$

Assuming no horizontal variation of the basic state pressure, i.e.,  $\frac{\partial \bar{p}}{\partial x} = \frac{\partial \bar{p}}{\partial y} = 0$ ,

and neglecting terms that are products of perturbation (therefore small, for the purposes of a linear theory) quantities, and using a beta-plane approximation, i.e.,  $f = y\beta$ , we obtain:

$$\frac{\partial u'}{\partial t} - y\beta v' = -\frac{1}{\rho_0} \frac{\partial p'}{\partial x} - F_x \quad (4.7)$$

$$\frac{\partial v'}{\partial t} + y\beta u' = -\frac{1}{\rho_0} \frac{\partial p'}{\partial y} - F_y \quad (4.8)$$

$$\frac{\partial p'}{\partial t} = -\bar{p} \left( \frac{\partial u'}{\partial x} + \frac{\partial v'}{\partial y} \right) - \tilde{Q} - F_p \quad (4.9)$$

Non-dimensionalization is done by selecting a length scale, L, a time scale, T, and a pressure scale P, such that  $(x, y) = L(x^*, y^*)$ ;  $\left(\frac{\partial}{\partial x}, \frac{\partial}{\partial y}\right) = \frac{1}{L} \left(\frac{\partial}{\partial x^*}, \frac{\partial}{\partial y^*}\right)$ ;  $t = Tt^*$ ;  $(u', v') = \frac{L}{T}(u^*, v^*)$ , and  $p' = Pp^*$ , where the starred quantities are non-dimensional. Applying these to (4.7), (4.8), and (4.9) we obtain:

$$\frac{L}{T^2} \frac{\partial u^*}{\partial t^*} - \frac{L^2 \beta}{T} y^* v^* = -\frac{P}{\rho_0 L} \frac{\partial p^*}{\partial x^*} - F_x \quad (4.10)$$

$$\frac{L}{T^2} \frac{\partial v^*}{\partial t^*} + \frac{L^2 \beta}{T} y^* u^* = -\frac{P}{\rho_0 L} \frac{\partial p^*}{\partial y^*} - F_y \quad (4.11)$$

$$\frac{P}{T} \frac{\partial p^*}{\partial t^*} = -\frac{\bar{p}}{T} \left( \frac{\partial u^*}{\partial x^*} + \frac{\partial v^*}{\partial y^*} \right) - \tilde{Q} - F_p \quad (4.12)$$

Rearranging, we obtain

$$\frac{\partial u^*}{\partial t^*} - \beta L T y^* v^* = -\frac{P T^2}{\rho_0 L^2} \frac{\partial p^*}{\partial x^*} - \frac{T^2}{L} F_x \quad (4.13)$$

$$\frac{\partial v^*}{\partial t^*} + \beta L T y^* u^* = -\frac{P T^2}{\rho_0 L^2} \frac{\partial p^*}{\partial y^*} - \frac{T^2}{L} F_y \quad (4.14)$$

$$\frac{\partial p^*}{\partial t^*} = -\frac{\bar{p}}{P} \left( \frac{\partial u^*}{\partial x^*} + \frac{\partial v^*}{\partial y^*} \right) - \frac{T}{P} \tilde{Q} - \frac{T}{P} F_p \quad (4.15)$$

If we select  $P = \bar{p} = \rho_0 g H$  and require that  $\frac{P T^2}{\rho_0 L^2} = 1$ , we obtain  $(\frac{L}{T}) = \sqrt{\frac{\bar{p}}{\rho_0}} = \sqrt{gH} = C$ , which is the phase speed of gravity waves. Selecting  $L = \sqrt{\frac{C}{2\beta}}$  and  $T = \sqrt{\frac{1}{2\rho_0 C}}$ , and substituting in the system above, we obtain

$$\frac{\partial u^*}{\partial t^*} - \frac{1}{2} y^* v^* = -\frac{\partial p^*}{\partial x^*} - \sqrt{\frac{1}{2\beta C^3}} F_x \quad (4.16)$$

$$\frac{\partial v^*}{\partial t^*} + \frac{1}{2} y^* u^* = -\frac{\partial p^*}{\partial y^*} - \sqrt{\frac{1}{2\beta C^3}} F_y \quad (4.17)$$

$$\frac{\partial p^*}{\partial t^*} = - \left( \frac{\partial u^*}{\partial x^*} + \frac{\partial v^*}{\partial y^*} \right) - \sqrt{\frac{\rho_0}{2\beta C^2}} \tilde{Q} - \sqrt{\frac{\rho_0}{2\beta C^2}} F_p \quad (4.18)$$

Let us assume that the non-dimensional friction is proportional to the non-dimensional wind speed, and that the non-dimensional pressure dissipation is proportional to the non-dimensional pressure with a proportionality constant  $\epsilon$ , i.e.,  $\sqrt{\frac{1}{2\beta C^3}} F_x = \epsilon u$ ,  $\sqrt{\frac{1}{2\beta C^3}} F_y = \epsilon v$ ,  $\sqrt{\frac{\rho_0}{2\beta C^2}} F_p = \epsilon p$ . Let us also denote  $\sqrt{\frac{\rho_0}{2\beta C^2}} \tilde{Q} = Q$ , and drop the asterisks from the notation. The linearized non-dimensional shallow water equation system for a stationary perturbation ( $\partial/\partial t = 0$ ) can now be written simply as

$$\epsilon u - \frac{1}{2} yv = - \frac{\partial p}{\partial x} \quad (4.19)$$

$$\epsilon v + \frac{1}{2} yu = - \frac{\partial p}{\partial y} \quad (4.20)$$

$$\epsilon p + \frac{\partial u}{\partial x} + \frac{\partial v}{\partial y} = -Q \quad (4.21)$$

where  $y$  is the non-dimensional northward distance,  $x$  is the non-dimensional eastward distance,  $(u, v)$  are the non-dimensional zonal and meridional winds, respectively,  $p$  is the non-dimensional pressure perturbation, and  $Q$  is the non-dimensional heating rate.

The non-dimensional vertical velocity in this model is

$$w = \epsilon p + Q \quad (4.22)$$

This system of equations can be reduced to a single equation for  $v$

$$\epsilon^3 v + \frac{1}{4} \epsilon y^2 v - \epsilon \frac{\partial^2 v}{\partial x^2} - \epsilon \frac{\partial^2 v}{\partial y^2} - \frac{1}{2} \frac{\partial v}{\partial x} = -\epsilon \frac{\partial Q}{\partial y} - \frac{1}{2} y \frac{\partial Q}{\partial x} \quad (4.23)$$

If the dissipative factor epsilon is assumed to be small, the initial term can be neglected. Also, if the east–west wavenumber is small (i.e., the east–west scale large), the third term can be neglected as well. These approximations are equivalent to setting  $\epsilon v = 0$  in the second equation, i.e., the eastward flow is in geostrophic balance with the pressure gradient.

### 4.1.1 Solutions to the Gill Model

For the solutions of the dissipational shallow water equations we introduce two new variables,

$$q = p + u \quad (4.24)$$

$$r = p - u \quad (4.25)$$

By adding together (4.19) and (4.21), we get

$$\varepsilon q + \frac{\partial q}{\partial x} + \frac{\partial v}{\partial y} - \frac{1}{2} yv = -Q. \quad (4.26)$$

Similarly, by subtracting (4.19) from (4.21) we get

$$\varepsilon r - \frac{\partial r}{\partial x} + \frac{\partial v}{\partial y} + \frac{1}{2} yv = -Q, \quad (4.27)$$

and (4.20) can be written as

$$\frac{\partial q}{\partial y} + \frac{1}{2} yq + \frac{\partial r}{\partial y} - \frac{1}{2} yr = 0. \quad (4.28)$$

The free solutions to this system of equations, i.e., the solution for  $Q = 0$  is in the form of parabolic cylinder functions  $D_n(y)$ . The forced solutions are obtained when all variables are expanded in terms of these basis functions  $D_n(y)$ :

$$\begin{pmatrix} q(x, y, t) \\ r(x, y, t) \\ v(x, y, t) \\ Q(x, y, t) \end{pmatrix} = \sum_{n=0}^{\infty} \begin{pmatrix} q_n(x, t) \\ r_n(x, t) \\ v_n(x, t) \\ Q_n(x, t) \end{pmatrix} D_n(y) \quad (4.29)$$

The parabolic cylinder functions  $D_n(y)$  have the following useful properties:

$$\frac{dD_n(y)}{dy} + \frac{1}{2} yD_n = nD_{n-1}, \quad n \geq 1 \quad (4.30)$$

$$\frac{dD_n(y)}{dy} - \frac{1}{2} yD_n = -D_{n+1}, \quad n \geq 0 \quad (4.31)$$

Substituting (4.29) into (4.26) through (4.28) we obtain, respectively:

$$\varepsilon \sum_{n=0}^{\infty} q_n D_n + \sum_{n=0}^{\infty} \frac{\partial q_n}{\partial x} D_n + \sum_{n=0}^{\infty} v_n \frac{dD_n}{dy} - \frac{1}{2} y \sum_{n=0}^{\infty} v_n D_n = - \sum_{n=0}^{\infty} Q_n D_n \quad (4.32)$$

$$\varepsilon \sum_{n=0}^{\infty} r_n D_n - \sum_{n=0}^{\infty} \frac{\partial r_n}{\partial x} D_n + \sum_{n=0}^{\infty} v_n \frac{dD_n}{dy} + \frac{1}{2} y \sum_{n=0}^{\infty} v_n D_n = - \sum_{n=0}^{\infty} Q_n D_n \quad (4.33)$$

$$\sum_{n=0}^{\infty} q_n \frac{dD_n}{dy} + \frac{1}{2} y \sum_{n=0}^{\infty} q_n D_n + \sum_{n=0}^{\infty} r_n \frac{dD_n}{dy} - \frac{1}{2} y \sum_{n=0}^{\infty} r_n D_n = 0 \quad (4.34)$$

Equation 4.32 can be rewritten as

$$\sum_{n=0}^{\infty} \left( \varepsilon q_n + \frac{\partial q_n}{\partial x} \right) D_n + \sum_{n=0}^{\infty} v_n \left( \frac{dD_n}{dy} - \frac{1}{2} y D_n \right) = - \sum_{n=0}^{\infty} Q_n D_n \quad (4.35)$$

Using the property of the parabolic cylinder functions given by (4.31), this becomes

$$\sum_{n=0}^{\infty} \left( \varepsilon q_n + \frac{\partial q_n}{\partial x} \right) D_n - \sum_{n=0}^{\infty} v_n D_{n+1} = - \sum_{n=0}^{\infty} Q_n D_n, \quad (4.36)$$

or

$$\left( \varepsilon q_0 + \frac{\partial q_0}{\partial x} \right) D_0 + \sum_{n=0}^{\infty} \varepsilon \left( q_{n+1} + \frac{\partial q_{n+1}}{\partial x} \right) D_{n+1} - \sum_{n=0}^{\infty} v_n D_{n+1} = -Q_0 D_0 - \sum_{n=0}^{\infty} Q_{n+1} D_{n+1} \quad (4.37)$$

Equation 4.36 has to be satisfied for every term in the summation, since the parabolic cylinder functions form a basis. Equating the coefficients by multiplying  $D_0$ , we obtain

$$\varepsilon q_0 + \frac{\partial q_0}{\partial x} = -Q_0 \quad (4.38)$$

Equating the coefficients by multiplying  $D_{n+1}$  for every  $n$ , we obtain

$$\varepsilon q_{n+1} + \frac{\partial q_{n+1}}{\partial x} - v_n = -Q_{n+1} \quad (4.39)$$

Following a similar procedure, from (4.33) we obtain

$$\varepsilon r_{n-1} - \frac{\partial r_{n-1}}{\partial x} + nv_n = -Q_{n-1} \quad (4.40)$$

And from (4.34) we obtain

$$q_1 = 0 \quad (4.41)$$

and

$$r_{n-1} = (n+1)q_{n+1} \quad (4.42)$$

We look for solutions for two special cases – heating that is symmetric about the equator, of the form

$$Q(x, y) = F(x)D_0(y) = F(x)e^{-\frac{1}{4}y^2}, \quad (4.43)$$

and heating that is antisymmetric about the equator, of the form

$$Q(x, y) = F(x)D_1(y) = yF(x)e^{-\frac{1}{4}y^2}. \quad (4.44)$$

With such forms of the heating function, the solutions involve only parabolic cylinder functions of order up to three.

$$D_0 = e^{-\frac{1}{4}y^2} \quad (4.45)$$

$$D_1 = ye^{-\frac{1}{4}y^2} \quad (4.46)$$

$$D_2 = (y^2 - 1)e^{-\frac{1}{4}y^2} \quad (4.47)$$

$$D_3 = (y^3 - 3y)e^{-\frac{1}{4}y^2}. \quad (4.48)$$

If we let the forcing vary smoothly in some localized neighborhood of  $x = 0$ , and have the form:

$$F(x) = \begin{cases} \cos kx & |x| < L \\ 0 & |x| \geq L \end{cases}$$

where  $k = \pi/(2L)$  is the east–west wave number, we can now look at the effects of symmetric and asymmetric forcing.

### (i) Symmetric forcing

For the symmetric forcing case, the form of the heating is given by (4.43), i.e., the only non-zero coefficient  $Q_n$  corresponds to the case  $n = 0$  and is given by

$$Q_0 = F(x) \quad (4.49)$$

There are two components of the response to such heating. The first component comes from the solution to (4.38) and involves only  $q_0$ . This solution represents an eastward propagating Kelvin wave, with decaying amplitude. The wave moves at unit speed with decay rate  $\epsilon$ , hence its spatial decay rate is also  $\epsilon$ . Such eastward propagating wave does not carry any signal to the west; therefore the solution is zero for the  $x < -L$  part of the domain. Thus the part of the solution associated with  $q_0$  is given by:

$$\begin{aligned} (\epsilon^2 + k^2)q_0 &= 0 && \text{for } x < -L \\ (\epsilon^2 + k^2)q_0 &= -\epsilon \cos kx - k(\sin kx + e^{-\epsilon(x+L)}) && \text{for } |x| \leq L \\ (\epsilon^2 + k^2)q_0 &= -k(1 + e^{-2\epsilon L})e^{\epsilon(L-x)} && \text{for } x > L \end{aligned} \quad (4.50)$$

Using (4.24), (4.25), (4.39), and (4.22), the solution for this Kelvin wave is given by

$$p = \frac{1}{2}q_0(x)e^{-\frac{1}{\varepsilon}y^2} \quad (4.51)$$

$$u = \frac{1}{2}q_0(x)e^{-\frac{1}{\varepsilon}y^2} \quad (4.52)$$

$$v = 0 \quad (4.53)$$

$$w = \frac{1}{2}(\varepsilon q_0(x) + F(x))e^{-\frac{1}{\varepsilon}y^2}. \quad (4.54)$$

The second component of the solution for a symmetric forcing corresponds to substituting  $n = 1$  into (4.39), (4.40), and (4.42), which then give

$$v_1 = \frac{dq_2}{dx} + \varepsilon q_2 \quad (4.55)$$

$$r_0 = 2q_2 \quad (4.56)$$

$$\frac{dq_2}{dx} - 3\varepsilon q_2 = Q_0 \quad (4.57)$$

This corresponds to the  $n = 1$  long planetary wave which propagates westwards at speed of  $1/3$ , thus having a spatial decay rate of  $3\varepsilon$ . Since the  $n = 1$  wave is westward propagating, it carries no information to the east, i.e. the solution is zero for the  $x > L$  part of the domain. The solution of (4.57) is given by

$$\begin{aligned} ((2n+1)^2\varepsilon^2 + k^2)q_{n+1} &= -k\left(1 + e^{-2(2n+1)\varepsilon L}\right)e^{(2n+1)\varepsilon(x+L)} && \text{for } x < -L \\ ((2n+1)^2\varepsilon^2 + k^2)q_{n+1} &= -(2n+1)\varepsilon \cos kx + k\left(\sin kx - e^{(2n+1)\varepsilon(x-L)}\right) && \text{for } |x| \leq L \\ ((2n+1)^2\varepsilon^2 + k^2)q_{n+1} &= 0 && \text{for } x > L \end{aligned}$$

with  $n = 1$

$$(4.58)$$

The detailed solution for the pressure and velocity components follows from (4.24), (4.25), (4.55), (4.56), (4.57), (4.22), and (4.50), (4.51), (4.52), namely,

$$p = \frac{1}{2}q_2(x)(1 + y^2)e^{-\frac{1}{\varepsilon}y^2} \quad (4.59)$$

$$u = \frac{1}{2}q_2(x)(y^2 - 3)e^{-\frac{1}{\varepsilon}y^2} \quad (4.60)$$

$$v = (F(x) + 4\epsilon q_2(x))ye^{-\frac{1}{\theta}y^2} \quad (4.61)$$

$$w = \frac{1}{2}(F(x) + \epsilon q_2(x)(1 + y^2))e^{-\frac{1}{\theta}y^2}. \quad (4.62)$$

The total solution for the symmetric heat source placed on the equator can be mapped out by summing the solution for  $n = 0$  (Eqs. 4.46, 4.47, 4.48, 4.49) and for  $n = 1$  (Eqs. 4.59, 4.60, 4.61, 4.62). This is easy to calculate since all variables are represented purely by analytical functions. The symmetric heat source solution is shown in Fig. 4.1a–d.

The forcing is equivalent to the representation of the area of deep convection over the Maritime continent. The solution then for symmetric heating about the equator in Fig. 4.1a shows the easterly trades flowing parallel to the equator into the forcing region, consistent with a pressure trough found at the equator (Fig. 4.1b, c(ii)). Gill (1980) interpreted the easterlies to the east of the forcing as a result of the Kelvin wave propagating eastward in the presence of damping. Since the Kelvin wave has no meridional component, the easterlies are relatively more trapped in the equatorial latitudes. Likewise, the westerlies to the west of the forcing was interpreted in Gill (1980) as a result of the westward propagation of the damping Rossby wave. However, unlike the Kelvin wave, the Rossby wave has two symmetrical (about the equator) cyclonic lows straddling the equator in Fig. 4.1b. Since the equatorial Kelvin wave speed is about three times more than the Rossby wave, the damping distance of the Kelvin wave is proportionately larger than that for the Rossby wave. This is because the zonal integral of the zonal wind perturbation is nearly zero at the equator. As a result the easterlies occupy a wider region to the east of the heating compared to the westerlies west of the heating, which also implies that the westerlies associated with Rossby waves must be stronger than the zonal winds associated with Kelvin waves.

The rising motion over the area of heating is part of a larger east–west (Walker) circulation (Fig. 4.1c(i)), typical over the tropical Pacific Ocean. Similarly, another cell of the east–west circulation reminiscent of that over the tropical Indian Ocean (Fig. 4.1c(i)) with surface westerlies to the west of the forcing (Fig. 4.1b) are also evident. The zonally averaged solution of the Gill atmosphere also shows the typical Hadley type circulation with symmetric meridional cells on both sides of the equator (Fig. 4.1d(ii)).

## (ii) Antisymmetric forcing

We shall next derive the solution, obtained in a similar manner, for an antisymmetric heat source consisting of a heat source at roughly 10N and a heat sink at roughly 10S. This source/sink pair produces some very interesting heat-induced circulations. For the antisymmetric heat source, the form is given by (4.49), i.e.,

$$Q_1 = F(x) \quad (4.63)$$

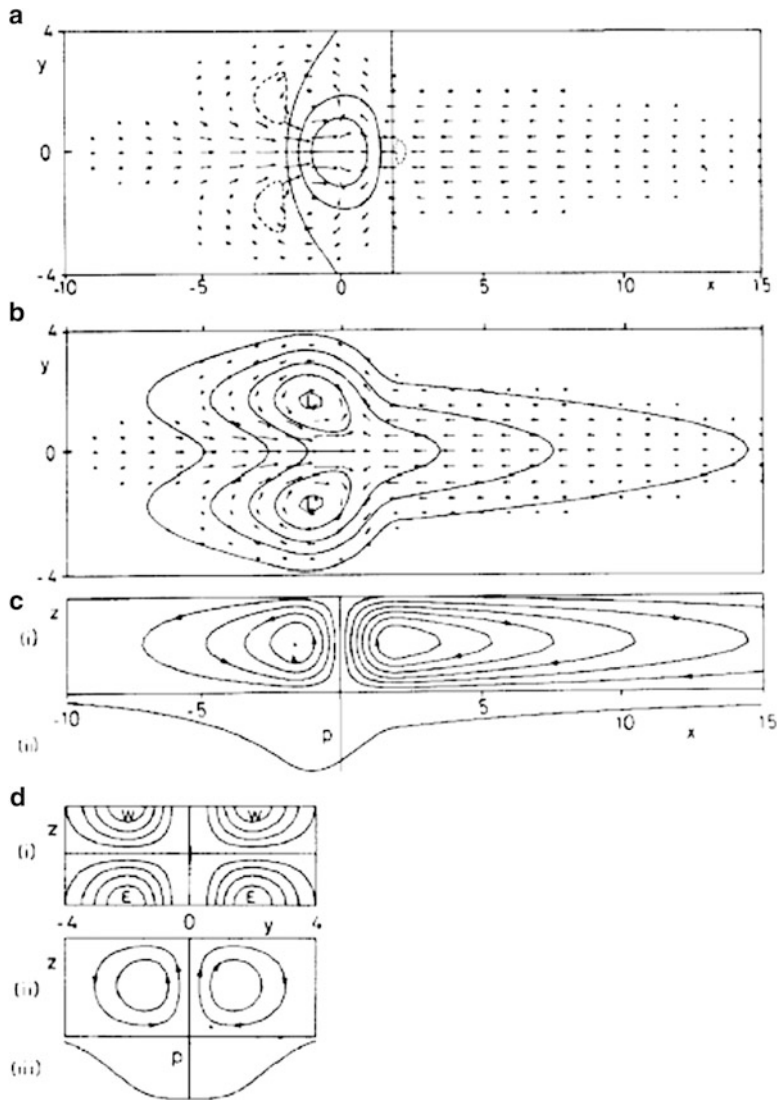


**Fig. 4.1** Solution of symmetric heating about the equator. The low level wind vectors are superposed with (a) contours of vertical velocity (contours at  $-0.1, 0, 0.3, 0.6$ ) and (b) contours of perturbation pressure (contour interval 0.3). (c) The meridionally integrated solution showing (i) stream function and (ii) perturbation pressure. (d) The zonally integrated solution showing (i) contours of zonal velocity (E marking the low level easterlies and W marking the upper level westerlies), (ii) stream function, and (iii) perturbation pressure (From Gill 1980)

Again, the response consists of two parts. The first one corresponds to the long  $n = 0$  mixed planetary gravity wave, for which (4.39), and (4.40) give

$$\begin{aligned} q_1 &= 0 \\ v_0 &= Q_1 \end{aligned} \quad (4.64)$$

This part has no effect outside the forcing region because long mixed waves do not propagate.

The second part of the solution arises from the long  $n = 2$  planetary wave for which (4.39), (4.42), and (4.40) give respectively

$$v_2 = \frac{dq_3}{dx} + \epsilon q_3 \quad (4.65)$$

$$r_1 = 3q_3 \quad (4.66)$$

$$\frac{dq_3}{dx} - 5\epsilon q_3 = Q_1 \quad (4.67)$$

The solution of (4.67) is given by (4.58) with  $n = 2$ . The detailed solution that follows for the pressure and the horizontal and vertical motion is then obtained as

$$p = \frac{1}{2}q_3(x)y^3 e^{-\frac{1}{\Phi}y^2} \quad (4.68)$$

$$u = \frac{1}{2}q_3(x)(y^3 - 6y)e^{-\frac{1}{\Phi}y^2} \quad (4.69)$$

$$v = (F(x)y^2 + 6\epsilon q_3(x)(y^2 - 1))e^{-\frac{1}{\Phi}y^2} \quad (4.70)$$

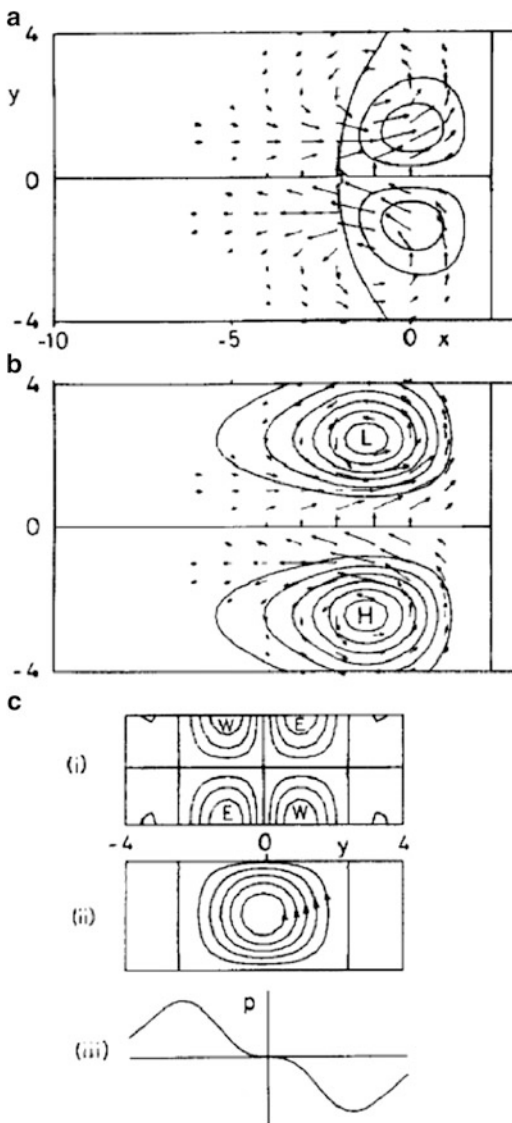
$$w = \left( F(x)y + \frac{1}{2}\epsilon q_3(x)y^3 \right) e^{-\frac{1}{\Phi}y^2}. \quad (4.71)$$

The solution for the antisymmetric heating is shown in Fig. 4.2a–c.

Unlike the symmetric heating, the antisymmetric heating solutions in Fig. 4.2 display cyclonic (anticyclonic) circulation in the heated (cooled) hemisphere. Furthermore, there is no wind response to the east of the heating in Fig. 4.3 because of the absence of equatorially symmetric eastward propagating Kelvin waves. It may be noted that the asymmetric heating produces one meridional cell (Fig. 4.2c (ii)) with rising branch of this cell in the heated hemisphere. This solution is similar to the zonally averaged circulation seen earlier in the Solstitial seasons in Chap. 1.

Gill (1980) however indicate that the circulation pattern consistent with the Asian summer monsoon heating is realized to a large extent by adding the solutions of the symmetric and asymmetric heating of the Gill atmosphere. It then produces

**Fig. 4.2** The solution for antisymmetric heating about the equator. (a) The low level wind fields are superposed with contours of vertical velocity (contour interval 0.3). (b) Contours of perturbation pressure (contour interval 0.3), and (c) zonally integrated solution showing (i) contours of zonal velocity, (ii) stream function contours, and (iii) perturbation pressure (From Gill 1980)



cyclonic circulation with rising motion in the heated hemisphere and corresponding sinking motion with anticyclonic circulation in the cooled hemisphere.

An interesting extension of the symmetric and antisymmetric heating solutions of the Gill atmosphere was proposed in Zhang and Krishnamurti (1987). Here they first computed global tropical distributions of heat sources and sinks using satellite data sets. This can be done from a mix of net radiation and rainfall estimates from satellites. Given such a heat source distribution, one can in principle expand this field into a number of zonal harmonic components and a number of meridional

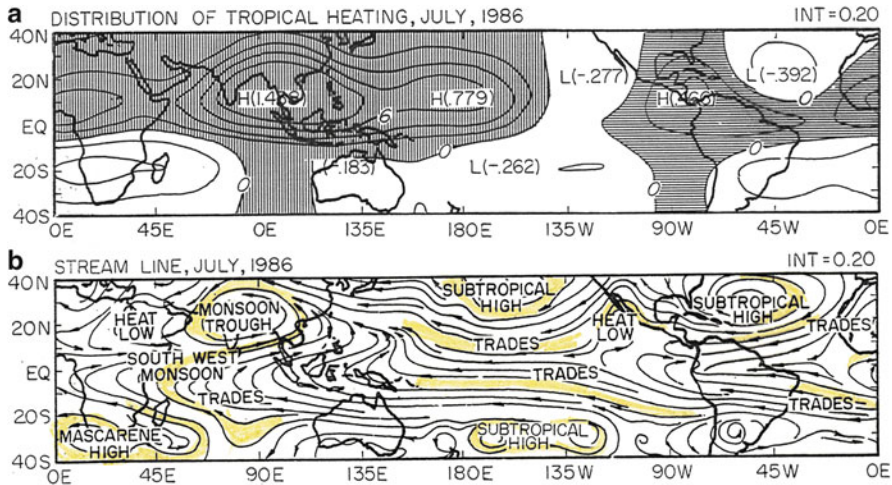


**Fig. 4.3** (a) The vertically integrated heating distribution retrieved from OLR observations for July 1986 and (b) Gill's solution of motion field at low level for the prescribed heating (shown in a) (From authors unpublished work based on Zhang and Krishnamurti 1996)

parabolic cylinder functions. Roughly three waves in the zonal direction and roughly three empirical parabolic cylinder functions (through  $D_3$ ) can represent the vertically integrated heating climatology reasonably well for the large scales. That analytical representation of the heating can be inserted in Gill's frame of reference and one can solve for the heating induced circulations over the entire tropics. Figure 4.3a, b illustrate these solutions from Zhang and Krishnamurti (1996). Figure 4.3a shows the truncated vertically integrated heating field for July 1986 based on satellite data sets. Figure 4.3b shows the exact analytical solution for the motion field from this approach. We note that most major features of the tropical climatology such as the northern and the southern hemisphere trades, the Inter Tropical Convergence zone, the summer monsoon circulation, the monsoon trough, the heat lows over Sahara and the subtropical highs are all captured by this analytical solution. This merely says that over the tropical latitudes there is a close relationship between the heat sources and the circulations.

## 4.2 Desert Heat Lows

The heat lows found over the deserts of the tropics and subtropics are a major component of the global circulation. These are shallow low pressure systems, generally found below 850 mb, that form during late spring and last through early fall over the arid and semi-arid tropical and subtropical regions. The central pressure in these systems lies between about 1,000 and 1,010 mb. Figure 4.4 illustrates the geographical locations where such systems are found during the

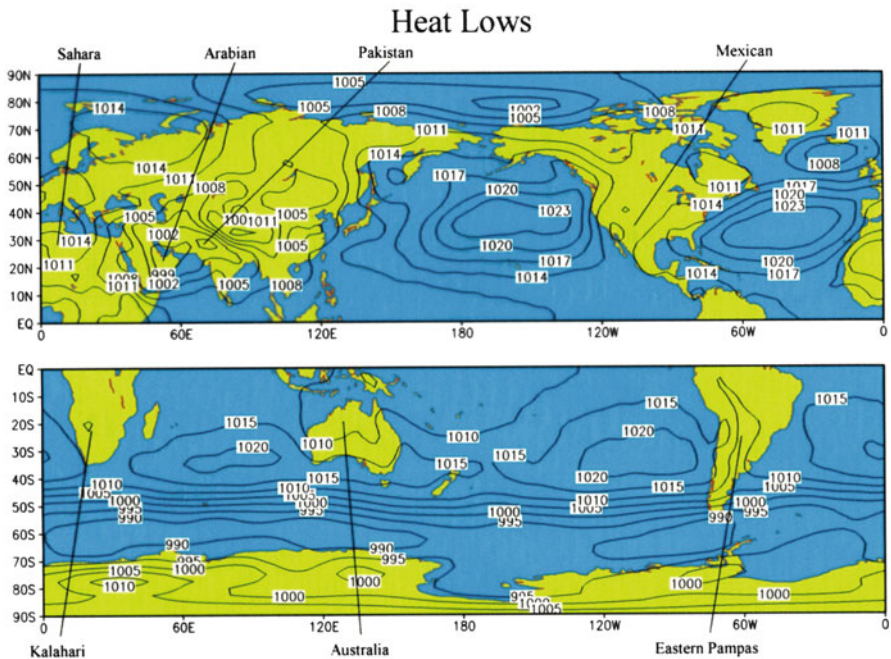


**Fig. 4.4** July (top) and January (bottom) sea level pressure (mb) illustrating the summer heat lows in the northern and southern hemispheres respectively (Based on authors unpublished work)

summer seasons of the two hemispheres. Here we show the July and January sea level pressure distribution over the northern and southern hemispheres respectively. This identifies the locations of heat lows over Sahara, the Arabian Peninsula, Pakistan, Mexico, South Africa, Australia, and Argentina.

Satellites that measure the Earth's radiative budget show that the tropics, as well as in the summer hemisphere extratropics, the incoming radiation exceeds the outgoing radiation. The converse is true over the winter hemisphere extratropics. The areas of the desert heat lows over the tropics and subtropics however are an exception. Here, the outgoing radiation exceeds the incoming radiation resulting in a net loss of radiation to outer space.

A unique feature of the tropical and subtropical desert regions is their high surface albedo, i.e., large ratio of reflected to incident solar radiation at the Earth's surface. The albedo at these locations can be as large as 40 %. The low humidity and lack of clouds of the desert atmosphere allow a substantial part of the incident solar radiation at the top of the atmosphere to reach the Earth's surface. A relatively large percentage of this radiation, due to the high albedo, is reflected back up to the top of the atmosphere.

The high ground temperature over the desert regions is another factor that contributes to the net loss of radiation. According to the Stefan-Boltsman law, the long-wave radiation emitted at the Earth's surface is proportional to the fourth power of the surface temperature. Since the daytime surface temperatures over the

desert regions are of the order of  $50^{\circ}\text{C}$  ( $323^{\circ}\text{K}$ ), this results in very large values of terrestrial radiation radiated upwards into the atmosphere. Unimpeded by atmospheric moisture or clouds, much of this terrestrial (long-wave) radiation reaches the top of the atmosphere where it exits into outer space.

It would seem that the radiative loss observed over the heat lows would call for a net cooling of the temperature over these regions. However, the thermal stratification and soundings over the desert regions during the summer season change little from one day to the next. It follows then that the heat budget of the heat low calls for large lateral transport of energy into the system. This subject is addressed in more detail further in this chapter.

The following sections are based on a field study of a heat low over the Empty Quarter of Saudi Arabia, described in Blake et al. (1983). The field study involved a combination of surface station measurements and aircraft flight-level and dropwindsonde measurements. The results are representative of a typical desert heat low structure.

#### 4.2.1 *Diurnal Change Over the Heat Lows*

At nighttime, when the supply of solar radiation ceases, the clear skies and dry atmosphere of the desert allow for a high rate of radiative cooling of the ground. While daytime surface temperatures can be as high as  $45\text{--}50^{\circ}\text{C}$ , the nighttime temperatures can drop down as low as  $15\text{--}25^{\circ}\text{C}$ . Figure 4.5 shows the surface air temperature and sea level pressure over a heat low site of Saudi Arabia. These measurements come from automatic surface weather observing instruments that were deployed at a site called Sheroara in the Saudi Arabian Desert.

The minimum surface temperature is found between 4 and 6 AM local time. As soon as the sun rises, the temperatures rapidly start to increase. The fastest rate of surface temperature warming is between 6 and 11 AM local time. The maximum temperature is found in the early afternoon hours.

The sea level pressure exhibits a semi-diurnal as well as a diurnal change. The semidiurnal tide can draw amplitudes of the order of several milibars for the sea level pressure. A sample of daytime versus nighttime sea level pressures in the Saudi Arabian Heat Low is illustrated in Fig. 4.6. During daytime hours (top two panels), the central pressure of the heat low is of the order of 1,004 mb. During the nighttime (bottom panel), descent and divergence prevail and the heat low is essentially washed out. It is evident that this is not a very strong low-pressure system when compared with tropical waves and depressions.

Typical day versus night soundings of potential temperature are illustrated in Fig. 4.7. Shown for comparison is a sounding for the US standard atmosphere. The potential temperature  $\theta$  for two daytime soundings (solid and medium-dashed line) shows a near constant  $\theta$  up to around 650 mb, which corresponds to the top of the dust layer. Dry convective thermals erode the superadiabatic lapse rates and produce a neutral lapse rate up to about the 650 mb level. During nighttime the surface layer

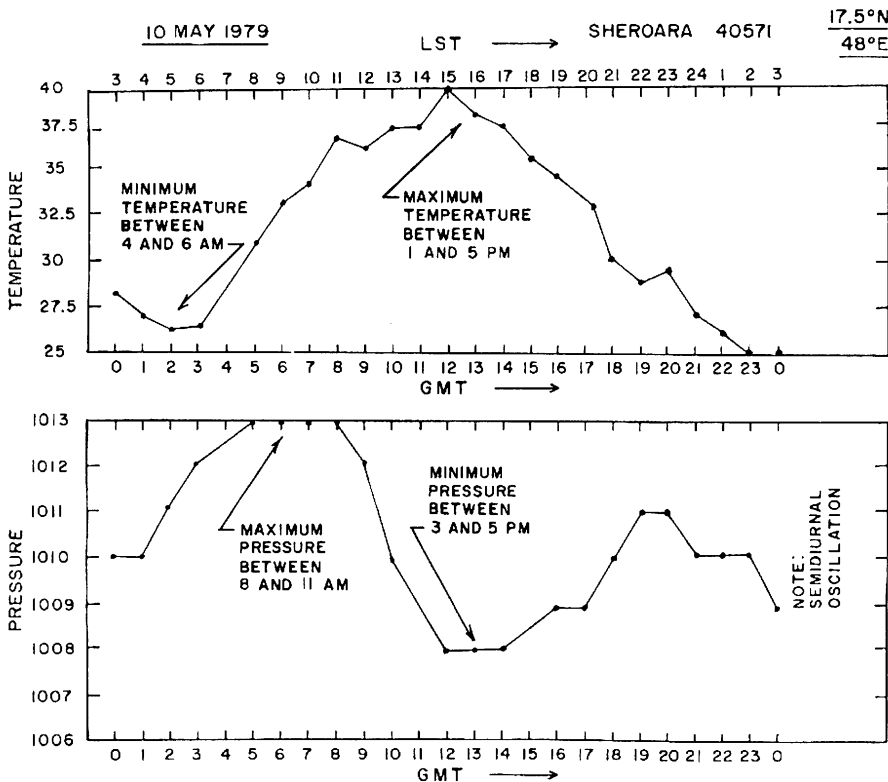


**Fig. 4.5** Example of diurnal variation of surface temperature (top) and surface pressure (bottom) at the Sheroara site (From Blake et al. 1983)

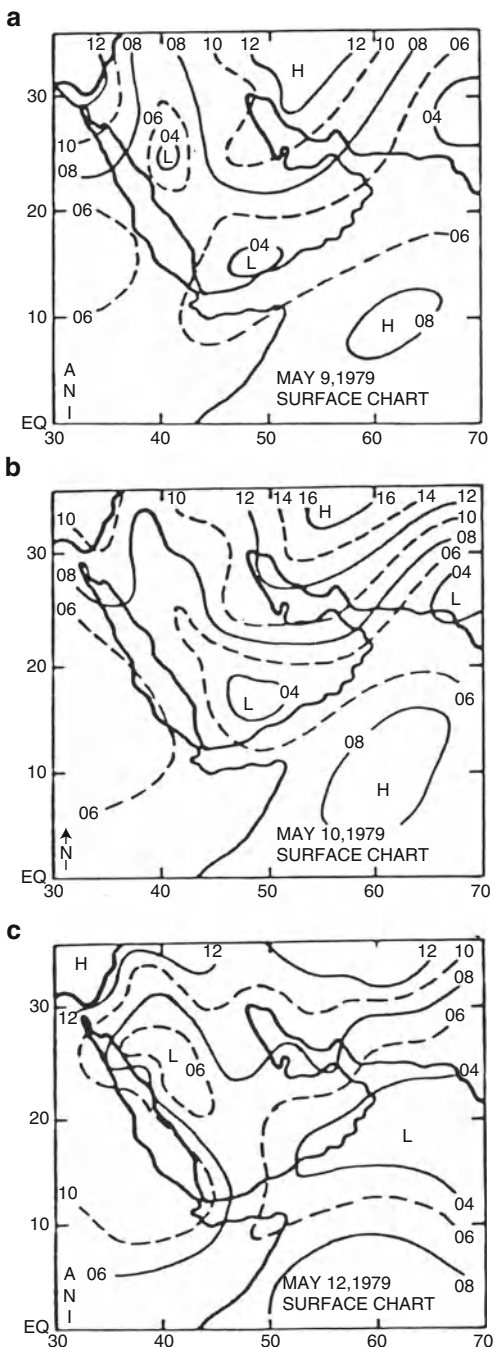
gets stabilized and  $\theta$  increases rapidly because of the surface cooling. Such day-night differences of soundings are very typical over tropical/subtropical heat lows.

The well-mixed layer is also evidenced from an analysis of the specific humidity data sets over the Empty Quarter. That is illustrated in Fig. 4.8. Here again we see nearly constant values of specific humidity with the top near the 650 mb level.

#### 4.2.2 Vertical Motion and Divergence Structure of Heat Lows

A schematic vertical circulation structure of a heat low is presented in Fig. 4.9. The heat low is a very shallow phenomenon in the vertical. At the surface level, air converges into the low, and diverges out near the 800 mb level. Aloft there is a deep layer of convergence in the upper troposphere that descends on top of the heat low.

**Fig. 4.6** Examples of daytime (top two panels) and nighttime (bottom panel) surface analyses over Saudi Arabia. Isopleths show sea level pressure departure from 1,000 mb  
(From Blake et al. 1983)



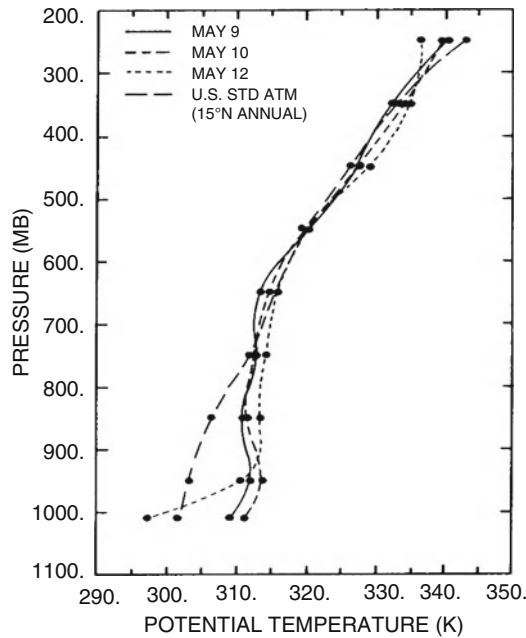


**Fig. 4.7** Average vertical profile of potential temperature (K) from two daytime (solid and medium-dashed lines) and one nighttime (short-dashed line) flight missions over the Saudi Arabian Heat Low. Shown for comparison is the US Standard Atmosphere profile (long-dashed line) (From Blake et al. 1983)

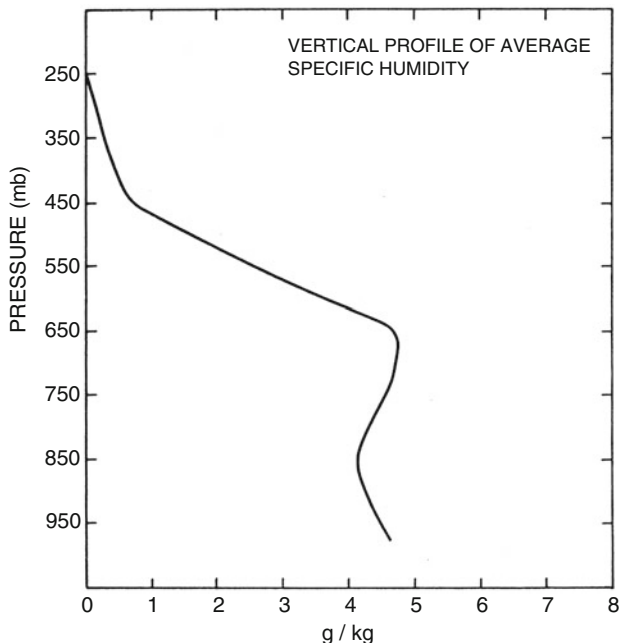


**Fig. 4.8** Average vertical profile of specific humidity ( $\text{g kg}^{-1}$ ) from two daytime flight missions over the Saudi Arabian Heat Low (From Blake et al. 1983)

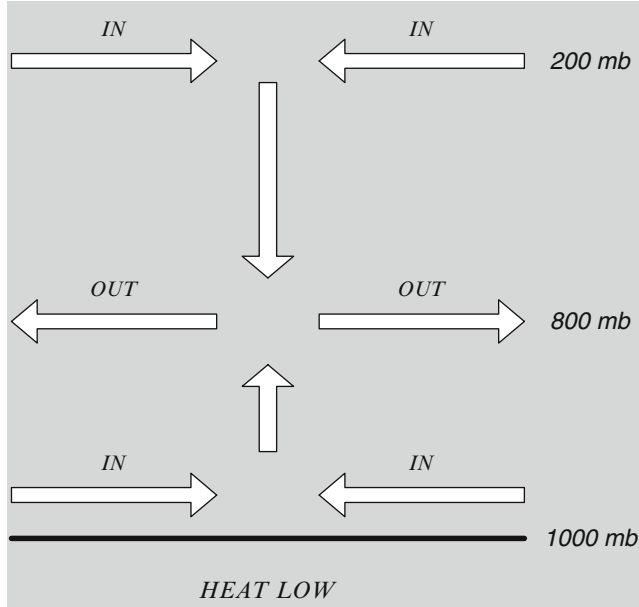


**Fig. 4.9** Schematic diagram of the heat low circulation

The divergence/vertical velocity structure above a heat low has been estimated using research aircraft data sets, Blake et al. 1983. A NASA research aircraft carried on board sensors to measure flight level winds and deployed dropwindsondes to obtain vertical profiles of the horizontal winds. The accuracy of flight-level winds was of the order of  $1 \text{ ms}^{-1}$ . There was an inertial navigation system that provided a high level of accuracy for horizontal winds. The dropwindsondes were tracked by an Omega system that had accuracy of the order of  $3\text{--}4 \text{ m s}^{-1}$ . Several wide swaths of aircraft traversing over the heat low by flights crisscrossing the region provided an extensive data coverage. The flight duration was of the order of 8 h. These data sets, centered on the middle of the flight time, i.e.,  $+/- 4 \text{ h}$ , were regarded as synoptic data sets. There are a large number of locations  $(x_i, y_i)$  where wind data  $(u_i, v_i)$  were available for the flight level and from the dropwindsondes. Via a least square minimization it is possible to represent the horizontal winds at each pressure level by linear surfaces. Assuming an arbitrary reference origin of  $(x = 0, y = 0)$ , and given a totality of wind data from one day of flight, it is possible to analyze the data spatially using a linear multiple regression, i.e.,

$$u(p) = a_1(p)x + a_2(p)y + a_3(p) \quad (4.72)$$

$$v(p) = b_1(p)x + b_2(p)y + b_3(p) \quad (4.73)$$

where the  $a_1, a_2, a_3$  and  $b_1, b_2, b_3$  are pressure level-dependent coefficients obtained linear regression of the data points  $(u_i, v_i)$  at all locations  $(x_i, y_i)$  at pressure level  $p$ . This results in a planar surface expansion of the wind field over the small region of the heat low. Once the coefficients are determined, the horizontal divergence at any pressure level is given by

$$D = \frac{\partial u}{\partial x} + \frac{\partial v}{\partial y} = a_1 + b_2 \quad (4.74)$$

This divergence at any pressure level does not vary in  $x$  and  $y$ . Because of errors in the wind measurements and the fact that not all data are synoptic, some errors are bound to be there in these divergence estimates at each level. We can define a corrected divergence  $D_C$  by the relationship  $D_C = D + \epsilon|D|$  where  $\epsilon$  is a constant. This assumes that the error in divergence is proportional to the magnitude of divergence. The vertical integral of the total divergence over a tropospheric column should be very close to zero. By setting

$$\frac{1}{g} \int_{p_{SFC}}^{p_{TOP}} D_C dp = 0 \quad (4.75)$$

where  $p_{SFC}$  is the surface pressure and  $p_{TOP}$  is the pressure at the top of the troposphere, we can obtain a value of  $\epsilon$ , i.e.,

$$\epsilon = \frac{- \int_{p_{SFC}}^{p_{TOP}} D dp}{\int_{p_{SFC}}^{p_{TOP}} |D| dp}. \quad (4.76)$$

Thus, knowing the uncorrected divergence  $D$  we can obtain a vertical profile of the corrected divergence  $D_C$  at each level. The vertical velocity  $\omega$  can next be obtained by vertically integrating the continuity equation, i.e.,  $\frac{\partial \omega}{\partial p} = -D_C$ . Here, as a boundary condition one can use  $\omega(p_{SFC}) = 0$ .

Two daytime and a nighttime profiles of  $D_C$  and  $\omega$  are illustrated in Fig. 4.10. The daytime profiles show rising motion below 850 mb surface and a descent above that pressure level in the troposphere. This result is consistent from two successive day time data sets. This corresponds to a shallow layer of convergence in the heat low below the 900 mb level, capped by a strong divergence near the 850 mb level. Above 700 mb, a weak convergence is apparent over the entire

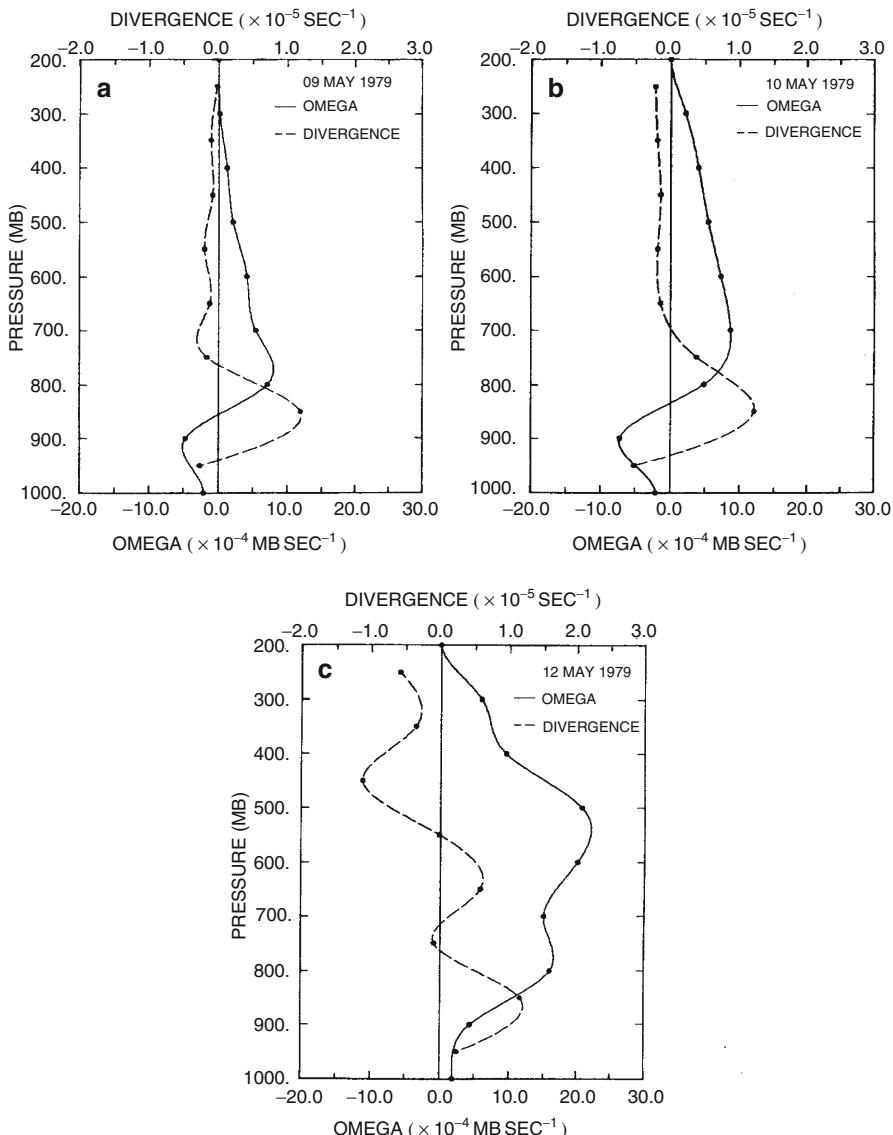


**Fig. 4.10** Average horizontal divergence and vertical velocity from two daytime (*top*) and one nighttime (*bottom*) flight missions over the Saudi Arabian Heat Low (From Blake et al. 1983)

tropospheric column. At night time, the heat low is essentially washed out and the downward motion and divergence extend to the lowest levels. This vertical structure of the vertical motion has important implications for the heat budget of the heat low.

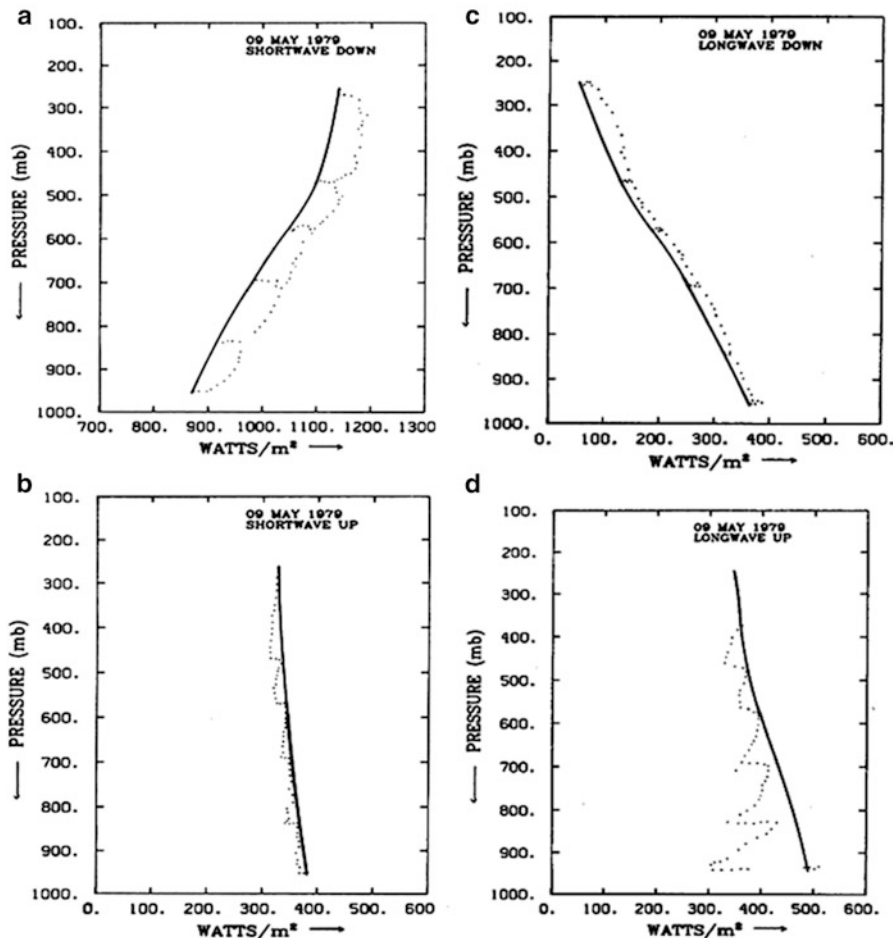


**Fig. 4.11** Example of daytime measurements of vertical profiles of (a) downward shortwave, (b) upward shortwave, (c) downward longwave, and (d) upward longwave irradiances over the Saudi Arabian Heat Low. Units in  $\text{W m}^{-2}$  (From Blake et al. 1983)

#### 4.2.3 Vertical Profiles of Radiative Transfer Over the Heat Low

A research aircraft is an excellent platform for providing vertical profiles of radiative fluxes. The lateral size of the heat low is roughly 700 by 300 km. This can be traversed and covered adequately by a 5–6 h flight. A NASA aircraft flew at the 237 mb level and stair-stepped down to 950 mb several times during the summer of 1979. This aircraft carried radiation measuring instruments (periheliometers and pyranemometers) that were mounted at the top and bottom. These measured the downward and upward fluxes of short and long wave irradiances. The stair-stepping provided vertical profiles of the radiative fluxes. Figure 4.11 illustrates the daytime

measurements of these vertical profiles. This data set is very important in our understanding of the heat budget of the heat low.

The solar constant,  $S_0$ , has an approximate value of  $1,370 \text{ W m}^{-2}$ . The incident solar radiation at the top of the atmosphere over the heat low would have a value less than that, since the solar radiation  $S$  is given by  $S = S_0 \cos \zeta$  where  $\zeta$  is the zenith angle. The zenith angle is derived by the relationship

$$\cos \zeta = \sin \varphi \sin \delta + \cos \varphi \cos \delta \cos H,$$

where  $\varphi$  is the latitude,  $\delta$  is the declination of the sun, and  $H$  is the local hour angle of the sun, measured from local noon. Obviously, the zenith angle varies by latitude, season, and hour of the day. At the flight level of 237 mb the value of  $S$  was  $1,100 \text{ W m}^{-2}$ . The lower value of  $S$  compared to the solar constant is due to the zenith angle at Saudi Arabia and to the absorption of solar radiation by the atmosphere above the 237 mb level. The downward directed solar radiation slowly depletes as we proceed down the vertical column. The solar radiation that eventually reaches the Earth's surface over the Empty Quarter is only  $870 \text{ W m}^{-2}$ . This depletion arises primarily from dust aerosols that absorb short wave radiation, and secondarily from atmospheric water vapor. The surface albedo over the desert heat low is around 40 %. Thus  $395 \text{ W m}^{-2}$  of the solar radiation is reflected back by the earth's surface. That diffuse radiation proceeds upwards and a part of it is absorbed by the dust aerosols and water vapor of the column.

The downward directed long wave radiation at the 237 mb level is very small (about  $20 \text{ W m}^{-2}$ ). The source of it is the long wave radiation emitted by the atmosphere between 237 mb and the top of the atmosphere. As we proceed down in the column, the downward directed long wave radiation increases because of the emissions from the column above any reference level. The amount that reaches the Earth's surface is around  $385 \text{ W m}^{-2}$ . This downward directed long wave radiation is contributed by the dust aerosols and the column of air above the ground. The surface radiative budget determines the top soil temperature, which, during the day time, is on the order of  $50^\circ\text{C}$ . The corresponding upward flux of longwave radiation is around  $500 \text{ W m}^{-2}$ . That upward directed longwave radiation again sees an absorption and reemission by the dust laden column of atmosphere above the ground. About  $340 \text{ W m}^{-2}$  pass upward at the aircraft flight level of 237 mb.

Imbedded in this story is the rate of warming or cooling of the atmosphere at any level of the atmospheric column. It is measured by the relation

$$\frac{\partial T}{\partial t} = -\frac{g}{C_p} \frac{\partial F}{\partial p},$$

where  $F$  denotes any one of the aforementioned fluxes. The total warming or cooling comes from adding all of the contributions from the long and short wave irradiances. Thus the rate of warming or cooling is generally expressed in units of  $^\circ\text{C/day}$ . The rates of warming for two daytime flights and an early morning

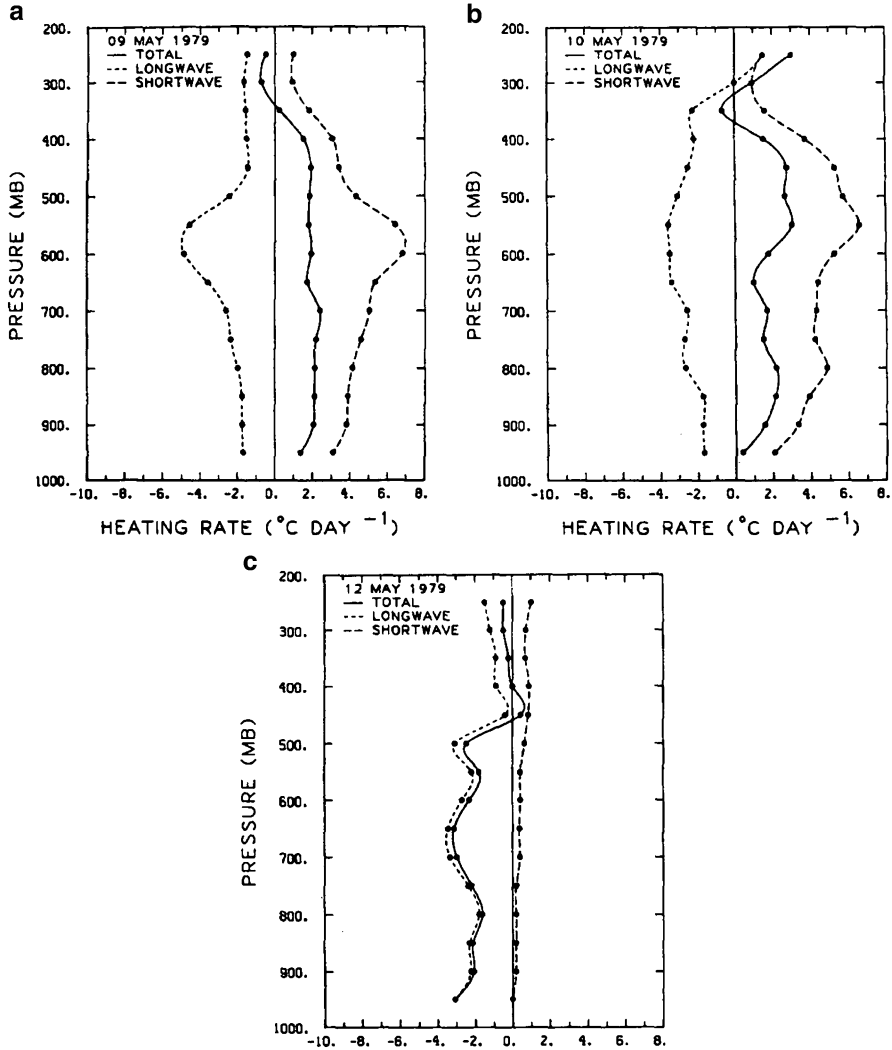


**Fig. 4.12** Vertical distribution of the longwave, shortwave, and net radiative heating (cooling) rates (a) 9 May, (b) 10 May, (c) 12 May (From Blake et al. 1983)

hour flight were calculated. In Fig. 4.12 we show these rates of warming as a function of pressure. In order to calculate this heating, one needs to calculate  $\partial F/\partial p$  over a layer of thickness  $\Delta p$ . The up and down fluxes from the aircraft observations were used over a layer 50mb deep. The results show an unusual warming by short wave radiation, which approaches  $6^{\circ}\text{C}/\text{day}$ . That rate of warming is largely attributed to the dust layer. The long wave cooling rate lies between 1 and  $2^{\circ}\text{C}/\text{day}$  and is uniform between the day and night hours. Thus one conclusion we can draw in reference to the heat budget of the air column above the heat low is that

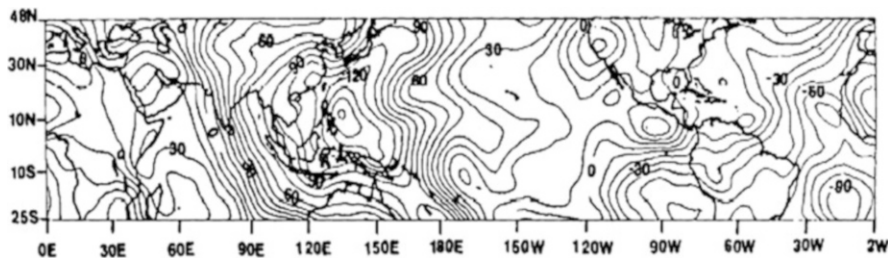


**Fig. 4.13** Observed 200 mb velocity potential averaged over the period 9–12 May, 1979. Units of  $10^{-6} \text{ m}^2 \text{s}^{-2}$  (Computed from NCEP-NCAR reanalysis)

short wave flux convergence contributes to a net warming of the column. The full story of the heat budget is addressed in the following section.

#### 4.2.4 Descent Above the Heat Low and Lateral Teleconnections

The descent over the heat lows often teleconnects to neighboring weather systems. The Saudi heat carries a substantial descending air that is known to teleconnect to the monsoons of South Asia. The 200 mb level velocity potential field is ideally suited for examining such teleconnections. Here we define the divergent wind by the equation

$$\mathbf{V}_\chi = -\nabla\chi$$

Following this sign convention, the divergent wind blows from high values of  $\chi$  towards low values of  $\chi$ . Figure 4.13 illustrates the velocity potential averaged over the period May 10 to May 12, 1979 when the heat low was prominently present over Saudi Arabia. The divergent outflows from the Asian Monsoon are clearly seen to teleconnect with the inflows over the region of the heat low at the 200 mb level. That air descends over the heat low. The adiabatic warming of the descending air sustains a warm column of air that in turn can remove (wash out) the superadiabatic layers that emanate from the strong surface heating of the desert. One of the inhibiting factors for these superadiabatic lapse rates is the divergence near the 850 mb level. Divergence generates stability thus counteracting the surface generated superadiabatic lapse rates. The descent from aloft contributes to the magnitudes of divergence at the 800 mb level. The process of stabilization by divergence is discussed in chapter X of this book.

The monsoonal teleconnection is unique for the Saudi Arabian heat low. Other heat lows generally teleconnect to the ITCZ in their vicinity. There is the question of why do such teleconnections occur in the first place. The monsoonal convection carries a large mass of ascending air. The compensating descent of mass generally occurs in the vicinity of the ascent. Such a dipole structure of ascent and descent is commonly seen for all scales of atmospheric divergent motions.

### 4.3 Heat Budget of the Heat Low

The heat budget of a heat low is computed over a domain of Arabia. The latitudinal spread of the domain is between x deg N and Y deg N the longitudinal spread extends from x deg E to Y deg E. This covers the general area of the surface heat low of Arabia. The period considered here is May 1979. The components of the heat budget i.e. the surface flux of sensible heat, surface flux of latent heat, downward flux of short wave radiation, reflected short wave radiation, downward flux of long wave radiation, the upward flux of the long wave radiation and the upper tropospheric import of moist static energy are all shown in Table 4.1a. Along the vertical layers covering 100 to 700, 700 to 400 and 400 to 100 hPa are considered here to portray a picture of the heat budget of the heat low. We next make use of the moist static energy equation (Equation 14.14, this is fully derived in chapter 14 section 14.3.2). In the flux form this equation can be written as:

$$\frac{\partial \overline{E_m}}{\partial t} = -\bar{\mathbf{u}} \cdot \nabla \overline{E_m} - \bar{\omega} \frac{\partial \overline{E_m}}{\partial p} - \frac{\partial}{\partial p} (\bar{\omega}' \overline{E'_m}) + LE_S + Q_{SEN} + Q_{RAD}$$

(symbols are explained in chapter 14, section 14.4.2)

**Table 4.1a** Heat budget of the Saudi Arabian heat low for the period May 1979. The units are in Watts/m<sup>2</sup>

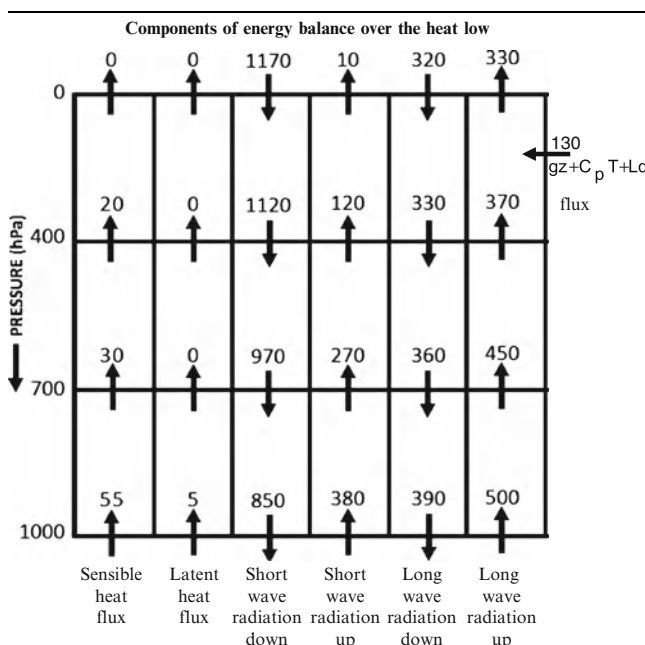
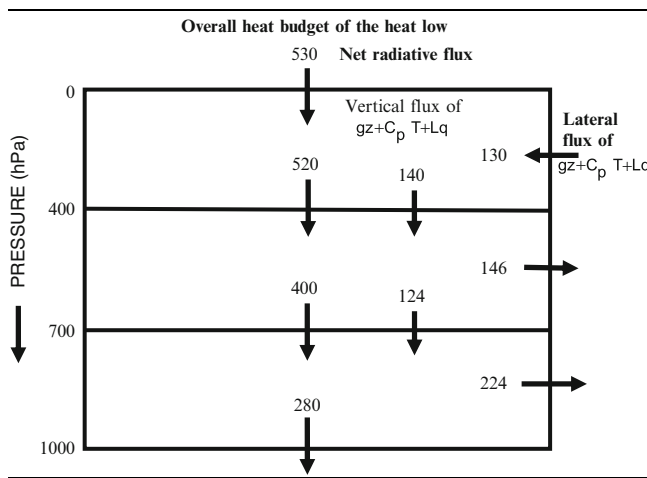


**Table 4.1b** Heat budget of the Saudi Arabian heat low for the period May 1979. The units are in Watts/m<sup>2</sup>



This equation is next integrated over the mass of each of these vertical layers. That integration provides the fluxes of the moist static energy across the horizontal and vertical boundaries of these layers. The complete heat budget of the heat low now includes the surface fluxes of sensible and latent heat, the net radiative flux components and the advection of the moist static energy are shown in Table 4.1b. That advection into the heat low comes mostly from the eastern wall, i.e. the monsoonal teleconnection. The downward fluxes of moist static energy at 400 and 700 hPa surfaces are respectively 140 and 124 W/m<sup>2</sup>. The lateral import of moist static energy in the upper troposphere is around 130 W/m<sup>2</sup>. The heat low exports a sizable amount of heat from Arabia. That export is largest near the 800 hPa level where the outflow layer of the heat low resides. All of this lower tropospheric export is largely across the southern wall towards the Arabian Sea. That contributes to the strength of the top of the Arabian Sea inversion layer. The net radiation carries the largest numbers starting at around 530 W/m<sup>2</sup> at the top (100 hPa level) and decreasing to 280 W/m<sup>2</sup> at the Earth's surface. The heat budget of the heat low requires an import of energy of around 130 W/m<sup>2</sup> from the monsoon for the maintenance of the thermal stratification that does not vary much from one day to the next.

The day-to-day maintenance of these soundings is a rather complex issue that requires an understanding of the balance among several entities, such as:

- Surface energy balance and related fluxes of sensible heat, long and short wave radiation
- The role of dust in the absorption of short wave radiation and its subsequent impact on the long wave radiation from the vertical air column

- The removal of superadiabatic lapse rates from the subgrid scale by dry convection and by the descent of upper tropospheric air.
- The teleconnection with the monsoon, where the compensating ascent is accounted for and from where a substantial input of energy ( $gz + C_p T + Lq$ ) occurs laterally at the upper troposphere into the region of the heat low.

## References

- Blake, D.W., Krishnamurti, T.N., Low-Nam, S.V., Fein, J.S.: Heat low over the Saudi Arabian Desert during May 1979 (Summer MONEX). *Mon. Weather Rev.* **111**, 1759–1775 (1983)
- Gill, A.E.: Some simple solutions for heat-induced tropical circulations. *Q. J. R. Met. Soc.* **106**, 447–462 (1980)
- Zhang, Z., Krishnamurti, T.N.: A generalization of Gill's heat-induced tropical circulation. *J. Atmos. Sci.* **53**, 1045–1052 (1996)

# Chapter 5

## Monsoons

### 5.1 Definition

The monsoons of the world are defined through the seasonal reversal of large-scale surface winds. The best place to see an illustration of this phenomenon is in the domain of the Indian Monsoon where the southwesterly surface winds of the summer monsoon get replaced by the northeasterly surface winds of the winter monsoon, as shown in Fig. 5.1.

The seasonal reversal of the monsoonal surface winds is not always very clear-cut – some instances, such as the Arizona-Mexico Monsoon, do not satisfy this definition, as will be discussed further in this chapter.

Another important feature of the monsoon is the heavy precipitation associated with the monsoon onset. This chapter shall address, in some detail, different stages of the monsoon season, and a number of aspects of the monsoonal circulations.

### 5.2 Monsoon Domain

Ramage (1971) defined a global monsoon domain based on the Asian, African and Australian monsoon systems. That domain is illustrated in Fig. 5.2. This illustration schematically portrays the surface wind reversal between the Winter Monsoon (relative to the Northern Hemisphere) shown by solid lines, and its Summer counterpart, shown by dashed lines.

Not shown in the above illustration are the domains of the American Monsoons. Those include the Arizona-Mexico monsoon of the Northern Hemisphere Summer months, and the South American Monsoon related to the semiannual continental pressure changes centered over Brazil.

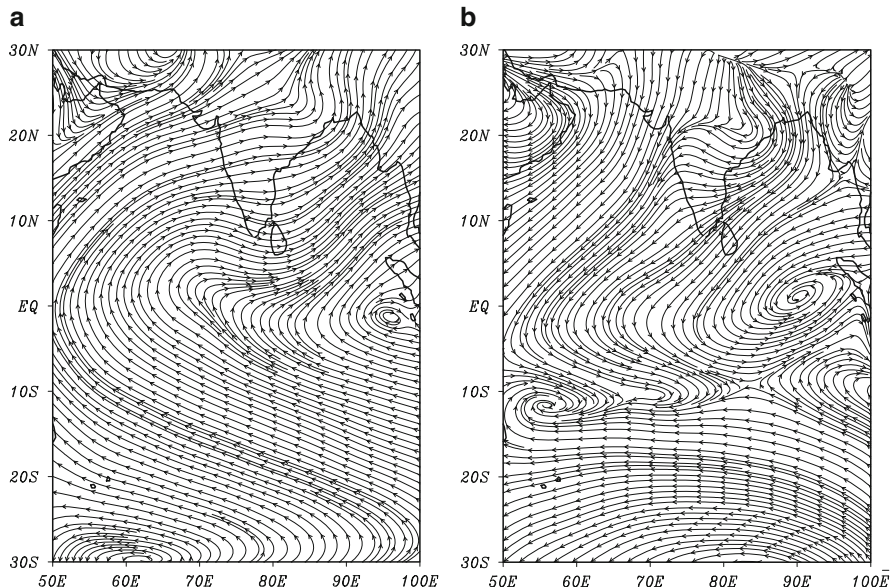


**Fig. 5.1** Climatological 925 mb streamlines over the Indian monsoon region for the month of (a) July, and (b) January (Computed from NCEP-NCAR reanalysis)

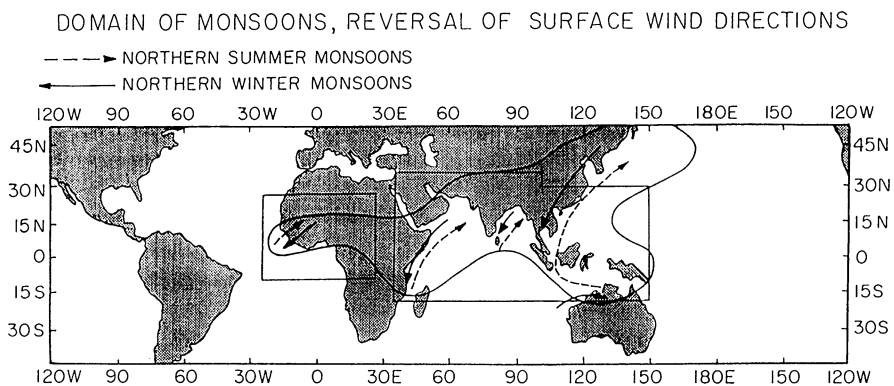


**Fig. 5.2** Domain of monsoons (After Ramage 1971)

### 5.3 Differential Heating and the Monsoon

The seasonal reversal of winds is known to be related to large-scale heat sources and sinks. In the case of the Asian Summer Monsoon, heavy rains north of 10°N over India, Indochina and China are associated with a belt of strong convective heating. Another source of heating in the region – often referred to as an ‘elevated heat source’ – is the Tibetan Plateau. This arises from the fact that the solar radiation is

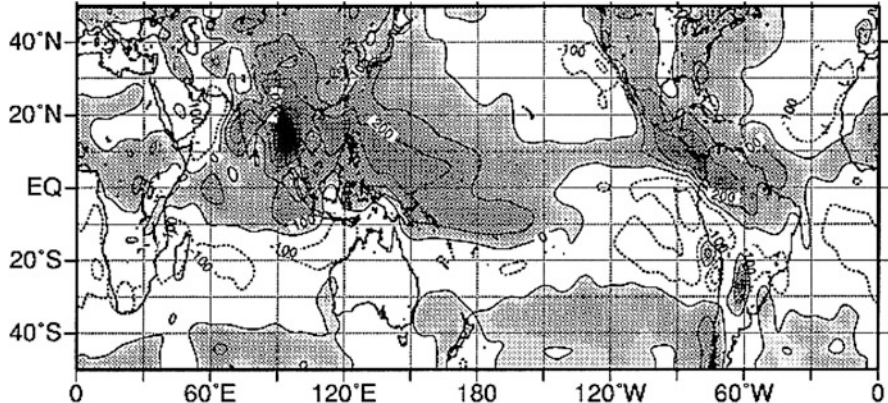


**Fig. 5.3** Vertically integrated apparent heat source ( $Q_1$ ) for a 15-year mean (1980–94) Northern summer season. Positive values are shaded. Units of  $\text{Wm}^{-2}$  (After Yanai and Tomita 1998)

absorbed by the elevated ground of the Plateau, resulting in significant upward sensible heat fluxes which are communicated further up through convection. The heat sink of the summer monsoon of Asia resides largely over the Mascarene High (around  $30^\circ\text{S}$  and  $60^\circ\text{E}$ ) and the southern part of the South China Sea, where the anticyclonic flows are associated with low-level divergence and descent and a net radiational cooling.

Figure 5.3 from a study by Yanai and Tomita (1998) illustrates the typical heat sources and sinks during the Northern Hemisphere summer season (June-July-August). This figure is based on a mapping of the vertically integrated apparent heat source  $Q_1$  derived from the first law of thermodynamics using atmospheric reanalysis data sets.

The apparent heat source  $Q_1$  is defined as  $Q_1 = \frac{d\bar{s}}{dt}$ , where  $\bar{s}$  is the dry static energy of the large-scale flow, *i.e.*  $\bar{s} = g\bar{z} + C_p\bar{T} + L\bar{q}$ . In this context, the bar indicates a large-scale ( $\sim 100$  km) averaged variable. The complete equation governing the change of dry static energy is given by

$$\begin{aligned} Q_1 &= \frac{d\bar{s}}{dt} \\ &= \frac{\partial \bar{s}}{\partial t} + \bar{\nabla}_H \cdot \nabla \bar{s} + \bar{\omega} \frac{\partial \bar{s}}{\partial p} \\ &= \bar{Q}_R + L(\bar{c} - \bar{e}) - \frac{\partial \bar{s}' \bar{\omega}'}{\partial p} \end{aligned}$$

Here  $\bar{\nabla}_H$  is the large-scale horizontal velocity vector,  $\bar{\omega}$  is the large scale vertical velocity,  $\bar{Q}_R$  is the large-scale averaged value of net radiation,  $\bar{c}$  and  $\bar{e}$  are the large-scale averages of condensation and evaporation, and  $-\frac{\partial \bar{s}' \bar{\omega}'}{\partial p}$  is the vertical eddy flux convergence of dry static energy by the sub-grid-scale processes.

In the absence of radiation, condensation, evaporation, and eddy flux convergence,  $Q_1 = 0$  and therefore the dry static energy (and the potential temperature) of large-scale flows is conserved. The more important case for Tropical meteorology is that of non-zero values of  $Q_1$ , which implies the presence of heat sources and sinks.  $Q_1$  is usually expressed in units of either  $\text{Wm}^{-2}$  or  $^{\circ}\text{C day}^{-1}$ . The radiative contribution to  $Q_1$  is generally on the order of  $1^{\circ}\text{C day}^{-1}$  (and is usually negative, *i.e.*, a net cooling). In most cloud-free areas that tends to be the leading term in the expression for the apparent heat source. In areas of deep convective systems, on the other hand, where convective heating and eddy flux convergence are the dominant terms,  $Q_1$  is on the order of  $10\text{--}50^{\circ}\text{C day}^{-1}$ .

The differential heating seen in Fig. 5.3 is responsible for the divergent vertical circulations with ascending lobes centered over the general regions of strong heat sources and descending lobes over the heat sink regions. Such circulations are best illustrated via the velocity potential and divergent wind (see Fig. 2.8 in Chap. 2).

## 5.4 A Principal Axis of the Asian Monsoon

At this stage it is important to recognize the seasonal migration of the heat source that ties in the Winter and Summer Monsoons. In the Northern Hemisphere winter, the belt of heavy monsoon rainfall is seen over Northern Australia, Southern Malaysia and Borneo. As the season advances, this belt of heavy rain shows a month-by-month northward progression. By the beginning of spring this belt is located over Central and Northern Malaysia. By early May it has migrated to Myanmar, and by the middle of June it arrives over the eastern foothills of the Himalayas. The rainfall amounts in these heavy precipitation belts are very large – on the order of  $3 \times 10^3 \text{ mm per season}$  (see Fig. 2.11 in Chap. 2). Figure 5.4, from Chang (2005), illustrates the seasonal propagation of the heat source associated with the heavy monsoonal precipitation between the months of July and February. The line described by the heat source locations in different months forms the principal axis of the Asian Monsoon.

## 5.5 Key Elements of the Asian Summer and Winter Monsoon

Some key features of the Asian Summer and Winter Monsoon are illustrated in Fig. 5.5. In this schematic, the lower tropospheric flow is represented by solid arrows, and the upper tropospheric flow is marked with dashed arrows.

In the summer season (left side of Fig. 5.5), note the following important features:

- (i) The Mascarene high of the Southern Hemisphere located near  $30^{\circ}\text{S}$  and  $60^{\circ}\text{E}$ .
- (ii) The southeast trade winds of the Southern Indian Ocean extending into a counterclockwise flow around the Mascarene high.

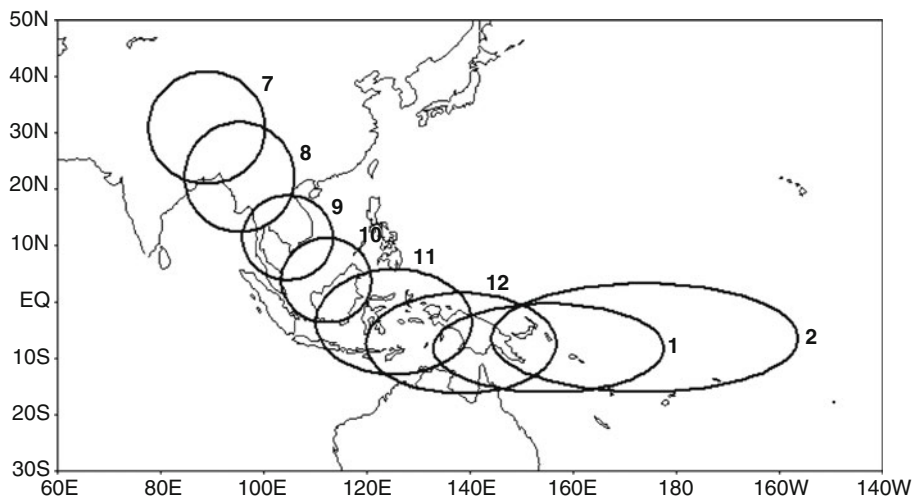


**Fig. 5.4** Propagation and extent of the monsoonal heat sources between the months of July (marked by a 7) and February (marked by 2) (After Chang et al. 2004)

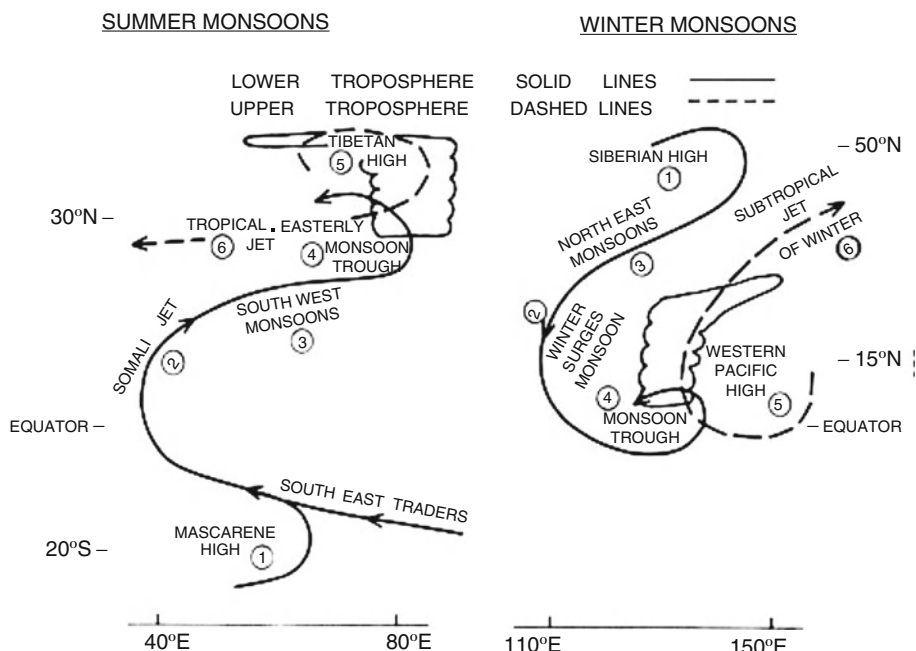


**Fig. 5.5** Schematic diagram of the summer (left) and winter (right) monsoon complex. Solid lines indicate lower tropospheric flow, dashed lines indicate upper tropospheric flow

- (iii) The cross-equatorial flow along the Arabian Sea shores of Kenya, east of the Kenya highlands, with southerly winds on the order of  $10 \text{ ms}^{-1}$ .
- (iv) The Somali Jet. This is a continuation of the cross-equatorial low-level flow as it exits to the east of the Horn of Africa. The Somali Jet is a major element of the Asian Monsoon. It carries westerly winds (as strong as  $50 \text{ ms}^{-1}$  on certain days) offshore from Northern Somalia over the Arabian Sea at an altitude of about 1 km above the ocean. The climatological seasonal mean winds of the Somali Jet are in excess of  $15 \text{ ms}^{-1}$ .
- (v) The southwesterly monsoonal flow over the Arabian Sea. This is a major element of the Asian Summer Monsoon. This southwesterly flow has two branches – one along  $15^\circ\text{N}$  and another one moving south towards the Central Arabian Sea and Southern India.
- (vi) The Monsoon trough of North-Central India between  $15^\circ\text{N}$  and  $25^\circ\text{N}$ . The southwesterly winds carrying moist air from the Arabian Sea and the Bay of Bengal flow counterclockwise around this trough.
- (vii) The heavy rains of the Indian Monsoon. The monsoonal precipitation is strongly influenced by the orography of the region. The heaviest rains occur along the eastern foothills of the Himalayas and at the western slopes of the Western Ghats that lie along the west coast of India.
- (viii) The Tibetan high. This is a major thermal high pressure system located in the upper troposphere above the Monsoon trough. Between the Monsoon trough at the surface levels and the Tibetan high of the upper troposphere resides a warm troposphere that is largely maintained by deep cumulus convection of the heavy monsoon rains and the heating of the Tibetan Plateau.
- (ix) The tropical easterly jet (TEJ) located near  $10^\circ\text{N}$  over the southern flanks of the Tibetan high.

The counterpart to the Summer Monsoon described above is the Winter Monsoon system (shown in the right side of Fig. 5.5), where the following features are of importance:

- (i) The Siberian high pressure system. This is a counterpart to the Mascarene high of the Summer Monsoon. Climatologically, the Siberian high is located near  $50^\circ\text{N}$  and  $125^\circ\text{E}$ . This is a region of significant heat sink in the troposphere of the northern hemisphere during winter.
- (ii) The northeasterly lower tropospheric flow. This can be regarded as a counterpart to the southeast trades of the Summer Monsoon.
- (iii) Wind surges carried by the northwesterly monsoonal flow seen along the western shores of the South China Sea. The winds in these surges can be as strong as  $15 \text{ ms}^{-1}$ , and are normally associated with cyclonic disturbances in the central part of the South China Sea. These winds are not quite as strong as those of the Somali jet.
- (iv) The Monsoon trough, located north of the equator in December and south of the equator in the months of January and February. The Monsoon trough is the

- locale of the heavy rains of the Winter Monsoon over Northern Australia, Southern Peninsular Malaysia and Borneo.
- (v) The West Pacific high. This is a counterpart to the Tibetan high. It resides over the region of heavy monsoon rains and is strongest near the 200 mb level.
  - (vi) The subtropical jet stream of winter (STJW). This is one of the strongest wind systems of the troposphere. It is located near the northern flanks of the West Pacific high, south of Japan.

## 5.6 Monsoon Onset and Withdrawal Isochrones

The annual cycle of passage of monsoon rains from Northern Australia to the eastern foothills of the Himalayas and back is an important component of the monsoon. This passage is best portrayed from isochrones of onset and withdrawal dates. Figure 5.6 illustrates how the isochrones of the onset dates of the monsoon progress northwestward between May and July. This northwestward progression seems to be strongly influenced by the semi-arid land surface in the northwest. The onset dates over Pakistan are relatively late since the monsoon has to work against the drying effect of the semi-arid land surface. Modeling of the monsoon onset isochrones has been successfully demonstrated in several forecasts although understanding of the land-atmosphere coupling involved is lacking. It does not seem that the isochrones' northwestward propagation is due to steering by the prevailing winds. The lower troposphere experiences southwesterly monsoonal flow while the upper troposphere sees northeasterly winds – a fact that speaks against a steering-by-winds argument.

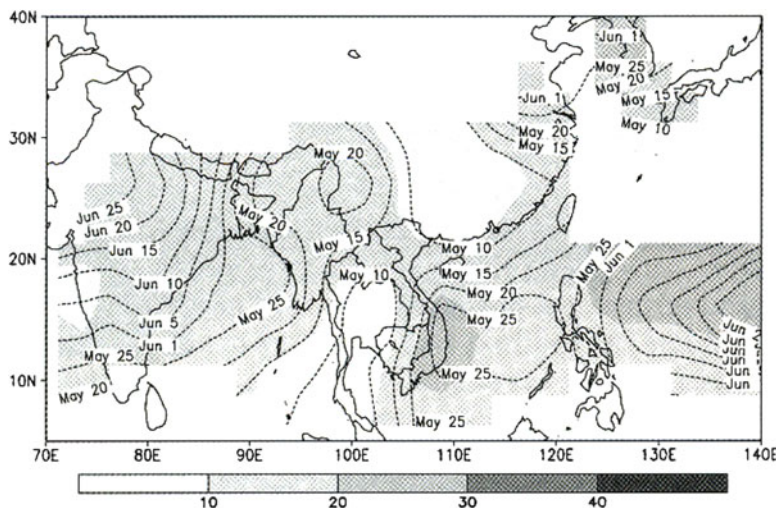


**Fig. 5.6** Climatological isochrones of onset of the Asian summer monsoon based on the period (1979–1999). Shading indicates the standard deviation (in days) of the onset date (From Janowiak and Xie 2003)

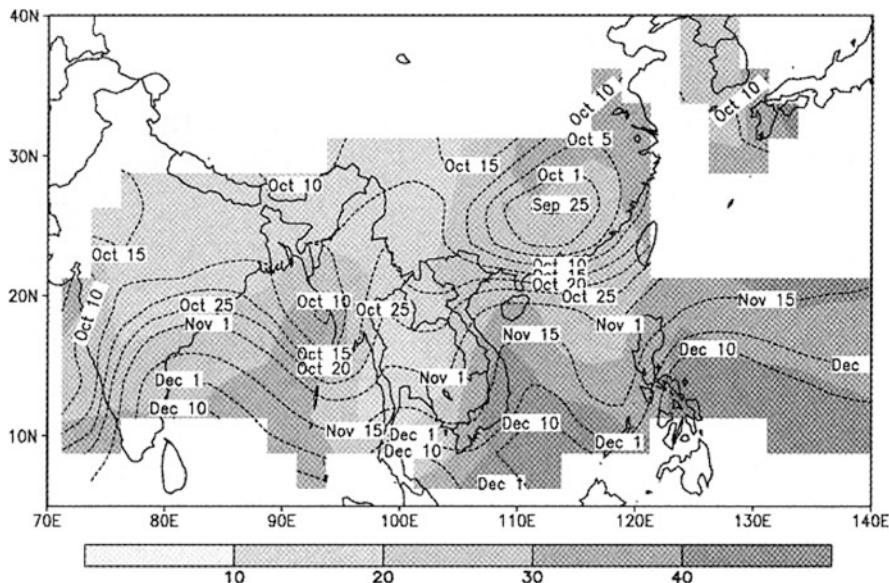


**Fig. 5.7** Climatological isochrones of withdrawal of the Asian summer monsoon based on the period (1979–1999). Shading indicates the standard deviation (in days) of the onset date (From Janowiak and Xie 2003)

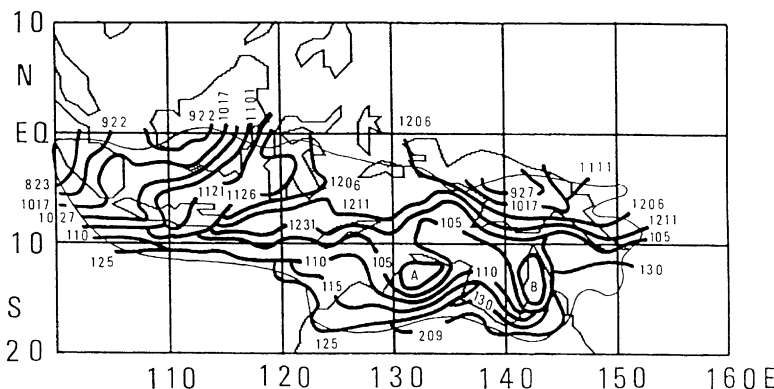


**Fig. 5.8** Isochrones of monsoon onset over the Maritime Continent (From Tanaka 1994)

The dates of withdrawal of the Asian monsoon are shown in Fig. 5.7. What is seen here is a reverse propagation of the last monsoon rainfall, moving from the northwest to the southeast towards Indonesia.

The onset and retreat of the monsoon across the Maritime Continent can be seen in Figs. 5.8 and 5.9 taken from Tanaka (1994). In the Maritime Continent region, as one proceeds from the Northern Hemisphere summer to the Northern Hemisphere

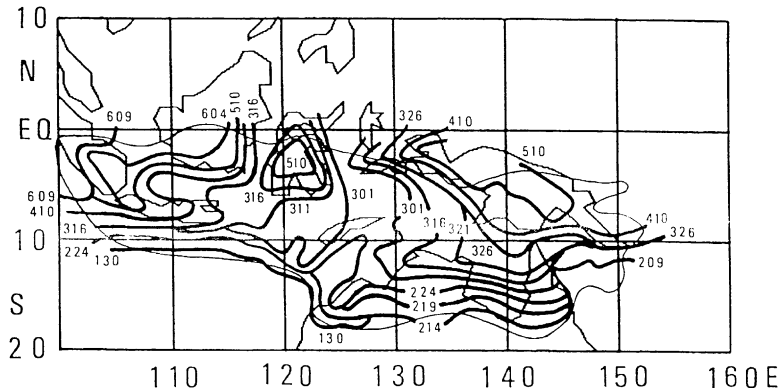


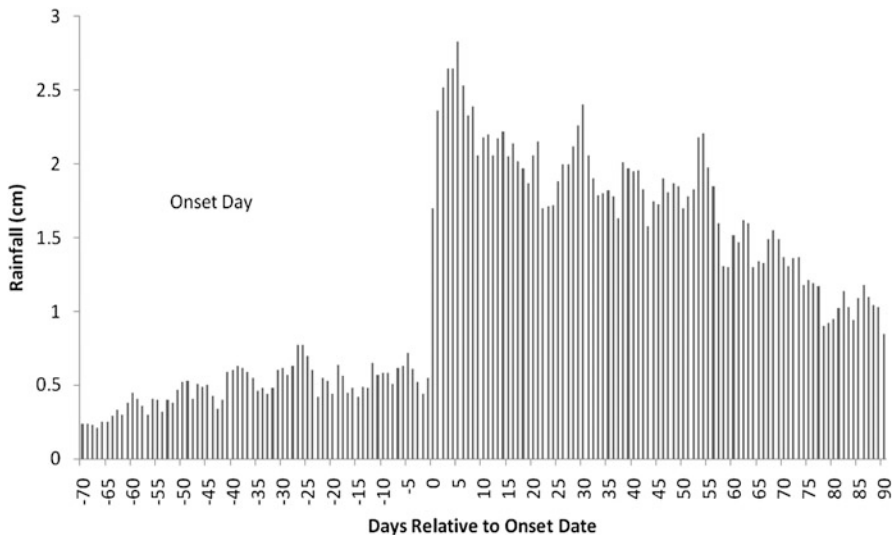
**Fig. 5.9** Isochrones of monsoon withdrawal over the Maritime Continent (From Tanaka 1994)

winter, the isochrones of monsoon onset move southwards. The converse is the case for the transition from summer to winter monsoon. Figures 5.8 and 5.9 illustrate, respectively, the isochrones for the dates of the onset and withdrawal of monsoon rains from Tanaka's study. Here the three (four) digit numbers MDD (MMDD) denote M (MM) for the month and DD for the day. The complex nature of isopleths as they march across the region is due to the topography, equatorial passage, and the influence of neighboring oceans.

In a recent study Krishnamurti et al. (2012) examined the modeling sensitivity to various parameters for the northward march of the onset isochrones related to the establishment of monsoon over India. To the south of the isochrone the atmosphere carried a large population of deep convective clouds and a deep moist layer (between the surface level to nearly 400 hPa level) The spring season dryness north of the isochrone was slowly wetted by stratiform rains from the anvils of clouds. That results in an increase of buoyancy, increase of soil moisture and the growth of clouds to the north where there were few clouds previously. The northward steering of the isochrone was largely carried out by the northward directed divergent circulation of the local Hadley cell. The CLOUDSAT imagery is very useful to look at the time history of the meteorological asymmetry across the onset isochrone.

## 5.7 Features of the Monsoon Onset

Almost every year, a spectacular onset of summer monsoon rains occurs over the southwest coast of India, in the province of Kerala. This feature is generally seen during the first week of June. The variability of the onset date over Kerala is on the order of 1–2 weeks at most. Because of this variability from 1 year to the next, it is useful to construct a composite at day 0 (the date of onset) and days prior to or after that date. Such a composite using 80 years of daily rainfall data is shown in



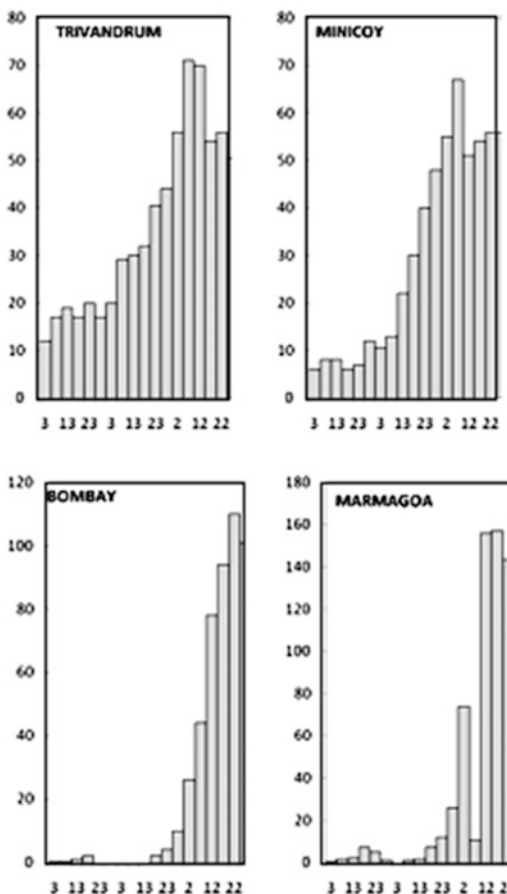
**Fig. 5.10** Composite climatology of daily rainfall amount as a function of time before or after onset date over Kerala (After Ananthakrishnan and Soman 1988)

Fig. 5.10. The ordinate denotes daily rainfall totals and the abscissa shows the composite time relative to the onset date. The sudden and dramatic jump in precipitation illustrates the spectacular nature of the monsoon onset.

If one were to simply perform a calendar day average using many years of data, one would still see the rapid increase of rain as the onset occurs, although the picture would be less dramatic. Examples of such calendar-day averaged precipitation amounts for four rainfall sites over the southwest coast of India are shown in Fig. 5.11. Two of the sites, Marmagao and Bombay (Mumbai), clearly display a spectacular onset of monsoon around June 2 and June 12 respectively. The other two sites, Trivandrum and Minicoy, display a slower increase of rainfall through late May and early June. Similar features are noted in most other regions where monsoon onset occurs. Figure 5.12, based on Raj (1992), illustrates the onset of winter monsoon rain over the southwest coast of India during the month of November. Here again we see a spectacular onset of winter monsoon rain when the compositing is done with respect to the onset day using some 90 years of data.

## 5.8 Onset of Monsoon and the Wall of Moisture from the South

The arrival from the south of a wall of moisture at the time of Monsoon onset was first documented from satellite data sets, Joshi et al. (1990), including from water vapor imagery. Recent advances in four-dimensional data assimilation have made it



**Fig. 5.11** Climatological precipitation amounts as a function of calendar date for four sites. Units of mm day<sup>-1</sup> (After Krishnamurti 1979)

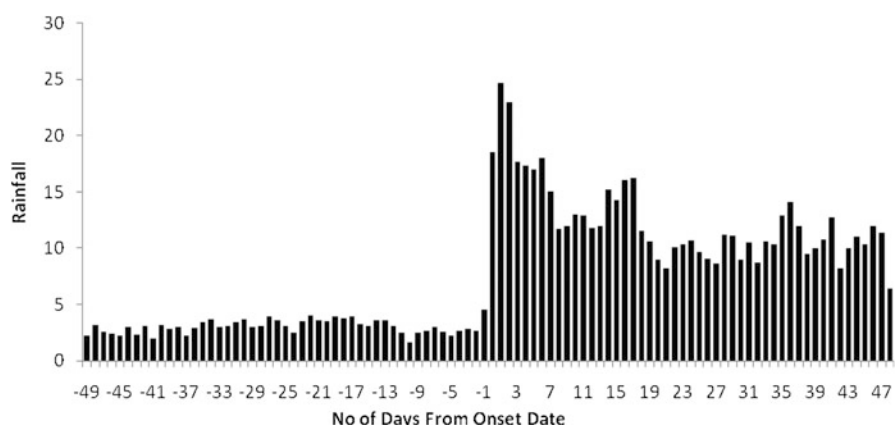


**Fig. 5.12** Composite climatology of daily rainfall amount as a function of time before or after onset date over Tamil Nadu (After Raj 1992)

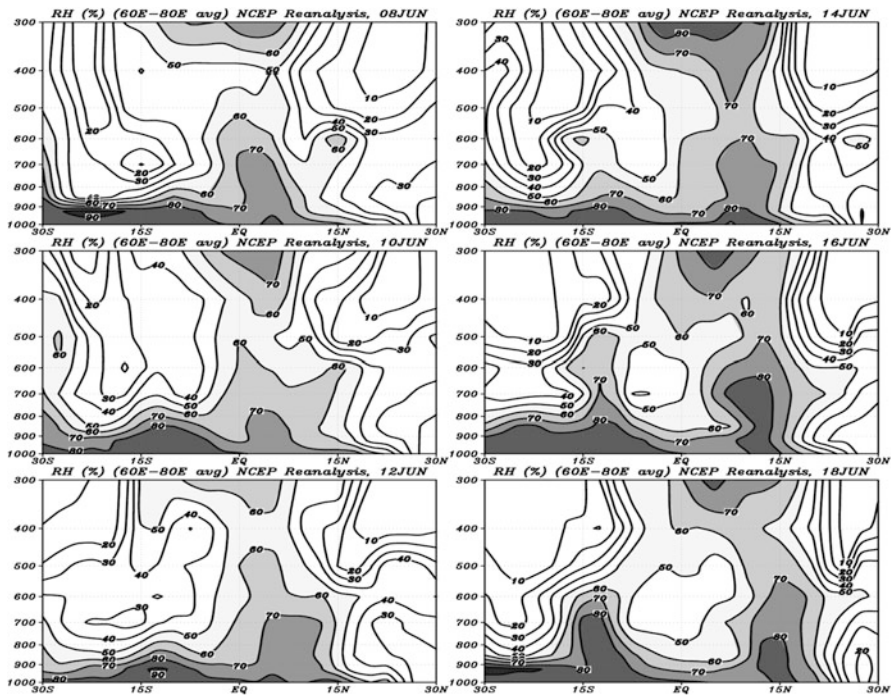


**Fig. 5.13** A sequence of daily latitude-pressure cross-sections of relative humidity values (in %), averaged between  $60^{\circ}\text{E}$  and  $80^{\circ}\text{E}$  for the period 08 June 1979–18 June 1979 (Computed from NCEP-NCAR reanalysis)

possible to obtain somewhat realistic daily analyses of moisture making it possible to see this feature on a daily basis.

Figure 5.13 shows a series of meridional cross sections of relative humidity from NCEP reanalysis covering the period June 8, 1979 through June 18, 1979 (12 UTC) at intervals of every 2 days. This is a vertical cross section in the meridional plane of a zonal average between  $60^{\circ}\text{E}$  and  $80^{\circ}\text{E}$ . The relative humidity is contoured at 10 % Intervals; values higher than 60 % are shaded. One can clearly see a vertical wall of moisture moving north from roughly  $5^{\circ}\text{N}$  to  $15^{\circ}\text{N}$  during this 11 day period. The onset of Monsoon rains in 1979 occurred around June 8th at Kerala ( $8^{\circ}\text{N}$ ), and made it to  $15^{\circ}\text{N}$  by the 16th of June. This meridional passage of a vertical wall of moisture is an annual feature during the onset of monsoon. The passage of moisture and the stronger winds during the onset period result in low-level convergence of moisture flux ahead of the wall that contributes to the water budget of the heavy rains.

## 5.9 Cooling of the Arabian Sea Following the Onset of Monsoon

The monthly mean sea surface temperatures of a large area of the Arabian Sea show a marked cooling between the months of May through July of each year. Observations show that this cooling follows the onset and the strengthening of surface winds.

The buildup of strong low-level zonal winds over the Central Arabian Sea following the onset of monsoon results in a stronger zonal wind stress which can be expressed by the bulk aerodynamic formula  $\tau_x = -C_d \rho_a (u^2 + v^2)^{1/2} u$ , where  $u$  and  $v$  are the surface wind components in the zonal and meridional directions,  $C_d$  is the surface bulk aerodynamic drag coefficient, and  $\rho_a$  is the surface air density. The rate of near-equatorial upwelling can be expressed by,  $w_s = -\frac{\beta \tau_x}{r^2 \rho}$ , where  $\beta = \frac{\partial f}{\partial y}$ . The increased wind stress associated with the strengthening monsoonal winds causes stronger upwelling, which in turn translates into an influx of cooler water into the surface layer.

During the Global Weather Experiment a number of surface- as well as space-based observing systems provided valuable data sets. Over the region of the Arabian Sea during the First GARP Global Experiment (FGGE), the relevant observing platforms included: geostationary satellites providing high-resolution low cloud motion vectors; research aircraft providing dropwindsonde data; constant level balloons providing meteorological information at the 1 km level; the world Weather Watch network providing surface and upper air observations; the merchant ships providing a vast collection of marine data collected; and FGGE research ships providing meteorological as well as oceanographic observations.

Shown here are results on the cooling of the Arabian Sea based on data sets for a 17-day period between June 11 and June 27, 1979, when the data density was largest, due to the activities of the GARP Monsoon Experiment over the Arabian Sea and the Indian Ocean. Another important feature of this period was the rapid cooling of the Arabian Sea captured in these data sets (Düing and Leetmaa 1980) during June, July and August. Here we shall explore the role of the strong winds during the onset with respect to this phenomenon.

Shown in Fig. 5.14 is a typical streamline/isotach chart with the cloud winds observations during FGGE. It illustrates the data density and flow features over the Arabian Sea on a representative day. The wind speeds (units of  $\text{ms}^{-1}$ ) are shown as dashed lines. During this time the Arabian Sea low-level monsoon flows were well established, and a monsoon depression was evident over the northern Bay of Bengal.

A number of ships participated in the GARP Monsoon Experiment; Fig. 5.15 illustrates the time variability of winds and sea surface temperatures measured by one of them. Within a matter of a day or two after the onset of strong winds around June 11, 1979, the sea surface temperatures exhibit a drop in temperature by 2–3°C. The remaining ships measured very similar histories. This rapid response of the ocean to the strong monsoon winds occurs not only near the western Arabian Sea

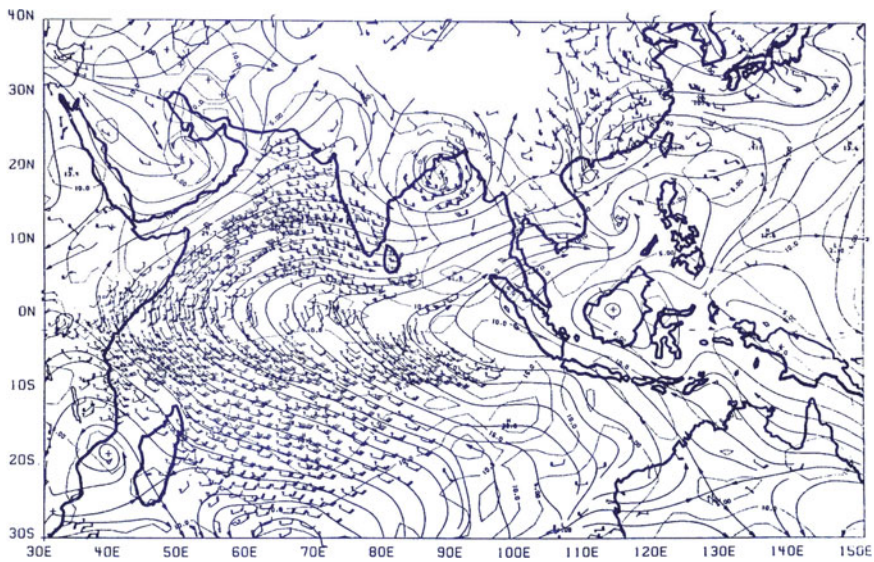


**Fig. 5.14** A typical streamline (solid lines) and isotachs (dashed lines) chart during the Earth Radiation Budget Experiment (ERBE). Space and surface observations plotted as wind barbs

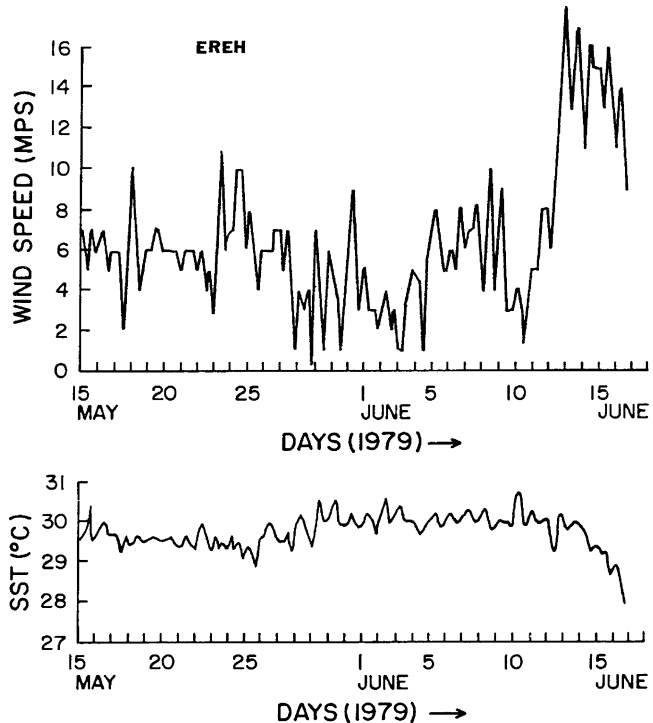


**Fig. 5.15** Sea level wind speed ( $\text{ms}^{-1}$ , top) and SST ( $^{\circ}\text{C}$ , bottom) measured by ship EREH, located at 0N, 49E between 16 May and 25 May, 1979, and at 7N 66.3E between 1 June and 16 June, 1979 (After Krishnamurti 1985)

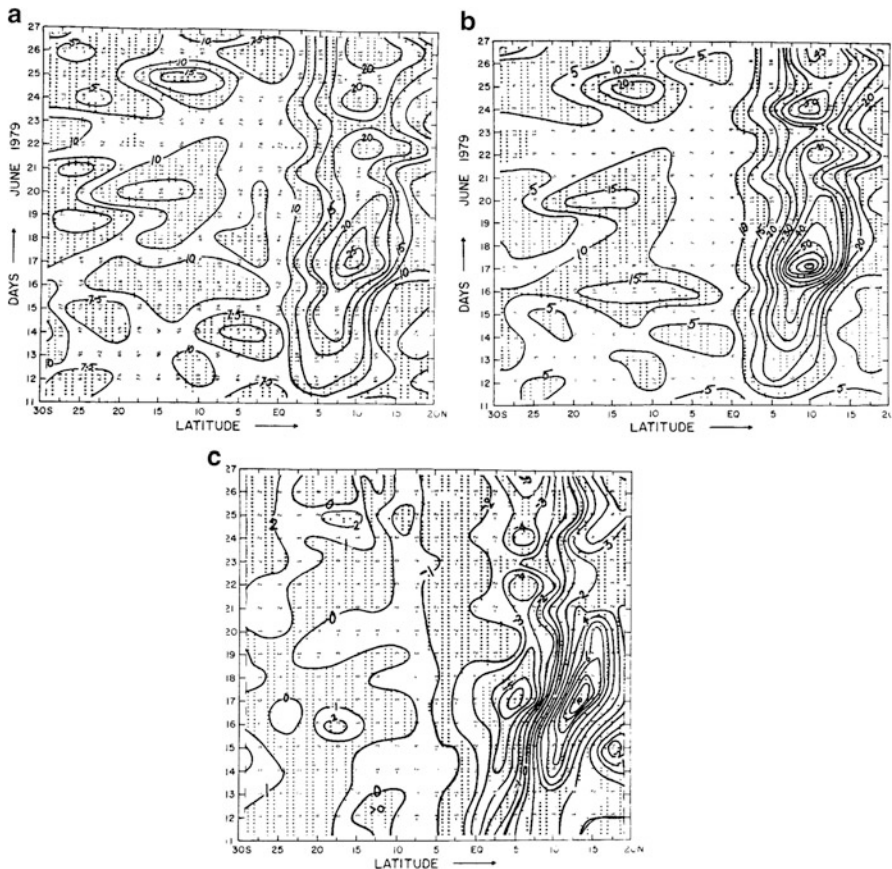


**Fig. 5.16** Time-latitude distribution of the 55E–70E averaged (a) surface wind speed ( $\text{ms}^{-1}$ ), (b) surface wind stress ( $\times 10^{-3} \text{Nm}^{-2}$ ), and (c) wind stress curl ( $\times 10^{-7} \text{Nm}^{-2}$ ) (After Krishnamurti 1985)

over the region of the Somali jet near Socotra, but also much farther east near 60°E. During this period a tropical cyclone – named the Onset Vortex – formed over the Arabian Sea and covered the period June 14 to June 20, 1979. It started as a tropical depression that became a tropical storm with winds as large as 60 knots during the onset period over the Eastern and Central Arabian Sea. This onset vortex was likely a prime contributor to the initiation of the cooling of the Arabian Sea during the summer of 1979 and also during many other years. Over open oceans, quite far away from the Somali and the Arabian upwelling regions, the winds associated with this tropical storm, as well as the eastward extension of the low level jet, together contributed to large magnitudes of wind stress and the wind stress curl.

The most striking feature during the 17 days is the evolution of the strong winds with the onset of the monsoons in this region was the presence of the onset vortex (Krishnamurti et al. 1981). The strongest zonally averaged surface winds (Fig. 5.16a), 25  $\text{ms}^{-1}$  (about 50 knots) on the 17th are attributed to the strong

monsoonal flows as well to the presence of the onset vortex. Between the 11th and 17th of June, strong winds build up and thereafter they prevail around  $10^{\circ}\text{N}$ . The intensity of the southeast trades around  $20^{\circ}\text{S}$  is of the order of  $10 \text{ ms}^{-1}$ . The trades exhibit considerable fluctuations in their intensity. The wind stress (Fig. 5.16b), computed via the bulk aerodynamic formula, acquires magnitudes as large as  $0.65 \text{ Nm}^{-2}$  during the onset period and thereafter remains as large as  $0.4 \text{ Nm}^{-2}$  around  $10^{\circ}\text{N}$ . Over the region of the southeast trades the wind stress fluctuates between  $0.05$  and  $0.15 \text{ Nm}^{-2}$ . Overall, the most spectacular feature in this time latitude section is the evolution of the monsoon, which overwhelms the trade winds.

As is to be expected, the equatorial belt (which lies between the southeast trades of the winter hemisphere and the southwest monsoons of the summer hemisphere) has the smallest wind stress. Figure 5.16c illustrates the corresponding evolution of the wind stress curl. Over the region of the monsoons, the strong belt of wind stress is divided into a positive and a negative wind stress curl field. The wind stress curl acquires its largest magnitude (about  $10^{-6} \text{ Nm}^{-3}$ ) around  $12.5^{\circ}\text{N}$ ; this is about an order of magnitude larger than the values in the trade wind belt. The latter also exhibits regions of positive (around  $20^{\circ}\text{S}$ ) and negative (around  $7.5^{\circ}\text{N}$ ) belts of the wind stress curl. The extremely large values of the wind stress curl are quite analogous to magnitudes one finds during tropical storm passage. The region south of the onset vortex experiences very strong winds due to the superposition (as well as the interaction) of the vortex and the mean flow.

Another latitude/time section was constructed from the available marine and ship observations of the sea surface temperatures. This is illustrated in Fig. 5.17. The most striking feature of this diagram is the evolution of the cold temperatures over the region of the strong positive wind stress curl, again somewhat reminiscent of the cooling of tropical oceans in the wake of hurricanes. Sea surface temperatures (SST) are coldest in the winter hemisphere. The trade wind belt exhibits small oscillations in the amplitude of SST variation. On the other hand, around  $10\text{--}15^{\circ}\text{N}$ , SST values drop from  $30^{\circ}\text{C}$  to around  $17.5^{\circ}\text{C}$  over the zonal belt between  $50^{\circ}\text{E}$  and  $70^{\circ}\text{E}$ . The centers of cooling appear to respond to strong winds very quickly.

At around  $10\text{--}20^{\circ}\text{N}$  between June and August, the sea surface temperatures are known to increase over the Atlantic and Pacific Oceans. The anomalous situation over the Indian Ocean, where a cooling is known to occur almost every year, has been a subject of great interest to monsoon oceanographers and meteorologists (Düing and Leetmaa 1980). There are a number of possible mechanisms that can contribute to the cooling of the Arabian Sea:

- (i) The onset of monsoons brings in extensive cloud cover with large amounts of high-level cirrus over the Arabian Sea. This acts to diminish the incoming solar radiation. The cooling of the Arabian Sea is generally not attributed to this effect because the oceanic response to solar radiation has a lag of 1–2 months, while the observed cooling starts almost immediately after the onset of strong winds.
- (ii) Southward flux of heat by ocean currents is contributed by clockwise oceanic eddies over the western Arabian Sea. This was estimated by Düing and

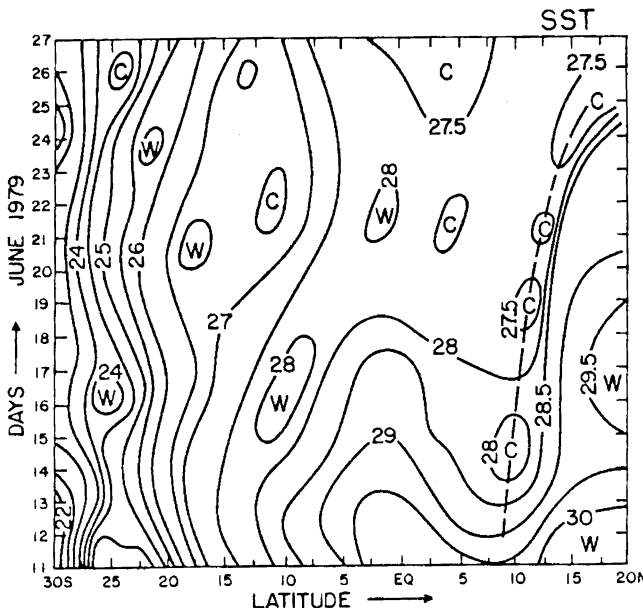


**Fig. 5.17** Time-latitude distribution of the  $55^{\circ}\text{E}$ – $70^{\circ}\text{E}$  averaged sea surface temperature ( $^{\circ}\text{C}$ ) (After Krishnamurti 1985)

- Leetmaa (1980). The related cooling of the northern Arabian Sea by the equatorward transport appears to be quite small.
- (iii) Coastal upwelling and downstream shedding of cold eddies: the premise that pockets of cold anomalies form in the Somali and Arabian upwelling regions and are advected eastward by the broadscale Somali currents is a possibility. There is some evidence of that from satellite observations. The rapid response of SST to the rapid evolution of strong winds in the central and eastern Arabian Sea during the onset precludes this possibility since this requires an eastward advective speed of the cold pockets, from the upwelling regions off the east African coast, comparable to the wind speeds in the low-level atmospheric jet. The oceanic advection is known to be much smaller.
  - (iv) Strong evaporation in the region of strong winds is a possible candidate. However, again, the available budgets of evaporative cooling do not favor such an intense cooling. This effect needs to be assessed in detail with the boundary layer humidity flux measurements for disturbed and undisturbed conditions. The sea state over this region is highly turbulent during the onset of monsoons. Flights made with low-level aircraft find a very large number of white caps with a greenish water color, indicating almost hurricane force surface winds during the passage of the onset vortex. With the large sea spray and strong winds, it is conceivable that evaporative cooling was underestimated in the past.

- (v) Strong wind stress-induced upwelling over the mid-ocean: Over the Central and Eastern Arabian Sea ( $50\text{--}70^{\circ}\text{E}$ ) around  $10^{\circ}\text{N}$ , a rapid cooling of sea surface temperatures occurs a day or two after the commencement of strong winds. The axis of cooling on a latitude time section coincides with the axis of the strongest positive wind stress curl.

## 5.10 Some Onset-Related Dynamical Fields

It is possible to break down the daily winds  $\vec{V}_H$  into a rotational ( $\vec{V}_\psi$ ) and a divergent ( $\vec{V}_\chi$ ) part, i.e.,  $\vec{V}_H = \vec{V}_\psi + \vec{V}_\chi$ . The corresponding kinetic energies of these components are  $\frac{1}{2}(\vec{V}_\psi \cdot \vec{V}_\psi)$  and  $\frac{1}{2}(\vec{V}_\chi \cdot \vec{V}_\chi)$ . As the Monsoon onset occurs, the lower tropospheric flow of the monsoon over the Arabian Sea shows a large increase of the wind magnitude  $|\vec{V}_H|$ . This increase is largely due to a strengthening of the rotational component  $|\vec{V}_\psi|$ . Over large areas of the Arabian Sea the maximum winds increase from roughly  $5\text{ ms}^{-1}$  to almost  $15\text{ ms}^{-1}$ . This leads to a manifold increase of the total kinetic energy  $K$ . Since the winds are dominated by the rotational component, a substantial part of total kinetic energy increase stems from the rotational kinetic energy  $K_\psi$ . This rapid increase of  $K$  and  $K_\psi$  seems to occur roughly 4–7 days prior to the occurrence of heavy rains over the west coast of India. Figure 5.18 illustrates the time histories of 700 mb  $K_\psi$  and  $K_\chi$ , area-averaged

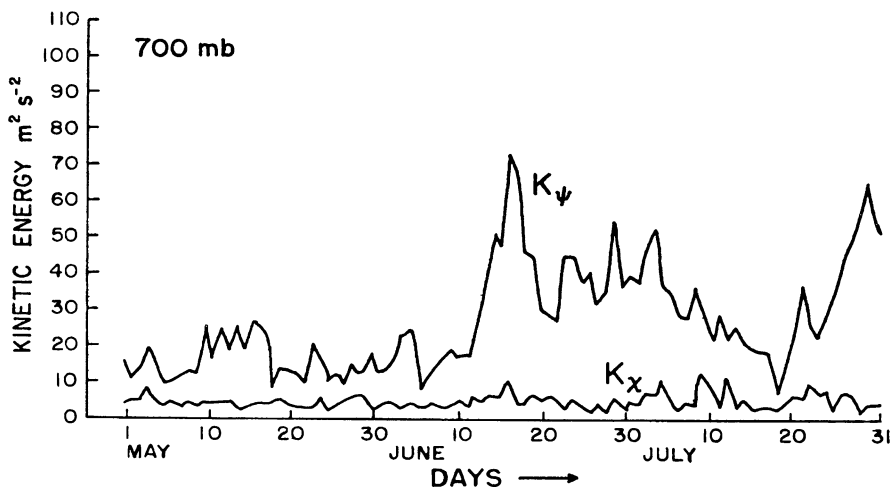


**Fig. 5.18** 700 mb rotational ( $K_\psi$ ) and divergent ( $K_\chi$ ) kinetic energy averaged over  $50^{\circ}\text{E}\text{--}120^{\circ}\text{E}$  and  $0^{\circ}\text{N}\text{--}20^{\circ}\text{N}$  prior for the period 1 May to 31 July 1979. The monsoon onset occurs on 17 July (After Krishnamurti and Ramanathan 1982)

between 50°E and 120°E and 0–20°N, before, during and after the onset of monsoon rain for the year 1979.

This figure shows the dramatic increase of  $K_y$  at the time of onset date of June 17th over the region. The rotational kinetic energy  $K_y$  averaged over a monsoon domain can be regarded as an empirical predictor for the onset of monsoon rain.

Another interesting aspect of the Monsoon onset is the increase of kinetic energy on a planetary scale. In order to demonstrate this, one can consider the kinetic energy of different zonal wave numbers for different days as the onset occurs. A first step in such an exercise is to take the zonal ( $u$ ) and meridional ( $v$ ) winds along a latitude circle as a function of longitude  $\lambda$  and expand them into Fourier series in the zonal direction, i.e.,  $u(\lambda) = \sum_{n=0}^N u_n e^{in\lambda}$  and  $v(\lambda) = \sum_{n=0}^N v_n e^{in\lambda}$ , where  $u_n$  and  $v_n$  are the Fourier coefficients for the  $n$ -th wave number. Thus  $u_0$  and  $v_0$  denote wave number zero, i.e., the zonal mean;  $u_1$  and  $v_1$  denote zonal wave number 1 of the zonal and meridional wind respectively, and so on. This Fourier expansion is done at one vertical level and one latitude circle at a time. After such a breakdown of the wind into its harmonic components, one can average these through the depth of the troposphere and over a belt of tropical latitudes (such as 0–30°N). The average kinetic energy for a particular wave number  $n$  is expressed by

$$\overline{\overline{K}_n} = \frac{1}{\int_{p_T}^{p_S} \int_{y_1}^{y_2} \int_{\lambda}^{\lambda} d\lambda dy dp} \int_{p_T}^{p_S} \int_{y_1}^{y_2} \int_{\lambda}^{\lambda} \frac{u_n^2 + v_n^2}{2} d\lambda dy dp$$

This has units of  $\text{m}^2\text{s}^{-2}$ . Fig. 5.19a–c illustrates the explosive growth of the kinetic energy contained at planetary scales (i.e., wave number 1) as the onset occurs. Shown here are the spectra for pre-onset (6 June, 1979), onset (18 June 1979) and post-onset (28 June 1979). This shows that the monsoon pronouncedly manifests on a planetary scale. This planetary scale can also be seen from the illustration of the divergent wind in Fig. 2.8.

Yanai (1992) noted a reversal of the meridional temperature gradient  $\frac{\partial T}{\partial y}$  as yet another indicator of the onset of monsoon. The meridional temperature gradient for the 200–500 mb layer between 5°N and 25°N is generally negative prior to the month of May, as seen in Fig. 5.20. This temperature gradient reverses sign and becomes positive around the period of onset of monsoon over Myanmar and the South China Sea (roughly 85–110°E). A similar reversal of temperature gradient is also seen at the longitudes of India (70–85°E) during early June. The practical utility of the parameter  $\frac{\partial T}{\partial y}$  as a forecast tool needs examination.

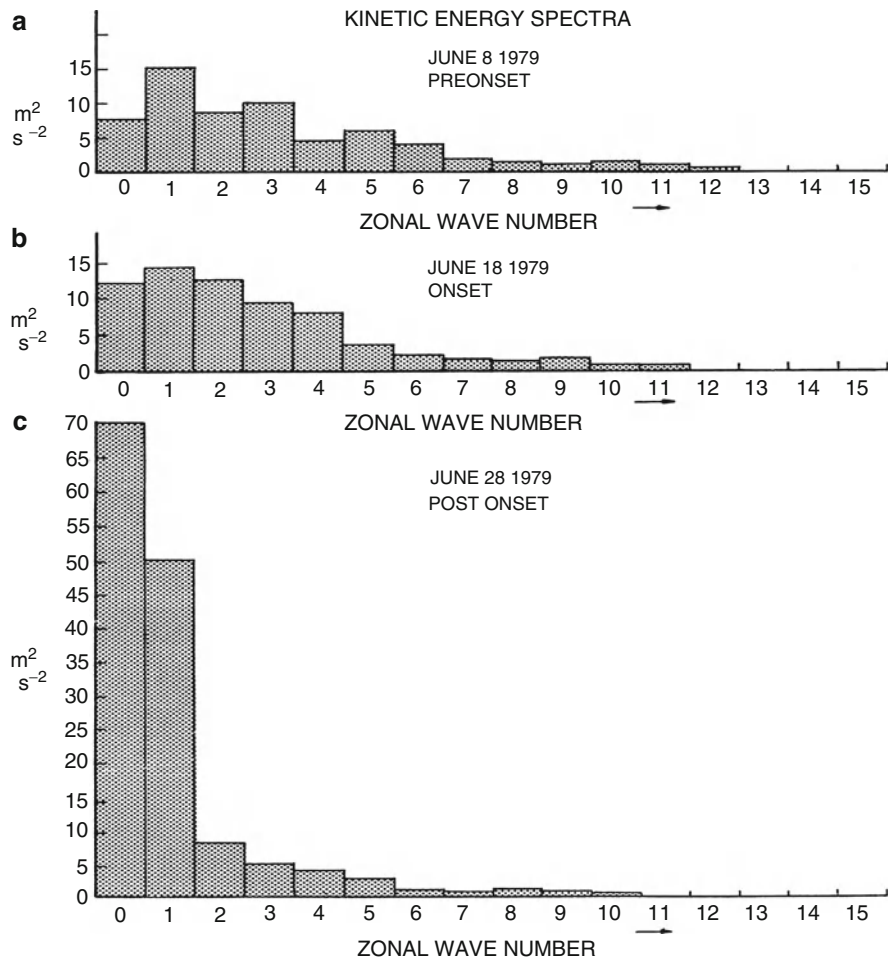


**Fig. 5.19** Kinetic energy spectra as a function of zonal wave number for (a) pre-onset, (b) onset, and (c) post-onset of monsoon. Units of  $m^2 s^{-2}$  (Computed from NCEP-NCAR reanalysis data)

## 5.11 $\psi\chi$ Interactions

The framework of  $\psi\chi$  interactions is a powerful tool for the understanding of the role of differential heating in the driving of the monsoon. In order to address the  $\psi\chi$  interactions, we start with:

- (i) The vorticity equation:

$$\frac{\partial \zeta}{\partial t} + \vec{V}_H \cdot \nabla(\zeta + f) + \omega \frac{\partial \zeta}{\partial p} + (\zeta + f) \nabla \cdot \vec{V}_H + \vec{k} \cdot \nabla \omega \times \frac{\partial \zeta}{\partial p} = F_\zeta \quad (5.1)$$

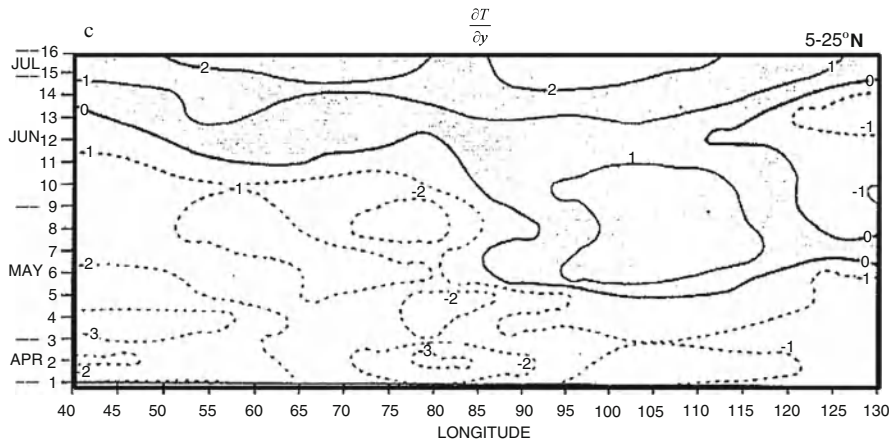


**Fig. 5.20** Meridional temperature gradient  $\frac{\partial T}{\partial y}$  between April and July, averaged between  $5^{\circ}\text{N}$  and  $25^{\circ}\text{N}$  (After Yanai et al. 1992)

(ii) The divergence equation

$$\frac{\partial D}{\partial t} + \nabla \cdot (\vec{V}_H \cdot \nabla \vec{V}_H) + \nabla \cdot \left( \omega \frac{\partial \vec{V}_H}{\partial p} \right) + \nabla \cdot (f \vec{k} \times \vec{V}_H) + \nabla^2 \phi = F_D \quad (5.2)$$

(iii) The First Law of thermodynamics

$$\frac{\partial C_p T}{\partial t} + \vec{V}_H \cdot \nabla C_p T + \omega s = F_T + G_T \quad (5.3)$$

(iv) The continuity equation

$$D + \frac{\partial \omega}{\partial p} = 0 \quad (5.4)$$

(v) The hydrostatic law

$$\alpha + \frac{\partial \phi}{\partial p} = 0 \quad (5.5)$$

The horizontal wind vector  $\vec{V}_H$  can be separated into a rotational and divergent part,  $\vec{V}_\psi$  and  $\vec{V}_\chi$  respectively, as

$$\vec{V}_H = \vec{V}_\psi + \vec{V}_\chi \quad (5.6)$$

The rotational wind is defined as  $\vec{V}_\psi = \vec{k} \times \nabla \psi$ , and the divergent wind is defined as  $\vec{V}_\chi = -\nabla \chi$ , where  $\psi$  is the streamfunction, and  $\chi$  is the velocity potential. The relative vorticity is given by

$$\zeta = \vec{k} \cdot \nabla \times \vec{V}_H = \vec{k} \cdot \nabla \times \vec{V}_\psi = \nabla^2 \psi \quad (5.7)$$

and the divergence is given by

$$D = \nabla \cdot \vec{V}_H = \nabla \cdot \vec{V}_\chi = -\nabla^2 \chi \quad (5.8)$$

The total kinetic energy per unit mass is given by  $K = \frac{1}{2} \vec{V}_H \cdot \vec{V}_H$ . Expanding this in terms of rotational and divergent wind, one obtains

$$\begin{aligned} K &= \frac{1}{2} \vec{V}_H \cdot \vec{V}_H = \frac{1}{2} (\vec{V}_\psi + \vec{V}_\chi) \cdot (\vec{V}_\psi + \vec{V}_\chi) \\ &= \frac{1}{2} (\vec{V}_\psi \cdot \vec{V}_\psi) + \frac{1}{2} (\vec{V}_\chi \cdot \vec{V}_\chi) + \vec{V}_\psi \cdot \vec{V}_\chi \\ &= \frac{1}{2} |\nabla \psi|^2 + \frac{1}{2} |\nabla \chi|^2 - J(\psi, \chi) \end{aligned} \quad (5.9)$$

Note also that the Jacobian, which represents the energy interaction between the rotational and divergent part, satisfies the identity  $J(\psi, \chi) \equiv \vec{k} \times \nabla \psi \cdot \nabla \chi$ . One can denote

$$\begin{aligned} K_\psi &\equiv \frac{1}{2} |\nabla \psi|^2 \\ K_\chi &\equiv \frac{1}{2} |\nabla \chi|^2 \end{aligned} \quad (5.10)$$

Equation 5.9 can then be written as

$$K = K_\psi + K_\chi - J(\psi, \chi) \quad (5.11)$$

It can be shown that the vorticity (5.1) can be rewritten in terms of the streamfunction and the velocity potential as

$$\begin{aligned} \frac{\partial}{\partial t} \nabla^2 \psi &= -J(\psi, \nabla^2 \psi + f) + \nabla \chi \cdot \nabla (\nabla^2 \psi + f) - \omega \frac{\partial}{\partial p} \nabla^2 \psi \\ &\quad + (\nabla^2 \psi + f) \nabla^2 \chi - \nabla \omega \cdot \nabla \frac{\partial \psi}{\partial p} + J\left(\omega, \frac{\partial \chi}{\partial p}\right) + F_\zeta \end{aligned} \quad (5.12)$$

The divergence (5.2) can be written in terms of the streamfunction and velocity potential as

$$\begin{aligned}\frac{\partial}{\partial t} \nabla^2 \chi &= \nabla^2 \left[ \frac{1}{2} (\nabla \psi)^2 + \frac{1}{2} (\nabla \chi)^2 - J(\psi, \chi) \right] - (\nabla^2 \psi)^2 - \nabla \psi \cdot \nabla (\nabla^2 \psi) \\ &\quad - \omega \frac{\partial}{\partial p} \nabla^2 \chi - J \left( \omega, \frac{\partial \psi}{\partial p} \right) - \nabla \omega \cdot \nabla \frac{\partial \chi}{\partial p} - \nabla f \cdot \nabla \psi \\ &\quad + J(f, \chi) + J(\nabla^2 \psi, \chi) + f \nabla^2 \psi + \nabla^2 \phi + F_D\end{aligned}\quad (5.13)$$

Note that

$$\psi \frac{\partial}{\partial t} \nabla^2 \psi = \nabla \cdot \left( \psi \nabla \frac{\partial \psi}{\partial t} \right) - \frac{\partial}{\partial t} \left( \frac{|\nabla \psi|^2}{2} \right) \quad (5.14)$$

$$\chi \frac{\partial}{\partial t} \nabla^2 \chi = \nabla \cdot \left( \chi \nabla \frac{\partial \chi}{\partial t} \right) - \frac{\partial}{\partial t} \left( \frac{|\nabla \chi|^2}{2} \right) \quad (5.15)$$

Noting the definitions given by (5.10), this means that

$$\frac{\partial}{\partial t} K_\psi = -\psi \frac{\partial}{\partial t} \nabla^2 \psi + \nabla \cdot \left( \psi \nabla \frac{\partial \psi}{\partial t} \right) \quad (5.16)$$

$$\frac{\partial}{\partial t} K_\chi = -\chi \frac{\partial}{\partial t} \nabla^2 \chi + \nabla \cdot \left( \chi \nabla \frac{\partial \chi}{\partial t} \right) \quad (5.17)$$

An area average of a quantity  $a$  is defined as

$$\bar{a} = \frac{1}{A} \iint_{x y} a \, dx dy, \quad (5.18)$$

where the area is  $A = \iint_{x y} dx dy$ . The vertical average of  $\bar{a}$ , denoted here as  $\bar{\bar{a}}$  is given by

$$\bar{\bar{a}} = \frac{1}{\int_p dp} \int_p a \, dp, \quad (5.19)$$

Note that over a closed domain for any arbitrary vector  $\vec{a}$  and scalars  $a$  and  $b$ ,

$$\iint_{x y} (\nabla \cdot \vec{a}) \, dx dy = 0 \quad (5.20)$$

$$\iint_{x y} J(a, b) \, dx dy = 0 \quad (5.21)$$

Also, if  $a = 0$  at the top and bottom boundary,

$$\int_p \frac{\partial a}{\partial p} dp = 0 \quad (5.22)$$

In view of (5.20), (5.21), and (5.22), it is convenient to express as many of the terms of the energy equation into the form of a divergence of a vector or a Jacobian of two scalars, so that integration of the energy equation over a closed domain would lead to the vanishing of all such terms.

To obtain the energy equation for the rotational and divergent components, one can multiply (5.12) by  $\psi$  and (5.13) by  $\chi$  to obtain, respectively,

$$\begin{aligned} \psi \frac{\partial}{\partial t} \nabla^2 \psi &= -\psi J(\psi, \nabla^2 \psi + f) + \psi \nabla \chi \cdot \nabla (\nabla^2 \psi + f) - \psi \omega \frac{\partial}{\partial p} \nabla^2 \psi \\ &\quad + \psi (\nabla^2 \psi + f) \nabla^2 \chi - \psi \nabla \omega \cdot \nabla \frac{\partial \psi}{\partial p} + \psi J\left(\omega, \frac{\partial \chi}{\partial p}\right) + F_\psi \end{aligned} \quad (5.23)$$

$$\begin{aligned} \chi \frac{\partial}{\partial t} \nabla^2 \chi &= \chi \nabla^2 \left[ \frac{1}{2} (\nabla \psi)^2 + \frac{1}{2} (\nabla \chi)^2 - J(\psi, \chi) \right] - \chi (\nabla^2 \psi)^2 \chi \nabla \psi \cdot \nabla (\nabla^2 \psi) \\ &\quad - \chi \omega \frac{\partial}{\partial p} \nabla^2 \chi - \chi J\left(\omega, \frac{\partial \psi}{\partial p}\right) - \chi \nabla \omega \cdot \nabla \frac{\partial \chi}{\partial p} - \chi \nabla f \cdot \nabla \psi \\ &\quad + \chi J(f, \chi) + \chi J(\nabla^2 \psi, \chi) + \chi f \nabla^2 \psi + \chi \nabla^2 \phi + F_\chi \end{aligned} \quad (5.24)$$

where  $F_\psi = \psi F_\zeta$  and  $F_\chi = \chi F_D$ . The terms on the right side of (5.23) can be rearranged as follows

$$-\psi J(\psi, \nabla^2 \psi + f) = -J\left(\frac{\psi^2}{2}, \nabla^2 \psi + f\right) \quad (5.25)$$

$$\begin{aligned} -\psi \nabla \omega \cdot \nabla \frac{\partial \psi}{\partial p} - \psi \omega \frac{\partial}{\partial p} \nabla^2 \psi &= -\psi \left[ \nabla \cdot \left( \omega \nabla \frac{\partial \psi}{\partial p} \right) - \omega \nabla^2 \frac{\partial \psi}{\partial p} \right] - \psi \omega \frac{\partial}{\partial p} \nabla^2 \psi \\ &= -\psi \nabla \cdot \left( \omega \nabla \frac{\partial \psi}{\partial p} \right) \\ &= -\nabla \cdot \left( \psi \omega \nabla \frac{\partial \psi}{\partial p} \right) + \omega \nabla \psi \cdot \nabla \frac{\partial \psi}{\partial p} \\ &= -\nabla \cdot \left( \psi \omega \nabla \frac{\partial \psi}{\partial p} \right) + \omega \frac{\partial}{\partial p} \frac{|\nabla \psi|^2}{2} \\ &= -\nabla \cdot \left( \psi \omega \nabla \frac{\partial \psi}{\partial p} \right) + \frac{\partial}{\partial p} \frac{\omega |\nabla \psi|^2}{2} - \frac{|\nabla \psi|^2}{2} \frac{\partial \omega}{\partial p} \\ &= -\nabla \cdot \left( \psi \omega \nabla \frac{\partial \psi}{\partial p} \right) + \frac{\partial}{\partial p} \frac{\omega |\nabla \psi|^2}{2} - \frac{|\nabla \psi|^2}{2} \nabla^2 \chi \end{aligned} \quad (5.26)$$

$$\begin{aligned}
& \psi \nabla \chi \cdot \nabla (\nabla^2 \psi + f) + \psi (\nabla^2 \psi + f) \nabla^2 \chi \\
&= \psi \nabla \chi \cdot \nabla (\nabla^2 \psi) + \psi \nabla \chi \cdot \nabla f + \psi \nabla^2 \psi \nabla^2 \chi + \psi f \nabla^2 \chi \\
&= \nabla \cdot (\psi \nabla^2 \psi \nabla \chi) - \nabla^2 \psi \nabla \psi \cdot \nabla \chi - \psi \nabla^2 \psi \nabla^2 \chi + \psi \nabla^2 \psi \nabla^2 \chi \\
&\quad + \nabla \cdot (\psi f \nabla \chi) - \nabla \psi \cdot f \nabla \chi + \psi f \nabla^2 \chi \\
&= \nabla \cdot (\psi \nabla^2 \psi \nabla \chi) - \nabla^2 \psi \nabla \psi \cdot \nabla \chi \\
&\quad + \nabla \cdot (\psi f \nabla \chi) - \nabla \psi \cdot f \nabla \chi + \psi f \nabla^2 \chi
\end{aligned} \tag{5.27}$$

$$\psi J \left( \omega, \frac{\partial \chi}{\partial p} \right) = J \left( \omega \psi, \frac{\partial \chi}{\partial p} \right) - \omega J \left( \psi, \frac{\partial \chi}{\partial p} \right) \tag{5.28}$$

Upon substituting (5.25) through (5.28) into (5.23) and integrating the resulting equation over a closed domain, one obtains

$$\frac{\partial}{\partial t} \bar{K}_\psi = \overline{\overline{f \nabla \psi \cdot \nabla \chi}} + \overline{\overline{\nabla^2 \psi \nabla \psi \cdot \nabla \chi}} + \overline{\nabla^2 \chi \frac{|\nabla \psi|^2}{2}} + \overline{\overline{\omega J \left( \psi, \frac{\partial \chi}{\partial p} \right)}} + \overline{\overline{F_\psi}} \tag{5.29}$$

Next, consider the first law of thermodynamics. Since

$$s = C_p T - \alpha = C_p \frac{\partial T}{\partial p} + \frac{\partial \phi}{\partial p}, \tag{5.30}$$

$$\begin{aligned}
-\omega s &= -\omega \frac{\partial}{\partial p} (C_p T + \phi) \\
&= -\frac{\partial}{\partial p} [\omega (C_p T + \phi)] + (C_p T + \phi) \frac{\partial}{\partial p} \omega \\
&= -\frac{\partial}{\partial p} [\omega (C_p T + \phi)] + (C_p T + \phi) \nabla^2 \chi
\end{aligned} \tag{5.31}$$

equation (5.3) can be rewritten as

$$\begin{aligned}
\frac{\partial}{\partial t} C_p T &= J(C_p T, \psi) + \nabla \chi \cdot \nabla (C_p T) \\
&\quad + (C_p T + \phi) \nabla^2 \chi - \frac{\partial}{\partial p} [\omega (C_p T + \phi)] + F_T + G_T
\end{aligned} \tag{5.32}$$

Note that

$$\begin{aligned}
\nabla \chi \cdot \nabla (C_p T) + (C_p T + \phi) \nabla^2 \chi &= \nabla \chi \cdot \nabla (C_p T) + \nabla \cdot (C_p T \nabla \chi) \\
&\quad - \nabla \chi \cdot \nabla (C_p T) + \nabla \cdot (\phi \nabla \chi) - \nabla \phi \cdot \nabla \chi \\
&= \nabla \cdot (C_p T \nabla \chi) + \nabla \cdot (\phi \nabla \chi) - \nabla \cdot (\chi \nabla \phi) + \chi \nabla^2 \phi
\end{aligned} \tag{5.33}$$

Therefore, integrating the thermodynamic equation over a closed domain leads to an equation for the tendency of the available potential energy, APE.

$$\frac{\partial}{\partial t} \overline{\overline{APE}} = \overline{\chi \nabla^2 \phi} + \overline{\overline{F_T}} + \overline{\overline{G_T}} \quad (5.34)$$

For the derivation of the  $\chi$ -energy equation, consider that in the absence of diabatic heating and friction, the total energy is conserved, i.e.,

$$\frac{\partial}{\partial t} \overline{\overline{APE + K}} = \frac{\partial}{\partial t} \overline{\overline{APE + K_\psi + K_\chi}} = 0 \quad (5.35)$$

Hence

$$\begin{aligned} \frac{\partial}{\partial t} \overline{\overline{K_\chi}} &= -\frac{\partial}{\partial t} \overline{\overline{APE}} - \frac{\partial}{\partial t} \overline{\overline{K_\chi}} \\ &= -\overline{\chi \nabla^2 \phi} - \overline{f \nabla \psi \cdot \nabla \chi} - \overline{\nabla^2 \psi (\nabla \psi \cdot \nabla \chi)} \\ &\quad - \frac{1}{2} \overline{|\nabla \psi|^2 \nabla^2 \chi} - \omega J \left( \psi, \frac{\partial \chi}{\partial p} \right) + \overline{\overline{F_\chi}} \end{aligned} \quad (5.36)$$

where  $\overline{\overline{F_\chi}} = -\overline{\overline{F_T}} - \overline{\overline{G_T}} - \overline{\overline{F_\psi}}$ . Equations 5.29, 5.36, and 5.34 provide expressions for the rate of change of the rotational and divergent kinetic, and the potential energy, respectively, integrated over a closed domain. In the case of an open domain, these equations contain additional boundary flux terms given, respectively, by  $\overline{\overline{B_\psi}}$ ,  $\overline{\overline{B_\chi}}$  and  $\overline{\overline{B_T}}$ . The boundary flux term in the rotational kinetic energy equation is given by:

$$\begin{aligned} B_\psi &= \nabla \cdot \left( \psi \nabla \frac{\partial \psi}{\partial t} \right) + J \left( \frac{\psi^2}{2}, \nabla^2 \psi + f \right) \\ &\quad - J \left( \omega \psi, \frac{\partial \chi}{\partial p} \right) + \nabla \cdot \left( \psi \omega \frac{\partial}{\partial p} \nabla \psi \right) \\ &\quad - \frac{\partial}{\partial p} \omega \frac{|\nabla \psi|^2}{2} - \nabla \cdot [\psi (\nabla^2 \psi + f) \nabla \chi] \end{aligned} \quad (5.37)$$

the boundary flux term in the divergent kinetic energy equation is given by:

$$\begin{aligned} B_\chi &= \nabla \cdot \left( \chi \frac{\partial \psi}{\partial t} \nabla \chi \right) + J \left( \frac{\chi^2}{2}, \nabla^2 \psi + f \right) + J \left( \omega \chi, \frac{\partial \chi}{\partial p} \right) \\ &\quad - \nabla \cdot \left\{ \chi \nabla \left[ \frac{|\nabla \psi|^2}{2} + \frac{|\nabla \chi|^2}{2} - J(\psi, \chi) \right] - \nabla \chi \left[ \frac{|\nabla \psi|^2}{2} + \frac{|\nabla \chi|^2}{2} - J(\psi, \chi) \right] \right\} \\ &\quad - \frac{\partial}{\partial p} \left\{ \omega \left[ \frac{|\nabla \psi|^2}{2} - J(\psi, \chi) \right] \right\} + \nabla \cdot \left\{ \chi \nabla \psi (\nabla^2 \psi + f) + \chi \omega \frac{\partial}{\partial p} \nabla \chi \right\} \end{aligned} \quad (5.38)$$

and the boundary flux term in the available potential energy equation is given by

$$B_T = J(C_p T, \psi) + \nabla \cdot (C_p T \nabla \chi) + \nabla \cdot (\varphi \nabla \chi) - \nabla \cdot (\chi \nabla \phi) \quad (5.39)$$

We shall next address the issue of the maintenance of the monsoon.

In a statistical steady state of a mature monsoon (after the onset), disregarding the boundary terms, the  $\psi$ - $\chi$  equations can be written as

$$\overline{\overline{K_\chi \cdot K_\psi}} + \overline{\overline{F_\psi}} = 0 \quad (5.40)$$

$$\overline{\overline{APE \cdot K_\chi}} - \overline{\overline{K_\chi \cdot K_\psi}} + \overline{\overline{F_\chi}} = 0 \quad (5.41)$$

$$-\overline{\overline{APE \cdot K_\chi}} + \overline{\overline{F_T}} + \overline{\overline{G_T}} = 0 \quad (5.42)$$

where  $\overline{\overline{K_\chi \cdot K_\psi}} \equiv \overline{\overline{f \nabla \psi \cdot \nabla \chi}} + \overline{\overline{\nabla^2 \psi \nabla \psi \cdot \nabla \chi}} + \overline{\overline{\nabla^2 \chi \frac{|\nabla \psi|^2}{2}}} + \overline{\overline{\omega J(\psi, \frac{\partial \chi}{\partial p})}}$  is the rate of conversion of divergent to rotational kinetic energy, and  $\overline{\overline{APE \cdot K_\chi}} = -\overline{\overline{\chi \nabla^2 \phi}}$  is the rate of conversion of available potential to divergent kinetic energy. The following inequality arguments are useful for an analysis of the maintenance of a steady-state monsoon:

- (i) The dissipation of rotation kinetic energy is negative ( $F_\psi < 0$ );
- (ii) Therefore  $\overline{\overline{K_\chi \cdot K_\psi}} >$  must be positive.
- (iii) The dissipation of divergent kinetic energy is negative ( $F_\chi < 0$ );
- (iv) Since  $-\overline{\overline{K_\chi \cdot K_\psi}}$  is negative and  $F_\chi$  is negative, it follows that  $\overline{\overline{APE \cdot K_\chi}}$  is positive.
- (v) Since  $-\overline{\overline{APE \cdot K_\chi}}$  is negative and  $F_T$  is negative, it follows that  $G_T > |F_T|$ .

Note that the following salient covariances are present in the above inequalities:

$$\overline{\overline{APE \cdot K_\chi}} \sim - \int_{p_T}^{p_S} \int_{y_1}^{y_2} \int_{x_1}^{x_2} \frac{\omega T}{p} dx dy dp$$

$$\overline{\overline{G_T}} \sim \int_{p_T}^{p_S} \int_{y_1}^{y_2} \int_{x_1}^{x_2} HT dx dy dp$$

The inequality argument simply states that for the maintenance of a steady state monsoon (which is largely defined by the domain-averaged rotational kinetic energy) a differential heating defined by a net positive covariance of heating and temperature is needed. This implies that if heating occurs where the air is relatively warm and the cooling occurs where the air is relatively cold (within the entire domain) a monsoon can be maintained. In this context the differential heating is not a vector  $\nabla H$  pointing from the cooling to the heating region but is one that carries

a net positive value for the  $HT$  covariance. The term  $\langle APE \cdot K_x \rangle$  is an important vehicle that transforms the  $APE$  generated from the above differential heating to rotational kinetic energy, arising from the net positive value of the covariance  $-\frac{\omega T}{p}$ . This calls for a net ascent of warmer air and descend of cooler air within the monsoon domain.

## 5.12 The Heaviest Rainfall of the Summer Monsoon

Cherrapunji, located at  $25.15^{\circ}\text{N}$  and  $91.44^{\circ}\text{E}$  is known to be one of the雨iest regions of the world. It is located at a height of 1,290 m above sea level. Its normal long-term mean monsoon season rainfall between 1 June and 15 September is on the order of  $10^4$  mm, or 10 m. The topography of the monsoon region is shown in Fig. 5.21.

Here the letter X marks the approximate location of Cherrapunji. This region is marked by high mountains to the north and to the east. The large-scale monsoonal flow brings in a moist current from the Bay of Bengal. The flow is counterclockwise around the monsoon trough whose axis is located near  $23\text{--}25^{\circ}\text{N}$ . The mesoscale structure of the circulation in the vicinity of this region of steep topography is not well studied. The rainfall in the region has a large diurnal variability. Most of the heavy rainfall occurs during late night to early morning hours. The day-to-day rainfall variability at Cherrapunji is illustrated in Fig. 5.22 for a period covering 1 May through 10 August, 1979 (a below-normal monsoon rainfall year).

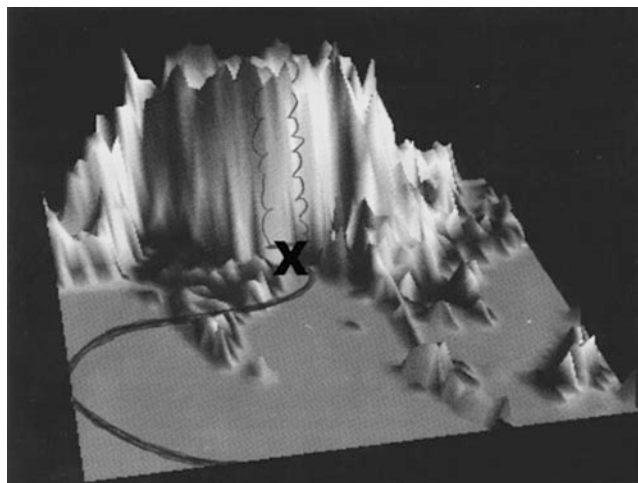


**Fig. 5.21** A 3-D perspective of the terrain of the Himalayas. The location of Cherrapunji is marked with an X

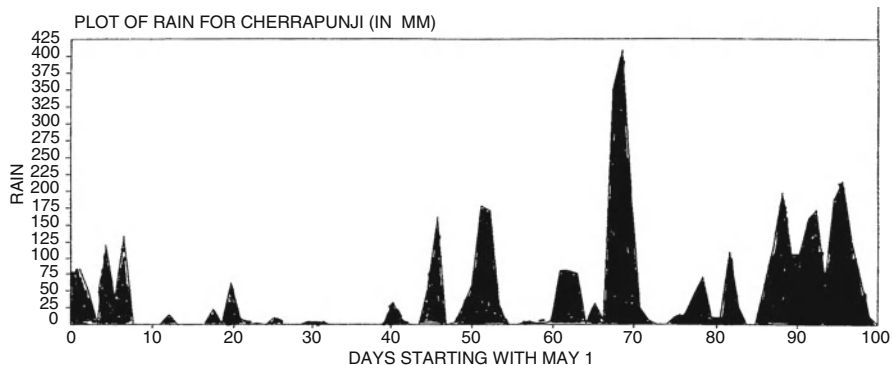


**Fig. 5.22** Daily rainfall amounts at Cherrapunji for the period 1 May – 10 August, 1979. Units of mm

The vertical scale is the daily rainfall total in millimeters. There are instances – e.g. around 10 July – when the rainfall total is as large as 400 mm/day (or roughly 16 in./day). There is a marked variability in the day-to-day rainfall that clearly illustrates the dry and wet spells on the quasi-biweekly and the ISO time-scales. The mean rainfall for the 100 day period shown in Fig. 5.22 is around  $50 \text{ mm day}^{-1}$ . Most of this rain is orographic and deep-convectional in nature and many of these high rain events last for 3–6 h each day. The hourly rain rates are exceedingly large in this region.

## 5.13 Breaks in the Indian Monsoon

A break in the monsoon is a temporary cessation of rains during the monsoon season. Many of these breaks, according to Ramamurthy (1969), last for 3–5 days while some have lasted for periods as long as 17–20 days. Figure 5.23, from Gadgil and Joseph (2003), illustrates the daily value of total rain over entire India for the drought year of 1972. This was a year of a long lasting break that lasted for almost a month. It was also an El Nino year.

The field of outgoing long wave radiation (OLR) provides a geographical picture of wet or dry areas. Low values of OLR imply high clouds and rainy areas, whereas higher values of OLR imply clearer rain free areas. Typical values of OLR for rainy areas of the monsoon are around  $195 \text{ Wm}^{-2}$ ; in clear areas these are around  $245 \text{ Wm}^{-2}$ . Gadgil and Joseph (2006) have provided an analysis of these fields (in terms of anomalies with respect to climatological mean values of OLR). Figure 5.24 shows the anomalies and total values of the OLR for the break and the active periods, from an analysis based on 18 years of OLR data (1972–1989). This figure illustrates that during a break period, positive OLR anomalies ( $+20\text{--}30 \text{ Wm}^{-2}$ ) prevail; these are replaced by strong negative anomalies ( $-20 \text{ Wm}^{-2}$ ) during the active spells.

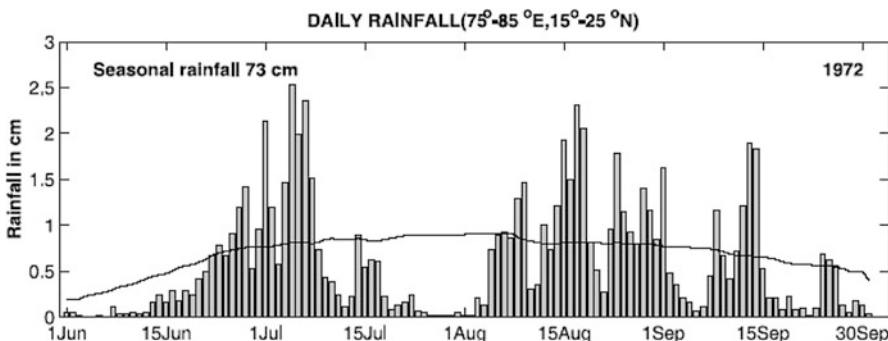


**Fig. 5.23** Daily rainfall (bars) over central India during the summer of 1972. Units of cm (From Gadgil and Joseph 2003)

Total OLR values above  $225 \text{ W m}^{-2}$  are indicative of break periods, whereas values below  $225 \text{ W m}^{-2}$  typify active periods. The monsoon break/active spells are relatively large-scale events, as Fig. 5.24 illustrates. The negative OLR anomalies associated with active spells spread from the northern Arabian Sea all the way to the vicinity of the  $130^{\circ}\text{W}$  longitude, covering a large area of the Pacific Ocean. The ITCZ over most of the equatorial Pacific seems to be somewhat more active during the periods of active monsoons.

Krishnan et al. (2000) have examined the antecedents of breaks in the monsoon. They noted that when a break occurs, the monsoon trough is weaker than the climatological monsoon trough. One can determine the antecedents of breaks by composing a large number of past cases of breaks. This can be done in steps of  $0, \pm 3, \pm 6, \pm 9$ , and  $\pm 12$  days. Such composites with respect to day 0 of major meteorological events are very useful, particularly when the standard deviation of the composited fields is relatively small. Figure 5.25 illustrates the composite of 18 cases of breaks performed by Krishnan et al. (2000). This shows that there is an antecedent history to these breaks going back to almost 12 days. There is a clear suggestion that the higher OLR values move north from the near-equatorial latitudes (day  $-12$ ) towards  $20^{\circ}\text{N}$  (day 0). Thereafter one sees a northward passage of the low values of OLR from the equatorial latitudes towards  $20^{\circ}\text{N}$ . This successive passage of positive and negative values of OLR anomalies is a part of the Intraseasonal Oscillation (ISO) [discussed in detail in chapter X] that seems to suggest a modulation of monsoon weather by the cyclonic and anticyclonic entities of the ISO. This raises the question of whether the cause of the breaks and active spells resides in the near-equatorial latitudes, since that is where the anomalies are first seen prior to their arrival at  $20^{\circ}\text{N}$ .

This is reminiscent of comments made, during a conference, by Dr James Sadler and Professor Suki Manabe. Sadler had noted large positive sea level pressure anomalies at the near equatorial latitudes that moved north in a matter of roughly 10 days and weakened the monsoon trough at  $20^{\circ}\text{N}$  and a break in the monsoon rains followed. He attributed the cause to something happening at the equatorial

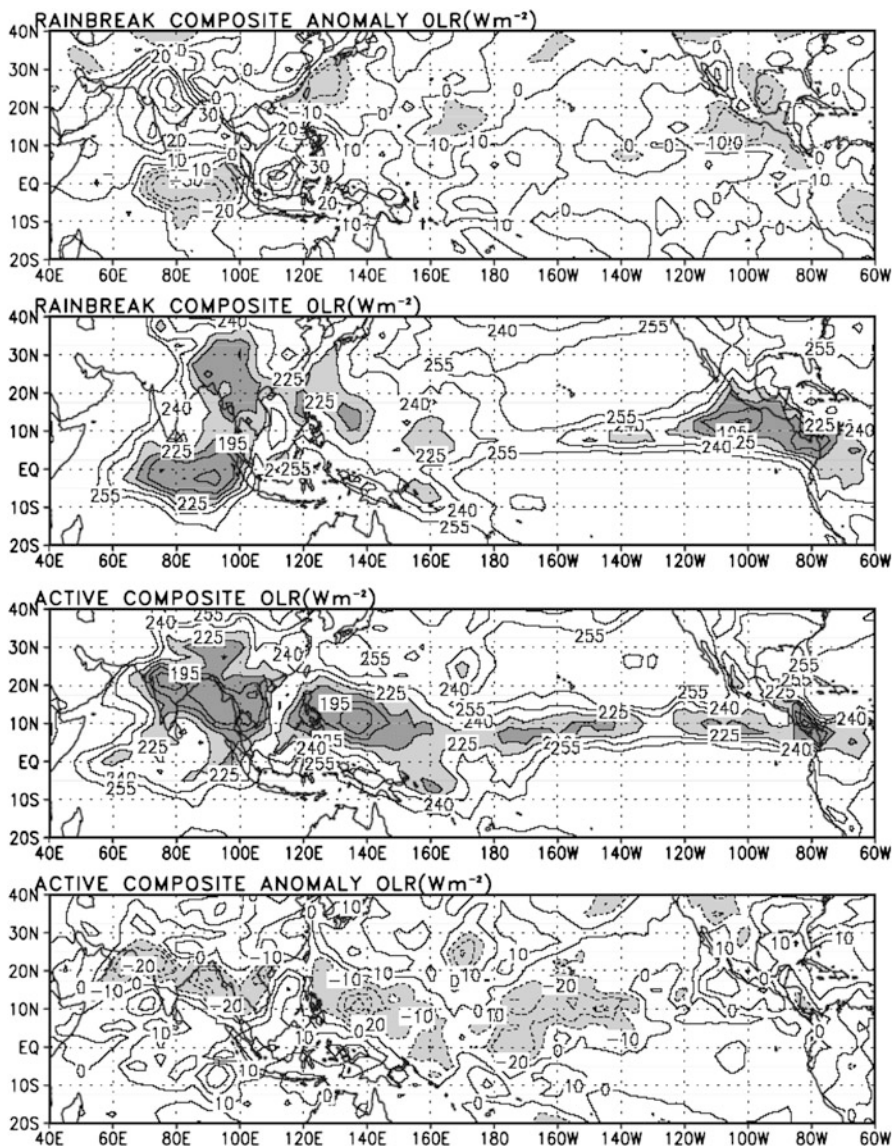


**Fig. 5.24** OLR and OLR anomaly for composite break (top two) and active (bottom two) periods (From Gadgil and Joseph 2003)

latitude. Manabe quipped “What if a guy in the north had telephoned that guy in the south to come north, then who is the cause?” What Manabe felt was that it might have been the case that first the heat sources over the foothills of the Himalayas and the Tibetan Plateau had weakened, and the northward motion of a higher pressure anomaly from the Equatorial latitudes could simply have been a response to that.

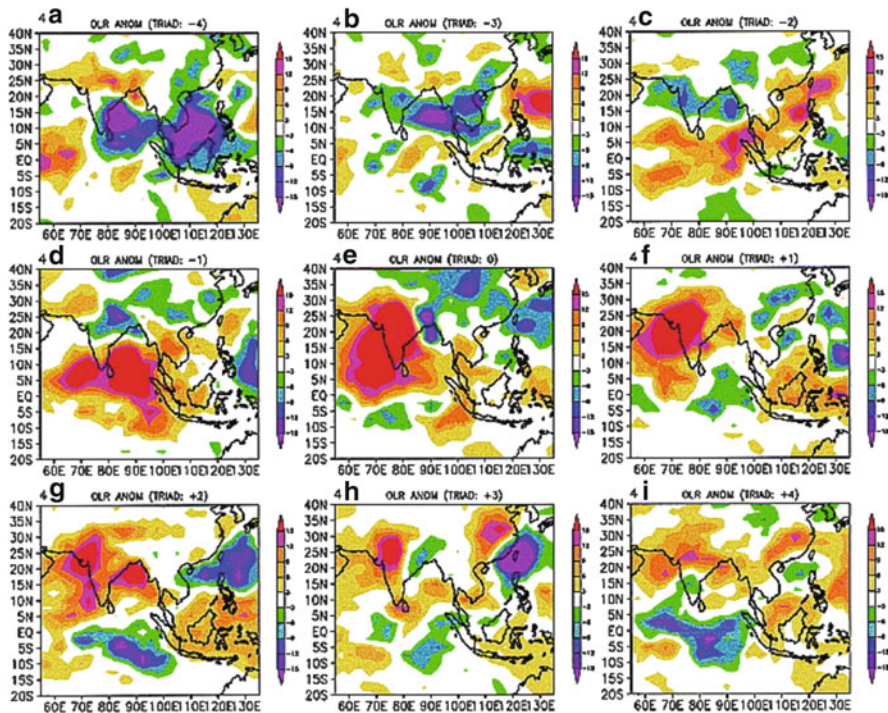
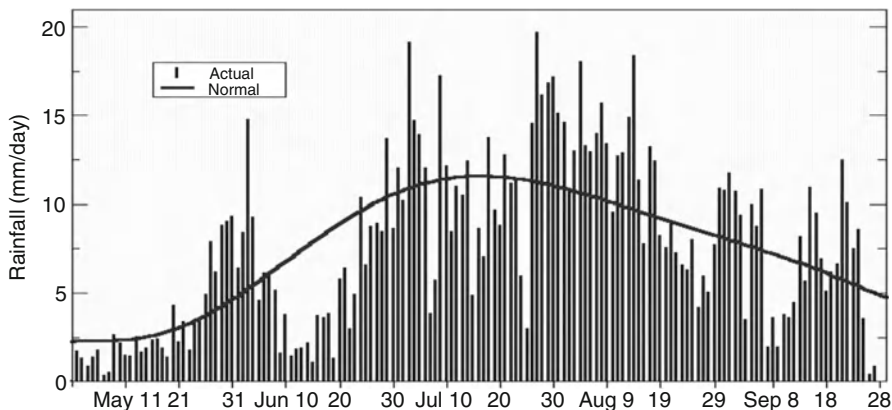


**Fig. 5.25** Sequence of composited OLR anomalies showing the evolution of monsoon breaks: (a) day – 12, (b) day – 9, (c) day – 6, (d) day – 3, (e) day 0, (f) day + 3, (g) day + 6, (h) day + 9, and (i) day + 12. Contour interval  $3 \text{ Wm}^{-2}$  (From Krishnan et al. 2000)

Careful numerical experimentation can answer such questions on pull or push. This also conveys a word of caution on any quick interpretations for the cause and effect for any phenomenological scenario that one might observe.

## 5.14 Active, Break and Withdrawal Phases of Indian Monsoons

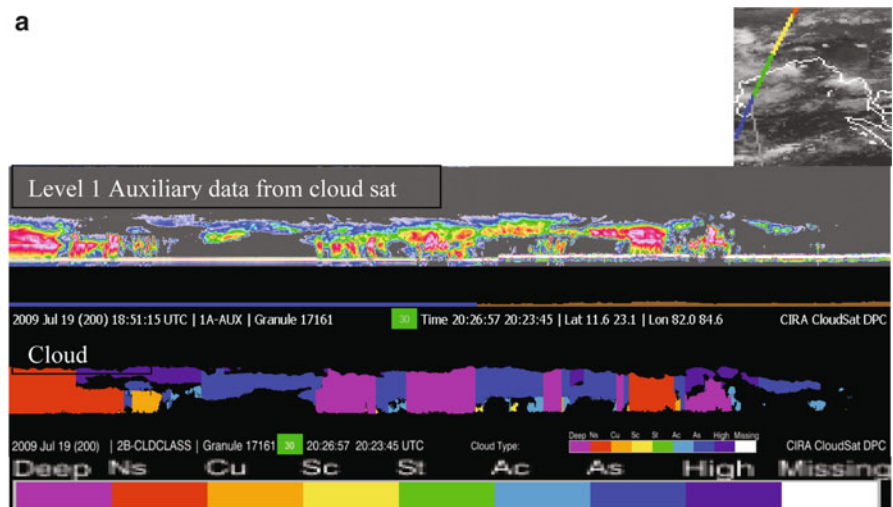
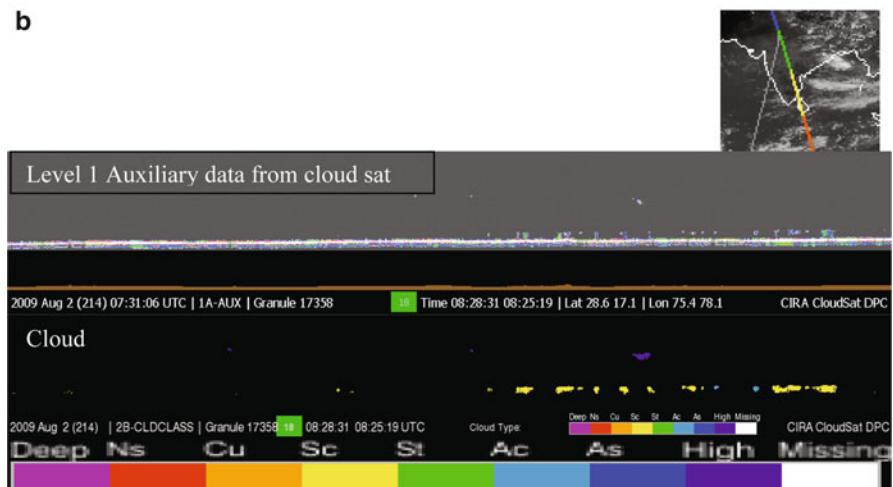
Figure 5.26 is an example of a popular diagram that is prepared annually by the India Meteorological Department. It shows the daily time history of rainfall totals (for each day) during the active monsoon season. The daily rainfall totals are shown by vertical bars. Also shown in this illustration is the long-term calendar day climatology (shown by a solid line). Daily values above or below that line show periods of active and break (less active) periods of rain. This illustration clearly shows the onset, active, break, revival and the withdrawal phases of the monsoon. Besides short-term variability on synoptic time scales on the order of 4–8 days, there are also prominent peaks in rainfall variability on periods of the order of



**Fig. 5.26** Daily all-India observed rainfall for 2006 (bars) and climatological daily rainfall values (line) (From India Met. Department archive)

2 weeks (quasi-biweekly) and 30–60 days (ISO time scale). This type of variability can be assessed using numerical algorithms for power spectra and digital filters. Those are described briefly in the appendices A1 and A2 of this book. The synoptic time scale disturbances generally move westwards to north-westwards at speeds of roughly  $5\text{--}7^\circ$  longitude per day between  $15^\circ$  and  $25^\circ\text{N}$ . They have an east–west wavelength of roughly 3,000 km. The quasi-biweekly mode is westward propagating and has its largest amplitude around  $15\text{--}20^\circ\text{N}$ ; there is evidence of such modes originating in the Pacific Ocean, crossing the Indochina peninsula and moving into the Bay of Bengal. The ISO over the summer monsoon belt is identified as a meridionally propagating low-frequency mode that moves from near  $5^\circ\text{S}$  to the foothills of the Himalayas with a propagation speed of roughly  $1^\circ$  latitude per day. It has a meridional wavelength of roughly 3,000 km; its passage is characterized by alternate clockwise and counterclockwise gyres that successively move northwards. These clockwise and counterclockwise flows contribute to parallel and antiparallel anomalies of flows with respect to the climatological flows. The parallel flows strengthen the inflowing moisture supply from the ocean and tend to enhance the monsoon rainfall; the converse is the case when the climatological flows are opposed by antiparallel anomalies.

In a recent study, Krishnamurti et al. (2010) noted some important antecedents for the dry spell of the summer monsoon over India. They noted that during wet spells the back trajectories, (covering 10 days from central India) of air show that almost all that air between the surface and the 400 hPa levels have an oceanic origin. During dry spells the flows between the surface level and the 850 hPa level are still of oceanic origin, whereas the air between 800 and the 400 hPa levels originate from the Arabian desert regions. That region was shown to carry a deep blocking anticyclone between the 700 and the 300 hPa levels. Air moving around this deep blocking high provides very dry descending air towards the northern

**a****b**

**Fig. 5.27** (a) For active monsoon day: 19th July 2009. The satellite pass is shown on top right. The vertical structure of clouds as seen by CloudSat along the satellite track is shown here illustrates a very active monsoon. The bottom panel illustrates the cloud types. (b) For monsoon break days: 2nd August 2009. The satellite pass is shown on top right. The vertical structure of clouds as seen by CloudSat along the satellite track is shown here illustrates a very total absence of clouds. The bottom panel illustrates the cloud types

Arabian Sea and towards central India. That study carries some interesting dynamical antecedents for this scenario linking dry spells of the monsoon to the dry air incursions from the desert. The CLOUDSAT imagery provides a clear distinction between the clouds during wet spells and the lack of it during the dry spells, Figs. 5.27a, b. The MODIS satellite of NASA is also an important observational platform since it clearly shows the incursion of heavy aerosol optical depths from dust incursions during the dry spell.

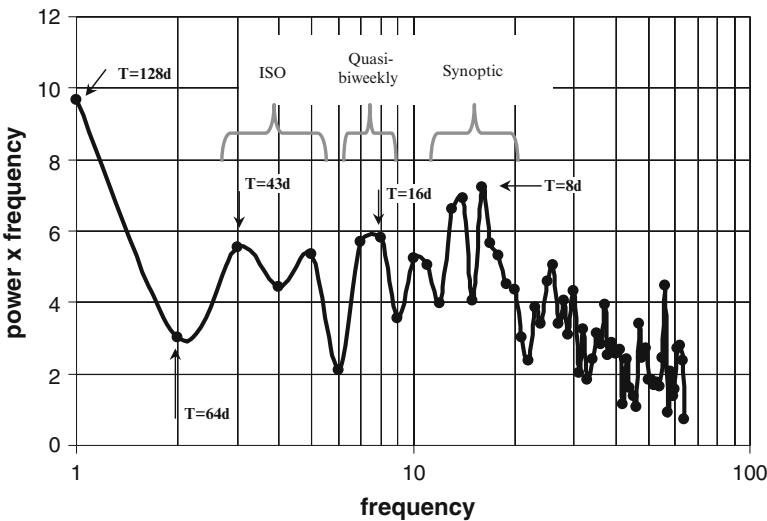


**Fig. 5.28** Ten-year-averaged (1979–1988) power spectrum of all-India rainfall, based on daily data between 1 May and 7 October

Figure 5.28 illustrates the average power spectra of all-India summer monsoon (May 1 through October 7) rainfall data sets for the years 1979 through 1988. The algorithm for computing the power spectra is described in the appendix of this book. The diagram shown here shows the spectral power times frequency along the ordinate, and the frequency (in cycles per 128 days) along the abscissa, using a logarithmic scale. The salient features in this power spectrum are the large signals on the MJO time scale (20–60 days), the quasi-biweekly time scale and the synoptic time scale between 4 and 8 days. These are three important time scales in the monsoon environment. We shall be discussing these in various sections of this book.

## 5.15 The Somali Jet

The Somali jet is one of the most prominent wind systems of the lower troposphere during the Asian summer monsoon. Its strongest winds are found during the months of June, July and August at a height of roughly 1 km above the Earth's surface off the coast of Somalia and extending over the northern Arabian Sea. Figure 5.29, from Findlater (1971), shows the climatological horizontal spread of this jet for the month of June at the 1 km level over the Arabian Sea. This figure is based on the best available at the time data – largely pilot balloon and rawinsonde measurements. Seen here is the extension of the southern hemisphere trades with a maximum wind speed ( $\sim 15 \text{ ms}^{-1}$ ) over the northern part of Madagascar. This flow reaches the coast of Kenya where it makes a northward traverse across the equator. Further, the flow

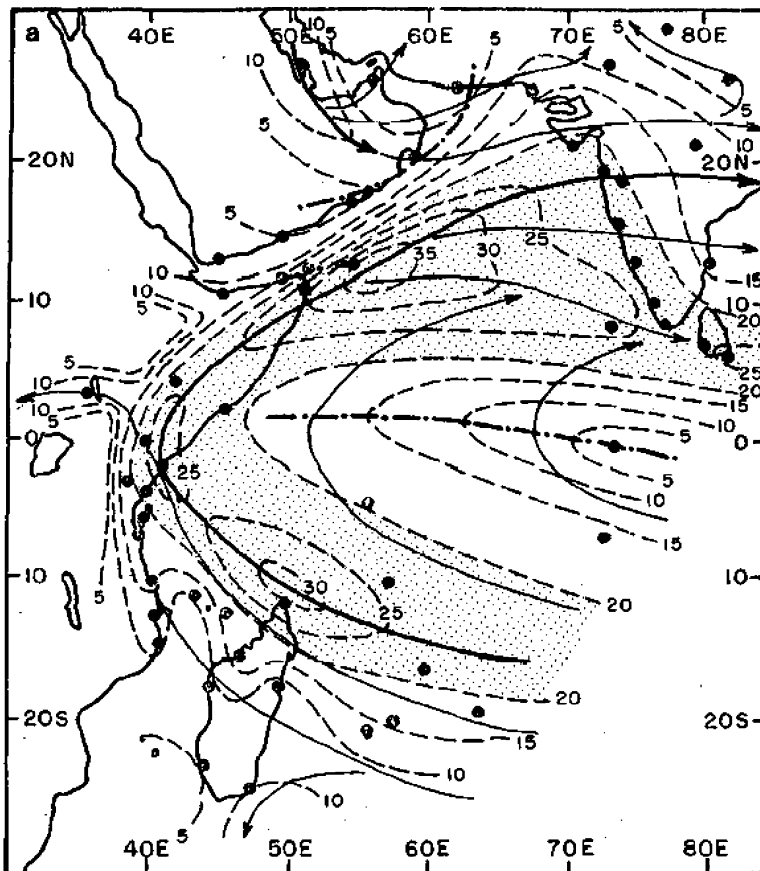


**Fig. 5.29** July streamlines (arrows) and isotachs (dashed lines), in knots, at 1 km height for the Somali jet (Adapted from Findlater 1969)

starts to turn eastward, acquiring a wind maximum of around  $17.5 \text{ ms}^{-1}$  off the coast of Somalia (hence the name ‘Somali jet’). Thereafter this climatological flow splits into two branches – one moving towards India (near  $17^\circ\text{N}$ ), and a second one moving towards the southern part of Sri Lanka (near  $5^\circ\text{N}$ ).

This split is an interesting climatological feature that has raised an important question, namely, are there instances in which the two branches of the jet are simultaneously in existence (i.e., are there days on which the jet is actually split), or is the appearance of branching a consequence of climatological averaging of days during which the jet is in the more southern location and days in which it is in the more northern location. Modern data sets have sufficiently high resolution in time and space to allow for an easy answer to the above question. The data sets that are currently available on a routine basis are similar to those shown in Fig. 5.13, largely coming from cloud-tracked winds via geostationary satellites. The satellites currently present over this region include India’s INSAT and the

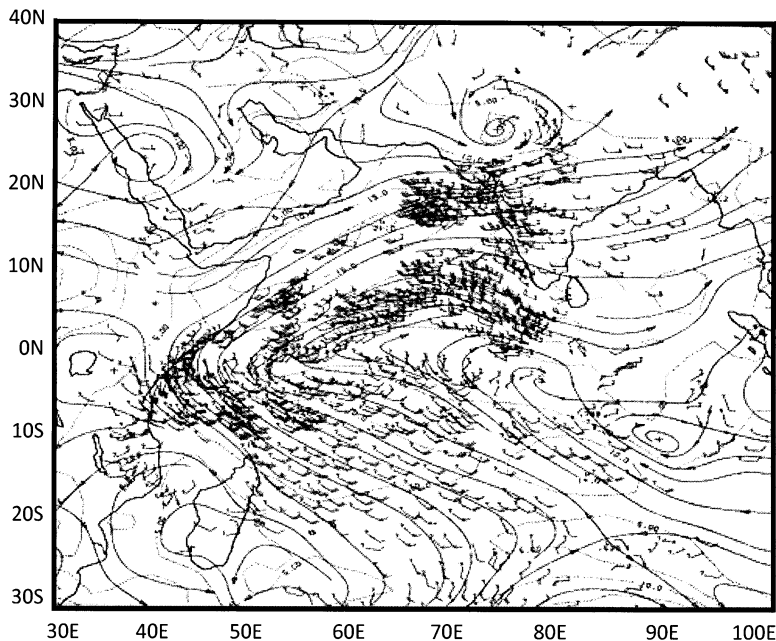


**Fig. 5.30** 850 mb analysis for 16 July 1979, illustrating the simultaneous existence of both branches of the Somali jet

French METEOSAT-East. A look at the daily winds obtained from this rich data source reveals that instances of simultaneous existence of both branches of the jet do indeed occur, as illustrated in Fig. 5.30.

The Somali jet plays an important role in the water budget of the Asian Summer Monsoon. The strong surface winds (on the order of  $5 \text{ ms}^{-1}$ ) over the northern Arabian Sea contribute to a large amount of surface evaporation. It has been estimated that about 50 % of the moisture needed to account for the monsoon rainfall comes from evaporation over the Arabian Sea (Pisharoty 1965).

The Kenya highlands and the Ethiopian mountains serve as a western boundary for the Somali jet. This is illustrated in Fig. 5.31, from Findlater (1969). Shown here are monthly mean vertical cross-sections of the meridional component of the Somali jet winds for May through October. The jet maximum winds are seen at approximately 1 km above sea level, just to the east of the Kenya highlands. The strongest monthly mean winds (about  $12.5 \text{ ms}^{-1}$ ) are seen during the summer months of June, July and August. The Somali jet is the fastest wind system in the low latitudes over the lower troposphere. On individual days, in undisturbed weather conditions, winds as high as  $50 \text{ ms}^{-1}$  have been recorded at the 1 km level at Alula, near the Horn of Africa.

The Somali jet largely owes its existence to the differential heating between the heat source along the principal axis of the monsoon (see Fig. 5.4) and the heat sink

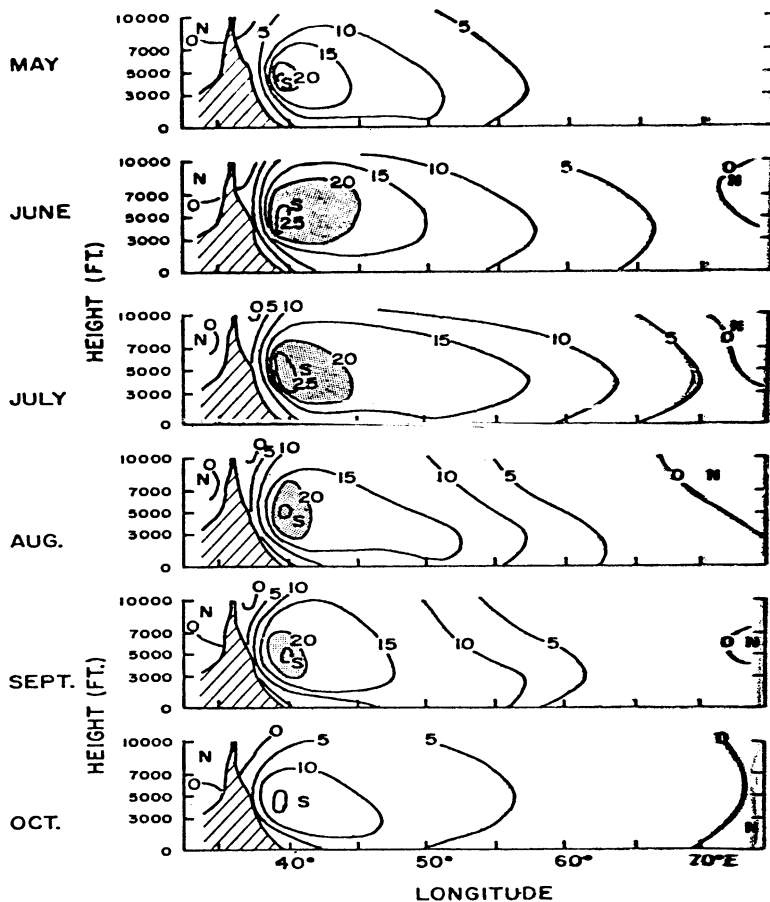


**Fig. 5.31** Climatological monthly mean vertical cross-section of the meridional component (in knots) of the Somali jet for the months of May through October (Adapted from Findlater 1969)

of the Southwestern Indian Ocean. This is schematically depicted in Fig. 5.32 which illustrates the steady northward migration of the monsoon gyre over the Arabian Sea. As the heat source migrates from Indonesia to the foothills of the Himalayas a low-pressure area (the monsoon trough) follows along at sea level. To the south of the monsoon trough westerly winds prevail, extending well into the Arabian Sea.

It is worth noting that the average westerly wind along the Somali jet at the 1 km level is on the order of  $10 \text{ ms}^{-1}$ , of which a large proportion, about 60 %, is contributed by the rotational (*i.e.* non-divergent) component of wind, and the remaining 40 % is due to the divergent component. For details on the computation of the divergent and rotational components of the wind – an important exercise in meteorology – see Sect. 5.13 of this chapter.

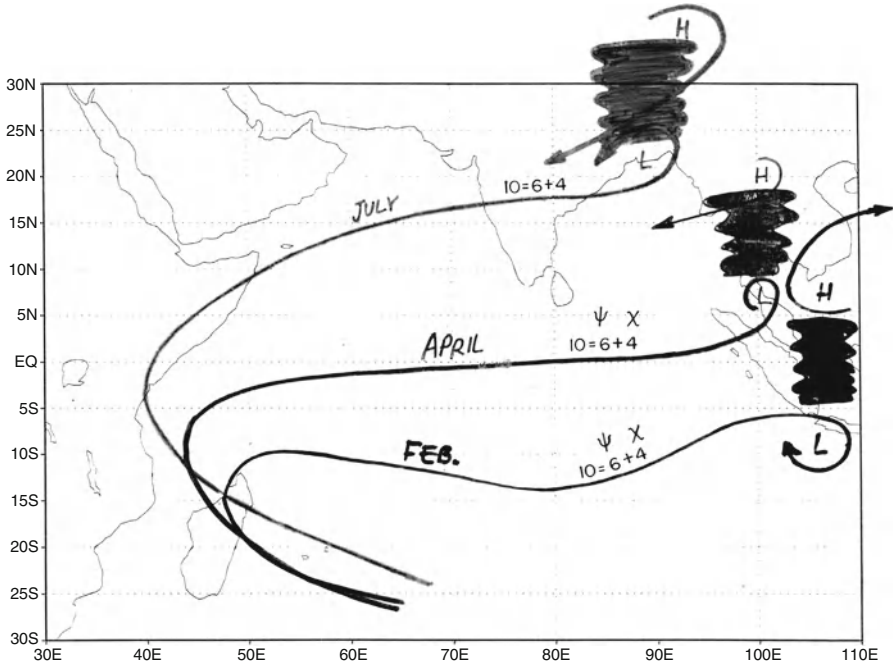


**Fig. 5.32** A schematic illustration of the northward passage of the monsoon gyre

## 5.16 Boundary Layer Dynamics of the Somali Jet

The horizontal equations of motion can be scaled in an interesting manner to define in a gross way some realizable boundary layer structures. Here we shall follow the procedure outlined by Mahrt and Young (1972). The zonal equation of motion, neglecting vertical advection, may be written in the form

$$\frac{\partial u}{\partial t} + u \frac{\partial u}{\partial x} + v \frac{\partial u}{\partial y} - fv = -g \frac{\partial z}{\partial x} + F_x \quad (5.43)$$

i.e., *Tendency (T) + Horizontal Advection (A) + Coriolis Force (C) = Pressure Gradient Force (P) + Friction (F)*. We shall use the following scaling to non-dimensionalize the above equation:

$$u = U u' \quad (5.44)$$

$$\frac{\partial}{\partial x} = \left( \frac{U}{\beta} \right)^{1/2} \frac{\partial}{\partial x'} \quad (5.45)$$

$$f = \beta y \quad (5.46)$$

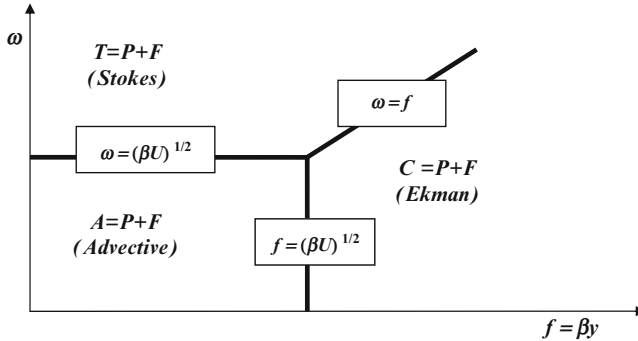


**Fig. 5.33** A schematic illustration of the Ekman, advective and Stokes regimes (After Mahrt and Young 1972)

$$\frac{\partial}{\partial t} = \omega \frac{\partial}{\partial t'} \quad (5.47)$$

where  $\omega$  is a characteristic frequency. In the boundary layer  $P$  and  $F$  are expected to be the dominant terms; the question is, how do  $T$ ,  $A$ , and  $C$  compare with these for different ranges of values of  $\omega$ . The scaling of the above equations gives:

$$\omega U \frac{\partial u'}{\partial t'} + \frac{U^2}{(U/\beta)^{1/2}} \left( u' \frac{\partial u'}{\partial x'} + v' \frac{\partial u'}{\partial y'} \right) - f U v' = P + F \quad (5.48)$$

or

$$\omega \frac{\partial u'}{\partial t'} + (U\beta)^{1/2} \left( u' \frac{\partial u'}{\partial x'} + v' \frac{\partial u'}{\partial y'} \right) - \beta y v' = \frac{P + F}{U}. \quad (5.49)$$

There are three time scales here, namely  $\omega^{-1}$ ,  $(U\beta)^{-1/2}$ , and  $(\beta y)^{-1}$ . Consider the following three cases:

- (i) If  $\omega^{-1} > (\beta y)^{-1}$  and  $(U\beta)^{-1/2} > (\beta y)^{-1}$ , then  $C$ ,  $P$  and  $F$  are the dominant terms, i.e., there is an Ekman balance.
- (ii) If  $(U\beta)^{-1/2} < (\beta y)^{-1}$  and  $(U\beta)^{-1/2} < \omega^{-1}$ , then the dominant terms are  $A$ ,  $P$  and  $F$  i.e., determining what is called an advective, or drift, boundary layer.
- (iii) If  $\omega^{-1} < (\beta y)^{-1}$  and  $(U\beta)^{-1/2} > \omega^{-1}$ , then the dominant terms are  $T$ ,  $P$  and  $F$ . This is called a Stokes regime.

Figure 5.33 is a diagram showing the above three regimes in the  $\omega$ - $f$  space. One is often interested in knowing which of the above three cases is the appropriate one in a given sub-region of the large-scale tropical boundary layer. There also exist, of course, broad transition regions where one would expect to see the overlapping influence of two of the above regions at the same time. In the middle

latitudes the boundary layer (i.e., the lowest kilometer) is typically in Ekman balance. In the Northern Hemisphere, Ekman layer the winds are generally veering (turning clockwise) with height, while in the Southern Hemisphere they are generally backing (turning counterclockwise) with height.

An interesting series of numerical experiments on the dynamical structure of the boundary layer was carried out by Mahrt and Young (1972). Here the solutions of the following system of boundary layer equations were integrated for a prescribed pressure field:the equations of motion,

$$\frac{\partial u}{\partial t} + v \frac{\partial u}{\partial y} + w \frac{\partial u}{\partial z} - fv = -\frac{1}{\rho_0} \frac{\partial p}{\partial x} + K \frac{\partial^2 u}{\partial z^2} \quad (5.50)$$

$$\frac{\partial v}{\partial t} + v \frac{\partial v}{\partial y} + w \frac{\partial v}{\partial z} + fu = -\frac{1}{\rho_0} \frac{\partial p}{\partial y} + K \frac{\partial^2 v}{\partial z^2} \quad (5.51)$$

and the mass continuity equation,

$$\frac{\partial v}{\partial y} + \frac{\partial w}{\partial z} = 0. \quad (5.52)$$

These equations describe flows in a meridional-vertical plane. The eddy diffusion coefficient  $K$  is prescribed, and the pressure field is given as a linear field of the form  $p = ax + by + c$ . The above system of three equations thus contains three unknowns, namely  $u$ ,  $v$  and  $w$ . One integrates the above system from an initial Ekman solution. This is not possible near the equator; there a linear interpolation of the Ekman solution on either side of the equator is necessary to define the initial wind field. The meridional plane usually extends from the middle latitudes of the two hemispheres. At the northern and southern boundaries one uses time-invariant Ekman solutions to define the boundary conditions. A good horizontal and vertical resolution is important for this numerical problem. Mahrt and Young used a vertical resolution of 200 m and a horizontal resolution of 50 km in their integration of the above system of equations.

Here we shall illustrate a particular application of Mahrt and Young's framework that was carried out by Krishnamurti and Wong (1979) as a part of a study of the boundary layer of the East African low-level jet of the northern summer. In this study the meridional distribution of the pressure gradient force was prescribed along 60°E. The model extends from 15° to 25°N. The major results of the boundary layer simulations are shown in Figs. 5.32 and 5.33. Figure 5.34 illustrates the horizontal winds in the meridional plane at 60°E, showing the cross-equatorial flows and a low level jet (the Somali jet) near 12°N. The simulated winds are reasonable when compared with observations. Knowing the long-term steady-state motion field one can compute the various terms in the equations of motion.

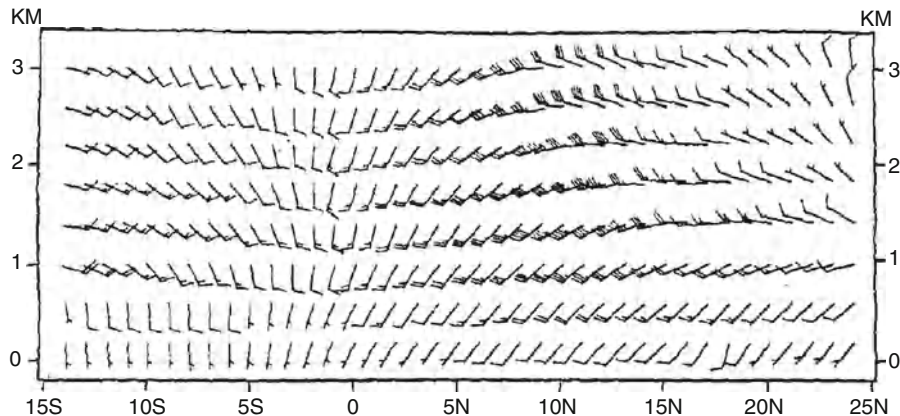


**Fig. 5.34** Horizontal wind barbs in a meridional-vertical plane for an experiment with a height-dependent diffusion coefficient  $K$  (From Krishnamurti and Wong 1979)

The balance of forces in the boundary layer is found to settle to a set of values quite different from that of the initial Ekman layer ( $C \approx P + F$ ). This is shown in Fig. 5.34. Here the simulations show a surface layer near the ground, where the essential balance of forces is between the pressure gradient and friction forces ( $P + F \approx 0$ ), regardless of latitude. Above the surface layer there is a friction layer, where the essential balance of forces in the subtropics is of Ekman type. However, closer to the equator the boundary layer is of the advective type, with the balance of forces being between the horizontal advection, pressure gradient, and friction terms at the equator and among the horizontal advection, Coriolis, pressure gradient, and frictional terms just away from the equator. Aside from the important equatorial regions, there are two other features of interest in the boundary layer of this region: the Somali jet and an ITCZ over the northern Arabian Sea. The calculations show that the Somali jet is located at the poleward edge of the region where the horizontal advective term becomes less important. The ITCZ is noted to form in the general region between the advective and Ekman boundary layers, a result first noted by Mahrt. The aforementioned study and the balance of forces diagram (Fig. 5.35) are very pertinent to the tropical boundary layer.

The above framework is not suitable for investigating time variations of the boundary layer. By prescribing a pressure force, it also limits investigations of thermodynamic inputs, such as air-sea interactions, diurnal variations, etc. Work in these important areas of the boundary layer structure would require a different approach.

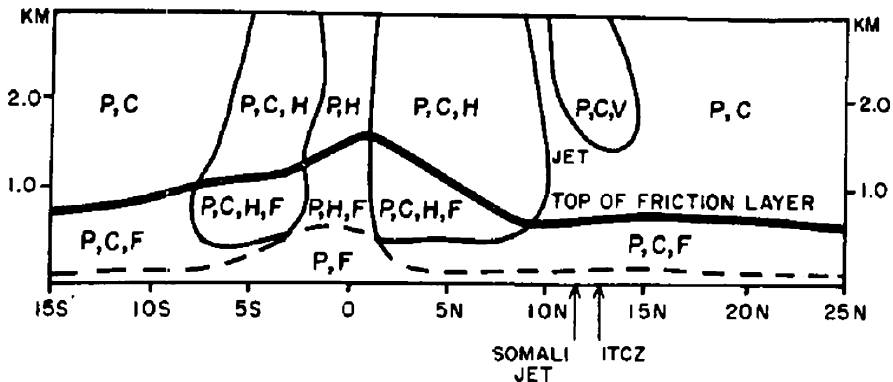


**Fig. 5.35** A schematic illustration of the various regimes determined by the dominant balance of forces, indicated by the letters P for the pressure gradient force, C for the Coriolis force, H for the horizontal advection, V for the vertical advection, and F for the friction. The *dashed line* indicates the top of the surface layer (From Krishnamurti and Wong 1979)

## 5.17 Upwelling in the Somali Jet Region

The strong surface winds of the Somali jet provide some of the strongest wind stress in undisturbed weather conditions. The surface wind stress can be as large as that encountered in tropical storms, i.e. as high as  $4\text{--}6 \text{ Nm}^{-2}$ . The US Navy took a fleet of four ships along the coast of Somalia on August 11 and 12 1975, to measure the sub-surface ocean temperatures over the Arabian Sea. The sub-surface temperatures at the 100 m depth are shown in Fig. 5.36a. Here we see some of the coldest sub-surface waters for any tropical site. The water temperatures are as cold as  $13^\circ\text{C}$ . The surface temperatures of SST over this region were close to  $24^\circ\text{C}$ . This is a region with a very steep thermocline, where strong wind stress leads to strong upwelling that penetrates to a greater depth bringing in colder water from greater depth resulting in the coldest water anywhere in the tropics in the near surface layers. The ocean bottom slope off the Somalia coast is very steep, as illustrated by the bottom topography shown in Fig. 5.36b. The coldest waters lie over a region where the bottom is at around 3,000 m. The interior Arabian Sea waters have a depth of slightly over 5,000 m.

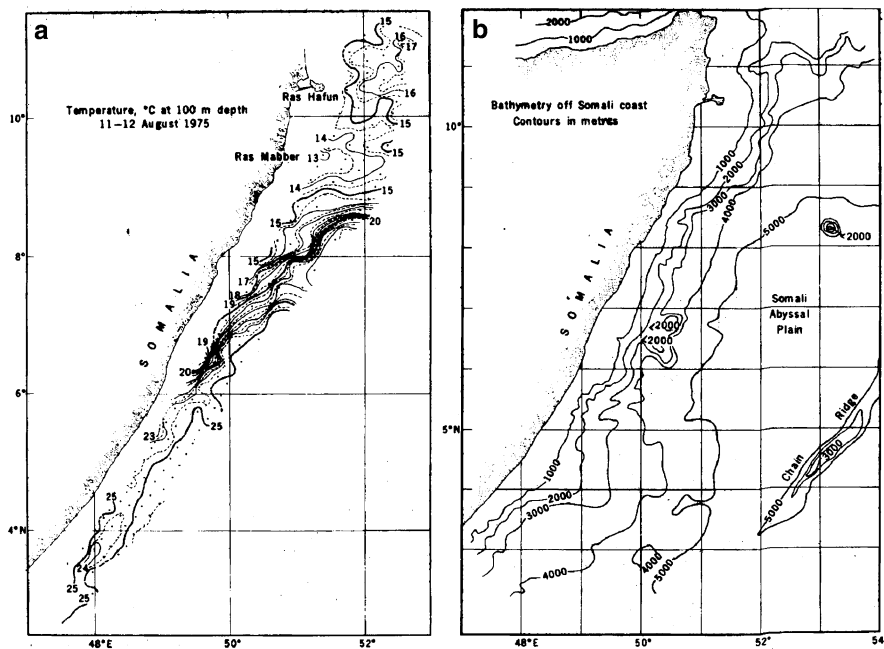


**Fig. 5.36** (a) Temperature ( $^{\circ}\text{C}$ ) at 100 m depth in the Somali current during the peak of summer monsoon in 1975; (b) bottom topography (m) off the Somali coast (From Bruce 1973)

## References

- Ananthakrishnan, R., Soman, M.K.: The onset of the southwest monsoon over Kerala: 1901–80. *J. Climatol.* **8**, 283–296 (1988)
- Bruce, J.G.: Large-scale variations of the Somali current during the southwest monsoon, 1970. *Deep-Sea Res.* **20**, 837–846 (1973)
- Chang, C.P., Harr, P.A., McBride, J., Hsu, H.H.: The maritime continent monsoon. In: Chang, C.P. (ed.) *East Asian Monsoon*, pp. 107–150. World Scientific, Hackensack (2004). Chapter 3
- Chang, C. P.: The maritime continent monsoon. The global monsoon system: research and forecast. WMO/TD Rep. 1266, pp. 156–178 (2005)
- Düing, W., Leetmaa, A.: Arabian Sea cooling: a preliminary heat budget. *J. Phys. Oceanogr.* **10**, 307–312 (1980)
- Findlater, J.: A major low-level air current near the Indian Ocean during the northern summer. *Quart. J. Roy. Soc.* **95**, 362–380 (1969)
- Findlater, J.: Mean monthly airflow at low levels over the western Indian Ocean. *Geophys. Memo.* **16**, 1–53 (1971)
- Gadgil, S., Joseph, P.V.: On breaks of the Indian monsoon. *Proc. Indian Acad. Sci. Earth Planet. Sci.* **112**, 529–558 (2003)
- Janowiak, J.E., Xie, P.: A global-scale examination of monsoon-related precipitation. *J. Climate* **16**, 4121–4133 (2003)
- Krishnamurti, T.N.: Compendium of Meteorology for Use by Class I and Class II Meteorological Personnel. Volume II, Part 4—Tropical Meteorology. Aksel Wiin-Nielsen, World Meteorological Organization - WMO (WMO-No. 364) (1979)

- Krishnamurti, T.N.: Summer monsoon experiment- a review. *Mon. Weather Rev.* **113**, 1590–1626 (1985)
- Krishnamurti, T.N., Ramanathan, Y.: Sensitivity of the monsoon onset to differential heating. *J. Atmos. Sci.* **39**, 1290–1306 (1982)
- Krishnamurti, T.N., Thomas, A., Simon, A., Kumar, V.: Desert air incursions, an overlooked aspect, for the dry spells of the Indian summer monsoon. *J. Atmos. Sci.* **67**, 3423–3441 (2010)
- Krishnamurti, T.N., Wong, V.: Compendium of meteorology - for use by class I and II Meteorological Personnel: Volume II, part 4 - Tropical meteorology T.N. Krishnamurti; Aksel Wiin-Nielsen, World Meteorological Organization - WMO, (WMO No. 364). A planetary boundary layer model for the Somali Jet. *J. Atmos. Sci.* **36**, 1895–1907 (1979)
- Krishnamurti, T.N., Ardanuy, P., Ramanathan, Y., Pasch, R.: The onset-vortex of the summer monsoon. *Mon. Weather Rev.* **109**, 344–363 (1981)
- Krishnamurti, T., Simon, A., Aype, T., Mishra, A., Sikka, D., Niyogi, D., Chakraborty, A., Li, L.: Modeling of forecast sensitivity of the march of monsoon isochrones from Kerala to New Delhi, the first 25 days. *J. Atmos. Sci.* (2012). doi:10.1175/JAS-D-11-0170.1, in press
- Krishnan, R., Zhang, C., Sugi, M.: Dynamics of breaks in the Indian summer monsoon. *J. Atmos. Sci.* **57**, 1354–1372 (2000)
- Mahrt, L.J., Young, J.A.: Some basic theoretical concepts of boundary layer flow at low latitudes. Published in *Dynamics of tropical atmosphere*, 411–420 (1972)
- Pisharoty, P.R.: Evaporation from the Arabian Sea and the Indian Southwest monsoon. *Proc. Int. Indian Ocean Expedition. Pisharoty, P.R. (ed.)*, 43–54 (1965)
- Raj, Y.E.A.: Objective determination of northeast monsoon onset dates over coastal Tamil Nadu for the period 1901–90. *Mausam* **43**, 273–282 (1992)
- Ramage, C.S. (ed.): *Monsoon Meteorology*. International geophysical series, vol. 15. Academic, New York (1971). 296pp
- Ramamurthy, K.: Monsoons of India, some aspects of the ‘Break in the Indian Southwest Monsoon during July and August’. *Forecasting Manual No.IV-18.3*, India Meteorological Department, Pune, pp. 1–57 (1969)
- Tanaka, M.: The onset and retreat dates of the austral summer monsoon over Indonesia, Australia and New Guinea. *J. Met. Soc. Jpn.* **72**, 255–267 (1994)
- Yanai, M., Tomita, T.: Seasonal and interannual variability of atmospheric heat sources and moisture sinks as determined from NCEP–NCAR reanalysis. *J. Climate* **11**, 463–482 (1998)
- Yanai, M., Li, C., Song, Z.: Seasonal heating of the Tibetan Plateau and its effects on the evolution of the Asian summer monsoon. *J. Meteor. Soc. Japan* **70**, 319–351 (1992)

# Chapter 6

## Tropical Waves and Tropical Depressions

### 6.1 Introduction

Tropical waves can be very difficult to locate on synoptic maps, especially in the western Pacific and in the Southern Hemisphere. Such waves, referred to as tropical waves, easterly waves, African waves, etc., are perturbations of the tropical easterlies that propagate westward, at a phase speed of roughly  $5\text{--}7^{\circ}$  longitude/day, sometimes accompanied by clouds and precipitation and pressure changes. Tropical waves can be identified in satellite imagery. The amount of precipitation that a small island in the path of the wave receives is not always proportional to the strength of the wave, as evidenced by the amount of cloudiness seen in the satellite imagery. This is because the amount of cloudiness and weather associated with the wave can change quickly and because rainfall tends to be organized into mesoscale systems which may or may not move directly over the island weather station. Tropical waves moving off the African coast into the eastern Atlantic usually have little convection due to the relatively cold waters and the dry air flowing off the Sahara Desert to the north of the wave. These waves may be tracked across the eastern Atlantic in satellite imagery by following an “inverted-V” cloud pattern, as pointed out by Frank (1968). The inverted-V pattern indicates a perturbation in the wind field possessing a weak vorticity maximum.

Sixty percent of all tropical cyclones form from tropical waves. Many of the category 3, 4 and 5 hurricanes form from tropical waves. Tropical waves produce most of the summer precipitation in the Atlantic Basin. The National Hurricane Center (NHC) tracks tropical waves and writes annual summaries of their occurrence in the Atlantic region. Tropical waves in the Atlantic can also be seen in winter but at lower latitudes compared to summer. These produce much of the winter rain in northern South America.

Figure 6.1 shows a vertical cross-section through a tropical wave as it would typically be seen in the Caribbean region. Ahead of the wave axis are northeasterly winds, low level divergence, sinking motion, and suppressed cloudiness.

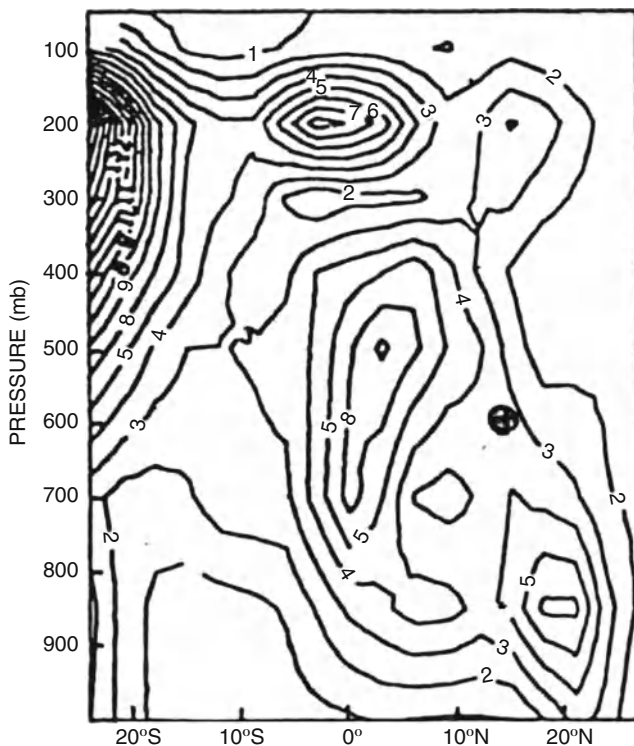


**Fig. 6.1** Meridional section along  $9^\circ\text{W}$  of the meridional wind variance ( $\text{m}^2 \text{ s}^{-2}$ ) for waves of 3–5 day period for August-September 1985. Circled plus sign indicates mean position of the African easterly jet (After Reed et al. 1988)

Behind the wave axis are southeasterly winds, low level convergence, rising motion, and enhanced convection. The wave axis tilts towards the east, and the wind shift is most noticed around 10,000 feet (700 mb). This schematic is of a strong wave. Often, however, the waves are very weak and the wind shift is difficult to locate. It is helpful to look at 24 h surface pressure changes, as there is a couplet of pressure change associated with the wave passage, with falling pressure ahead and rising pressure behind the wave axis. Waves that have not yet developed into tropical cyclones can produce up to five inches of rain, or virtually none at all, as they pass a given location. Thus they pose a very difficult forecast problem even if they do not undergo further development.

The behavior of a tropical wave is strongly influenced by its environment. Extensive research has shown that the tropical waves from the extremely active Atlantic hurricane season of 1995 were really no different from tropical waves of less active years, but a higher percentage of the tropical waves were able to develop into tropical cyclones because of a very favorable larger scale environment of that year.

If a wave is in a westerly sheared environment, as is typical for the Atlantic, the convection will break out to the east of the trough axis. If there is little shear, as in the eastern Pacific where the Mexican anticyclone is found aloft, the convection will be near the wave axis. Finally, if there is easterly shear, as found over West Africa, convection will break out to the west of the wave axis.

In the Atlantic, tropical waves can be tracked from Africa into the Caribbean and then into the eastern Pacific, using:

- (a) Time sections for station in Africa, the Cape Verde Islands, and the Caribbean, focusing on wind shifts aloft and 24 h 1,000 mb height changes; and
- (b) Satellite imagery, whereby the wave axis is located relative to the cloudiness using the above rules concerning vertical shear (e.g. for westerly shear, the wave axis would be located to the west of the observed cloudiness).

The following cautions must be observed in trying to track tropical waves. Typically, one will not see all the classic features falling in place for a given wave, i.e., wind shift, pressure changes, and convection in the proper relation to the wave axis. Flare-ups of convection associated with upper level features must not tempt one to mis-locate the tropical wave axis. A wave should not be dropped just because convection cannot be seen in the satellite imagery, since convection is not the only indicator of the presence of a wave. Convection associated with orography in Central America must not tempt one to mis-locate the tropical wave axis.

Using the above considerations, tropical waves may be tracked from Africa into the Eastern Pacific. Most of the hurricanes in the eastern Pacific develop from perturbations from the Atlantic, as they move into a favorable environment characterized by relatively low surface pressures and upper level divergence associated with the Mexican anticyclone.

African easterly waves (AEFs) range in length from 1,500 to 4,000 km, with 2,500 km being the most cited length. The wave period ranges from 2.5 to 5.5 days, with a majority of studies reporting the period as 3–5 days. The waves move westward at about 8 m/s, or about 5–7° degrees of longitude per day, and are described as originating anywhere from the west coast of Africa to 32°E, with a majority of studies reporting the region of origin as 15–30°E. Finally, African waves are described as reaching their maximum amplitude somewhere in the region from 10°E to 20°W, but with a majority of studies reporting maximum development in the range 5–20°W, or near the west African coast.

There has been considerable debate on how wave amplitude and structures vary in the vertical. Burpee (1972) reported maximum amplitude in the meridional wind spectra as 1–2 m/s near 700 mb. A number of studies have reported two regions of wave activity in the lower troposphere below 700 mb (i.e., 850 mb, 2,000 feet, surface, depending on the study). One region is located near 20°N, coincident with the surface position of the monsoon trough over North Africa, and the other region is located in the equatorial rain belt to the south, around 10°N. (Carlson (1969), Burpee (1974), Reed et al. (1977), Ross (1985), Reed et al. (1988b), Duvel (1990), Thorncroft (1995), Pytharoulis and Thorncroft (1999), Thorncroft and Hodges (2001)).

Pytharoulis and Thorncroft (1999) point out that more attention should be given to the wave regime following the northern track, and to the relationship between the disturbances that follow the two tracks. They cite one reason for giving more attention to the low level structures to the north of the jet; some of these disturbances move over the ocean and could be associated with tropical cyclone formation.

Thorncroft and Hodges (2001) found that there was a strong positive correlation between the frequency of 850 mb wave activity at the West African coast between 10 and 15°N and the frequency of Atlantic tropical cyclones, based on 20 years of data. Tropical cyclone frequency may not vary with the total number of AEWs passing into the Atlantic, but with the number of such waves that have significant low-level amplitude. The vertical structure of the waves may, therefore, be a very important factor in their relation to tropical cyclone formation. It is clear that the study of the low level structure and behavior of AEWs is of considerable importance for our understanding of tropical meteorology over Africa and in the Atlantic basin.

## 6.2 Barotropic Instability

### 6.2.1 Necessary Conditions for the Existence of Barotropic Instability

Consider a wind field that consists of a zonal basic flow with a superimposed perturbation, i.e.,

$$u = U(y) + u', \quad v = v'. \quad (6.1)$$

The stream function  $\Psi$  is defined through

$$u = -\frac{\partial \Psi}{\partial y}, \quad v = \frac{\partial \Psi}{\partial x}. \quad (6.2)$$

The basic flow stream function is given by  $\bar{\Psi}(y)$  such that  $-\frac{\partial \bar{\Psi}}{\partial y} = U$ .

The perturbation stream function  $\Psi'$  is defined through

$$u' = -\frac{\partial \Psi'}{\partial y}, \quad v' = \frac{\partial \Psi'}{\partial x}. \quad (6.3)$$

The barotropic vorticity equation for a flow on a beta-plane is given by

$$\frac{\partial}{\partial t} \nabla^2 \Psi = -J(\Psi, \nabla^2 \Psi) - \beta \frac{\partial \Psi}{\partial x}. \quad (6.4)$$

When linearized for the flow described above, it becomes

$$\frac{\partial}{\partial t} \nabla^2 \Psi' = -U \frac{\partial}{\partial x} \nabla^2 \Psi' - \left( \beta - \frac{\partial^2 U}{\partial y^2} \right) \frac{\partial \Psi'}{\partial x}. \quad (6.5)$$

The perturbation stream function can be expressed as:

$$\Psi' = \psi(y) e^{i\mu(x-ct)}, \quad (6.6)$$

where  $c$  is the complex phase speed and  $\mu$  is the wave number. Upon substitution of (6.6) into (6.5), we obtain:

$$(U - c) \left( \frac{d^2 \psi}{dy^2} - \mu^2 \psi \right) - \left( \frac{d^2 U}{dy^2} - \beta \right) \psi = 0. \quad (6.7)$$

Let us assume a current of finite width centered at  $y = 0$  with rigid boundaries at  $y = \pm D$ . The assumption of rigid boundaries necessitates vanishing of the normal velocities at those boundaries, i.e.,

$$v(x, \pm D, t) = v'(x, \pm D, t) = \frac{\partial}{\partial x} \psi(\pm D) e^{i\mu(x-ct)} = i\mu \psi(\pm D) e^{i\mu(x-ct)} = 0, \quad (6.8)$$

from which it follows that

$$\psi(\pm D) = 0. \quad (6.9)$$

Both the phase speed and the amplitude function  $\psi(y)$  are complex. Let  $\psi^*$  be the complex conjugate of  $\psi$ . Multiplying (6.7) by  $\psi^*$ , we obtain

$$(U - c) \left( \psi^* \frac{d^2 \psi}{dy^2} - \mu^2 \psi^* \psi \right) - \left( \frac{d^2 U}{dy^2} - \beta \right) \psi^* \psi = 0. \quad (6.10)$$

Since  $\psi^* \psi = |\psi|^2$ ,  $\psi^* \frac{d^2 \psi}{dy^2} = \frac{d}{dy} \left( \psi^* \frac{d\psi}{dy} \right) - \frac{d\psi^*}{dy} \frac{d\psi}{dy}$ , and  $\frac{d\psi^*}{dy} \frac{d\psi}{dy} = \left| \frac{d\psi}{dy} \right|^2$ , after division by  $(U - c)$  equation (6.7) becomes:

$$\frac{d}{dy} \left( \psi^* \frac{d\psi}{dy} \right) - \left| \frac{d\psi}{dy} \right|^2 - \mu^2 |\psi|^2 - \left( \frac{d^2 U}{dy^2} - \beta \right) \frac{|\psi|^2}{(U - c)} = 0. \quad (6.11)$$

Integrating (6.11) from  $-D$  to  $D$ , we obtain:

$$\int_{-D}^D \left[ \frac{d}{dy} \left( \psi^* \frac{d\psi}{dy} \right) - \left| \frac{d\psi}{dy} \right|^2 - \mu^2 |\psi|^2 \right] dy = \int_{-D}^D \left( \frac{d^2 U}{dy^2} - \beta \right) \frac{|\psi|^2}{(U - c)} dy. \quad (6.12)$$

Since  $\psi$  vanishes at  $y = \pm D$ , both its real and imaginary parts should vanish at  $y = \pm D$ , and hence  $\psi^*$  also vanishes at  $y = \pm D$ . As a result, the first term of (6.12) is zero. Multiplying (6.12) by the complex conjugate of  $(U - c)$ , we get:

$$\int_{-D}^D \left[ -\left| \frac{d\psi}{dy} \right|^2 - \mu^2 |\psi|^2 \right] dy = \int_{-D}^D \left( \frac{d^2 U}{dy^2} - \beta \right) \frac{|\psi|^2}{|(U - c)|^2} (U - c)^* dy. \quad (6.13)$$

The complex phase speed can be written as a sum of a real and an imaginary component, *i.e.*,  $c = c_r + ic_i$ . Thus

$$(U - c)^* = (U - c_r + ic_i). \quad (6.14)$$

Because of this, equation (6.13) has both a real and an imaginary part. The imaginary part of (6.13) is given by

$$c_i \int_{-D}^D \left( \frac{d^2 U}{dy^2} - \beta \right) \frac{|\psi|^2}{|(U - c)|^2} dy = 0 \quad (6.15)$$

For an amplifying wave, it is necessary that the phase speed have a non-zero imaginary component, *i.e.*,  $c_i \neq 0$ . In such a case, the only way for (6.15) to be satisfied is for the integral to vanish. The integral can only vanish if  $\left( \frac{d^2 U}{dy^2} - \beta \right)$  changes sign at least once in the interval  $y = \pm D$ . Thus the necessary condition for barotropic instability is:

$$\left. \left( \frac{d^2 U}{dy^2} - \beta \right) \right|_{y=y_k} = 0 \text{ for some } y_k \in (-D, D). \quad (6.16)$$

This is equivalent to stating that, in order for a perturbation to be amplifying in a zonal barotropic flow, it is necessary that

$$\frac{d}{dy} \left( -\frac{dU}{dy} + f \right) = \frac{d\zeta_a}{dy} = 0 \text{ for some } y_k \in (-D, D), \quad (6.17)$$

or in other words, that the absolute vorticity of the flow must have a minimum or a maximum somewhere within the basic current.

### 6.2.2 Finite Difference Methods for Studying Barotropic Instability in the Tropics

The second-order differential equation for the unknown amplitude of the perturbation stream function (6.7) can be used to determine the scale corresponding to the fastest growing perturbations in a zonal basic flow. A finite-difference procedure for obtaining a numerical solution to this problem is described below.

Consider a south–north domain spanning from  $y = \pm D$ , with a grid distance of  $\Delta y$ . Let  $j$  be the grid point index in the latitudinal direction, spanning  $j = 1, 2, \dots, J-1, J$ , corresponding to  $y = -D, -D + \Delta y, \dots, D - \Delta y, D$ . From (6.9) we know that the boundary conditions for the problem are  $\psi(\pm D) = 0$ , or, in terms of the index  $j$ ,  $\psi_1 = \psi_J = 0$ . For any point  $j$  within the domain, the second derivative of  $\psi$  can be approximated using finite differences as

$$\frac{d^2\psi}{dy^2}\Big|_j \approx \frac{\psi_{j+1} + \psi_{j-1} - 2\psi_j}{\Delta y^2} \quad (6.18)$$

With this, (6.7) can be expressed in the following finite difference form:

$$(U_j - c)\frac{\psi_{j+1} + \psi_{j-1} - 2\psi_j}{\Delta y^2} - \mu^2\psi_j - \left(\frac{U_{j+1} + U_{j-1} - 2U_j}{\Delta y^2} - \beta\right)\psi_j = 0. \quad (6.19)$$

Both the complex phase speed  $c$  and the complex amplitude function  $\psi$  are unknown at this stage. In order to determine whether a perturbation is amplifying or not, we need to determine whether there is an imaginary component to the phase speed. A positive imaginary component of the phase speed would dictate an amplification of the perturbation, while a negative imaginary component would dictate exponential decay. In order obtain a solution, all terms involving  $\psi$  in the interior of the domain are collected, the boundary conditions  $\psi_1 = \psi_J = 0$  are applied, and a resulting matrix equation for the column vector of  $(\psi_j)$  is written in the form:

$$(\mathbf{B} - c\mathbf{D}) \begin{pmatrix} \psi_2 \\ \psi_3 \\ \vdots \\ \psi_{J-2} \\ \psi_{J-1} \end{pmatrix} = 0, \quad (6.20)$$

where  $\mathbf{B}$  and  $\mathbf{D}$  are known matrices that are functions of  $U, \mu, \beta$ , and  $\Delta y$ . We seek a non-zero solution for the perturbation amplitude, i.e., a non-trivial solution to (6.20). This means

$$|\mathbf{B} - c\mathbf{D}| = 0. \quad (6.21)$$

Solving (6.21) yields the complex eigenvalues for the phase speed  $c$ . Knowing the eigenvalues, the corresponding eigenvectors can be calculated. The eigenvalue with the largest positive imaginary component will correspond to the fastest growing perturbation for the given wave number  $\mu$ . In order to determine what scale has the maximum growth rate, the eigenvalues of  $c$  for a range of values of  $\mu$  are calculated. The growth rate  $\mu c_i$  determines the scale that has the maximum perturbation amplification. Thus one can construct a stability diagram with a plot of the horizontal shear  $dU/dy$  as a function of the scale  $\mu$ . One can also construct the eigenstructure of the most unstable wave by substituting in (6.6) the values of  $\mu$  and  $c$  that yield maximum growth rate, and the corresponding eigenvector  $\psi$ .

## 6.3 Combined Barotropic-Baroclinic Instability

### 6.3.1 Necessary Conditions for the Existence of Combined Barotropic-Baroclinic Instability

We shall not go into a lengthy derivation of the conditions for combined barotropic-baroclinic instability. This is generally derived from a linearized quasigeostrophic system of equations. Unlike the necessary condition for the existence of purely barotropic instability, which uses the conservation of absolute vorticity as an underlying principle, the study of combined barotropic-baroclinic instability is done in the framework of conservation of potential vorticity. Here a basic zonal current  $U(y, p)$  is prescribed and perturbations are described with respect to that basic flow. The quasigeostrophic potential vorticity  $\zeta_p$  is defined as:

$$\zeta_p = \nabla^2 \Psi + f + \frac{\partial}{\partial p} \left( \frac{f_0^2}{\sigma} \frac{\partial \Psi}{\partial p} \right)$$

where  $f_0$  is the mean value of the Coriolis parameter  $f$ ,  $\Psi$  is the stream function, and  $\sigma$  is the dry static stability parameter. The necessary condition for the existence of combined barotropic-baroclinic instability is expressed by the requirement that

$$\frac{\partial \zeta_p}{\partial y} = \left( \beta - \frac{\partial^2 U}{\partial y^2} \right) - \frac{\partial}{\partial p} \left( \frac{f_0^2}{\sigma} \frac{\partial U}{\partial p} \right)$$

must change sign somewhere within the domain of interest. The basic flow  $U(y, p)$  is given and the north south gradient of potential vorticity has to vanish within the domain in order for the necessary condition to be satisfied. The term  $\left( \beta - \frac{\partial^2 U}{\partial y^2} \right)$  constitutes the contribution from the barotropic dynamics, and the term  $- \frac{\partial}{\partial p} \left( \frac{f_0^2}{\sigma} \frac{\partial U}{\partial p} \right)$

**Table 6.1** Estimates of individual terms in the horizontal gradient of mean potential vorticity in units of  $10^{-11} \text{ m}^{-1} \text{s}^{-1}$ . Terms were evaluated at 700 mb from the monthly mean cross-section at 5°E over West Africa during northern summer (Based on Burpee 1972)

Latitude	$-\frac{\partial^2 U}{\partial y^2}$	$\beta$	$-f_0^2 \left( \frac{\partial}{\partial p} \frac{1}{\sigma} \right) \frac{\partial U}{\partial p}$	$-\frac{f_0^2}{\sigma} \frac{\partial^2 U}{\partial p^2}$	$\frac{\partial \zeta_p}{\partial y}$
5.0°N	4.8	2.2	-0.2	-2.0	4.8
7.5°N	6.4	2.2	-0.2	-2.0	6.4
10.0°N	-1.2	2.2	-0.3	-4.0	-3.3
12.5°N	-5.2	2.2	-0.4	-8.0	-11.4
15.0°N	-4.0	2.2	-0.3	-4.0	-6.1
17.5°N	0.0	2.2	-0.4	-2.0	-0.2
20.0°N	0.6	2.2	-0.2	-2.0	0.6
22.5°N	2.8	2.2	-0.1	0.0	4.9
25.0°N	0.0	2.2	0.0	0.0	2.2

represents the baroclinic contribution. The horizontal temperature gradient and resulting thermal wind-related vertical wind shear  $\frac{\partial U}{\partial p}$  are not large enough to satisfy the condition for free baroclinic instability. Even over Africa adjacent to the Sahara Desert where the north-south temperature gradients in the air near the surface are around  $1 \text{ K}/100 \text{ km}$ , free baroclinic modes do not exist. However the barotropic modes can force a baroclinic mode to be present over the tropics. Thus often we see a change of sign for  $\frac{\partial \zeta_p}{\partial y}$  from the barotropic term but not from the baroclinic term. But often in many areas of tropical wave growth such as West Africa we will see the combined barotropic and baroclinic terms contributing to a change of sign of  $\frac{\partial \zeta_p}{\partial y}$ . The low-level easterly jet over northwest Australia also satisfies the same conditions.

That is illustrated in the following tables, which show the various terms in the expansion over West Africa, taken from Burpee (1972) and over northwestern Australia from an unpublished work by Krishnamurti. There are five columns showing respectively the horizontal shear, the beta term, two terms showing the effects of vertical wind shear, and finally, the sum of all these terms. The rows in the tables show different latitudes. The sum of the first two terms denotes the barotropic effects. A change of sign in the sum of the first two terms (as a function of latitude) reflects that the necessary condition for the existence of barotropic instability is satisfied by the data set. This is true for the two low-level jets considered here. The sum of all of the terms also shows a change of sign as a function of latitude, thus satisfying the existence of the combined instability. The question naturally arises – what is the implication if the necessary condition is satisfied by a data set? (Table 6.1)

Here our interpretation is that wave disturbances propagating westward on the cyclonic shear side of the low-level jet could draw energy from the horizontal as well as the vertical shear of the basic current, i.e., the low level jet (Table 6.2).

**Table 6.2** Estimates of individual terms in the horizontal gradient of mean potential vorticity in units of  $10^{-11} \text{ m}^{-1}\text{s}^{-1}$ . Terms were evaluated at 700 mb from the monthly mean cross-section at 125°E over northwestern Australia during southern summer (Based on unpublished work (Krishnamurti))

Latitude	$-\frac{\partial^2 U}{\partial y^2}$	$\beta$	$-f_0^2 \left( \frac{\partial}{\partial p} \frac{1}{\sigma} \right) \frac{\partial U}{\partial p}$	$-\frac{f_0^2}{\sigma} \frac{\partial^2 U}{\partial p^2}$	$\frac{\partial \zeta_p}{\partial y}$
5.0°S	-0.3	2.2	4.6	2.5	9.0
7.5°S	-0.0	2.2	5.9	1.4	9.5
10.0°S	0.3	2.2	-1.9	1.5	2.1
12.5°S	3.5	2.2	-0.1	1.0	6.6
15.0°S	-0.2	2.2	-0.4	-1.8	-0.2
17.5°S	-5.8	2.2	0.3	-2.7	-6.0
20.0°S	-0.8	2.2	-0.2	-5.2	-4.0
22.5°S	2.9	2.2	-0.1	-5.3	-0.3
25.0°S	0.8	2.2	0.2	-5.4	-2.2

In order to go one step beyond this stage towards confirming whether such energy exchanges indeed occur in the maintenance of the wave disturbances, further diagnostic and prognostic studies are needed. Such studies have been carried out by Reed et al. (1977), Norquist et al. (1977) and Krishnamurti et al. (1979a) over West Africa. These studies essentially confirm the importance of baroclinic and barotropic energy exchanges for the maintenance of the wave disturbances.

Finally, it is important to recognize another point of similarity between these two wave disturbances. Most Atlantic hurricanes are known to form from the African waves. Likewise, a large number of tropical storms of the southern Indian Ocean form out of westward propagating wave disturbances that originate in the general region of north of Australia, Indonesia and southern Malaysia.

### 6.3.2 Initial Value Approach to the Combined Instability

This section deals with an initial value approach to the problem of combined barotropic-baroclinic instability including the effects of cumulus convection. For such a combined problem the initial value approach is necessary since the conventional linear instability approach is not possible due to the non-separability of these effects in the equation for wave growth. In the initial value approach the following steps, following Rennick (1976), are involved. First, one writes down the system of five equations and five unknowns (the two horizontal equations of motion, the first law of thermodynamics, the hydrostatic law, and the continuity equation). The problem posed like this is three dimensional in space. The motion is assumed to be hydrostatic, and a heat source  $Q$  is included. This system of equations is then linearized with respect to a time-averaged basic zonal flow on a meridional-vertical plane, i.e.,  $\bar{u}(y, p)$ , where the bar denotes space-time average on

scales of the order of the wavelength and life span of a perturbation. This zonal flow is intended to represent the African Easterly Jet (AEJ). The basic state also includes a temperature field  $\bar{T}(y, p)$  in the same meridional-vertical plane. This basic state temperature field is linked to the basic state's zonal wind by the thermal wind relationship. The basic state does not have any meridional wind ( $\bar{v}(y, p) = 0$ ) nor any vertical motion ( $\bar{\omega}(y, p) = 0$ ). The resulting linearized equations are solved by a low order spectral model that is described below. The solutions of this system are obtained for each assigned zonal wave number  $k$ . For each wave the growths of eddy kinetic energy arising from barotropic, baroclinic, and convective processes are evaluated. The following describes the implementation of the initial value approach to combined instability.

The linearized system of the momentum equation, the first law of thermodynamics, the hydrostatic balance, and the mass continuity equation are expressed by:

$$\frac{\partial u'}{\partial t} + \bar{u} \frac{\partial u'}{\partial x} + \frac{\partial \bar{u}}{\partial y} v' + \frac{\partial \bar{u}}{\partial p} \omega' - fv' + \frac{\partial \phi'}{\partial x} = 0 \quad (6.22)$$

$$\frac{\partial v'}{\partial t} + \bar{u} \frac{\partial v'}{\partial x} + fv' + \frac{\partial \phi'}{\partial y} = 0 \quad (6.23)$$

$$\frac{\partial T'}{\partial t} + \bar{u} \frac{\partial T'}{\partial x} + \frac{\partial \bar{T}}{\partial y} v' + \sigma \omega' = Q' \quad (6.24)$$

$$\frac{\partial \phi'}{\partial p} + \frac{RT'}{p} = 0 \quad (6.25)$$

$$\frac{\partial u'}{\partial x} + \frac{\partial v'}{\partial y} + \frac{\partial \omega'}{\partial p} = 0 \quad (6.26)$$

where the symbols have the usual meanings.  $Q'$  denotes the diabatic heating,  $\sigma = -\frac{\bar{T}}{\bar{\theta}} \frac{\partial \bar{\theta}}{\partial p}$  is the dry static stability, and primes denote perturbations with respect to the mean state. The diabatic heating used by Rennick is a form of a very simple cumulus parameterization scheme. It is simply expressed by the relationship  $Q' = \begin{cases} -\alpha \omega_B & \text{if } \omega_B < 0 \\ 0 & \text{if } \omega_B \geq 0 \end{cases}$ , where  $\alpha$  is a constant and  $\omega_B$  is the vertical velocity at the top of the boundary layer (i.e. around 900 mb level). If the vertical velocity is upward ( $\omega_B < 0$ ) there is convective heating; otherwise, the heating is set to zero. This type of conditional heating is often used in linear dynamical problems.

Requiring that Dine's compensation be satisfied for all times, we may set

$$\frac{\partial}{\partial t} \left( \int_{p_{00}}^0 \frac{\partial \omega'}{\partial p} dp \right) = 0. \quad (6.27)$$

Combining the momentum and the mass continuity equations, (6.27) becomes

$$\left( \frac{\partial^2}{\partial x^2} + \frac{\partial^2}{\partial y^2} \right) \int_{p_{00}}^0 \phi' dp = \int_{p_{00}}^0 \left( \frac{\partial \eta'}{\partial x} + \frac{\partial \xi'}{\partial y} \right) dp, \quad (6.28)$$

where  $\eta' = \frac{\partial u'}{\partial t} + \frac{\partial \phi'}{\partial x}$  and  $\xi' = \frac{\partial v'}{\partial t} + \frac{\partial \phi'}{\partial y}$ . Equation 6.28 can be transformed using the hydrostatic relation (6.25) to yield

$$\left( \frac{\partial^2}{\partial x^2} + \frac{\partial^2}{\partial y^2} \right) \phi'(p_{00}) = -\frac{1}{p_{00}} \int_{p_{00}}^0 \left[ \frac{\partial \eta'}{\partial x} + \frac{\partial \xi'}{\partial y} + \left( \frac{\partial^2}{\partial x^2} + \frac{\partial^2}{\partial y^2} \right) R \int_{p_{00}}^p \frac{T'}{p^*} dp^* \right] dp \quad (6.29)$$

This is an elliptic equation whose solution provides the lower boundary condition  $\phi'(p_{00})$ . In principle, the solution consists of marching in time with the momentum (6.22) and (6.23) and the thermal equations (6.24) to obtain future values of  $u'$ ,  $v'$  and  $T'$ . Equation 6.29 is a Poisson equation that determines  $\phi'$  at the lower boundary. The hydrostatic law (6.25) provides  $\phi'$  at all other levels and finally the vertical velocity comes from the mass continuity equation given by (6.26).

In order to solve the initial value problem, Rennick (1976) proposed a solution of the form

$$F(x, y, p, t) = F_1(y, p, t) \sin kx + F_2(y, p, t) \cos kx, \quad (6.30)$$

where  $F$  is any of the dependent variables  $u$ ,  $v$ ,  $\omega$ ,  $T$ , or  $\phi$ . Equation 6.30 describes a single wave with wave number  $k$ . The idea here is to take one wave at a time and study its growth. The wave number  $k$  with a corresponding wavelength  $L = 2\pi/k$  is one whose growth is under investigation. One substitutes the above expression (6.30) for  $u$ ,  $v$ ,  $\omega$ ,  $T$  and  $\phi$  into (6.22) through (6.26), and the resulting five equations are multiplied by either  $\sin kx$  or  $\cos kx$  and integrated over the wavelength  $L$  of the disturbance. This integration along  $x$  over the wave length  $L$  is an implementation of the Fourier transformation method. It will allow us to obtain the Fourier transform for each of our equations. In the process the trigonometric dependence along  $x$  will disappear from the system of equations. This is due to the fact that integrals of  $\sin kx$ ,  $\cos kx$  and  $\sin kx \cos kx$  vanish upon integration from 0 to  $2\pi$ , whereas the integrals of  $\sin^2 kx$  and  $\cos^2 kx$  from 0 to  $2\pi$  do not vanish.

This results in the following ten equations which represent the spectral equations of the model. Note that there are now twice the number of equations, one for the sine part, and one for the cosine part.

$$\frac{\partial u_1}{\partial t} - k\bar{u}u_2 + \frac{\partial \bar{u}}{\partial y}v_1 + \frac{\partial \bar{u}}{\partial p}\omega_1 - fv_1 - k\phi_2 = 0 \quad (6.31)$$

$$\frac{\partial u_2}{\partial t} + k\bar{u}u_1 + \frac{\partial \bar{u}}{\partial y}v_2 + \frac{\partial \bar{u}}{\partial p}\omega_2 - fv_2 + k\phi_1 = 0 \quad (6.32)$$

$$\frac{\partial v_1}{\partial t} - k\bar{u}v_2 + fu_1 + \frac{\partial \phi_1}{\partial y} = 0 \quad (6.33)$$

$$\frac{\partial v_2}{\partial t} + k\bar{u}v_1 + fu_2 + \frac{\partial \phi_2}{\partial y} = 0 \quad (6.34)$$

$$\frac{\partial T_1}{\partial t} - k\bar{u}T_2 + \frac{\partial \bar{T}}{\partial y}v_1 + \sigma\omega_1 = Q_1 \quad (6.35)$$

$$\frac{\partial T_2}{\partial t} + k\bar{u}T_1 + \frac{\partial \bar{T}}{\partial y}v_2 + \sigma\omega_2 = Q_2 \quad (6.36)$$

$$\frac{\partial \phi_1}{\partial p} + \frac{RT_1}{p} = 0 \quad (6.37)$$

$$\frac{\partial \phi_2}{\partial p} + \frac{RT_2}{p} = 0 \quad (6.38)$$

$$-ku_2 + \frac{\partial v_1}{\partial y} + \frac{\partial \omega_1}{\partial p} = 0 \quad (6.39)$$

$$ku_1 + \frac{\partial v_2}{\partial y} + \frac{\partial \omega_2}{\partial p} = 0 \quad (6.40)$$

The solution of  $\phi$  at the boundaries requires the specification of  $\phi_1$  and  $\phi_2$  at the two north-south boundaries. These are both set to zero to assure a closed domain, i.e.,  $v' = 0$ . The lower boundary condition given by (6.29) is also cast into two similar equations, namely:

$$\left( -k^2 + \frac{\partial^2}{\partial y^2} \right) \phi_1(p_{00}) = -\frac{1}{p_{00}} \int_{p_{00}}^0 \left[ -k\eta_2 + \frac{\partial \xi_1}{\partial y} + \left( -k^2 + \frac{\partial^2}{\partial y^2} \right) R \int_{p_{00}}^p \frac{T_1}{p^*} dp^* \right] dp \quad (6.41)$$

$$\left(-k^2 + \frac{\partial^2}{\partial y^2}\right)\phi_2(p_{00}) = -\frac{1}{p_{00}} \int_{p_{00}}^0 \left[ k\eta_1 + \frac{\partial\xi_2}{\partial y} + \left(-k^2 + \frac{\partial^2}{\partial y^2}\right)R \int_{p_{00}}^p \frac{T_2}{p^*} dp^* \right] dp, \quad (6.42)$$

where  $\eta_1 = \frac{\partial u_1}{\partial t} - k\phi_2$ ,  $\eta_2 = \frac{\partial u_2}{\partial t} + k\phi_1$ ,  $\xi_1 = \frac{\partial v_1}{\partial t} + \frac{\partial\phi_1}{\partial y}$ , and  $\xi_2 = \frac{\partial v_2}{\partial t} + \frac{\partial\phi_2}{\partial y}$ .

The numerical solution to the system of (6.31) through (6.39) with boundary conditions given by (6.41) and (6.42) is relatively straightforward. Rennick utilizes the following predictor-corrector for the time differencing (or marching) of  $u$ ,  $v$  and  $T$ :

$$\begin{aligned} F^{(n+1)} &= F^n + G^n \Delta t \\ F^{n+1} &= \frac{1}{2} \left( F^{(n+1)} + F^n \right) + G^{(n+1)} \Delta t \end{aligned} \quad (6.43)$$

This is a two-step predictor-corrector scheme. In the first step of the scheme, a temporary predicted value of  $F$  at time step  $n + 1$ ,  $F^{(n+1)}$ , is calculated using the value of  $F$  at the current time step  $n$ ,  $F^n$ , and the current value of the right hand side of the predictive equation given by  $G^n$ . The second step of the scheme calculates the corrected value of  $F$  at time step  $n + 1$ ,  $F^{n+1}$ , using the temporary  $F^{(n+1)}$ ,  $F^n$  and the recalculated value of  $G^{(n+1)}$ . Centered differences may be used for all spatial derivatives. Thus one can integrate this system for a given scale and examine the growth of the wave.

The combined instability itself is addressed after the fact from an examination of the energetics of such a model. Here the zonal kinetic energy is simply  $ZKE = \frac{1}{2}\bar{u}^2$ . The eddy kinetic energy is given by  $EKE = \frac{1}{2}(u'^2 + v'^2)$ . The equation for the rate of change eddy kinetic energy is obtained from a multiplication of the zonal and the meridional momentum equations by  $u'$  and  $v'$  respectively, adding the two equations together, and integrating. Similarly, the rate of change of eddy available potential energy,  $EAPE$ , is obtained from the first law of thermodynamics. The resulting equations for  $EKE$  and  $EAPE$  are

$$\frac{\partial EKE}{\partial t} = \frac{\Delta p}{g} \left( -\frac{\partial \bar{u}}{\partial y} [u'v'] - \frac{\partial \bar{u}}{\partial p} [u'\omega'] - \frac{R}{p} [T'\omega'] - \frac{\partial}{\partial y} [\phi'v'] - \frac{\partial}{\partial p} [\phi'\omega'] \right) \quad (6.44)$$

$$\frac{\partial EAPE}{\partial t} = \frac{\Delta p}{g} \left( \frac{R}{\sigma p} \frac{\partial \bar{T}}{\partial y} [T'v'] + \frac{R}{p} [T'\omega'] + \frac{R}{\sigma p} [T'Q'] \right) \quad (6.45)$$

These denote the time rate of change of eddy kinetic and eddy available potential energy, respectively, of the modeled atmosphere. The brackets here represent a zonal average over one wavelength. An examination of graphs of these energies as a function of time can be used to assess the relative importance of the barotropic and

baroclinic processes. In (6.44) the first two terms,  $-\frac{\partial \bar{u}}{\partial y}[u'v'] - \frac{\partial \bar{u}}{\partial p}[u'\omega']$ , represent the barotropic energy conversion of zonal to eddy kinetic energy. If this is positive, the eddy kinetic energy, *EKE*, grows at the expense of the zonal kinetic energy, *ZKE*. The term  $-\frac{R}{p}[T'\omega']$  is the baroclinic energy conversion term. If warm air rises and relatively cooler air descends over the domain in consideration, then the eddy available potential energy, *EAPE*, is converted into eddy kinetic energy, *EKE*. The terms  $-\frac{\partial}{\partial y}[\phi'v'] - \frac{\partial}{\partial p}[\phi'\omega']$  represent the boundary fluxes, implying that the African waves could be driven by external influences, although generally this effect is very small. In the equation for eddy available potential energy, the first term,  $\frac{R}{\sigma p} \frac{\partial \bar{T}}{\partial y}[T'v']$ , represents the conversion between zonal and eddy available potential energies. The second term,  $\frac{R}{p}[T'\omega']$ , denotes the conversion of eddy available potential energy to eddy kinetic energy by the baroclinic processes. Note that this term appears with opposite sign in (6.44) and (6.45), since it represents the energy that *EAPE* loses to *EKE*, which is the same as the energy *EKE* gains from *EAPE*. The last term in (6.45) is the generation term for the *EAPE* due to convective heating. If convective heating occurs where it is warm (note that there is no cooling with the conditional definition of convection used here), this term denotes the generation of *EAPE*.

The following summarizes the theories and conclusions that can be made regarding the different processes responsible for the formation of African easterly waves:

- (a) Many observational studies suggest that horizontal shear flow instability may be an important mechanism for the initial formation of disturbances. This is the barotropic instability problem. Krishnamurti et al. (1979a) calculated a function  $\langle K_Z \rightarrow K_E \rangle = -\bar{u} \frac{\partial}{\partial y}[u'v']$ , averaged over a domain covering West Africa and the eastern Atlantic Ocean. This function measures the barotropic energy exchange between the zonal mean flow and the eddies within that domain. Carrying out those computations for an entire hurricane season it was noted that the lower tropospheric flows of that region show a rather large exchange of energy from the easterly zonal flows to the African waves. The term  $-\frac{\partial}{\partial y}[u'v']$  denotes the convergence of meridional eddy flux of momentum. If there is a net convergence of westerly eddy flux (i.e.  $\frac{\partial}{\partial y}[u'v'] > 0$ ) in the region of the easterly mean flow, the easterly jet weakens. In the barotropic framework this implies that the loss of energy for the easterly zonal flows must go to the waves since the total kinetic energy is an invariant for barotropic flows. Thus there is considerable interest in the barotropic shear flow dynamics of the West African low level jet.

- (b) There is a simple theory based on the meridional profile of mean zonal flows and the zonally averaged vorticity that provides insight on the possibility for wave growth in shearing flows. This theory goes back to the days of Rayleigh (1919).
- (c) If such a minimum for absolute vorticity is found it implies that wave growth in such an environment is possible.
- (d) It is possible to construct a diagram showing the barotropic growth rate as a function of the horizontal scale of waves for a prescribed shear flow. This can be done using a finite difference method.
- (e) The region of the African easterly jet carries both horizontal and vertical wind shear. The horizontal shear often satisfies the necessary condition for the growth of waves. The finite difference method often suggests that waves on the order of 3,000 km are most unstable in this region since they carry the largest growth rates. One needs to ask what about the prevailing vertical wind shear? The north-south temperature gradient of air in the lower troposphere is  $<1^{\circ}\text{C}$  per degree latitude. That is too small a temperature gradient for the free growth of baroclinically unstable waves. However vertical shear could still provide some energy for the free growth of waves when horizontal shear is a robust energy source. This would be a forced baroclinic growth in the presence of barotropic growth. This is normally labeled as the combined barotropic-baroclinic instability.
- (f) There is a mathematical difficulty in the linear stability analysis for the combined barotropic-baroclinic instability problem. The two mechanisms (barotropic and baroclinic) are non-separable and therefore that the conventional linear approach to stability assessment can not be applied. The initial value approach takes the basic state to be time invariant function in the latitude/pressure plane. Time dependent linear perturbations are introduced and a linear system of closed equations is obtained for these perturbations of a given horizontal scale. This system is integrated forward in time to examine the growth of different imposed scales. This way the growth of a single imposed scale at a time is studied. In that sense this is a single-wave spectral model. A Fourier transform of the closed system of equations removes the spatial dependence while keeping only the time dependent amplitude functions for the different variables. After a number of such integrations in time are carried out, one carries out energy exchange computations for the rate of growth of the eddy kinetic energy of the imposed scale of the wave. These exchanges include the barotropic, baroclinic, and heating-induced (from cumulus convection) processes. This is a numerical initial value approach for addressing the combined instability problem that overcomes the difficulties of the eigenvalue approach of linear stability analysis.
- (g) The primary result of Rennick (1976) study is that African waves primarily draw their energy from the horizontal shear flows of the African low-level jet. The roles of the vertical shear and convection in supporting the growth of the eddy kinetic energy of African waves are also non-trivial. During the formation stage of the African waves the most important role is that of horizontal shear (the barotropic processes). Next in importance is the role of vertical shear (i.e. the baroclinic processes), followed by convection.

## 6.4 Dual Parts of African Waves

Recent observations and analysis have shown that two clusters of tracks of African waves exist over the eastern Atlantic Ocean. The African easterly jet of the northern summer season is located roughly near  $13^{\circ}\text{N}$  and has its maximum winds (on the order of  $30\text{ ms}^{-1}$ ) near the 600 mb level. Clusters of tracks of westward moving African waves have been noted both to the north and south of the African easterly jet. Figure 6.2 from Reed et al. (1988) illustrates a plot of the meridional wind covariance of storms (measured by the frequency of disturbance passage as a function of latitude and pressure) on the time scale of 3–4 days.

This vertical cross section of the frequency shows a pronounced wave activity near the 600 mb level south of the jet near  $9^{\circ}\text{N}$ . This is the latitude of the primary African waves that lie on the cyclonic shear side of the African easterly jet. To the north of the easterly jet lies the Saharan jet where the heat low and low level convergence associated with it is the seat of a second family of African waves. These carry a large meridional wind variance near the 850 mb level at about  $20^{\circ}\text{N}$ . The waves south of the latitude of the African easterly jet tend to be moister whereas the ones north of the jet tend to be dust-laden and considerably drier as they diverge out of Africa into the eastern Atlantic Ocean. The location of the African easterly jet in Fig. 6.1 is shown by a symbol X. There are intraseasonal differences in the frequency of the two families of African waves. In the months of June and July more cyclonic relative vorticity (magnitudes greater than  $4 \times 10^{-5}\text{ ms}^{-1}$ ) is noted for the northern family of waves while during the months

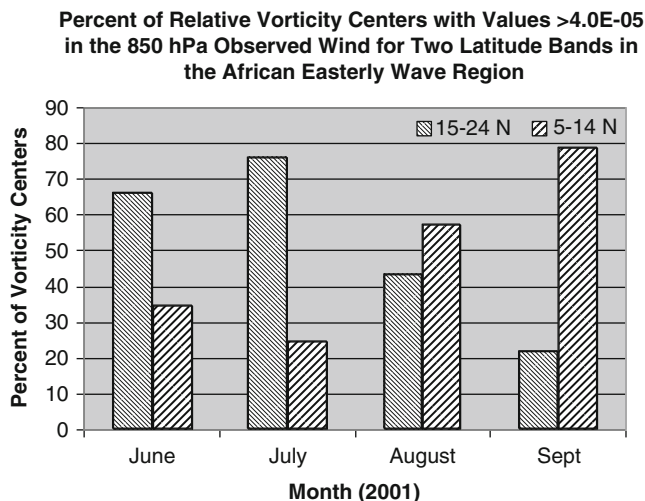


**Fig. 6.2** Percent of observed 850 hPa relative vorticity centers of magnitude greater than  $4.0 \times 10^{-5}$  in two latitude bands, 5N–14N and 15N–24N, distributed by month, June–September of 2001, in the African easterly wave region (35W–15E and 5S–30N) (From Ross and Krishnamurti 2007)

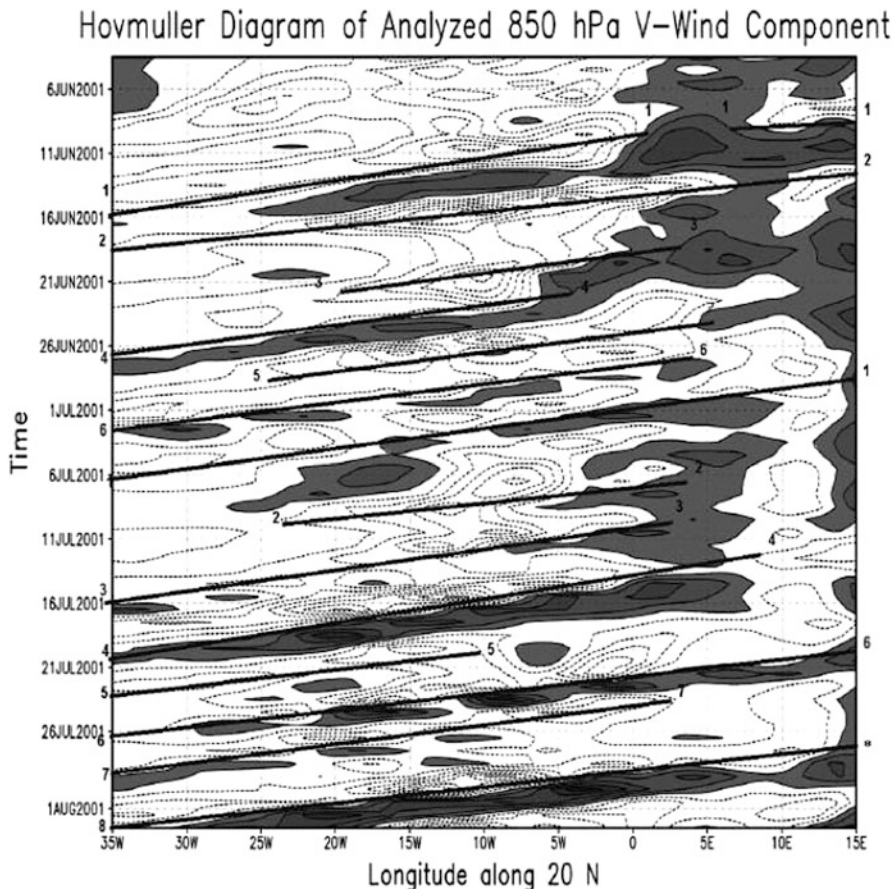


**Fig. 6.3** Hovmuller diagrams of analyzed (observed) 850 hPa meridional wind component ( $\text{ms}^{-1}$ ) in the longitude band 15E–35W for: June–July of 2001 along 20N. Positive values (southerly wind component) are shown with *solid lines*, and negative values (northerly wind component) are shown with *broken lines*. Propagation of African easterly waves is depicted by lines sloping from upper right to lower left and numbered consecutively for each month (From Ross and Krishnamurti 2007)

of August and September the southern family of waves is dominant. This is illustrated in Fig. 6.3 from a recent study by Ross and Krishnamurti (2007).

The Atlantic hurricane season generally lasts from June through November. The earlier part of the season is largely dominated by the waves in the northern part of the domain, whereas the latter part of the season sees more of the southern waves. However a certain number of northern waves (near 25 %) can be seen throughout the season. These can occur simultaneously both north and south of the African easterly jet. The westward propagation of these two families of African waves can be best illustrated via a Hovmuller diagram of the meridional winds. Figures 6.4 and 6.5 shows these diagrams for the longitude belt 35W to 15E for the early (June, July) and late (August, September) parts of the hurricane season.

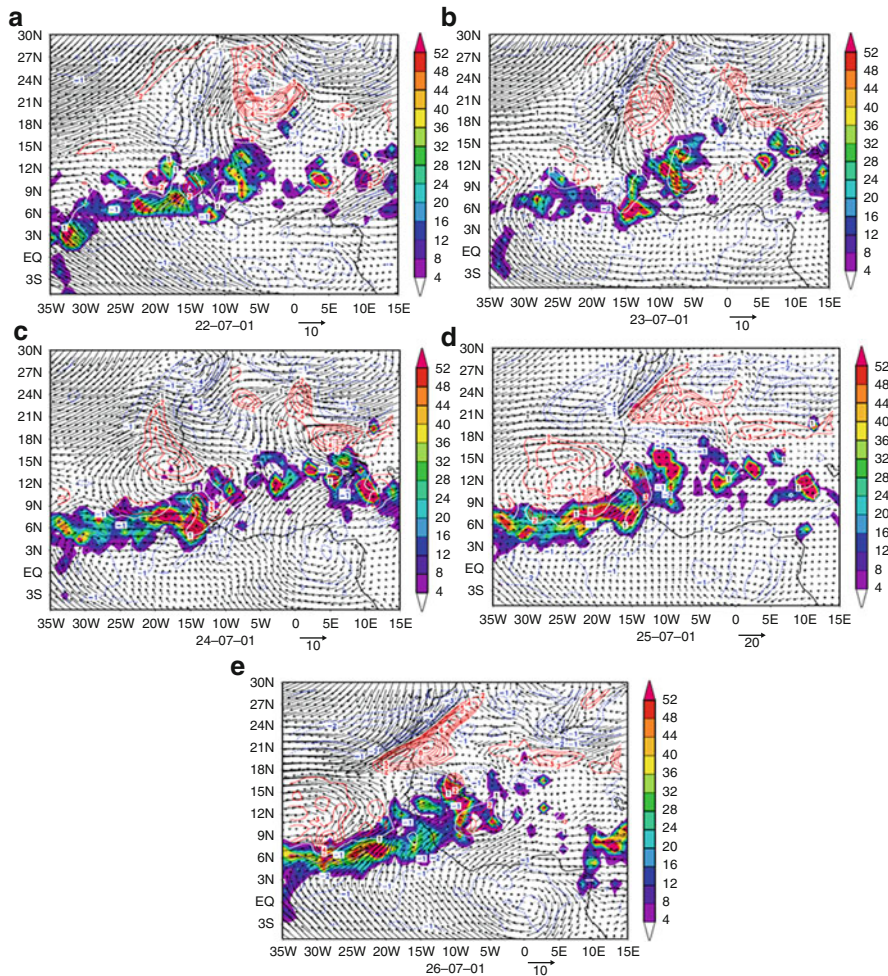


**Fig. 6.4** Observed 850 hPa vector wind and relative vorticity ( $10^{-5} \text{ s}^{-1}$ ), along with observed 24 h precipitation ( $\text{mm day}^{-1}$ ), for wave 6 in July (precursor to Tropical Storm Barry) during the five-day period 22–26 July 2001: (a) top left 1200 UTC 22 July 2001, (b) top right 1200 UTC 23 July 2001, (c) middle left 1200 UTC 24 July 2001, (d) middle right 1200 UTC 25 July 2001, (e) bottom 1200 UTC 26 July 2001 (From Ross and Krishnamurti 2007)

Roughly 14 waves can be noted along the 20N latitude for the early season, and roughly the same number of waves near 10N for the late season. These longitude-time sections are at the 850 mb level where the maximum meridional wind intensity is on the order of  $3\text{--}6 \text{ ms}^{-1}$ . The southern waves are somewhat stronger in intensity. These waves travel eastward at a speed of roughly 70 km/day. Following the work

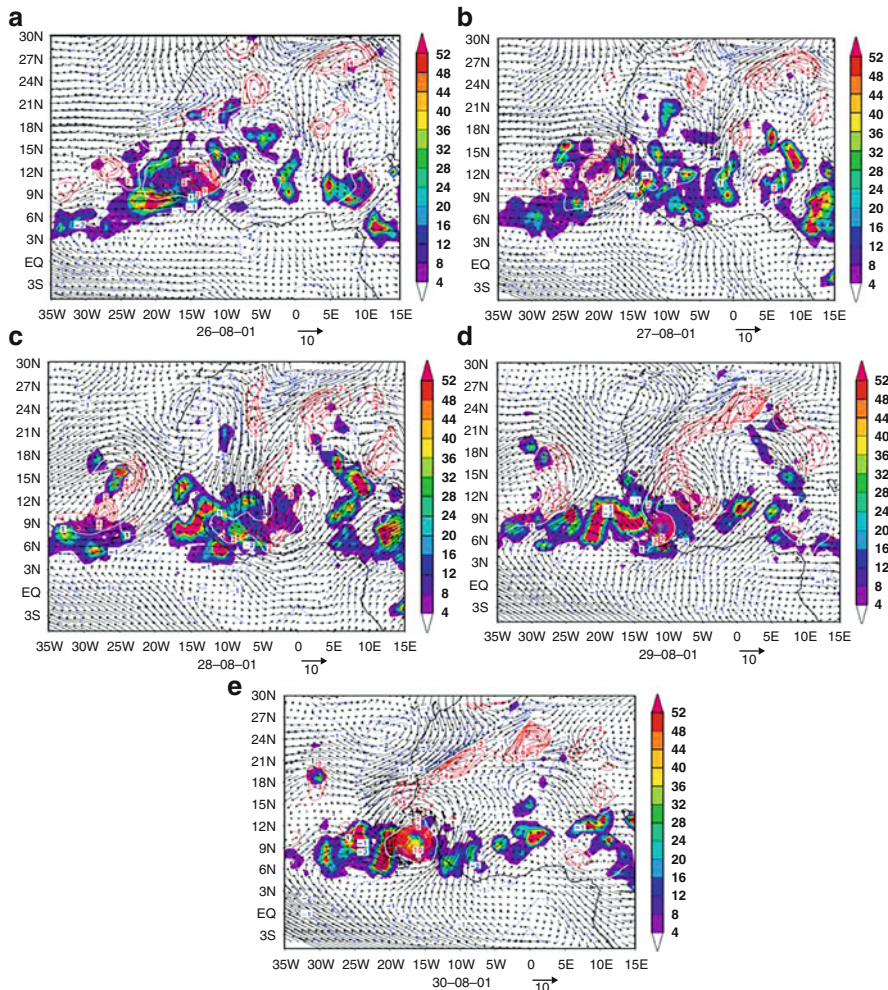


**Fig. 6.5** Observed 850 hPa vector wind and relative vorticity ( $10^{-5} \text{ s}^{-1}$ ), along with observed 24 h precipitation ( $\text{mm day}^{-1}$ ), for wave 6 in August (precursor to Hurricane Erin) during the five-day period 26–30 August 2001: (a) top left 1200 UTC 26 August 2001, (b) top right 1200 UTC 27 August 2001, (c) middle left 1200 UTC 28 August 2001, (d) middle right 1200 UTC 29 August 2001, (e) bottom one 1200 UTC 30 August 2001 (From Ross and Krishnamurti 2007)

of Ross and Krishnamurti (2007), we shall next illustrate the formation of a tropical cyclone and of a hurricane from these two families of African waves. Figures 6.4 and 6.5 shows a sequence of 850 mb charts showing the westward passage of two waves – a northern and a southern one. The northern wave (Fig. 6.4) moved southwestward and eventually formed tropical storm Barry in July 2001. The

southern wave (Fig. 6.5) moved due west and formed hurricane Erin in August 2001. Although such northern and southern waves often stay somewhat separated in latitude when they are simultaneously present, they do sometimes merge and have been known to form major hurricanes.

## References

- Burpee, R.W.: The origin and structure of easterly waves in the lower troposphere of North Africa. *J. Atmos. Sci.* **29**, 77–90 (1972)
- Burpee, R.W.: Characteristics of North African easterly waves during summers of 1968 and 1969. *J. Atmos. Sci.* **31**, 1556–1570 (1974)
- Carlson, T.N.: Synoptic histories of three African disturbances that developed into Atlantic hurricanes. *Mon. Weather Rev.* **97**, 256–276 (1969)
- Duvel, J.P.: Convection over tropical Africa and the Atlantic Ocean during northern summer part II: modulation by easterly waves. *Mon. Weather Rev.* **118**, 1855–1868 (1990)
- Frank, N.: The “Inverted V” cloud pattern—an easterly wave? *Mon. Weather Rev.* **97**, 130–140 (1968)
- Krishnamurti, T.N., Pan, H.L., Chang, C.B., Ploshay, J., Walker, D., Oodally, A.W.: Numerical weather prediction for GATE. *J. Roy. Met. Soc.* (1979a) (To appear in the October issue of the Quart)
- Norquist, C.C., Recker, E.E., Reed, R.J.: The energetics of African wave disturbances as observed during phase III of GATE. *Mon. Weather Rev.* **105**, 334–342 (1977)
- Pytharoulis, I., Thorncroft, C.D.: The low-level structure of African easterly waves in 1995. *Mon. Weather Rev.* **127**, 2266–2280 (1999)
- Rayleigh, L.: The traveling cyclone. *Mon. Weather Rev.* **47**, 644 (1919)
- Reed, R.J., Norquist, D.C., Recker, E.E.: The structure and properties of African wave disturbances as observed during phase III of GATE. *Mon. Weather Rev.* **105**, 317–333 (1977)
- Reed, R.J., Klinker, E., Hollingsworth, A.: The structure and characteristics of African easterly wave disturbances as determined from the ECMWF operational analysis/forecast system. *Meteor. Atmos. Phys.* **38**, 22–33 (1988)
- Rennick, M.A.: The generation of African waves. *J. Atmos. Sci.* **33**, 1955–1969 (1976)
- Ross, R.S.: Diagnostic studies of African Easterly waves observed during GATE. Technical report, National Science Foundation Grant No.TM-7825857, Department of Earth Sciences, Millersville University of PA, pp. 375 (1985)
- Ross, R.S., Krishnamurti, T.N.: Low-level African easterly wave activity and its relation to tropical cyclone activity in 2001. *Mon. Weather Rev.* **135**, 3950–3964 (2007)
- Thorncroft, C.D.: An idealized study of African easterly waves part III. *Q. J. Roy. Meteor. Soc.* **121**, 1589–1614 (1995)
- Thorncroft, C.D., Hodges, K.: African easterly wave variability and its relationship to Atlantic tropical cyclone activity. *J. Climate* **14**, 1166–1179 (2001)

# Chapter 7

## Madden Julian Oscillation

### 7.1 Observational Aspects

The Madden Julian Oscillation, often abbreviated as MJO, is a major feature of the tropical circulation. It manifests as quasi-periodic fluctuations in the sea level pressure and wind structure, and consequently – in the sea surface temperature, convection and rainfall. The time scale of the phenomenon is, on average, about 30–60 days. It was first discovered by Madden and Julian (1971) as they studied the zonal winds and the sea level pressure in a 10-year long record of tropical data. The MJO time scales carry a significant proportion of the atmospheric variance in the tropics.

In order to see this phenomenon clearly, a band pass filter in time is usually applied. Once the filtering is done, the MJO sea level pressure anomaly manifests as a planetary wave that moves from west to east, completing a full circle around the globe in about 40 days. The largest anomaly (roughly a few mb) are found in the equatorial latitudes, particularly over the equatorial Indian Ocean and the equatorial western Pacific Ocean. The seasonal and geographical distributions of the 850 mb zonal wind anomalies associated with the MJO are shown in Fig. 7.1a–d. Some of the prominent features seen here are the build-up of the zonal wind anomalies over the near-equatorial latitudes during the spring and summer seasons of the northern hemisphere. During these two seasons, large anomalies reside over the Arabian Sea and extend eastwards. The values during summer (the summer monsoon season) are as large as  $3\text{--}5 \text{ ms}^{-1}$ . These values are sufficiently large that one can in fact see the presence of this eastward propagating MJO wave in such wind field data sets.

By the fall season the Indian and Pacific Ocean amplitudes of the zonal wind anomalies on the MJO time scale cover a smaller area. During the winter months most of the tropics carry weaker amplitudes, on the order of  $1\text{--}2 \text{ ms}^{-1}$ . The MJO in the tropics stands out because it carries a sizable proportion of the total variance of the wind field. It is interesting to note that some of the largest amplitudes of oscillation of the zonal wind on the time scale of 20–60 days reside polewards of the  $50^\circ$  latitudes. Here the amplitude reaches as high as  $9 \text{ ms}^{-1}$ , mostly over the oceanic regions.

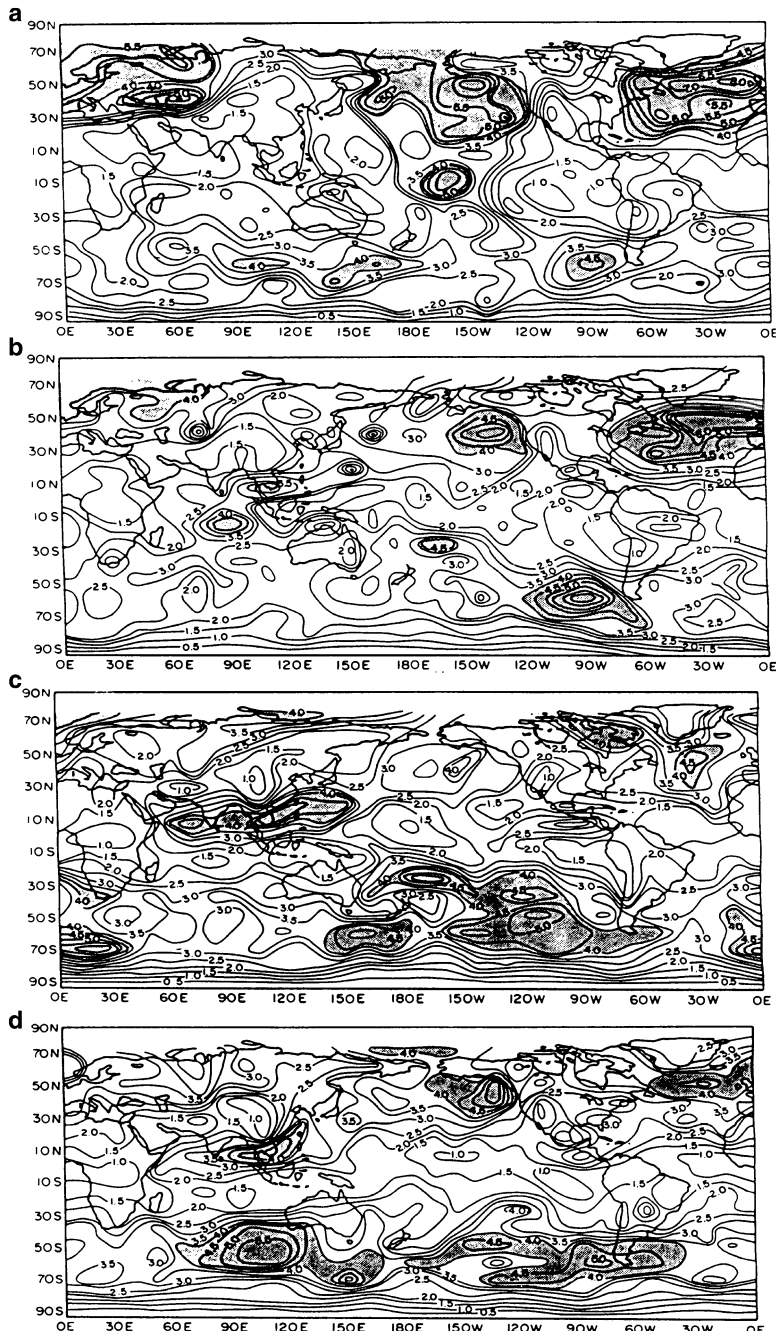


**Fig. 7.1** Maximum zonal wind at 850 mb of frequency filtered motions during individual seasons ( $\text{ms}^{-1}$ ) (a) winter, (b) spring, (c) summer and (d) fall (After Krishnamurti et al. 1992a)

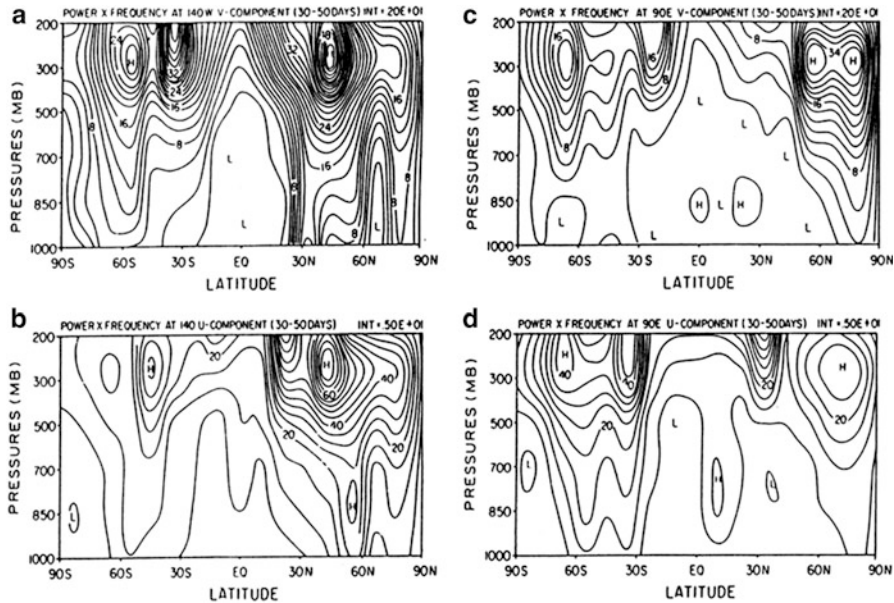


**Fig. 7.2** Vertical distribution of power spectra (power times frequency) analyzed as function of latitude and pressure for the following variables: (a) v component at 140°W, (b) u component at 140°W, (c) v component at 90°E, (d) u component at 90°E (After Krishnamurti et al. 1992a)

This mid-latitude/polar feature however is not called the MJO. Over the high latitudes – in the region of the Icelandic and Aleutian lows of the northern hemisphere, and polewards of the roaring 40°s of the southern hemisphere – the MJO time scale oscillation contributes less to the total variance. Here the dominant time scale is around 4–6 days. If one looks at the vertical structure of the power spectra of the MJO time scale we note that the largest power again resides in these high latitudes of the polar region (Fig. 7.2). Here we show a plot of the power spectra (power times frequency) plotted for different latitudes and pressure levels. In this illustration we show the power spectra for the meridional and zonal components of the winds at 140°W (eastern Pacific) and 90°E (Monsoon) regions. Most of the large power can be seen polewards of 40° latitude over the upper troposphere. At 90°E one can see the large power of the zonal wind near 850 mb reflecting the Monsoonal modulation on the time scale of the MJO. These results are based on year long data sets and show the importance of this time scale for the monsoon.

The MJO wave is baroclinic in the tropical latitudes and is quasibarotropic over the higher latitudes. This is best seen from the vertical structure of the phase of the MJO wave. Figure 7.3 illustrates the amplitude of the zonal wind from an year-long data set for two tropical sites (left) and two polar sites (right). The phase of the zonal wind (westerlies are shaded, easterlies are unshaded) shows a clear reversal from the lower to the upper troposphere. Such change of phase is absent over the higher latitudes. This is what we mean by the more baroclinic structure for the MJO time

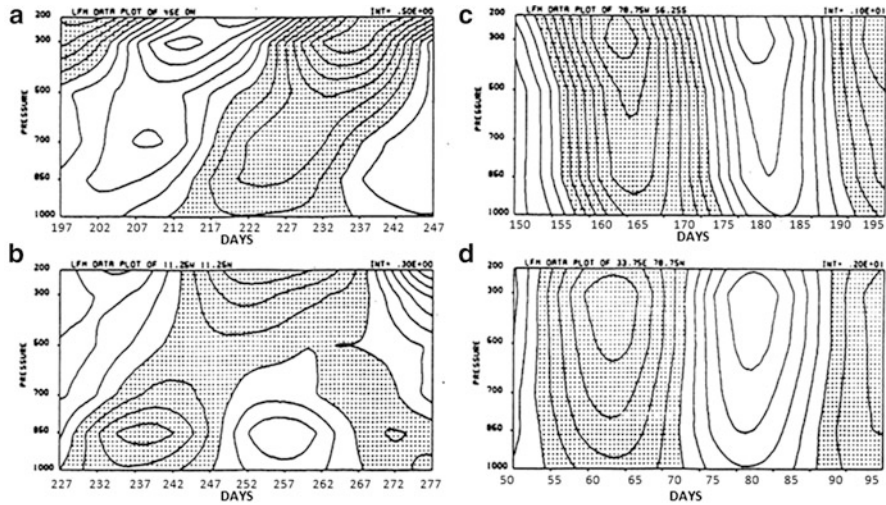


**Fig. 7.3** Pressure–time analysis of the zonal wind on the time scale of 30–50 days for two tropical grid points (a) and (b) and for two higher latitude points (c) and (d). The units are  $\text{ms}^{-1}$ . Shaded area denotes negative values. The interval of analysis is shown on the top right of each panel (After Krishnamurti et al. 1992a)

scale over the tropics and a more barotropic structure in the extratropics. The MJO is intimately connected to organized tropical convection that prefers a lower pressure in the lower troposphere and a higher pressure aloft. Over the higher latitudes this time scale may be more dynamically driven.

The globally eastward propagating MJO wave over the tropics is a divergent wave. It carries convergence or divergence over one half of the wave as it progresses eastwards. This can be seen from the velocity potential maps. The velocity potential  $\chi$  is defined from the equation

$$\nabla^2 \chi = -\nabla \cdot \vec{V} = -\nabla \cdot \vec{V}_\chi, \quad (7.1)$$

where the divergent component of the wind is  $\vec{V}_\chi = -\nabla \chi$  and  $\vec{V}$  is the total wind. To map the field of  $\chi$  one needs to first perform an analysis of the wind field  $\vec{V}$ . Figure 7.4 illustrates a sequence of charts at intervals of every 5 days that shows the zonal passage of the MJO wave. This wave during 1979 traversed around the globe in roughly 30 days. These are the velocity potential charts that were obtained from local time filtering of the wind ( $u, v$ ) at each grid location first and the divergence  $-\nabla^2 \chi$  computed next. The field of  $\chi$  is obtained from a solution of the Poisson equation  $\nabla^2 \chi = -\nabla \cdot \vec{V}$ . This MJO wave is a long wave with most of its variance in the zonal wave numbers 1 and 2. Half of this wave carries low values of  $\chi$  and the other half carries high values. That implies in fact that the wave has alternating features of divergence and convergence. The tropical weather seems to be modulated by the passage of these waves, i.e. a convergent part of the wave in the lower troposphere favors weather activity and vice versa.

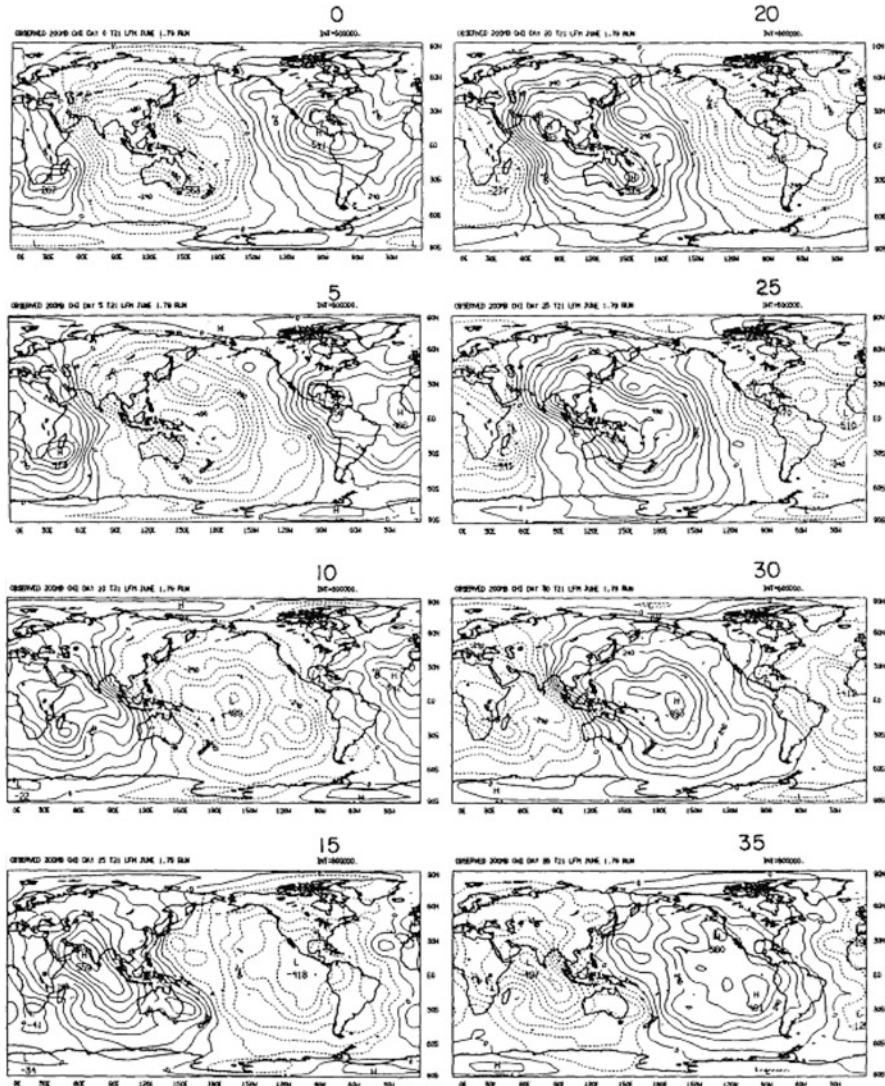
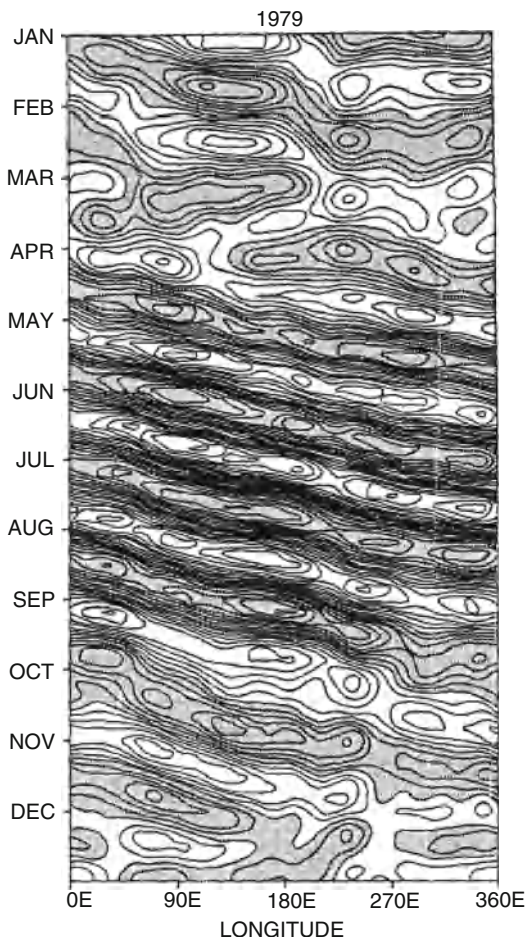


**Fig. 7.4** Panels of the velocity potential at 200 mb based on observed wind. Interval of isopleths  $60 \times 10^{-6} \text{ m}^2 \text{s}^{-1}$ . Day 0 is 1 June 1979. Maps are shown at intervals of 5 days. After Krishnamurti et al. (1992b)

The eastward propagation of the MJO wave can be illustrated with a Hovmöller diagram of the velocity potential (Fig. 7.5). Here the longitudes are shown along the abscissa and the ordinate denotes time for an entire year. The time-filtered velocity potential  $\chi$  on the time scale of the MJO averaged between  $5^\circ\text{S}$  and  $5^\circ\text{N}$  is illustrated here. Here we see this spectacular phenomenon of MJO. These waves for nearly

**Fig. 7.5** An x-t diagram of the 200 mb velocity potential during the FGGE year. This represents an average from 50S to 50N. The contour interval is  $1.3 \times 10^6 \text{ m}^2 \text{s}^{-1}$  (After Krishnamurti et al. 1985)



the entire year propagate around the Earth on a time scale of roughly 40 days. The amplitudes of the waves are largest between April and October. The largest amplitudes are seen over the Asian and west Pacific Ocean longitudes. As stated before, the passage of an upper air divergence seems to modulate the weather as this slow moving wave goes by.

That modulation of weather was illustrated by Nakazawa (1988). He showed that an envelope of this MJO wave carries within it (over regions of lower tropospheric convergence) considerable meso-convective precipitating cloud elements. Those individual elements are seen clearly to move westwards and the entire envelope moves eastwards. The cloud elements normally move westward at a speed of roughly  $5\text{--}10^\circ$  longitude/day, whereas the envelope moves eastward at a rate of roughly  $10^\circ$  longitude/day. These two time scales clearly carry some interesting scale interactions that will be discussed in Chap. 8.

There is a monsoonal anomaly in this zonal propagation that is evident if we look at latitudes between 5°N and 30°N over Asia. While the near-equatorial wave on the MJO time scale moves eastward, the off-equatorial wave over Asia seems to carry a meridionally propagating component. This off-equatorial component of the MJO wave is not simply propagating eastwards. There is a meridional propagation of a wave that is called “intraseasonal oscillation”, or ISO. This has a meridional wave length of roughly 3,000 km and propagates at a speed of about 1° latitude/day. It carries again alternating phases of divergence and convergence in the lower troposphere, carrying disturbed and undisturbed weather respectively. This meridionally moving feature is on the same time scale as the MJO. It appears to be a reflected Rossby gravity wave, i.e. the equatorial Kelvin wave (the eastward propagating MJO) being reflected by the Sumatra mountains. That has not been proven but deserves to be examined. This meridionally propagating intraseasonal oscillation called the monsoonal ISO is a divergent wave. The meridional passage of winds, especially at the 850 mb level, can illustrate this wave from time filtered data sets (Fig. 7.6). Those are troughs and ridges of waves that alternately pass northward from the equatorial latitudes. This figure illustrates roughly one cycle of this major phenomenon. The point to note here is that the summer monsoon climatology at 850 mb that carries the trade wind easterlies, the cross equatorial flow offshore from Kenya, the Somali jet east of the Horn of Africa (near Somalia) and the southwesterly monsoonal flow over the central Arabian Sea is modulated by the passage of the ISO wave northwards over South Asia and South East Asia. This passage of the ISO waves tends to strengthen or weaken the southwest monsoon current over the Arabian Sea. These are called parallel and antiparallel flows with respect to climatology. The modulation of monsoon weather by the passage of ISO waves depends on the strengthening (parallel) or weakening (antiparallel) of the climatological southwesterly monsoon. One can also carry out band pass filtering of rainfall data or of the OLR data as a proxy for clouds and see the passage of weather that is a part of the ISO waves. The variables where this feature is most conspicuous include: specific humidity, precipitation, total winds, clouds, and divergence.

Several studies have been carried out on the place of origin of these ISO waves. The seat of origin seems to be the southern equatorial trough near 5°S. That is a pressure trough – a clockwise wind near 5°S, best seen in the climatology of the lower troposphere during the summer months. A July climatology of low level winds is shown in Fig. 7.7 where the southern equatorial trough can be readily seen. To illustrate the meridional passage of this regime one can show latitude/time plots of variables such as the zonal wind and the relative vorticity at the 850 mb level during selected weeks of ISO passage. Those are illustrated in Fig. 7.8a, b. Here the time filtered data on the time scale of MJO/ISO for the zonal wind and the relative vorticity are shown at the 850 mb level. We clearly see the origin of the ISO waves near 0–5°S latitudes. The waves move northward carrying alternating components of westerlies and easterlies (amplitude about  $3 \text{ ms}^{-1}$ ) and of cyclonic and anticyclonic vorticity (amplitude about  $0.5 \times 10^{-5} \text{ s}^{-1}$ ). Additionally, we note

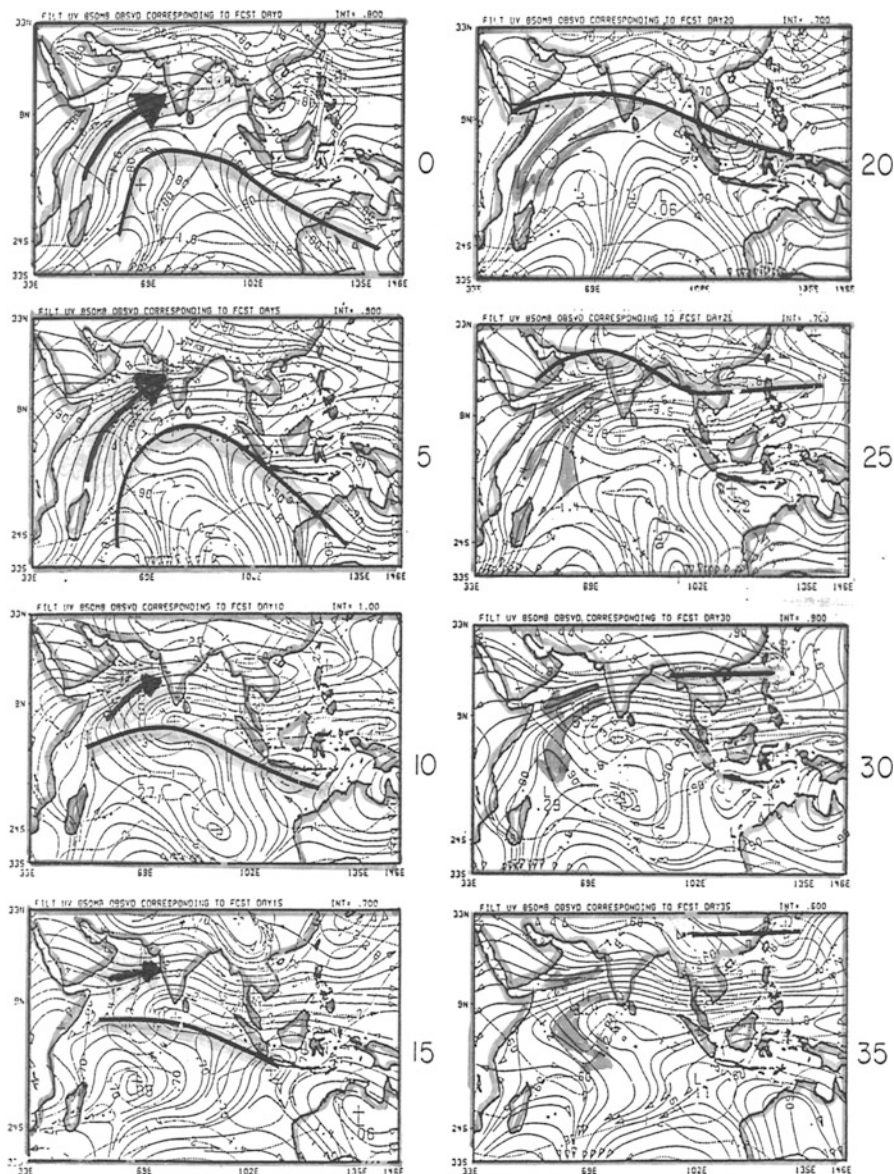


**Fig. 7.6** A sequence of 950 mb observed flow fields (time filtered on the scale of 30–50 days) for the experiment on dry spell over India. Streamlines (solid lines) and isotachs (dashed lines) are shown here. Units of  $\text{ms}^{-1}$

an emanating component of a weaker ISO wave moving southwards from the southern equatorial trough. This feature is not well understood at the present time. The modulation of weather during the monsoon months from the northward moving component of the ISO wave has been well documented.

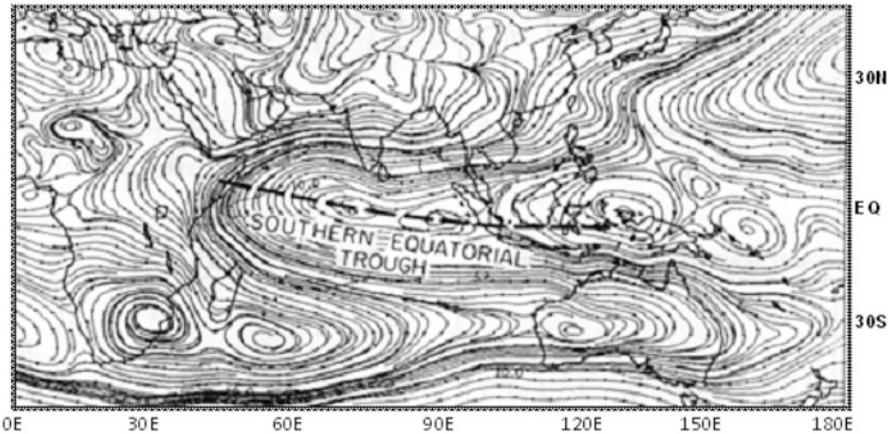


**Fig. 7.7** Climatology of the 850 mb streamlines based on FGGE data set for July 1979. The southern equatorial trough is emphasized here as a source region for the meridionally propagating low frequency waves (After Krishnamurti et al. 1992b)

## 7.2 Theory of the MJO

Lau and Peng (1987) presented a theory for those eastward propagating Madden Julian waves that traverse around the earth in roughly 40 days. This theory states that these waves undergo an interaction with convection that can be studied by a mechanism called wave CISK. This being a promising theory, we present an outline of it here.

In their analysis Lau and Peng (1987) make use of a global model that is described by the following vorticity and divergence equations, the mass continuity equation, the first laws of thermodynamics and the hydrostatic law. This constitutes a closed system of five equations for the vorticity, divergence, temperature, surface pressure, and the geopotential height. In a  $\sigma$ -coordinate system these are:

$$\frac{\partial \zeta}{\partial t} = -\nabla \cdot (\zeta + f)\vec{V} - \vec{k} \cdot \nabla \times \left( RT\nabla q + \dot{\sigma} \frac{\partial \vec{V}}{\partial \sigma} - \vec{F} \right) \quad (7.2)$$

$$\frac{\partial D}{\partial t} = -\vec{k} \cdot \nabla \times (\zeta + f)\vec{V} - \nabla \cdot \left( RT\nabla q + \dot{\sigma} \frac{\partial \vec{V}}{\partial \sigma} - \vec{F} \right) - \nabla^2 \left( \phi + \frac{\vec{V} \cdot \vec{V}}{2} \right) \quad (7.3)$$

$$\frac{\partial T}{\partial t} = -\nabla \cdot T\vec{V} + TD + \dot{\sigma}\gamma - \frac{RT}{C_p} \left( D + \frac{\partial \dot{\sigma}}{\partial \sigma} \right) + H_T \quad (7.4)$$

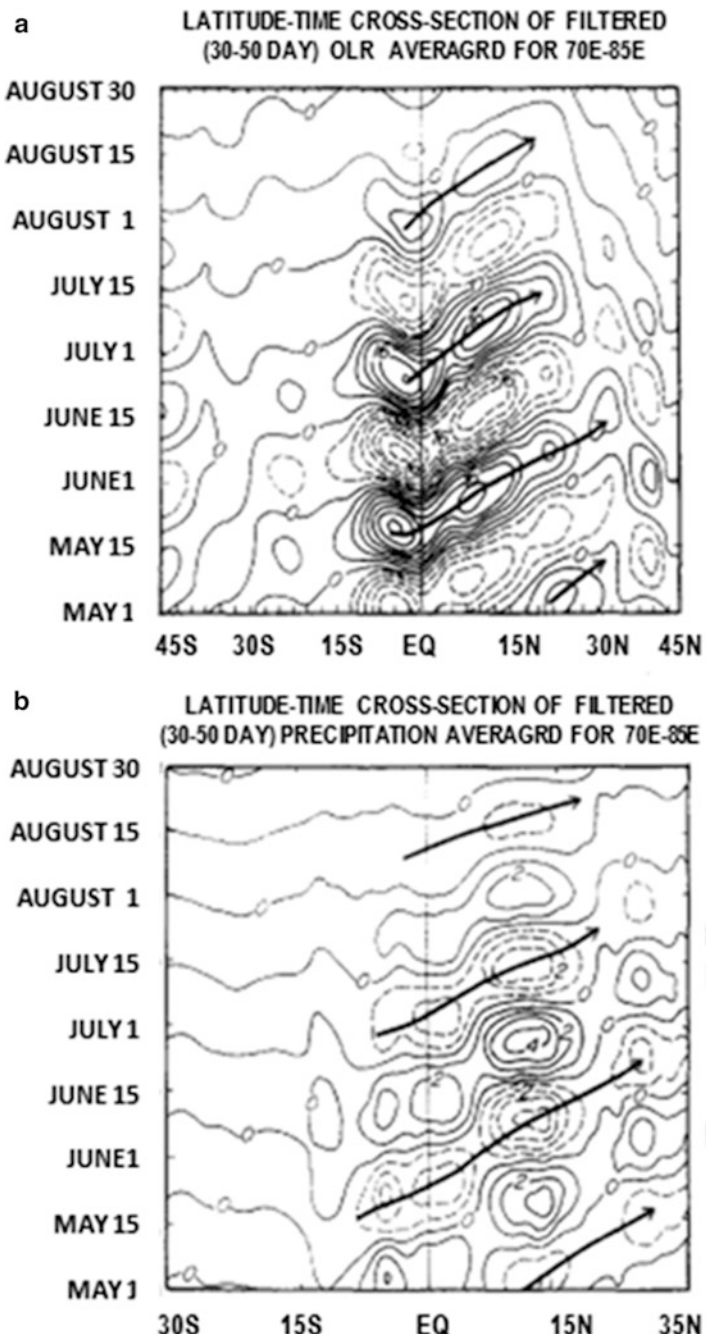


**Fig. 7.8** Latitude-time cross-section of 30–50 days time filtered (a)  $u$  wind ( $\text{ms}^{-1}$ ) and (b) vorticity ( $\text{s}^{-1}$ ) at 850 mb (After Krishnamurti et al. 1997)

$$\frac{\partial q}{\partial t} = -\vec{V} \cdot \nabla q - D - \frac{\partial \dot{\sigma}}{\partial \sigma} \quad (7.5)$$

$$\sigma \frac{\partial \phi}{\partial \sigma} = -RT, \quad (7.6)$$

where  $\zeta$  is the vorticity,  $D$  is the divergence,  $\vec{V}$  is the horizontal wind vector,  $T$  is the temperature,  $q = \ln p_s$ , i.e., the logarithm of the surface pressure,  $\gamma = RT/c_p\sigma - \partial T/\partial \sigma$  is the static stability parameter,  $\vec{F}$  is the frictional force, and  $H_T$  represents the diabatic heat sources and sinks.

The model used by Lau and Peng (1987) was a standard global spectral model that was run at a resolution of 15 wave (Rhomboidal Truncation), with five levels in the vertical. The global spectral model is a forecast model which carries certain physical parameterization models; see any standard text (e.g. Krishnamurti et al. 2006) for details on such modeling. In their work Lau and Peng (1987) included the following features in their global spectral model:

1. Rayleigh friction for dissipation. This is of the form  $-K\zeta$  in the vorticity equation and  $-KD$  in the divergence equation.
2. Newtonian Cooling of the form  $-KT$  as proxy for net radiative cooling in the thermal equation of the first law of thermodynamics.
3. No surface topography.
4. Convective heating is the only form of diabatic heating that is included.

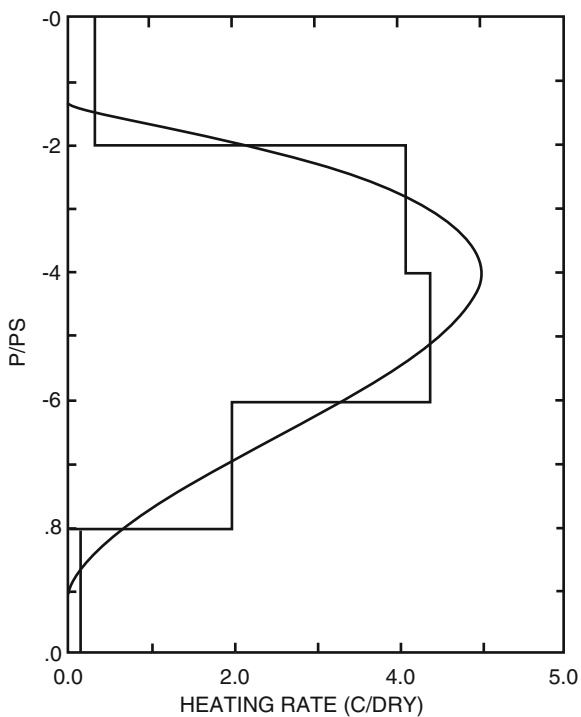
They introduce a conditional convective heating defined by the equation:

$$Q(\sigma) = \begin{cases} -m\eta(\sigma)rLq_{sat}(T_5)D_5\Delta\sigma/C_p & D_5 < 0 \\ 0 & D_5 \geq 0 \end{cases} \quad (7.7)$$

This heating  $Q$  is defined on sigma surfaces. The relationship between this  $Q$  and  $H_T$  in (7.4) is given by  $H_T = \frac{1}{C_p}\frac{\theta}{T}Q$ .  $D_5$  is the divergence at the lowest model level (level 5) which is at the  $\sigma = 0.9$  surface i.e. close to 900 mb level.  $r$  is the prevailing relative humidity at the  $\sigma = 0.75$  surface (roughly 750 mb level). Only level convergence influences the heating (there is no cooling mechanisms here).  $q_{sat}$  is the saturation specific humidity at the temperature  $T_5$  at the  $\sigma = 0.90$  level.  $\eta(\sigma)$  is a normalized vertical profile of heating (whose vertical integral is 1).

The conditional instability of the first kind refers to the growth of small perturbations in a conditionally unstable atmosphere. This is based on a linear analysis that was carried out by Kuo (1961) and Lilly (1960). They noted that the most unstable (i.e. the most amplifying) mode in such an atmosphere was on the cloud scale of the order of few km. Since tropical disturbances on the scale on the order of 3,000 km abound in the tropics (such as easterly waves) Charney and Eliassen (1964) proposed a theory for shifting the scale of instability from few kilometers to several 1,000 km scale. This is known as the conditional instability of the second kind, or CISK. This requires, mathematically, that the heating be

**Fig. 7.9** Vertical structure of heating profile (Adopted from Lau and Peng 1987). Actual values used in the model layer are shown as discrete solid lines. Units in  $^{\circ}\text{C day}^{-1}$



independent of the internal vertical velocity of the growing perturbations. The analysis of the growth of linear perturbations, in a conditionally unstable atmosphere, with heating proportional to the Ekman pumping (vertical velocity) at the top of the boundary layer shows that the growth rates are indeed on scales much larger than the cloud scales.

The CISK produced by the internal waves such as gravity, Kelvin, mixed gravity Rossby and Rossby waves in the absence of any explicit Ekman pumping is defined as wave CISK (Lindzen 1974). In the CISK mechanism, low level convergence is provided by the passing of lower tropospheric waves, the effectiveness of Ekman pumping close to the equator seems dubious. Internal waves are highly convergent and need no Ekman pumping to produce CISK. The latent heat release processes are case dependent and are similar to those of CISK.

Figure 7.9 shows the vertical structure of the internal heating in this five-layer model. At every grid point that encounters mass convergence,  $D_5 < 0$ , the vertical structure given by  $\eta(\sigma)$  is imposed following (7.7) which dictates the amplitude of the overall heating. The initial horizontal structure of the external heating is described in Fig. 7.10. This is a zonally asymmetric dipole of heating (solid lines) and cooling (dashed lines). This is initially inserted as an external forcing and after a model spin up that takes about 5 days, the external heating is removed and from an internal heating that moves with the Kelvin wave. The time longitude section of the 300 mb zonal wind ( $\text{ms}^{-1}$ ) along the equator is shown in Fig. 7.11. This clearly

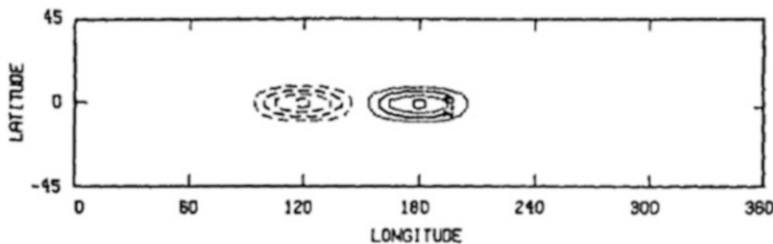


**Fig. 7.10** Spatial structure of the oscillating dipole heat source with a 44-day period at Day 77 when positive (negative) heating is strongest over  $180^\circ$  ( $120^\circ$ ) longitude. Contour starts at  $1^\circ\text{C}$  for every  $2^\circ\text{C}$  (After Lau and Peng 1987)

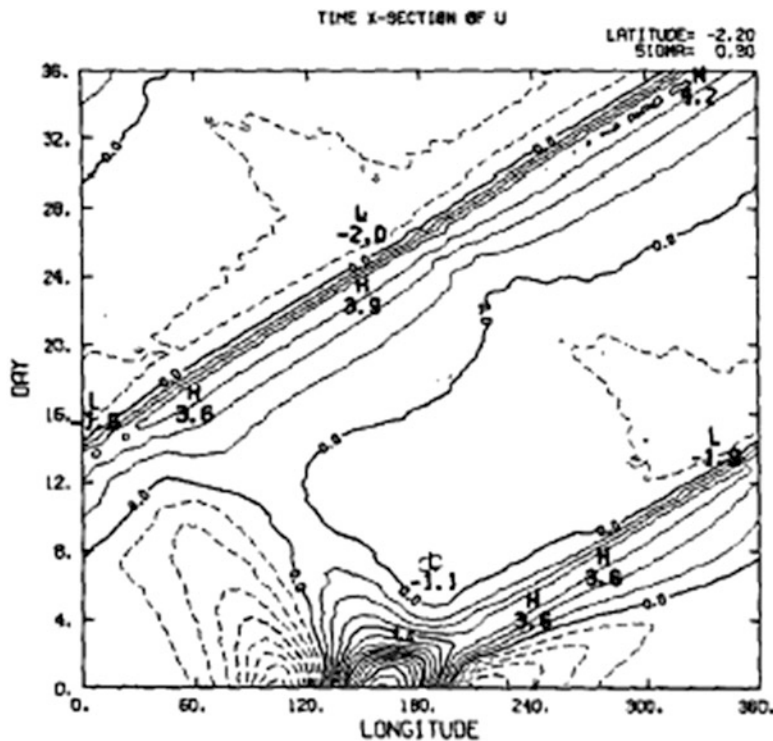


**Fig. 7.11** Time longitude section of 300 mb zonal wind ( $\text{ms}^{-1}$ ) from an idealized experiment where CISK like heating is prescribed (After Lau and Peng 1987)

shows the zonal propagation of the zonal wind anomalies that carry an amplitude of roughly  $3\text{--}4 \text{ ms}^{-1}$  which is close to the observed values. This illustration also shows the initial spin up period of roughly 5 days that was imposed. Strong westerlies and weak easterlies propagate eastward around the globe in roughly 25 days. This wave is driven by the free dynamics of the Kelvin waves plus the forced dynamics from the wave CISK. The march of precipitation follows a similar cycle that is shown in

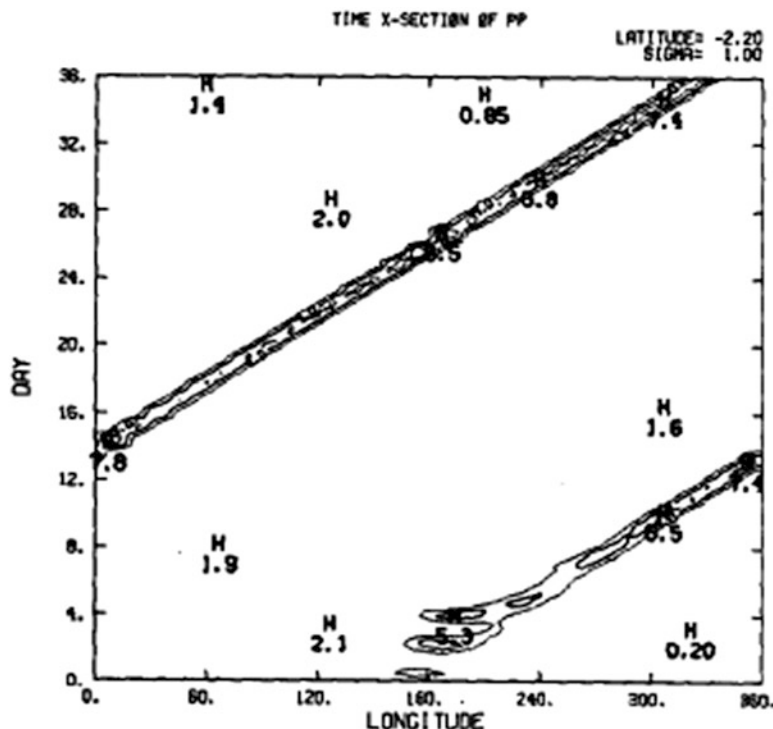


**Fig. 7.12** Same as Fig. 7.11 but for precipitation ( $\text{mm day}^{-1}$ ) (After Lau and Peng 1987)

Fig. 7.12. This was a successful theory and modeling effort for Lau and Peng (1987). Their essential finding could be summarized by stating that one needs a simple wave CISK (i.e. heating proportional to the surface convergence of traversing waves) to model the eastward propagating MJO phenomenon. The waves in question here are long planetary waves (wave numbers 1 and 2). The amplitudes of wind perturbations were reasonably modeled. The phase speed of the eastward propagating MJO of roughly  $20 \text{ ms}^{-1}$  in this experiment was twice what is observed. Lau and Peng (1987) attribute that difference to the slowing down effects of more realistic ocean atmosphere coupling and imply the need for modeling of super cloud clusters.

Wave CISK is normally applied to synoptic scale tropical waves with wavelengths on the order of few 1,000 km. This application of wave CISK on scales on the order of 10,000 km for planetary scale Kelvin waves is clearly open to question since this requires a modulation of convection by convergence on the scale of this planetary wave. It is more likely that a number of smaller scale waves and smaller scale convection is organized on the scale of MJO. Those were not resolved by the simple model configuration of Lau and Peng (1987). A richer spectrum of scales is seen in more recent modeling studies of the MJO.

Randall et al. (2003) proposed that the modeling of the MJO would require the modeling of the deep convective elements that form a super cloud cluster. Towards this end they designed a global model (with prescribed monthly mean ocean temperatures) that carried explicit clouds. In such a model they were able to replicate many features of the MJO.

Other scientists, such as Saha et al. (2006) point out that a coupled atmosphere ocean model is necessary for the simulation of MJO since that time scale is present in the SST anomaly fields.

### 7.3 Westerly Wind Bursts in the MJO

The MJO signal in the zonal wind is fairly robust. Surface and 850 mb winds have been examined in a number of studies and it has been noted that in the equatorial latitudes the westerly phase of the MJO is often accompanied by strong wind surges. This signature is sufficiently strong that it is also seen in the total zonal wind i.e. the total wind (not just the wind anomaly) is also westerly in the equatorial latitudes. This is observed in the Indian Ocean and the western Pacific Ocean. A westerly wind burst in the equatorial latitudes creates a cyclonic shear of the horizontal wind in both hemispheres across this wind belt. Often in these regions of strong cyclonic shear vortices form that eventually become tropical depressions leading to tropical cyclones (or typhoons). A spectacular example of such an event is shown in Fig. 7.13 where two pairs of tropical cyclones have formed on either side of the equator – one over the Arabian Sea/Indian Ocean and the other over the Bay of Bengal/Indian Ocean. This event occurred during May 2003. The 850 mb winds of the westerly wind burst in the equatorial latitudes was on the order of  $15 \text{ ms}^{-1}$ .

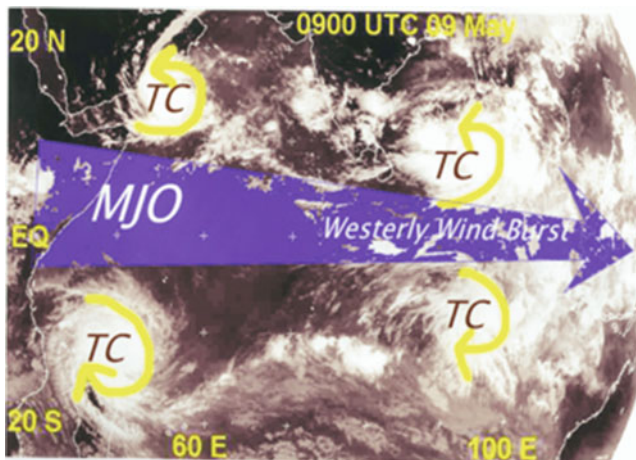


**Fig. 7.13** Two pairs of tropical cyclones during a westerly wind burst seen on May 9, 2003

## 7.4 The MJO Connection During the Birth and Demise of ENSO

Considerable observational evidence has accumulated to show that some westerly phases of the MJO extend eastwards into the Pacific Ocean in the formative stages of an El Nino event. This is illustrated in Fig. 7.14 from Krishnamurti et al. (2000). These are Hovmöller diagrams (longitude/time) averaged over the equatorial belt 5°S to 5°N of the daily zonal wind at the 850 mb level. The westerly wind anomalies at the MJO time scale are shaded. Rectangular boxes indicate the period of El Nino onset. These tend to coincide with the periods during which there is a marked eastward propagation of the westerly MJO-scale anomalies. The periods when the westerly wind phases of the MJO extend into the Pacific Ocean seem to coincide with the onset of El Nino for the years 1968–69, 1971–72, 1976, 1981–82, 1991–92, 1992–93, and 1996–97. That aspect of the weakening of the lower tropospheric easterlies originating in the Indian Ocean was also illustrated in Chap. 4, Sect. 4.3 and Fig. 4.4. This appears to be an important antecedent feature of the El Nino in most years.

There is also some evidence of the role of MJO activity on the in the equatorial Indian Ocean playing a role in the termination of El Nino events. Takayabu et al. (1999) reported on the termination of the El Nino of the 1997/98 season. They examined equatorial Hovmöller diagrams for precipitation, sea surface temperatures and surface winds and found a strong MJO with a strong easterly phase propagating into the Pacific Ocean. This event coincided with the abrupt termination of the El Nino of the 1997–98 (cf Fig. 7.2 in Takayabu et al. 1999). In the second half of May 1998 the sea surface temperatures cooled to below 27°C at around 120°W over the eastern Pacific Ocean. This highlighted the end of the warm phase of the 1997–98 El Nino. The other notable feature of that figure is the strong easterlies representing a build-up of the Pacific trades. During May of 1998 the propagation of strong easterly winds from the Indian Ocean to the equatorial Pacific Ocean (3°S to 3°N) is clearly evident.

## 7.5 Wave Energy Flux Across the Tropics

The linear theories of Eliassen and Palm (1961) and later by Yanai and Lu (1983) provide the following equation to describe the wave energy flux across a latitude circle:

$$\overline{\phi' v'} = (\bar{u} - c) \left[ \overline{u' v'} - \frac{1}{\sigma_o} \frac{\partial \bar{u}}{\partial p} \overline{v' \partial \phi'} \right]$$

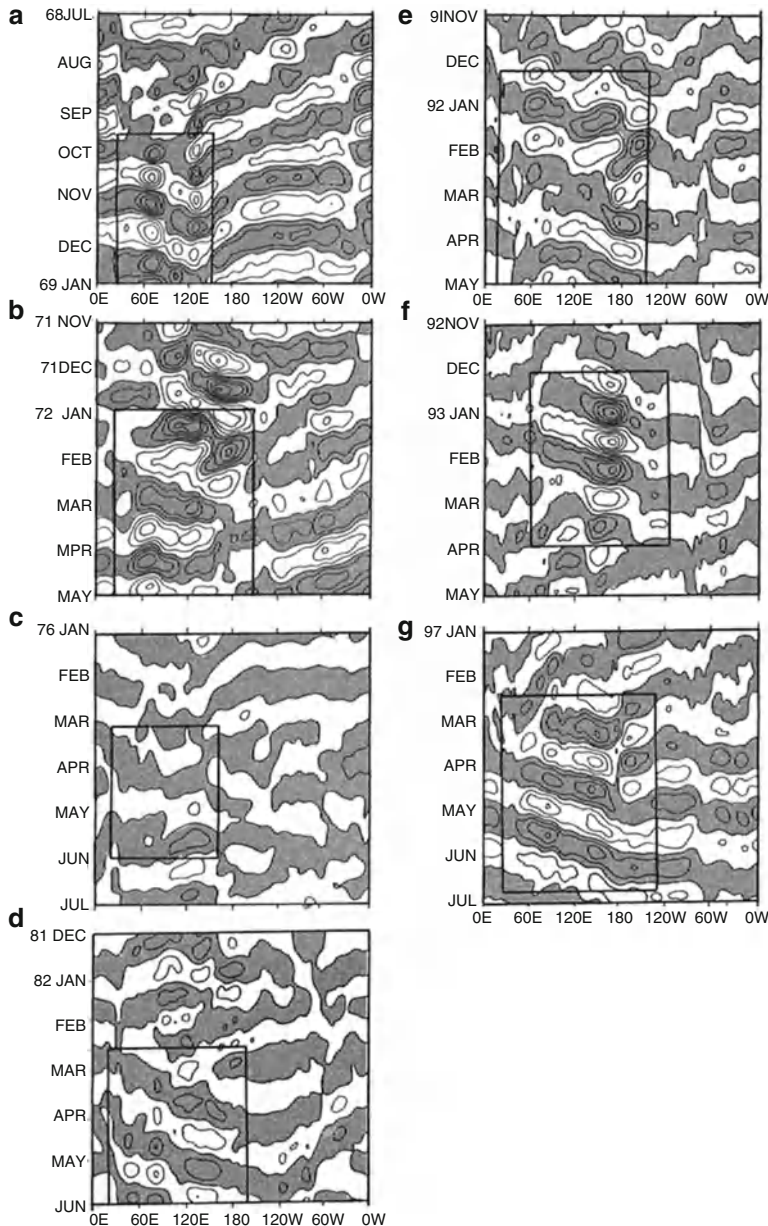


**Fig. 7.14** Longitude–time sections of the time-filtered (30–60 days) zonal winds at 850 mb. Shaded areas denote westerly anomalies. Results for different El Niño years ((a) 1968–69, (b) 1971–72, (c) 1976, (d) 1981–82, (e) 1991–92, (f) 1992–93, and (g) 1996–97). Boxes indicate the time of El Niño onset (After Krishnamurti et al. 2000)

Here  $\phi'v'$  denotes the wave energy flux across a latitude circle;  $\bar{u}$  is the zonally averaged zonal wind;  $c$  is the phase speed of the wave;  $u'v'$  denotes the meridional eddy flux of momentum;  $\sigma_o$  is a reference dry static stability;  $\frac{\partial \bar{u}}{\partial p}$  denotes the vertical shear of the zonally averaged zonal wind;  $\frac{v'\partial\phi'}{\partial p}$  is a measure of the meridional heat flux across a latitude circle.

It is clear that when  $u-c$  goes to zero the wave energy flux vanishes. Thus a major conclusion was drawn that this latitude where  $u-c$  vanishes is a critical latitude and a barrier that does not permit any wave energy exchange from tropics to middle latitudes to occur and vice versa. That means that tropical wave activity cannot influence the higher latitudes, nor can the extratropical wave activity directly influence the tropics across such a barrier. This was an accepted result in many subsequent studies. There is however a major flaw in this linear theory. Almost all scales of motion including the zonally averaged flows carry temporal variabilities on many time scales. Those include variabilities in biennial, annual, MJO, ENSO and decadal time scales. The nature of this problem changes as soon as we include the presence of such other time scales. That becomes a problem of wave energy flux in the frequency domain, Krishnamurti et al. (1997). In that formulation  $\bar{u}$  is no more a constant, nor are other time averaged terms. Nonlinearity is present in such a formulation in the starting equations from which the wave energy fluxes are derived. We shall not present a derivation of that equation here, except to state that it is possible to write an expression for  $\overline{\phi'v'}$  that includes many more terms. Those terms arise from the complete dynamical and the thermodynamical equations including all of the non linear advective terms. Given reanalysis data sets, in principle, one can compute such wave energy fluxes. One then asks the question does the wave energy flux still vanish or is it near zero around the critical latitudes of the linear problem. Computations of such quantities do suggest that the total wave energy flux across the liner theory based critical latitudes are indeed very small. This might suggest that the linear theory is being confirmed from the inclusion of non linear terms of the complete equations. However one can take a further step with these equations. These complete wave energy flux equations can be cast in a frequency domain and one can ask what are the fluxes within certain windows of time scales. One such question is what goes on at the MJO time scale. That question was addressed by Krishnamurti et al. 1997. They found that the critical latitude is not a barrier in the frequency domain, large amounts of wave energy flux escapes from the tropics to the higher latitudes across the barrier since  $\bar{u}$  is not a constant but has a temporal variability on the MJO time scale. At higher frequencies, on the other hand, wave energy flux returns to the tropics from the extratropics. Although the total wave energy flux, summed over all frequency windows is small, there is a large communication between the tropics and the higher latitudes at individual frequencies. In that light the MJO time scale is very interesting since it sees a substantial exchange of energy between the tropics and the middle latitudes.

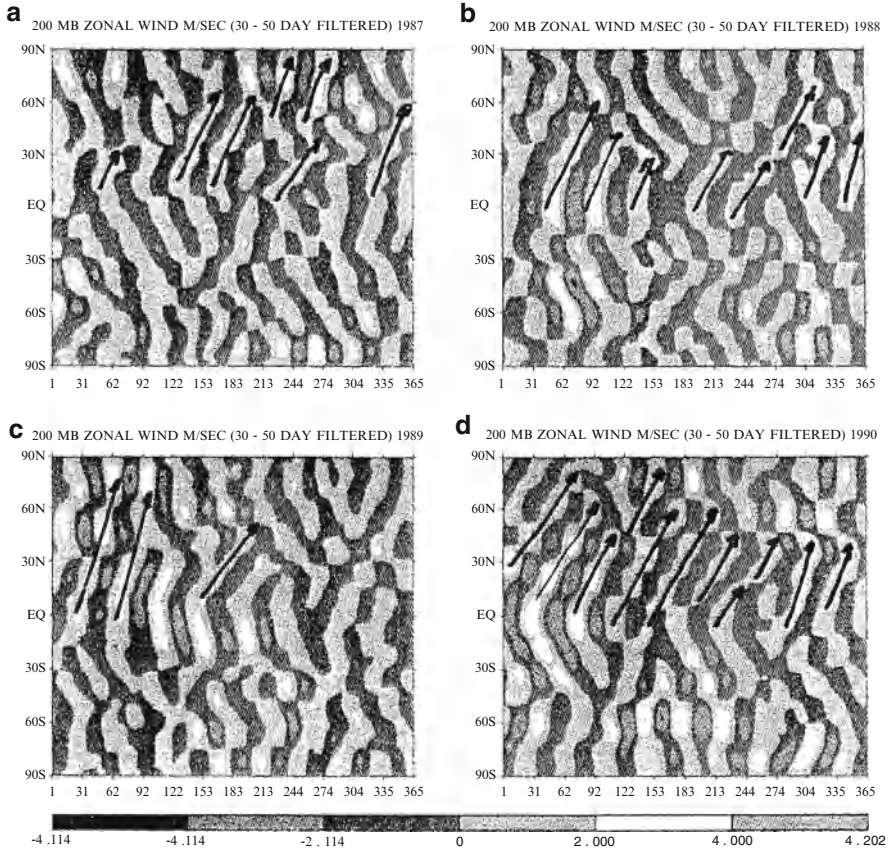


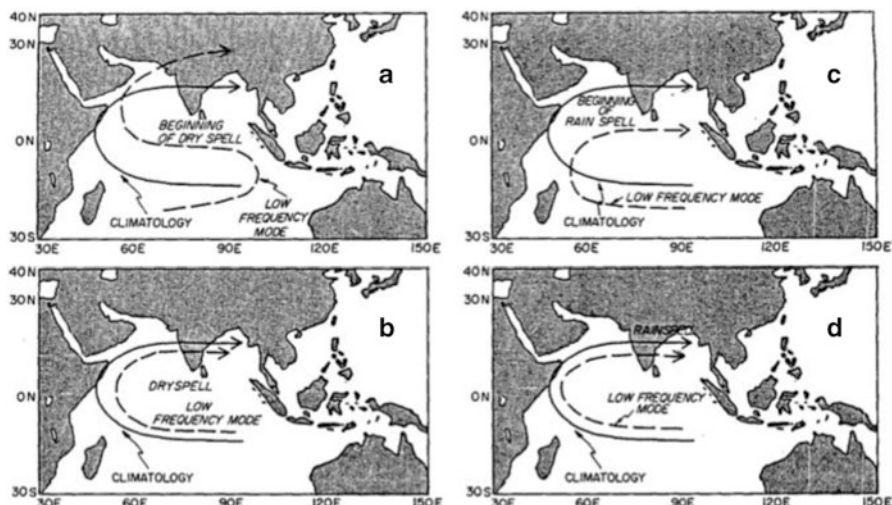
**Fig. 7.15** Latitude-time diagram of meridional wave energy flux  $\bar{\phi}'v'$  on the time scale of 30–50 days. Four separate years of result are shown for the years (a) 1987, (b) 1988, (c) 1989, and (d) 1990 here. The ordinate denotes latitude, the abscissa denotes day of the year. Units are  $J\text{m}^{-1}$

An illustration of wave energy flux as a function of latitude and time in days is shown in Fig. 7.15. This is a vertical integral of the wave energy flux through the troposphere and is zonally averaged. What we see here is a substantial meridional propagation of wave energy flux from the tropics to the higher latitudes. The latitude belt 30–60 N latitudes show a rightward slope for these fluxes, meaning a northward flux as a function of time. It also suggests a strong convergence of wave energy flux near 60 N. There exists a large variance for the zonal wind anomalies on the time scale of 30–60 days, (the MJO time scale) at around 60 N latitude. The linear theory fails to connect the tropical signals on the MJO time scale with those of the higher latitudes. The selective fluxes across the critical latitude are possible in the frequency domain, making it possible to have a communication between the tropics and the higher latitudes.

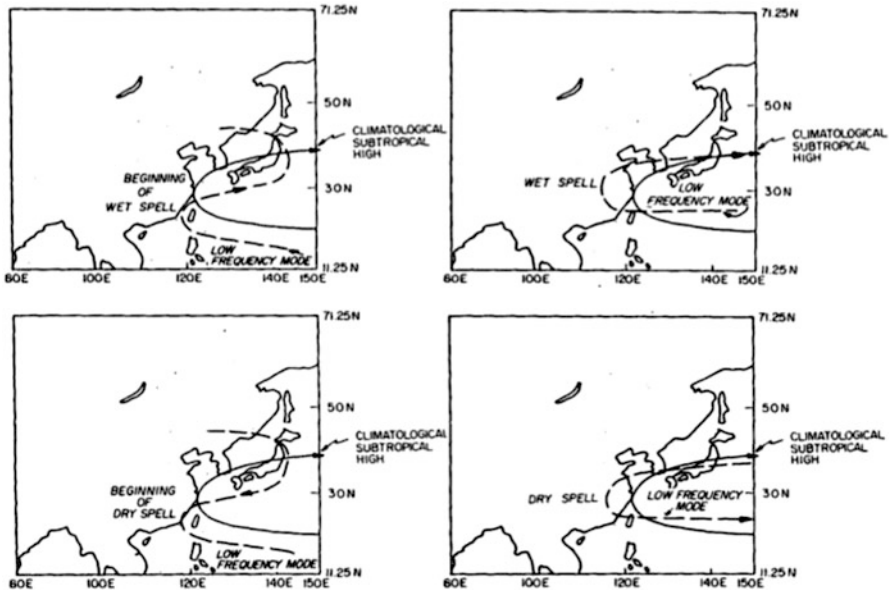
## 7.6 Real Data Forecasts of ISO

In a series of modeling experiments Krishnamurti et al. (1990, 1992b, 1995) showed that it is possible to predict at least one cycle of the passage of an ISO wave of the Indian, the Chinese and the Australian Monsoon. The premise of these studies is based on the fact that the superposition of the intraseasonal circulation anomalies and the climatological circulations favors enhanced or deficient rainfall anomalies. This is illustrated schematically in Figs. 7.16, 7.17, and 7.18 for the Indian, the Chinese and the Australian components of the monsoon respectively.

In the case of the Indian monsoon, the climatological southwesterly flow is weakened by the transients (intraseasonal component; Fig. 7.16a, b) resulting in the dry spell of the monsoon. Likewise during the wet spell of the Indian monsoon the southwesterly flow is enhanced by the intra-seasonal component (Fig. 7.16c, d) of the low level flow. Similarly the modulation of the climatological West Pacific subtropical high by the intra-seasonal component of the low level flow (~850 mb) leads to the wet and dry spells of the Chinese monsoon (Fig. 7.17). In the context of the Australian monsoon it is the modulation of the inter-tropical convergence zone in between 10 and 15 S that undergoes modulation from the passage of the intraseasonal modes as illustrated in Fig. 7.18.

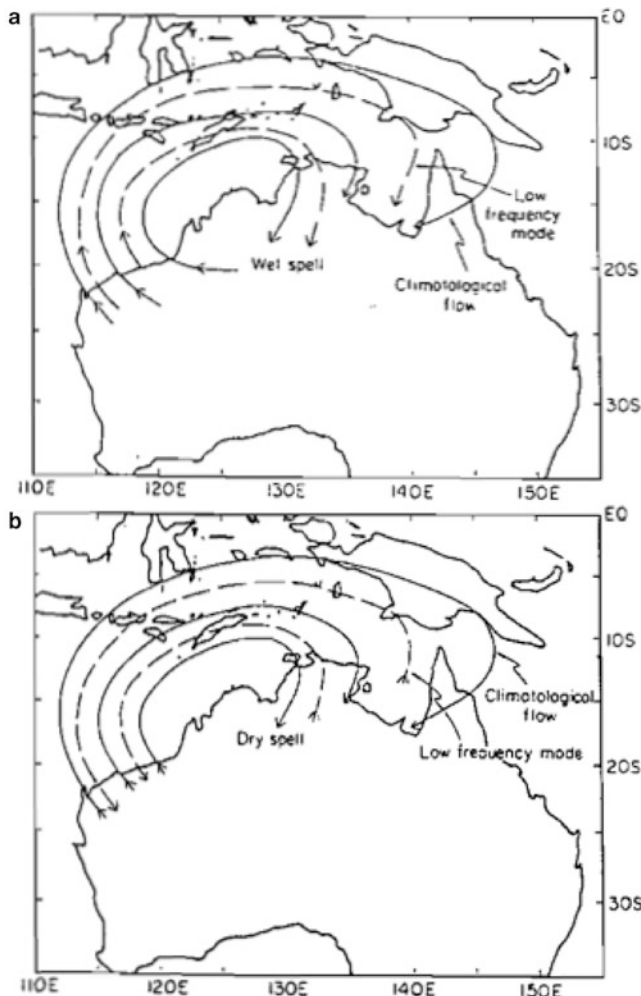


**Fig. 7.16** Schematic pictures of (a, b) anti-parallel and (c, d) parallel flows that produce anomalous dry and wet periods of the Indian monsoon (After Krishnamurti et al. 1992b)



**Fig. 7.17** Same as Fig. 7.16 but for the Chinese monsoon (After Krishnamurti et al. 1992b)

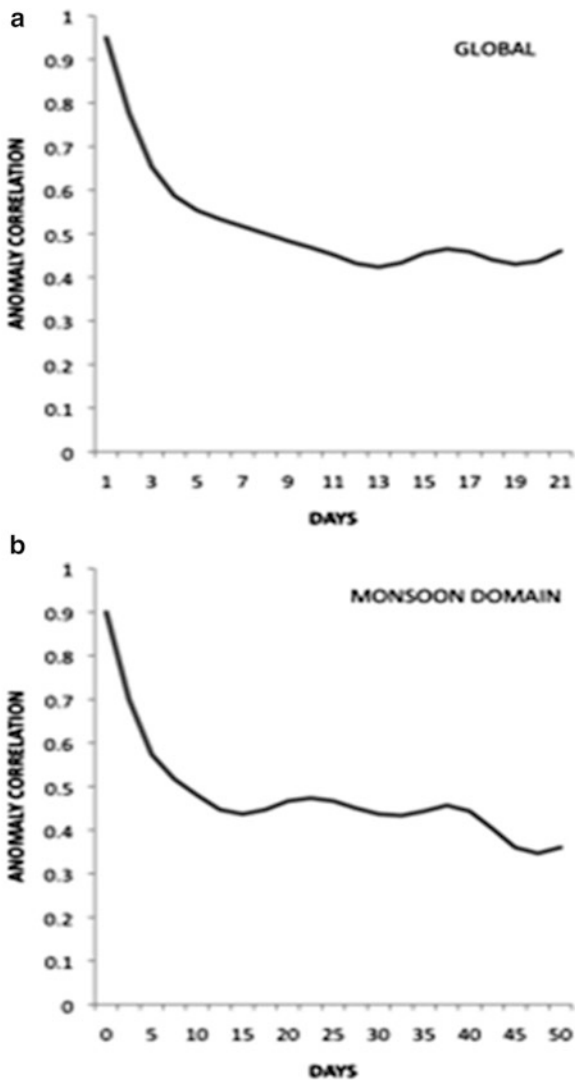
Krishnamurti et al. (1990, 1992b, 1995) proposed an initialization technique for an atmospheric model that could predict one cycle of this intra-seasonal mode. This intialization technique was based on the fact that the growth of the very high frequency variability during the integration of the model contaminated the forecasts of the intra-seasonal modes. Furthermore, it was felt that the SST carries an anomaly on the timescale of the ISO, which follows from an earlier observational study (Krishnamurti et al. 1988). Therefore, a low band pass filter was used on the SST to retain the intra-seasonal modes from the past 120 days prior to day 0 (or start) of the forecast at every ocean grid point of the model. These anomalies were then simply extrapolated into the future preserving their recent past amplitudes. However its phase was varied based on extrapolation of the past cycle that was obtained from the observed SST. Likewise all the all the atmospheric variables were also low pass filtered and only the low frequency anomalies were retained at day zero of the forecast. Figure 7.19a, b show the typical error growth for a month from such an initialized forecast for 850 mb winds for the globe and for the Asian monsoon region. In these forecasts the anomaly correlation was over 0.5 at day 30 of the forecast.



**Fig. 7.18** Schematic illustration of the (a) parallel and (b) anti-parallel flow that produces wet and dry spells of the Australian monsoon (After Krishnamurti et al. 1995)

The full forecast of the 850 hPa winds (time filtered on the scale of 30–60 days) is displayed in Fig. 7.20 at 5 day intervals. For comparison the corresponding observations are shown in Fig. 7.21. The predicted ISO waves in Fig. 7.20 show a remarkable agreement during the first phase of the ISO with the corresponding observations in Fig. 7.21, suggesting that this method of removing high frequencies initially and including an oceanic forcing can provide a prediction of the ISO.

**Fig. 7.19** Anomaly correlation of 850 mb winds for (a) global and (b) monsoon domain from the initialization experiments for low frequency variability forecasts (After Krishnamurti et al. 1992b)



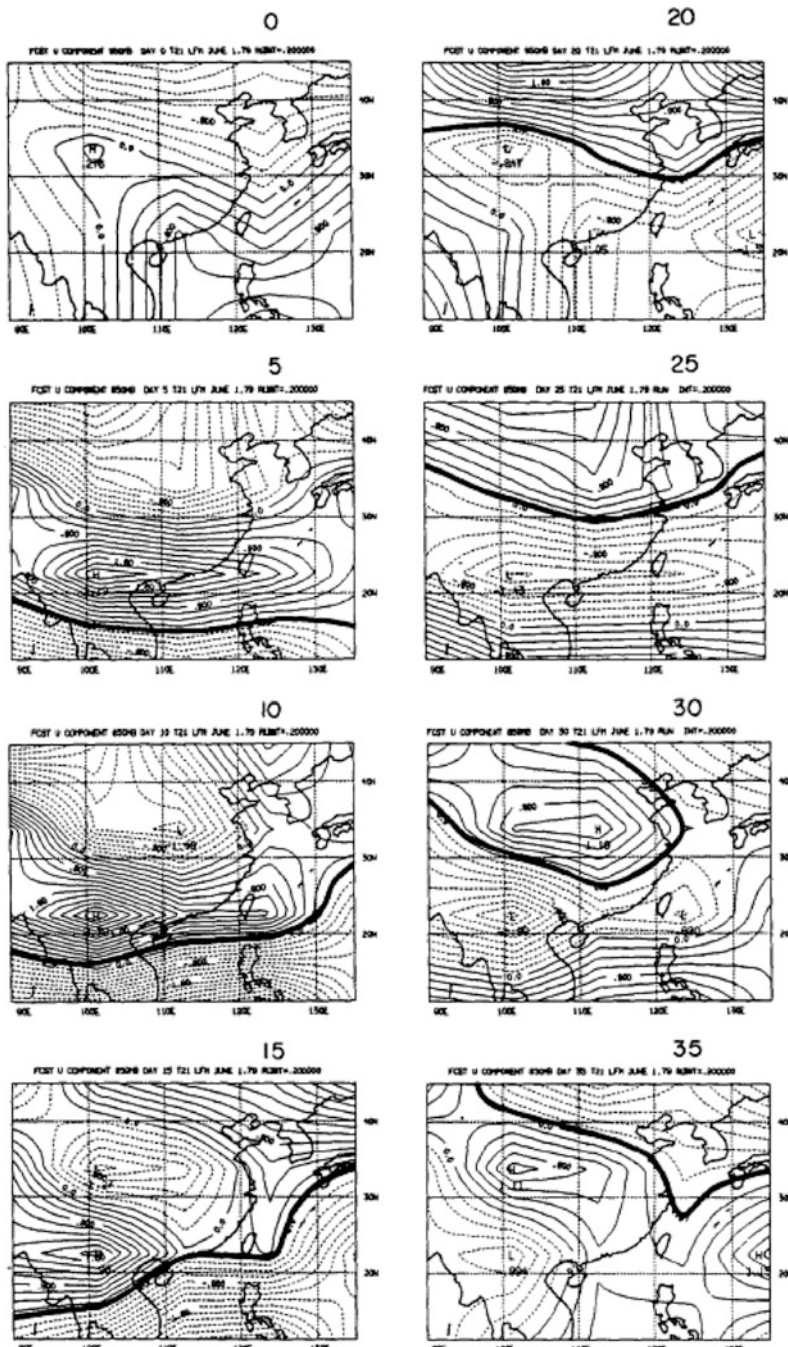


**Fig. 7.20** Panels of the 850 mb zonal winds ( $\text{ms}^{-1}$ ) based on the intraseasonal forecasts. Day 0 is June 1, 1979. Maps are shown at intervals of 5 days (After Krishnamurti et al. 1992b)

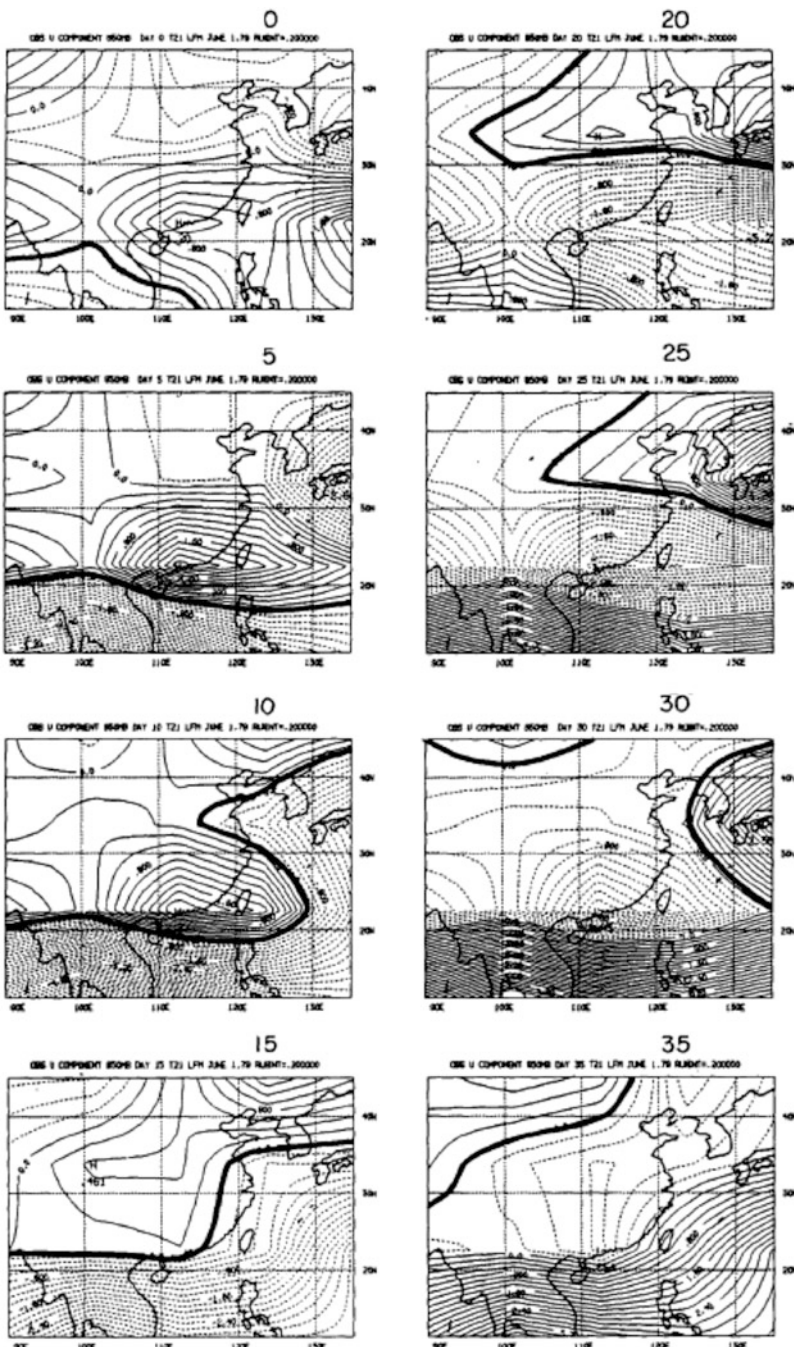


**Fig. 7.21** Same as Fig. 7.20 but from observations (ECMWF'S FGGE analysis for MONEX year 1979) (After Krishnamurti et al. 1992b)

## References

- Charney, J., Eliassen, A.: On the growth of the hurricane depression. *J. Atmos. Sci.* **21**, 68–75 (1964)
- Eliassen, A., Palm, E.: On the transfer of energy in stationary mountain waves. *Geof. Pub.* **3**, 1–23 (1961)
- Krishnamurti, T.N., Jayakumar, P.K., Sheng, J., Surgi, N., Kumar, A.: Divergent circulations on the 30–50-day time scale. *J. Atmos. Sci.* **42**, 364–375 (1985)
- Krishnamurti, T.N., Oosterhof, D., Mehta, A.V.: Air-sea interaction on the time scale of 30–50 days. *J. Atmos. Sci.* **45**, 1304–1322 (1988)
- Krishnamurti, T.N., Subramaniam, M., Oosterhof, D., Daughenbaugh, G.: On the predictability of low frequency modes. *Meteorol. Atmos. Phys.* **44**, 131–166 (1990)
- Krishnamurti, T.N., Sinha, M.C., Krishnamurti, R., Oosterhof, D., Comeaux, J.: Angular momentum, length of day, and monsoonal low frequency mode. *J. Meteorol. Soc. Jpn.* **70**(1B), 131–166 (1992a)
- Krishnamurti, T.N., Subramaniam, M., Daughenbaugh, G., Oosterhof, D., Xue, J.: One month forecasts of wet and dry spells of the monsoon. *Mon. Weather Rev.* **120**, 1191–1223 (1992b)
- Krishnamurti, T.N., Han, S.-O., Misra, V.: Prediction of wet and dry spells of the Australian Monsoon. *Int. J. Climatol.* **15**, 753–771 (1995)
- Krishnamurti, T.N., Sinha, M.C., Misra, V., Sharma, O.P.: Tropical-middle latitude interactions viewed via wave energy flux in the frequency domain. *Dyn. Atmos. Oceans* **27**(1997), 383–412 (1997)
- Krishnamurti, T.N., Bachiochi, D., LaRow, T., Jha, B., Tewari, M., Chakraborty, D.R., Correa-Torres, R., Oosterhof, D.: Coupled atmosphere–ocean modeling of the El Niño of 1997–98. *J. Climate* **13**, 2428–2459 (2000)
- Krishnamurti, T.N., Bedi, H., Hardiker, V., Ramaswamy, L.: An Introduction to Global Spectral Modeling. Springer, 317pp. 2nd, rev. and enlarged ed (2006)
- Kuo, H.L.: Convection in conditionally unstable atmosphere. *Tellus* **13**, 441–459 (1961)
- Lau, K.M., Peng, L.: Origin of low-frequency (intraseasonal) oscillations in the tropical atmosphere. Part I: The basic theory. *J. Atmos. Sci.* **44**, 950–972 (1987)
- Lilly, D.K.: On the theory of disturbances in a conditionally unstable atmosphere. *Mon. Weather Rev.* **88**, 1–17 (1960)
- Lindzen, R.S.: Wave-CISK in the tropics. *J. Atmos. Sci.* **31**, 156–179 (1974)
- Madden, R.A., Julian, P.R.: Detection of a 40–50 day oscillation in the zonal wind in the tropical Pacific. *J. Atmos. Sci.* **28**, 702–708 (1971)
- Nakazawa, T.: Tropical super clusters within intraseasonal variations over the western Pacific. *J. Meteorol. Soc. Jpn.* **66**, 823–839 (1988)
- Randall, D., Khairoutdinov, M., Arakawa, A., Grabowski, W.: Breaking the cloud parameterization deadlock. *Bull. Am. Meteorol. Soc.* **84**(11), 1547–1564 (2003)
- Saha, S., et al.: The NCEP climate forecast system. *J. Climate* **19**, 3483–3517 (2006)
- Takayabu, Y.N., Iguchi, T., Kachi, M., Shibata, A., Kanzawa, H.: Abrupt termination of the 1997–98 El Niño in response to a Madden-Julian oscillation. *Nature* **402**, 279–282 (1999)
- Yanai, M., Lu, M.-M.: Equatorially trapped waves at the 200 mb level and their association with convergence of wave energy flux. *J. Atmos. Sci.* **40**, 2785–2803 (1983)

# Chapter 8

## Scale Interactions

### 8.1 Introduction

The tropical atmospheric circulation contains a number of spatial and temporal scales of motion. In terms of temporal scales – or frequency domain – these range from scales of a few seconds (for turbulent motions), through semi-diurnal and diurnal scales, synoptic (2–7 day) scales, semi-biweekly scales, Madden-Julian oscillation scales (30–60 days), annual cycle, ENSO, PDO, etc. In terms of spatial scales – or wave number domain – the scales range from a few mm for turbulent processes, few 100 m for cloud-scale motions, few 100 km for tropical disturbances, few 1,000 km for the African easterly waves, and so on.

These scales do not exist separately from one another, but instead are in constant interplay. The formalism describing this communication is called ‘scale interaction’. The mathematical formulation of scale interactions is somewhat complicated, but the physical interpretations are elegant. Scale interaction is a central topic in the atmosphere–ocean dynamics and thermodynamics. It is possible to calculate the rate of change of kinetic or potential energy of a given scale (either spatial or temporal) as a result of its interactions with any other scales based on either observations or numerical model data sets.

An interesting example of scale interactions is the following. It is well known that deep cumulus convection drives a hurricane/typhoon/tropical cyclone. The scale of deep cumulus convection (the cumulonimbus clouds) is only on the order of a few km, whereas the scale of the hurricane is on the order of 100 km and larger. How do these diverse spatial scales communicate with each other? This is the type of question that is addressed by the scale interaction approach.

## 8.2 Wave-Number Domain

The only way energy can be transferred between scales (excluding the mean) is via triad interactions; a triad of waves with wave numbers  $n, m$  and  $k$  interact if and only if  $k + m = n$ , or  $-k + m = n$ , or  $k - m = n$ . These are the so called trigonometric selection rules (see Saltzman 1957).

Symbolically, the changes in kinetic and potential energy for wave number  $n$  and for the zonal mean are given by

$$\frac{\partial K_n}{\partial t} = \langle K_0 \rightarrow K_n \rangle + \langle K_{n,m} \rightarrow K_k \rangle + \langle P_n \rightarrow K_n \rangle + \langle F_n \rightarrow K_n \rangle$$

$$\frac{\partial K_0}{\partial t} = - \sum_n \langle K_0 \rightarrow K_n \rangle + \langle P_0 \rightarrow K_0 \rangle + \langle F_0 \rightarrow K_0 \rangle$$

$$\frac{\partial P_n}{\partial t} = \langle P_0 \rightarrow P_n \rangle + \langle P_{k,m} \rightarrow P_n \rangle - \langle P_n \rightarrow K_n \rangle + \langle H_n \rightarrow P_n \rangle$$

$$\frac{\partial P_0}{\partial t} = - \sum_n \langle P_0 \rightarrow P_n \rangle - \langle P_0 \rightarrow K_0 \rangle + \langle H_0 \rightarrow P_0 \rangle$$

where  $K_n$  and  $K_0$  represent the kinetic energy of wave number  $n$  and wave number 0 (the zonal mean) respectively; similarly,  $P, F$  and  $H$  are the available potential energy, frictional dissipation and the heating, respectively, at the wave number indicated by the subscript. The terms in triangular brackets indicate exchanges (positive in the direction of the arrow). These exchanges can be analyzed as follows:

(a) Zonal to wave exchange of kinetic energy

$$\begin{aligned} \langle K_0 \rightarrow K_n \rangle = & - \left[ \Phi_{uv}(n) \frac{\cos \varphi}{a} \frac{\partial}{\partial \varphi} \left( \frac{U(0)}{\cos \varphi} \right) - \Phi_{vv}(n) \frac{1}{a} \frac{\partial V(0)}{\partial \varphi} \right. \\ & \left. + \Phi_{u\omega}(n) \frac{\partial U(0)}{\partial p} + \Phi_{v\omega}(n) \frac{\partial V(0)}{\partial p} - \Phi_{uu}(n) V(0) \frac{\tan \varphi}{a} \right] \end{aligned}$$

is the conversion of the kinetic energy of the zonal mean to kinetic energy of wave number  $n$  (see Appendix 1 for the meaning of symbols and for the derivation of the conversion equations). This is more or less a barotropic energy exchange that invokes the covariance among the zonally averaged motion and the eddy flux of momentum.

## (b) Waves to waves exchange of kinetic energy

$$\begin{aligned} \langle K_o \rightarrow K_n \rangle = & \sum_{\substack{m=-\infty \\ m \neq 0}}^{\infty} \left\{ U(m) \left( \frac{1}{a \cos \varphi} \Psi_{uu_\lambda}(m, n) + \frac{1}{a} \Psi_{vu_\varphi}(m, n) \right. \right. \\ & + \Psi_{ow_p}(m, n) - \frac{\tan \varphi}{a} \Psi_{uv}(m, n) \Big) \\ & + V(m) \left( \frac{1}{a \cos \varphi} \Psi_{uv_\lambda}(m, n) + \frac{1}{a} \Psi_{vv_\varphi}(m, n) \right. \\ & + \Psi_{ow_p}(m, n) + \frac{\tan \varphi}{a} \Psi_{uu}(m, n) \Big) \\ & - \frac{1}{a \cos \varphi} \frac{\partial}{\partial \varphi} [\cos \varphi (U(m) \Psi_{vu}(m, n) + V(m) \Psi_{vv}(m, n))] \\ & \left. \left. - \frac{\partial}{\partial p} (U(m) \Psi_{ow}(m, n) + V(m) \Psi_{ov}(m, n)) \right) \right\} \end{aligned}$$

is the non-linear exchange of kinetic energy among different scales. This is a triplet interaction, since a triple product is involved. The three scales ( $m$ ,  $k$  and  $n$ ) have to be related by the requirement that  $m + k = n$  or  $m - k = n$  or  $-m + k = n$ , or else the energy exchange is zero.

- (c) Wave to wave conversion between available potential and kinetic energy  
 $\langle P_n \rightarrow K_n \rangle = -\frac{R}{p} \Phi_{T\omega}(n)$  is the conversion of the potential energy of the wave number  $n$  to the kinetic energy of the same wave number. This is a quadratic (in-scale) interaction.
- (d) Wave to wave conversion between friction and kinetic energy  
 $\langle F_n \rightarrow K_n \rangle$  is the conversion between frictional dissipation and kinetic energy. This also is a quadratic (in-scale) interaction. It would be expected to be negative, since friction is a sink of kinetic energy.
- (e) Zonal conversion between available potential and kinetic energy  
 $\langle P_0 \rightarrow K_0 \rangle = -\frac{R}{p} \Phi_{T\omega}(0)$  is the conversion of zonally averaged potential energy to zonally averaged kinetic energy. This is the Hadley cell vertical overturning, with warm air rising and cold air sinking.
- (f) Zonal to wave exchange of available potential energy  
 $\langle P_0 \rightarrow P_n \rangle = - \left[ \frac{C_p \gamma}{a} \Phi_{Tv}(n) \frac{\partial Y(0)}{\partial \phi} + \frac{\gamma p^\mu}{\mu} \left\{ \Phi_{T\omega}(n)'' \frac{\partial \bar{\theta}''}{\partial p} \right\} \right]$  is the potential energy exchange between the zonally averaged flow and wave number  $n$ . It relates to the heat flux from the zonal mean to the scales of the waves.

(g) Waves to waves exchange of available potential energy

$$\begin{aligned} \langle P_{m,n} \rightarrow P_k \rangle &= C_p \gamma \sum_{\substack{m=-\infty \\ m \neq 0}}^{\infty} Y(m) \left( \frac{1}{a \cos \varphi} \Psi_{uT_\lambda}(m, n) + \frac{1}{a} \Psi_{vT_\phi}(m, n) \right. \\ &\quad \left. + \Psi_{\omega T_p}(m, n) + \frac{R}{C_p p} \Psi_{\omega T}(m, n) \right) \\ &\quad - \frac{1}{a \cos \varphi} \frac{\partial}{\partial \varphi} \cos \varphi Y(m) \Psi_{vT}(n, m) - \frac{\partial}{\partial p} Y(m) \Psi_{\omega T} \end{aligned}$$

is the non-linear potential energy exchange between scales. This is a triad interaction among a triplet of waves that satisfies the selection rule.

(h) Generation of wave available potential energy

$\langle H_n \rightarrow P_n \rangle = \gamma \Phi_{Th}(n)$  is the generation of available potential energy at wave number  $n$  from heating. This involves a covariance among heating and temperature on the scale of wave number  $n$ . This term is quadratic.

(i) Generation of zonal available potential energy

$\langle H_0 \rightarrow P_0 \rangle = \gamma \Phi_{Th}(0)$  is the generation of available potential energy at the scale of the zonal mean from heating. This generation is achieved by the covariance of zonally averaged heating and temperature.

The totality of interactions is illustrated schematically in Fig. 8.1.

The total energy budget in the wave number domain for a selected scale  $n$  has to include the following components:

(a) Exchanges involving quadratic non-linearities (i.e. in-scale exchanges):

- Generation or loss of available potential energy from heat sources or sinks on the scale of  $n$ ;
- Conversion between kinetic and available potential energy on the scale of  $n$ ,
- Conversion between the kinetic energy of the zonal mean and the kinetic energy of scale  $n$ , and
- Conversion between the potential energy of the zonal mean and the potential energy of scale  $n$ .

(b) Exchanges involving triple product non-linearities (i.e. cross-scale exchanges):

- Triplet potential energy exchanges with wave numbers  $m$  and  $k$  such that  $n = \pm(m \pm k)$ , and
- Triplet kinetic energy exchanges with wave numbers  $m$  and  $k$  such that  $n = \pm(m \pm k)$ .

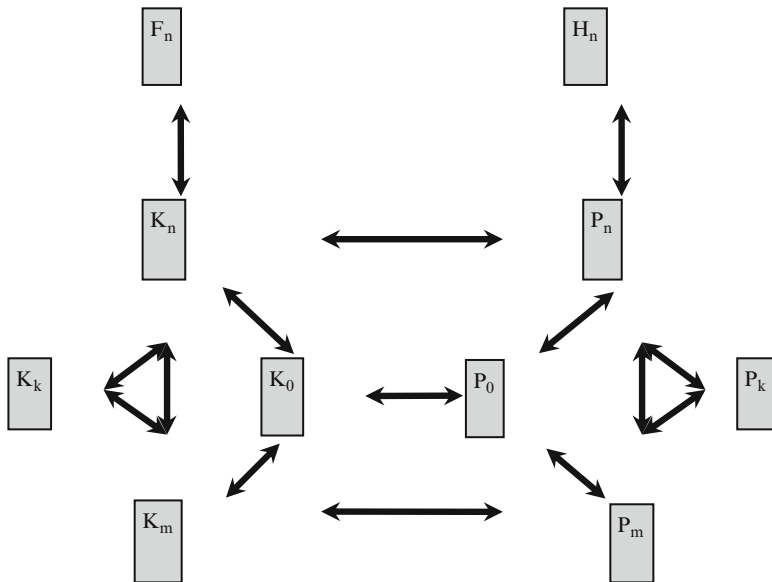


**Fig. 8.1** Schematic illustration of the possible energy exchanges among the mean (subscript 0) and different scales (subscripts k, m, n)

### 8.3 Frequency Domain

A similar approach can be used to derive equations for the energy exchanges in a frequency domain. In that case, the Fourier decomposition of variables would be in time, instead of space, i.e.,  $f(t) = \sum_{n=-\infty}^{\infty} F(n)e^{i2\pi n t/T}$ , where T is the length of the data set. In this case, n would denote the wave frequency (instead of wave number). Oscillations in time can be separated into a long term mean ( $n = 0$ ), low-frequency modes (small n), and high frequency modes (large n). For an energy exchange among oscillations with frequencies n, m and k to take place, it is necessary that the selection rule  $k = \pm(m \pm n)$  be satisfied. For example, if one uses a year-long data set ( $T = 365$  days), the synoptic scale oscillations (2.5–5 days) have frequencies m,  $n = (146-73)$ . Madden-Julian oscillations, on the other hand have typical periods of 30–50 days, or  $k = (12-7)$ . The allowable interactions between MJO and the synoptic time scales then are:

$$\begin{aligned} m &= 146, n = 139, k = 7; m = 146, n = 138, k = 8; \dots; m = 146, n = 134, \\ &\quad k = 12; \\ m &= 145, n = 138, k = 7; m = 145, n = 137, k = 8; \dots; m = 146, n = 133, \\ &\quad k = 12; \\ m &= 85, n = 78, k = 7; m = 85, n = 77, k = 8; \dots; m = 85, n = 73, k = 12 \end{aligned}$$

## 8.4 Frequency Domain Examples

The maintenance of the MJO is an attractive problem for scale interactions. The time scale of the MJO (roughly 20–60 days) can in principle interact with several other time scales such as:

- (i) The tropical disturbance time scales (4–7 days); this would include tropical waves and depressions.
- (ii) The annual cycle.
- (iii) The El Niño-Southern Oscillation time scales.
- (iv) The long-term mean state, i.e., the climatology.

Sheng and Hayashi (1990a, b) examined this problem using 30 years of past global analysis data sets. The most important result they obtained was that the synoptic scale typical waves (on the time scales of 4–7 days) supplied kinetic energy towards the maintenance of the MJO time scale (20–60 days). This kinetic energy exchange from the synoptic to the MJO time scale invokes a number of triads of frequencies of which two frequencies generally reside in the synoptic time scales and one in the MJO time scale (the time scale is the inverse of the frequency). One such example is composed of 5 day and 6 day times scales interacting with the 30 day time scale, i.e.,  $1/30 = 1/5 - 1/6$ . This satisfies the selection rule  $n_{MJO} = n_{synoptic1} - n_{synoptic2}$ .

Some of the other findings of the Sheng and Hayashi studies are

- There is another family of triads that can provide potential energy to the scale of the MJO. These exchanges were generally quite small.
- The potential energy for the MJO time scale is largely received from in-scale heating on the MJO time scale.
- Kinetic energy on the MJO time scale also builds from overturnings (potential to kinetic energy conversion via the net ascent of warmer air and a descent of colder air on the same time scale). This is a smaller contribution compared to the triad exchange of kinetic energy for the synoptic to the MJO time scale.

This brings out interactions among triplets of waves. In a recent study, Krishnamurti et al. (2003) asked what scales were most important for the latent heat fluxes from the ocean to the atmosphere over the tropics on the time scale of MJO. They found again those triplet interactions of waves where two of the waves are in the synoptic range and one is in the MJO range stood out. A large number of such triplets of waves contribute to these latent heat fluxes. Recent results at the surface and at the top of the planetary boundary layer are shown in Figs. 8.2 (a through h) and 8.3 (a through h). These two illustrations show the respective annual fluxes for the tropical Indian and Western Pacific Oceans.

In these two illustrations, panels (a) through (h) show the following:

- (a) Map of the total fluxes on the time scale of the MJO.
- (b) Map of the total fluxes on the time scale of the MJO arising solely from the interactions of the MJO time scale with the synoptic time scale of 3–7 days.

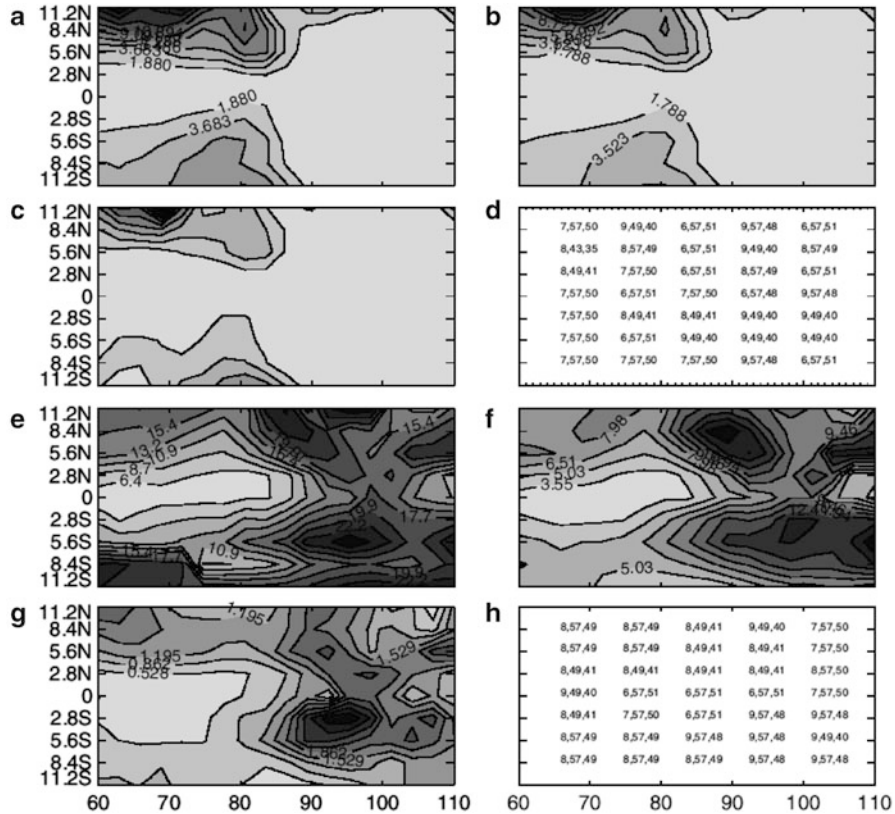


**Fig. 8.2** Latent-heat fluxes ( $\text{Wm}^{-2}$ ) over the Indian Ocean region. (a) Total latent-heat fluxes on the time-scale of the MJO across the constant-flux layer. (b) Total fluxes of latent heat across the constant-flux layer on the time-scale of the MJO arising from interaction of the MJO with the synoptic time-scale of 2–7 days. (c) Fluxes of latent heat contributed by salient (strongest contributing) triad interactions in the surface layer. (d) Salient triad interaction frequencies contributing to latent-heat fluxes on the time-scale of the MJO across the constant-flux layer. (e) Total latent-heat fluxes on the time-scale of the MJO in the planetary boundary layer (PBL) at 850 hPa. (f) Total latent-heat fluxes in the PBL on the time-scale of the MJO arising from interaction of the MJO time-scale with the synoptic time-scale of 2–7 days. (g) Latent-heat fluxes contributed by the salient triad interactions in the PBL. (h) Salient triad interaction frequencies contributing to latent-heat fluxes on the time-scale of the MJO in the PBL at 850 hPa (After Krishnamurti et al. 2003)

- (c) Contribution to the total fluxes in Panel b that arise from triads (MJO time scale interacting with pairs of synoptic time scale frequencies).
- (d) Salient triads of Panel c. A triad denoted as 7, 57, 50 is interpreted as follows. The time scales are 364/7, 364/57, and 364/50 days respectively. Here the triplet interactions involve a triple product of the surface wind  $V$ , the saturation specific humidity  $q_s$  at the ocean temperature  $T$ , and the stability-dependent drag coefficient  $CD$ .

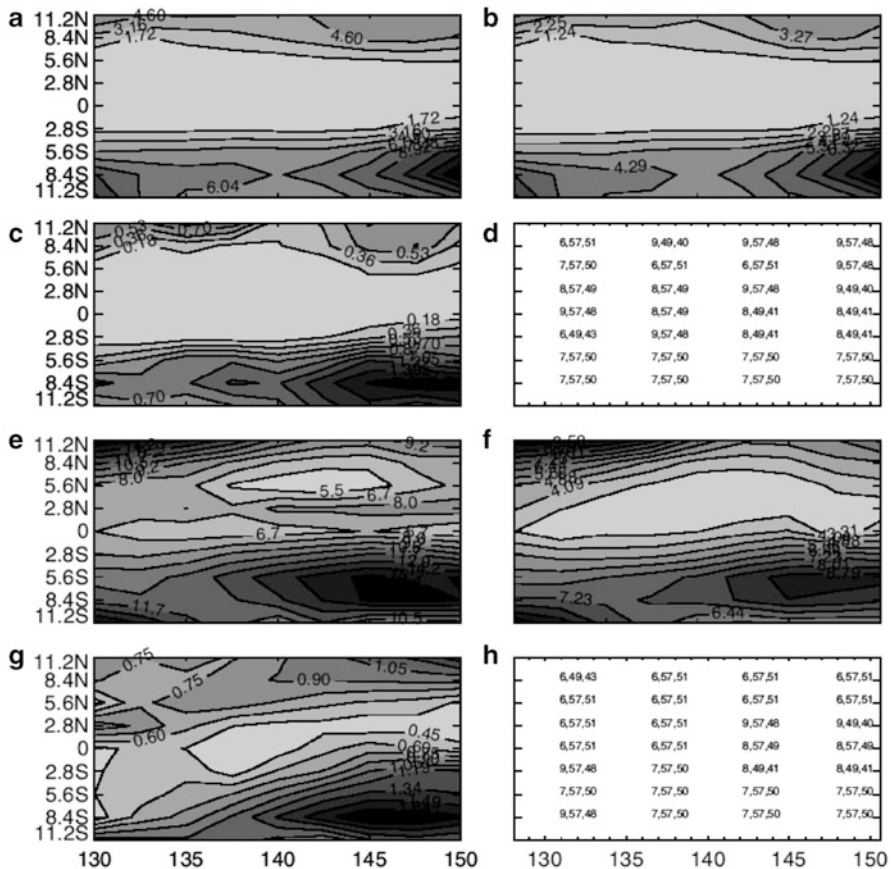


Fig. 8.3 As in Fig. 8.2, but for the West Pacific Ocean (After Krishnamurti et al. 2003)

Panels (a) through (d) refer to the constant flux layer, i.e., the surface level. Panels (e) through (h) show the same respective fields as panels (a) through (d) but at the top of the planetary boundary layer. All fluxes are in units of  $\text{Wm}^{-2}$ . The results over the Indian Ocean are quite similar to those over the Pacific. In summary, a substantial fraction of the total annual fluxes (nearly 15 %) occur on the time scale of MJO. Such fluxes on the MJO time scale from the ocean to the atmosphere require SST variability on the same scale. The synoptic disturbances (4–7 day time scales) seem to tap this energy from the ocean at the MJO time scale. If SST variability were very small on the MJO time scale, then the latent heat flux on the MJO time scale would be very small as well. It was found that there are some salient triads (illustrated in panels (d) and (h)) that contribute to a substantial portion of the total fluxes on the MJO time scale. These seem to involve MJO and the synoptic time scales.

The mechanism of the MJO that emerges from computations of scale interactions are as follows: Organized clouds are not found on the entire MJO scale encircling the global tropics. Clouds are thus not organized on the scale of the MJO. Where we do see clouds seemingly relating to an MJO wave, such as over the monsoon belt and the western tropical Pacific Ocean, are in fact clouds that relate to synoptic and mesoscale disturbances over those regions. The magnitude of convergence and divergence on the scale of the MJO is of the order of  $10^{-6}$  to  $10^{-7}$  is too weak to organize deep convection on the scale of the MJO. There is sufficient evidence to state that clouds are organized on the scales of tropical synoptic waves and imbedded mesoscale motions within the synoptic scales. In this context the term “organization of convection” implies organization of clouds around the scale of a synoptic disturbance, organization of the large centers contributing to the covariance of convective heating and temperature for the generation of available potential energy on the scale of organized convection and the synoptic scale disturbances. Furthermore the covariance of vertical velocity and temperatures also occurs on these same organized scales to provide eddy kinetic energy to the scale of that synoptic scale disturbance. This is a mechanism for the maintenance of the synoptic scales over the Asian monsoon and the western tropical pacific belts. These quadratic nonlinearities (these covariances) support inscale processes. The clouds not organized about the synoptic scale fail to meet the trigonometric selection rules and the entire scenario weakens. The next component of this scenario is on the maintenance of the MJO. That invokes an organization of dynamics. Here a pair of synoptic scales (such as 5 and 6 day time scale disturbances) can interact with a member of the MJO time scale (such as the 30 day time scale, because  $1/5-1/6 = 1/30$  meets the triad selection rule) and provides energy to the MJO time scale. This energy exchange dictated by triads largely arises from the non liner advective dynamics terms and hence calls for an organization of dynamics to meet the energy exchange and the maintenance of the MJO.

## 8.5 Wave-Number Domain Examples

### 8.5.1 Global Tropics

In the context of the Asian summer monsoon the scale interactions are very revealing of the mechanisms for its maintenance. As the monsoon onset occurs, the planetary scale monsoon flow (zonal wave numbers 1 and 2) builds up very fast. Figure 8.4 shows the kinetic energy spectra before, during and after onset, as a function of zonal wave number. This kinetic energy is a mass averaged quantity between  $50^{\circ}\text{E}$  and  $150^{\circ}\text{E}$ ,  $30^{\circ}\text{S}$  and  $40^{\circ}\text{N}$ , and between the surface and 100 hPa level. This clearly shows that soon after the onset in the month of June the planetary scale (i.e. wave numbers 1 and 2) show an explosive gain of energy. This planetary

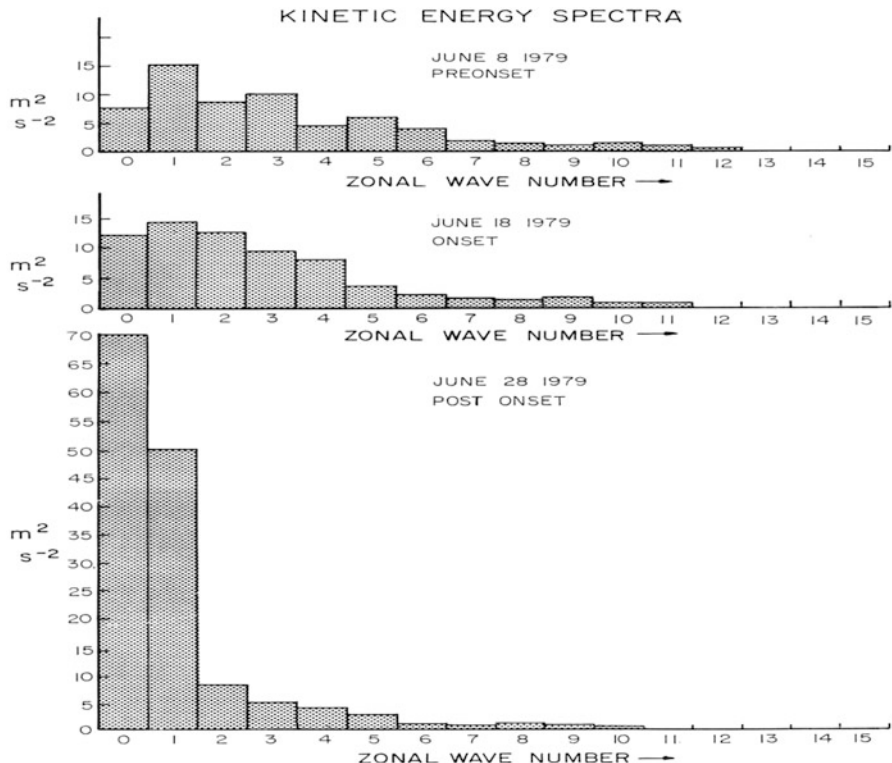


**Fig. 8.4** Kinetic energy spectra (averaged between  $50^\circ\text{E}$  and  $150^\circ\text{E}$ ,  $30^\circ\text{S}$  and  $40^\circ\text{N}$ , and surface to 100 hPa) before (top), during (middle) and after (bottom) the onset of the 1979 monsoon (Computed from NCEP-NCAR reanalysis data)

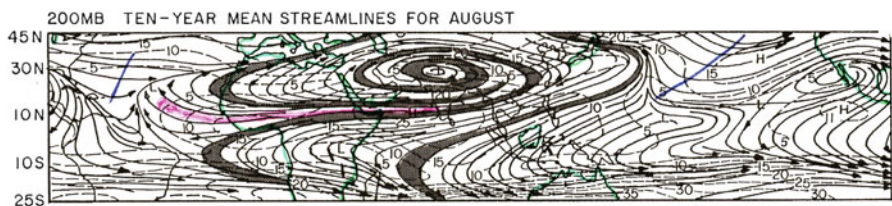


**Fig. 8.5** Mean August streamlines at 200 hPa (Computed from NCEP-NCAR reanalysis)

scale can be seen in Fig. 8.5 where the time mean flows at 200 hPa are shown. This shows the geographical extent of the planetary scale monsoon as revealed by the buildup of the Tibetan High after the onset of the monsoon. This stretch of the monsoon extends for roughly  $20^\circ\text{W}$  to the date line in the Pacific Ocean. The troposphere below this upper anticyclonic complex is warm largely maintained by cumulus convection over Asia. The time averaged thermal field is illustrated in Fig. 8.6 that shows the 300 hPa temperatures. An east–west thermal asymmetry is

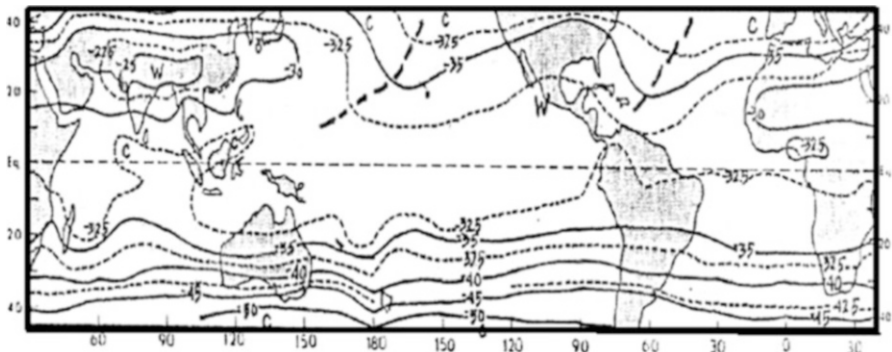


**Fig. 8.6** Mean summer temperature ( $^{\circ}\text{C}$ ) at 300 hPa (Computed from NCEP-NCAR reanalysis)

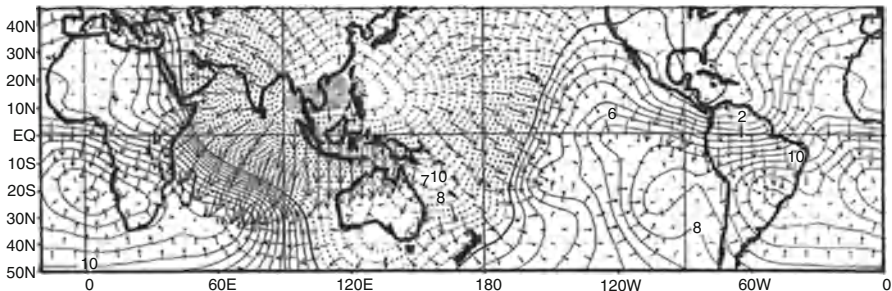


**Fig. 8.7** Mean 200 hPa velocity potential ( $106\text{m}^2\text{s}^{-2}$ ) and divergent wind (CDAS/reanalysis) for August 1996

also a part of this planetary scale feature. Cold lobes are found in the subtropical middle Atlantic and the middle Pacific. These are the places where the mid-oceanic upper troughs reside. Another related feature of importance in the context of scale interactions are the divergent east–west circulations that show slow ascent of mass in the region of the upper anticyclone and a slow descent in the region of the upper trough. This is best seen from the geometry of the velocity potential and the streamlines of the divergent wind (Fig. 8.7).

A schematic diagram (from Kanamitsu et al. 1972) of the gross energetics of the tropics for the summer season, derived using a scale interaction approach, is presented in Fig. 8.8. This illustrates the following scenario: There is a pronounced differential heating ( $H_L$ ) in the east–west direction on the scale of long waves. This builds the available potential energy ( $P_L$ ) on the scale of the long waves. The divergent east–west circulations carry a net covariance of vertical velocity and temperature, i.e.,  $-\frac{\omega_T T_L}{p} > 0$  and generate kinetic energy of the long waves. In the zonally averaged sense the summer Hadley cell energetics is also an important component of this scenario. Zonally averaged heating  $H_Z$  near  $10^{\circ}\text{N}$  and net cooling

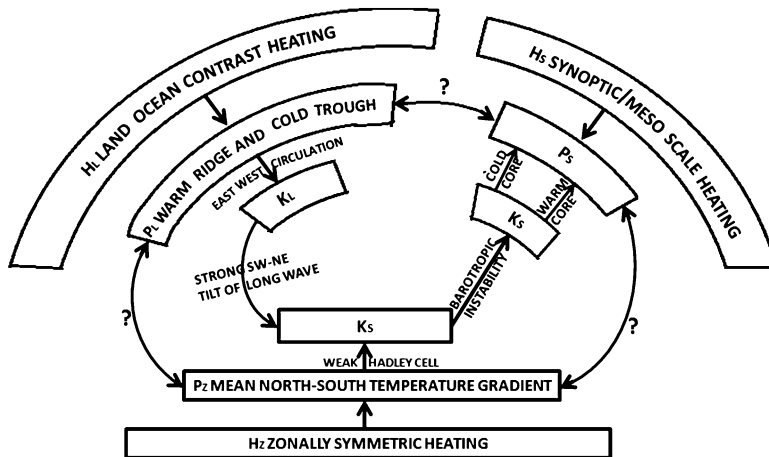


**Fig. 8.8** Diagram of the energy exchanges in the tropical atmosphere for the zonal mean, short, medium and long waves (After Krishnamurti 1979). Units of  $10^{-6} \text{m}^2 \text{s}^{-3}$

near  $25^\circ\text{S}$  generate zonal available potential energy  $P_Z$ . The Hadley overturning of mass generates kinetic energy  $K_Z$  from the ascent of warmer air near  $10^\circ\text{N}$  and a descent in the southern hemisphere near  $25^\circ\text{S}$ .

Shorter time and space scale disturbances, indicated by the subscript S, include tropical waves, depressions and storms. Some are cold core disturbances while others are characterized by a warm core. These can have a conversion from the available potential to the eddy kinetic energy or vice versa, depending on the structure and thermal status.

A number of other arms of the schematic diagram shown in Fig. 8.8 show the lateral energy exchanges among scales that signify scale interactions. Non-linear kinetic energy exchanges from the longer to the shorter waves of the tropical have been demonstrated. There is also considerable evidence of the transfer of kinetic energy from the zonal scales to these shorter scales (Krishnamurti et al. 1975b). The non-linear exchange of potential energy among scales is somewhat uncertain; however current data suggest a down-the-scale transfer from long waves  $P_L$  to shorter waves  $P_S$ . Over the monsoon complex, a long wave giant sea breeze line system sets up. This large scale system supplies energy to other scales via the mechanism of scale interaction.

### 8.5.2 Hurricanes

Another application of the scale interaction approach is towards understanding the scale interactions within a hurricane. There a cylindrical coordinate system is used, and the Fourier decomposition is done in the azimuthal direction. Azimuthal wave

number zero corresponds to the hurricane mean circulation, wave numbers one and two correspond to the hurricane asymmetry, and higher wave numbers can be related to contributions on the cloud scales. There are energy exchanges among various forms of energy such as zonal and eddy energies for kinetic and potential and nonlinear exchanges among the same types such as kinetic to kinetic, and eddy available to eddy available, these are exchanges among different scales. Appendix 1 provides the mathematical formulations.

- (i)  $\langle P_o \cdot K_o \rangle$  is the generation of eddy available potential energy and its transformation to eddy kinetic energy, which is the storm's kinetic energy, relies on the magnitudes of two covariances. These are the products of convective heating and temperature, and of the vertical velocity and temperature. The eye wall warming compared to the surroundings and the descent around the eye wall and the rain bands plus the convective heating in heavy rain areas contribute to these processes.
- (ii)  $\langle P_l \cdot K_l \rangle$  The scale of a hurricane can be assessed from a Fourier analysis of winds along the azimuthal coordinate for inner radii that includes the maximum wind belt. Such an analysis reveals that most of the azimuthal variance resides in the azimuthal mean, i.e. wave number zero, and the first two or three long waves around the azimuthal coordinate (here expressed in a local cylindrical coordinate about the storm's center as the origin). These long waves and the wave number zero are the ones that contribute the most to the conversion of eddy available potential energy to eddy kinetic energy for the hurricane scale. That arises from the vertical overturning, the Hadley type overturning for wave number zero. This happens also on the long wave scales where the rising of warm air the descent of relatively cooler air contributes this covariance and hence to a strengthening of the hurricane. The end result of such energy conversions is the increase of eddy kinetic energy and the strengthening of the hurricane. Disruption of the organization of convection can also, in a reverse manner lead to a weakening of a hurricane.
- (iii)  $\langle P_c \cdot K_c \rangle$  is the energy conversion from eddy available potential to eddy kinetic energy  $P_c$  to  $K_c$  on cloud scales can only generate kinetic energy on the cloud scales and not on the hurricane scale. The reason for that is this conversion invokes a quadratic nonlinearity among vertical motion and temperature and all such quadratic processes can only do in-scale conversions.
- (iv)  $\langle H_o \cdot P_o \rangle$  is the generation of available potential energy on the cloud scale  $H_o$  to  $P_o$  defines the generation from heating on the cloud scale where it is already warm and cooling where it is relatively less warm. This is a quadratic term and will only describe an in-scale process hence this does not address directly the hurricane scales. The covariance of cloud scale convective heating and the cloud scale temperatures are involved in this computation.
- (v)  $\langle H_l \cdot P_l \rangle$  is an important component of hurricane energetics. Here the heating generates available potential energy on the long azimuthal hurricane scales by heating where it is warm and cooling where it is less warm.
- (vi)  $\langle H_c \cdot P_c \rangle$  generate available potential energy on small scales.

- (vii)  $\langle P_s \cdot P_l \rangle$   $P_s$  to  $P_l$  denotes a transfer of available potential energy among the short and the long wave scales. This computation invokes triple product nonlinearity and calls for sensible heat transfer among the short and the long waves via heat transfer that can be up or down the thermal gradient of the long waves. That transfer is from long to short waves if the short waves transfer sensible heat from the long to the short waves (thus building the latter) or vice versa. This is not found to be a major contributor to the overall driving of a hurricane energetics.
- (viii)  $\langle K_s \cdot K_l \rangle$  is the direct energy exchange of kinetic energy among short and long waves. This invokes a triple product non linearity, such that generally two short waves interact with a long wave resulting in a gain or a loss of kinetic energy for the long wave. That sign of exchange is dictated by the covariance of the local long wave flows and the convergence of eddy momentum flux by the short waves. If the planetary scale monsoon builds the long scales kinetic energy from the available potential energy of long waves that energy is generally dispersed to shorter waves by this triad of wave mechanism. In a hurricane this nonlinear exchange is not a very important contributor for the mutual exchanges among azimuthal long and short waves.
- (ix)  $\langle K_0 \cdot K_l \rangle$  – The exchange from  $K_0$  to  $K_l$  denotes the conventional barotropic process from zonal to long waves scales. This invokes the covariance of azimuthally averaged flows and the convergence of eddy flux of momentum by the long wave scales. In hurricane dynamics, and also for the planetary scale monsoon, this is an important contributor.
- (x)  $\langle K_0 \cdot K_s \rangle$  – The exchange of kinetic energy from the azimuthally averaged zonal kinetic energy to short wave scales is simply another component of the barotropic stability/instability problem. This invokes the covariance of zonal flows and the eddy convergence of flux of kinetic energy by the shorter waves. This is a nontrivial effect but does not directly seem to be important for the hurricane scales.
- (xi)  $\langle P_o \cdot P_l \rangle$  – The exchange  $P_o$  to  $P_l$  of available potential energy from the azimuthally averaged motions to the scale of long azimuthal waves  $\langle P_o \cdot P_l \rangle$  is an important ingredient of hurricane dynamics. The wave number zero, i.e. the azimuthal mean carries the warm core and it exchanges available potential
- (xii)  $\langle P_o \cdot P_c \rangle$  – This denotes the exchange of potential energy from the zonal available potential energy to that of long waves. This relates to sensible heat flux down or up the thermal gradient of the azimuthally averaged flows.

Organization of convection occurs when individual cumulonimbus clouds or cloud clusters evolve into a large-scale cluster over a period of time (Moncrieff 2004). In a simple linear model it is a positive feedback loop, whereby intense latent heating generates lifting, creates divergence aloft, and lowers the pressure at the surface. Lower surface pressure increases the pressure gradient at low levels and creates stronger low level winds. This leads to stronger convergence into the center of the storm and enhanced convection. The whole process then repeats itself.

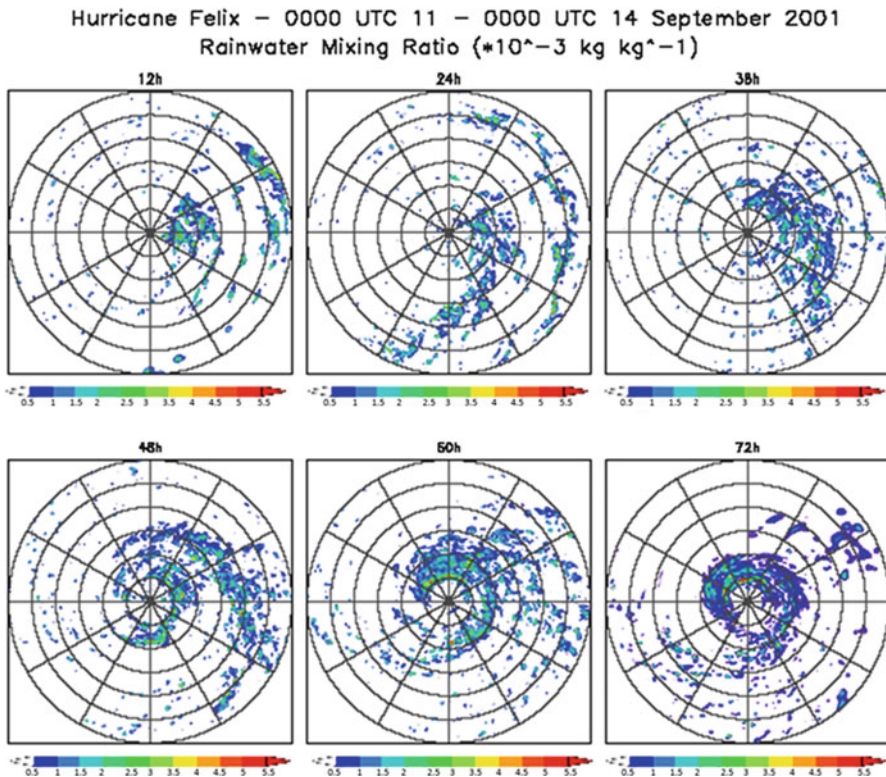


**Fig. 8.9** Distribution of rainwater mixing ratio ( $\times 10^{-3} \text{ kg kg}^{-1}$ ) at 900 mb for hours 12, 24, 36, 48, 60, and 72 of the forecast for Hurricane Felix shown in storm centered coordinates. Radial increments are  $0.5^\circ$  ( $\sim 56 \text{ km}$ )

To show organization of convection in the simulated hurricanes, the amplitude spectra of the rainwater mixing ratio at various wavenumbers was examined. Rainwater mixing ratio was chosen as it can indicate the features of deep convective cloud elements in a hurricane (Krishnamurti et al. 2005). Organization of convection was illustrated in this way for three reasons: (1) amplitude is the measure of the strength of the signal, (2) it can be shown that as the storm is forming, the strength of the signal of certain wavenumbers increases, and (3) the part of the storm in which organization is occurring can be ascertained, i.e., determine which radii have the strongest signals. Each rainwater mixing ratio data point in cylindrical coordinates at the 900 mb level for all hurricane simulations was Fourier transformed and time-radius plots of the amplitude spectra were then plotted for wavenumbers 0, 1, 2, and 25. Because the energy falls off very rapidly beyond wavenumber 3, we have lumped all other wavenumbers beyond this together and refer to them collectively as the “cloud-scale”. Hence, wavenumber 25 was randomly chosen as a representative for any cloud-scale harmonic.

Figures 8.9 and 8.10 show the predicted rainwater mixing ratio ( $\text{kg kg}^{-1}$ ) at 900 mb and winds at 900 mb, respectively, for the 72 h forecast for Hurricane Felix.

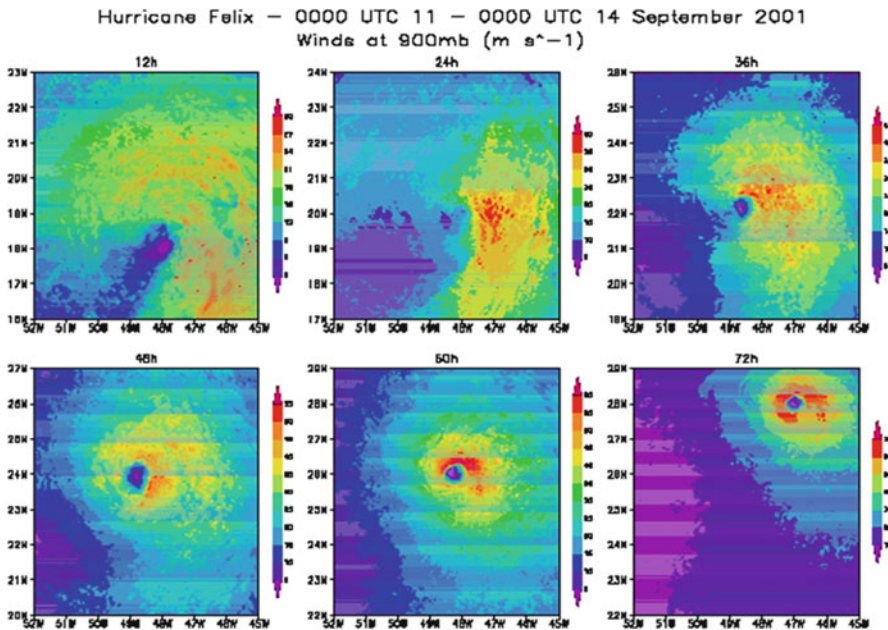


**Fig. 8.10** Winds ( $\text{m s}^{-1}$ ) at 900 mb for hours 12, 24, 36, 48, 60, and 72 of the forecast for Hurricane Felix. Partial 1.67 km domain is shown

From 120 to 36 h, the storm was very asymmetrical with maximum values of rainwater mixing ratio occurring to the southeast and east of the storm center and the maximum winds at 900 mb occurring to the east of the storm center. Hence, a stronger signal from wavenumber 1 during these hours would be expected. From 48 to 72 h, the storm becomes increasingly more symmetric and the largest values of amplitude can be expected to occur in wavenumber 0. However, the storm is still somewhat asymmetrical.

The central issue in the energetics is that deep cumulus convection drives a hurricane only from an azimuthal organization of clouds on the scale of the hurricane. Plethora of single clouds, if they are not organized, then they cannot contribute to the generation of available potential energy and its disposition to the kinetic energy of a hurricane. Intensity changes can be expected as the organization evolves. In the early stages of a hurricane formation dynamical instabilities play an important role in organizing convection by providing a steering of clouds along a circular geometry. That happens in barotropic processes when shear flow vorticity is transformed into curvature flow.

The hurricane scales are largely described by azimuthal wave numbers 0, 1, 2 and 3. The mechanism of a mature hurricane energetics relies on the organization of convection on the hurricane scale. On these scales convective heating and temperature carry a large positive value for their covariance; this generates available potential energy on the scale of the hurricane. That energy is disposed off to

kinetic energy for all those respective azimuthal scales 0, 1, 2 and 3 by the individual scale vertical overturning. This is largely the warm air rising and the relatively cooler air descending. That is the conversion of available potential energy to the eddy kinetic energy for each scale that happens separately mathematically since this is an inscale process. Both of the above energy processes are described by quadratic nonlinearities. The other energy exchanges to other shorter scales carry much smaller magnitudes. The barotropic exchanges from azimuthally averaged flow kinetic energy to hurricane scales can also be somewhat important. The nonlinear triad interactions are generally small but are non-trivial.

The total available potential energy for all scales summed together is shown in Fig. 8.11. The histograms show these results for wave numbers in groups. These results are grouped for inner radii less than 40 km and for larger outer radii greater than 40 km. Overall the results show the largest contributions from the wave number 0 which are the azimuthally averaged modes.

The conversions for wave numbers 1 and 2 are about half as large as those for wave number domain for the middle latitude zonally averaged jet, wave number 180 was in fact small and even fluctuating in sign for different smaller scales. The energetics in the wave number domain for the middle latitude zonally averaged jet, wave number 0, is opposite to that for a hurricane's azimuthal wave number 0. Waves provide energy to the wave number 0 in the former case whereas they seem to remove the energy from the hurricane circulation. The former is generally regarded as a low Rossby number phenomenon whereas the latter is clearly one where the Rossby number exceeds one. Although the cloud scales are very small close to wave number 80, the organization of convection makes the available potential energy at wave number 0 and also for the long waves as the primary contribution (Fig. 8.12).

Figure 8.13 is a schematic diagram of the directions of energy transfer for the mature stage of Hurricane Katrina of 2005. It illustrates the difference between the energy exchanges in the inner radii of a hurricane and the exchanges near the area of maximum winds. At the inner radii the sinking of warm air (thermally indirect circulation) leads to a conversion of kinetic to potential energy. The converse is true outside the inner radii. In the inner radii, both the kinetic energy transfer and the potential energy transfer is generally from the scales of the asymmetry and clouds to the azimuthal mean. Again, the converse is true outside of this region.

## Appendix 1: Derivation of Equations in Wave-Number Domain

The classical Lorenz approach separates the motion into zonal mean and eddy, and stationary and transient. Here we shall show an approach developed by Saltzman (1957) for the wave number domain and expanded by Hayashi (1980) for use in the frequency domain.

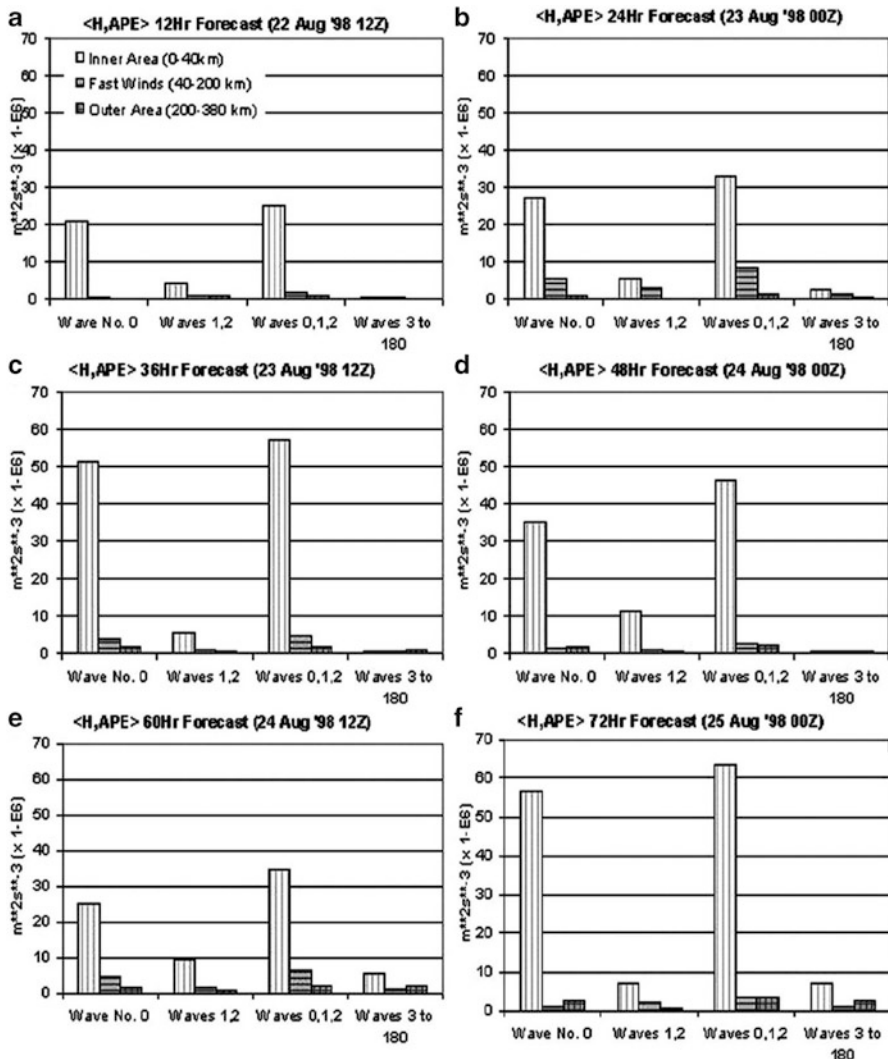


**Fig. 8.11** Generation of available potential energy for Hurricane Bonnie. Three different histograms in each panel represent three regions—inner area (0–40 km), fast winds (40–200 km), and outer area (200–380 km). Forecast times are (a) 12, (b) 24, (c) 36, (d) 48, (e) 60, and (f) 72 h of the model output. Units are  $m^2 s^{-3} (\times 10^{-6})$  (After Krishnamurti et al. 2005)

We shall follow the procedure adopted by Salzman (1957) to derive the equations for the rate of growth of a scale (wavenumber  $n$ ) as it interacts with the zonal mean flow or with any other scales. This requires some preliminaries on Fourier transforms.

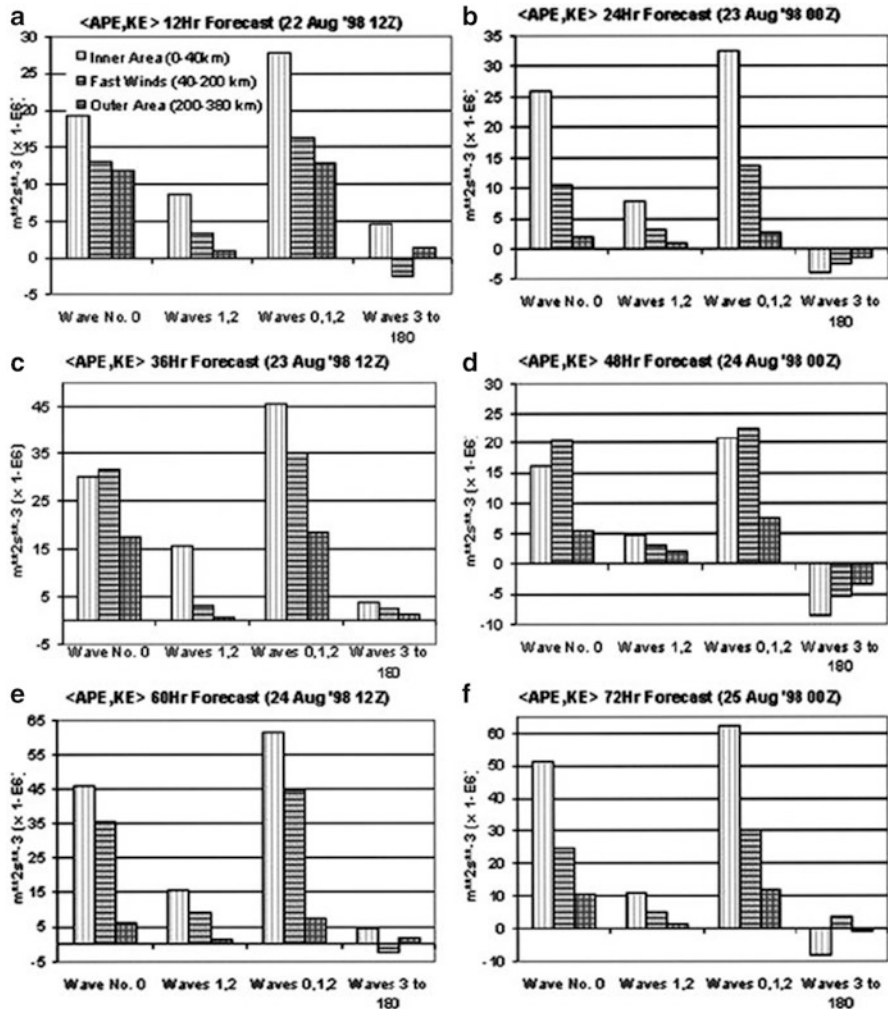
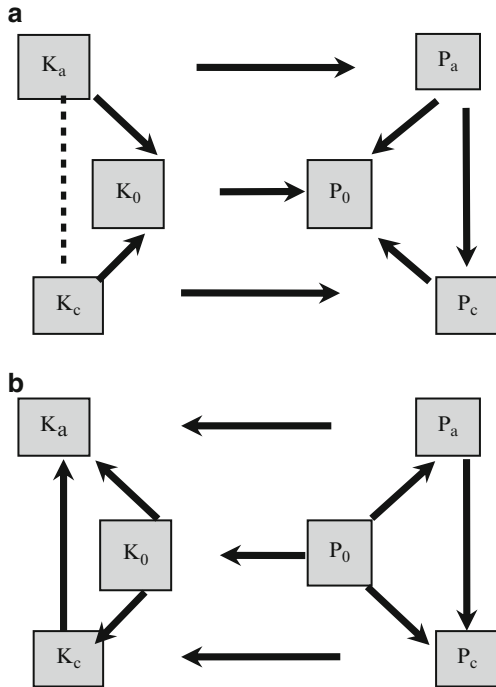


**Fig. 8.12** Generation of kinetic energy by vertical overturning for Hurricane Bonnie. Three different histograms in each panel represent three regions—inner area (0–40 km), fast winds (40–200 km), and outer area (200–380 km). Forecast times are (a) 12, (b) 24, (c) 36, (d) 48, (e) 60, and (f) 72 h of the model output. Units are  $m^2 s^{-3} (\times 10^{-6})$  (After Krishnamurti et al. 2005)

Any smooth variable can be subjected to Fourier transform along a latitude circle:

$$f(\lambda) = \sum_{n=-\infty}^{\infty} F(n) e^{in\lambda}, \quad (8.1)$$

**Fig. 8.13** Schematic diagram of the directions of energy transfer for the mature stage of hurricane Katrina (2005) (a) inwards of the area of maximum winds, and (b) outside of this area



where the complex Fourier coefficients  $F(n)$  are given by

$$F(n) = \frac{1}{2\pi} \int_0^{2\pi} f(\lambda) e^{-in\lambda} d\lambda. \quad (8.2)$$

The Fourier transform of the product of two functions can be expressed as:

$$\frac{1}{2\pi} \int_0^{2\pi} f(\lambda) g(\lambda) e^{-in\lambda} d\lambda = \frac{1}{2\pi} \int_0^{2\pi} \sum_{k=-\infty}^{\infty} F(k) e^{ik\lambda} \sum_{m=-\infty}^{\infty} G(m) e^{im\lambda} e^{-in\lambda} d\lambda. \quad (8.3)$$

From the orthogonality property of the exponents it follows that the only non-zero contribution from this integral arises when  $k + m - n = 0$ , i.e.,  $k = n - m$ . The expression for the Fourier transform of the product of two functions then becomes

$$\frac{1}{2\pi} \int_0^{2\pi} f(\lambda) g(\lambda) e^{-in\lambda} d\lambda = \sum_{m=-\infty}^{\infty} F(n-m) G(m) \quad (8.4)$$

This relationship relating the product of two functions to their Fourier transforms is known as Parseval's Theorem. Since the Fourier coefficients are independent of  $\lambda$ , the Fourier expansion of the derivative of a function with respect to  $\lambda$  is

$$\frac{\partial f(\lambda)}{\partial \lambda} = \sum_{n=-\infty}^{\infty} F(n) \frac{\partial e^{in\lambda}}{\partial \lambda} = \sum_{n=-\infty}^{\infty} i n F(n) e^{in\lambda} \quad (8.5)$$

The derivative of a function with respect to any other independent variable  $\alpha$  is simply

$$\frac{\partial f(\lambda)}{\partial \alpha} = \sum_{n=-\infty}^{\infty} \frac{\partial F(n)}{\partial \alpha} e^{in\lambda} \quad (8.6)$$

Here we will start with the equations of motion, mass continuity, the hydrostatic law and the first law of thermodynamics. Next, we shall perform a Fourier transform of all the above equations. Using these, we shall then derive an eddy kinetic energy equation  $K_n$  for the single zonal harmonic wave  $n$ . We will also derive a similar equation for the available potential energy of a single harmonic  $P_n$ . We will next sort these equations to examine the rates of growth (or decay) of  $K_n$  and  $P_n$  as they interact with other waves or as they interact with the zonal flows and vice versa.

The equations of motion in spherical coordinate system with hydrostatic assumption are:

- The zonal equation of motion:

$$\frac{\partial u}{\partial t} = -\frac{u}{a \cos \varphi} \frac{\partial u}{\partial \lambda} - \frac{v}{a} \frac{\partial u}{\partial \varphi} - \omega \frac{\partial u}{\partial p} + v \left( f + \frac{u \tan \varphi}{a} \right) - \frac{g}{a \cos \varphi} \frac{\partial z}{\partial \lambda} - F_1, \quad (8.7)$$

- The meridional equation of motion:

$$\frac{\partial v}{\partial t} = -\frac{u}{a \cos \varphi} \frac{\partial v}{\partial \lambda} - \frac{v}{a} \frac{\partial v}{\partial \varphi} - \omega \frac{\partial v}{\partial p} - u \left( f + \frac{u \tan \varphi}{a} \right) - \frac{g}{a} \frac{\partial z}{\partial \varphi} - F_2 \quad (8.8)$$

- The continuity equation:

$$\frac{\partial \omega}{\partial p} = - \left( \frac{1}{a \cos \varphi} \frac{\partial u}{\partial \lambda} + \frac{1}{a} \frac{\partial v}{\partial \varphi} - \frac{v \tan \varphi}{a} \right) \quad (8.9)$$

- The hydrostatic equation:

$$\frac{\partial z}{\partial p} = - \frac{RT}{gp} \quad (8.10)$$

- The First law of thermodynamics:

$$\frac{dT}{dt} = \frac{h}{C_p} + \frac{\omega RT}{C_{pp}} \quad (8.11)$$

where  $\lambda$  is the longitude,  $\varphi$  is the latitude,  $p$  is the pressure,  $u$  and  $v$  are the eastward and northward wind components,  $\omega$  is the pressure vertical velocity,  $z$  is the pressure surface height,  $a$  is the earth's radius,  $T$  is the temperature,  $f$  is the Coriolis parameter,  $R$  is the ideal gas constant,  $C_p$  is the specific heat at constant pressure,  $F_1$  and  $F_2$  are the  $u$  and  $v$  components of the frictional force and  $h$  is the heating.

Equations 8.7 through 8.11 form a closed system for the dependent variables ( $u$ ,  $v$ ,  $\omega$ ,  $z$ ,  $T$ ) provided the heating  $h$  is known. Based on this system, in the following section we shall derive the equations for the scale interactions involving the kinetic and potential energy.

Integrating (8.7) through (8.11) from 0 to  $2\pi$ , and using the notation listed in the table below, one can write down the Fourier transforms of these variables:

Variable	$u(\lambda)$	$v(\lambda)$	$\omega(\lambda)$	$z(\lambda)$	$T(\lambda)$
Fourier transform	$U(n)$	$V(n)$	$\Omega(n)$	$Z(n)$	$Y(n)$

We shall next do the Fourier transform of the closed set of Eqs. 8.7 through 8.11 as follows:

- The zonal equation of motion:

$$\begin{aligned} \frac{\partial U(n)}{\partial t} = & - \sum_{m=-\infty}^{\infty} \left[ \frac{im}{a \cos \varphi} U(m) U(n-m) + \frac{1}{a} U_\varphi(m) V(n-m) \right. \\ & \left. + U_p(m) \Omega(n-m) - \frac{\tan \varphi}{a} U(m) V(n-m) \right] \\ & - \frac{ing}{a \cos \varphi} Z(n) + f V(n) - F_1(n) \end{aligned} \quad (8.12)$$

- The meridional equation of motion:

$$\begin{aligned} \frac{\partial V(n)}{\partial t} = & - \sum_{m=-\infty}^{\infty} \left[ \frac{im}{a \cos \varphi} V(m) U(n-m) + \frac{1}{a} V_\varphi(m) V(n-m) \right. \\ & \left. + V_p(m) \Omega(n-m) + \frac{\tan \varphi}{a} U(m) U(n-m) \right] \\ & - \frac{g}{a} Z(n) - f U(n) - F_2(n) \end{aligned} \quad (8.13)$$

– The mass continuity equation:

$$\Omega_p(n) = - \left[ \frac{in}{a \cos \varphi} U(n) + \frac{1}{a} V_\varphi(n) - \frac{\tan \varphi}{a} V(n) \right] \quad (8.14)$$

– The hydrostatic equation

$$Z_p(n) = - \frac{R}{gp} Y(n) \quad (8.15)$$

– The first law of thermodynamics:

$$\begin{aligned} \frac{\partial Y(n)}{\partial t} = & - \sum_{m=-\infty}^{\infty} \left[ \frac{im}{a \cos \varphi} Y(m) U(n-m) + \frac{1}{a} Y_\varphi(m) V(n-m) \right. \\ & \left. + Y_p(m) \Omega(n-m) - \frac{R}{C_p p} Y(m) \Omega(n-m) \right] \\ & - \frac{1}{C_p} H(n) \end{aligned} \quad (8.16)$$

Equations 8.12, 8.13, 8.14, 8.15, and 8.16 form a closed system for the Fourier amplitudes of the dependent variables. The zonally averaged kinetic energy is given by

$$\bar{k} = \frac{1}{2\pi} \int_0^{2\pi} \frac{u^2 + v^2}{2} d\lambda = \frac{U(0)^2 + V(0)^2}{2} + \sum_{n=1}^{\infty} [|U(n)|^2 + |V(n)|^2]. \quad (8.17)$$

The first term on the right hand side is the kinetic energy of the zonal mean. The second term is the sum of the spectral eddy kinetic energy corresponding to all wavenumber  $n$ , given by  $K(n) = |U(n)|^2 + |V(n)|^2$ .

Similarly to (8.12) and (8.13), equations can be written for  $\frac{\partial U(-n)}{\partial t}$  and  $\frac{\partial V(-n)}{\partial t}$ . Multiplying (8.12) with  $U(-n)$  and (8.13) with  $V(-n)$  and the expressions for  $\frac{\partial U(-n)}{\partial t}$  and  $\frac{\partial V(-n)}{\partial t}$  by  $U(n)$  and  $V(n)$  respectively, and adding the resulting equations together, one obtains an equation for the rate of change of the kinetic energy of wave number  $n$ :

$$\begin{aligned}
\frac{\partial K(n)}{\partial t} = & \sum_{\substack{m=-\infty \\ m \neq 0}}^{\infty} \left\{ U(m) \left( \frac{1}{a \cos \varphi} \Psi_{uu_\lambda}(m, n) + \frac{1}{a} \Psi_{vu_\varphi}(m, n) + \Psi_{wu_p}(m, n) - \frac{\tan \varphi}{a} \Psi_{uv}(m, n) \right) \right. \\
& + V(m) \left( \frac{1}{a \cos \varphi} \Psi_{uv_\lambda}(m, n) + \frac{1}{a} \Psi_{vv_\varphi}(m, n) + \Psi_{vw_p}(m, n) + \frac{\tan \varphi}{a} \Psi_{uu}(m, n) \right) \\
& - \frac{1}{a \cos \varphi} \frac{\partial}{\partial \varphi} [\cos \varphi (U(m) \Psi_{vu}(m, n) + V(m) \Psi_{vv}(m, n))] \\
& \left. - \frac{\partial}{\partial p} (U(m) \Psi_{wu}(m, n) + V(m) \Psi_{vw}(m, n)) \right\} \\
& - \left[ \Phi_{uv}(n) \frac{\cos \varphi}{a} \frac{\partial}{\partial \varphi} \left( \frac{U(0)}{\cos \varphi} \right) - \Phi_{vv}(n) \frac{1}{a} \frac{\partial V(0)}{\partial \varphi} + \Phi_{uw}(n) \frac{\partial U(0)}{\partial p} \right. \\
& \left. + \Phi_{vw}(n) \frac{\partial V(0)}{\partial p} - \Phi_{uu}(n) V(0) \frac{\tan \varphi}{a} \right] \\
& - \left[ \frac{1}{a \cos \varphi} \Phi_{uz_\lambda}(n) + \frac{1}{a} \Phi_{vz_\varphi}(n) \right] - [\Phi_{uF_1}(n) + \Phi_{uF_2}(n)]
\end{aligned} \tag{8.18}$$

Where

$$\begin{aligned}
\Psi_{ab}(m, n) &= A(n - m)B(-n) + A(-n - m)B(n), \text{ and} \\
\Phi_{ab}(n) &= A(n)B(-n) + A(-n)B(n),
\end{aligned}$$

where  $a$  and  $b$  are any two dependent variables, and  $A$  and  $B$  are their respective Fourier transforms. Subscripts in (8.19) indicate derivatives, i.e., for example,  $u_\lambda \equiv \frac{\partial u}{\partial \lambda}$ . (8.18) is the equation for the rate of change of kinetic energy  $K(n)$  for a particular wave number  $n$ . On the face of it this looks like a complex mess. However it can be sorted out to make it physically attractive and interpretable.

In a symbolic form Eq. 8.18 can be expressed as

$$\frac{\partial K_n}{\partial t} = <(K_m, K_p) \cdot K_n> + <K_0 \cdot K_n> + <P_n \cdot K_n> + F_n$$

The terms on the right hand side are as follows:

- (i) The first term denotes the transfer of kinetic energy to the scale of  $n$  from pairs of other wave numbers  $m$  and  $p$ . This follows a trigonometric selection rule, i.e.  $n = m + p$  or  $n = |m - p|$  for an exchange; if the three wave numbers  $n$ ,  $m$  and  $p$  do not satisfy the selection rule, the exchanges are zero. This is an important dynamical term in scale interactions since it allows three different scales to interact resulting in gain or loss of energy from one to the other two. This permits ‘out of scale’ energy exchanges.

- (ii) The second term denotes the gain of energy by a wave number  $n$  when it interacts with the zonal flow 0. This is also identified as barotropic energy exchange and can be related to horizontal shear flow instabilities.
- (iii) The third term denotes a growth of kinetic energy  $K_n$  from the eddy available potential energy on the same scale  $P_n$ . This is an in-scale ( $n$ ) energy transfer. This is largely defined by the domain integral of  $-\frac{\Phi_\theta(\omega, T)}{p}$ , i.e. it largely involves the covariance of vertical velocity  $\omega$  and the temperature  $T$  on the scale of  $n$ . If within a domain of interest warm air is rising and relatively colder air is sinking, this covariance would be positive and the net contribution to  $\frac{\partial K_n}{\partial t}$  would be positive, and vice versa.
- (iv) The last term denotes the net gain or loss of kinetic energy  $K_n$  for a scale  $n$  from frictional dissipation.

The eddy available potential energy of a wave number  $n$  is defined as  $P(n) = C_p \gamma |Y(n)|^2$ , where  $\gamma = -\frac{R^2}{C_p p^{R/C_p}} \left( \frac{\partial \theta}{\partial p} \right)^{-1}$ . In a similar manner, we obtain

$$\begin{aligned} \frac{\partial P(n)}{\partial t} &= C_p \gamma \sum_{\substack{m=-\infty \\ m \neq 0}}^{\infty} Y(m) \left( \frac{1}{a \cos \varphi} \Psi_{uT_z}(m, n) + \frac{1}{a} \Psi_{vT_\theta}(m, n) + \Psi_{\omega T_p}(m, n) + \frac{R}{C_p p} \Psi_{\omega T}(m, n) \right) \\ &\quad - \frac{1}{a \cos \varphi} \frac{\partial}{\partial \varphi} \cos \varphi Y(m) \Psi_{vT}(n, m) - \frac{\partial}{\partial p} Y(m) \Psi_{\omega T} \\ &\quad - \left[ \frac{C_p \gamma}{a} \Phi_{Tv}(n) \frac{\partial Y(0)}{\partial \varphi} + \frac{\gamma p^\mu}{\mu} \left\{ \Phi_{T\omega}(n)'' \frac{\partial \bar{\theta}''}{\partial p} \right\} \right] \\ &\quad + \frac{R}{p} \Phi_{T\omega}(n) + \gamma \Phi_{Th}(n) \end{aligned} \tag{8.19}$$

as the expression for the local rate of change of the available potential energy of wave number  $n$  due to non-linear interactions with wave numbers  $m$  and  $n \pm m$ , interactions with the mean flow (wave number zero), and quadratic (in-scale) interactions (wave number  $n$ ).

## Appendix 2: A Simple Example

Let us assume for simplicity that we are given an equation of motion

$$\frac{\partial u}{\partial t} = -\frac{u}{a \cos \varphi} \frac{\partial u}{\partial \lambda} \tag{8.20}$$

The zonal wind  $u(\lambda, t)$  can be expanded into Fourier series, following Eq. 8.1 as

$$u(\lambda) = \sum_{n=-\infty}^{\infty} U(n)e^{in\lambda}, \quad (8.21)$$

where the complex Fourier coefficients  $U(n)$  are given, following (8.2), by

$$U(n) = \frac{1}{2\pi} \int_0^{2\pi} u(\lambda)e^{-in\lambda} d\lambda. \quad (8.22)$$

Also, by the Parseval's theorem (from Eq. 8.3),

$$\frac{1}{2\pi} \int_0^{2\pi} (u(\lambda))^2 e^{-in\lambda} d\lambda = \sum_{m=-\infty}^{\infty} U(n)U(n-m). \quad (8.23)$$

Now if both sides of (8.20) are multiplied by  $1/(2\pi)$  and integrated over a longitude circle, the resulting tendency equation for the  $n$ th complex Fourier coefficient of the zonal wind can be written as

$$\frac{\partial U(n)}{\partial t} = - \sum_{m=-\infty}^{\infty} \frac{i(n-m)}{a \cos \varphi} U(m)U(n-m) \quad (8.24)$$

A similar equation can be written for  $U(-n)$ , i.e.,

$$\frac{\partial U(-n)}{\partial t} = - \sum_{m=-\infty}^{\infty} \frac{i(-n-m)}{a \cos \varphi} U(m)U(-n-m) \quad (8.25)$$

Multiplying (8.25) by  $U(n)$  and (8.24) by  $U(-n)$  and adding the results together, after noting that  $K(n) = |U(n)|^2$  and thus

$$\frac{\partial K(n)}{\partial t} = U(n) \frac{\partial U(-n)}{\partial t} + U(-n) \frac{\partial U(n)}{\partial t}, \quad (8.26)$$

yields the following expression for the rate of change of kinetic energy of the  $n$ th wave number:

$$\begin{aligned} \frac{\partial K(n)}{\partial t} = & - \sum_{m=-\infty}^{\infty} \frac{i}{a \cos \varphi} U(m)[(n-m)U(n-m)U(-n) \\ & + (-n-m)U(-n-m)U(n)] \end{aligned} \quad (8.27)$$

In the case of  $m = 0$ , the right-hand side of (25) becomes

$$-\frac{i}{a \cos \varphi} U(0)[nU(n)U(-n) - nU(-n)U(n)] \equiv 0 \quad (8.28)$$

It can also be easily shown that the contributions of  $m = -n$  and  $m = n$  cancel each other out, so that the final form of (8.25) becomes

$$\begin{aligned} \frac{\partial K(n)}{\partial t} = & - \sum_{\substack{m=-\infty \\ m \neq 0 \\ m \neq \pm n}}^{\infty} \frac{i}{a \cos \varphi} U(m)[(n-m)U(n-m)U(-n) + (-n-m)U(-n-m)U(n)] \end{aligned} \quad (8.29)$$

Since  $m \neq 0$  and  $m \neq \pm n$ , there are no quadratic interactions taking place in this problem. The calculation of the triplet interactions can be illustrated with a simplified example where only waves with wave numbers  $\pm 1$ ,  $\pm 2$  and  $\pm 3$  are considered. For such a case, the kinetic energy of wave number 1 can be expressed, using (8.29), as

$$\begin{aligned} \frac{\partial K(1)}{\partial t} = & - \frac{i}{a \cos \varphi} U(2)[-U(-1)U(-1) - 3U(-3)U(1)] \\ & - \frac{i}{a \cos \varphi} U(-2)[3U(3)U(-1) + U(1)U(1)] \\ & - \frac{i}{a \cos \varphi} U(3)[-2U(-2)U(-1)] \\ & - \frac{i}{a \cos \varphi} U(-3)[2U(2)U(1)] \end{aligned} \quad (8.30)$$

Or, after rearranging,

$$\begin{aligned} \frac{\partial K(1)}{\partial t} = & - \frac{i}{a \cos \varphi} [-U(1)U(2)U(-3) + U(-1)U(-2)U(3) \\ & - U(-1)U(-1)U(2) + U(1)U(1)U(-2)] \end{aligned} \quad (8.31)$$

Each of the complex Fourier coefficients has both a real and an imaginary component, i.e., for any wave number  $n$ ,

$$U(n) = U_R(n) + iU_I(n) \quad (8.32)$$

where subscript R indicates the real component, and subscript I the imaginary one. If we use (8.32) to express all the Fourier coefficients in (8.31) and perform the multiplication, we obtain

$$\begin{aligned} \frac{\partial K(1)}{\partial t} = & -\frac{2}{a \cos \varphi} [U_I(1)U_R(2)U_R(3) + U_R(1)U_I(2)U_R(3) \\ & + U_R(1)U_R(2)U_I(3) - U_I(1)U_I(2)U_I(3) \\ & + U_I(1)U_R(1)U_R(2) + U_R(1)U_I(1)U_R(2) \\ & + U_R(1)U_R(1)U_I(2) - U_I(1)U_I(1)U_I(2)] \end{aligned} \quad (8.33)$$

## References

- Hayashi, Y.: Estimation of non-linear energy transfer spectra by the cross-spectral method. *J. Atmos. Sci.* **37**, 299–307 (1980)
- Kanamitsu, M., Krishnamurti, T.N., Depardine, C.: On scale interactions in the tropics during northern summer. *J. Atmos. Sci.* **29**, 698–706 (1972)
- Krishnamurti, T.N.: Compendium of Meteorology for Use by Class I and Class II Meteorological Personnel. Volume II, Part 4-Tropical Meteorology. WMO, vol. 364. World Meteorological Organization, Geneva (1979)
- Krishnamurti, T.N., Kanamitsu, M., Godbole, R.V., Chang, C.B., Carr, F., Chow, I.H.: Study of a monsoon depression. I. Synoptic structure. *J. Meteor. Soc. Japan* **53**, 227–239 (1975b)
- Krishnamurti, T.N., Chakraborty, D.R., Cubukcu, N., Stefanova, L., Vijaya Kumar, T.S.V.: A mechanism of the Madden-Julian Oscillation based on interactions in the frequency domain. *Q. J. Roy. Meteorol. Soc.* **129**, 2559–2590 (2003)
- Krishnamurti, T.N., Pattnaik, S., Stefanova, L., Vijaya Kumar, T.S.V., Mackey, B.P., O’Shay, A.J., Pasch, R.J.: The hurricane intensity issue. *Mon. Weather Rev.* **133**, 1886–1912 (2005)
- Moncrieff, M.W.: Analytic representation of the large-scale organization of tropical convection. *J. Atmos. Sci.* **61**, 1521–1538 (2004)
- Saltzman, B.: Equations governing the energetics of the larger scales of atmospheric turbulence in the domain of the wave number. *J. Meteorol.* **14**, 513–523 (1957)
- Sheng, J., Hayashi, Y.: Observed and simulated energy cycles in the frequency domain. *J. Atmos. Sci.* **47**, 1243–1254 (1990a)
- Sheng, J., Hayashi, Y.: Estimation of atmospheric energetics in the frequency domain in the FGGE year. *J. Atmos. Sci.* **47**, 1255–1268 (1990b)

# **Chapter 9**

## **El Niño and Southern Oscillation**

### **9.1 Introduction**

The Southern Oscillation is a sea level pressure oscillation over the equatorial latitudes between the Eastern Pacific and the Indian Ocean. El Niño is a phenomenon that is characterized by the occurrence of warmer than normal sea surface temperatures over the Central and Eastern Equatorial Pacific Ocean. These two phenomena are intimately interwoven, so much so that they are usually considered together, under the name of ENSO, or El Niño-Southern Oscillation. The Southern Oscillation has a time scale of roughly 4–6 years. Within that period warm SST anomalies over the Central and Eastern Pacific Ocean (El Niño) are followed by cold SST anomalies (La Niña). This chapter is devoted to the observational, theoretical and modeling aspects of ENSO.

### **9.2 Observational Aspects**

The Southern Oscillation is a phenomenon manifesting as a seesaw pattern in the sea level pressure between the Indian Ocean (Darwin, in northern Australia) and the Eastern Pacific Ocean (Tahiti, in French Polynesia). This oscillation has a time scale of roughly 4–6 years and amplitude on the order of a few millibars. It bears the name of the Southern Oscillation due to the fact that its largest amplitudes are found in the Southern Hemisphere, between the Equator and 5°S. The long-term annual mean climatology is such that at the equatorial latitudes the sea level pressure on the Eastern Pacific side is higher than that on the Indian Ocean side. The Southern Oscillation can be regarded as a superimposed pressure oscillation on top of this long-term annual mean. The geographic extent of the oscillation is best seen from a well-known illustration from Trenberth and Shea (1987) that shows the point correlations of annual mean sea level pressure of all points around the globe with the annual mean sea level pressure at a reference point in the Indian Ocean taken as

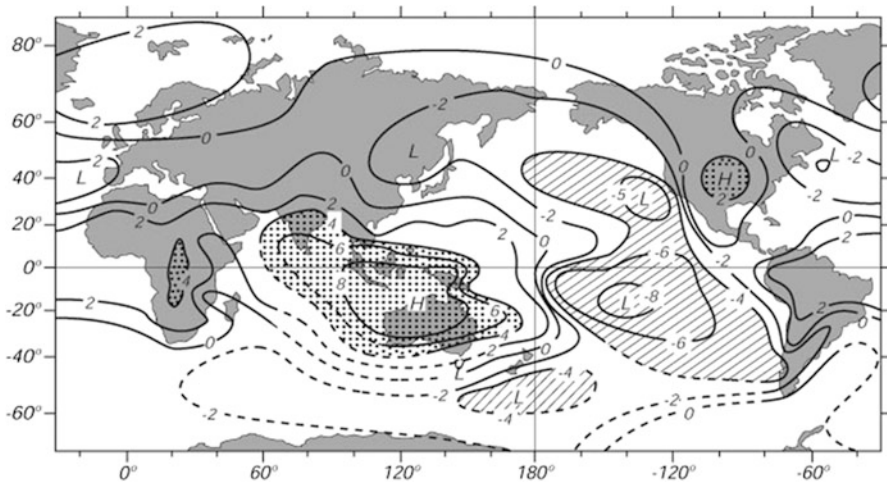


**Fig. 9.1** Correlation ( $\times 10$ ) of the annual mean sea level pressure with the annual mean sea level pressure at Darwin (From Trenberth and Shea 1987)

Darwin, Australia (Fig. 9.1). These point correlations are high in the vicinity of Darwin, with a maximum value of 100 % at Darwin itself (since the correlation of a time series with itself is, naturally, perfect). As one moves away from Darwin, the correlations decrease, and at some point go to zero. As one increases the distance from Darwin and nears Tahiti, the correlations become strongly negative, reaching a value of about negative 80 % at Tahiti. It is these two locations, Darwin and Tahiti, that are the principal dipole centers of the Southern Oscillation. The large negative correlation indicates that the time series of annual mean sea level pressure at these two sites are almost perfectly out of phase.

The difference in sea level pressure anomalies between Darwin and Tahiti is used to define a standardized index called the Southern Oscillation Index (SOI). The SOI is positive when the sea level pressure is above normal at Tahiti and below normal at Darwin. In the reverse situation, the SOI is negative. It has been established that persistent negative SOI tends to relate to above normal sea surface temperatures in the Eastern Tropical Pacific, a condition indicative of El Niño. Conversely, persistent positive SOI relates to below normal Eastern Tropical Pacific sea surface temperatures that are indicative of La Niña.

El Niño is a phenomenon characterized by persistent (for three or more months) above normal sea surface temperatures over the Central and Eastern Equatorial Pacific. Its counterpart, La Niña, is characterized by persistent below normal sea surface temperatures in the same region. As an El Niño occurs, the warm ocean temperatures of the equatorial latitudes support intensified ITCZ convection with a large longitudinal extent of nearly 2,000 km. The deep convection drives a divergent circulation all around the belt it occupies. This divergent circulation can be broken down into a zonal and a meridional component. Figure 9.2 shows two typical winter season schematics of the zonal part of the divergent circulations – one for an El Niño

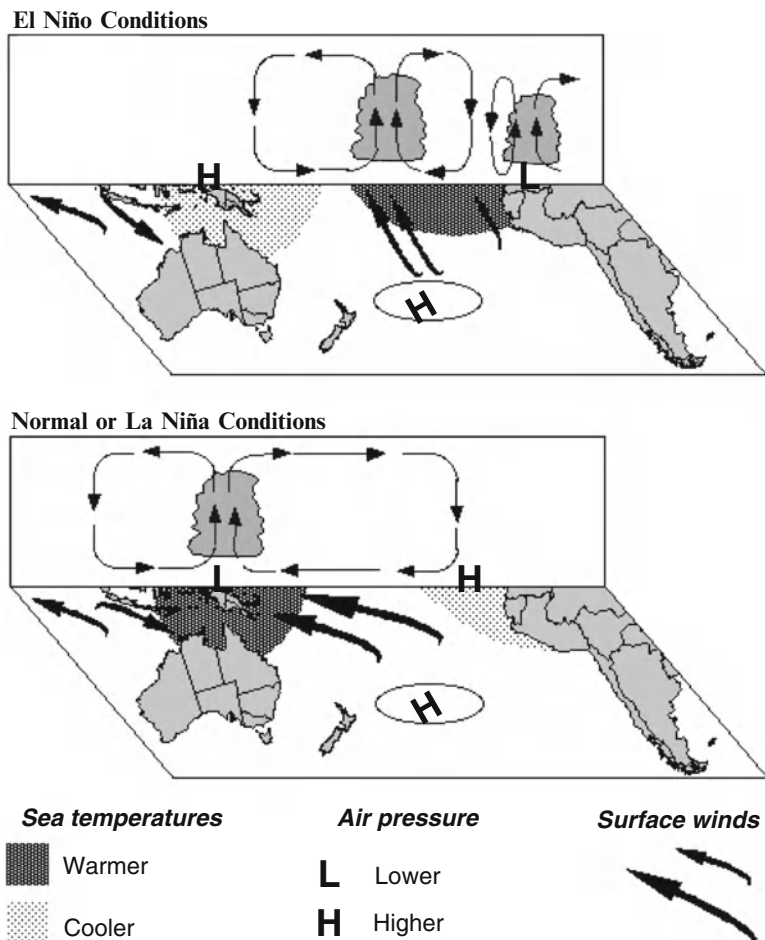


**Fig. 9.2** Schematic of the atmospheric circulation during El Niño (*top*) and normal or La Niña (*bottom*) conditions (Adapted from Partridge 1994)

year and one for a neutral year. This illustration shows that the divergent circulation anomaly during an El Niño year carries prominent rising motion over the warm waters of the Central Pacific Ocean. In normal years this feature is located further west and is part of the winter monsoon circulation of the Indonesian region. This vertical circulation of the normal years is called the Walker circulation. It is an east–west vertical divergent circulation gyre that ascends near Indonesia and descends over the Eastern Pacific Ocean. The seasonally averaged divergent zonal winds have magnitude on the order of a few meters per second, while the vertical motions are on the order of a few centimeters per second. The occurrence of El Niño causes a disruption of the normal divergent circulation and shifts the locations of both the ascending and descending lobes. The location of the descending lobes of the

divergent circulation is of particular climatic interest, since the descent is associated with suppressed convection and, consequently, inhibited precipitation. One of the regions most regularly affected by this is eastern Australia, where the majority of El Niño events result in dryness and lack of rains. Other regions that can be affected, although with less regularity, by the El Niño-related position shift of the descending lobes include East Africa, the Indian Monsoon area, China, Malaysia and the Philippines. To what degree a particular El Niño episode affects any of the above regions depends on a number of contributing factors – such as the prevailing large-scale zonal winds and the thermal stratification over the tropics and extratropics – that help determine the positioning of the descending lobes.

## 9.3 The ENSO Scenario

The following are elements of an ENSO scenario that are based on the observational chronology of events during its life cycle:

### 9.3.1 *Arrival of a Sea Level Pressure Anomaly at the Near-Equatorial Latitudes*

Nearly 80 years of sea level pressure data are currently available over the global belt. Although the coverage of sea level pressure measurements has varied over these years, the data is still useful for many research purposes. If one takes a long-term mean of the sea level pressure, taking all the years of daily data, one finds that in the mean, over the equatorial latitudes the pressure is higher over the Eastern Pacific compared to the Western Pacific Ocean. Superimposed on that long-term mean are sea level pressure anomalies on many different time scales. On the time scale of ENSO (i.e. 4–6 year period) there exist pressure anomalies with amplitudes on the order of a few millibars. These anomalies strengthen and weaken the east–west pressure differential of the long-term mean. Such modulation of the east–west pressure differential impacts the strength of the trade winds of the Pacific Ocean. The trades of the Northern and Southern Pacific Ocean are modulated on the time scale of ENSO. The modulation of the east–west differential of the equatorial pressure field is related to the systematic arrival of sea level pressure anomalies from higher latitudes to the equatorial latitudes. An arrival of a high-pressure anomaly over the Western Pacific and a lower-pressure anomaly to the Eastern Pacific can result in a weakening of the trades and vice versa during the amplification of the trades. Figures 9.3a, b illustrates two examples of such pressure anomalies that weaken the east–west pressure gradient resulting in weaker trades as the El Niño for the years 1961–62 and 1971–72 were first noted to occur. These anomaly charts are shown at intervals of every 6 months. El Niño refers to a warming of sea surface

temperatures over the Eastern and Central Equatorial Pacific Ocean that is described more fully in the following subsections. As we proceed further in time these anomalies propagate away from the equator with a reversal of the anomaly pressure gradient in the east–west direction and a strengthening of the trades as an El Niño event completes its cycle.

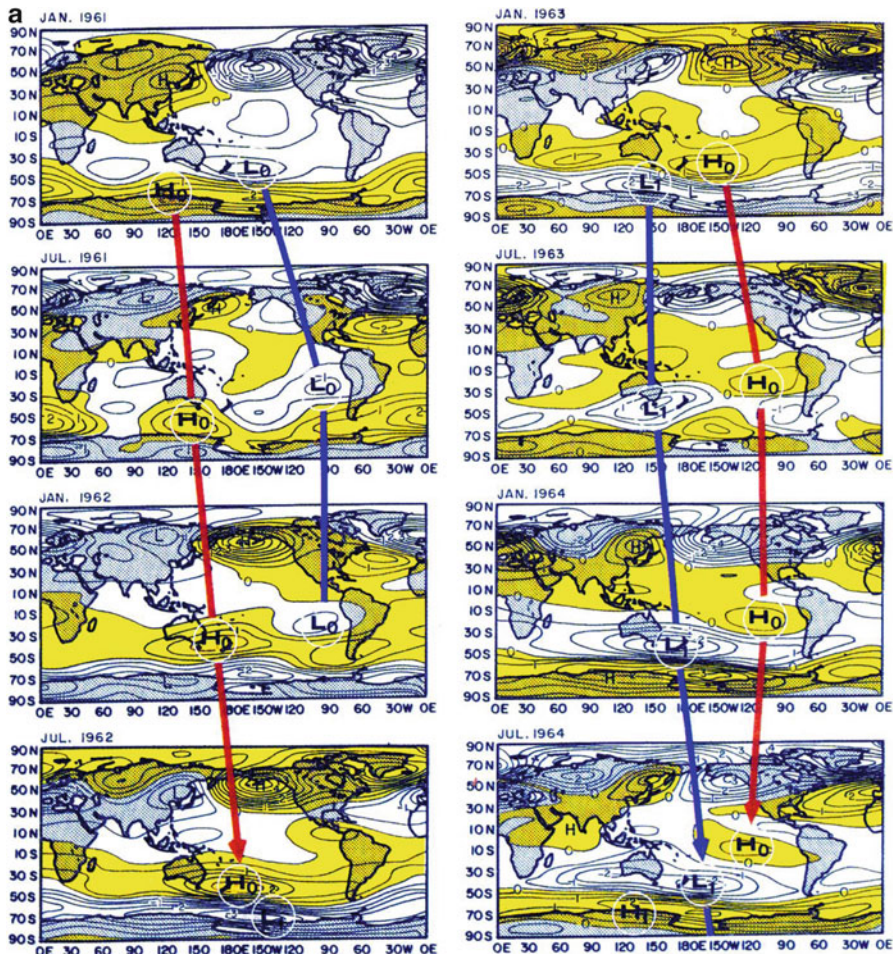


**Fig. 9.3** (a) Time filtered sea level pressure at 30–50 month time scale from January 1961 through July 1964 at intervals of 6 months. Zonal wave numbers 0, 1, 2, and 3 are included in the analysis. The contour interval is 0.5 hPa. The shaded region denotes positive pressure anomalies (Adapted from Krishnamurti et al. 1986). (b) Same as Fig. 9.3a but for the years 1969 through 1972

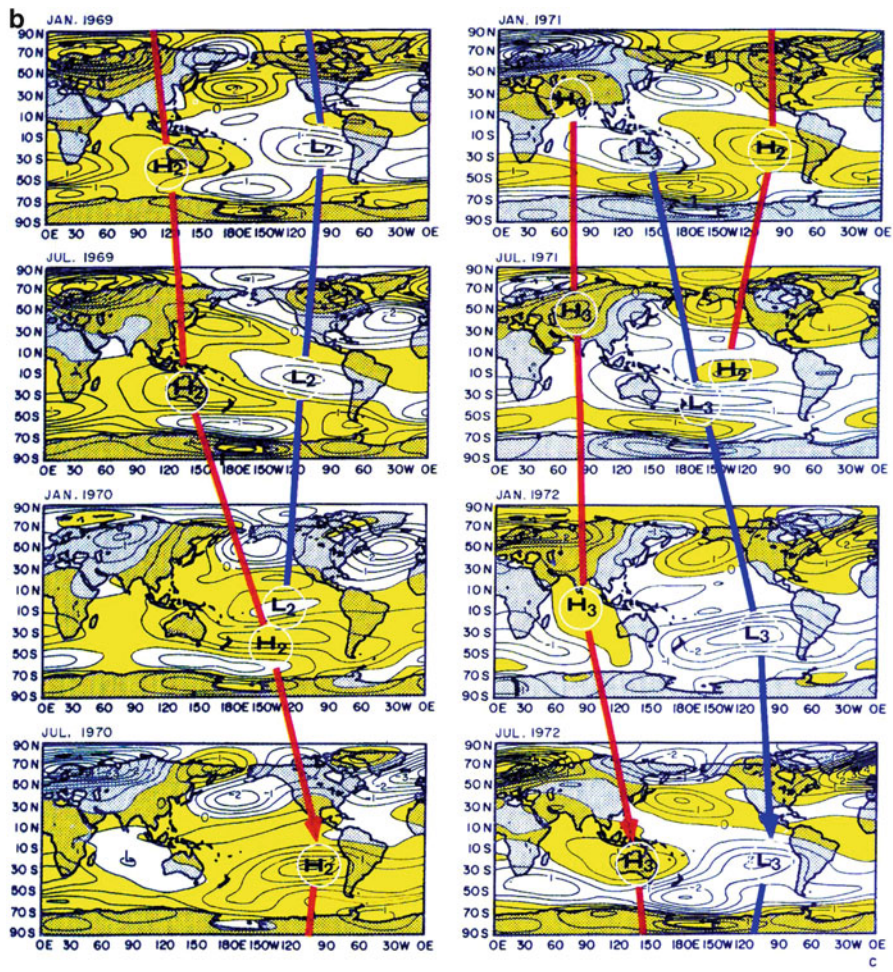
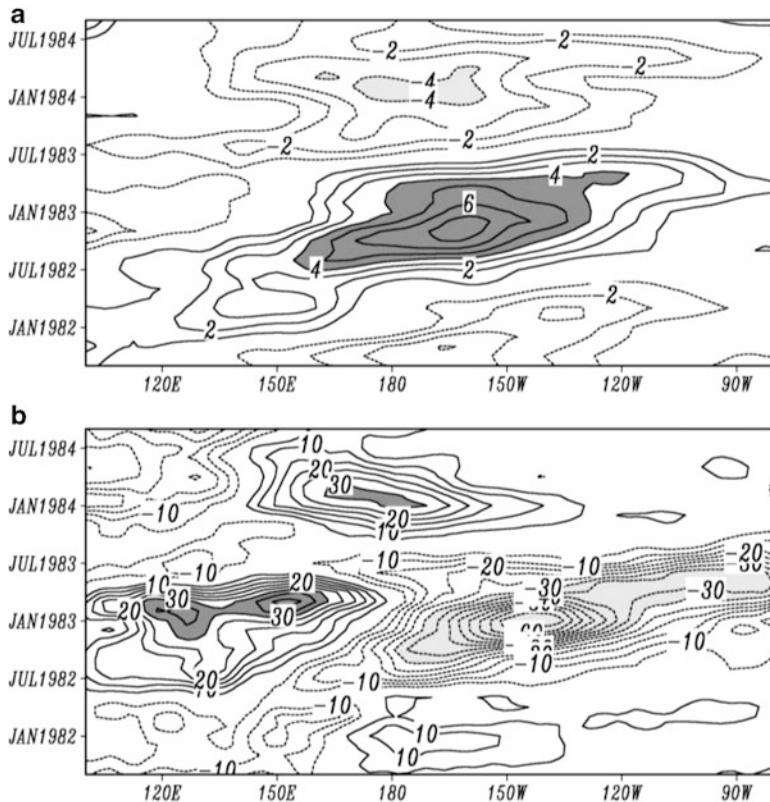


Fig. 9.3 (continued)

### 9.3.2 Trade Winds

The amplification and weakening of the trades on the time scale of ENSO are illustrated in Fig. 9.4a. This shows the zonal winds for the near equatorial belt 5S–5N. This is a time-longitude (Hovmöller) diagram that shows the strong trades followed by weaker trades and again the establishment of stronger trades. The total strength of the trades is of the order of  $10 \text{ ms}^{-1}$ . The modulation of the trades on the time scales of ENSO is on the order of  $2\text{--}3 \text{ ms}^{-1}$ . An interesting aspect of this Hovmöller diagram is the latitude and time of start of the weakening of the trades. Several months prior to the weakening of the trades over the Pacific Ocean it is already noted to occur over the Indian Ocean. That is related to an earlier weakening of the zonal pressure gradient over the Indian Ocean. The SLP anomalies seem to arrive over



**Fig. 9.4** (a) Time-longitude cross-sections of (a) 850 mb zonal wind anomalies ( $\text{ms}^{-1}$ ), and (b) OLR anomalies ( $\text{Wm}^{-2}$ ), averaged between  $5^{\circ}\text{S}$  and  $5^{\circ}\text{N}$  for the Pacific

the Indian Ocean, weakening the zonal pressure gradient well prior to that over the Pacific Ocean. In this instance a high pressure anomaly arrives over the Equatorial Indian Ocean side and a lower pressure anomaly arrives over the Equatorial Eastern Pacific.

### 9.3.3 Piling of Water Over the Western Pacific Ocean

The strong trade phase of ENSO lowers the mean sea level over the Eastern shores of the Pacific Ocean and the converse is seen over the Western Pacific Ocean. These are features that are seen regularly. The observational tools for monitoring the sea level over the global oceans come from satellites such as the TOPEX/Poseidon and its successor Jason-1. These are satellites that carry onboard radar altimeters and a global positioning system (GPS) that can be used to estimate the sea level anomalies (with respect to a long-term mean) with accuracy within several millimeters. Such satellite altimeter measurements have been available since 1992 as 10-day averages.

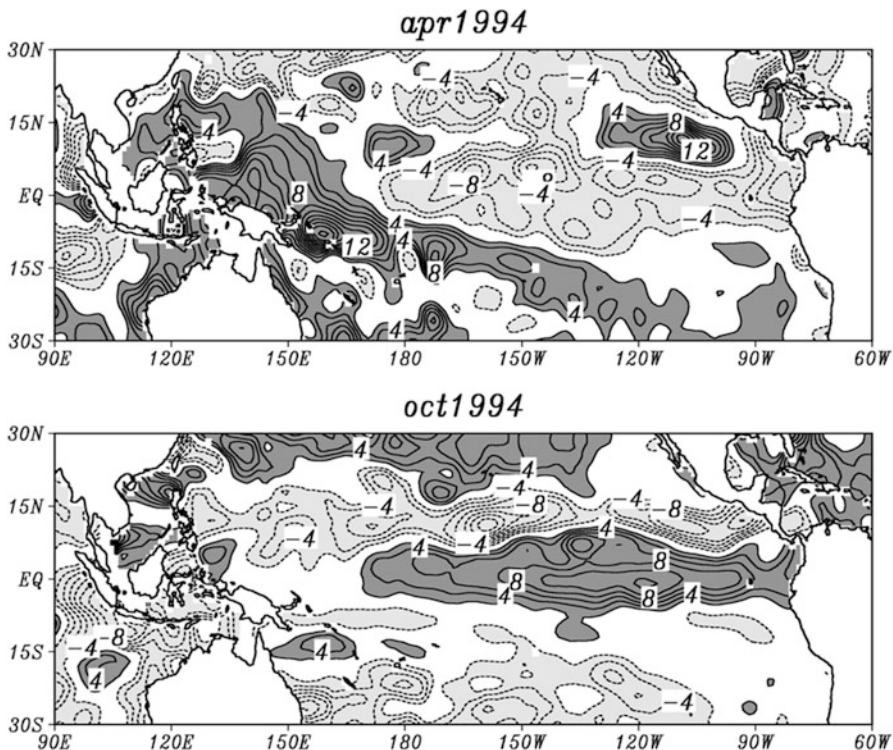


**Fig. 9.5** Ocean surface height anomalies for April 1994 (top) and October 1994 (bottom)

Figure 9.5 shows the ocean surface topography from the TOPEX/Poseidon data set before and during an El Niño episode. During normal conditions (Fig. 4.3a), the Eastern Tropical Pacific displays below average ocean surface heights, while the Western Tropical Pacific displays above average ocean surface heights. During an El Niño episode (Fig. 4.3b), the gradient of ocean surface anomalies reverses sign, with the Eastern Tropical Pacific Ocean surface height anomaly becoming positive.

### 9.3.4 Thermocline Transitions

The oceanic transitions occurring between a normal, La Niña, and El Niño years are schematically illustrated in Fig. 9.6. The mean climatological water level, indicated by the sloping solid line, is the average ocean surface level for all years, and does not vary between normal and ENSO years. Also shown are the water level and thermocline (a line that separates a body of warmer surface water from the cold bottom water) depth for a normal (top), La Niña (middle) and El Niño (bottom) year.

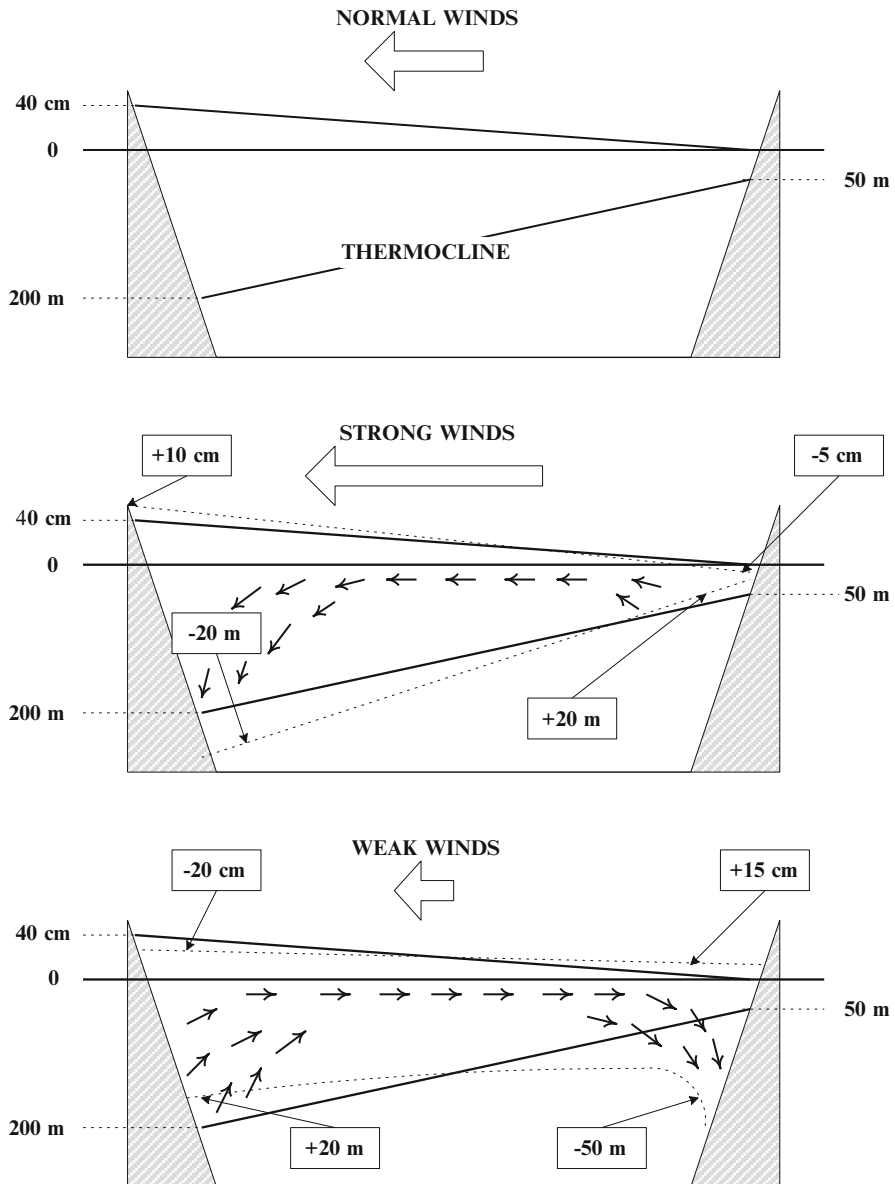


**Fig. 9.6** A schematic of the surface trades and the ocean surface and thermocline response for a normal (top), La Niña (middle), and El Niño (bottom) years

The true water level, shown by a dashed line, varies with the phases of ENSO. During normal non-ENSO conditions prior to the onset of El Niño, stronger trades prevail and pile the water over the western ocean, and reducing the ocean surface level over the East Pacific. As a result, the normal ocean surface in the western part

of the domain is higher than that in the Eastern Pacific Ocean. During El Niño, the weakening of the trades leads to the reduction of this effect. As a result, the anomalies of the ocean surface height show positive values over the Eastern Pacific, and negative values over the Western Pacific.

The thermocline also responds to these changes. The normal thermocline rises over the western oceans during El Niño years by about 20 m and depresses over the eastern oceans by about 50 m. These changes are related to the anomalous circulation gyres over the upper oceans. On a longitude-height cross-section over the western portion of the Pacific Ocean this anomalous circulation is counter-clockwise during normal years but becomes clockwise during El Niño years. A consequence of the clockwise gyre is a downwelling of water over the eastern oceans where the net upwelling is reduced by the anomalous flow. A direct result of such reduction of upwelling is the relative lack of cooling of surface waters that prevails over the eastern ocean. That diminishment of cooling is viewed as the occurrence of warm ocean temperature anomaly that is the El Niño phase.

### ***9.3.5 Typical SST Anomalies, Normal and El Niño Years***

A sequence of SST anomaly (SSTA) charts at intervals of 6 months covers the life cycle of the El Niño event of 1987 (Fig. 9.7). Illustrated here is the period June 1986 through December 1989. These are based on Reynolds and Smith (1994) data sets. The dark shading illustrates the warm SSTA regions and the light shading has cold SSTA anomalies. The anomalies are with respect to long term average (for the respective month).

In June 1986 the Eastern Pacific is characterized by cold SSTA with amplitude of the order of  $-0.5$  to the  $-1.0^{\circ}\text{C}$ . By December 1986 this region already sees a warming which becomes most intense by June 1987. The warming persists throughout 1987 and is reversed by June 1988. Thereafter a cold phase persists over the Eastern Pacific Ocean. The amplitude of the cold anomaly is most intense ( $-2.5^{\circ}\text{C}$ ) in December 1988 (a La Niña year). Thereafter the cold anomaly decreases to values between  $-0.5^{\circ}\text{C}$  and  $-1.0^{\circ}\text{C}$ . An interesting feature is a cold cap (a horse shoe pattern) around the warm SSTA of El Niño events. This can be seen particularly well in the December 1987 patterns. The warm anomalies are encircled to the northwest and the southwest by cold anomalies whose amplitudes are of the order of  $-0.5^{\circ}\text{C}$ . A converse feature is also noted during the La Niña phase (see December 1988), where a warm cap encircles the cold SSTA in somewhat similar manner.

It should be noted that there are many inter-El Niño differences from one El Niño event to the next. Some events have SSTA warm anomalies with amplitudes as large as  $4\text{--}5^{\circ}\text{C}$  and others are very mild. The meridional width (or spread) of warm SSTA over the Eastern Pacific Ocean can be very large for some events, such as during December 1987, whereas there are other events where the feature is narrower. The same is true of the cold phase SSTA of the La Niña events.

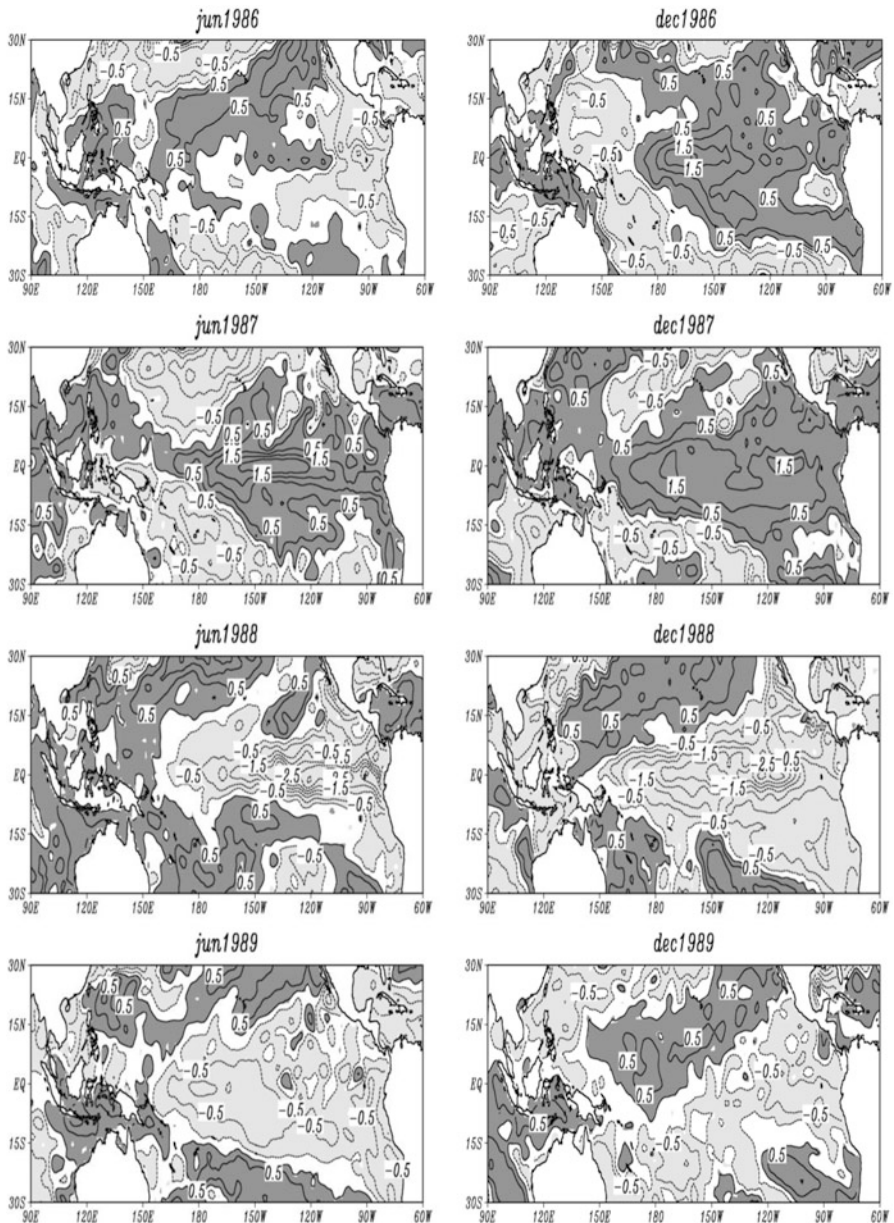


**Fig. 9.7** Sequence of SST anomalies ( $^{\circ}$ K) from June 1986 to December 1989 in 6-month intervals

A very narrow extent of cold SSTA near the equatorial belt over the Eastern Pacific in a cold phase can have a cap of warm water enclosing it rather close to the equator. In such cases the weather impacts of the cold phase can be quite similar to those of a warm phase.

### ***9.3.6 The Pacific North American Pattern (PNA)***

The Pacific North American Pattern, or PNA, is a grand teleconnection wave train that is the result of an external stationary Rossby wave. It emanates from the region of the oceanic warm SSTA during El Niño years, makes roughly a great circle route starting from the Equatorial Central Pacific and terminates over the Southeastern United States. Along this pathway of the great circle route, alternating high and low pressure systems constitute this stationary wave train. This is an upper tropospheric feature with largest amplitude between 200 and 300 mb levels. When the warm SSTA are established in the Eastern Pacific, the equatorial region is characterized by deep convection. Above the region in the upper troposphere we find two high pressure areas straddling the equator near  $5^{\circ}\text{S}$  and  $5^{\circ}\text{N}$ . The near-equatorial convection cannot sustain an anticyclonic circulation over the equatorial latitudes because of the vanishing Coriolis force. As a result, the upper highs tend to get established just north (clockwise flows) and south (counterclockwise flows) of the equator. These highs extend between  $+/-5^{\circ}$  and  $+/-10^{\circ}$  degree latitudes. They initiate a wave train that is illustrated in Fig. 9.8. Illustrated here are the 200 mb geopotential height anomalies for January 1983, an El Niño year. These are alternating high and low pressure areas. The low adjacent to the near-equatorial upper level high is found over the subtropical Eastern Pacific Ocean. This is followed by a high that is located over the Northwestern United States. Downstream from that resides an upper low over the Southeastern United States.

It is possible to model this wave train using a simple shallow water model on a beta plane where the potential vorticity is conserved. A heat source related to the convective heating over the equatorial warm SSTA can be mimicked in a shallow water system via the prescription of a diabatic mass flux in the mass continuity equation. Using an initial basic flow that is a seasonal zonal average, the model simulates a PNA pattern. The PNA is often called an external Rossby wave, since the heat source that generates it resides in the equatorial belt, outside of the tropics.

### ***9.3.7 A River of Westerlies That Nearly Encircles the Globe Emanating from the El Niño Region***

This is a well-known upper tropospheric feature of the El Niño. The region between the first upper tropospheric high and the next low of the PNA over the Eastern Pacific Ocean is characterized by upper tropospheric westerlies. Those westerlies cross the Eastern Pacific, Mexico, West Africa, the Arabian Sea, India, and on to the tropical Pacific Ocean. An example of this belt of westerlies is illustrated in Fig. 9.9. These westerly wind anomalies are a major disruptor of tropical organized convection. They weaken the easterly jet over West Africa and weaken the amplitude and precipitation of African waves. As these westerlies traverse over India they weaken the monsoon lows and monsoon depression that normally produce heavy rains.

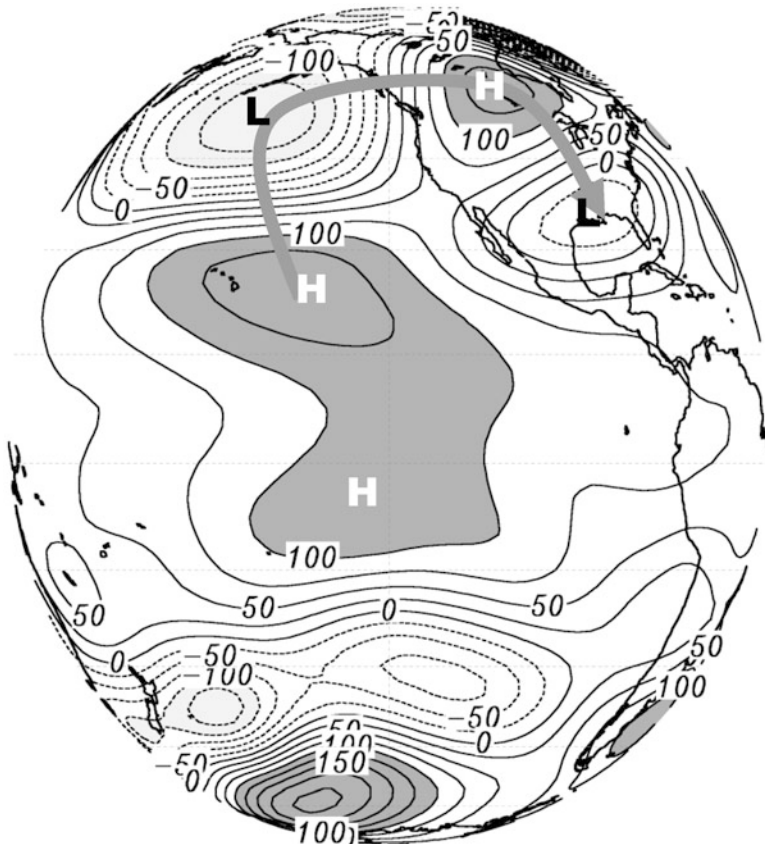


**Fig. 9.8** 200 mb geopotential height anomalies for January 1983 illustrating the PNA pattern

Although this pattern is first seen at the time of onset of the El Niño (mostly at the start of a winter season) the anomalous westerlies last for almost 6–9 months, impacting the climate of the following summer seasons. These anomalous westerlies of the upper troposphere can also impact the hurricanes and typhoons of the Atlantic and Pacific oceans. The role of increased vertical wind shear has generally been one that diminishes organized convection and rain.

## 9.4 Coupled Modeling of ENSO

We shall next discuss a simple coupled model of ENSO that consists of two parts – an atmospheric component, based on a model developed by Adrian Gill (1980) which is described in Chap. 4 of this textbook, and an ocean component based on a model developed by Zebiak and Cane (1987).

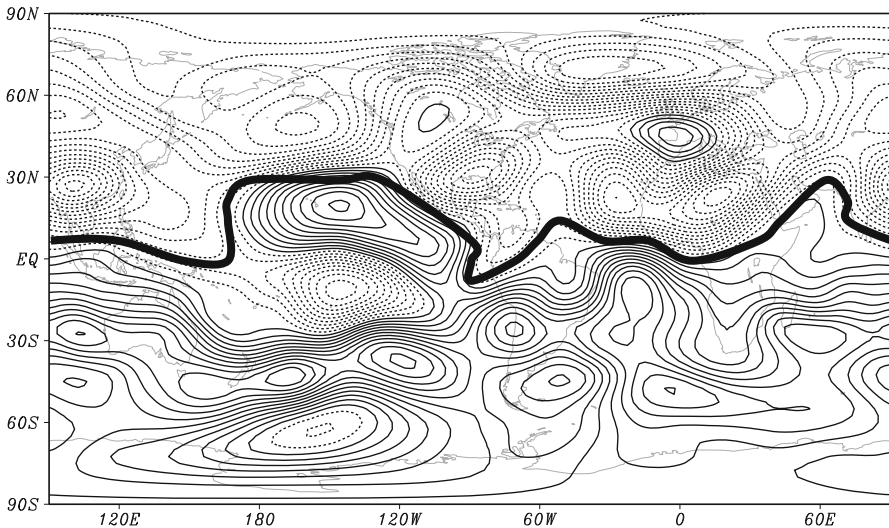


**Fig. 9.9** 200 mb stream function during an El Niño event, January 1983. The river of strong westerlies, originating near the date line north of the anticyclone centered near 15N, is shown by a bold line

#### 9.4.1 Zebiak-Cane Ocean Model

Zebiak and Cane (1987) proposed a simple model for the response of the ocean upwelling and sea surface temperatures to the surface wind stress, which can be used as a tool for understanding the mechanism of El Niño. They considered a 1<sup>1</sup>/2-layer ocean model, which is equivalent to a 2-layer model whose lower layer has a fixed depth. The ocean currents are modeled using a linearized version of the dynamical equations. In the thermodynamical equation, which is used for modeling the temperature, the non-linear terms are retained.

Let  $\vec{u}_1$  and  $\vec{u}_2$  denote the upper and lower layer ocean current vectors,  $H_1$  and  $H_2$  – the upper and lower layer mean depths,  $p_1$  and  $p_2$  – the mean dynamic pressures in the upper and lower layer,  $\vec{\tau}$  – the surface wind stress,  $h$  – the upper layer depth anomaly, and  $w_s$  – the rate of entrainment of lower-layer water into the surface layers. The equations of motion for the two layers and the mass continuity equation are expressed by the linearized shallow water equations on a beta plane. The momentum equation for the ocean current in the upper layer is given by

$$\frac{\partial \vec{u}_1}{\partial t} + f \vec{k} \times \vec{u}_1 = -\nabla p_1 + \frac{\vec{\tau}}{\rho H_1} - \frac{K(\vec{u}_1 - \vec{u}_2)}{H_1} - r \vec{u}_1. \quad (9.1)$$

Here  $r$  and  $K$  are frictional parameters:  $-\frac{K(\vec{u}_1 - \vec{u}_2)}{H_1}$  represents the vertical diffusion and  $-r \vec{u}_1$  represents the Rayleigh friction. This equation expresses the

balance between the local change of the current plus the Coriolis force on one side, with the sum of the pressure gradient force, the wind stress term, the vertical diffusion, and Rayleigh friction on the other side. An analogous equation for the second layer can be written in the form:

$$\frac{\partial \vec{\mathbf{u}}_2}{\partial t} + f \vec{\mathbf{k}} \times \vec{\mathbf{u}}_2 = -\nabla p_2 + \frac{K(\vec{\mathbf{u}}_1 - \vec{\mathbf{u}}_2)}{H_2} - r \vec{\mathbf{u}}_2 \quad (9.2)$$

The bottom layer does not experience the direct effect of the surface wind stress  $\vec{\tau}$ , hence there is no wind stress term here. The mass continuity equation is expressed by

$$\frac{\partial h}{\partial t} + H_2 \nabla \cdot \vec{\mathbf{u}}_2 = -w_s - rh, \quad (9.3)$$

This equation carries a local change of the free surface height plus divergence of the lower layer on the left hand side, and the sum of the rate of entrainment from the lower to the upper layer and the Rayleigh friction term  $-rh$  on the right side. The entraining vertical velocity at the surface layer is expressed by the relation.

$$w_s = H_1 \nabla \cdot \vec{\mathbf{u}}_1 \quad (9.4)$$

The above four equations carry the variables  $\vec{\mathbf{u}}_1$ ,  $\vec{\mathbf{u}}_2$ ,  $p_1$ ,  $p_2$ ,  $h$ , and  $w_s$  (note that the first two are vector equations). Some simplifications are invoked to close this system. If a shearing vector  $\vec{\mathbf{u}}_s$  is defined as  $\vec{\mathbf{u}}_s = \vec{\mathbf{u}}_1 - \vec{\mathbf{u}}_2$ , by subtracting (9.2) from (9.1), one can obtain an equation for the shearing vector:

$$\frac{\partial \vec{\mathbf{u}}_s}{\partial t} + f \vec{\mathbf{k}} \times \vec{\mathbf{u}}_s = -\nabla(p_1 - p_2) + \frac{\vec{\tau}}{\rho H_1} - r_s \vec{\mathbf{u}}_s. \quad (9.5)$$

Zebiak and Cane simplify this equation by dropping the local change and the pressure gradient force to obtain a balance among the friction, the Coriolis force, and the wind stress, i.e.,

$$r_s \vec{\mathbf{u}}_s + f \vec{\mathbf{k}} \times \vec{\mathbf{u}}_s = \frac{\vec{\tau}}{\rho H_1} \quad (9.6)$$

Given the wind stress  $\vec{\tau}$  from an atmospheric model, such as that from the Adrian Gill model described in the previous section, one can derive the shearing current  $\vec{\mathbf{u}}_s$ . The zonal and meridional components of the shearing current  $\vec{\mathbf{u}}_s$  are given by

$$r_s u_s - f v_s = \frac{\tau_x}{\rho H_1} \quad (9.7)$$

$$r_s v_s + f u_s = \frac{\tau_y}{\rho H_1} \quad (9.8)$$

Eliminating first  $v_s$  and then  $u_s$  between these two equations one obtains

$$u_s = \frac{1}{r^2 + f^2} \frac{r\tau_x + f\tau_y}{\rho H_1} \quad (9.9)$$

$$v_s = \frac{1}{r^2 + f^2} \frac{-f\tau_x + r\tau_y}{\rho H_1} \quad (9.10)$$

Since near the equator  $f$  is small,  $\frac{1}{r^2 + f^2} \approx \frac{1}{r^2}$ . Assuming the equatorial flow is almost zonal, the meridional wind stress can be neglected, i.e.  $\tau_y \approx 0$ . With these approximations, (59) and (60) become

$$u_s = \frac{\tau_x}{r\rho H_1} \quad (9.11)$$

$$v_s = \frac{-f\tau_x}{r^2\rho H_1} \quad (9.12)$$

If the lower layer is assumed to be nearly-geostrophic, i.e., have zero divergence, the entrainment velocity  $w_s$  can be approximated as

$$w_s \approx H_1 \nabla \cdot \vec{\mathbf{u}}_s \quad (9.13)$$

Substituting the expressions for  $u_s$  and  $v_s$  into the equation for the entrainment velocity, one obtains

$$w_s = H_1 \left( \frac{\partial u_s}{\partial x} + \frac{\partial v_s}{\partial y} \right) = \frac{1}{r\rho} \frac{\partial \tau_x}{\partial x} - \frac{1}{r^2\rho} \left( \frac{\partial f}{\partial y} \tau_x + f \frac{\partial \tau_x}{\partial y} \right). \quad (9.14)$$

Since  $\frac{\partial \tau_x}{\partial x} = 0$ ,  $f \approx 0$  and  $\frac{\partial f}{\partial y} = \beta$ , this finally becomes

$$w_s = -\frac{\beta \tau_x}{r^2 \rho} \quad (9.15)$$

This is a very useful expression for the upwelling velocity  $w_s$  near the equator that is driven by the wind stress  $\tau_x$ . The next step in this analysis is to obtain the

ocean current for a reduced-gravity model where  $-\frac{1}{\rho} \nabla p_1$  is replaced by  $-g' \nabla h$ . Here  $g'$  is the reduced gravity defined as  $g' = g \frac{\rho'}{\rho_0}$ , where  $g$  is the normal gravitational acceleration, and  $\rho'$  is density perturbation around a reference density  $\rho_0$ . The shallow water equations for the upper layer now take on the form:

$$\frac{\partial \vec{\mathbf{u}}_1}{\partial t} + f \vec{\mathbf{k}} \times \vec{\mathbf{u}}_1 = \frac{\vec{\tau}}{\rho H_1} - r \vec{\mathbf{u}}_1 - g' \nabla h \quad (9.16)$$

$$\frac{\partial h}{\partial t} + H \nabla \cdot \vec{\mathbf{u}}_1 = -rf \quad (9.17)$$

This system carries two equations and two unknowns. It can be solved for  $\vec{\mathbf{u}}_1$  and  $h$  given a prescribed surface wind stress  $\vec{\tau}$  as a numerical marching-in-time problem using a standard time differencing scheme such as the leapfrog scheme (see Krishnamurti et al. 2006). This provides solutions for  $\vec{\mathbf{u}}_1$  and  $h$  as a function of time, all forced by the prescribed surface wind stress  $\vec{\tau}$ .

The above procedure provides with solutions for  $\vec{\mathbf{u}}_s$ ,  $w_s$ ,  $\vec{\mathbf{u}}_1$ , and  $h$ . The bottom layer current  $\vec{\mathbf{u}}_2$  is simply obtained from the relationship  $\vec{\mathbf{u}}_2 = \vec{\mathbf{u}}_1 - \vec{\mathbf{u}}_s$ . The procedure so far involves solely dynamics, in isolation from the oceanic thermodynamics. In order to address the El Nino problem, these solutions are now used to numerically solve the temperature tendency equation, as described below.

From the first law of thermodynamics applied to the ocean temperatures, the equation for the surface layer temperature is expressed by

$$\frac{\partial T}{\partial t} + \vec{\mathbf{u}}_1 \cdot \nabla T + M(w_s) \frac{T - T_e}{H_1} = \frac{Q}{H_1}, \quad (9.18)$$

Where  $T$  is the surface layer temperature and  $T_e$  is the temperature of water that is entrained from the bottom layer to the surface layer.  $Q$  is a measure of the surface heating. The function  $M(w_s)$  is defined as

$$M(w_s) = \begin{cases} w_s & \text{if } w_s > 0 \\ 0 & \text{if } w_s \leq 0 \end{cases} \quad (9.19)$$

In other words, if upwelling occurs ( $w_s > 0$ ) then  $M(w_s)$  is simply equal to  $w_s$ . If there is no upwelling, the entire term is set to zero. According to this equation, the sum of the local change of temperature and the horizontal and vertical temperature advections equals the total diabatic heating at the surface.  $T_e$  is a reference temperature of the bottom layer that is somewhat arbitrarily assigned in the Zebiak-Cane model. The next step is to write down the equation for the mean temperature  $\bar{T}$ , which is a long-term monthly mean for a specific month, as

$$\frac{\partial \bar{T}}{\partial t} + \overline{\vec{u}_1} \cdot \nabla \bar{T} + M(\bar{w}_s) \frac{\bar{T} - \bar{T}_e}{H_1} = \frac{\bar{Q}}{H_1}, \quad (9.20)$$

where the bar denotes a long term mean, and a prime denotes the anomaly with respect to that mean. The equation for the surface temperature anomaly is obtained by subtracting (9.18) from (9.20). The resulting equation is

$$\begin{aligned} \frac{\partial T'}{\partial t} + \overline{\vec{u}_1} \cdot \nabla (\bar{T} + T') + \overline{\vec{u}_1} \cdot \nabla T' \\ + (M(\bar{w}_s + w'_s) - M(\bar{w}_s)) \frac{\bar{T} - \bar{T}_e}{H_1} + M(\bar{w}_s + w'_s) \frac{T' - T'_e}{H_1} = \frac{Q'}{H_1} \end{aligned} \quad (9.21)$$

The various terms on the left hand side can be interpreted, from left to right, as: the local change of surface temperature anomaly; the horizontal advection of total temperature by the anomalous upper-layer current; the horizontal advection of temperature anomaly by the mean upper-layer current; the vertical advection of the mean temperature by the anomalous entrainment; and the vertical advection of the anomalous temperature by the total current. The sum of all these terms equals the diabatic heating anomaly. The diabatic heating anomaly could involve net radiation, sensible heat and evaporative heat flux at the ocean–atmosphere interface.

The vertical advection terms contain the quantities  $\frac{\bar{T} - \bar{T}_e}{H_1}$  and  $\frac{T' - T'_e}{H_1}$  which represent  $\frac{\partial \bar{T}}{\partial z}$  and  $\frac{\partial T'}{\partial z}$  respectively. Zebiak and Cane (1987) parameterize the temperature anomaly of the water entrained from the lower level,  $T'_e$ , by an empirical equation

$$T'_e = \gamma T'_{sub} + (1 - \gamma) T' \quad (9.22)$$

where  $T'_{sub}$  is the specified sub-surface temperature anomaly, and  $0 < \gamma \leq 1$  is an efficiency factor for the mixing of the subsurface and surface waters. With this, the final form of the temperature anomaly equation that was used by Zebiak and Cane has the form

$$\begin{aligned} \frac{\partial T'}{\partial t} = -\overline{\vec{u}_1} \cdot \nabla (\bar{T} + T') - \overline{\vec{u}_1} \cdot \nabla T' - \gamma(M(\bar{w}_s + w'_s) - M(\bar{w}_s)) \frac{\partial \bar{T}}{\partial z} \\ - \gamma M(\bar{w}_s + w'_s) \frac{T' - T'_{sub}}{H_1} - \alpha T' \end{aligned} \quad (9.23)$$

Here the entrained temperature anomaly has been expanded in terms of  $\gamma$  and the heating has been replaced by a Newtonian cooling term  $- \alpha T'$  to represent the net radiative effect at the ocean surface;  $\frac{\partial \bar{T}}{\partial z} = \frac{\bar{T} - \bar{T}_{sub}}{H_1}$  is the lapse rate of the climatological temperature. This equation provides a first-order understanding of the formation

of warm SST anomalies during an El Niño event. The mechanism that it portrays starts with the weakening of the trades. Such weakening implies a weaker easterly zonal wind stress from the atmospheric forcing. In the context of (65) this precipitates a reduction of the magnitude of  $w_s$ . The entrainment velocity is still positive because the easterly wind stress from the weaker trade winds implies a smaller magnitude but still negative  $\tau_x$ . The smaller  $w_s$  due to the weaker trades implies reduced upwelling and weaker entrainment. Note that in the region of the equatorial trades  $\bar{w}_s$  – the climatological rate of entrainment – is also weakly positive. Since the climatological lapse rate is generally positive, in the case of anomalously strong trades the term  $-\gamma(M(\bar{w}_s + w'_s) - M(\bar{w}_s))\frac{\partial T}{\partial z}$  is more strongly negative, compared to the case of weaker trades. The term  $-\gamma M(\bar{w}_s + w'_s)\frac{T' - T'_{sub}}{H_1}$  acts in the same manner during changes in the trade wind strength. Of the two terms above, the latter carries the larger magnitudes and is the big player for explaining the onset of El Niño in the Zebiak-Cane model. This is a rather straightforward scenario whereby a weakening of the trade winds leads to smaller negative values of  $\tau_x$ , which leads to smaller positive values of  $w_s$ , which in turn reduces the magnitude of vertical advection, which then contributes to a smaller negative value for the temperature anomaly tendency  $\frac{\partial T'}{\partial t}$ . Note that  $\gamma$  is positive, During the start of an El Niña the trades have become weaker, thus the upwelling is weaker and so is the wind stress and the wind stress curl, hence  $\bar{w}_s$  and  $w'_s$  are weaker but positive, gamma is positive,  $T' - T'_{sub}$  is positive and  $H_1$  is positive, hence the entire term contributes to weak negative tendency (minus sign in front of that term). When one compares that with a La Niña event the stronger trades makes all above quantities more positive and the tendency (because of the minus sign in front of this term) makes it more negative, i.e. more cooling tendency during a La Niña. Thus the El Niño warming is infact a reduced cooling of the surface layer SST due to the weaker upwelling. This is the underlying theme of the El Niño that is built in the design of the Zebiak-Cane model.

#### 9.4.2 Results from the Zebiak-Cane Model

It is possible to run the life cycle of an El Niño simply using observed monthly mean surface winds to drive the ocean model. The wind stress  $\tau_x$  can be obtained from bulk aerodynamic formula  $\tau_x = C_d \rho_a (u^2 + v^2)^{1/2} u$ , where  $u$  and  $v$  are the surface wind components in the zonal and meridional direction,  $C_d$  is the surface bulk aerodynamic drag coefficient, and  $\rho_a$  is the surface air density. The drag coefficient value is generally taken as  $1.4 \times 10^{-3}$  (non dimensional). In addition to the observed wind stress, for the ocean model one also needs the climatology of all the appropriate variables in equation (9.6). Given such data sets one can make long term integrations of the ocean model. Figure 9.10 illustrates the results of such a simulation of the El Niño/Southern Oscillation. Shown here is the initial SST

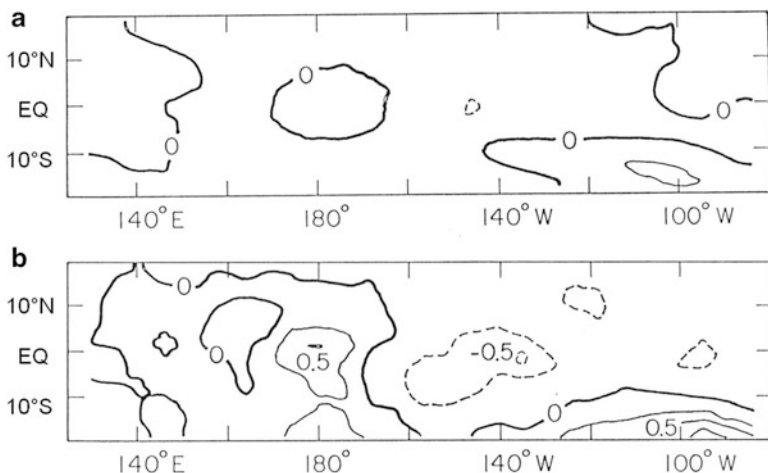


**Fig. 9.10** Model (a) and observed (b) SST anomalies in °C for December one year prior to the onset of El Niño

anomaly field as used by the model and as derived from observed estimates for December for 1 year prior to the occurrence of El Niño. The initial differences between these two fields arise due to spin-up of the model to the initial state. A spin-up of the ocean model is generally carried out using many years of observed wind stresses and the observed sea surface temperatures using a Newtonian relaxation procedure. This forces the surface fields to these imposed forced values. During this process the deeper ocean comes to equilibrium with respect to the surface fields.

The differences between the observed SST and the model SST for the initial state in Fig. 9.10 are not very critical since the subsequent wind forcing in the ensuing months carries out a realistic El Niño. Figures 9.11 and 9.12 show (a) the modeled fields, and (b) the observed fields of sea surface temperature anomalies for the months of May and December respectively for the year of the El Niño. In these illustrations we see clearly a successful simulation of the warm SST anomalies from the imposed observed wind forcing. It is possible to simulate SST anomalies of the order of 3°C from such a simple model.

The above example portrays results from the Zebiak-Cane ocean model that is driven by the imposed winds from real data, without using any atmospheric model.

Alternatively, the atmospheric forcing can be provided by Gill's atmospheric model run in a forecast mode by adding the local time tendency term in its momentum and mass continuity equations. Gill's solutions for the symmetric and the antisymmetric cases were obtained for a steady state linear model. The atmospheric model used by Zebiak and Cane for the modeling of the ENSO cycle was indeed Gill's model; however they had to drop the assumption of steady state in order to bring in a time dependent coupling of their ocean model with this atmospheric model. The diabatic mass flux term in the mass continuity equation of Gill's model should also include some form of parameterization of convective

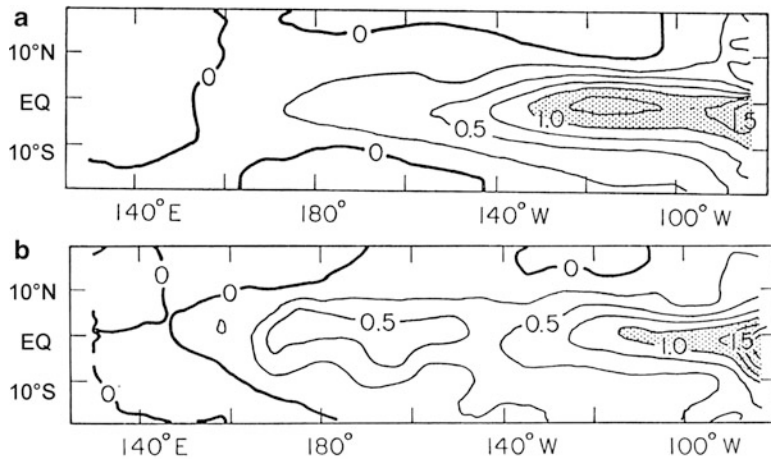


**Fig. 9.11** Model (a) and observed (b) SST anomalies in °C for May of the year of El Niño

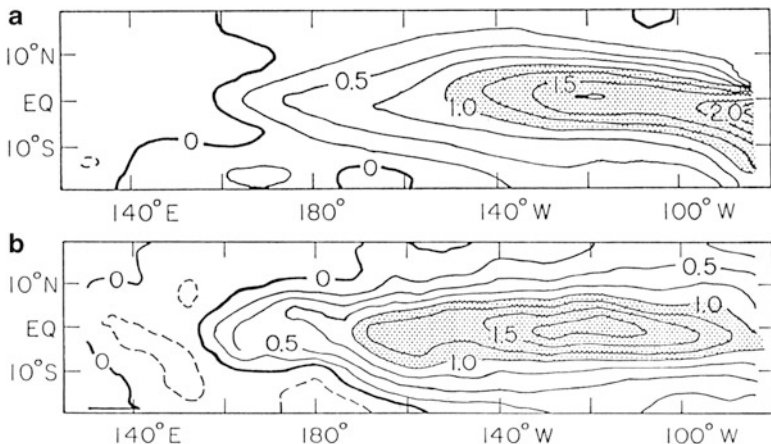


**Fig. 9.12** Model (a) and observed (b) SST anomalies in °C for December of the year of El Niño

heating that is important for the tropics. A simple form of such heating for the Gill model could be of the form  $Q = \eta w$  where  $w$  is the vertical velocity at the interface of the two layers (the upper layer is essentially a mirror image of the lower layer), and  $\eta$  is a constant. Such coupled modeling (where a Gill-type model is combined with the Zebiak-Cane model) requires an initial spin-up using observed monthly mean wind stresses derived from the surface winds. The ocean model is first run in spin-up mode for some 60 years of integration. The occurrence of El Niño and La Niña episodes can be noted during the spin-up. After the ocean model reaches equilibrium, the atmospheric model is introduced in place of the observed

atmospheric forcing, thereby setting up the coupled modeling system. The parameterized heating now plays a role by defining a heating (or lack of it) for the atmospheric model. This type of model is self-sustained, meaning that it will keep generating alternating episodes of El Niño and La Niña conditions for the duration of integration.

## 9.5 ENSO Theory

One of the popular theories to explain ENSO is the delayed oscillator theory (Schopf and Suarez 1988; Suarez and Schopf 1988; Battisti and Hirst 1989). From its initial presentation it has undergone several modifications thereafter to improve its conformity to the observed ENSO behavior.

Bjerknes (1966, 1969) made the first attempt to relate the large SST anomalies over the Eastern Equatorial Pacific to coupled air-sea interaction. He indicated a positive feedback involving SST anomalies (SSTA) in the Eastern Equatorial Pacific Ocean, zonal gradient of the Equatorial Pacific SST, the overlying tradewinds and ocean upwelling. A positive SSTA in the Eastern Equatorial Pacific reduces the zonal gradient of Equatorial Pacific SST, which in turn slows the trade winds that consequently reduces the upwelling in the Eastern Equatorial Pacific causing further warming in the region. The arguments can be reversed to explain the growth of the cold ENSO events. However a major shortcoming of the Bjerknes mechanism is that it fails to explain the transition from one (warm or cold) state of ENSO to the other.

Schopf and Suarez (1988); Suarez and Schopf (1988), and Battisti and Hirst (1989) proposed the delayed oscillator theory to explain the quasi-periodic oscillation of ENSO. The theory implies that a westerly zonal wind stress anomaly in the Central Equatorial Pacific excites a downwelling equatorial Kelvin wave that propagates rapidly to the eastern boundary. The downwelling Kelvin wave in the shallow thermocline region of the Eastern Pacific raises the SSTA. These SSTA then grow further from the local air-sea interaction as explained in the Bjerknes mechanism. In the meanwhile, the westward propagating Rossby wave from the forcing region in the Central Pacific is reflected as an upwelling Kelvin wave from the western boundary, which upon reaching the Eastern Pacific interferes with the downwelling Kelvin wave and the coupled instability to lead to the termination of the warm event and initiate the cold event.

Although this theory could explain the transition between the phases of ENSO, the simulated period of ENSO from this theory was too short in comparison to the observations. The transit time for the Kelvin and the Rossby waves to travel back and forth in the basin was found to be too short relative to the observed ENSO period. Cane et al. (1990) argued that the growth of the SSTA in the Eastern Equatorial Pacific from local coupled instability required multiple reflections of the equatorial waves to reverse the phase of ENSO.

However, Schneider et al. (1995) using an empirical delayed oscillator equation suggested that time delays from equatorially trapped Kelvin and Rossby waves cannot alone explain the low frequency ( $>4$  year period) oscillation of ENSO. In an elaborate set of theoretical experiments conducted with Zebiak and Cane (1987) model, Kirtman (1997) showed the critical role of the off-equatorial (beyond  $7^{\circ}$  latitude in either hemisphere) Rossby waves in determining the low frequency oscillation of ENSO. He showed that the meridional structure of the zonal wind stress anomaly in the Central Pacific influences the ENSO period: relatively broad (narrow) meridional structures lead to long (short) ENSO periods. The argument here is that the broad zonal wind stress anomalies invoke off-equatorial Rossby waves, which travel much slower than the equatorial Rossby waves. Furthermore, they destructively interfere with the upwelling Kelvin waves thereby reducing the amplitude of the latter. Both of these features of the off-equatorial Rossby waves result in increasing the period of the ENSO in Zebiak and Cane Model compared to ENSO generated from a narrower meridional spread of the equatorial zonal wind stress anomaly. Kirtman (1997) showed that without the effects of the off-equatorial Rossby waves at the western boundary, an ENSO with two year period was generated regardless of the meridional structure of the zonal wind stress anomaly in the Central Equatorial Pacific Ocean. Kirtman (1997) concluded that the reflection of the gravest (first meridional) mode of the Rossby wave from the western boundary is necessary to produce the ENSO oscillation, while the period of this oscillation is determined by the off-equatorial Rossby waves.

Many of the current dynamic coupled models that produce ENSO-like oscillation in the Equatorial Pacific Ocean conform to the delayed oscillator theory. There are however other competing theories like the advective-reflective oscillator (Picaut et al. 1997), the Western Pacific oscillator (Weisberg and Wang 1997), recharge-discharge theory (Jin 1997a, b), and the unified oscillator (Wang 2001) that have also made an attempt to explain the ENSO oscillation.

## References

- Battisti, D.S., Hirst, A.C.: Interannual variability in a tropical atmosphere–ocean model: influence of the basic state, ocean geometry, and non-linearity. *J. Atmos. Sci.* **46**, 1687–1712 (1989)
- Bjerknes, J.: A possible response of the atmospheric Hadley circulation to equatorial anomalies of ocean temperature. *Tellus* **18**, 820–828 (1966)
- Bjerknes, J.: Atmospheric teleconnections from the equatorial Pacific. *Mon. Weather Rev.* **97**, 163–172 (1969)
- Cane, M.A., Münnich, M., Zebiak, S.E.: A study of self-excited oscillations of the tropical ocean–atmosphere system. Part I: linear analysis. *J. Atmos. Sci.* **47**, 1562–1577 (1990)
- Gill, A.E.: Some simple solutions for heat-induced tropical circulations. *Q. J. Roy. Meteor. Soc.* **106**, 447–462 (1980)
- Jin, F.F.: An equatorial ocean recharge paradigm for ENSO Part I: conceptual model. *J. Atmos. Sci.* **54**, 811–829 (1997a)
- Jin, F.F.: An equatorial ocean recharge paradigm for ENSO. Part II: a stripped down coupled model. *J. Atmos. Sci.* **54**, 830–847 (1997b)

- Kirtman, B.P.: Oceanic Rossby wave dynamics and the ENSO period in a coupled model. *J. Climate* **10**, 1690–1704 (1997)
- Krishnamurti, T.N., Chu, S.-H., Iglesias, W.: On the sea level pressure of the southern oscillation. *Meteor. Atmos. Phys.* **34**, 385–425 (1986)
- Krishnamurti, T.N., Chakraborty, A., Krishnamurti, R., Dewar, W.K., Clayson, C.A.: Seasonal prediction of sea surface temperature anomalies using a suite of 13 coupled atmosphere–ocean models. *J. Climate* **19**, 6069–6088 (2006)
- Partridge, I.J.: Will It Rain? The Effects of the Southern Oscillation and El Niño on Australia, 2nd edn. Dept. of Primary Industries, Brisbane (1994). 51pp
- Picaut, J., Masia, F., du Penhoat, Y.: An advective-reflective conceptual model for the oscillatory nature of the ENSO. *Science* **277**, 663–666 (1997)
- Reynolds, R.W., Smith, T.N.: Improved global sea surface temperature analysis using optimal interpolation. *J. Climate* **7**, 929–948 (1994)
- Schneider, E.K., Huang, B., Shukla, J.: Ocean wave dynamics and El Niño. *J. Climate* **8**, 2415–2439 (1995)
- Schopf, P.S., Suarez, M.J.: Vacillations in a coupled ocean–atmosphere model. *J. Atmos. Sci.* **45**, 549–566 (1988)
- Suarez, M.J., Schopf, P.S.: A delayed action oscillator for ENSO. *J. Atmos. Sci.* **45**, 3283–3287 (1988)
- Trenberth, K.E., Shea, D.J.: On the evolution of the southern oscillation. *Mon. Weather Rev.* **115**, 3078–3096 (1987)
- Wang, C.: A unified oscillator model for the El Niño-Southern oscillation. *J. Climate* **14**, 98–115 (2001)
- Weisberg, R.H., Wang, C.: A western Pacific oscillator paradigm for the El Niño-Southern oscillation. *Geophys. Res. Lett.* **24**, 779–782 (1997)
- Zebiak, S.E., Cane, M.A.: A model El Niño/Southern oscillation. *Mon. Weather Rev.* **115**, 2262–2278 (1987)

# Chapter 10

## Diabatic Potential Vorticity Over the Global Tropics

### 10.1 Introduction

Most readers are familiar with the basic concepts of conservation of absolute vorticity and potential vorticity. The conservation of absolute vorticity is generally used in a two-dimensional context, where the effects of heat sources and sinks, divergence, vertical motion and friction are ignored and the vertical component of the vorticity, i.e.,  $\nabla \times \mathbf{V} + f$  is conserved following a parcel. The conservation of potential vorticity, on the other hand, is properly applied to three-dimensional motions of parcels on isentropic surfaces, following the seminal work of Ertel. Here again the heat sources and sinks and the friction terms are ignored. The effects of divergence and vertical motion, however, are retained. In a very simplistic sense, we can use the following two approximate equations:

$$\frac{d\zeta_a}{dt} = -\zeta_a \nabla \cdot \mathbf{V} \quad (10.1)$$

$$\frac{d\Gamma_d}{dt} = \Gamma_d \nabla \cdot \mathbf{V} \quad (10.2)$$

The former is a vorticity equation, where  $\zeta_a$  is the absolute vorticity, and the latter is a stability equation, where  $\Gamma_d = -g \frac{\partial \theta}{\partial p}$  is the dry static stability. The first equation tells us that divergence ( $\nabla \cdot \mathbf{V} > 0$ ) reduces the absolute vorticity, i.e.,  $\frac{1}{\zeta_a} \frac{d\zeta_a}{dt} < 0$ . The second equation indicates that divergence ( $\nabla \cdot \mathbf{V} > 0$ ) generates stability, i.e.,  $\frac{1}{\Gamma_d} \frac{d\Gamma_d}{dt} > 0$ . We can eliminate the divergence from the above equations by introducing the adiabatic potential vorticity  $\zeta_p = \zeta_a \Gamma_d$  to obtain

$$\frac{d}{dt} \zeta_p = 0 \quad (10.3)$$

This is the equation for conservation of potential vorticity. It states that for frictionless adiabatic motions the potential vorticity is conserved following the parcel.

For most of the tropics, however, heat sources and sinks are present in abundance, making the assumption of adiabatic motion invalid. It has been noted that one cannot make even a 1 day forecast of circulations in the tropical rainy areas using the conservation of potential vorticity given by (10.3) as an underlying principle. Hence, we must address the diabatic potential vorticity equation.

## 10.2 Diabatic Potential Vorticity Equation

The diabatic potential vorticity equation takes into account the heat sources and sinks, and thus provides a more accurate formulation of the problem. The natural framework for the diabatic potential vorticity equation uses the potential temperature as a vertical coordinate. The quasi-static version of the complete Ertel Potential Vorticity Equation in such isentropic coordinates is expressed by (Bluestein 1993) as:

$$\begin{aligned} \frac{d}{dt} \left( -\zeta_{a\theta} g \frac{\partial \theta}{\partial p} \right) &= \left( -\zeta_{a\theta} g \frac{\partial \theta}{\partial p} \right) \frac{\partial}{\partial \theta} \frac{d\theta}{dt} + \left\{ \nabla \frac{d\theta}{dt} \cdot \frac{\partial (\mathbf{V} \times \mathbf{k})}{\partial \theta} \right\} g \frac{\partial \theta}{\partial p} \\ &\quad - \{ \nabla \cdot (\mathbf{F} \times \mathbf{k}) \} g \frac{\partial \theta}{\partial p} \end{aligned} \quad (10.4)$$

where the isentropic absolute vorticity is given by:

$$\zeta_{a\theta} = \left( \frac{\partial \nu}{\partial x} \right)_\theta - \left( \frac{\partial u}{\partial y} \right)_\theta + \frac{u}{a} \tan \varphi + f \quad (10.5)$$

and the isentropic potential vorticity is expressed by:

$$\zeta_{p\theta} = -g \zeta_{a\theta} \frac{\partial \theta}{\partial p} \quad (10.6)$$

where  $\varphi$  and  $\theta$  are the latitude and potential temperature respectively. The reference to quasi-static indicates that vertical motion and its acceleration appears in (10.4) and yet the system is not non-hydrostatic i.e., vertical acceleration does not change gravity. The dry static stability,  $-g \frac{\partial \theta}{\partial p}$ , is generally positive unless superadiabatic layers are present. The absolute and the potential vorticities,  $\zeta_{a\theta}$  and  $\zeta_{p\theta}$ , are generally positive over the Northern Hemisphere and are generally negative

over the Southern Hemisphere, except for the cross-equatorial meanders of the zero potential vorticity isopleth.

By substituting (10.6) into (10.4) we find that the local rate of change of isentropic potential vorticity is given by:

$$\begin{aligned}\frac{\partial}{\partial t} \zeta_{p\theta} = & -\mathbf{V} \cdot \nabla \zeta_{p\theta} - \frac{d\theta}{dt} \frac{\partial \zeta_{p\theta}}{\partial \theta} + \zeta_{p\theta} \frac{\partial}{\partial \theta} \frac{d\theta}{dt} + \left\{ \nabla \frac{d\theta}{dt} \cdot \frac{\partial(\mathbf{V} \times \mathbf{k})}{\partial \theta} \right\} g \frac{\partial \theta}{\partial p} \\ & - \{ \nabla \cdot (\mathbf{F} \times \mathbf{k}) \} g \frac{\partial \theta}{\partial p}\end{aligned}\quad (10.7)$$

In other words, on an isentropic surface,

*Local rate of change of PV = Horizontal advection of PV  
+ Vertical differential of heating + Horizontal differential of heating  
+ Friction term.*

If the last three terms on the right hand side are neglected, (10.7) reduces to the familiar adiabatic equation for the conservation of potential vorticity. Retaining these three terms allows us to account for the generation or destruction of potential vorticity due to horizontal or vertical heating differentials and friction. Calculation of the potential vorticity budget involves the calculation of all terms using variables interpolated to isentropic surfaces.

## 10.3 Application of the Diabatic Potential Vorticity Equation to the Global Tropics

The order of magnitude of the different terms on the right hand side of (10.7) can be estimated from scale analysis consideration applied to the global tropics, as follows.

### 10.3.1 Potential Vorticity

The potential vorticity is defined as  $\zeta_{p\theta} = -\zeta_{a\theta} g \frac{\partial \theta}{\partial p}$ . In order to estimate the typical potential vorticity values, consider that  $g = 9.8 \text{ ms}^{-2}$ ,  $\zeta_{a\theta} \approx 10^{-4} \text{ s}^{-1}$ , and the typical vertical change of potential temperature for the large-scale tropical environment can be estimated to be  $\frac{\partial \theta}{\partial p} \approx \frac{5^\circ C}{100 \text{ mb}} \approx 5 \times 10^{-4} \text{ kg}^{-1} \text{ m s}^2 \text{ K}$ . Thus we obtain

$\zeta_{p\theta} \approx 5 \times 10^{-7} \text{ kg}^{-1} \text{ m}^2 \text{ s}^{-1} \text{ K}$  as a typical value for the isentropic potential vorticity over the tropics. The global tropical distribution of the potential vorticity for a given day is shown in Fig. 10.1a.

### 10.3.2 Horizontal Advection of Potential Vorticity

The horizontal advection of potential vorticity is given by  $-\mathbf{V} \cdot \nabla \zeta_{p\theta}$ . The order of magnitude for the horizontal wind is  $\mathbf{V} \approx 10 \text{ ms}^{-1}$ . The horizontal scale of typical tropical circulation systems can be taken as about 300 km, leading to an estimate for  $\nabla \approx \frac{1}{1000 \text{ km}} = 10^{-6} \text{ m}^{-1}$ . From these and the previously estimated potential vorticity  $\zeta_{p\theta} \approx 5 \times 10^{-7} \text{ kg}^{-1} \text{ m}^2 \text{ s}^{-1} \text{ K}$ , we obtain  $-\mathbf{V} \cdot \nabla \zeta_{p\theta} \approx 5 \times 10^{-12} \text{ kg}^{-1} \text{ m}^2 \text{ s}^{-2} \text{ K}$  as a typical order of magnitude for the large scale horizontal potential vorticity advection.

### 10.3.3 Vertical Advection of Potential Vorticity

The vertical advection of potential vorticity is given by  $-\frac{d\theta}{dt} \frac{\partial \zeta_{p\theta}}{\partial \theta}$ . A measure of the heating rate  $\frac{d\theta}{dt}$  can be obtained from typical tropical values of the apparent heat source  $Q_1$  based on several studies e.g. Luo and Yanai (1984). Typically these heating rates are on the order of  $5 \text{ K day}^{-1}$ . Noting that  $\frac{d\theta}{dt} = \left(\frac{p_0}{p}\right)^{\frac{R}{C_p}} \frac{dT}{dt}$ , a heating rate of  $5 \text{ K day}^{-1}$  in the lower troposphere roughly translates to  $\frac{d\theta}{dt} \approx 6 \times 10^{-5} \text{ K s}^{-1}$ . The vertical differential of potential vorticity  $\left(\frac{\partial \zeta_{p\theta}}{\partial \theta}\right)$  is of the order of  $10^{-7}$ . Then the order of magnitude of the vertical advection of potential vorticity is around  $10^{-12} \text{ kg}^{-1} \text{ m}^2 \text{ s}^{-2} \text{ K}$ .

### 10.3.4 Vertical Differential Heating

The vertical differential heating term is given by  $\zeta_{p\theta} \frac{\partial}{\partial \theta} \frac{d\theta}{dt}$ . This is the leading diabatic term of the potential vorticity equation. Based on typical profiles of the apparent heat sources over the eastern Atlantic (GATE) and western Pacific (TOGA-COARE; Johnson 1984), it is safe to state that  $\frac{\partial}{\partial \theta} \frac{d\theta}{dt}$  is generally greater

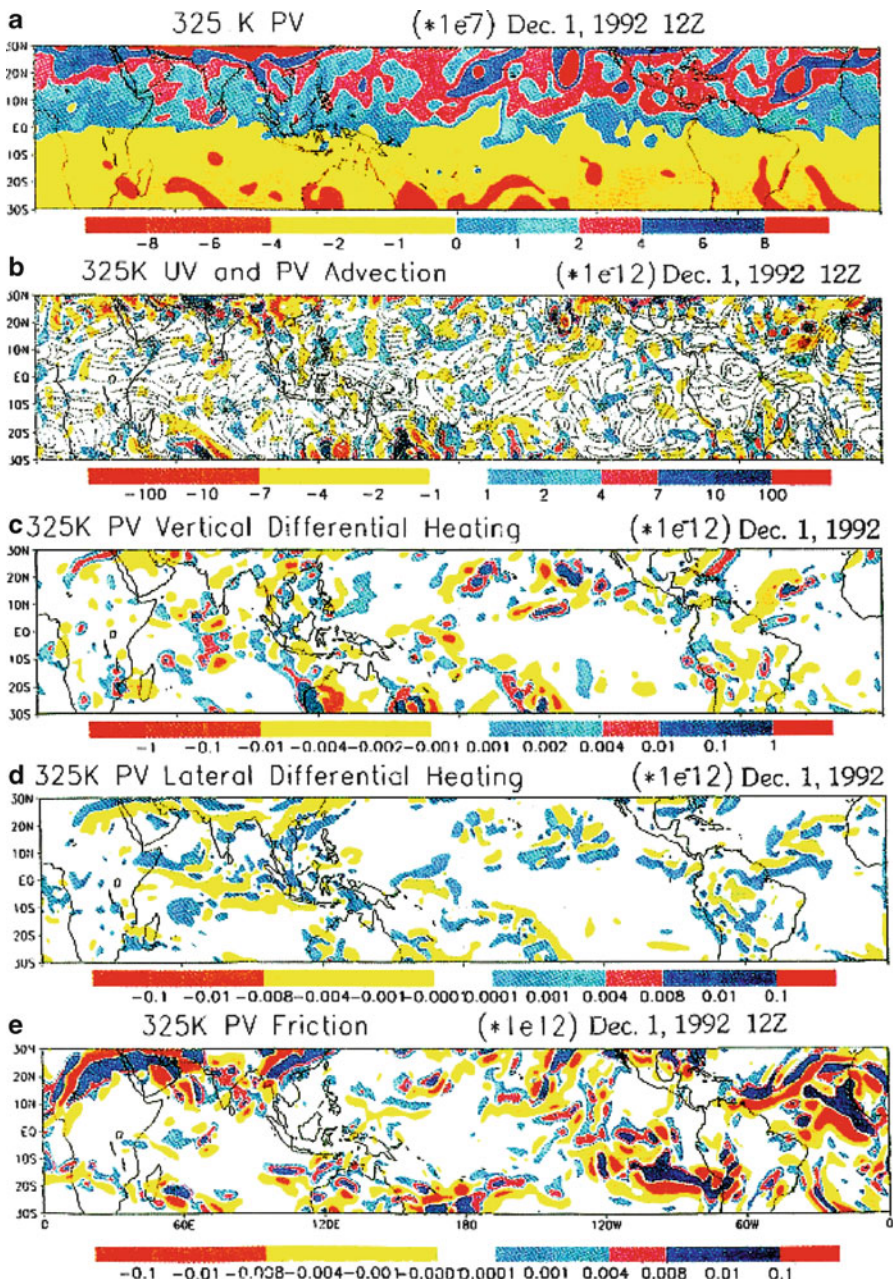


**Fig. 10.1** Potential vorticity budget related fields for Dec. 1 1992, 12 UTC at 325 K isentropic surface. (a) Potential vorticity ( $\times 10^{-7} \text{ kg}^{-1}\text{m}^2\text{s}^{-1} \text{ K}$ ) (b) Advection of potential vorticity ( $\times 10^{-12} \text{ kg}^{-1}\text{m}^2\text{s}^{-1} \text{ K}$ ) (c) Vertical differential of potential vorticity ( $\times 10^{-12} \text{ kg}^{-1}\text{m}^2\text{s}^{-1} \text{ K}$ ) (d) Lateral differential of potential vorticity ( $\times 10^{-12} \text{ kg}^{-1}\text{m}^2\text{s}^{-1} \text{ K}$ ) (e) Frictional contributions to tendency of potential vorticity ( $\times 10^{-7} \text{ kg}^{-1}\text{m}^2\text{s}^{-1} \text{ K}$ ) (From Krishnamurti et al. 2000)

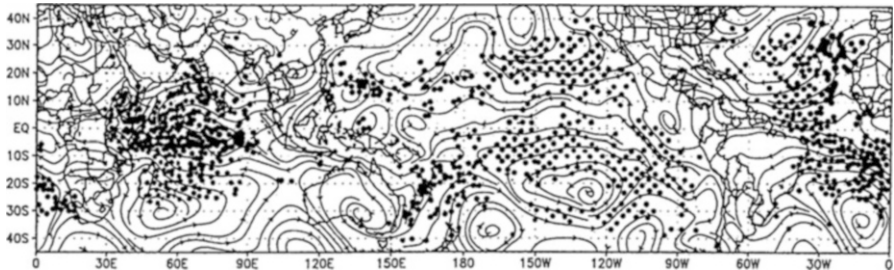


**Fig. 10.2** 850 mb flow field and positions of cloud wind vectors for July 16, 1979, 00 UTC. The black dots denote positions where low cloud motions were extracted for this map time from the tracking of low clouds (shallow stratocumulus) from five geostationary satellites (From Krishnamurti 1985)

than zero in the lower troposphere and is generally less than zero above the maximum convective heating in the upper troposphere.

Since the isentropic potential vorticity  $\zeta_{p\theta}$  is generally positive in the Northern Hemisphere, the effect of such a convective heating (as observed in TOGA-COARE or GATE) is to generate potential vorticity in the lower troposphere and to destroy it in the upper troposphere. An issue for consideration may be the scale and extent of influence of this term. That can be answered from an examination of the charts of the apparent heat source,  $Q_1$ , from data sources such as those produced by Luo and Yanai (1984) and several others; however it is readily apparent that this term would be large in a region of heavy meso-convective precipitation. Large values of  $\frac{d\theta}{dt}$  exist not only where individual deep convective clouds are present, but they also prevail over the downdraft regions of the clouds and on scales larger than the clouds themselves. Since  $Q_1 \approx C_p \left( \frac{p}{po} \right)^{\frac{R}{C_p}} \frac{d\theta}{dt}$ , large values of  $\zeta_{p\theta} \frac{\partial}{\partial \theta} \frac{d\theta}{dt}$  can be expected where the vertical gradient of the apparent heat source  $Q_1$  is large. This implies that the following regions of the tropics, on synoptic scales, can experience a generation of potential vorticity from the differential heating along the vertical: the ITCZ, monsoon and tropical depressions, tropical waves, tropical cyclones, tropical squall systems, rainfall systems and mid tropospheric cyclones, etc.

The global tropical belt are significantly populated by shallow stratocumulus clouds as seen typically in satellite imagery. This observation is also based on the large number of cloud-tracked winds that were extracted during the global experiment First Global Atmospheric Research Program [GARP] Global Experiment (FGGE). Most of those low cloud motion vectors came from tracking the propagation of shallow stratocumuli that could be viewed from the high-resolution imagery of geostationary satellites. Figure 10.2 illustrates the distribution of a delayed collection of low cloud motion vectors during FGGE. This shows that shallow stratocumuli abound over the undisturbed tropical oceans. This illustrates, of course, only a small portion of the possible distribution of stratocumuli since the satellite surveillance did not see all the shallow clouds.

We can expect a substantial cooling of the tropical troposphere near the level of the tops of these shallow stratocumulus clouds. The tropospheric rate of cooling over these levels in the cloud-free atmosphere is usually much smaller. Thus the field of  $\frac{\partial}{\partial \theta} \frac{d\theta}{dt}$  is expected to be negative below the cloud top and positive above the cloud top. This shallow convective heating should not be confused with the total heating in a tropical disturbance that largely comes from the heating related to the deep cumulus convection. The latter has a maximum heating somewhere in the middle troposphere and carries a positive vertical gradient of the heating term in the lower troposphere. Whereas in the region of shallow convection, the cloud top cooling can locally reverse that vertical gradient largely from radiative effects. Thus the diabatic contribution to the generation of potential vorticity dictated by the vertical heating gradient would be positive above the tops of these shallow clouds and negative below in the northern hemisphere. Therefore diabatic forcing can contribute to the generation or destruction of potential vorticity over these regions. The question remains: what are the magnitudes and time scales of this diabatic forcing, and how do these values compare with the advection of potential vorticity?

The vertical differential  $\frac{\partial}{\partial \theta} \frac{d\theta}{dt}$  has an approximate magnitude of about  $10^{-5} s^{-1}$ . This is obtained from order of magnitude considerations of cumulus scale heating. Given  $\frac{\partial}{\partial \theta}$  to be of the order of  $10^{-1}$  (i.e., looking vertically across  $10^\circ$  separation of adiabats and a heating rate following Yanai's estimates of apparent heating of  $10^\circ C day^{-1}$  [which is roughly  $10^5 s l$ ]), we obtain a value of this heating to be around  $10^{-5} s^{-1}$ .

Given that  $\zeta_{p\theta} \approx 5 \times 10^{-7} kg^{-1} m^2 s^{-1} K$ , we obtain an estimate for the value of  $\zeta_{p\theta} \frac{\partial}{\partial \theta} \frac{d\theta}{dt} \approx 5 \times 10^{-12} kg^{-1} m^2 s^{-2} K$ . Further, the radiative cooling near the top of the clouds on synoptic scales can be estimated to be of the order  $5-10 K day^{-1}$ , Chen and Cotton (1987). Thus the order of these terms in regions of shallow stratocumulus is estimated to be  $\zeta_{p\theta} \frac{\partial}{\partial \theta} \frac{d\theta}{dt} \approx 2 \times 10^{-12} kg^{-1} m^2 s^{-2} K$ . This implies that somewhere near 700 mb (where the tops of the shallow stratocumuli are located) one can expect to see a substantial diabatic generation of potential vorticity.

### 10.3.5 Horizontal Differential Heating

The term in the diabatic potential vorticity equation that carries the effects of the horizontal heating differential is  $\left( \nabla \frac{d\theta}{dt} \cdot \frac{\partial(\mathbf{V} \times \mathbf{k})}{\partial \theta} \right) g \frac{\partial \theta}{\partial p}$ . Over a beta plane the horizontal differential heating term can be expressed as  $-g \frac{\partial \theta}{\partial p} \left[ \frac{\partial u}{\partial \theta} \frac{\partial}{\partial y} \frac{d\theta}{dt} - \frac{\partial v}{\partial \theta} \frac{\partial}{\partial x} \frac{d\theta}{dt} \right]$ . The dry static stability  $-g \frac{\partial \theta}{\partial p}$  is generally positive; therefore the generation or destruction of

potential vorticity from horizontal differential heating is determined by the sign of the bracketed term, which represents the lateral heating. This term is in fact somewhat analogous to the twisting term of the vorticity equation with pressure as a vertical coordinate, viz.  $\frac{\partial \omega}{\partial y} \frac{\partial u}{\partial p} - \frac{\partial \omega}{\partial x} \frac{\partial v}{\partial p}$ . In the isentropic frame of reference  $\frac{d\theta}{dt}$  is an analogue to the vertical velocity  $\omega$  (in the pressure coordinate system) and  $\frac{\partial \mathbf{V}}{\partial \theta}$  denotes the equivalent vertical wind shear. Since the twisting term is generally small in the pressure coordinate system, one might also expect this lateral heating term to be small in the potential vorticity equation. However, as we shall see, that turns out not to be the case across regions of strong wind shears and strong lateral heating gradients in the tropics.

To estimate the order of magnitude of the lateral heating term we can assume that the meridional wind  $v$  is small, and simply examine the magnitudes of  $-g \frac{\partial \theta}{\partial p} \left( \frac{\partial u}{\partial \theta} \frac{\partial}{\partial y} \frac{d\theta}{dt} \right)$ . Using  $g \approx 9.8 \text{ ms}^{-2}$ ,  $\frac{\partial \theta}{\partial p} \approx 5 \times 10^{-4} \text{ kg}^{-1} \text{ m s}^2 \text{ K}$ ,  $u \approx 10 \text{ ms}^{-1}$ ,  $\frac{\partial u}{\partial \theta} \approx 3 \text{ ms}^{-1} \text{ K}^{-1}$ ,  $\frac{\partial}{\partial y} \approx \frac{1}{1000 \times 10^3 \text{ m}}$ ,  $\frac{d\theta}{dt} \approx 6 \times 10^{-5} \text{ K s}^{-1}$ , we obtain  $-g \frac{\partial \theta}{\partial p} \times \left( \frac{\partial u}{\partial \theta} \frac{\partial}{\partial y} \frac{d\theta}{dt} \right) \approx 10^{-12} \text{ kg}^{-1} \text{ m}^2 \text{ s}^{-2} \text{ K}$  as the order of magnitude for the lateral heating term.

### 10.3.6 Frictional Contribution

The contribution of friction to the local rate of change of potential vorticity is given by  $-\{\nabla \cdot (\mathbf{F} \times \mathbf{k})\} g \frac{\partial \theta}{\partial p}$ .  $\mathbf{F}$  can be estimated by the relation  $-g \frac{\partial \boldsymbol{\tau}}{\partial p}$ , where  $\boldsymbol{\tau}$  is the surface stress. On a beta plane,

$$\nabla \cdot (\mathbf{F} \times \mathbf{k}) = -g \frac{\partial}{\partial p} \nabla \cdot (\boldsymbol{\tau} \times \mathbf{k}) = -g \frac{\partial}{\partial p} \left[ \frac{\partial \tau_y}{\partial x} - \frac{\partial \tau_x}{\partial y} \right] = \left( \frac{\partial F_y}{\partial x} - \frac{\partial F_x}{\partial y} \right) \quad (10.8)$$

where

$$F_x = -g \frac{\partial \tau_x}{\partial p} \text{ and } F_y = -g \frac{\partial \tau_y}{\partial p} \quad (10.9)$$

Since the static stability  $\left(-g \frac{\partial \theta}{\partial p}\right)$  is generally positive, the vertical variation of the curl of the wind stress, depending on its sign, contributes to the generation or destruction of the potential vorticity. In the vicinity of regions of strong surface

cyclonic vorticity the term  $-g \frac{\partial}{\partial p} \left[ \frac{\partial \tau_y}{\partial x} - \frac{\partial \tau_x}{\partial y} \right]$  tends to have a dipole structure with neighboring strong positive and negative centers. Thus we can expect to see both generation and destruction of potential vorticity in the vicinity of strong surface vorticity. The vertical structure of the surface fluxes generally displays a similar but weaker pattern of the potential vorticity generation and destruction aloft in the lower troposphere.

If we use typical magnitudes of  $\mathbf{F}$  from global model computations based on the surface similarity theory and note that the frictional contribution to the rate of change of potential vorticity contains the curl of the surface wind stress, where the wind stresses is expressed by:

$$\begin{aligned}\tau_x &= C_D \rho |\mathbf{V}| u \\ \tau_y &= C_D \rho |\mathbf{V}| v\end{aligned}\tag{10.10}$$

where  $C_D$  is the stability dependent drag coefficient, then using the relations (10.9) between the frictional force and the stress, and assuming that

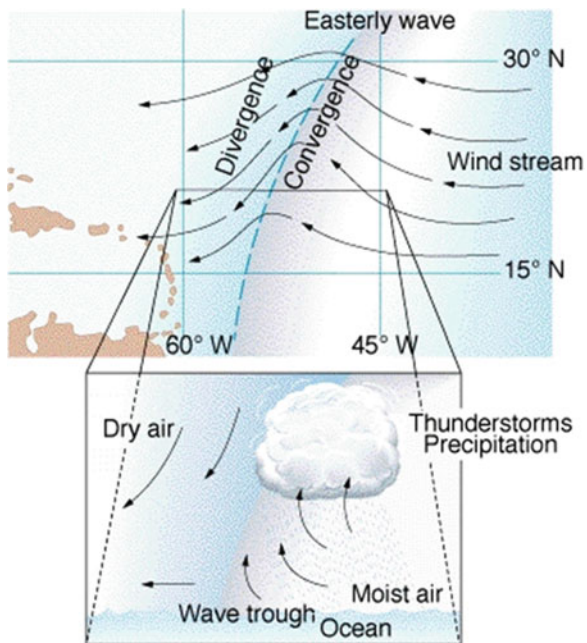
$$\begin{aligned}C_D &\approx 1.4 \times 10^{-3}, \rho \approx 1.2 \text{ kgm}^{-2}, |\mathbf{V}| \approx 10 \text{ ms}^{-1}, \Delta p \approx 100 \text{ mb}, \Delta x \approx \Delta y \\ &\approx 300 \times 10^3 \text{ m},\end{aligned}$$

we obtain a typical value for the friction term of the potential vorticity equations as  $10^{-12} \text{ kg}^{-1} \text{ m}^2 \text{ s}^{-2} \text{ K}$ . This value is typical near the Earth's surface. At higher levels it can become much smaller.

## 10.4 Application of the Diabatic Potential Vorticity Equation to Hurricanes

The hurricanes are characterized by substantial amounts of deep cumulus convection. This deep convection is particularly strong along the eye wall and the rain bands. There, one of the most important diabatic contributions to the potential vorticity is given by the vertical differential heating term, i.e.,  $\zeta_{p\theta} \frac{\partial}{\partial \theta} \frac{d\theta}{dt}$ . For the Northern Hemisphere, hurricane regions generally have positive potential vorticity  $\zeta_{p\theta}$ . Below the level of maximum convection,  $\frac{\partial}{\partial \theta} \frac{d\theta}{dt}$  is positive. This, combined with the positive potential vorticity, leads to  $\frac{\partial}{\partial t} \zeta_{p\theta} > 0$ . In regions of heavy precipitation, such as that found in the eye wall of a hurricane, the difference in

**Fig. 10.3** A schematic diagram of an Easterly wave showing the convergence and associated convection of moist air (From U. of Arizona, <http://geog.arizona.edu/~comrie/geog230/tropical.htm>)



the heating rate  $\frac{d\theta}{dt}$  can reach up to about  $50 \text{ K day}^{-1}$  over an atmospheric depth of  $5 \text{ km}$ . Over this depth of atmosphere, the potential temperature changes by about  $5 \text{ K}$ . All this translates to  $\frac{\partial}{\partial \theta} \frac{d\theta}{dt} \approx 10^{-4} \text{ s}^{-1}$ . The potential vorticity of a hurricane is on the order of  $10^{-6} \text{ kg}^{-1} \text{ m}^2 \text{ s}^{-1} \text{ K}$ . Thus the rate of change of potential vorticity resulting from such differential heating can be quite large, of the order of  $10^{-10} \text{ k g}^{-1} \text{ m}^2 \text{ s}^{-2} \text{ K}$ , which is comparable to (or even somewhat larger than) the horizontal advection of potential vorticity in a hurricane. These two effects – differential heating and horizontal advection of potential vorticity – can contribute to an increase of intensity of the hurricane from the following arguments.

Both the horizontal advection of potential vorticity and the diabatic potential vorticity contribution from  $\zeta_{p\theta} \frac{\partial}{\partial \theta} \frac{d\theta}{dt}$  can lead to a local increase of potential vorticity. In regions of heavy rains, convergence in the lower troposphere reduces the dry static stability (see 10.2). Since the potential vorticity is increasing while the dry static stability is decreasing, an increase of absolute vorticity must take place. Since the Coriolis parameter is virtually constant for slow zonally moving disturbances, this results in a large increase of relative vorticity, which implies a stronger cyclonic circulation, i.e., a stronger storm.

Figure 10.3 is a schematic sketch of an idealized easterly wave with its region of precipitation, lower tropospheric mass convergence and diabatic heating. We can summarize the relationship between generation of potential vorticity and strengthening of tropical disturbances by saying that:

- (i) Deep convection-related convective heating generates diabatic potential vorticity in the lower troposphere.
- (ii) At the same time, the mass convergence lowers the dry static stability in the same region.
- (iii) If the potential vorticity increases and the dry static stability decreases, then, since the potential vorticity is the product of the dry static stability and the absolute vorticity, the absolute vorticity must be increasing.
- (iv) The Earth's vorticity (the Coriolis parameter) is not changing significantly during the passage of a tropical wave. Since the absolute vorticity is the sum of the relative vorticity and the Earth's vorticity, and the absolute vorticity is increasing, it follows that the relative vorticity must be increasing.
- (v) An increase of relative vorticity implies a strengthening of the tropical wave, possibly into a storm, or the intensification of an existing storm.

Another term that provides a substantial contribution to the generation of potential vorticity in a hurricane is the horizontal differential heating term in the potential vorticity equation, i.e.  $\left( \nabla \frac{d\theta}{dt} \cdot \frac{\partial(\mathbf{V} \times \mathbf{k})}{\partial\theta} \right) g \frac{\partial\theta}{\partial p}$ . The heating gradient across a hurricane eye wall can be substantial. Along a radial line extending from the storm center outwards, we can approximate this term by the expression  $-g \frac{\partial\theta}{\partial p} \left( \frac{\partial V_\theta}{\partial\theta} \frac{\partial}{\partial r} \frac{d\theta}{dt} \right)$ , where  $V_\theta$  is the tangential component of the wind. The change of  $\frac{d\theta}{dt}$  along the radial direction over the approximately 10 km thickness of a typical eye wall can be substantial. As a result, the lateral heating term can also acquire a value of close to  $10^{-10} kg^{-1} m^2 s^{-2} K$ . This again can lead to a large enhancement of potential vorticity and consequent storm intensification.

## References

- Bluestein, H.B.: Synoptic-Dynamic Meteorology in Midlatitudes: Vol II, Observations and Theory of Weather Systems. Oxford University Press, New York (1993). 594pp
- Chen, C., Cotton, W.R.: Internal structure of a small mesoscale convective system. Mon. Weather Rev. **44**, 2951–2977 (1987)
- Johnson, R.H.: Partitioning tropical heat and moisture budgets into cumulus and mesoscale components: implications for cumulus parameterization. Mon. Weather Rev. **112**, 1590–1601 (1984)
- Krishnamurti, T.N.: Summer monsoon experiment – a review. Mon. Weather Rev. **113**, 1590–1626 (1985)
- Krishnamurti, T.N., Jha, B., Bedi, H.S., Mohanty, U.C.: Diabatic effects on potential vorticity over the global tropics. J. Meteor. Soc. Jpn. **78**, 527–542 (2000)
- Luo, H., Yanai, M.: The large-scale circulation and heat sources over the Tibetan Plateau and surrounding areas during the early summer of 1979. Part II: heat and moisture budgets. Mon. Weather Rev. **112**, 966–989 (1984)

# Chapter 11

## Tropical Cloud Ensembles

### 11.1 Introduction

As one proceeds from the west coast of a continent, such as California in North America or Morocco in Northwest Africa, towards the near-equatorial oceanic ITCZ, one notes the following transition in the predominant species of tropical clouds: coastal stratus, stratocumulus, fair weather cumulus, towering cumulus and cumulonimbus. This is a typical scenario over the Pacific and Atlantic Oceans of the two hemispheres. The Asian Monsoon carries some of its own cloud features over the Indian Ocean. Figure 11.1 is a collage of cloud types and typical rainfall distributions over the tropics during the northern summer. This identifies precipitation features, such as those from the ITCZ, typhoon, monsoon, and near coastal phenomena. The precipitation illustrated here was estimated from microwave radiances received by the TRMM satellite. A plethora of clouds types abound in the tropics. Dynamics, physics, and microphysics are important interrelated scientific areas for these clouds' life cycles. Modeling of the life cycle of individual clouds and cloud ensembles and representation of the effects of unresolved clouds in large scale environment are areas of importance for tropical meteorology. The ocean, land surface, and planetary boundary layer large scale wind systems and thermal and humidity stratification have a large control over the nature of evolving clouds.

A background in Cloud Physics is necessary for the understanding of different cloud types and their life cycle. Motions on meso-convective space and time scales have a large influence on these life cycles. The problem is further compounded by the need to know aerosol-cloud interactions, cloud radiative interactions, as well as the mutual interactions among cloud microphysics, dynamics, and other physical processes. Clouds seem to organize from the relatively small scales of the sea breeze to large scales, such as the monsoon. Thus there is a coexistence of clouds and the motion fields on many space and time scales. We allude to some of these issues in the chapter on scale interactions.

A widely used measure of convective instability is the Convective Available Potential Energy, or CAPE. CAPE represents the vertically integrated amount of

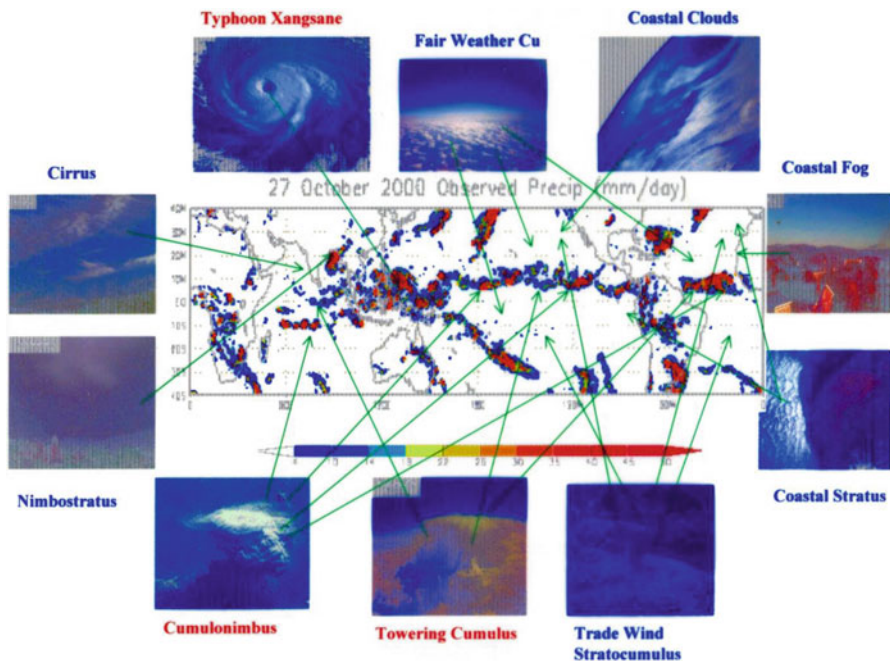


**Fig. 11.1** A collage of cloud types and typical rainfall distributions over the tropics during the northern summer

buoyant energy that would be released if a parcel were lifted up to an equilibrium level. It is measured in units of  $\text{J kg}^{-1}$ . It is usually estimated using a skew-T-log-p diagram. The higher the value of CAPE, the larger the potential for development of deep convection. Negative values of CAPE represent a stable environment. Values of CAPE between 0 and  $1,000 \text{ J kg}^{-1}$  are considered marginally unstable; between  $1,000$  and  $2,500 \text{ J kg}^{-1}$  – moderately unstable; between  $2,500$  and  $4,000 \text{ J kg}^{-1}$  – very unstable; and finally, values above  $4,000 \text{ J kg}^{-1}$  are considered representative of an extremely unstable atmosphere.

A number of instability measures are important for the understanding of convection. Those can be found in introductory texts on meteorology. The student should be familiar with concepts such as absolute instability, conditional instability, potential instability, etc.

In this chapter we have taken the modeling approach as one that provides some insights on processes that are important for the understanding of buoyancy-driven dry convection, modeling of the non-precipitating shallow stratocumulus and the modeling of cloud ensembles. This approach clearly has its flaws – none of the model examples presented here are perfect. They are based on a number of assumptions and hence have many limitations. Nevertheless, these models are quite useful compared to looking at pictures of clouds and satellite imagery and

gross interpretations that are never very complete in terms of providing insights on the complex interactions we spoke of above. The modeling approach is better suited as an avenue for understanding, provided one is mindful of its limitations.

## 11.2 Understanding Simple Buoyancy-Driven Dry Convection

Here we shall show an example of a buoyancy-driven cloud model. This model has applications for the understanding of dry convection over warm land surfaces. It describes the growth of a buoyancy-driven cloud element in a neutral sounding, i.e., a sounding with an initial stratification that has a constant potential temperature in the vertical. It is possible to develop a rather simple model on an  $x$ - $z$  plane to study the growth of such a cloud using a simplified two dimensional vorticity equation, the first law of thermodynamics and the mass continuity equation.

Dry convection thermals originate over hot surfaces, such as deserts, where the lowest layers of the atmosphere have superadiabatic lapse rates. Driven by the heating above the surface layer, buoyant thermals, also known as buoyancy driven elements, are generated. These buoyancy driven elements act to destroy the superadiabatic lapse rates. In a hydrostatic environment,

$$0 = -\frac{\partial p}{\partial z} - \rho g \quad (11.1)$$

For a buoyant parcel with a density of  $\rho'$  the vertical acceleration is given by

$$\frac{dw}{dt} = -\frac{1}{\rho'} \frac{\partial p'}{\partial z} - g \quad (11.2)$$

Assuming continuity of pressure across the buoyant element, i.e.,  $\frac{\partial p'}{\partial z} = \frac{\partial p}{\partial z}$  and using the equation of state,

$$p = \rho RT \quad (11.3)$$

the vertical equation of motion (11.2) can be written as

$$\frac{dw}{dt} = -g \frac{T' - T}{T}. \quad (11.4)$$

A buoyancy-driven simple cloud model was first developed by Malkus and Witt (1959) and by Nickerson (1965). This elementary model is most illustrative for the

understanding of dry convection. It is a simple two-dimensional model on the zonal plane ( $x, z$ ) where the velocity components are defined in terms of the stream function  $\psi$  as

$$u = \frac{\partial \psi}{\partial z} \quad (11.5)$$

and

$$w = -\frac{\partial \psi}{\partial x}, \quad (11.6)$$

thus ensuring that the continuity equation

$$\frac{\partial u}{\partial x} + \frac{\partial w}{\partial z} = 0 \quad (11.7)$$

is satisfied. The vorticity equation and the first law of thermodynamics in the  $x$ - $z$  plane are written by the relations

$$\frac{\partial \eta}{\partial t} = J(\psi, \eta) - g\phi + \nu \nabla^2 \eta \quad (11.8)$$

$$\frac{\partial \phi}{\partial t} = J(\psi, \phi) + \frac{Q}{\theta_0} + \nu \nabla^2 \phi \quad (11.9)$$

Here  $\eta$  is the relative vorticity given by  $\eta = \frac{\partial u}{\partial z} - \frac{\partial w}{\partial x} = \nabla^2 \psi$ ;  $\phi = \frac{\theta - \theta_0}{\theta_0}$  is the normalized potential temperature excess of a parcel with a potential temperature  $\theta_0$  with respect to the environment  $\theta$ ;  $\nu$  is the viscosity coefficient; and  $Q$  denotes the diabatic heating which is defined below. Basically, the problem is regarded as a system of two equations and two unknowns,  $\psi$  and  $\phi$ . Once  $\psi$  is solved for, one can find  $u$  and  $w$  from (11.5) and (11.6). This problem still needs the definition of the heating  $Q$  and the boundary conditions and initial states for  $\psi$  and  $\phi$ . The lateral boundary condition for  $\psi$  utilizes a mirror image at  $x = 0$  and a Neuman boundary condition  $\frac{\partial \psi}{\partial x} = 0$  at  $x = L$ . Over the north and south boundaries  $\psi$  is set to zero and  $\phi$  is set to a constant value. An elevated initial potential temperature excess is defined by

$$\theta - \theta_0 = 0.5 \cos \frac{\pi x}{320} \cos^2 \frac{\pi(z - 100)}{400} \quad (11.10)$$

and this excess resides within  $0 \leq x \leq 160m$  and  $100 \leq z \leq 300m$ . The diabatic heating  $Q$  is defined by

$$Q = Q_0 \cos \frac{\pi x}{320} \cos^2 \frac{\pi(z - 100)}{40} \quad (11.11)$$

and resides within  $0 \leq x \leq 160m$  and  $80 \leq z \leq 120m$ . This is a continuous heat source at the base of the warm bubble defined by (11.10). It resides above the Earth's surface between 80 and 120 m and defines an initial buoyancy element. The initial vertical stratification is a neutral state ( $\theta_0 = \text{const}$ ). As the system of equations is integrated, the buoyancy element rises and forms a mushroom cloud near  $x = 0$ . This growth of the buoyant element is very illustrative of the growth of shallow dry convection.

Figure 11.2a–c shows the results of the model cloud growth at 2, 6 and 10 min after the start of the integration. Here the solid lines represent the potential temperature excess (in °C) and the dashed lines represent the stream function (in  $m^2 s^{-1}$ ). This shows that the potential temperature excess grows in the form of a plume and ends up using most of the initial buoyancy. The life time of this buoyant element is roughly 15 min. Also note that, because of the imposed symmetry about  $x = 0$ , the left half of the cloud (not shown here) is a mirror image of what the right half (shown here), resulting in a mushroom-shaped cloud.

## 11.3 Understanding Simple Buoyancy-Driven Shallow Moist Convection

### 11.3.1 A Simple Cloud Model

The simple cloud model following Murray and Anderson (1965) is a simple non-precipitating shallow convection model. It allows for the formation of liquid water in a supersaturated environment, and for the evaporation of liquid water in a non-saturated environment. Fallout of rain is not permitted. The total moisture (liquid water and water vapor) is thus conserved. An outline of this two-dimensional ( $x$ - $z$ ) cloud model is presented here.

The vorticity equation is expressed by

$$\frac{\partial}{\partial t} \nabla^2 \psi = -J(\psi, \nabla^2 \psi) + \frac{g}{T_M} \frac{\partial T'}{\partial x} + \nu_M \nabla^4 \psi, \text{i.e.,} \quad (11.12)$$

$$\text{Local Change of Vorticity} = \text{Vorticity Advection} + \text{Buoyancy Term} + \text{Friction}$$

Here  $\psi$  is a stream function in the vertical plane ( $x, z$ ) where  $T_M$  is a mean temperature for the entire domain and is a constant.  $T'$  is the departure of the local

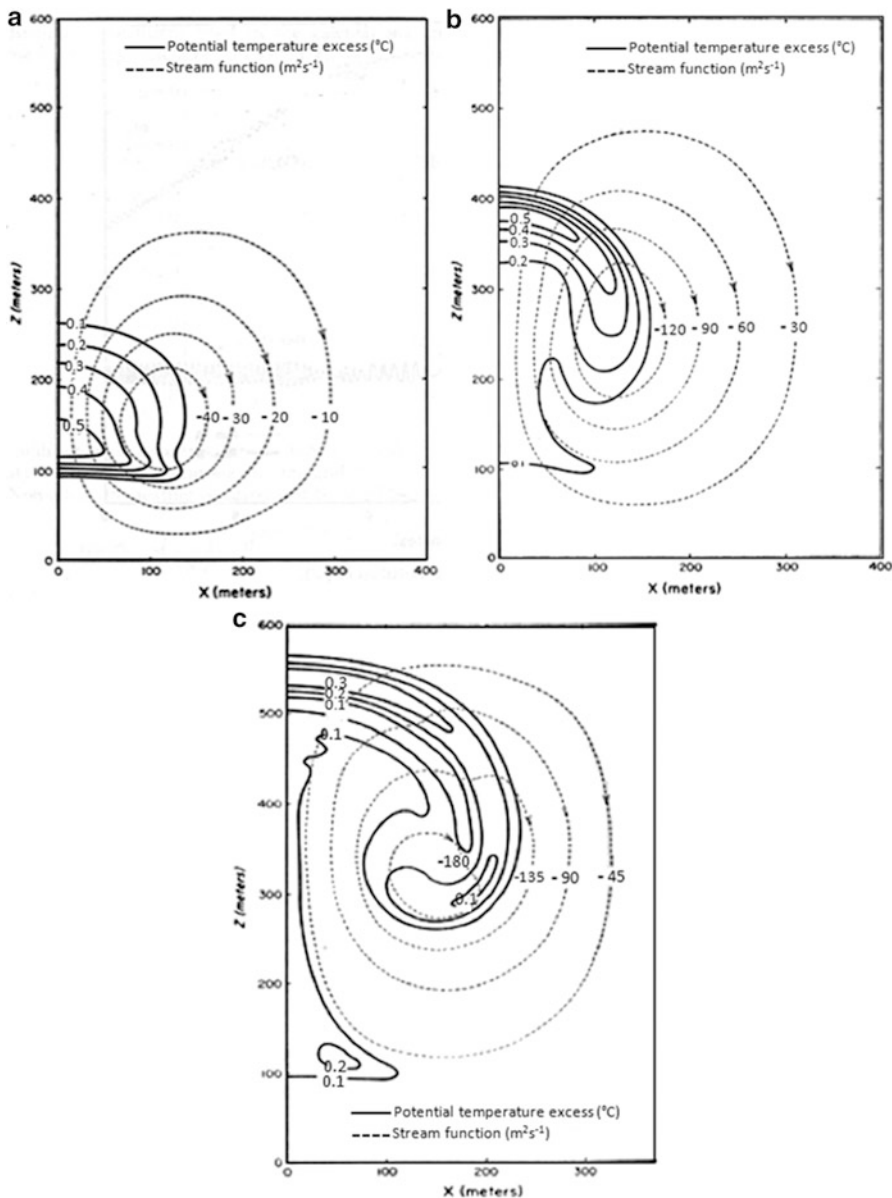


**Fig. 11.2** Configuration of the buoyant element at (a) 2, (b) 6, and (c) 10 min after the beginning of integration. Solid lines show the potential temperature excess ( $^{\circ}\text{C}$ ), and dashed lines show the stream function ( $\text{m}^2\text{s}^{-1}$ ) (From Nickerson 1965)

temperature  $T$  from a horizontal ( $x$ ) average.  $\nu_M$  is a diffusion coefficient for the eddy flux of momentum. The stream function is related to the  $u$  and  $w$  velocity components via the relations

$$\frac{\partial \psi}{\partial z} = u \quad (11.13)$$

and

$$\frac{\partial \psi}{\partial x} = -w, \quad (11.14)$$

so that the continuity equation

$$\frac{\partial u}{\partial x} + \frac{\partial w}{\partial z} = 0 \quad (11.15)$$

is satisfied.

According to (11.12), the buoyancy field ( $\frac{\partial T'}{\partial x} > 0$ ) contributes to vorticity generation, i.e., to  $\frac{\partial}{\partial t} \nabla^2 \psi > 0$ . This increase in vorticity will, in general, lead to a cellular stream function geometry on the  $x$ - $z$  plane with an enhancement of the velocities  $u$  and  $w$  in different parts of the buoyant cell. This is the mechanism via which buoyancy can initiate motion from an initial state of rest. If  $T'$  is locally large and positive, then on either side of it there would be regions of  $\frac{\partial T'}{\partial x} > 0$  and  $\frac{\partial T'}{\partial x} < 0$  respectively. The rising motion that results in the center will have two sinking lobes on either side.

Any numerical model that is designed to study the time evolution of a phenomenon should have the following ingredients:

- (i) Independent variables;
- (ii) Dependent variables;
- (iii) Closed system of equations
- (iv) Finite differencing schemes for the above;
- (v) Boundary conditions; and
- (vi) Initial conditions.

In this problem,  $x$ ,  $z$  and  $t$  are the independent variables. The dependent variables are  $u$ ,  $v$ ,  $\psi$ ,  $T'$ ,  $q_l$  and  $q_v$ , where  $q_l$  and  $q_v$  are, respectively, the specific humidity of liquid water content and that of the water vapor. We need six equations for these six unknowns to close and solve this system. The principal numerical schemes needed for this modeling include a time differencing scheme for marching forward and a Poisson solver to obtain the streamfunction from vorticity. Details on such schemes can be found in texts on numerical methods such as Krishnamurti and Bounoua (1996).

The thermal energy equation is taken as

$$\frac{dT}{dt} = -w \frac{g}{C_p} + \left( \frac{dT}{dt} \right)_{ph} + \nu_T \nabla^2 T, \quad (11.16)$$

where

$$T = T_M + T_0(z) + T'. \quad (11.17)$$

$T_0(z)$  is the initial stratification of temperature of the undisturbed state and is known, and  $T_M$  is the (constant) mean domain value. Equation 11.16 describes the change of temperature  $T$  from which the changes of  $T'$  can be deduced.  $\left( \frac{dT}{dt} \right)_{ph}$  is the diabatic change of temperature due to phase change – either condensational heating or evaporative cooling. The changes in liquid water and water vapor respectively arising from phase changes and diffusion may be expressed by:

$$\frac{dq_l}{dt} = \left( \frac{dq_l}{dt} \right)_{ph} + \nu_q \nabla^2 q_l \quad (11.18)$$

$$\frac{dq_v}{dt} = \left( \frac{dq_v}{dt} \right)_{ph} + \nu_q \nabla^2 q_v \quad (11.19)$$

Equations 11.12 through 11.19 constitute a closed system provided the phase change terms are adequately defined. To that end, if  $q_v > q_{vs}$ , where  $q_{vs}$  is the saturation value, the disposition of supersaturation is parameterized from the relation

$$\left( \frac{dq_v}{dt} \right)_{ph} = -\frac{q_v - q_{vs}}{\Delta t} \quad (11.20)$$

Once saturation is reached, the local change for (11.19) is set to zero. Furthermore, one sets

$$\left( \frac{dq_l}{dt} \right)_{ph} = -\left( \frac{dq_v}{dt} \right)_{ph} \quad (11.21)$$

Thus saturation results in removal of water vapor and the formation of an equivalent amount of liquid water.

Liquid water in an unsaturated environment evaporates until the environment is saturated. This is expressed by

$$\left( \frac{dq_l}{dt} \right)_{ph} = -\frac{q_{vs} - q_v}{\Delta t} \quad (11.22)$$

This is the parameterization for the evaporative process. Again, an equivalent increase in water vapor in the water vapor equation is defined by the relation

$$\left( \frac{dq_v}{dt} \right)_{ph} = - \left( \frac{dq_l}{dt} \right)_{ph} \quad (11.23)$$

The condensation heating or evaporative cooling for the thermal equation is next defined by the statement

$$C_p \left( \frac{dT}{dt} \right)_{ph} = -L \left( \frac{dq_v}{dt} \right)_{ph} \text{ or } C_p \left( \frac{dT}{dt} \right)_{ph} = +L \left( \frac{dq_l}{dt} \right)_{ph} \quad (11.24)$$

Here one must use the appropriate sign for heating or cooling within the first law of thermodynamics.

The diffusion terms are needed for the suppression of computational waves which could otherwise grow to unrealistic sizes depending on the kind of numerical prediction algorithm one uses. This issue shall not be discussed here.

The system is now closed. The solution procedure involves the following steps:

- (i) An initial buoyancy and an initial state of no motion are specified to start the computation. The initial buoyancy can be in the  $T'$  field or it can be introduced via the moisture and thus in the initial horizontal gradient of virtual temperature.
- (ii) The vorticity (11.12) yields a new value of the stream function; this in turn gives the values of  $u$  and  $w$  from (11.13) and (11.14).
- (iii) The two moisture equations provide new values of  $q_l$  and  $q_v$ .
- (iv) The thermal (11.24) provide a prediction of the temperature  $T$  and thus the temperature deviation  $T'$  field

### 11.3.2 Initial and Boundary Conditions and Domain Definition

At  $x = 0$ , the horizontal gradient  $\partial/\partial x$  of all quantities is set to zero, and the stream function is a constant at  $z = 0$ ,  $z = z_T$  and  $x = x_R$  (the bottom, top and right boundaries of the domain). The perturbation temperature  $T'$  vanishes at these boundaries. The liquid water content is set to zero at the boundaries, and is also initially set to zero over the entire domain. Initially there is no horizontal gradient of water vapor  $q_v$  and carries an initial vertical stratification. The initial thermal stratification shows a conditional instability for the  $T_0(z)$  field in the lower troposphere. A perturbation in the  $T'$  field is used to introduce an augmentation of the virtual temperature that supplies the initial buoyancy perturbation necessary for the growth of convection.

The domain is an  $8,000 \text{ m} \times 8,000 \text{ m}^2$  within which there are grid points at every 250 m in the  $x$  and  $z$  directions. In the actual simulations of the cloud Murray and Anderson set  $\nu_M = 500 \text{ m}^2 \text{ s}^{-1}$  and  $\nu_q = \nu_T = 0$ . The time step for calculations is 15 s, which satisfies the linear stability criterion.

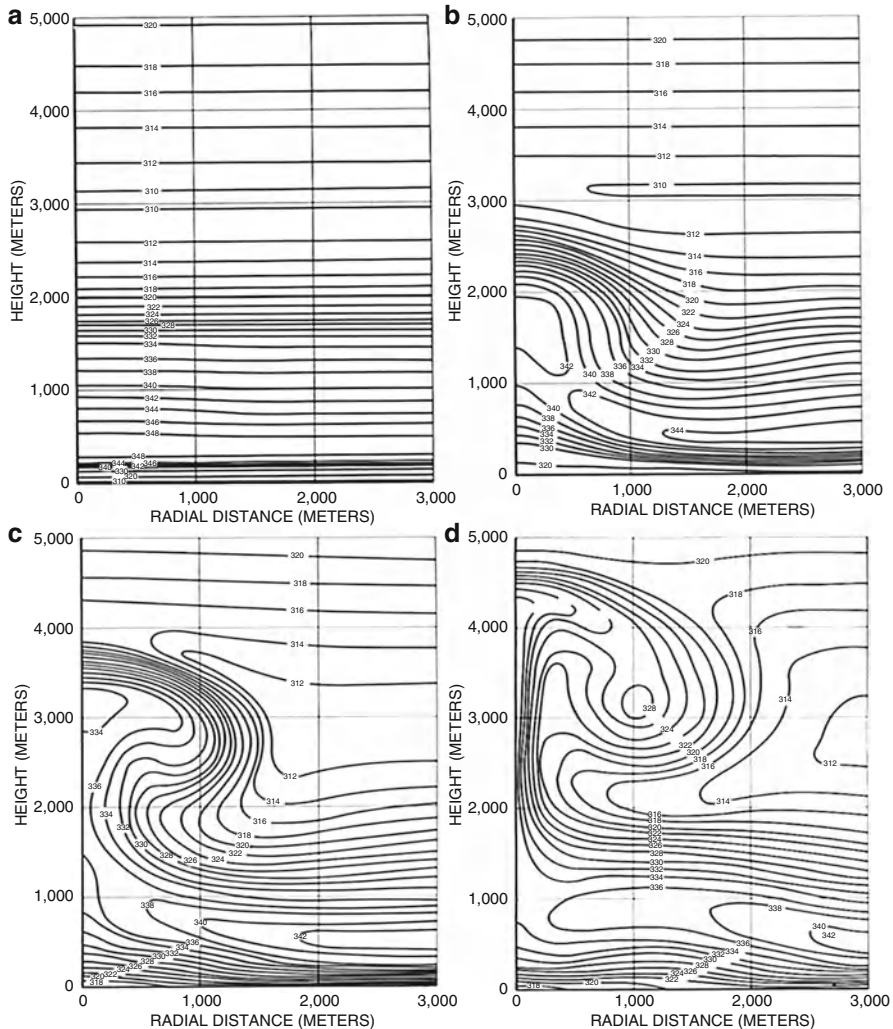
### 11.3.3 Numerical Model Results

Figure 11.3a–d shows the evolution of the equivalent potential temperature  $\theta_e$  at forecast times of 0, 10, 15, and 20 min from the beginning of integration. The initial state distribution of  $\theta_e$  has a minimum at the 3 km height. This initial state is conditionally unstable. Near the ground, in the lowest half kilometer, the initial state contains a stable layer. The initial buoyancy perturbation is placed above this surface stable layer to initiate the cloud growth. As time proceeds to 10, 15, and 20 min one sees the growth of the cloud streamfunction and the evolution of the  $\theta_e$  field. The distortion of the  $\theta_e$  isopleths by the evolving wind as a function of time is very impressive. This evolution reduces the overall conditional instability over the  $x$ - $z$  plane as the cloud grows within it. The  $x$ -averaged reduction of the slope of  $\theta_e$  is illustrated in Fig. 11.4. This shows that a single cloud can substantially reduce the conditional instability of the environment. Counteracting forcings must then come into play in order to restore the conditional instability of the large scale tropics (see Chap. 14).

The time history of vertical velocity and temperature departure at the axis of the cloud ( $x = 0$ ) is shown in Fig. 11.5a, b. These are height-time sections covering the life cycle of the model cloud. Figure 11.5a shows the evolution of the axis-centered vertical velocity  $w$  ( $\text{m s}^{-1}$ ) for 40 min of integration. The upward motion starts almost immediately, reaching a maximum value of nearly  $13 \text{ ms}^{-1}$  at a height of 2.8 km above the ground 14 min after the initial time. After that the cloud dies out by around 24 min. Thereafter mostly weak downward flows prevail. The attendant temperature departure  $T'$  (i.e., the warm and cold anomalies with respect to the initial state horizontal average of temperature) is shown in Fig. 11.5b. By around 12 min the latent heating provides a warm anomaly on the order of  $5^\circ\text{C}$  at a height of 2.8 km. After 16 min this warm core weakens and narrows to  $2^\circ\text{C}$  near the 3 km level.

A very interesting aspect of this cloud model is the buoyancy-induced overshooting of vertical motion. This overshooting of vertical motion above the cloud results in cloud evaporation and adiabatic cooling and a narrow cold cap above the cloud is seen. This cold cap has a temperature anomaly of  $-4^\circ\text{C}$  and lasts through roughly 28 min of integration.

Figure 11.6a–d shows the corresponding history of the growth of the streamfunction  $\psi$  on the  $x$ - $z$  plane (solid lines) and of the liquid water mixing ratio (dashed lines) for times 5, 10, 15, and 20 min. The isopleths for the liquid water mixing ratio starting at values  $\geq 0.4 \text{ g kg}^{-1}$  outline the shape of the model cloud (generally, visible clouds in the tropics have liquid water mixing ratios in excess of this threshold value). In the first 15 min of this time history one sees the



**Fig. 11.3** x-z cross-sections of the model potential temperature at time (a) top left 0, (b) top right 10, (c) bottom left 15, and (d) bottom right 20 min illustrating the evolution of the model moist shallow convection (From Murray et al. 1965)

spectacular growth of the model cloud and the associated circulation described by the streamfunction. Thereafter the cloud slowly starts to weaken. However, it remains active near the axis ( $x = 0$ ) at a height of near 3.5 km. At 20 min, the horizontal size of the cloud is around 1 km, and its vertical extent is about 4 km.

These numerical results can be regarded as a simulation of the life cycle of a shallow non-precipitating stratocumulus cloud.

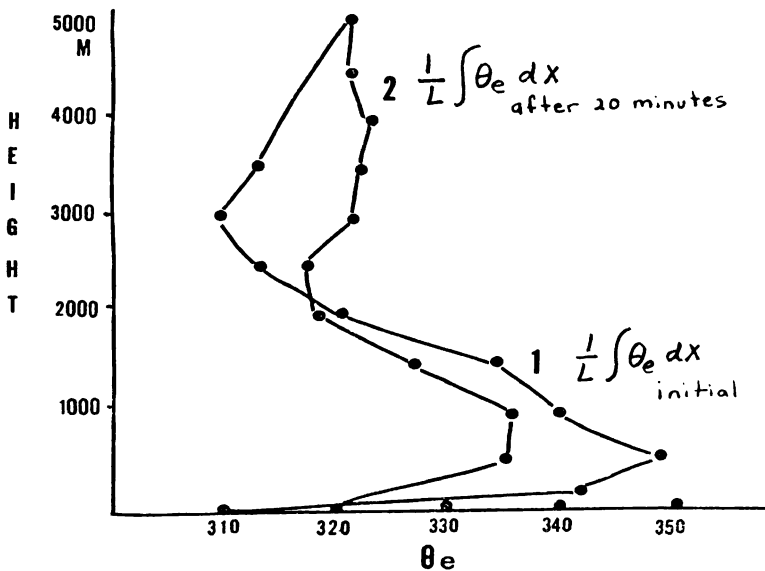


**Fig. 11.4** Vertical profiles of horizontally averaged potential temperature at the initial time and 20 min into the integration

## 11.4 A Cloud Ensemble Model

There are several cloud ensemble models that have been developed in recent years. These models include several forms of water substance, including vapor, liquid and ice phase. In this section we will provide a description of one such model that was developed by Tao and Simpson (1993).

### 11.4.1 Kinematics and Thermodynamics

The equation of state is given by

$$p = \rho RT(1 + 0.61q_v) \quad (11.25)$$

where  $p$ ,  $\rho$  and  $T$  are the pressure, density and temperature of the air, and  $(1 + 0.61q_v)$  is the virtual temperature correction for air with specific humidity  $q_v$ . In the following equations the Exner pressure  $\pi$  will be used; it is defined as

$$\pi = (p/p_0)^{R/C_p}, \quad (11.26)$$

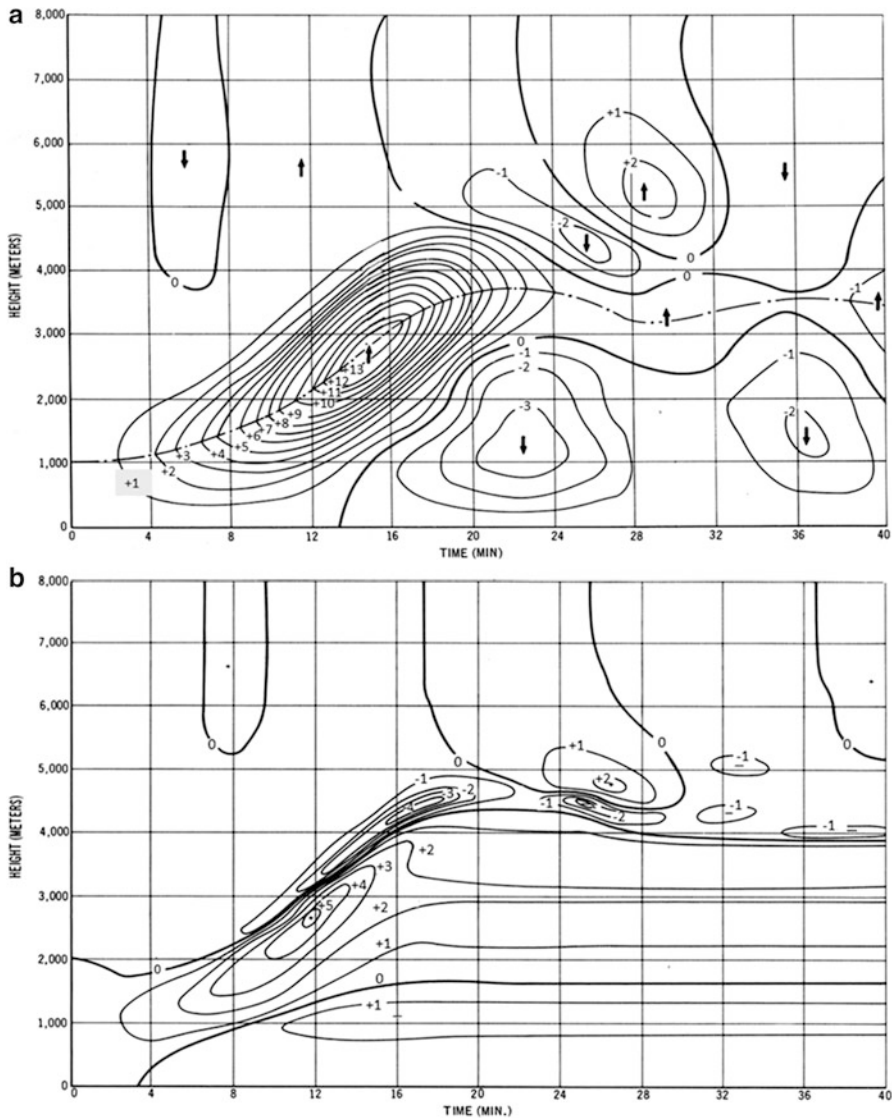


**Fig. 11.5** Time-height cross-sections of (a) top vertical velocity, and (b) bottom temperature departure. Centered at  $x = 0$  (From Murray and Anderson 1965)

where  $p_0$  is a reference pressure. The virtual potential temperature is defined as

$$\theta_v = \theta(1 + 0.61q_v) \quad (11.27)$$

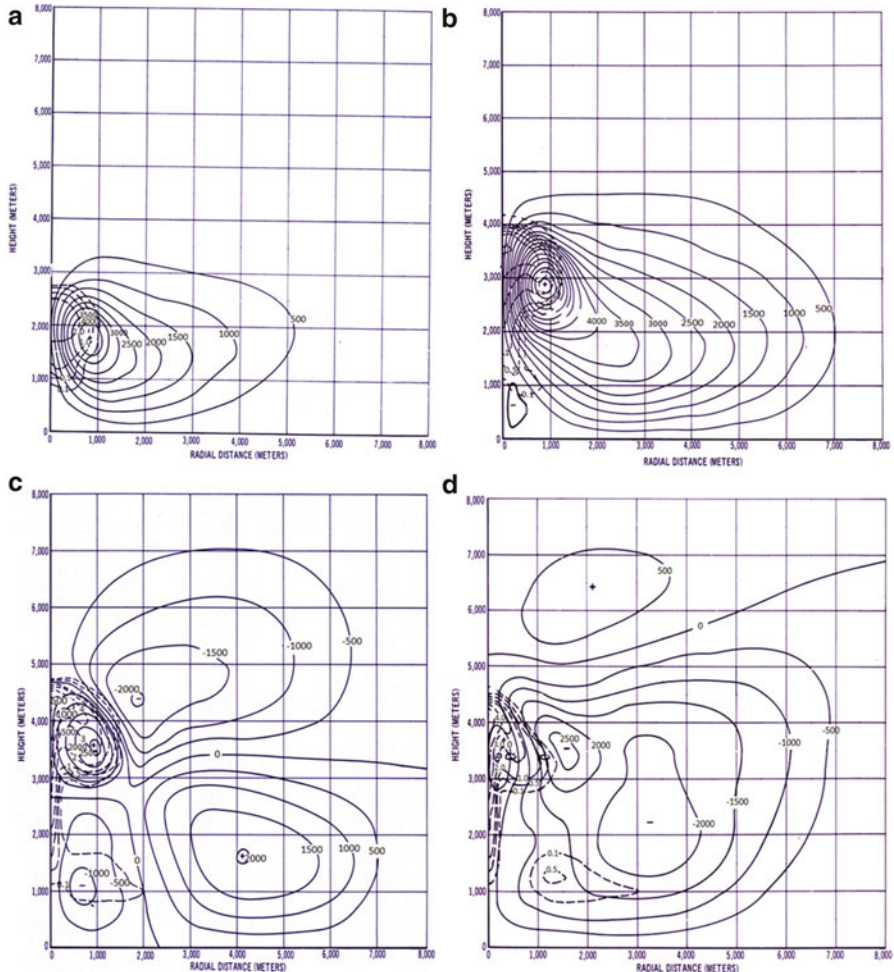


**Fig. 11.6** Streamlines (solid) and liquid water mixing ratio (dashed) at (a) 10, (b) 15, (c) 20 and (d) 25 min (From Murray and Anderson 1965)

Using the definition of potential temperature,  $\theta = T(p_0/p)^{R/C_p}$ , or in other words,  $\theta = T/\pi$ , the three equations of motion can be written as:

$$\frac{\partial u}{\partial t} = -\frac{\partial}{\partial x}(uu) - \frac{\partial}{\partial y}(uv) - \frac{1}{\bar{\rho}} \frac{\partial}{\partial z}(\bar{\rho}uw) - C_p \bar{\theta} \frac{\partial \pi'}{\partial x} + fv + D_u \quad (11.28)$$

$$\frac{\partial v}{\partial t} = -\frac{\partial}{\partial x}(uv) - \frac{\partial}{\partial y}(vv) - \frac{1}{\bar{\rho}} \frac{\partial}{\partial z}(\bar{\rho}vw) - C_p \bar{\theta} \frac{\partial \pi'}{\partial y} - fu + D_v \quad (11.29)$$

$$\frac{\partial w}{\partial t} = -\frac{\partial}{\partial x}(uw) - \frac{\partial}{\partial y}(wv) - \frac{1}{\bar{\rho}} \frac{\partial}{\partial z}(\bar{\rho}ww) - C_p \bar{\theta} \frac{\partial \pi'}{\partial z} + g \left( \frac{\theta'}{\theta} + 0.61q'_v - q_l \right) + D_w \quad (11.30)$$

In these equations  $u$ ,  $v$  and  $w$  are the zonal, meridional and vertical wind components;  $g$  is the acceleration of gravity;  $q_l$  is the mixing ratio of liquid water plus that of ice. Primes denote departures from the corresponding horizontal area-average. The horizontal area averages in turn are denoted by an overbar.  $D_u$ ,  $D_v$  and  $D_w$  are the momentum diffusion rates of the sub-grid scales in the three respective directions. The thermodynamic energy equation is written as

$$\begin{aligned} \frac{\partial \theta}{\partial t} = & -\frac{\partial}{\partial x}(u\theta) - \frac{\partial}{\partial y}(v\theta) - \frac{1}{\bar{\rho}} \frac{\partial}{\partial z}(\bar{\rho}w\theta) + D_\theta \\ & + \frac{L_v}{C_p}(c - e_c - e_r) + \frac{L_f}{C_p}(f_r - m) + \frac{L_s}{C_p}(d - s) + Q_R \end{aligned} \quad (11.31)$$

where  $L_v$ ,  $L_f$  and  $L_s$  denote, respectively, the latent heats of condensation, fusion and sublimation;  $c$ ,  $e_c$ , and  $e_r$  are the rates of condensation, evaporation of cloud water, and evaporation of cloud droplets respectively;  $f_r$  and  $m$  are the rates of freezing of raindrops and of melting of snow, graupel or hail;  $d$  and  $s$  are the rates of deposition and sublimation of ice particles.  $Q_R$  is the radiative heating or cooling, and  $D_\theta$  is the horizontal diffusion rate of potential temperature.

The equation for the specific humidity of water vapor can be written as

$$\frac{\partial q_v}{\partial t} = -\frac{\partial}{\partial x}(uq_v) - \frac{\partial}{\partial y}(vq_v) - \frac{1}{\bar{\rho}} \frac{\partial}{\partial z}(\bar{\rho}wq_v) + D_{q_v} - (c - e_c - e_r) - (d - s) \quad (11.32)$$

Here  $D_{q_v}$  is the horizontal diffusion rate for water vapor.

### 11.4.2 Cloud Microphysics

We will next address the water substance components of the model and their rates of growth. A drop size distribution function  $N(D)$  is assumed as

$$N(D) = N_0 e^{-\lambda D}$$

i.e. the number of drops  $N$  (per unit volume of space) of a given size  $D$  is inversely proportional to that size.  $N_0$ , the value of  $N$  at  $D = 0$ , is called an intercept parameter.  $\lambda$  is called the slope of the particle size distribution and is empirically expressed by

$$\lambda = \left( \frac{\pi \rho_x N_0}{\rho q_x} \right)^{1/4} \quad (11.33)$$

where  $\rho_x$  and  $q_x$  are the density and mixing ratio of the specific hydrometeor.

The model uses values of the intercept parameter for graupel, snow and rain that are around 0.04, 0.04 and 0.08 cm<sup>-4</sup> respectively. The densities for graupel, snow and rain are respectively 0.4 g cm<sup>-3</sup>, 0.1 g cm<sup>-3</sup> and 1 g cm<sup>-3</sup>. For cloud ice, the model assumes a single value of size with diameter of 2 × 10<sup>-3</sup> cm and a density of 0.917 g cm<sup>-3</sup>.

The prognostic equations for the components of the water substance include the following:

(a) Cloud water

$$\bar{\rho} \frac{\partial q_c}{\partial t} = -\frac{\partial}{\partial x}(\bar{\rho} u q_c) - \frac{\partial}{\partial y}(\bar{\rho} v q_c) - \frac{\partial}{\partial z}(\bar{\rho} w q_c) + \bar{\rho}(c - e_c) \\ - T_{qc} + D_{qc} \quad (11.34)$$

(b) Rain water

$$\bar{\rho} \frac{\partial q_r}{\partial t} = -\frac{\partial}{\partial x}(\bar{\rho} u q_r) - \frac{\partial}{\partial y}(\bar{\rho} v q_r) - \frac{\partial}{\partial z}[\bar{\rho} (w - V_r) q_r] + \bar{\rho}(-e_r + m - f_r) \\ - T_{qr} + D_{qr} \quad (11.35)$$

(c) Ice

$$\bar{\rho} \frac{\partial q_i}{\partial t} = -\frac{\partial}{\partial x}(\bar{\rho} u q_i) - \frac{\partial}{\partial y}(\bar{\rho} v q_i) - \frac{\partial}{\partial z}(\bar{\rho} w q_i) + \bar{\rho}(d_i - s_i) \\ - T_{qi} + D_{qi} \quad (11.36)$$

(d) Snow

$$\bar{\rho} \frac{\partial q_s}{\partial t} = -\frac{\partial}{\partial x}(\bar{\rho} u q_s) - \frac{\partial}{\partial y}(\bar{\rho} v q_s) - \frac{\partial}{\partial z}[\bar{\rho} (w - V_s) q_s] \\ + \bar{\rho}(d_s - s_s - m_s + f_s) - T_{qs} + D_{qs} \quad (11.37)$$

(e) Graupel

$$\bar{\rho} \frac{\partial q_g}{\partial t} = -\frac{\partial}{\partial x}(\bar{\rho} u q_g) - \frac{\partial}{\partial y}(\bar{\rho} v q_g) - \frac{\partial}{\partial z}[\bar{\rho} (w - V_g) q_g] \\ + \bar{\rho}(d_g - s_g - m_g + f_g) - T_{qg} + D_{qg} \quad (11.38)$$

On the right hand side of the above equations there are terms of the kind  $\bar{\rho}(c - e_c)$ ,  $\bar{\rho}(-e_r + m - f_r)$ ,  $\bar{\rho}(d_i - s_i)$ , etc. Taking (11.35) as an example,  $\bar{\rho} \frac{\partial q_r}{\partial t} = \dots + \bar{\rho}(-e_r + m - f_r) + \dots$ , the right hand side is interpreted as follows – evaporation ( $e_r$ ) and freezing ( $f_r$ ) reduce the mixing ratio of rain water  $q_r$ ,

therefore they figure in the equation with a minus sign; melting ( $m$ ) increases the mixing ratio of rain water, therefore it figures in the equation with a plus sign. Similar interpretation applies to the terms of this kind in all the above equations.

The transfer rates among the different hydrometeor species are denoted by  $T$  with the relevant subscript. These are expressed by the following equations:

$$T_{qc} = -\left(P_{sacw} + P_{raut} + P_{racw} + P_{sfw} + D_{gacw} + Q_{sacw}\right) - P_{ihom} - P_{imlt} - P_{idw} \quad (11.39)$$

$$T_{qi} = -\left(P_{saut} + P_{saci} + P_{raci} + P_{sfi} + D_{gaci} + W_{gaci}\right) + P_{ihom} - P_{imlt} + P_{idw} \quad (11.40)$$

$$T_{qr} = Q_{sacw} + P_{raut} + P_{racw} + Q_{gacw} - \left(P_{iacr} + D_{gacr} + W_{gacr} + P_{sacr} + P_{gfr}\right) \quad (11.41)$$

$$T_{qs} = P_{saut} + P_{saci} + P_{sacw} + P_{sfw} + P_{sfi} + \delta_3 P_{raci} + \delta_3 P_{iacr} + \delta_2 P_{sacr} - [P_{gacs} + D_{gacs} + W_{gacs} + P_{gaut} + (1 - \delta_2) P_{racs}] \quad (11.42)$$

$$T_{qg} = (1 - \delta_3) P_{raci} + D_{gaci} + W_{gaci} + D_{gacw} + (1 - \delta_3) P_{iacr} + P_{gacs} + D_{gacs} + W_{gacs} + P_{gaut} + (1 - \delta_2) P_{racs} + D_{gacr} + W_{gacr} + (1 - \delta_2) P_{sacr} + P_{gfr} \quad (11.43)$$

In these equations,

$$W_{gacr} = P_{wet} - D_{gacw} - W_{gaci} - W_{gacs}. \quad (11.44)$$

If the temperature is above freezing,

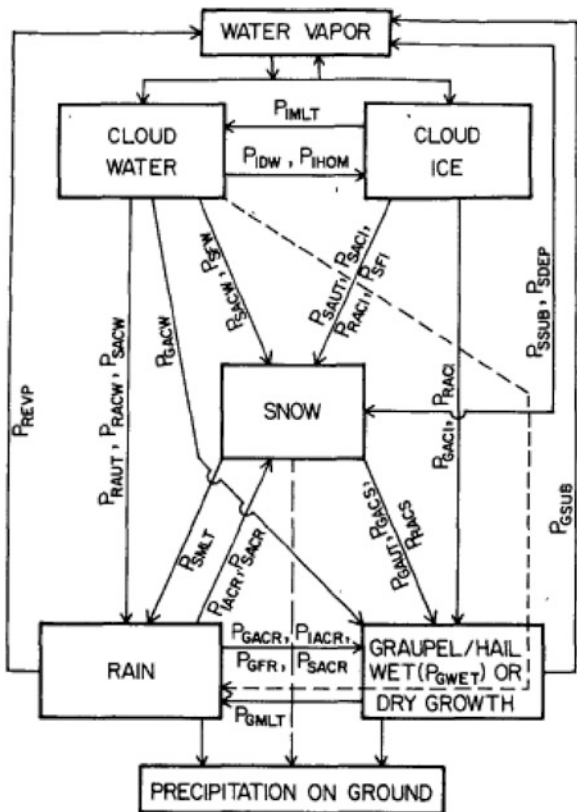
$$\begin{aligned} P_{saut} &= P_{saci} = P_{sacw} = P_{raci} = P_{iacr} = P_{sfi} = P_{sfw} = D_{gacs} = W_{gacs} \\ &= P_{gacs} = D_{gacr} = P_{gwet} = P_{racs} + P_{sacr} = P_{gfr} = P_{gaut} = P_{imlt} = 0, \end{aligned} \quad (11.45)$$

otherwise

$$Q_{sacw} = Q_{gacw} = P_{gacs} = P_{idw} = P_{ihom} = 0 \quad (11.46)$$

The symbols on the right hand sides of the equations for the transfer rates among different hydrometeor species (11.39) through (11.43) and in Eqs. 11.44 and 11.45 represent different processes as explained in Table 11.1 and illustrated schematically in Fig. 11.7. Each of these is explained in greater detail in Lin et. al. (1983) and Tao and Simpson (1993).

**Fig. 11.7** Cloud microphysical processes of the Goddard Cumulus Ensemble model (After Lin et al. 1983)



The three momentum equation (for  $u$ ,  $v$ ,  $w$ ), the first law of thermodynamics ( $\theta$ ), the water vapor equation for ( $q_v$ ) and the five microphysical process equation ( $q_c$ ,  $q_r$ ,  $q_i$ ,  $q_s$  and  $q_g$ ) constitute ten prognostic equations. The mass continuity and the equation of state bring in two more variables – the Exner pressure  $\pi$  (which is related to the pressure  $p$ ) and the density of air  $\bar{\rho}$ . In order to close this system of equations, the transfer rates that account for all conversion processes need to be calculated, usually by using suitable empirical parameterizations.

### 11.4.3 Conversion Processes

There are a number of conversion processes transforming one form of water within a cloud into another, as seen in (11.39) through (11.43) and Table 11.1. The transfer processes are generally modeled empirically based on microphysical field experiment results. The degree of empiricism and the number of parameters controlling the transfer are quite large. Cloud growth or decay in modeling studies is very

**Table 11.1** List of acronyms

Symbol	Meaning
$P_{dep}$	Depositional growth of cloud ice
$P_{int}$	Initiation of cloud ice
$P_{imlt}$	Melting of cloud ice to form cloud water
$P_{idw}$	Depositional growth of cloud ice at the expense of cloud water
$P_{ihom}$	Homogeneous freezing of cloud water to form cloud ice
$P_{iacr}$	Accretion of rain by cloud ice; producing snow or graupel depending on the amount of rain
$P_{raci}$	Accretion of cloud ice by rain; producing snow or graupel depending on the amount of rain
$P_{raut}$	Autoconversion of cloud water to form rain
$P_{racw}$	Accretion of cloud water by rain
$P_{revp} (e_r)$	Evaporation of rain
$P_{racs}$	Accretion of snow by rain; producing graupel if rain or snow exceeds threshold and $T < 273.16$ or rain if $T > 273.16$
$P(Q)_{sacw}$	Accretion of cloud water by snow; producing snow ( $P_{sacw}$ ) if $T < 273.16$ or rain ( $Q_{sacw}$ ) if $T > 273.16$
$P_{sacr}$	Accretion of rainby snow; producing graupel if rain or snow exceeds threshold; if not, produces snow
$P_{saci}$	Accretion of cloud ice by snow
$P_{saut}$	Autoconversion (aggregation) of cloud ice to form snow
$P_{sfw}$	Bergeron process (deposition and rimming) – transfer of cloud water to form snow
$P_{sfi}$	Bergeron process embryos (cloud ice) used to calculate transfer rate of cloud water to snow ( $P_{sfw}$ )
$P_{sdep} (d_s)$	Deposition growth of snow
$P_{ssub} (s_s)$	Sublimation of snow
$P_{smlt} (m_s)$	Melting of snow to form rain, $T > 273.16$
$P_{wacs}$	Accretion of snow by cloud water to form rain, $T > 273.16$
$P_{gaut}$	Autoconversion (aggregation) of snow to form graupel
$P_{gfr} (f_g)$	Probabilistic freezing of rain to form graupel
$D(Q)_{gacw}$	Accretion of cloud water by graupel
$D(W)_{gaci}$	Accretion of cloud ice by graupel
$D(W)_{gacr}$	Accretion of rain by graupel
$P_{gsub} (s_g)$	Sublimation of graupel
$P_{gmtl} (m_g)$	Melting of graupel to form rain, $T > 273.16$ . (In this regime $Q_{gacw}$ is assumed to be shed as rain)
$P_{gwet}$	Wet growth of graupel; may involve $W_{gacs}$ and $W_{gaci}$ and must include $D_{gacw}$ or $W_{gacr}$ , or both. The amount of $W_{gacw}$ which is not able to freeze is shed to rain

sensitive to the modeled values of these transfer processes. For illustrative purposes, parameterizations for three of these processes are described below.

(a) Autoconversion (cloudwater to rainwater,  $P_{raut}$ ):

This process consists of transforming the liquid water from cloud droplets to raindrops. Kessler (1969) formulated a simple parameterization of the role of

autoconversion of liquid water from raindrops with water content  $m$  (mass/volume) to raindrops with water content  $M$ . The autoconversion is formulated as

$$c_1 = \left[ \frac{\Delta q_l}{\Delta t} \right]_{auto} = k_a (q_c - q_{cr}) \quad (11.47)$$

and allows autoconversion process to take place only if the cloud water mixing ratio  $q_c$  is greater than a critical value  $q_{cr}$ . The values of  $q_{cr}$  and  $k_a$  used by Kessler are  $q_{cr} = 0.05 \text{ g kg}^{-1}$  and  $k_a = 0.001 \text{ s}^{-1}$

(b) Accretion (cloud water to rainwater,  $P_{racw}$ ):

The formulation of accretion follows Kessler (1969) and that of terminal velocity follows Srivastava (1967). After the embryonic rainfall droplets have been formed it is assumed that the water content converts into rain following an inverse exponential distribution function (Marshall-Palmer 1948)  $N(D) = N_0 e^{-\lambda D}$ , where  $N(D)$  is the number of raindrops per unit volume of diameter  $D$ , and  $\lambda = 3.67/D_0$ , where  $D_0$  is a threshold smallest diameter for the start of this process.

The cross-sectional area of the raindrop is  $\pi D^2/4$  and its terminal velocity is  $v_{TD}$  hence the volume swept by this raindrop per unit time is  $v_{TD}\rho q_c \pi D^2/4$ . The increase of mass of drops at each diameter is given by

$$\left[ \frac{\Delta q}{\Delta t} \right]_{acc} = \int_0^\infty v_{TD}\rho q_c \frac{\pi D^2}{4} N(D) dD \quad (11.48)$$

Assuming  $v_{TD} = 1500D^{1/2} \text{ cm s}^{-1}$  and integrating for all diameters, the relation used for the computation of accretion process is obtained as an exact solution of the integral above,

$$c_2 = \left[ \frac{\Delta q_l}{\Delta t} \right]_{acc} = \frac{1500\pi}{4} N_0 \rho \frac{\Gamma(3.5)}{\lambda^{3.5}} q_c \quad (11.49)$$

The rainwater mixing ratio is defined as

$$q_r = \int_0^\infty q_r D dD = \int_0^\infty N_0 e^{-\lambda D} \left[ \pi \frac{D^3}{6} \rho_w \right] dD \quad (11.50)$$

After integrating  $q_r = \pi \rho_w N_0 / \lambda^4$ , where  $\rho_w$  is the density of liquid water, the value of  $\lambda$  is obtained as an exact solution

$$\lambda = \left( \frac{4\pi\rho_w N_0}{q_r} \right)^{1/4} \quad (11.51)$$

Finally, from

$$v_T = \frac{\int_0^\infty q_{rD} v_{TD} dD}{\int_0^\infty q_{rD} dD} = \frac{\int_0^\infty q_{rD} v_{TD} dD}{q_r} \quad (11.52)$$

Substituting from (11.48) one finally obtains the final fall speed of raindrops as

$$v_T = \frac{1}{\pi \rho_w N_0 \lambda^{-4}} \int_0^\infty N_0 e^{-\lambda D} \left( \frac{\pi D^3}{6} \right) \rho_w 1500 D^{1/2} dD \quad (11.53)$$

Or, after solving the above integral exactly,

$$v_T = 1500 \Gamma(4.5) / \lambda^{1/2} \Gamma(4) \quad (11.54)$$

(c) Evaporation (cloud water to vapor,  $P_{revp}$ ):

The evaporation process follows to some extent the format of Murray and Anderson (1965) If the air is saturated the rate of change of the saturation mixing ratio of water vapor is the same as the rate of change of the saturation mixing ratio. On the basis of conservation of equivalent potential temperature under conditions of saturation mixing ratio is

$$\frac{dq_{vs}}{dt} = -Bw \quad (11.55)$$

and

$$B = \frac{1 - \frac{1}{\epsilon L} (C_p T - L q_{vs})}{C_p R T^2} g \quad (11.56)$$

$$L + \frac{L q_{vs} (\epsilon + q_{vs})}{C_p R T^2}$$

where  $\epsilon = 0.62195$  is the molecular weight of water vapor/molecular weight of dry air,  $L = 2.5 \times 10^6 \text{ J kg}^{-1}$  is the latent heat of evaporation, and  $C_p = 1,004 \text{ J kg}^{-1} \text{ K}^{-1}$  is the specific heat capacity of dry air. The amount of local change in the water vapor mixing ratio is then

$$\Delta q_v = -Bw \Delta t \quad (11.57)$$

In the case of upward motion this represents condensation and is accompanied by an equal and opposite change in cloud water mixing ratio and an increase in temperature, i.e.,

$$\Delta q_c = -\Delta q_v \quad (11.58)$$

$$\Delta T = \frac{L}{C_p} \Delta q_c \quad (11.59)$$

In the case of downward motion of saturated air, the same treatment is used. The increase of mixing ratio, however, accompanying this change is done through evaporation of cloud and/or rain. If cloud water is sufficient to accomplish this change, no rainwater is evaporated. If the cloud water is insufficient some rainwater is evaporated until the sum of cloud water and rainwater evaporation is enough to accomplish the change computed in (11.55).

#### 11.4.4 Modeling Results

In this section we will show some results from Tao and Simpson (1993) and McCumber et al. (1991). These results pertain to some aspects of cloud microphysical sensitivity to the passage of a tropical squall line. This squall line propagated from West Africa into the eastern Atlantic Ocean.

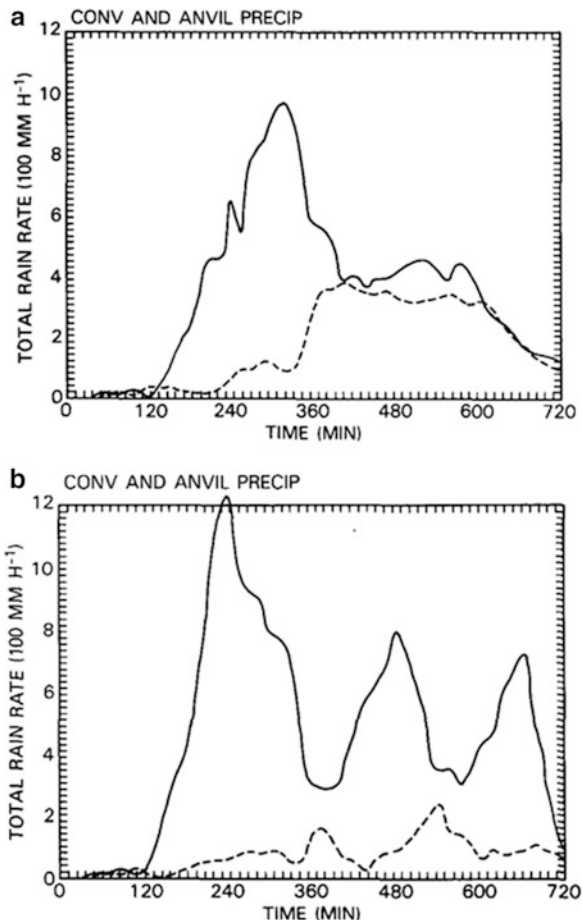
Microphysical sensitivity experiments show some interesting differences from the inclusion versus non inclusion of the ice phase. One of the results was the partitioning of the convective and anvil rain. These results covering a simulated domain of a squall line are shown in Fig. 11.8a, b. When ice phase is excluded the quantitative amount of heavy precipitation increases significantly (and unrealistically). The inclusion of ice brings this heavy precipitation to values that are an order of magnitude smaller and in agreement with observations. The depths of stratiform clouds were considerably reduced when ice was not included (Fig. 11.9a, b). The ice free run lacks a well defined anvil and also carries excessive cellular precipitating towers. This experiment without ice phase also conveyed a slower propagation speed for the squall line.

By using microphysics schemes with varying densities and intercept parameters for the different hydrometeors, one can study the sensitivity of cloud simulations to the distribution and parameterization of hydrometeors.

McCumber et al. (1991) used two experiments with different schemes for modeling the ice phase of water within the cloud. The schemes that he used were:

1. A graupel-only scheme, after Rutledge and Hobbs (1984), which has graupel and snow but no hail processes.
2. A hail-only scheme, after Lin et al. (1983), which has snow and hail but no graupel processes.

**Fig. 11.8** Total rain intensity integrated over the grid points designated as the convective and stratiform (anvil) regions from (a) ice run, and (b) ice-free run (Adapted from McCumber et al. 1991)



The main difference between graupel and hail is in the hydrometeors' density – the respective values are  $0.4 \text{ g cm}^{-3}$  and  $0.9 \text{ g cm}^{-3}$  – and in their size (graupel particles are generally much smaller).

In the graupel-only case (Fig. 11.10a) the vertical distribution of hydrometeors shows a predominance of graupel over snow particles in the convective and anvil regions. This is a result of the graupel particles being smaller than the snow particles and thus falling more slowly. As a consequence, in the graupel-only case, the melting and deposition of snow are second-order processes. In the hail-only case (Fig. 11.10b), because of the formation and rapid fall out of the hail stones, snow becomes the dominant precipitating hydrometeor within the anvil cloud. This large amount of snow accounts for larger amounts of melting and deposition of snow.

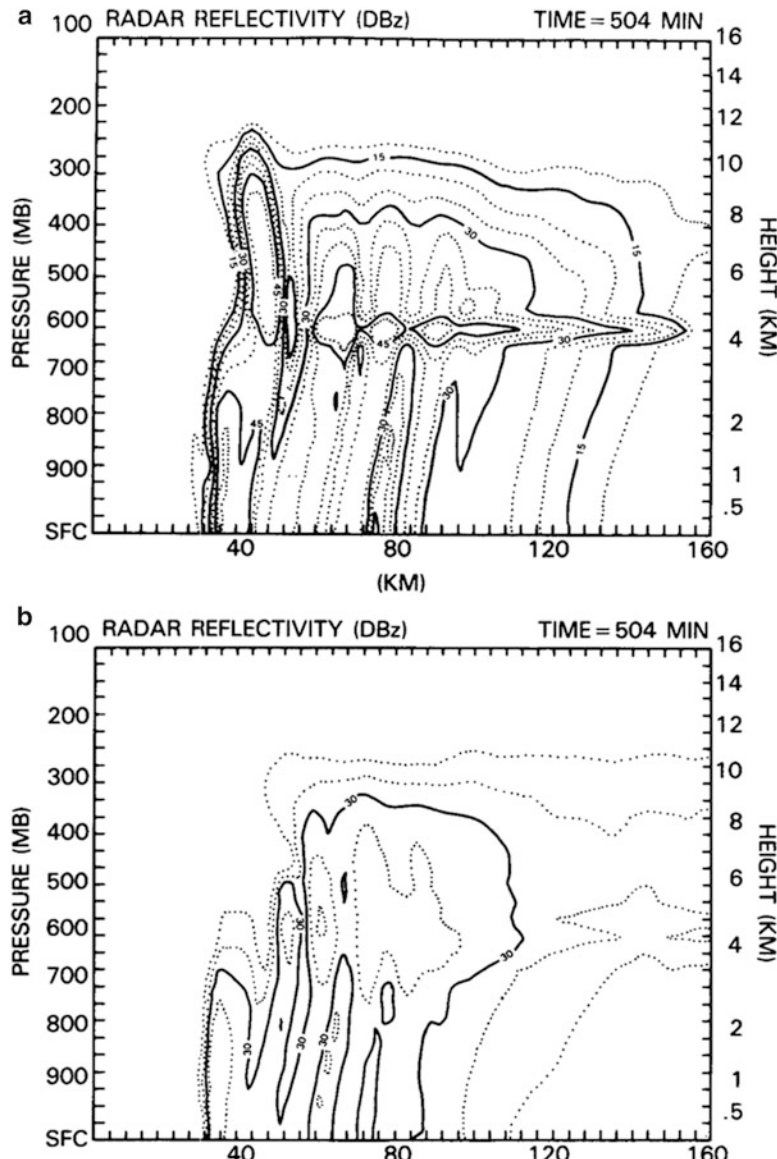


**Fig. 11.9** Vertical cross-section of a simulated tropical squall-type convective line at its mature stage from (a) ice run and (b) ice free run. The contour intervals show radar reflectivity at 5dBZ interval beginning from 10dBZ; contours are highlighted at intervals of 15dBZ. From McCumber et al. (1991)

The heating/cooling profiles along the vertical from the above two sensitivity experiments for a tropical squall type convective system are shown in Fig. 11.11b. The hail-only experiment is seen to be characterized by less

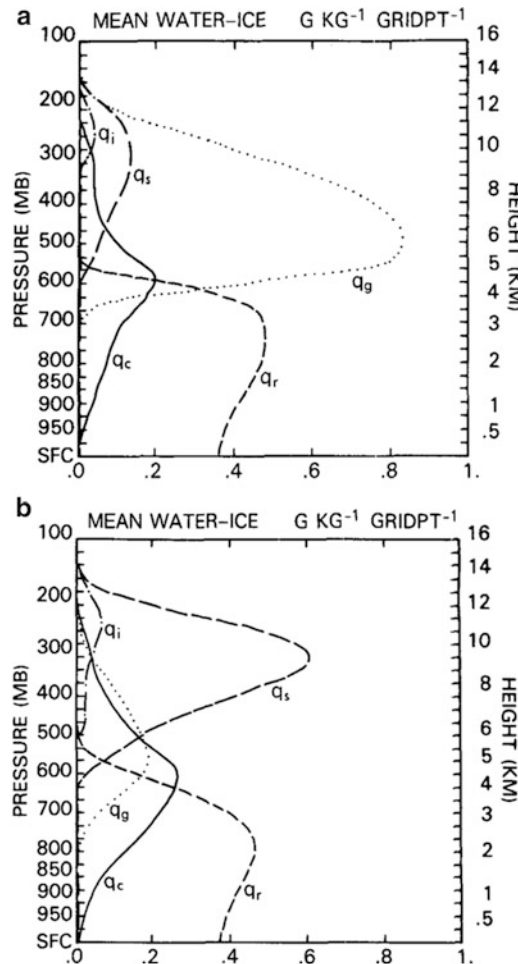
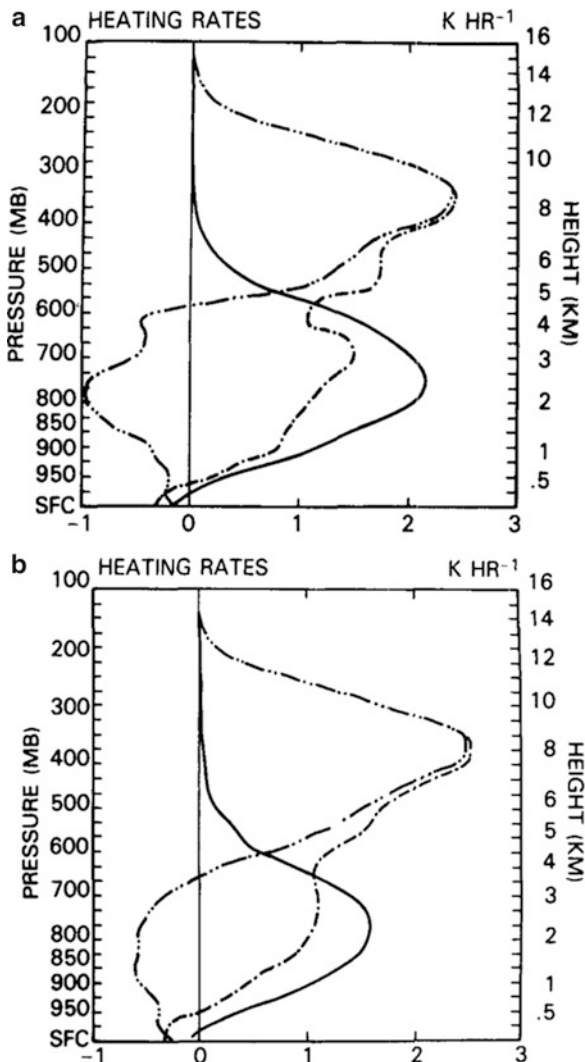


**Fig. 11.10** Mean water and ice hydrometeors (g/kg per grid pint) depicted as a function of height for tropical squall system simulations. The curves for the hydrometeors shown are rain ( $q_r$ , short dash), cloud water ( $q_c$ , solid), graupel/hail ( $q_g$ , dotted), cloud ice ( $q_i$ , dot-dash), and snow ( $q_s$ , long dash). The units in the figure are normalized with respect to the number of horizontal model grid points. (The unnormalized units are obtained by multiplying by 512 km). The top panel shows results from the graupel-only experiment, while the bottom panel shows results from the hail-only experiment (From McCumber et al. 1991)

diabatic cooling in the lower troposphere compared to the significant cooling in the graupel-only experiment (Fig. 11.11a). The cooling in the hail-only case is mainly attributed to the evaporation of rain and melting of snow (which falls more slowly than hail) and for the graupel-only case there is large scale melting of graupel in the lower troposphere which leads to enhanced lower tropospheric cooling.

**Fig. 11.11** Convective heating profiles ( $\text{K/h}$ ) computed for the last 5 h of 2D simulations for tropical squall type convective lines. Shown are the heating in the convective region (*solid*), heating in the anvil region (*double dot-dash*), and the total heating (*dot-dash*). (a) Graupel-only case, and (b) hail-only case (From McCumber et al. 1991)



## References

- Kessler, E.: On the distribution and continuity of water substance in atmospheric circulation. *Meteor. Monogr.* No **32**, Amer. Meteor. Soc., 84pp (1969)
- Krishnamurti, T.N., Bounoua, L.: An Introduction to Numerical Weather Prediction Techniques. CRC Press, Boca Raton (1996). 293pp
- Lin, Y.L., Farley, R., Orville, H.D.: Bulk parameterization of the snow field in a cloud model. *J. Climate Appl. Meteor.* **22**, 1065–1092 (1983)
- Malkus, J.S., Witt, G.: The Evolution of a Convective Element: A Numerical Calculation. *The Atmosphere and the Sea in Motion*, pp. 425–439. The Rockefeller Institute Press, New York (1959)

- Marshall, J.S., Palmer, W.M.K.: The distribution of raindrops with size. *J. Meteor.* **5**, 165–166 (1948)
- McCumber, M., Tao, W.-K., Simpson, J., Penc, R., Soong, S.-T.: Comparison of ice-phase microphysical parameterization schemes using numerical simulations of convection. *J. Appl. Meteor.* **30**, 985–1004 (1991)
- Murray, F.W., Anderson, C.E.: Numerical Simulation of the Evolution of Cumulus Towers, *Report SM-49230*, Douglas Aircraft Company, Inc., Santa Monica, 97pp (1965)
- Nickerson, E.C.: A numerical experiment in buoyant convection involving the use of a heat source. *J. Atmos. Sci.* **22**, 412–418 (1965)
- Rutledge, S.A., Hobbs, P.V.: The mesoscale and microscale structure and organization of clouds and precipitation in mid-latitude clouds. Part XII: a diagnostic modeling study of precipitation development in narrow cold frontal rainbands. *J. Atmos. Sci.* **41**, 2949–2972 (1984)
- Srivastava, R.C.: A study of the effects of precipitation on cumulus dynamics. *J. Atmos. Sci.* **24**, 36–45 (1967)
- Tao, W.-K., Simpson, J.: The Goddard Cumulus ensemble model. Part I: model description. *Terr. Atmos. Oceanic Sci.* **4**, 19–54 (1993)

# Chapter 12

## Tropical Boundary Layer

In this chapter we shall present a brief outline of the tropical boundary layer. This is the region of the atmosphere where the air/sea and air/land interactions take place and the surface fluxes of heat, momentum and moisture are generated and vertically distributed. Its structure is very important for studies of tropical convection and tropical disturbances, especially hurricanes, the ITCZ, waves and low-level jets, all of which require a detailed knowledge of the lowest 1 km of the atmosphere.

The boundary layer is characterized by strong turbulence and vertical mixing, which distribute the surface fluxes throughout its depth. Low clouds whose bases are close (about 1 km) to the land or ocean surface also help shape the boundary layer structure through downdrafts resulting from their internal circulations.

Compared to the ocean boundary layer, the boundary layer over land areas is more complex and less spatially homogeneous, due to the high variability in land surface characteristics. These characteristics play a significant role in determining the surface energy balance, and the fluxes of heat, momentum and moisture.

In this chapter we shall begin with the current status of observational knowledge. Some of the material presented here, although elementary, requires some knowledge of tropical convection. We shall also present some empirical and dynamical aspects of the tropical boundary layer in this chapter. The rapid advances of observational, theoretical, modeling and numerical approaches in the field make it difficult to present a complete picture here and only an overview is given.

### 12.1 Empirical Concepts

#### 12.1.1 *The Mixing-Length Concept*

A zonal wind perturbation  $u'$  at height  $z$  is the difference between the value of the mean zonal wind  $\bar{u}$  at  $z$  and its value at some distance away at a level  $z + l$ , i.e.,

$$u' = \bar{u}(z + l) - \bar{u}(z). \quad (12.1)$$

A Taylor expansion of  $u'$  around  $z$  gives

$$u' \approx l \frac{\partial \bar{u}(z)}{\partial z}. \quad (12.2)$$

The quantity  $l$  is representative of the local intensity of turbulence. Similar expressions can be written for  $\theta'$ ,  $v'$ ,  $w'$  and the moisture variable  $q'$ . If the flow is fully turbulent in three dimensions, then

$$|u'| \approx |v'| \approx |w'|, \quad (12.3)$$

And hence

$$w' \approx l \left| \frac{\partial \bar{u}}{\partial z} \right|. \quad (12.4)$$

The upward flux of momentum can be written as

$$F_u = \rho \overline{w' u'} = -\rho l^2 \left( \frac{\partial \bar{u}}{\partial z} \right) \left| \frac{\partial \bar{u}}{\partial z} \right| \quad (12.5)$$

(the minus sign is introduced to ensure that the flux is positive down the flux gradient.)

The above formula gives a parameterization of the turbulent flux of momentum as a function of the variation of  $\bar{u}$ . However, it should be noted that  $\bar{u}$  varies very rapidly near the ground. Hence, it is still necessary to have some means of defining the profile of  $\bar{u}$ .

### 12.1.2 The Wind Profile and Surface Drag

Near the ground one assumes that the mixing length is not related to the scale length of the large scale flow. It is assumed to be proportional to the distance from the ground, i.e.,

$$l \approx \kappa z \quad (12.6)$$

The coefficient  $\kappa$  is the von Karman constant. The concept of friction velocity  $u^*$  is defined by the relation

$$u^* = \left( - \frac{F_{u0}}{\rho} \right)^{1/2} \quad (12.7)$$

where  $\rho$  is the density of air and  $F_{u0}$  is the upward surface momentum flux. Since

$$F_{u0} = \rho \overline{w' u'} = -\rho l^2 \left( \frac{\partial \bar{u}}{\partial z} \right) \left| \frac{\partial \bar{u}}{\partial z} \right|, \quad (12.8)$$

we may write

$$-\frac{F_{u0}}{\rho} = l^2 \left( \frac{\partial \bar{u}}{\partial z} \right) \left| \frac{\partial \bar{u}}{\partial z} \right|, \quad (12.9)$$

or

$$u^{*2} = \left( \kappa z \frac{\partial \bar{u}}{\partial z} \right)^2. \quad (12.10)$$

From this is obtained the logarithmic law:

$$\bar{u}(z) = \frac{u^*}{\kappa} \ln \left( \frac{z}{z_0} \right), \quad (12.11)$$

where  $z_0$ , the roughness length, is a characteristic of the underlying surface, and is formally defined as the height at which the logarithmic wind profile goes to zero. The roughness length defines a length scale representative of the resistance that surface roughness elements offer to the turbulent flow. Empirical values are generally used for  $z_0$  over tropical oceans ( $\sim 0.4$ ), flat land areas ( $\sim 1.0$ ) and mountains ( $\sim 10.0$ ).

This formula relates the surface stress to the mean wind profile  $\bar{u}(z)$  in the lowest layers, since

$$\bar{u}(z) = \left( -\frac{F_{u0}}{\rho} \right)^{1/2} \frac{1}{\kappa} \ln \left( \frac{z}{z_0} \right). \quad (12.12)$$

If values for the von Karman constant  $\kappa$  and the surface roughness  $z_0$  are assumed, the above equation allows one to calculate  $\bar{u}(z)$ . The profile method can be used to estimate the magnitudes of turbulent momentum fluxes  $\overline{u' w'}$ . The procedure consists of making detailed measurements of the profile of  $\bar{u}(z)$  from ship-tethered balloons, masts or towers. Knowing  $\bar{u}(z)$ , an estimate of  $\overline{u' w'}$  is usually made from the relation  $\overline{u' w'} = -\rho l^2 \left( \frac{\partial \bar{u}}{\partial z} \right) \left| \frac{\partial \bar{u}}{\partial z} \right|$ . Profile methods can also be used to estimate turbulent fluxes of heat and moisture.

### 12.1.3 Bulk Aerodynamic Method

The bulk aerodynamic formulae relate stresses and fluxes of moisture and heat to large scale variables. These are based on experiments carried over ponds by G. I. Taylor back in the 1910s. The flux  $F_A$  of a quantity  $A$  from the earth's surface to the atmosphere is generally expressed by formulae of the type

$$F_A = C|\mathbf{V}_a|(A_s - A_a), \quad (12.13)$$

where  $C$  is a dimensionless parameter called a bulk aerodynamic coefficient or exchange coefficient,  $|\mathbf{V}_a|$  is the wind speed measured at the anemometer level (i.e., 10 m above the ground), and  $A_s$  and  $A_a$  denote the relevant flux variable measured at the earth surface and at the anemometer level respectively. Note that this formulation is such that a positive sign of  $F_A$  indicates an upward flux of  $A$ , while a negative sign indicates a downward flux.

For most tropical meteorological problems the recommended bulk aerodynamic formulae are

$$F_M = -C_M \rho |\mathbf{V}_a|^2 \quad (12.14)$$

for the momentum flux,

$$F_{SH} = C_S \rho C_p |\mathbf{V}_a| (T_s - T_a) \quad (12.15)$$

for the sensible heat flux, and

$$F_{LH} = C_L \rho L |\mathbf{V}_a| (q_s - q_a) \quad (12.16)$$

for the latent heat flux. Here  $T_s$  and  $q_s$  are the surface values of the temperature and specific humidity respectively, while  $T_a$  and  $q_a$  are the corresponding anemometer level values.  $C_p$  is the specific heat of air at constant pressure,  $L$  is the latent heat of evaporation, and  $\rho$  is the air density. Some standard values for the exchange coefficients ( $C_M$  for the momentum – often called a drag coefficient,  $C_S$  for the sensible heat, and  $C_L$  for the latent heat) are  $C_M = 1.1 \times 10^{-3}$ ,  $C_S = 1.4 \times 10^{-3}$ , and  $C_L = 1.6 \times 10^{-3}$ . The fluxes are normally expressed in units of  $\text{N m}^{-2}$  for the momentum, and  $\text{W m}^{-2}$  for the latent and sensible heat. A set of useful working formulae for calculating these fluxes is

$$F_M = -1.35 \times 10^{-3} |\mathbf{V}_a|^2, \quad (12.17)$$

$$F_{SH} = 1.72 |\mathbf{V}_a| (T_s - T_a), \quad (12.18)$$

and

$$F_{LH} = 4.9 \times 10^{-2} |\mathbf{V}_a| (q_s - q_a) \quad (12.19)$$

Here the anemometer level wind speed  $|\mathbf{V}_a|$  must be given in units of  $\text{ms}^{-1}$ ,  $T_s$  and  $T_a$  in units of K, and  $q_s$  and  $q_a$  in units of  $\text{g kg}^{-1}$  in order to get units of  $\text{N m}^{-2}$  for the momentum flux and units of  $\text{W m}^{-2}$  for the latent and sensible heat fluxes.

The bulk aerodynamic formulae shown above were designed for neutral stability conditions and wind speeds less than  $5.8 \text{ m s}^{-1}$ . For winds in excess of  $5.8 \text{ m s}^{-1}$  the drag coefficient is altered, based on empirical experience, as follows:

$$C_M = \begin{cases} C_{M0} = 1.1 \times 10^{-3} & \text{for } |\mathbf{V}_S| < 5.8 \text{ ms}^{-1} \\ C_{M0}(0.74 + 0.046|\mathbf{V}_S|) & \text{for } 5.8 \text{ ms}^{-1} \leq |\mathbf{V}_S| \leq 16.8 \text{ ms}^{-1} \\ C_{M0}(0.94 + 0.034|\mathbf{V}_S|) & \text{for } |\mathbf{V}_S| > 16.8 \text{ ms}^{-1} \end{cases} \quad (12.20)$$

Such accounting for the change in the value of the drag coefficient  $C_M$  with higher wind speeds is necessary when dealing with the high winds associated with tropical storms and hurricanes.

## 12.2 Observational Aspects of the Boundary Layer

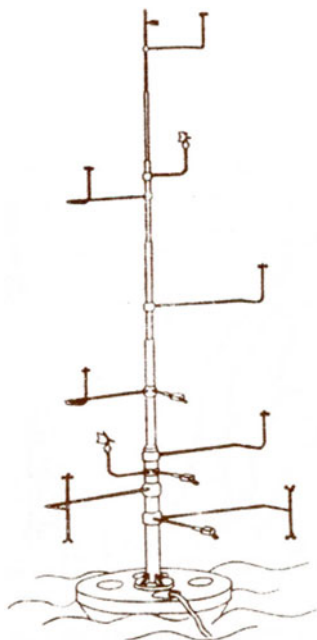
Observational studies of the turning of wind with height show that veering (turning clockwise with height) essentially dominates the flows north of the ITCZ in the northern hemisphere and backing (turning counterclockwise with height) is generally found south of the ITCZ. Historically, this was documented by data from the Line Island Experiment ( $2^\circ\text{N}$  to  $6^\circ\text{N}$  and  $157^\circ\text{W}$  to  $162^\circ\text{W}$ ) by Robitaille and Zipser (1970) and also by Estoque (1971) from the Christmas Island data.

The tropical boundary layer characteristics in clear areas, in undisturbed areas with shallow convection and in disturbed areas are generally found to be quite different from one another.

In the clear or undisturbed trade wind regions the tropical boundary layer is known to have the following well-defined layers:

- (i) A surface layer in the lowest 20 m where one finds a slight upward decrease of potential temperature and a decrease of moisture
- (ii) A mixed layer from a height of 20 m above the surface to approximately 100 m below the cloud base in which the potential temperature is nearly constant with height and the moisture content decreases only slightly with height.
- (iii) A transitional layer located just above the well-mixed layer below the cloud base. Here we note a stable layer with an increase of potential temperature and a decrease of moisture with height. This is usually a very thin layer with a thickness on the order of 100 m or less.
- (iv) A cloud layer usually several hundred meters deep where the moisture is still decreasing with height, the observed lapse rate in this region being close to the moist adiabatic lapse rate.

**Fig. 12.1** A schematic of a classical oceanic buoy for atmospheric observation



- (v) An inversion layer on top of the cloud layer in which the potential temperature increases rapidly and the moisture decreases rapidly with height. Its base can be regarded as a reference level that defines the thickness of the boundary layer.

During the summer of 1977 some early observational findings in the planetary boundary layer of the Eastern Atlantic (the GATE Experiment) were reported by a number of researchers in the field (J. Businger, W. Seguin, E. Augstein, M. Garstang, P. Lemone and others). A short summary of their important findings will be presented here. During the GATE experiment the boundary layer of the tropical trade wind and ITCZ region was explored using ships, buoys, tethered balloons and research aircraft. The methods used for determining fluxes in the lowest kilometer included the bulk aerodynamic method, the profile method, the budget method, and the dissipation method.

Figure 12.1 illustrates the Meteor Profile Buoy that was used in the GATE experiment. Instruments are mounted to measure profiles as well as eddy correlations at several heights in the lowest 8 m. These types of buoys are extremely useful for determining the vertical structure of the boundary layer near the surface. The vertical profiles of fluxes of momentum, heat, and moisture for the lowest several hundred meters can be obtained from towers, tethered balloons, and low flying aircraft. It should be noted that there are different types of errors that can arise in such types of measurements due to the orientation of the mast, rainfall on the anemometers and the effects of ocean waves. The methodology for flux

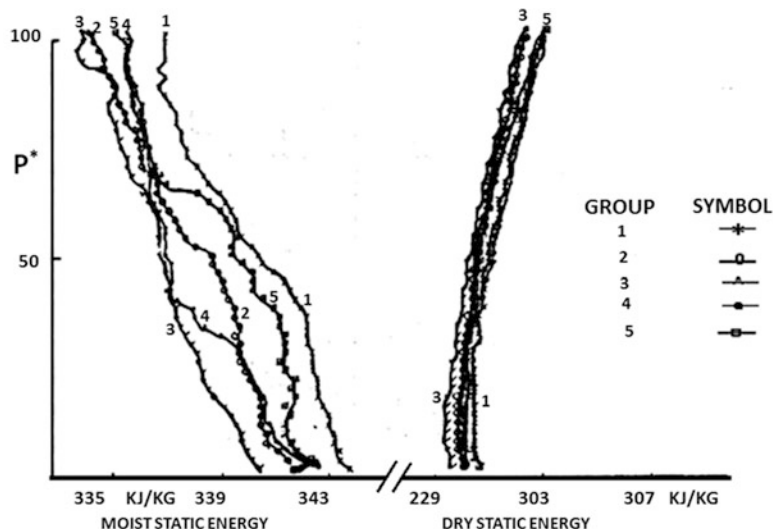


**Fig. 12.2** Mean vertical structure of moist and dry static energy by stage

correction is the eddy correlation method. These eddy correlations can be done in space and time as desired.

Based on radar measurements, Garstang and his co-workers define five echo categories associated with different stages of a disturbance passage to illustrate the behavior of the boundary layer. They can be defined as (1) stationary radar echoes with no precipitation, (2) growing radar echoes with precipitation, (3) decaying radar echoes, (4) disturbance wakes with no precipitation, and (5) stationary radar echoes with moderate convection.

The first stage signifies an undisturbed situation, the second stage – the arrival of a disturbance, the third stage – the period just after the passage of a disturbance, the fourth stage – the wake some time after the disturbance passage, and the final stage signifies a state close to the undisturbed situation. Figure 12.2 illustrates the mean vertical structure in the lowest 100 mb layer of the dry and moist static energy. (These parameters are defined in Chap. 14). The moist static energy shows a substantial decrease from the undisturbed to the disturbed stage in the lowest kilometer. The restoring of the mixed layer occurs with a gradual increase of static energy sequentially by classes. The dry static energy also shows a decrease as the disturbed state arrives over a station. Garstang also reported that the winds gradually increase in the lowest kilometer from the undisturbed state (1) to the disturbed state (3).

Figure 12.3a, b show typical sea surface fluxes during GATE of the buoyancy, sensible heat and latent heat in undisturbed and disturbed conditions. We note here that the buoyancy flux increases from roughly  $25 \text{ Wm}^{-2}$  to about  $40 \text{ Wm}^{-2}$  from the undisturbed to the disturbed state. The corresponding increase for sensible heat flux is from  $10 \text{ Wm}^{-2}$  to about  $40 \text{ Wm}^{-2}$  while for the latent heat flux it is from

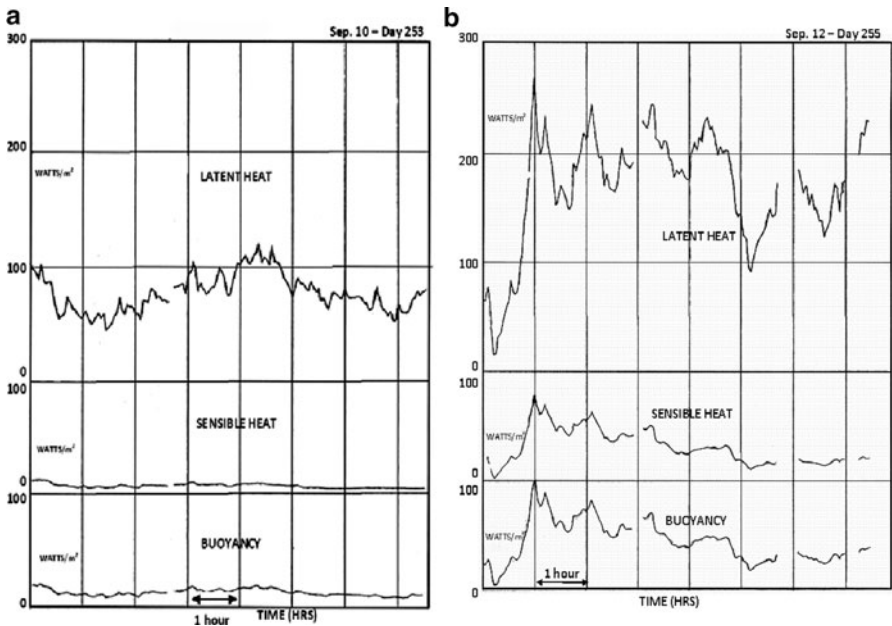


**Fig. 12.3** Sea surface fluxes during (a) undisturbed and (b) disturbed conditions (From Garstang 1977)

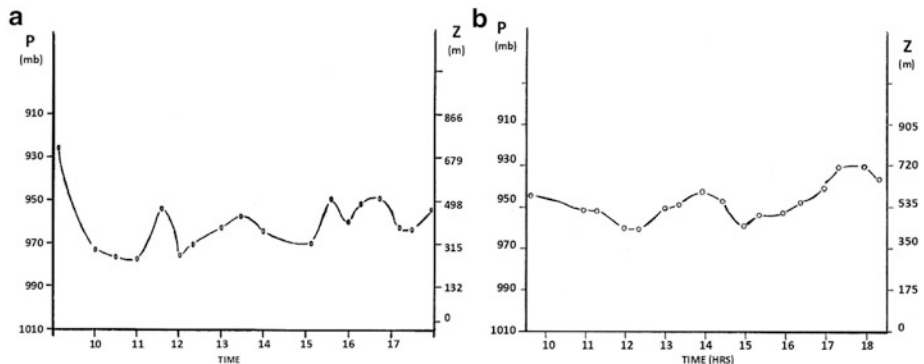


**Fig. 12.4** Dallas BLIS, height of the (a) undisturbed and (b) disturbed mixed layer (From Garstang 1977)

roughly  $80 \text{ Wm}^{-2}$  to  $200 \text{ Wm}^{-2}$ . This is consistent with the gradual increase of the surface wind speed alluded to earlier.

The height of the mixed layer (the layer in which the potential temperature is almost constant in height) is another important parameter. All the parameters are illustrated from GATE observations in Fig. 12.4a, b. We note that the height of

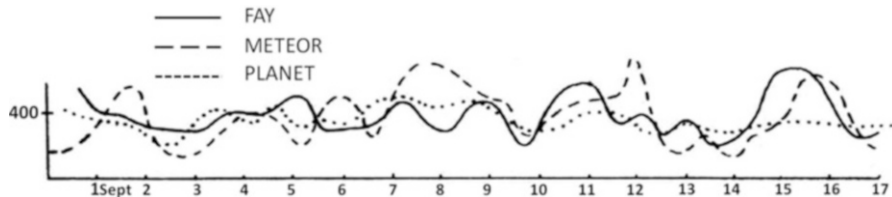


**Fig. 12.5** Height of the mixed layer, measured by three separate ships, as a function of time for a 17-day period in September of 1977 (From Garstang 1977)

**Table 12.1** Mean transitional layer and convective cloud base properties for undisturbed and disturbed conditions (From Garstang 1977)

Property	Undisturbed	Disturbed
Transitional layer depth	$23 \text{ mb} \pm 15 \text{ mb}$	$23 \text{ mb} \pm 14.7 \text{ mb}$
	$200 \text{ m} \pm 130 \text{ m}$	$200 \text{ m} \pm 130 \text{ m}$
Height of base of transitional layer	$953 \text{ mb} \pm 11.4 \text{ mb}$	$972 \text{ mb} \pm 14.9 \text{ mb}$
	$500 \text{ m} \pm 100 \text{ m}$	$330 \text{ m} \pm 130 \text{ m}$
Height of cloud base	$930 \text{ mb} \pm 14.6 \text{ mb}$	$948 \text{ mb} \pm 19.0 \text{ mb}$
	$700 \text{ m} \pm 130 \text{ m}$	$540 \text{ m} \pm 170 \text{ m}$
Height of lifting condensation level	$937 \text{ mb} \pm 8.7 \text{ mb}$	$952 \text{ mb} \pm 16.3 \text{ mb}$
	$640 \text{ m} \pm 75 \text{ m}$	$510 \text{ m} \pm 140 \text{ m}$

the mixed layer descends from roughly 550 m (during the undisturbed state) to around 300 m (in the moderately disturbed state). The lowering of the height of the mixed layer during disturbance passage is attributed to descending motion on large as well as small scales.

A long history of the height of the mixed layer for a 17 day period during GATE from observations taken by three ships at 1 h interval is illustrated in Fig. 12.5. It shows interesting fluctuations in both diurnal and 2–3-day time scales. The mean height is around 400 m.

A summary of the structure of the planetary boundary layer is presented in Table 12.1.

A summary of the surface fluxes based on budget studies is provided in Table 12.2, again taken from the GATE Workshop (1977) results. Here the symbols are:

$I_1$  = total latent + sensible heat flux from the ocean

$I_2$  = surface precipitation minus evaporation in energy units, and

$I_3$  = total net heating of the atmosphere due to condensation reaching the ground and sensible heat flux at the ocean.

Here a comparison of the results of the eastern Atlantic region (GATE) and the western Pacific region (Marshall Islands) is illustrated. It shows the convective

**Table 12.2** Values of  $I_1$ ,  $I_2$ , and  $I_3$  for GATE phase III and Marshall Islands (From Garstang 1977)

n	GATE 85	Marshall Islands 390
$I_1$	$180 \pm 40 \text{ W m}^{-2}$	$190 \pm 10 \text{ W m}^{-2}$
$I_2$	$280 \pm 80 \text{ W m}^{-2}$	$340 \pm 20 \text{ W m}^{-2}$
$I_3$	$460 \pm 80 \text{ W m}^{-2}$	$530 \pm 20 \text{ W m}^{-2}$

activity (measured in terms of total condensation heating) was larger in the western Pacific Ocean.

The above results are taken entirely from the results of the GATE Workshop (1977). The final analysis of all of the GATE boundary layer subprogram data will be of considerable interest. What is evident from much of this is that a more rational framework based on dynamical and thermodynamical principles is lacking. Hopefully, with further work such a basis will emerge to coordinate the many observational findings.

## 12.3 A Simple Model of the Tropical Boundary Layer

The Ekman spiral describes the characteristic turning of the wind with height in the boundary layer. Assuming a prescribed pressure fields and height-invariant horizontal pressure gradients, this turning of the wind with height is derived from the following equations:

$$-fv = -\frac{1}{\rho} \frac{\partial p}{\partial x} + k \frac{\partial^2 u}{\partial z^2} \quad (12.21)$$

and

$$fu = -\frac{1}{\rho} \frac{\partial p}{\partial y} + k \frac{\partial^2 v}{\partial z^2} \quad (12.22)$$

where  $k$  is an eddy diffusion coefficient. The boundary conditions necessary to solve the problem are: (1) the winds are in geostrophic balance at sufficient distance from the surface ( $u \rightarrow u_g$  and  $v \rightarrow 0$  as  $z \rightarrow \infty$ ), and (2) the winds are zero at the surface ( $u, v = 0$  at  $z = 0$ ).

This system was first solved by Akerblom for the atmosphere. The solution is of the form

$$u = u_g(1 - e^{-\gamma z} \cos \gamma z) \quad (12.23)$$

and

$$v = u_g e^{-\gamma z} \sin \gamma z \quad (12.24)$$

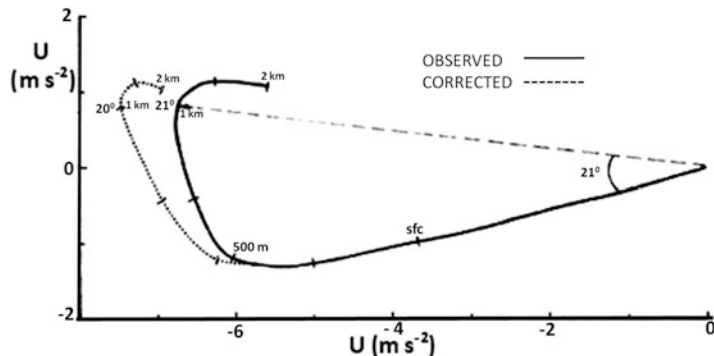


**Fig. 12.6** Observed and calculated hodographs at Swan Island derived from 2,070 observations. Elevation marks are shown at the surface, 150, 300, 500, 1,000, 1,500, and 2,000 m. Veering angle between the surface and 1,000 m is noted on each hodograph. Observed veering is  $21^\circ$  and calculated veering  $20^\circ$  (From Mahrt and Young 1972)

where  $\gamma = (f/2k)^{1/2}$  and the geostrophic wind components are  $(u_g = -\frac{1}{f\rho} \frac{\partial p}{\partial y}, v_g = 0)$ . The Ekman turning of wind with height is clockwise (veering) in the Northern Hemisphere and counterclockwise (backing) over the Southern Hemisphere. This analysis assumes that the geostrophic wind (and, consequently, the pressure gradient force) does not vary with height. To include such height variations (i.e., a consideration of the thermal wind effects) is a considerably more complicated matter but these can nevertheless be very important at all latitudes. If we assume that the variation of geostrophic wind with height is constant in the boundary layer, we can prescribe thermal wind corrections to the Ekman formulae given above.

With thermal wind corrections, the corresponding formulae for  $u$  and  $v$  become

$$u = \left( u_g - \frac{g}{fT} \frac{\partial T}{\partial y} z \right) (1 - e^{-\gamma z} \cos \gamma z) \quad (12.25)$$

and

$$v = \left( u_g - \frac{g}{fT} \frac{\partial T}{\partial y} z \right) e^{-\gamma z} \sin \gamma z \quad (12.26)$$

It has been found in practice that the thermal wind corrections provide an improvement when there are large cold surges and horizontal temperature contrasts. Applications of the above formulae have been described by Mendenhall (1967). Figure 12.6 from his study shows the close agreement between the observed and the calculated wind veer at Swan Island.

## 12.4 Surface Similarity Theory

The similarity theory is based on the principles of dimensional analysis and curve fitting to observational data. The purpose of such analysis is to find robust relationships between observed turbulent fluxes (based on tower measurements) and large scale variables. Such relationships would make possible the calculation of unknown fluxes based purely on large scale data sets. A successful application of this approach was first presented by Monin and Obukhov (1954).

In the 1950s and 1960s a number of scientists tried to relate observed measures of fluxes in the surface layer (<50 m above the earth surface) to large scale variables. Disappointingly, the plots of such data (measured fluxes against large scale variables) provided a wide scatter of points revealing no apparent relationships.

The breakthrough in understanding the relationship between turbulent fluxes and large scale variables came from the pioneering contribution of Monin and Obukhov (1954) and Businger et al. (1971). They designed a relationship X-Y space where the unknowns (i.e. the fluxes) and the knowns (i.e. the large scale variables) were contained in both the abscissa and the ordinate. These implied possible complex nonlinear relationships among fluxes and large scale variables. They first defined a characteristic velocity ( $u^*$ ), temperature ( $\theta^*$ ) and specific humidity ( $q^*$ ) by the relationships

$$F_M = u^{*2} = \overline{u'w'}_s \quad (12.27)$$

$$F_\theta = u^*\theta^* = -\overline{\theta'w'}_s \quad (12.28)$$

$$F_q = u^*q^* = -\overline{q'w'}_s \quad (12.29)$$

This way, the three unknowns of the problem, namely, the surface fluxes of momentum, heat and moisture are related to the three variables  $u^*$ ,  $\theta^*$  and  $q^*$ .

At this stage, a non-dimensional length scale  $L$ , called the Monin-Obukhov length, is defined as

$$L = \frac{u^{*2}}{\kappa\beta\theta^*} \quad (12.30)$$

where,  $\kappa$  is the von Karman constant ( $\kappa = 0.35 - 0.42$ ) and  $\beta = g/\theta_0$  where  $\theta_0$  is a reference temperature. The sign of  $L$  is determined from the sign of the heat flux, i.e.  $-\overline{\theta'w'}$ . If the flux is upward, then  $-\overline{\theta'w'}$  is positive. The stability of the surface layer is defined by the sign of  $L$  as follows:

$L > 0$	stable
$L = 0$	neutral
$L < 0$	unstable

It should be noted that at this stage all parameters discussed above are unknowns of the problem hence the stability itself is not known.

Often stability is expressed in terms of the sign of the bulk Richardson number, namely

$$Ri_B = \beta \frac{\partial \bar{\theta} / \partial z}{\left( \frac{du}{dz} \right)^2} \quad (12.31)$$

This is a ratio of the stability to the square of the wind shear. The thermal stability of the constant flux layer determines the sign of  $Ri_B$ , i.e.,

$$\begin{aligned} Ri_B > 0 &\quad \text{stable} \\ Ri_B = 0 &\quad \text{neutral} \\ Ri_B < 0 &\quad \text{unstable} \end{aligned}$$

For the surface layer tower data Businger et al. (1971) noted that the scatter of plots can be vastly reduced by using a non-dimensional shear and stability against a non-dimensional height  $z/L$ . This is expressed by the following universal relationships:

This universal functionality is clearly seen from the observational estimate of fluxes from different heights  $z$ , Fig. 12.7. Businger et al. (1971) used a plot of these functions using observed estimates against  $z/L$  and arrived at several curve fit-based relationships. In Fig. 12.7 we see a monotonic relationship for the non-dimensional shears and for the non-dimensional vertical gradient of potential temperature. The scatter is almost gone and a universal relationship has been found here from this representation of data. This is a major finding. Here the abscissa and the ordinate both carry the known, i.e., the vertical gradients and the unknowns, the fluxes. But these are easy to solve for. For the stable case these are:

$$\phi_m = \frac{\kappa z}{u^*} \frac{\partial \bar{u}}{\partial z} = \left( 1 - 15 \frac{z}{L} \right)^{-1/4} \quad (12.32)$$

$$\phi_h = \frac{\kappa z}{\theta^*} \frac{\partial \bar{\theta}}{\partial z} = 0.74 \left( 1 - 9 \frac{z}{L} \right)^{-1/2} \quad (12.33)$$

$$\frac{\kappa z}{q^*} \frac{\partial \bar{q}}{\partial z} = 0.74 \left( 1 - 9 \frac{z}{L} \right)^{-1/2} \quad (12.34)$$

For the unstable case, these are:

$$\frac{\kappa z}{u^*} \frac{\partial \bar{u}}{\partial z} = 1.0 + 4.7 \frac{z}{L} \quad (12.35)$$

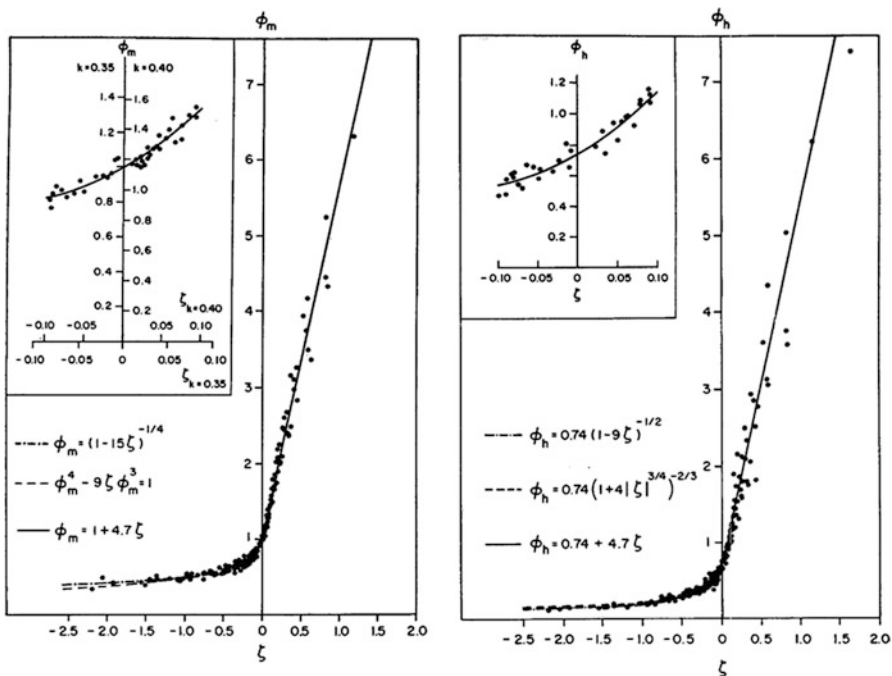


**Fig. 12.7** Comparison of dimensionless wind shear ( $\phi_m$ ) and dimensionless temperature gradient ( $\phi_h$ ) observations with dimensionless height ( $\zeta$ ) (Based on Businger et al. 1971)

$$\frac{\kappa z}{\theta^*} \frac{\partial \bar{\theta}}{\partial z} = 0.74 + 4.7 \frac{z}{L} \quad (12.36)$$

$$\frac{\kappa z}{q^*} \frac{\partial \bar{q}}{\partial z} = 0.74 + 4.7 \frac{z}{L} \quad (12.37)$$

The definition of  $L$  and the above equations for  $\frac{\partial \bar{u}}{\partial z}$ ,  $\frac{\partial \bar{\theta}}{\partial z}$  and  $\frac{\partial \bar{q}}{\partial z}$  constitute a closed system of nonlinear algebraic equations for  $L$ ,  $u^*$ ,  $\theta^*$  and  $q^*$ . These can be easily solved for the three unknowns making an extreme guess on  $L$  and then pursuing simple small increment  $\Delta L$  to a simple iteration scheme. In this process one solves for  $u^*$ ,  $\theta^*$  and  $L$  iteratively in sequence. The iterations are stopped when there is a convergence of the answer to an acceptable degree of tolerance. After acquiring the value of  $L$  one can simply solve for  $q^*$  in the equation for  $\frac{\partial \bar{q}}{\partial z}$ . This is a powerful model for estimating fluxes of momentum, sensible and latent heat in the surface layer. It is stability-dependent and hence is more accurate compared to the bulk aerodynamic method, since the latter only applies for neutral conditions.

Much further work is still needed for the so called Stable Planetary Boundary layer. This is a critical element for the boundary layer physics since this controls

the diurnal change over land and ocean areas. The boundary layer in turn has strong ties with the cloud layer and the entire precipitation physics. Factors such as turbulence, radiation, internal waves, mesoscale variability and terrain heterogeneity all need to be studied in considerable further detail to address the stable planetary boundary layer.

## 12.5 Scale Analysis of the Large-Scale Tropical Boundary Layer

The horizontal equations of motion can be called in an interesting manner to define in a gross way some realizable boundary layer structures. Here we shall follow the procedure outlined by Mahrt (1972).

The zonal equation of motion may be written in the form:

$$\frac{\partial u}{\partial t} + u \frac{\partial u}{\partial x} + v \frac{\partial u}{\partial y} - fv = -g \frac{\partial z}{\partial x} + F_x \quad (12.38)$$

or

Tendency ( $T$ ) + Advection ( $A$ ) + Coriolis force ( $C$ ) = Pressure gradient force ( $P$ ) + Friction ( $F$ ).

We shall use the following scaling to non-dimensionalize the above equations:

$$u = Uu' \quad (12.39)$$

$$v = Uv' \quad (12.40)$$

$$\frac{\partial}{\partial x} = \left(\frac{U}{\beta}\right)^{1/2} \frac{\partial}{\partial x'} \quad (12.41)$$

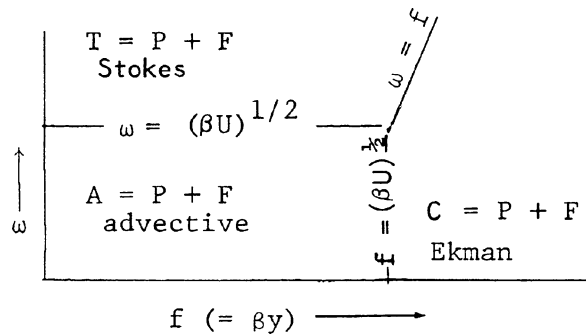
$$\frac{\partial}{\partial y} = \left(\frac{U}{\beta}\right)^{1/2} \frac{\partial}{\partial y'} \quad (12.42)$$

$$f = \beta y \quad (12.43)$$

$$\frac{\partial}{\partial t} = \omega \frac{\partial}{\partial t'} \quad (12.44)$$

where  $\omega$  is a characteristic frequency. In the boundary layer  $P$  and  $F$  are expected to be dominant terms and we wish to compare  $T$ ,  $A$ , and  $C$  with these for different ranges of values of  $\omega$ . The scaling of the above equation gives:

**Fig. 12.8** Regimes in the boundary layer (From Mahrt and Young 1972)



$$\omega U \left( \frac{\partial u'}{\partial t'} \right) + \frac{U^2}{(U/\beta)^{1/2}} \left( u' \frac{\partial u'}{\partial x'} + v' \frac{\partial u'}{\partial y'} \right) - f U v' = P + F, \quad (12.45)$$

or

$$\omega \left( \frac{\partial u'}{\partial t'} \right) + (U\beta)^{1/2} \left( u' \frac{\partial u'}{\partial x'} + v' \frac{\partial u'}{\partial y'} \right) - \beta y v' = \frac{P}{U} + \frac{F}{U}. \quad (12.46)$$

The vertical advection term is assumed to be small. There are three time scales here, namely,

$$\omega^{-1}, (U\beta)^{-1/2}, \text{ and } (\beta y)^{-1}.$$

Consider the following three cases:

- (i) If  $\omega < \beta y$  and  $(U\beta)^{1/2} < \beta y$  then  $C$ ,  $P$  and  $F$  are the dominant terms, i.e., we would expect an Ekman balance.
- (ii) If  $f = \beta y < (U\beta)^{1/2}$  and  $\omega < (U\beta)^{1/2}$  then the advective term  $A$  balances  $P + F$  and we have what is called an advective or drift boundary layer.
- (iii) Finally, if  $\omega > \beta y$  and  $\omega > (U\beta)^{1/2}$  then the tendency term  $T$  becomes dominant and is balanced by  $P + F$ . This is called a Stokes regime.

In the large scale tropical boundary layer one is often interested in knowing which of the above three cases is realized in a given region. Mahrt and Young (1972) illustrated the three regimes in an interesting diagram (Fig. 12.8). There also exist, of course, broad transition regions where one would expect to see the overlapping influence of two of the above regions at the same time. In the middle latitudes the dominant boundary layer regime tends to be Ekman balance, because of the relatively large values of  $y$ . In the tropics, the prevailing regimes are Stokes and advective balance.

## 12.6 Cross-Equatorial Flows and Planetary Boundary Layer Dynamics

An interesting series of numerical experiments on the dynamical structure of the boundary layer was carried out by Mahrt (1972). Here the solutions of the following system of boundary layer equations were integrated for a prescribed pressure field:

$$\frac{\partial v}{\partial t} = -v \frac{\partial v}{\partial y} - w \frac{\partial v}{\partial z} - fu - \frac{1}{\rho_0} \frac{\partial p}{\partial y} + k \frac{\partial^2 v}{\partial z^2} \quad (12.47)$$

$$\frac{\partial v}{\partial y} + \frac{\partial w}{\partial z} = 0. \quad (12.48)$$

These equations describe flow in a meridional vertical plane. The eddy diffusion coefficient is prescribed and the pressure field is given as a linear field of the form  $p = ax + by + c$ . The above system of two equations thus contains two unknowns, namely  $v$  and  $w$ . One integrates the above system from an initial Ekman solution. This is not possible near the Equator, since there the coriolis parameter in the denominator goes to zero. A linear interpolation of the Ekman solution on either side of the equator is therefore used to define the initial equatorial wind field. The meridional plane usually extends from the middle latitudes of the two hemispheres and at the northern and southern boundaries time invariant Ekman solutions can be used to define the boundary conditions. We have already shown how one can express the Ekman profile as a function of the geostrophic wind defined by a given pressure field. A good horizontal and vertical resolution is important for this numerical problem. Mahrt (1972) used a vertical resolution of 200 m and a horizontal resolution of 50 km in his integration of the above system of equations.

Here we shall illustrate a particular application of Mahrt's framework that was carried out by Krishnamurti and Wong (1979) as part of a study of the boundary layer of the east African low-level jet of the northern summer. In this study, the meridional distribution of the pressure gradient force was prescribed along 60°E. The model extends from 15°N to 25°N. The major results of the boundary layer simulations are shown in Figs. 12.3 and 12.4. Figure 12.9 illustrates the horizontal winds in the meridional plane at 60°E, showing the cross-equatorial flows and a low level jet (the Somali jet) near 12°N. Knowing the long-term steady-state motion field one can compute the various terms in the equations of motion.

The balance of forces in the boundary layer is found to settle to a set of values quite different from that of the initial Ekman layer, where the balance is between the forces of Coriolis, pressure gradient, and friction. The new balance of forces is schematically shown in Fig. 12.10.

The simulations show throughout the domain a surface layer near the ground where the predominant balance of forces is between the pressure gradient and friction forces (i.e.  $P + F = 0$ ).

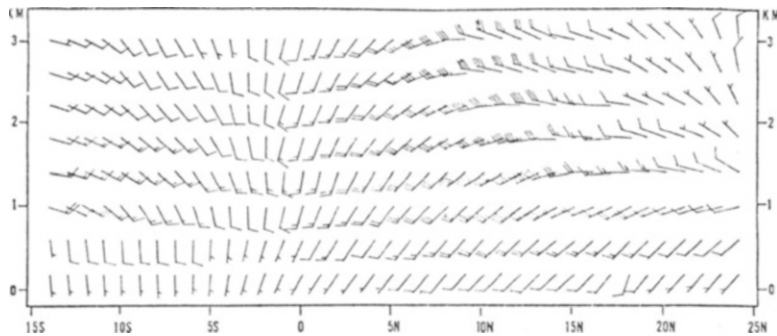


**Fig. 12.9** Winds barbs along a meridional-vertical plane along  $60^{\circ}\text{E}$  for an experiment with a height-dependent eddy diffusion coefficient. The winds are in knots (From Krishnamurti and Wong 1979)

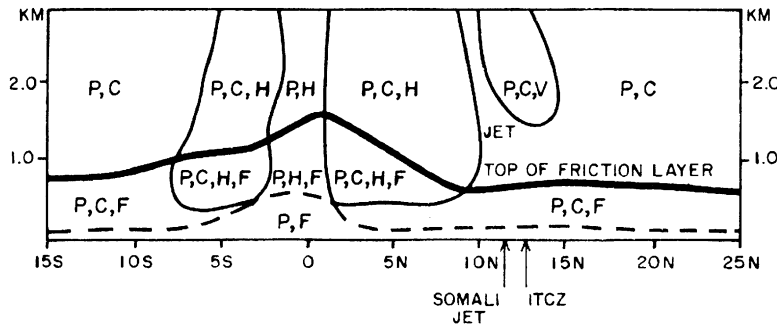


**Fig. 12.10** A schematic illustration of the various regimes and the significant forces in the boundary layer from the solution at day 50. The letters P, C, H, V, and F stand for pressure gradient, Coriolis, horizontal advection, vertical advection and the frictional terms respectively. In the different regimes only those relative forces are identified whose magnitudes exceed 0.3. The dashed line indicates the top of the surface layer (From Krishnamurti and Wong 1979)

Above this surface layer lies the friction layer. In the subtropics, this friction layer is characterized by an Ekman type balance of forces ( $C + P + F = 0$ ). In the equatorial friction layer the balance is between horizontal advection, pressure gradient, and friction terms ( $H + P + F = 0$ ). The near-equatorial friction layer combines the characteristics of the subtropics and the equatorial region – here the balance of forces is between the Coriolis, horizontal advection, pressure gradient, and friction terms ( $C + H + P + F$ ). The friction layer in the equatorial and near-equatorial regions is called an advective boundary layer, due to the strong relative influence of the horizontal advection term.

Aside from the important equatorial regions, there are two other features of interest in the boundary layer of this region: the Somali jet and an ITCZ over the northern Arabian Sea. The calculations show that the Somali jet is located at

the poleward edge of the region where the horizontal advective term becomes less important. The ITCZ is noted to form in the general region between the advective and Ekman boundary layers, a result first noted by Mahrt. The aforementioned study and the balance of forces diagram (Fig. 12.10) are very pertinent to the tropical boundary layer. This framework is not suited for investigating time variations of the boundary layer. By prescribing a pressure force this framework also limits investigations of thermodynamic inputs such as air-sea interaction, diurnal variations, etc. Work in these important areas of the boundary layer structure would require a different approach.

## References

- Businger, J.A., Wyngaard, J.C., Izumi, Y., Bradley, E.F.: Flux-profile relationships in the atmospheric surface layer. *J. Atmos. Sci.* **28**, 181–189 (1971)
- Estoque, M.A.: The planetary boundary layer wind over Christmas Island. *Mon. Weather Rev.* **99**, 193–201 (1971)
- Garstang, M.: Report of the U. S. GATE central program workshop by National Science Foundation and National Oceanic and Atmospheric Administration, pp 492 (1977)
- Krishnamurti, T.N., Wong, V.: A planetary boundary-layer model for the Somali Jet. *J. Atmos. Sci.* **36**, 1895–1907 (1979)
- Mahrt, L.J.: A numerical study of the influence of advective accelerations in an idealized, low-latitude planetary boundary layer. *J. Atmos. Sci.* **29**, 1477–1484 (1972)
- Mahrt, L.J., Young, J.A.: Some basic theoretical concepts of boundary layer flow at low latitudes. In: *Dynamics of the Tropical Atmosphere: Notes from the Colloquium: Summer 1972*, pp. 411–420. National Center for Atmospheric Research, Boulder, Colorado (1972)
- Mendenhall, B.R.: A statistical study of frictional wind veering in the planetary boundary layer. Department of Atmospheric Science, Colorado State University, Fort Collins, Colorado, Paper No. 116, 57 pp, (1967)
- Monin, A.S., Obukhov, A.M.: Basic laws of turbulent mixing in the ground layer of the atmosphere. *Akad. Nauk SSSR Geofiz. Inst. Tr.* **151**, 163–187 (1954)
- Robitaille, F.E., Zipser, E.J.: Atmospheric boundary layer circulations equatorward of the intertropica convergence zone. *Symposium on Tropical Meteorology*, University of Hawaii, Honolulu (1970)

# Chapter 13

## Radiative Forcing

### 13.1 Radiative Processes in the Tropics

Radiative transfer is very important for tropical/subtropical meteorology. The subtropical highs occupy a large part of the subtropics, the temperature does not change much here from 1 day to the next inspite of the fact that descending air is continually warmed up by the adiabatic descent. That warming is offset by radiative cooling. Accurate modeling of radiative cooling in the presence of lower tropospheric stratus and strato-cumulus is an important issue for the tropics. Dust and aerosols abound in Asia and Africa and well stretched into the Atlantic and their rates of warming/cooling by radiative effects are a central issue for the modeling of the monsoon and hurricanes. Immediately below the cloud base long wave radiative flux convergence often leads to a warming by the long wave radiative process. Those are also important modeling issues. The clear weather shallow startocumulus carry a field of long wave cloud top cooling that dictates the low temperatures of the base of the trade wind inversion that also needs understanding of cloud radiative transfer processes. Various regions of the troposphere of the tropics show radiative stabilization or destabilization that are important for the thermodynamical/dynamical interactions and require understanding of physical processes. The entire seat of diurnal change in the atmosphere relates to the zenith angle of the sun and the understanding of diurnal change requires a detailed interpretation of radiative transfer. The heat budget of the land surface carries the impacts of short and long wave radiation at the Earth's surface. These are areas where a considerable amount of research is needed to fully understand the role of land surface on the atmospheric processed. Even the Sea Surface Temperatures show a diurnal variability of the order of 0.5 C/day, that too has important implications for tropical buoyancy and clouds. There are major tropical circulations such as the Hadley and East West circulations that require understanding and careful modeling of radiative convective thermal balances.

The following areas of radiative transfer computations are important for a student to learn:

- (i) Vertical profiles of short wave radiation for the upward and downward fluxes.
- (ii) Vertical profiles of long wave radiation for the upward and downward fluxes.
- (iii) Role of clouds along the vertical coordinate – low, middle and high clouds; stratiform and convective clouds.
- (iv) Surface energy balance.

Students should develop an access to codes that perform the above computations starting from data sets of vertical profiles of temperature and specific humidity (Krishnamurti and Bounoua 1996). For the validation of such codes, they are usually run over regions where direct measurements are available, such as:

- (i) Direct observational estimates of radiative fluxes,
- (ii) Heating rates by long and short wave irradiances,
- (iii) Vertical distribution of cloud cover, and
- (iv) The components of the surface energy balance.

Such observations are generally available from special field experiments, such as GATE, TOGA/COARE and ARM, to name a few. Research aircraft flights provide direct measurements of the up and down irradiances for the long and short wave components. These experiments also provide direct estimates for the surface energy balance components and for the distribution of cloud cover.

This textbook will not address in any detail the theories of radiative transfer or its direct modeling; those can be found in specialized texts. Here we will focus on the radiative interactions that are relevant to tropical phenomenology.

## 13.2 Shallow Stratocumulus Clouds and Radiative Transfer

A well-known thermodynamical feature of the tropical lower troposphere is the  $\theta_e$  minimum that prevails near the 600 hPa level. That can be seen over nearly 90 % of the tropical oceanic areas. Since  $\theta_e$  is conserved for dry and moist adiabatic motion, a sudden appearance of a new  $\theta_e$  minimum can only be ascribed to a single thermodynamical process – radiation. Shallow stratocumulus clouds abound in the tropics. These clouds generally have bases near the 900 mb level and tops between 700 and 600 mb. Near the cloud top level, over a thin layer (roughly 10 mb) there is a large net radiative flux divergence, primarily due to the long wave irradiance. The radiative flux divergence in this thin layer engenders cooling rates as large as 20°C/day. Averaged over a 100 mb layer above the cloud top the cooling rates are often as large as 5°C/day. Such values are obtained from radiative transfer computations and/or special field experiments where research aircraft make direct measurements of the upward and downward fluxes of the short and long-wave

irradiances (Krishnamurti and Bounoua 1996) The meteorological significance of this  $\theta_e$  minimum will be discussed in Chap. 14 of this book. The combination of large surface evaporation and the above-described radiative cooling over shallow stratocumulus cloud tops is a major contributor for the maintenance of the conditional instability of the tropics. Deep convection contributes to an erosion of this conditional instability, whereas the shallow stratocumulus cloud top cooling contributes to its restoration.

Another feature worth noting is the radiative flux convergence that is nearly always found in a layer approximately 100 mb below the cloud base. In this region, near the 900 mb level, the long wave irradiances contribute to a slight warming – on the order of 0.5–1°C/day. The typical magnitude of the long-wave cooling in clear sky conditions over the large scale tropics are generally on the order of 1.5–2°C/day. In the presence of shallow stratocumulus clouds, this cooling is reduced or even eliminated in the region immediately below the cloud base. The steepness of the  $\theta_e$  vertical profile over the cloudy region is largely attributed to this cloud effect. A secondary factor contributing to this steepness is the vertical eddy flux convergence or divergence arising from cloud scale eddy motions. Another factor to consider is the cloud evaporation and the related cooling. However, in the context of conservation of  $\theta_e$ , that is an integral part of the moist adiabatic processes and not one that can contribute to a  $\theta_e$  minimum or to the steepness of the profile maintained above.

### 13.3 Surface Energy Balance

The components of the surface energy balance over land areas are of much interest for studies of tropical weather and climate. These components include the downward and upward fluxes of short and long wave radiation. The vertical fluxes of sensible and latent heat at the Earth's surface. Major swings in the values of these fluxes occur on a variety of time scales. Models for short and long wave irradiances and empirical surface flux formulae provide estimates for these components. These modeled values are always validated over limited parts of the tropics where field experiments and special measurements are available. Such a validation is an essential part of model improvement. One of the major limitations is that these observed estimates cover limited durations over limited areas of the Earth's surface, making it difficult to make global conclusions about the models' accuracy. The downward flux of solar radiation at the Earth's surface is a function of the zenith angle of the Sun, the local vertical distribution of atmospheric constituents, such as water vapor, carbon dioxide, ozone, and, most importantly, cloud cover. Given those vertical distributions of constituents one can calculate the short wave radiation received at the Earth's surface. As stated previously, this requires access to codes for radiative transfer, such as a band model for cloud radiation (see for example Krishnamurti and Bounoua 1996). The reflected short wave radiation is

a function of the surface albedo  $\alpha_S$ . Thus  $F_S^\uparrow = \alpha_S F_S^\downarrow$ . Tabulations of surface albedo are generally available from climate data centers.

The downward flux of long-wave radiation reaching the Earth's surface relies on the atmospheric vertical distribution of temperature, moisture, atmospheric constituents such as ozone, carbon dioxide, and clouds. These again can be calculated using column models of radiative transfer. The upward flux of long wave radiation from the Earth's surface generally assumes that the Earth's surface is a perfect black body with a temperature equal to the ground temperature  $T_g$ . With such an assumption, the upward flux of long-wave radiation is expressed as  $F_L^\uparrow = \sigma T_g^4$ , where  $\sigma$  is the Stefan-Boltzman constant. The clouds that are immediately overhead above the Earth's surface are also generally assumed to be radiating as perfect black bodies that emit downward long-wave radiation equal to  $\sigma T_{cb}^4$ , where  $T_{cb}$  is the air temperature of the cloud base. The perfect black body assumption is not usually applied to higher-altitude clouds, such as thin high level cirrus.

The upward fluxes of sensible and latent heat for the land surfaces can be estimated from a number of well-known empirical formulations, such as the bulk aerodynamic formulae or the surface similarity theory. These apply to a region near the Earth's surface over what is called a constant flux layer which is approximately 60 feet deep.

The transfer formulae for momentum, sensible heat and latent heat are usually expressed by the bulk aerodynamic formulae discussed in the previous chapter, namely,

$$F_M = -C_M \rho |\mathbf{V}_a|^2 \quad (13.1)$$

for the momentum flux,

$$F_{SH} = C_S \rho C_p |\mathbf{V}_a| (T_s - T_a) \quad (13.2)$$

for the sensible heat flux, and

$$F_{LH} = C_L \rho L |\mathbf{V}_a| (q_s - q_a) \quad (13.3)$$

for the latent heat flux. Here again  $T_g$  and  $q_g$  are the surface values of the temperature and specific humidity respectively, while  $T_a$  and  $q_a$  are the corresponding anemometer level values.  $C_p$  is the specific heat of air at constant pressure,  $L$  is the latent heat of evaporation, and  $\rho$  is the air density.

For land areas, an additional parameter is of importance – the ground water wetness. The surface flux of moisture/latent heat is significantly affected by the state of the soil moisture. This effect can be roughly accounted for by introducing a parameter  $\mu$  into the equation for the latent heat flux, i.e.,

$$F_{LH} = \mu C_L \rho L |\mathbf{V}_a| (q_g - q_a) \quad (13.4)$$

This parameter is generally related to the surface air's relative humidity. For saturated conditions  $\mu = 1$ , and decreases accordingly for lower relative humidities.

### 13.3.1 *Ground Temperature T<sub>g</sub>*

The surface energy balance is often used for obtaining the value of the ground temperature T<sub>g</sub> over land. This is achieved by treating T<sub>g</sub> an unknown in the surface energy balance equation.

$$0 \approx C_p \frac{\partial T_g}{\partial t} = F_S^\downarrow (1 - \alpha) + F_L^\downarrow - \sigma T_g^4 - C_{SH} C_p \rho |\mathbf{V}_a| (T_g - T_a) \\ - C_M L \rho |\mathbf{V}_H| \mu (q_g - q_a). \quad (13.5)$$

This equation has the form  $\sigma T_g^4 + A(T_g) = 0$ , where A is a linear function of the unknown, T<sub>g</sub>. Such an equation can be easily solved by standard methods, such as Newton–Raphson (Press et al. 1986). The procedure involves the following steps:

1. Define  $f(T_g) = \sigma T_g^4 + A(T_g) = 0$
2. Calculate  $f'(T_g) = \frac{\partial f(T_g)}{\partial T_g}$
3. Find a first guess of the surface temperature,  $T_g^0$ .
4. Use the following equation to find the n + 1th approximate value for T<sub>g</sub>  $T_g^{n+1} = T_g^n - \frac{f(T_g)}{f'(T_g)}$ .

This procedure is used to derive the surface temperature of land areas.

### 13.3.2 *Evaluating Moisture Fluxes for Hydrological Budgets and Water Cycle Studies*

The same surface energy balance equation is often used by hydrologists for obtaining estimates of surface evaporation over land areas. The procedure is the same as discussed in the previous section. Heavy rains over land areas are seldom contributed by local recycling of moisture. Most of the moisture participating in local heavy rains over land areas is accomplished by large horizontal eddy flux convergence. Evaporation of moisture from a previous storm cannot account for the source of moisture for the next major rain storm since the magnitude of the land evaporation is quite small. Local recycling of moisture is known to be an important source of moisture in typhoons where mesoscale winds can lead to large evaporation, but is otherwise seldom important over land areas.

### ***13.3.3 The Surface Sensible and Latent Heat Fluxes***

The following figures present the summer and winter climatologies from the ERA-40 atlas ([http://www.ecmwf.int/research/era/ERA-40\\_Atlas/docs/section\\_B/index.html](http://www.ecmwf.int/research/era/ERA-40_Atlas/docs/section_B/index.html)). The units of these fluxes are  $\text{Wm}^{-2}$ , and positive values indicate downward fluxes.

### ***13.3.4 Net Solar (Shortwave) Radiation at the Earth Surface***

This is the difference between the incoming solar radiation at the Earth's surface and the reflected part. The latter is a function of the surface albedo. The incoming solar radiation starts off as the solar constant ( $S = 1,370 \text{ Wm}^{-2}$ ) at the top of the atmosphere. By the time it passes through the atmosphere and clouds, this magnitude is significantly reduced. The net downward solar radiation at the Earth's surface is no larger than  $300\text{--}400 \text{ Wm}^{-2}$ . Figure 13.1a, b show the winter and summer net surface solar radiation fields. There is a clear reduction of the net surface solar radiation in the cloudy regions – the ITCZ, SPCZ and monsoon. This reduction due to the reduction of incoming (rather than increase in reflected) solar radiation. Larger values, exceeding  $200 \text{ Wm}^{-2}$  are seen over the subtropical oceans and the dry desert areas. The seasonal migration of the ITCZ and the monsoon are clearly reflected in these components of radiation climatology. The eastern portions of the subtropical highs (near the west coasts of the continents) display some of the largest values of net incoming solar radiation. These are regions of strong descent of tropospheric air, with associated low moisture content and little cloud cover. The land areas of the African and the Asian monsoons have the lowest values of net incoming solar radiation. Here the summer time values can be as low as  $60\text{--}80 \text{ Wm}^{-2}$ .

### ***13.3.5 Net Thermal (Longwave) Radiation at the Earth Surface***

The downward directed longwave radiation reaching the earth's surface is a function of the vertical structure of temperature, humidity, clouds and aerosols. In the context of global climate change, at longer time scales changes in the vertical profiles of CO<sub>2</sub> and O<sub>3</sub> can be important. Figure 13.2a, b illustrate the net thermal radiation for the winter and summer seasons. The net refers to the difference between the downward and upward fluxes of thermal radiation at the Earth's surface. The upward fluxes are simply estimated as  $\sigma T_g^4$ , where  $T_g$  is the surface temperature. Global fields of  $T_g$  are, as stated previously, obtained from the surface energy balance computations.  $\sigma T_g^4$  is generally larger in magnitude than the

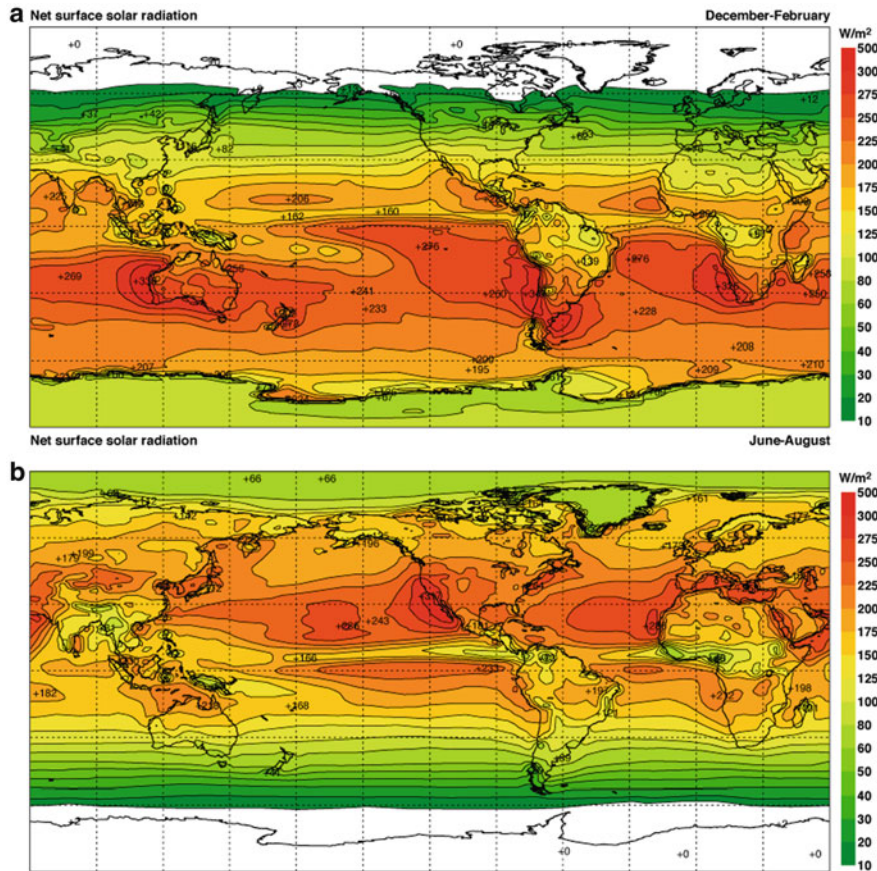


**Fig. 13.1** Climatological net surface solar (shortwave) radiation flux for December, January and February (top) and June, July and August (bottom). Units are  $\text{Wm}^{-2}$ . Positive fluxes are downward

incoming (downward directed) longwave radiation. As a result, nearly everywhere the net surface downward thermal radiation is negative, i.e., the net flux is upward. The largest values ( $-100$  to  $-150 \text{ Wm}^{-2}$ ) are found over the major desert areas described in Chap. 8. These regions of large upward fluxes of thermal radiation are characterized by heat lows. This problem is of interest to climate scientists who are studying desertification and the possible extensions of deserts. The tropics display the clear signatures of the ITCZ, SPCZ and the monsoon, where lower net upward fluxes of thermal radiation ( $-20$  to  $-50 \text{ Wm}^{-2}$ ) are found. These are cloudy areas and the oceanic fluxes are large. Here the cloud bases provide a stronger downward directed thermal radiation and the oceans are relatively cooler ( $T_g \sim 300 \text{ K}$ ) as compared to the warmer land areas of the tropics and subtropics. The subtropical highs of the winter and summer seasons generally have values of about  $-50$  to  $-70 \text{ Wm}^{-2}$ . The explanation for these relatively low values lies in the lack of

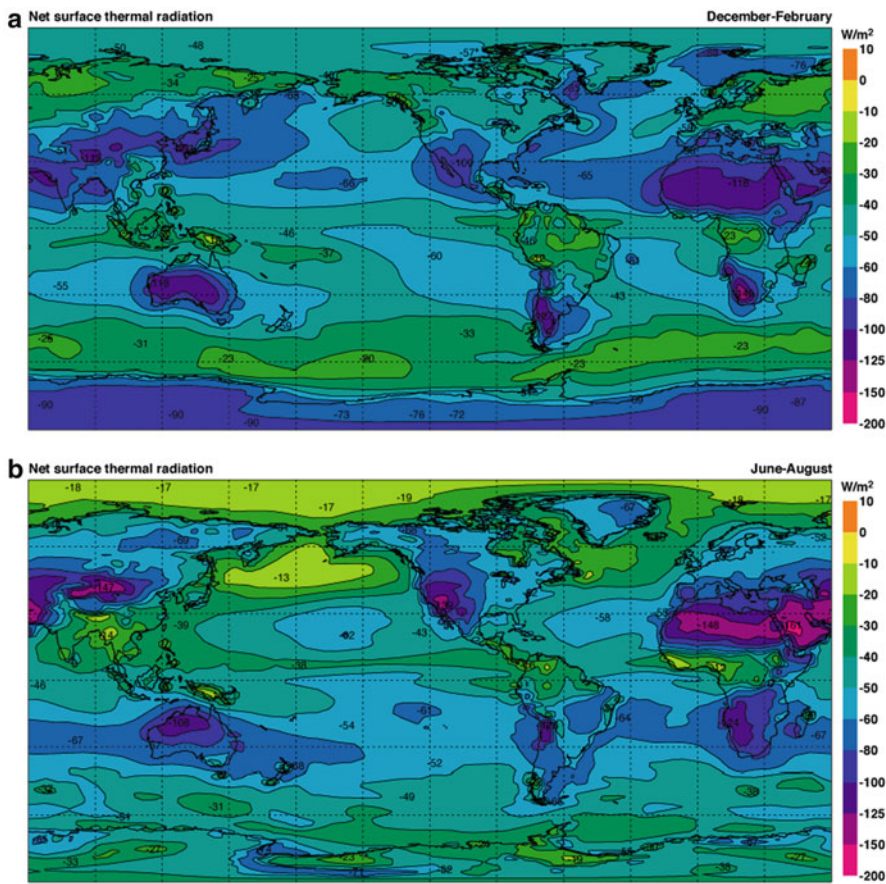


**Fig. 13.2** As in Fig. 13.1, but for surface thermal (longwave) radiation

clouds and rain. The geographical variability of the net surface thermal flux shown in Fig. 13.2a, b carries a lot of useful information for the atmospheric general circulation.

### 13.3.6 Surface Sensible Heat Flux

Figure 13.3a, b show the surface fluxes of sensible heat flux for the winter (December through January) and summer (June through August). Over the tropical oceans (30S–30N) the sensible heat fluxes are generally on the order of  $10\text{--}20 \text{ W m}^{-2}$ . The sensible heat fluxes generally are not large contributors to the energy balance of the tropics. Over land areas the summer time values can get as

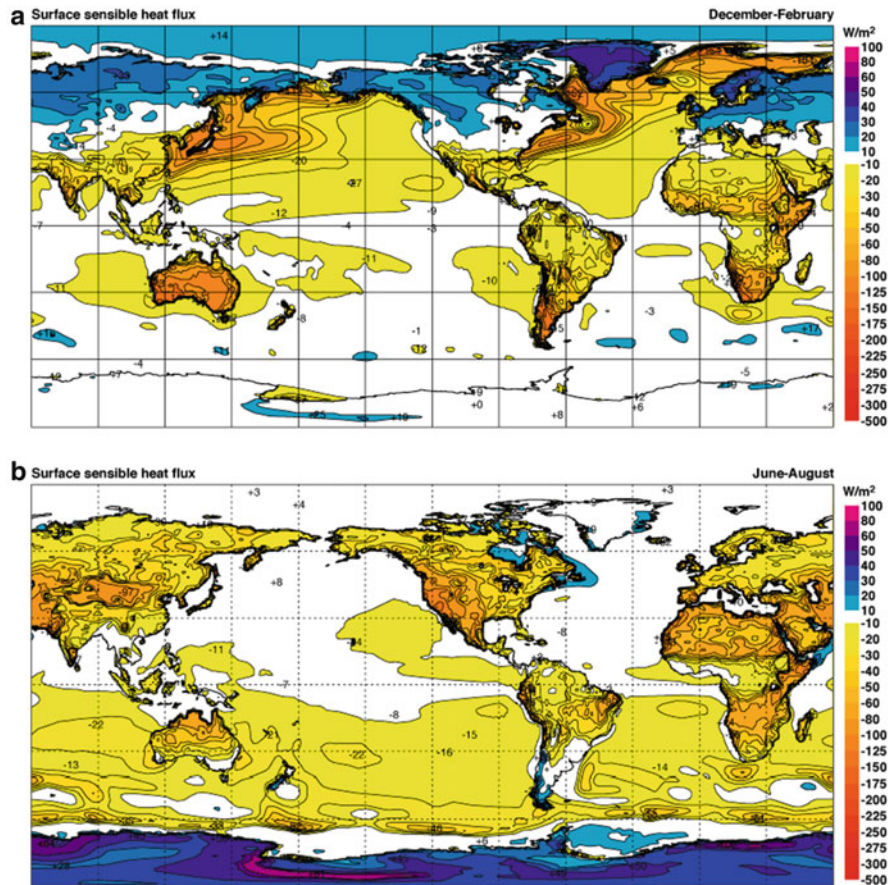


**Fig. 13.3** As in Fig. 13.1 but for sensible heat flux

large as  $60 \text{ W m}^{-2}$ . Such large values are noted over the desert areas (see the chapter on heat lows) of North Africa, Pakistan, Southwestern China, Australia, South America and Australia. Oceanic fluxes show a migration of larger values into the subtropics during the respective hemispheres' winters. In Fig. 13.3a and 13.3b we find some exceptional features along the Gulfstream and Kuroshio Currents of the western Atlantic and the Pacific Oceans respectively. These carry large sensible heat fluxes during the northern winter season at latitudes as far north as 40N. These respective seasonal fluxes approach values close to  $100 \text{ W m}^{-2}$ . These large fluxes occur when cold air outbreaks occur from the northwest over the warm coastal ocean currents. In the overall surface energy balance in monsoon phenomenology such as the life cycle of a monsoon season the role of sensible heat fluxes is nontrivial.

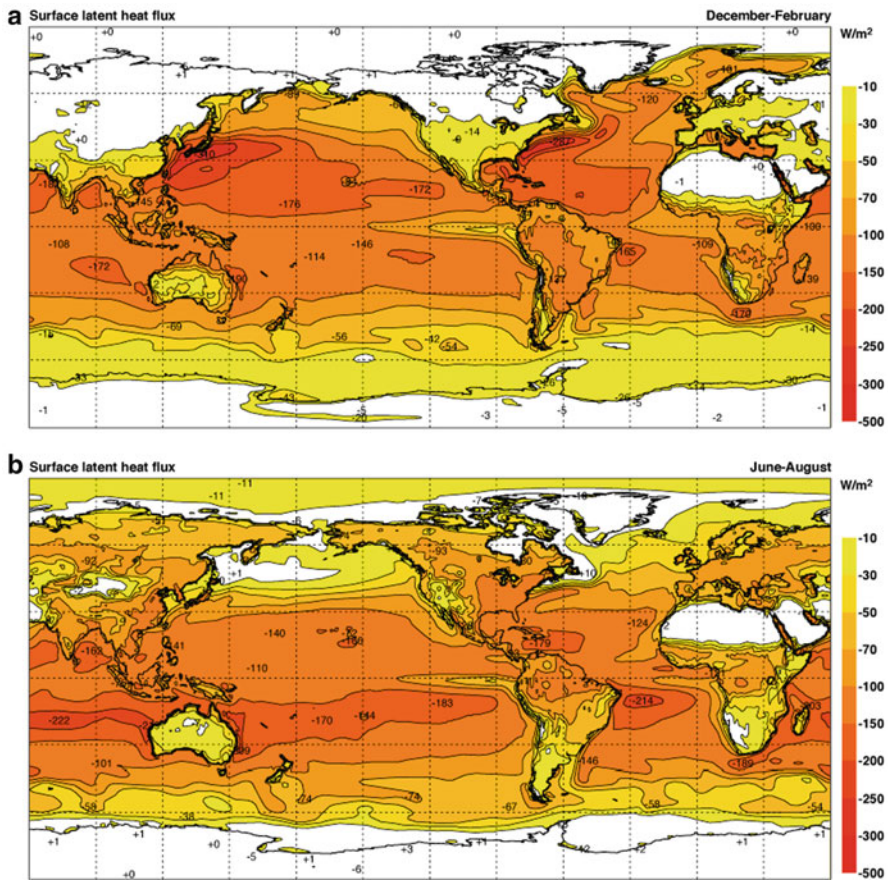


Fig. 13.4 As in Fig. 13.1 but for latent heat flux

### 13.3.7 Surface Latent Heat flux

The surface fluxes of latent heat are illustrated in Fig. 13.4a, b for the northern winter and summer respectively. The most important feature of the latent heat flux climatology are the larger fluxes over the trade wind belts. These seasonal fluxes are as large as  $175 \text{ Wm}^{-2}$ . Note that the daily values can be as large as  $300 \text{ Wm}^{-2}$  over the trades and can be as large as  $800 \text{ Wm}^{-2}$  over the strong wind regions of a typhoon. In Fig. 13.4a and 13.4b we also note somewhat stronger latent heat fluxes over the respective winter season trade wind belts. In this context it is important to note that stronger moisture and latent heat fluxes over the winter hemisphere trades get carried equatorwards and even across the equator towards the near-equatorial intertropical convergence zone. The winter trade winds are a main conveyor of moisture for the summer hemisphere ITCZ belts.

**Table 13.1** Climatological DJF (blue) and JJA (red) net surface fluxes at different geographical areas. The units are in  $\text{Wm}^{-2}$

	Asian Monsoon	SPCZ	ITCZ	Subtropical high	North African Desert
Sensible heat flux	-20 to -10	-20 to -10	-20 to +10	-20 to -10	-30 to -10
	-10 to +10	-20 to -10	-20 to +10	-10 to 10	-80 to -40
Latent heat flux	-200 to -100	-150 to -100	-150 to -70	-200 to -150	0
	-200 to -100	-200 to -100	-150 to -100	-150 to -100	0
Thermal radiation	-100 to -60	-50 to -30	-50 to -40	-80 to -60	-125 to -100
	-40 to -20	-50 to -40	-50 to -30	-60 to -50	-150 to -125
Solar radiation	+200 to +225	+150 to +200	+150 to +175	+80 to +100	+80 to +150
	+125 to +150	+125 to +175	+100 to +175	+225 to +275	+125 to +200

Strong latent heat fluxes are also a prominent feature over the Gulfstream and the Kuroshio currents. Here the cold sea drier air intrusions over the warmer (moist) oceanic coastal regions encounter very large fluxes on the order of  $200 \text{ Wm}^{-2}$ . Such fluxes can contain daily values as large as  $350 \text{ Wm}^{-2}$  in the cold sections of extratropical cyclones.

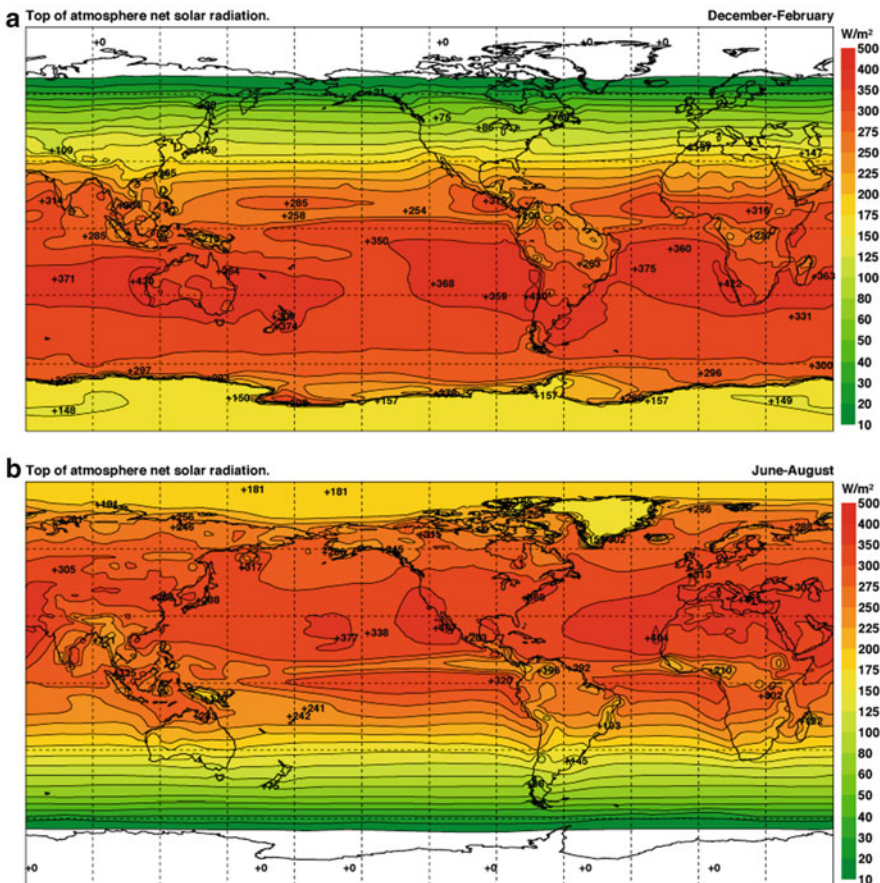
Over land areas of the tropics the latent heat fluxes are generally smaller than the oceanic values. Over most land areas the pattern of the latent heat fluxes resembles that of the rainfall climatology. The pattern of latent heat fluxes over land areas contains local anomalies near water bodies such as river basins and lakes. These anomalies are important for local weather.

Table 13.1 presents a summary of the winter and summer time fluxes over several areas of interest – the Asian monsoon, the SPCZ, the ITCZ, the North Atlantic subtropical high, and the North African desert. Note that over the land area (the North African desert in this case), the net energy budget at the surface is zero. This is consistent with (13.5) that derives the ground temperatures. The ocean areas, on the other hand, have a non-zero net energy budget. This residual has to be balanced with horizontal advection and vertical upwelling.

## 13.4 Top of the Atmosphere Net Radiation Fluxes

### 13.4.1 *The Net Solar Radiation at the Top of the Atmosphere*

The incoming solar radiation at any point at the top of the atmosphere is a function of the solar constant and the solar zenith angle. The solar constant is relatively constant, at around  $1,370 \text{ Wm}^{-2}$ . The solar zenith angle varies with the season but is essentially zonally symmetric. As a result, the incoming solar radiation field is very smooth. The more interesting field is that of the *net* solar radiation, that is, the difference between the incoming and outgoing solar radiation. The latter is a function of the planetary albedo which is strongly a function of the atmospheric structure and clouds within the



**Fig. 13.5** Same as Fig. 13.1 but for solar radiation at the top of the atmosphere

atmosphere and the radiation reflected by the Earth's surface. Since the atmospheric structure and clouds vary by season, and, depending on the location, the reflectivity of the Earth's surface may vary by season as well, the field of net solar radiation at the top of the atmosphere varies too. The fields of the net solar radiation for the northern hemisphere winter and summer are shown in Fig. 13.5a, b respectively. It is worth noting that the net solar radiation at the top of the atmosphere at any given location never exceeds  $400 \text{ W m}^{-2}$ . The values shown in Fig. 13.5a, b include both values from both day and night time 24 h averages for the entire season. During the night time, there is no incoming solar radiation. Since the only source of outgoing solar radiation is reflection, the night time net solar radiation is zero.

The winter and summer hemisphere tropics and subtropics have the largest values of net solar radiation, on the order of  $375 \text{ W m}^{-2}$ . The belt of maximum net solar radiation migrates by almost  $20^\circ$  of latitude between these summer and

winter, primarily in response to the solar zenith angle. The seasonally varying climatological cloud cover distribution largely controls the longitudinal variance of the net solar radiation. During the northern winter there are three major rain areas – Borneo, Congo and Brazil. These rain areas are characterized by large high cloud cover. The high cloud tops reflect a large fraction of the incoming radiation, which leads to a significant reduction of the net top of the atmosphere solar radiation. A similar effect is observed in the area of the Asian summer monsoon. Since sand is highly reflective, the desert areas have a large albedo. Additionally, the desert air is dry, so that there is very little absorption of solar radiation in the tropospheric column, resulting in an overall high planetary albedo over the deserts, and thus a relatively low net solar radiation at the top.

#### ***13.4.2 The Net Thermal Radiation at the Top of the Atmosphere***

Figure 13.6a, b describe the net outgoing longwave radiation for the northern winter and summer respectively. Clouds are a major contributor to this OLR climatology. The values shown in green color over the tropical latitudes carry values close to  $200 \text{ Wm}^{-2}$ . These are the major rain areas of the northern winter months ie the ITCZ, the SPCZ and the rainbelts of the Amazon, Congo and Borneo. During the northern summer the global ITCZ, West Africa Guinea coast and the Asian monsoon belt are characterized by high clouds and low values of OLR (i.e. black body radiation emanating from cold cloud tops residing near the 200 mb level). The orange colors abound over the subtropical oceans where the OLR values are between  $250$  and  $200 \text{ Wm}^{-2}$ . The latter areas are generally characterized by clear skies or fractional stratocumulus cloud cover. The largest OLR values are found over the desert areas of North Africa, Saudi Arabia and Pakistan where the seasonal average OLR values reach as high as  $300\text{--}325 \text{ Wm}^{-2}$ . Some large values are also noted near the Kalahari and the North Australian desert regions. Overall these illustrations largely reflect the deep cloud cover of the tropical latitudes.

### **13.5 Radiative Forcing for the Hadley and East–West Circulation**

The downward branch of the Hadley cell exists over the latitudes of the subtropical highs. The strongest downward motions are generally found over the southeastern parts of these subtropical highs. This descent of air results in adiabatic warming. Since no related temperature changes are noted in the soundings of the subtropical

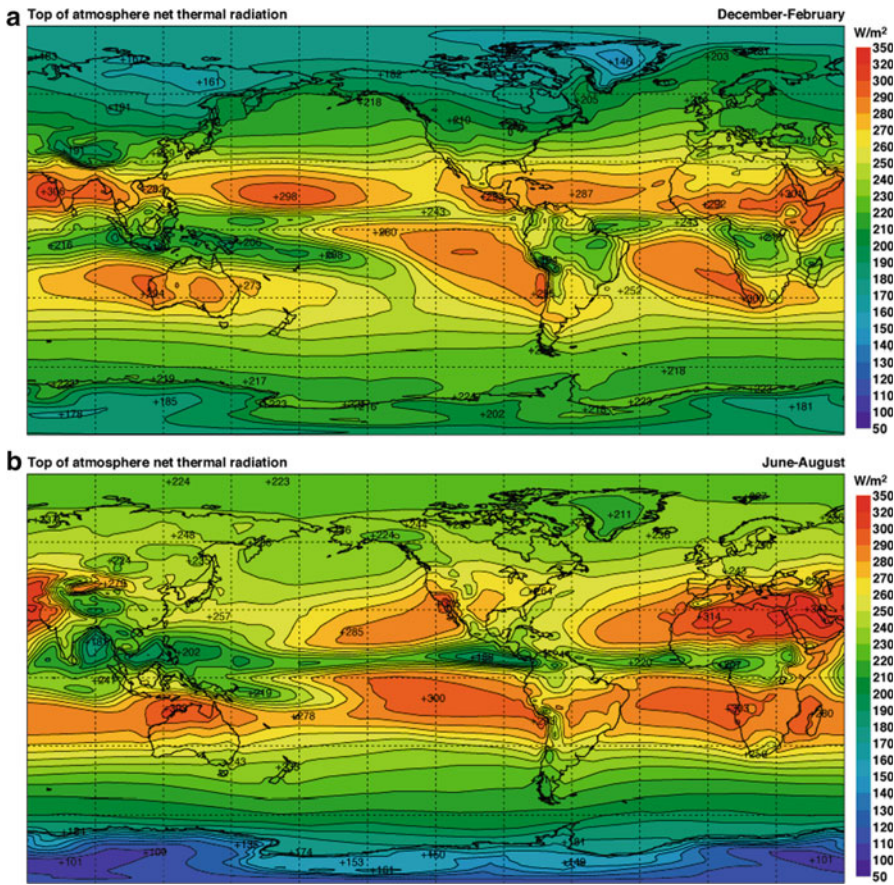


**Fig. 13.6** Same as Fig. 13.1 but for net outgoing long wave radiation at the top of the atmosphere

weather stations (such as the Azores) it is clear that the adiabatic warming is being offset by a steady radiative cooling in the regions of clear sky. This balance is often expressed by the relationship  $\omega \frac{T}{\theta} \frac{\partial \theta}{\partial p} = -\frac{H_{LWR}}{C_p}$ . It is possible to calculate the fields of these two terms for reanalysis data sets to illustrate that such a balance is indeed in place over the subtropical highs. The reanalysis data sets contain six-hourly values of the vertical velocity  $\omega$  and the temperature  $T$ . The cooling by the long-wave radiation,  $-H_{LWR}$ , is also available from the reanalysis data sets. These are based on a radiative transfer algorithm that computes the field of  $-H_{LWR}$  from given inputs of temperature and specific humidity profiles along the vertical coordinate and the vertical distribution of cloud cover following Krishnamurti and Bounoua (1996).

## 13.6 Life Cycle of the Monsoon

An interesting illustration of the surface energy balance is from the life cycle of the monsoon. This includes the following epochs of the Indian Monsoon: pre-onset, onset, active, break, revival, and withdrawal. These are based on rainfall activity. The computation of the components of the surface energy balance was carried out over a domain covering central India (Fig. 13.7). These computations were carried out on a daily basis for the year 2001. These epochs covered the following dates:

- Onset: June 13 (14 mm/day)
- First break: June 23 (2 mm/day)
- Revival: July 1 (23 mm/day)
- Second break: August 1 (1 mm/day)
- Second Revival: August 8 (15 mm/day)
- Withdrawal: August 16 (< 1 mm/day)

The numbers within parentheses illustrate the mean daily rainfall during the epochs. The data sets used for these computations of the components of the surface energy balance were extracted from the ERA-40 files of ECMWF. Figure 13.8 presents the components of the surface energy balance. Prior to the onset of the monsoon the net surface radiation largely balances the sensible heat flux. The soil during this pre-onset phase is very dry and surface latent heat flux is insignificant. In contrast, during the active phase after the onset the soil is wet and the afternoon surface soil temperatures  $T_g$  have dropped from near 50°C during the pre-onset, to around 30°C during the active phase. This drop in surface temperature is coincident with a large drop in the surface sensible heat flux. The wet soil contributes to a

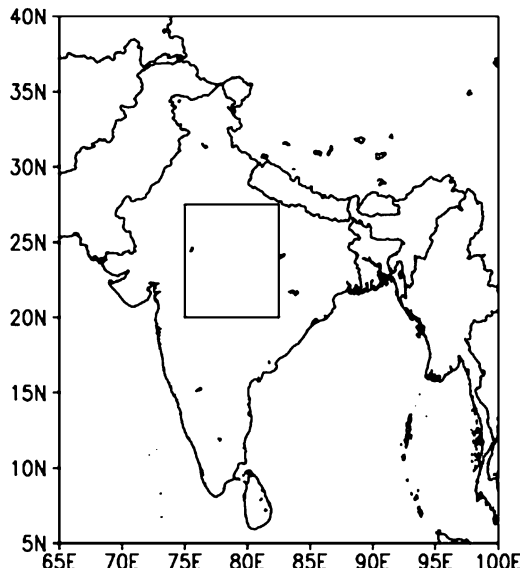


**Fig. 13.7** A map of central India where the estimates of surface energy balance were made

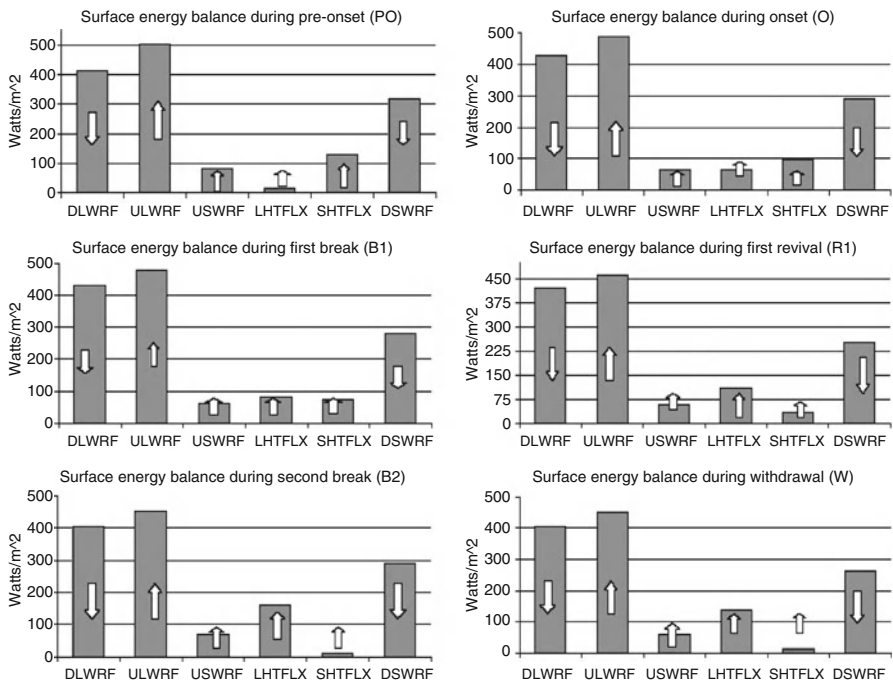


**Fig. 13.8** Components of surface energy fluxes over central India during different epochs

substantial increase of the latent heat flux. During this active (and also during the revival) phase there is a close balance between the net surface radiation and the latent heat flux. The break phase, when the rains diminish, is not quite like the pre-onset phase. During this break phase the sensible heat increases slightly whereas the latent heat diminishes somewhat leading to a surface energy balance between the net radiation and the surface fluxes of sensible and latent heat. During the break phase the cloud cover is generally much larger than during the pre-onset phase. Thus the net radiation reaching the earth's surface over central India is also less. The post-monsoon withdrawal season sees a very slow transition since the soil stays wet for a considerable length of time. Thus the immediate period after the withdrawal phase commences, after the revival, is similar to a break phase, except for the net radiation that starts to significantly. That diminution of net radiation during the withdrawal phase is attributed to the lower zenith angle of the Sun during September and continuing excessive cloud cover.

These transitions in the components of the surface energy balance are essentially common sense changes. There is much said about the surface energy balance in the meteorological literature, thus one is prompted to ask do these changes in the components of the surface energy balance provide any advance information on the behavior of that monsoon season. To answer such a question one needs to

examine several years of the life cycle of the monsoon in this context. Only by examining several years of data one can obtain some idea whether the transition of the surface energy balance carries any advance warning for the monsoon season.

The meanings of the x-axis labels are as follows:

DLWRF	Long wave radiation down at surface
ULWRF	Upward long wave radiation at surface
USWRF	Upward short wave radiation at surface
LHTFLX	Latent heat flux at surface
SHTFLX	Sensible heat flux surface
DSWRF	Downward short wave radiation at surface

## References

- Krishnamurti, T.N., Bounoua, L.: An Introduction to Numerical Weather Prediction Techniques.  
CRC Press, Boca Raton (1996). 293pp
- Press, W.H., Flannery, B.P., Teukolsky, S.A., Vetterling, W.T.: Numerical recipes, the art of scientific computing. Cambridge University press, New York (1986). 123pp

# Chapter 14

## Dry and Moist Static Stability

### 14.1 Introduction

Nearly 80 % of the soundings over the tropical oceans contain a lower tropospheric inversion. In the regions of the trade winds this is often referred to as a trade wind inversion. The strongest inversions are found over the eastern regions of the oceans. Convection, clouds, and turbulent mixing constantly work to erode them. Evidently, however, there are strong restoring forces that counteract the eroding effects and act to maintain the inversion.

Many tropical disturbances, such as tropical lows, depressions, tropical storms, and hurricanes have large amounts of clouds and vertical mixing. Despite the destabilizing influence of these disturbances, the tropical atmosphere remains stable, with an inversion somewhere within the lowest 2 km of the atmosphere. Since this stable tropical atmosphere is the large-scale environment – and thus the lateral boundary – for all tropical disturbances, it is important to understand its nature and reasons for existence.

Nearly 90 % of the tropics are characterized by the presence of conditional instability. Over most of the tropics, the moist static energy and the equivalent potential temperature decrease with height ( $-\frac{\partial \theta_e}{\partial p} < 0$ ) up to roughly the 700 mb level. In this layer the atmosphere is unstable in the moist static sense. In the dry static sense, the tropics are generally stable, i.e., the potential temperature increases with height ( $-\frac{\partial \theta}{\partial p} > 0$ ). These two features (moist instability and dry stability) of the tropical atmosphere constitute the conditional instability. There are several mechanisms that tend to destroy conditional instability; there are others that tend to restore it. Because of the prevalence of conditional instability over the entire tropics, the mechanisms for its maintenance are an important issue. This is discussed in the present chapter.

## 14.2 Some Useful Definitions

Under dry adiabatic conditions,  $C_p \frac{T}{\theta} \frac{d\theta}{dt} = \frac{d}{dt}(gz + C_p T) = 0$ . This relationship can be derived from the Poisson equation  $\theta = T \left( \frac{p_0}{p} \right)^{R/C_p}$  and the hydrostatic law,  $\frac{\partial z}{\partial p} = -\frac{RT}{gp}$ . This indicates that if a parcel is moving upward along a dry adiabat, the dry adiabatic lapse rate is  $\frac{\partial T}{\partial z}_{DA} = -\frac{g}{C_p}$ , or roughly  $10^\circ\text{C km}^{-1}$ . The analogous relation for moist adiabatic processes can be written as  $C_p \frac{T}{\theta} \frac{d\theta_e}{dt} = \frac{d}{dt}(gz + C_p T + Lq_s) = 0$ , where  $q_s$  is the saturation specific humidity at the temperature  $T$ , and  $\theta_e$  is the equivalent potential temperature.

The dry static stability can be expressed by

$$\Gamma_d = -C_p \frac{T}{\theta} \frac{\partial \theta}{\partial p} = -\frac{\partial}{\partial p}(gz + C_p T)$$

and the moist static stability can be expressed by

$$\Gamma_m = -C_p \frac{T}{\theta} \frac{\partial \theta_e}{\partial p} = -\frac{\partial}{\partial p}(gz + C_p T + Lq)$$

## 14.3 Dry and Moist Static Energy

In the following sections we shall present a short derivation of the equations governing the time rate of change of dry static energy  $E_d \equiv gz + C_p T$  and the moist static energy  $E_m \equiv gz + C_p T + Lq$ .

### 14.3.1 Dry Static Energy

Starting with the equations of motion in pressure coordinates,

$$\frac{\partial u}{\partial t} + u \frac{\partial u}{\partial x} + v \frac{\partial u}{\partial y} + \omega \frac{\partial u}{\partial p} = fv - g \frac{\partial z}{\partial x} - F_x \quad (14.1)$$

$$\frac{\partial v}{\partial t} + u \frac{\partial v}{\partial x} + v \frac{\partial v}{\partial y} + \omega \frac{\partial v}{\partial p} = -fu - g \frac{\partial z}{\partial y} - F_y \quad (14.2)$$

If we multiply (14.1) by  $u$  and (14.2) by  $v$  and add the resulting equations together, we obtain

$$\frac{dK}{dt} = -g \vec{u} \cdot \nabla z - \vec{u} \cdot \vec{F} = -g \left( \frac{dz}{dt} - \frac{\partial z}{\partial t} - \omega \frac{\partial z}{\partial p} \right) - \vec{u} \cdot \vec{F} \quad (14.3)$$

where  $K = (u^2 + v^2)/2$  is the kinetic energy per unit mass of air. From the hydrostatic law,

$$\frac{\partial z}{\partial p} = -\frac{RT}{gp} \quad (14.4)$$

Substituting this into (14.3) and rearranging, we obtain

$$\frac{d}{dt}(K + gz) = g \frac{\partial z}{\partial t} - \omega \frac{RT}{p} - \vec{u} \cdot \vec{F}. \quad (14.5)$$

Now we use the first law of thermodynamics,

$$C_p \frac{dT}{dt} = \omega \frac{RT}{p} + Q \quad (14.6)$$

where  $Q = \sum_i Q_i$  is the net heating obtained from the summation of all heat sources and sinks  $Q_i$ . Substituting this into (14.5) and rearranging, we obtain

$$\frac{d}{dt}(K + gz + C_p T) = g \frac{\partial z}{\partial t} + Q - \vec{u} \cdot \vec{F}. \quad (14.7)$$

Since  $C_p \approx 10^3 J kg^{-1} K^{-1}$  and  $T \approx 300 K$ ,  $C_p T \approx 3 \times 10^5 J kg^{-1} = 3 \times 10^5 m^2 s^{-2}$ . If we estimate  $|\vec{u}| \approx 100 m s^{-1}$ , we find that  $K \approx 5 \times 10^3 m^2 s^{-2}$ . Thus from scale analysis, we can see that  $K \ll C_p T$ . For this reason, we can neglect the kinetic energy  $K$  and its dissipation given by  $\vec{u} \cdot \vec{F}$  in (14.7). Furthermore, the pressure tendency term,  $g \frac{\partial z}{\partial t}$  is also usually neglected on the grounds that it is generally small compared with the other terms. Thus one obtains the important energy relation for the dry static stability

$$\frac{d}{dt}(gz + C_p T) = Q. \quad (14.8)$$

In the absence of heat sources and sinks the dry static stability is conserved following the parcel, i.e.,

$$\frac{d}{dt}(gz + C_p T) = 0 \quad (14.9)$$

This equation is synonymous with the equation of conservation of potential temperature, i.e.,

$$C_p \frac{T}{\theta} \frac{d\theta}{dt} = 0 \quad (14.10)$$

### 14.3.2 *Moist Static Energy*

The total heating of a unit mass of air,  $Q$ , is the sum of all the heat sources and sinks  $Q_i$ . To be specific,

$$Q = Q_{SEN} + Q_{EVC} + Q_{CON} + Q_{RAD}, \quad (14.11)$$

where  $Q_{SEN}$  is the sensible heat flux from the ocean or land surface,  $Q_{EVC}$  is the heating (negative, since it is in fact cooling) due to evaporation of cloud matter,  $Q_{CON}$  is the condensational heating, and  $Q_{RAD}$  is the radiative heating. Note that evaporation from the land surface or the ocean does not enter equation (14.11) since the evaporation only cools the underlying surface and can only affect the air temperature when it condenses again. The conservation of moisture requires that

$$\frac{dq}{dt} = E_S + E_C - P, \quad (14.12)$$

where  $E_S$  is the rate of evaporation from the underlying ocean or land surface,  $E_C$  is the rate of evaporation of cloud matter, i.e.,  $E_C = -Q_{EVC}/L$ , where  $L$  is the specific heat of evaporation, and  $P$  is the rate of precipitation per unit mass of air, i.e.,  $P = Q_{CON}/L$ . Thus in energy units, (14.12) can be rewritten as

$$L \frac{dq}{dt} = LE_S - Q_{EVC} - Q_{CON} \quad (14.13)$$

Combined with equation (14.11) this yields

$$Q = -L \frac{dq}{dt} + LE_S + Q_{SEN} + Q_{RAD} \quad (14.14)$$

Substituting this into the dry static energy equation given by (14.8), we obtain an expression for the rate of change of moist static energy following a parcel as

$$\frac{d}{dt} (gz + C_p T + Lq) = LE_S + Q_{SEN} + Q_{RAD} \quad (14.15)$$

Note that  $LE_C$  and  $P$  are implicitly included in this equation. It is evident that the moist static energy can be modified by surface fluxes of moisture and sensible heat, and by radiative processes. In the absence of surface fluxes and radiative heating or cooling, the moist static energy is conserved following a parcel.

## 14.4 Dry and Moist Static Stability

Maintenance of inversion layer and the moist conditional instability over the tropics

### 14.4.1 The Dry Static Stability Equation

This is an important framework for the understanding of the trade wind inversion. We start from the first law of thermodynamics,

$$C_p \frac{T}{\theta} \frac{d\theta}{dt} = \sum_i Q_i \quad (14.16)$$

where  $Q_i$  denotes all forms of diabatic heating, such as condensation heating, radiative heating or cooling, sensible heat flux from the Earth's surface (this includes the ocean surface), and the eddy convergence of heat flux. In flux form, the first law of thermodynamics is given by

$$\frac{\partial \theta}{\partial t} = -\nabla \cdot (\bar{\mathbf{u}}\theta) - \frac{\partial}{\partial p}(\omega\theta) + \frac{1}{C_p} \left( \frac{p}{p_0} \right)^{R/C_p} \sum_i Q_i \quad (14.17)$$

The advective form of the same equation is

$$\frac{\partial \bar{\theta}}{\partial t} = -\bar{\mathbf{u}} \cdot \nabla \bar{\theta} - \bar{\omega} \frac{\partial \bar{\theta}}{\partial p} - \nabla \cdot (\overline{\bar{\mathbf{u}}' \theta'}) - \frac{\partial}{\partial p} \overline{(\omega' \theta')} + \frac{1}{C_p} \left( \frac{p}{p_0} \right)^{R/C_p} \sum_i Q_i \quad (14.18)$$

The definition of dry static stability that we shall use here is

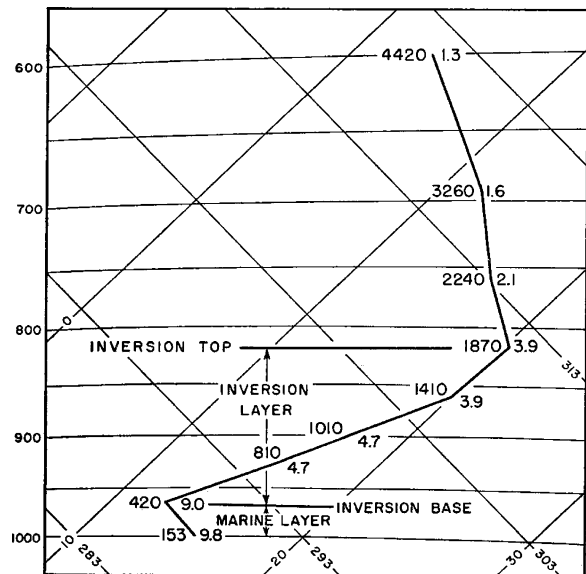
$$\bar{\Gamma}_d = -\frac{\partial \bar{\theta}}{\partial p} \quad (14.19)$$

Upon differentiation of the first law of thermodynamics with respect to  $p$  and changing the sign of the entire equation we obtain:

$$\begin{aligned} \frac{\partial \bar{\Gamma}_d}{\partial t} &= -\bar{\mathbf{u}} \cdot \nabla \bar{\Gamma}_d - \bar{\omega} \frac{\partial \bar{\Gamma}_d}{\partial p} - \bar{\Gamma}_d \frac{\partial \bar{\omega}}{\partial p} + \frac{\partial^2}{\partial p^2} \overline{(\omega' \theta')} - \frac{\partial}{\partial p} \\ &\times \left[ \frac{1}{C_p} \left( \frac{p_0}{p} \right)^{R/C_p} \sum_i Q_i \right] \end{aligned} \quad (14.20)$$

This is the dry static stability equation that states that the local change of dry static stability is influenced by the horizontal advection of dry static stability; the vertical advection of dry static stability; the second derivative of the vertical profile of eddy heat flux  $-\overline{\omega' \theta'}$ , which turns to be same as the vertical derivative of the vertical eddy convergence of flux of heat; the effect of large scale divergence on the dry static stability; and finally, the effects of the vertical derivative of each of the diabatic terms.

**Fig. 14.1** A typical sounding at the southern California coast in summer (From Neiburger et al. 1961)



A typical sounding of the trade wind inversion is shown in Fig. 14.1. This shows that, as we go up, the temperature first decreases up to the base of the inversion, thereafter it increases in the inversion layer, and after we reach the top of the inversion it decreases again. The humidity below the base of the inversion is high and decreases to rather low values above the inversion. The formation or destruction of such an inversion is the topic of this chapter.

What follows is a qualitative assessment of the effects of each term in (14.19). If the initial configuration is one without a trade wind inversion, one must discount the horizontal advection as a possible candidate for its formation since all the horizontal advection can do is carry an inversion from one place to another within a domain. The same is true of the vertical advection – it can only take an existing inversion at one vertical level and move it to another level. Thus, the two advective terms cannot contribute to the formation or the weakening of an inversion. Note, however, that differential advection can still be a contributing factor.

The largest source term that generates  $\bar{\Gamma}_d$  over eastern oceans is  $-\bar{\Gamma}_d \frac{\partial \bar{w}}{\partial p}$ . This is the divergence term. Note that divergence always creates stability and convergence erodes it. Over the eastern oceans, as will be illustrated later in this section, the subtropical highs carry a large field of surface divergence over their southeastern flanks. Here descending air from the deep troposphere continually encounters this positive divergence, generally located below the 600 mb level. As a consequence, descending parcels of air encounter an increase in the dry static stability. If no other processes were acting on the parcel then the largest static stability would reside at the land or ocean surface. However a number of counteracting processes exist that can generate or destroy the dry static stability. The descent and divergence over the

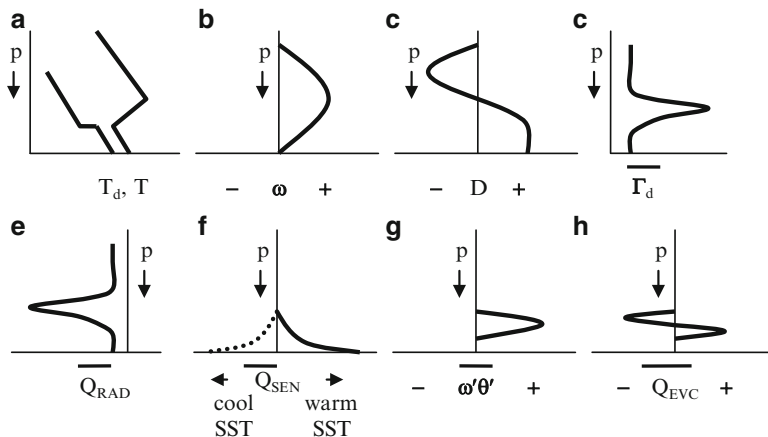


**Fig. 14.2** Schematic vertical profiles of (a) dew point temperature and temperature; (b) vertical velocity; (c) divergence; (d) dry static stability; (e) net radiative heating; (f) sensible heat flux; (g) turbulent heat flux; (h) cloud evaporative heating

eastern oceans generate a reservoir of strong stability that is eroded by a number of processes that ultimately maintain an inversion above the ocean at heights ranging from half a km above ocean to several km above the oceans.

Figure 14.2a–h illustrates schematics of vertical profiles that one sees over the eastern tropical oceans. These illustrations in sequence show the following:

- A typical sounding of temperature and dew point, showing an inversion, the marine layer, and the dry air aloft.
- A vertical profile of vertical velocity  $\omega$ . Positive  $\omega$  indicates sinking motion.
- A vertical profile of horizontal divergence, i.e.  $-\frac{\partial \omega}{\partial p}$ , showing the lower tropospheric divergence and upper tropospheric convergence.
- A vertical profile of dry static stability  $\bar{\Gamma}_d$ , showing the large stability of the inversion layer. Note that shallow stratocumulus and coastal stratus clouds tend to extend just above the base of the inversion. The cloud base is below the inversion.
- A vertical profile of net radiation, dominated by net radiative cooling from the top of the cloud layer of the shallow stratocumulus and coastal stratus. This carries opposite signs of  $-\frac{\partial Q_{RAD}}{\partial p}$  below and above the levels of maximum cooling.  $-\frac{\partial Q_{RAD}}{\partial p} > 0$  tends to lead to destabilization in the dry static sense. The following rule of thumb operates for all diabatic processes – cooling above a certain level and warming below that level leads to destabilization (and vice-versa).
- The sensible heat flux (Fig. 14.2f) and the turbulent heat flux associated with cloud turbulence (Fig. 14.2g) are usually strongly coupled. Between the surface layer and the top of the planetary boundary layer (whose top is around at a height of a few km), the surface fluxes generally diminish with height.

This diminution is often represented with a vertical diffusion (of momentum, temperature, or specific humidity) model. The diffusion coefficient always implies a down-the-gradient transport of the quantity in question. There are two cases for the sensible heat flux, depending on whether the ocean is warmer than the air or the ocean is colder than the air. If we separate the cloud turbulence from the surface sensible heat flux then the profile of the latter can be sketched as shown in Fig. 14.2f. This essentially shows a decay of heating or cooling from the surface layer to the top of the planetary boundary layer which resides near the 1 km level.

- (g) The turbulent mixing is represented by  $\frac{\partial^2}{\partial p^2} \overline{\omega' \theta'}$ . Note that the vertical eddy flux is given by  $-\overline{\omega' \theta'}$ . If the flux is upward  $-\overline{\omega' \theta'} > 0$  and vice versa. This turbulent heat flux plays a key role in elevating the inversion from the ocean surface to a height of one or more km. This acts to erode the stability.  $\frac{\partial^2}{\partial p^2} \overline{\omega' \theta'}$  tends to be negative in the region below the inversion. This is associated with a downward flux of sensible heat in the cloud layer (from cloud-scale vertical motions), i.e.,  $-\overline{\omega' \theta'} < 0$ . This downward flux arises from the fact that the temperature is increasing upwards in the inversion layer and vertical motions of clouds interacting with this vertical temperature gradient transport heat downwards. This happens regardless of whether the ocean is warmer or colder than the air above it.
- (h) Another possible contributor to the destabilization is the evaporation of clouds. Generally the clouds entrain moisture from the bottom of the clouds, condense this moisture into cloud water in the interior (and release heat in the process), and evaporate (and thus cool) at the cloud tops. This provides a vertical gradient of heating  $-\frac{\partial Q_{EVC}}{\partial p} < 0$ . This, along with the cloud top cooling, play a major role for the dry static destabilization of the lower troposphere.

#### 14.4.2 The Moist Static Stability Equation

The moist static energy equation is given by

$$\frac{d}{dt} (gz + C_p T + Lq) = LE_S + Q_{SEN} + Q_{RAD} \quad (14.21)$$

where  $E_S$  is the surface evaporative cooling,  $Q_{RAD}$  denotes net radiative heating, and  $Q_{SEN}$  is the sensible heating. With the definition of moist static energy, (14.14) can be rewritten as

$$\frac{d}{dt} E_m = LE_S + Q_{SEN} + Q_{RAD} \quad (14.22)$$

The grid-scale moist static energy equation is then

$$\frac{\partial \overline{E_m}}{\partial t} = -\bar{\mathbf{u}} \cdot \nabla \overline{E_m} - \bar{\omega} \frac{\partial \overline{E_m}}{\partial p} - \frac{\partial}{\partial p} \overline{(\omega' E_m')} + LE_S + Q_{SEN} + Q_{RAD} \quad (14.23)$$

The right hand side includes the horizontal and vertical advection of grid-scale moist static energy, the convergence of vertical eddy flux of moist static energy from sub-grid-scale motions, the evaporation at the Earth's surface and within clouds, and the sensible and net radiative heat fluxes. Upon differentiation of the above equation with respect to pressure, and changing the sign of the entire equation, one obtains:

$$\frac{\partial \overline{\Gamma_m}}{\partial t} = -\bar{\mathbf{u}} \cdot \nabla \overline{\Gamma_m} - \bar{\omega} \frac{\partial \overline{\Gamma_m}}{\partial p} - \overline{\Gamma_m} \frac{\partial \bar{\omega}}{\partial p} + \frac{\partial^2}{\partial p^2} \overline{(\omega' E_m')} - \frac{\partial}{\partial p} (LE_S + Q_{SEN} + Q_{RAD}) \quad (14.24)$$

Here the left hand side denotes the grid scale local change of moist static stability. The terms on the right hand side denote sequentially: the horizontal advection of moist static stability by the grid scale moisture field; the vertical advection by the grid-scale motion; the large-scale divergence term; the turbulent mixing term; and the effect of stabilization or destabilization by surface evaporation, cloud evaporation, sensible heat flux and net radiation.

The transition of the vertical profile of moist static stability from an undisturbed to a disturbed situation and its converse are important scientific issues. These mechanisms also differ between the eastern and western oceans. The terms in (14.23) can be interpreted as follows:

- (a) Horizontal advection of moist static stability simply conveys it from one region to another and is not considered an important contributor for the restoring or destroying of moist static stability. However differential advection at different vertical levels cannot be ruled out as a possible contributor.
- (b) The vertical advection of moist static stability can only convey it from one vertical layer to another and is not considered an important mechanism during the transition.
- (c) The divergence term which was a centerpiece for the formation of dry static stability is of less importance for the moist static stability where other terms seem to have the major role.
- (d) The flux of moist static energy leads to  $-\overline{(\omega' E_m')} > 0$  with lower values of  $-\overline{(\omega' E_m')}$  at the base and top of the clouds.  $\frac{\partial^2}{\partial p^2} \overline{(\omega' E_m')}$  across the cloud layer tends to be positive, thus contributing to a positive tendency of the moist static stability. This means that the cloud turbulence has a stabilizing effect. The arrival of tropical disturbances (and associated clouds) thus leads to a reduction of the sharp minimum of the  $\theta_e$  profile near the 700 mb level.

- (e) The role of radiation is central to this problem. Shallow stratocumulus and coastal stratus provide a large source of cloud-top cooling near the base of the inversion. It is important to note that over the minimum value of  $\theta_e$  found in a closed three-dimensional domain cannot be lowered by moist adiabatic processes, since these conserve  $\theta_e$ . It cannot be lowered by advection either, since the domain is closed and therefore there is nowhere for the lower  $\theta_e$  air to be brought in from. The most likely mechanism by which the  $\theta_e$  minimum in a closed domain can be lowered is radiative cooling. The gradient  $-\frac{\partial \theta_e}{\partial p}$  can be enhanced by radiative cooling from the cloud-tops near the 700 mb level and by enhanced evaporation at the ocean surface that could contribute to larger values of  $Lq$  at the lower level of the sloping  $\theta_e$  profile. The rule of thumb for interpreting the role of any diabatic term  $Q$  is that for stabilizing the moist static stability the requirement is that  $-\frac{\partial Q}{\partial p} > 0$ . This means that it is necessary to cool at a lower level and warm at a higher level. The stronger radiative cooling at the top of clouds provides a stabilization (or a reduction of the instability) for the layer below.
- (f) Surface evaporation adds moisture to the lower layer and this component of air-sea exchange contributes to a steepening of the  $\theta_e$  (or  $gz + C_p T + Lq$ ) profile from the enhanced value of  $\theta_e$  at the lower end.
- (g) Shallow stratocumulus clouds abound over the tropical ocean. They have a cloud base near the 900 mb level and a top near the 700 mb level. Evaporation of clouds occurs near its top and condensation is at levels below the top of these clouds. This provides a profile where  $-\frac{\partial Q}{\partial p} < 0$ . This has a strong destabilizing influence i.e. its contribution is towards  $\frac{\partial \Gamma_m}{\partial t} < 0$  and contributes to a steepening of the slope of  $\theta_e$ .

In summary, the dry static stability is constantly restored by the divergence term in the eastern subtropical oceans. Turbulent mixing, cloud top radiation, and cloud evaporation are factors that tend to erode the large dry static stability of the inversion layer. The moist static stability is restored constantly by the cloud top radiative cooling, surface evaporation, and the evaporation of clouds. The relevant clouds here are the shallow stratocumulus and the coastal stratus. The turbulent mixing in these clouds also contributes towards an increase of moist static stability.

## 14.5 Observational Aspects of the Trade Wind Inversion

Neiburger et al. (1961) compiled a detailed climatology of the Trade Wind Inversion that provides a very useful background. Neiburger's work was based on ship traverses and series of soundings over the Pacific Ocean, mainly east, south-east, and northeast of the Hawaiian Islands. This climatology covers the summer months. Figure 14.3 illustrates the climatology of the subtropical high of the

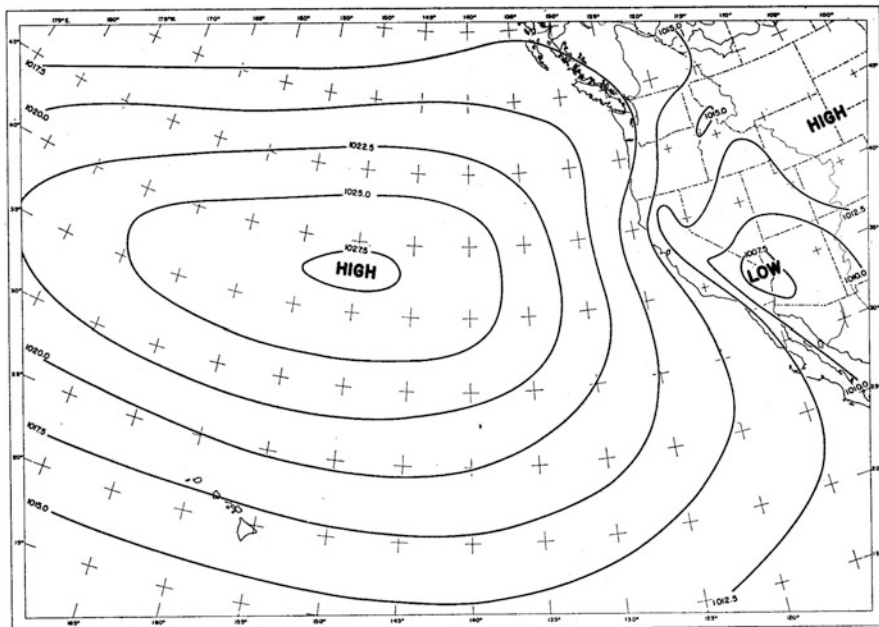


**Fig. 14.3** Normal sea level pressure in July (mb) (From Neiburger et al. 1961)

Eastern Pacific Ocean. This is a large high-pressure system that prevails over the region, similar structures are always seen off the east coast of North and South Africa, South America, and Australia. The central pressure of this high is around 1,027.5 mb. The eastern and especially the southeastern flanks of the subtropical highs are characterized by strong surface divergence of wind and descending motions.

Figure 14.4 illustrates the surface streamline of the subtropical high. The center of this circulation, during the Northern Summer months, is located near 40°N. A most conspicuous feature is the diffluent streamline in the Southeastern section where the diffuseness is associated with strong surface divergence of wind and descending air. These are regions of the strongest inversion. The coastal region from roughly 35°N to 20°N experiences strong divergence.

The Trade Wind Inversion in the coastal region is generally quite strong. Figure 14.1 illustrates a sounding for Los Angeles during the summer season. It shows several features that are worth noting:

- There is a marine layer with large specific humidity approximately 9.8–9.0 g/kg. In this layer the temperature decreases with height.
- The inversion base is located near 420 m. The temperature at the base of the inversion is around 14°C.
- In the inversion layer temperature increases, the top of the inversion is near 1,870 m, where the temperature is near 20°C.

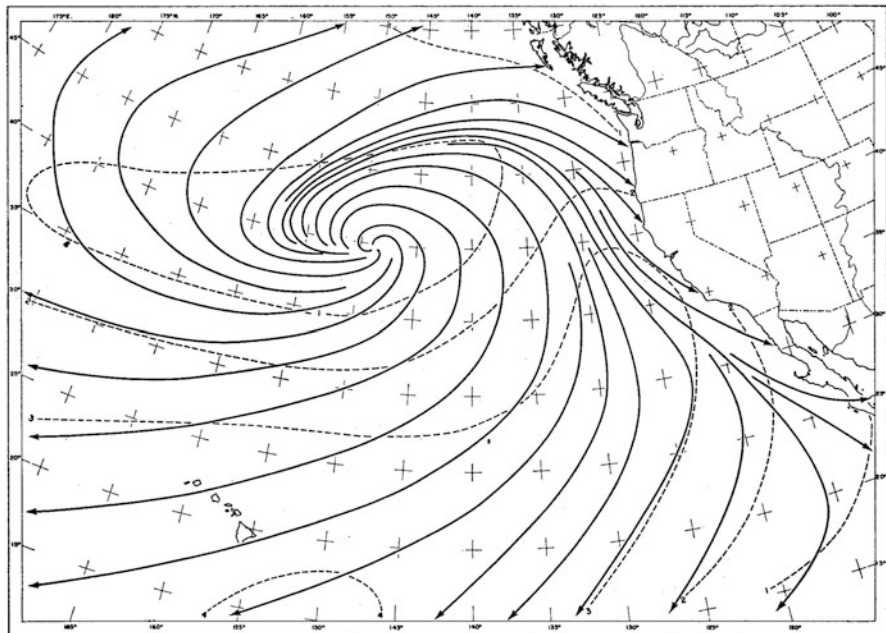


**Fig. 14.4** Normal resultant wind streamlines and isotachs in July (From Neiburger et al. 1961)

- (d) The specific humidity in the inversion layer decreases from roughly 9 g/kg to 3.9 g/kg.
- (e) Above the inversion layers, the temperature decreases with height at a lapse rate close to the dry adiabat.

The average height of the inversion base is shown in Fig. 14.5. The inversion base rises from 500 m to 2,000 m as one proceeds southwestward from California to Hawaii. The temperature at the base of the inversion is at about 10°C at both the California and Hawaii coasts (Fig. 14.6). Between those two locations there is a cold trough of temperature that reaches a minimum near 137.5°W and 37.5°N. This is a semi-permanent feature of the northern summer season. It does not affect the slow increase of the inversion base height encountered as one proceeds westward from the California coast.

The height and temperature at the inversion top are shown in Figs. 14.7 and 14.8. The height of the inversion top ranges from about 600 m at the California coast to around 2,400 m near Hawaii. The temperature at the top of the inversion ranges from about 22°C (near the coast of California and Mexico) to around 14°C in the vicinity of Hawaii. The temperature at the top of the inversion also carries features of the thermal trough that was seen for the base of the inversion.

The average increase of temperature and the average decrease of relative humidity from the bottom to the top of the inversion are shown in Figs. 14.9 and 14.10 respectively. The largest temperature raise and humidity decrease are clearly

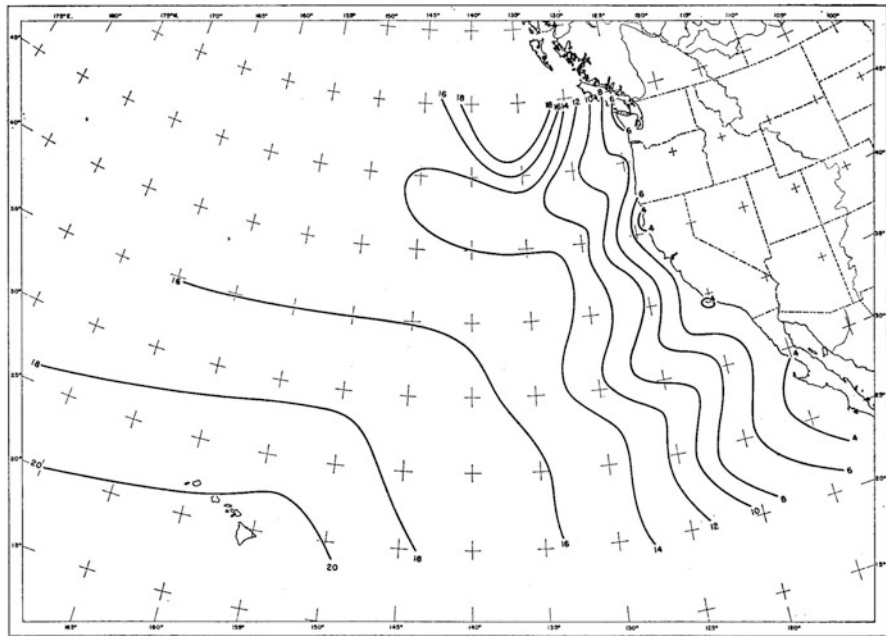


**Fig. 14.5** Average height of the inversion base during summer. Units of hundreds of meters (From Neiburger et al. 1961)

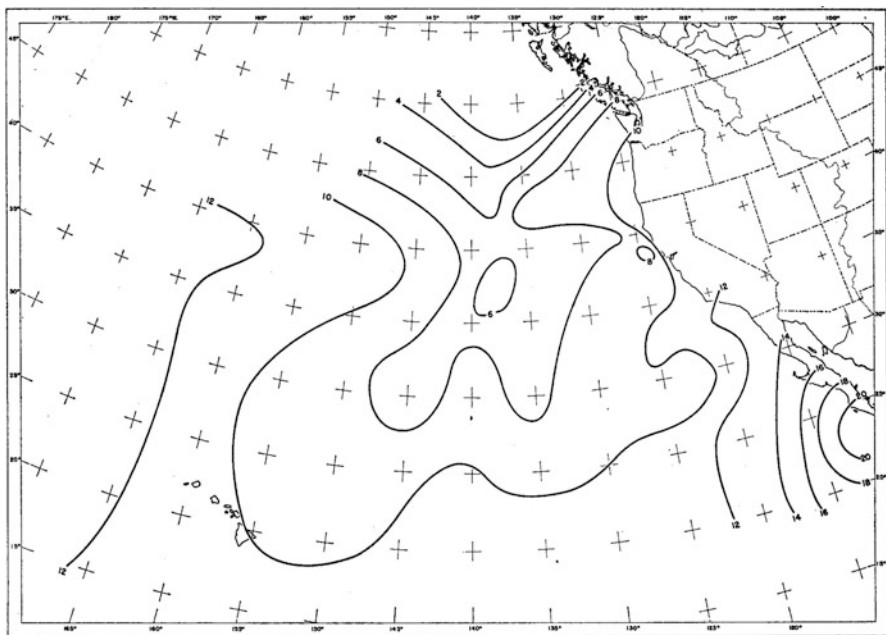


**Fig. 14.6** Average temperature of the inversion base during summer. Units of °C (From Neiburger et al. 1961)

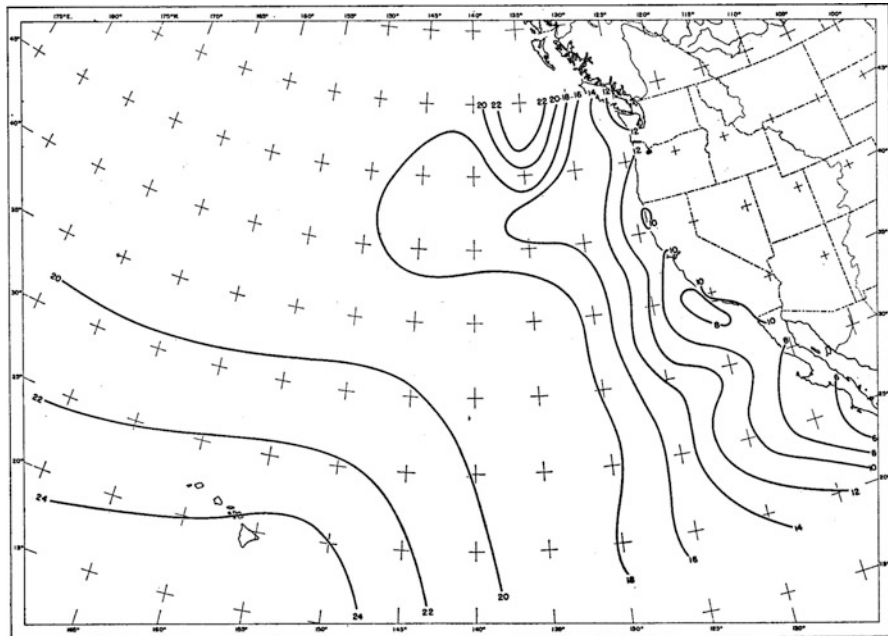


**Fig. 14.7** Average height of the inversion top during summer. Units of hundreds of meters (From Neiburger et al. 1961)

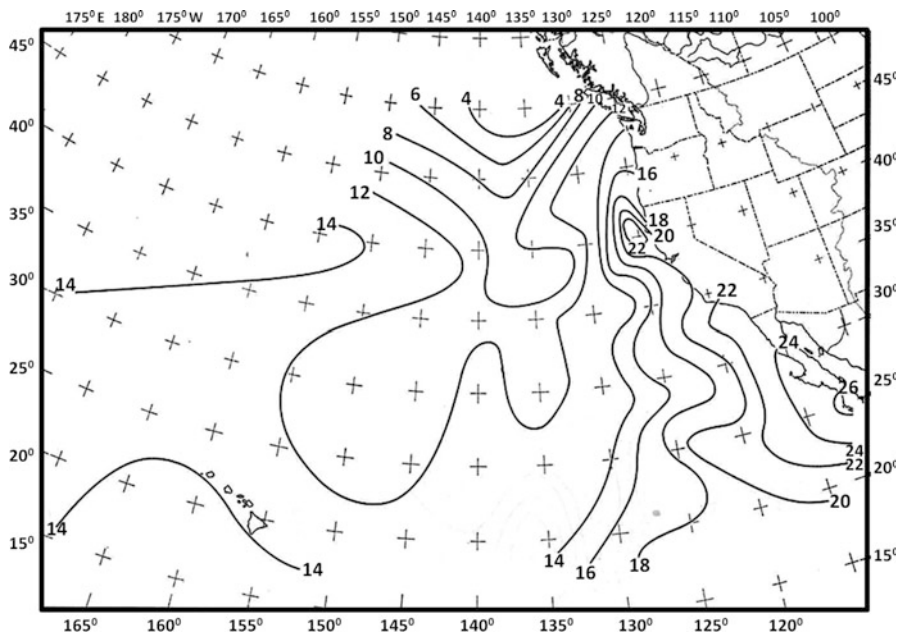


**Fig. 14.8** Average temperature of the inversion top during summer. Units of °C (From Neiburger et al. 1961)

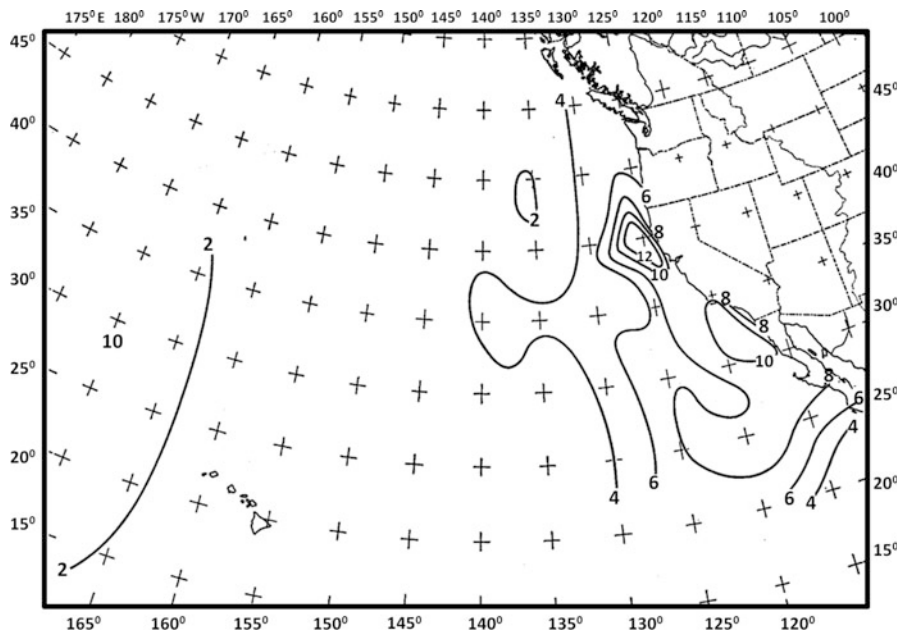


**Fig. 14.9** Average temperature increase from base to top of inversion during summer. Units of °C (From Neiburger et al. 1961)

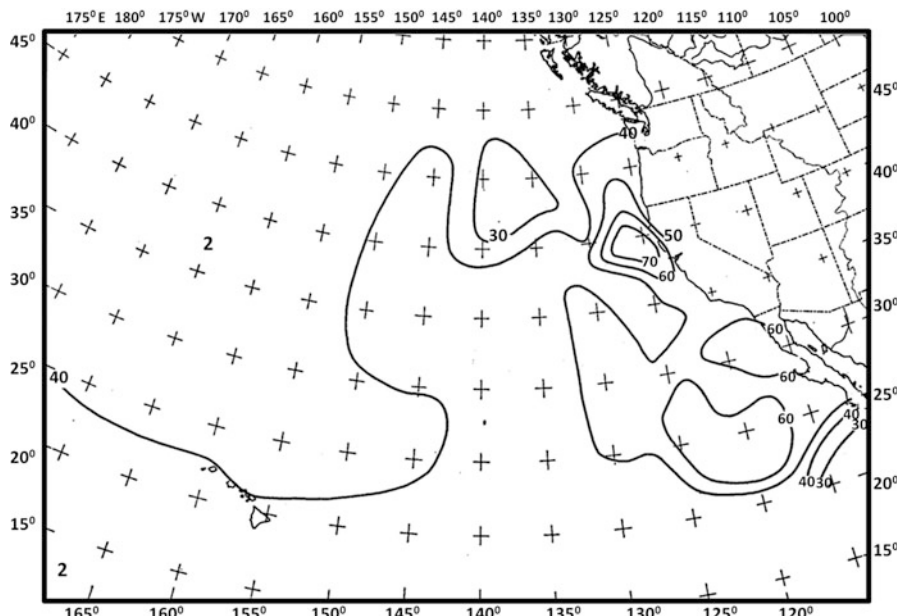


**Fig. 14.10** Average specific humidity decrease from base to top of inversion during summer. Units of % (From Neiburger et al. 1961)

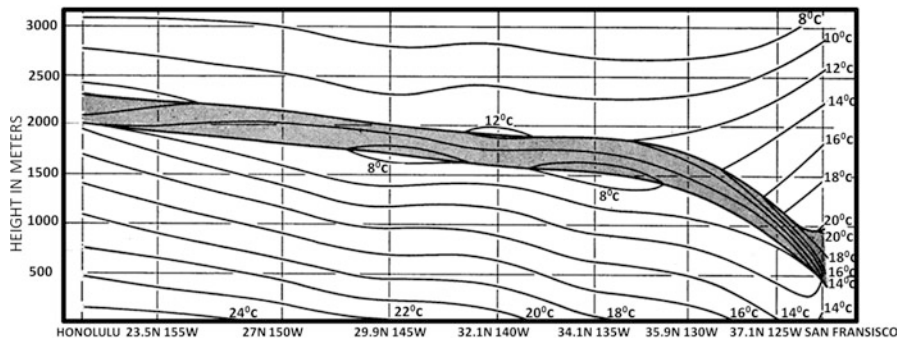


**Fig. 14.11** Average summer cross-section of temperature from San Francisco to Honolulu (From Neiburger et al. 1961)

over the eastern ocean ( $\sim 10^{\circ}\text{C}$  and 60–70 % respectively). Near Hawaii the temperature increase across the inversion is closer to  $2^{\circ}\text{C}$  and the humidity drop is around 40 %.

It is clear from these illustrations that in an undisturbed tropical environment the air above the inversion is quite dry compared to the marine air below the inversion. A vertical cross-section of air temperatures extending northeast from Honolulu to San Francisco is shown in Fig. 14.11. Here the shaded region shows the inversion layer. Its slope and the number of isotherms enclosed within it are indicative of the inversion strength.

Figure 14.12a, b shows typical fields of the dry and moist static stability for a summer day (12 UTC July 1, 2006) in the layer 1,000–700 mb. Over the entire tropics the dry static stability in this layer is positive, whereas the moist static stability is mostly negative. The units for both panels are  $\text{m}^3 \text{kg}^{-1}$ .

The dry static stability has values on the order of  $0.4\text{--}0.5 \text{ m}^3 \text{ kg}^{-1}$  over most of the tropics. The values are somewhat higher over the southern ocean (since this is the southern hemisphere winter season). The desert areas of the northern hemisphere, Sahara and Saudi Arabia, have some of the lowest values of dry static stability.

The moist static instability is largest (with values  $< -0.4 \text{ m}^3 \text{ kg}^{-1}$ ) over the storm areas of the western Pacific, the Asian Monsoon land area and the Caribbean Sea/Gulf of Mexico regions. The most negative values are over the Tibetan Plateau.

The atmosphere over the eastern oceans is normally very dry and as a consequence the vertical gradient of  $E_m \equiv gz + C_p T + Lq$  is very close to that of  $E_d \equiv gz + C_p T$ . There are some regions of positive moist static stability. These include the desert areas of Sahara and Saudi Arabia where the moisture content is extremely low. Other positive moist static stability areas are found over the relatively cool continents of the Southern Hemisphere where again the sign of moist static stability is largely dominated by that of the dry static stability.

It is important to know a gross distinction between disturbed and undisturbed vertical soundings. Since most tropical areas are undisturbed, inversions and low

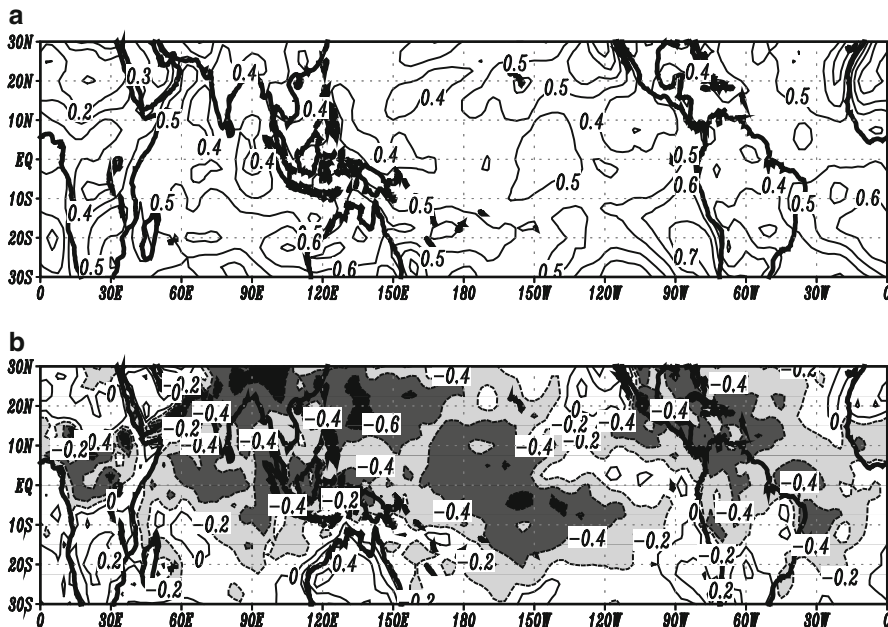


**Fig. 14.12** July 1, 2006 (12UTC) values of (a) dry static stability, and (b) moist static stability for the layer 1,000–700 mb. Units of  $\text{m}^3 \text{ kg}^{-1}$ . NCEP-NCAR reanalysis

humidities above the inversions are typically present. Disturbance passages deepen the moist layer in the soundings and thereby erode the stability. The undisturbed  $\theta_e$  profile normally shows a minimum near the 700 mb level. Below that level conditional instability normally prevails. In a disturbed situation the  $\theta_e$  profile shows a more nearly vertical profile and a sharp decrease in the conditional instability.

## Reference

Neiburger, M., Johnson, D.S., Chien, C.W.: Studies of the Structure of the Atmosphere Over the Eastern Pacific Ocean in Summer. The Inversion Over the Eastern North Pacific Ocean. University of California Publications in Meteorology, vol. 1, pp. 1–94. University of California Press, Berkeley (1961)

# Chapter 15

## Hurricane Observations

### 15.1 Introduction

The terms “hurricane”, “typhoon”, and “tropical cyclone” reflect only a difference in geographical location, but not of underlying physical principles. For this reason, when geographical considerations are not relevant, the above terms will be used more or less interchangeably throughout this book. The unique vertical structure of a hurricane can best be seen from a few vertical cross-sections that portray its wind, temperature, equivalent potential temperature, and clouds. Some of the classical illustrations of wind and temperature have come from an analysis of Hurricane Inez of 1966 by Hawkins and Imbembo (1976). Figure 15.1 is a cross-section across the hurricane that was produced using multiple aircraft reconnaissance data sets. The hurricane reconnaissance aircraft provided flight level winds and a center fix that enabled the construction of this inner core structure of the strong winds in a hurricane.

This cross section is roughly perpendicular to the direction of motion of the storm. There are several features of interest in this illustration. The strongest winds occur in the right quadrant (with respect to the motion of the hurricane), at a radial distance of roughly 10 nautical miles (18.5 km) from the storm’s center. In the hurricane’s inner core, the isotachs are vertically aligned, indicating the lack of strong vertical shear. Strong winds in excess of 100 kt (51.4 m/s) prevail to an altitude of roughly 30,000 feet (about 9 km). Radially, strong winds in excess of 50 kt (25.7 m/s) extend to a radius of roughly 40 nautical miles (74 km) from the storm’s center.

The difference in the wind intensity between the right and the left quadrants for the case shown in Fig. 15.1 is only about 15 knots (7.7 m/s). This asymmetry is partly translational (i.e. resulting from the addition of the storm motion vector to the circulation wind field) and partly arising from storm dynamics that may involve interactions among the azimuthally averaged flows and the translational asymmetry. The inner core of this storm has cyclonic circulation through the 100 mb level and even at 52,000 feet (15.8 km) above the sea level winds in excess of 20 kt (10.3 m/s)

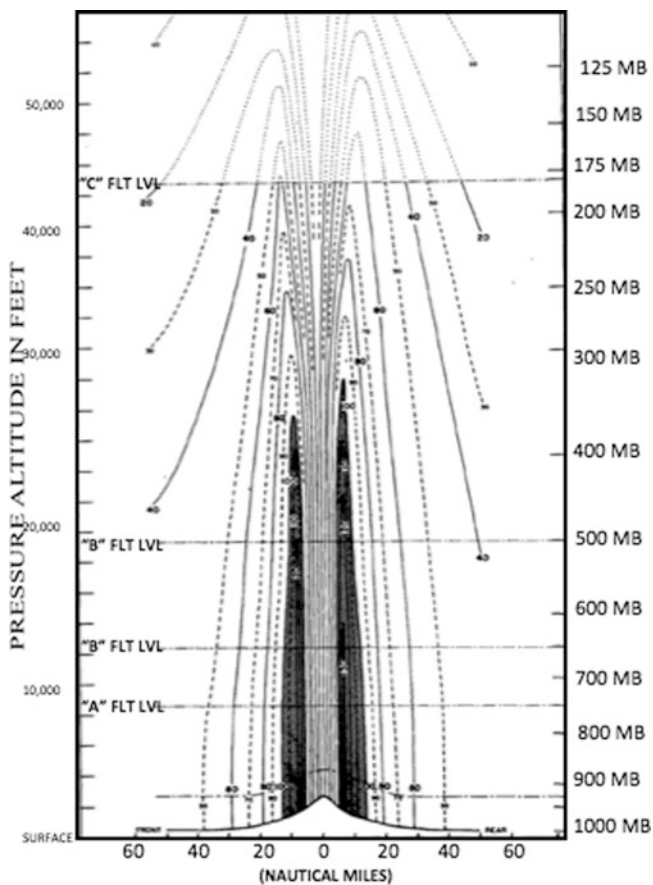


**Fig. 15.1** Storm-relative wind speeds for Hurricane Inez (From Hawkins and Imbembo 1976)

can be seen. Above roughly 55,000 feet (16.7 km) the cyclonic circulation in the inner core abates and is replaced by an anticyclonic circulation.

Figure 15.2, also from Hawkins and Imbembo (1976), illustrates the thermal structure of Hurricane Inez. Shown here is the temperature anomaly with respect to a mean tropical hurricane season sounding. Horizontal dotted lines show the aircraft flight levels where the data sets were available for analysis. The most striking feature here is the warm core of the hurricane that resides within 15 nautical miles (28 km) from the storm center and stretches throughout the troposphere, reaching a maximum temperature anomaly very high in the troposphere – at roughly 250 mb. This warm core is about  $16^{\circ}\text{C}$  warmer than the air some 200 nautical miles (370 km) away from the storm center. It is largely the result of organized cumulus convection around the eye wall of the hurricane. Most of this anomalous warming occurs at the edges of the clouds that provide a conversion of potential energy to sensible heat. The air in the eye wall clouds experiences moist adiabatic ascent

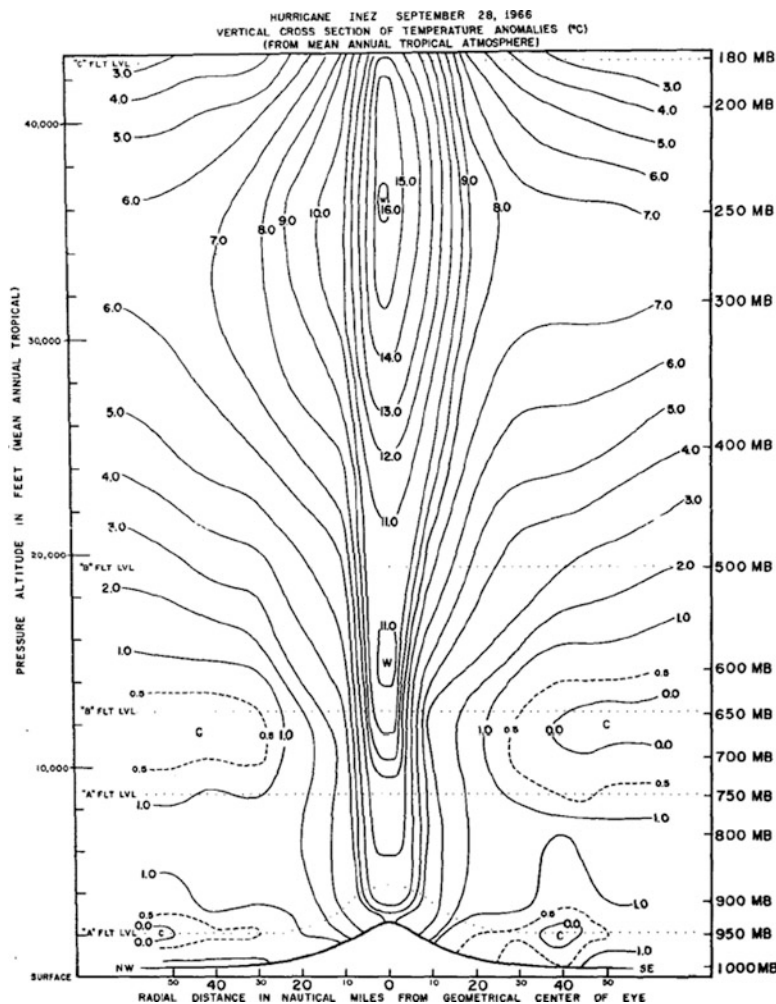


**Fig. 15.2** Vertical cross section of temperature anomaly for Hurricane Inez (From Hawkins and Imbembo 1976)

where the potential energy of the rising parcels is generated. Here buoyant motions provide the energy for vertical motions.

Another feature of interest in this diagrams is the presence of cold temperature anomalies near the 10,000 feet (3 km) level at radii >30 nautical miles (55 km). These cold anomalies are seen in both the right and the left sector. They are largely explained by the cloud top cooling of low clouds outside of the storm's inner core and from the evaporation of falling rain in the environment of the storm. Another notable feature of this illustration is the strong radial gradient of temperature at a distance of about 10 nautical miles (18.5 km) from the storm center. In spite of this

strong radial gradient of temperature, the winds shown in Fig. 15.1 do not change much with height (contrary to what would be implied by geostrophic thermal wind theory). That is explained from the very large differences between the geostrophic thermal wind and the gradient thermal wind in such strongly rotating systems.

For a system in gradient wind balance we can write

$$\frac{v_\theta^2}{r} + fv_\theta = -g \frac{\partial z}{\partial r}, \quad (15.1)$$

where  $v_\theta$  denotes the tangential wind, and the three terms represent the centrifugal, Coriolis, and pressure gradient forces respectively. Using the hydrostatic equation,

$$-g \frac{\partial z}{\partial p} = \frac{RT}{p}, \quad (15.2)$$

one can write its radial gradient as

$$-g \frac{\partial^2 z}{\partial p \partial r} = \frac{R}{p} \frac{\partial T}{\partial r}. \quad (15.3)$$

The gradient thermal wind is obtained upon differentiation of the gradient wind relation (15.1) with respect to pressure:

$$2 \frac{v_\theta}{r} \frac{\partial v_\theta}{\partial p} + f \frac{\partial v_\theta}{\partial p} = -g \frac{\partial^2 z}{\partial r \partial p} \quad (15.4)$$

The resulting equation for the gradient wind after substituting for  $[-g \frac{\partial^2 z}{\partial r \partial p}]$  from (15.3) into (15.4) is:

$$\frac{\partial v_\theta}{\partial p} = \frac{R}{p(2 \frac{v_\theta}{r} + f)} \frac{\partial T}{\partial r}. \quad (15.5)$$

The geostrophic thermal wind, on the other hand, is simply given by

$$\left. \frac{\partial v_\theta}{\partial p} \right|_{geostr} = \frac{R}{pf} \frac{\partial T}{\partial r} \quad (15.6)$$

For a given radial temperature gradient, the ratio of the geostrophic to the gradient thermal wind is

$$\frac{\left. \frac{\partial v_\theta}{\partial p} \right|_{geostr}}{\left. \frac{\partial v_\theta}{\partial p} \right|_{grad}} = \frac{2 \frac{v_\theta}{r} + f}{f} \approx \frac{2 \frac{v_\theta}{r}}{f} \quad (15.7)$$

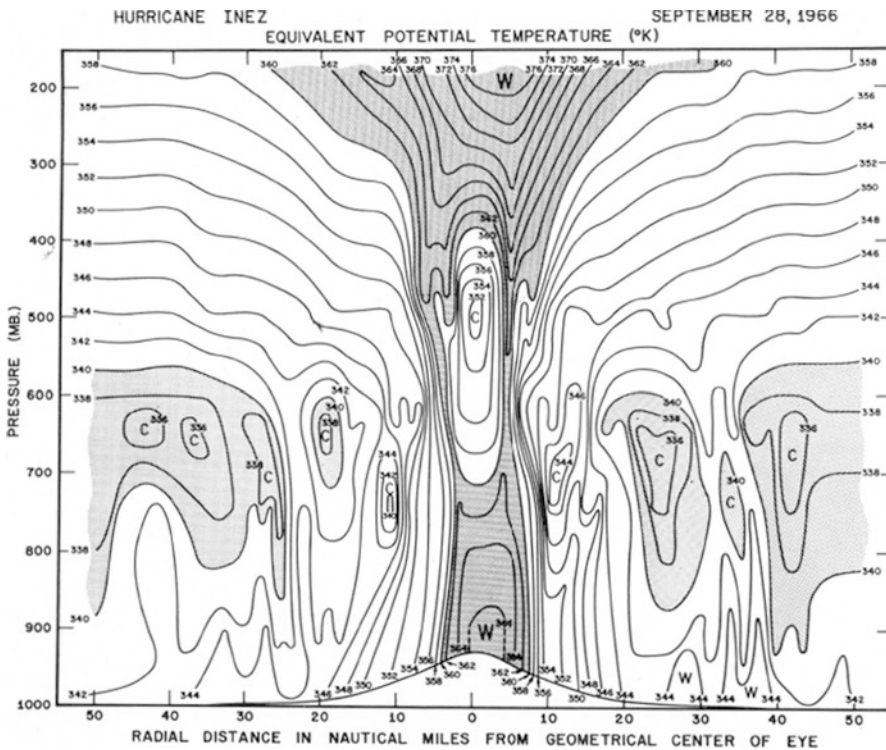


**Fig. 15.3** Vertical cross-section of equivalent potential temperature for Hurricane Inez on 28 September 1966 (From Hawkins and Imbembo 1976)

since  $2 \frac{v_0}{r} >$  in the inner core of a hurricane. The right hand side of (15.7) is on the order of 100. The gradient wind changes with height are therefore roughly 100 times smaller than those of the geostrophic thermal wind. Thus one finds a slow decrease of wind with height in a hurricane.

Another striking feature of a mature hurricane is the field of equivalent potential temperature,  $\theta_e$ , shown in Fig. 15.3, also based on Hawkins and Imbembo (1976). This diagram shows several important features. The eye wall region between 5 and 10 nautical miles (9–18 km) for the storm's center has a near-vertical orientation for the  $\theta_e$  isopleths. This is representative of undiluted ascent. At outer radii of approximately  $r > 25$  nautical miles ( $\sim 46$  km) low values of  $\theta_e$  are found near the 700 mb level. This is the familiar  $\theta_e$  minimum of the large scale tropical atmosphere. This  $\theta_e$  minimum is maintained by radiative cooling at the top of the stratocumuli that abound over the tropical oceans. The hurricane carries a strong low-level convergence of air in its planetary boundary layer. Weak inflows also prevail over a deep lower troposphere that continually brings in lower  $\theta_e$  air of the tropical environment into the circulation of the hurricane. Within the eye large values of  $\theta_e$  near the ocean surface are contributed by enhanced evaporation from the ocean.

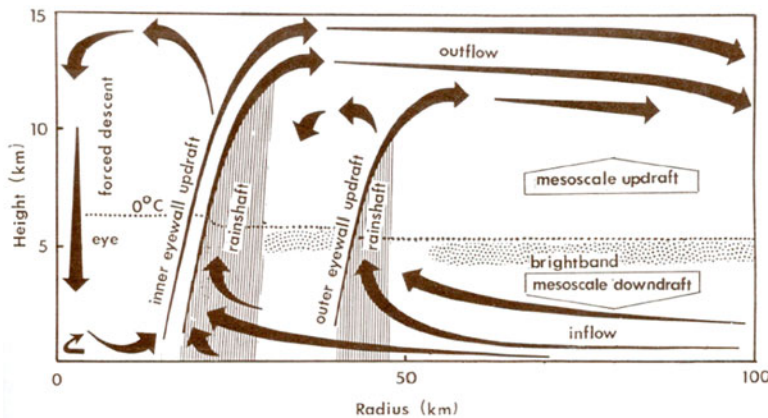


**Fig. 15.4** Schematic of the secondary circulation and precipitation distribution for a tropical cyclone (From Wiloughby 1988)

A schematic of the clouds and vertical circulation in a hurricane is illustrated in Fig. 15.4. This shows the eye wall and the rainband clouds, and the outer region clouds. A typical feature of the hurricanes is the inner cyclonic outflow over the top of the eye wall cloud, which is illustrated in Fig. 15.4. The downdrafts at the edges of the convective clouds are another important feature of the hurricanes (not shown).

Hurricanes and typhoons appear in varying sizes. Figure 15.5 shows examples of some intense cyclones (Choi Wan over Western Pacific, Wilma and Isabel over tropical Atlantic Oceans) that are characterized by a relatively symmetric eye wall with intense convection. In contrast relatively weaker cyclones like Loke and Winnie in Western Pacific Ocean are characterized sometimes by double eyewall structure with intervening cloud free regions and relative asymmetry.

## 15.2 Conventional Observations

Hurricane analysis and forecasts do require a data base of conventional observations. This includes data sets from a variety of sources, such as: the broadband radiosonde and rawinsonde networks, pilot balloons, surface and marine observations, cloud and water vapor winds, commercial aircraft-based wind and temperatures, oceanic buoys, the ARGO profiles global oceanic network, satellite-based sounders for temperature and humidity, precipitation estimates from surface, radar and satellites (microwave and radar). This broad scale data set must be supplemented by special observations in the inner core of a hurricane.

Big changes have occurred in the observing systems for the surveillance of the inner core of hurricanes. NASA and NOAA in US have deployed pilot less drones that carry radar, drop windsonde and various specialized instruments.

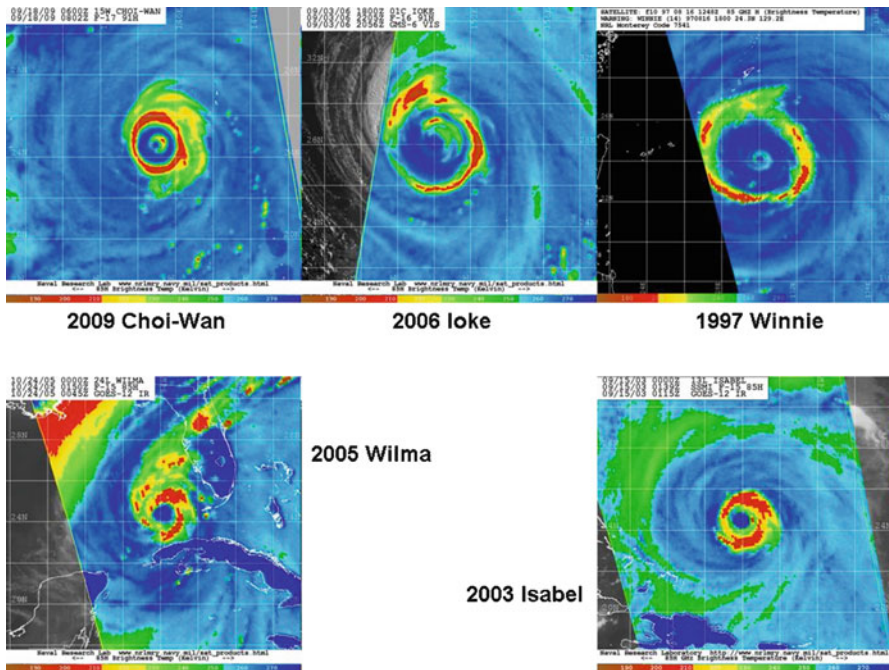
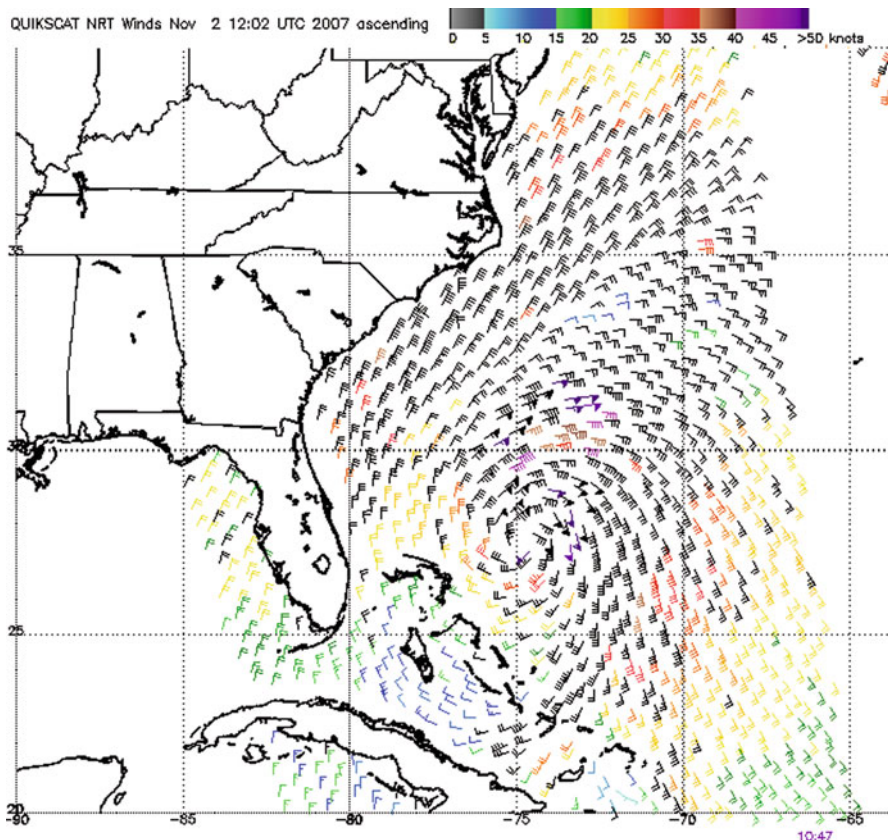


**Fig. 15.5** The figure shows the eye with different sizes in different typhoons and hurricanes (From Space Science and Engineering Center of the University of Wisconsin (Courtesy M. Sitkowski))

In the summer of 2010 no less than seven research aircraft participated in a joint effort to provide observations for hurricanes. Almost every hurricane within aircraft reach from the south east coast of US is currently monitored by surveillance aircraft. The inner core carries wind, temperatures moisture, pressure and microphysical observations from this.

### 15.2.1 *Observations of the Inner Core*

A **scatterometer** is a satellite-mounted microwave sensor that is used for the determination of the wind speed and direction over a water surface. It works by sending pulses of microwave energy to the surface and then measuring the return signal from the waves on the water surface; the wind direction and speed are then estimated based on the backscatter characteristics. Figure 15.6 illustrates Quik Scatterometer (QuikSCAT) winds for hurricane Noel on November 2, 2007. The color-coded scale of the winds is shown at the top of the figure. The maximum winds in this tropical storm are between 40 and 45 knots (20 and 23 m/s). Such surface



Note: 1)Times are GMT 2)Times correspond to 30N at right swath edge - time is right swath for overlapping swaths at 30N  
3)Data buffer is Nov 2 12:02 UTC 2007-22 hrs 4)Black barbs indicate possible rain contamination

NOAA/NESDIS/Office of Research and Applications

**Fig. 15.6** Illustration of QuickSCAT winds for hurricane Noel, November 2, 2007

winds are available daily over many regions of the tropics. This is a very useful database for mesoscale numerical weather prediction of tropical disturbances.

**Dropwindsondes** are a useful tropospheric profiling instrument that is often launched from reconnaissance aircraft. The United States have been using this platform for flights into hurricanes since the 1950s. At times as many as six research aircraft have made penetration into hurricanes. These fly at several levels from roughly a km above the ocean to almost 11 km above the ocean. Flight patterns are designed by mission scientists to meet the situation and the scientific needs of the day. The profiles include temperature, humidity, pressure altitude and winds. A dropwindsonde is deployed from an aircraft that carries the instrument package and a balloon. This is like a reverse radiosonde balloon; here the balloon is going down at a rate of roughly 300 m a minute. The balloon also carries a Global Positioning system (GPS) that transmits its position and hence the horizontal wind

estimate is made available. All of the data from the dropwindsonde are received at the aircraft and are transmitted to the Global Telecommunication System (GTS) for weather analysis (assimilation) and forecasting. Hurricane Humberto was located in the Atlantic Ocean on September 23 2001 when multiple research aircraft provided dropwindsonde data at several levels. Figure 15.7 shows a plot of such data at three different levels. It should be noted that in the absence of this data set the only tropospheric winds one can have over the ocean would be those from the tracking of clouds and water vapor from satellites. The dropwidsonde is a very high quality data for research and operations.

**Lidar Atmospheric Sensing Experiment (LASE)** detector is an airborne instrument that is used for measuring the vertical profiles of concentration of aerosols and water vapor. This lidar uses a laser pulse repeated at frequency of roughly 2–4 kHz at a wavelength of 730 nm. It has a field of view of roughly 1.23 mrad. It uses the absorption and scattering of different laser pulses to deduce the vertical structure of aerosol and water vapor distributions along the aircraft path. The LASE instrument can only see to the top of clouds but it cannot penetrate into clouds. It is, however, capable of providing profiles both below and above the aircraft flight level. Here we will show vertical time sections obtained using the LASE instrument aboard a research aircraft during a hurricane surveillance mission. The aircraft flight track along which this particular set of measurements was obtained is shown in Fig. 15.8.

NASA DC8 aircraft was flown into an easterly wave off the west coast of Africa on August 30, 2006 that eventually became a tropical storm. The vertical-time section along a south-to-north leg of the flight is shown in Fig. 15.9a, b. These show the aerosol and humidity concentration respectively as seen by the LASE instrument. Figure 15.9a, b show a heavy dust layer between the altitudes of 2 and 3 km. The moisture cross-section shows a marked drying as one proceeds north from 14°N to 20°N. The moist layer with specific humidity of the order of 12–14 g/kg near 14°N below 2 km narrows to a very shallow marine layer as we proceed north of 16°N. This is a unique data set for studying dust-loaded African waves that can become tropical storms as they move westward. A strong inversion caps the dust below the 3 km level in the eastern Atlantic Ocean.

Airborne expendable bathy-thermograph (AEBT) is a probe that measures the temperature profile in a water column. It consists of a thermistor enclosed in a case that is dropped from an aircraft.

## 15.3 Tropical Cyclones Over the Indian Ocean Basin

The post-monsoon months, mid-October to mid-December, and the pre-monsoon months of April through early June are well known for the formation of tropical cyclones over the Bay of Bengal and the Arabian Sea. The northern winter months of December through March are a period of tropical cyclone activity in the Indian

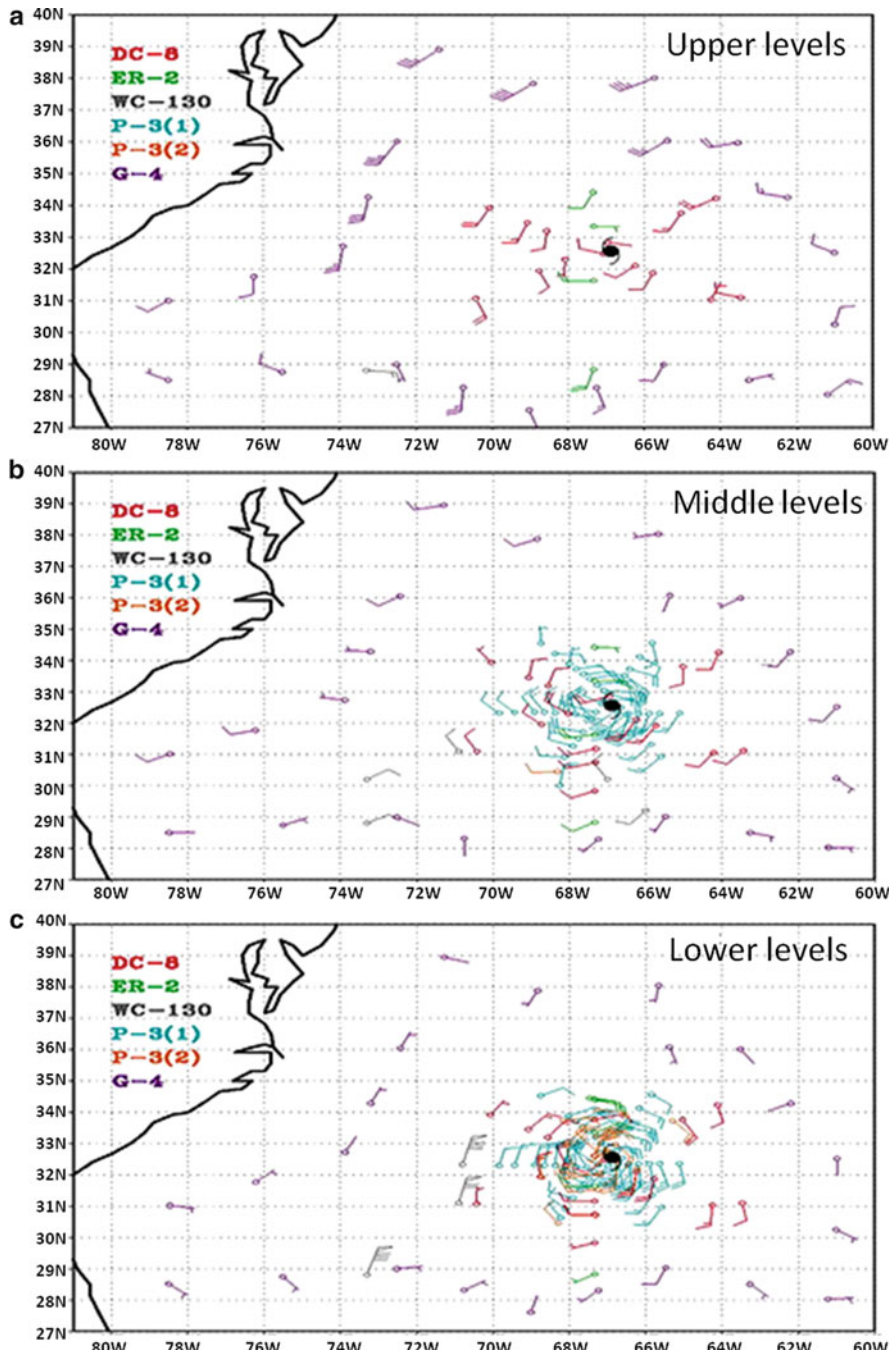


**Fig. 15.7** Sample coverage of dropsonde data from multiple aircraft for CAMEX-4 on 23 Sep 2001, Hurricane Humberto, at (a) upper level (300–200 mb), (b) middle level (400–600 mb), and (c) lower level (900–750 mb) (From Kamineni et al. 2006)

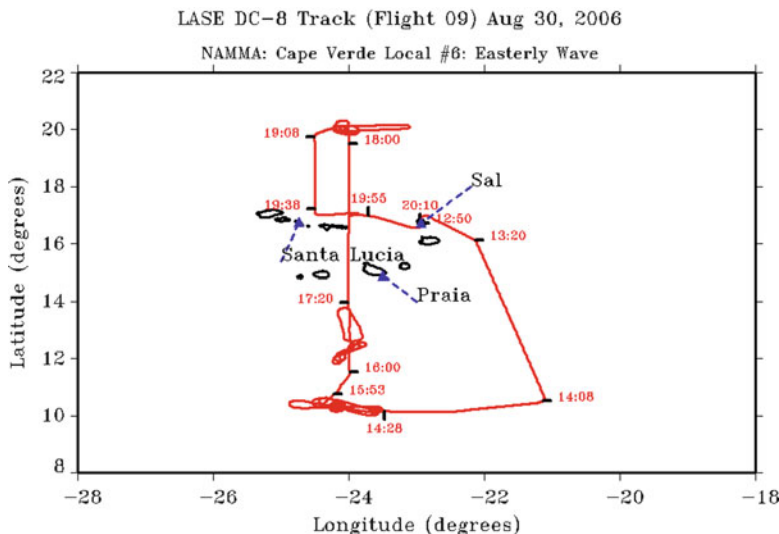


**Fig. 15.8** The flight track of NASA DC8, a research aircraft for the surveillance of an easterly wave on August 30, 2006 over the eastern Atlantic is shown here. Sal Island, shown here, is over the Cape Verde group of islands (From Browell et al. 1997)

Ocean on the opposite side of the equator, around 7°S to 15°S. All of this activity is centered on the following prevailing large scale conditions over these regions:

- (a) Weak vertical wind shear
- (b) Presence of cyclonic relative vorticity in the lower troposphere
- (c) Sea surface temperatures in excess of 27°C
- (d) Presence of moisture in the middle troposphere.

Figure 15.10 shows the climatological tracks of tropical cyclones over the Indian Ocean covering all seasons. This makes use of all available historical storm tracks over the Bay of Bengal and the Arabian Sea.

The regions most severely affected by the tropical cyclones over the Indian Ocean Basin include Bangladesh, Bengal and the East Coast of India, Mozambique in Africa, the Mascarene Islands, Madagascar and Northern Sri-Lanka. Losses of life and property are quite large since many of the tropical cyclones in this region are of category 2 in intensity or larger.

A number of tropical storms form near 10°N over the central Bay of Bengal and track northwestward. Some of these recurve towards Bangladesh. Often the antecedents of these tropical cyclones can be traced to easterly waves that propagate westwards from the western Pacific Ocean. These systems move westwards at a speed of roughly 5°longitude per day. As they arrive over a region of weak wind

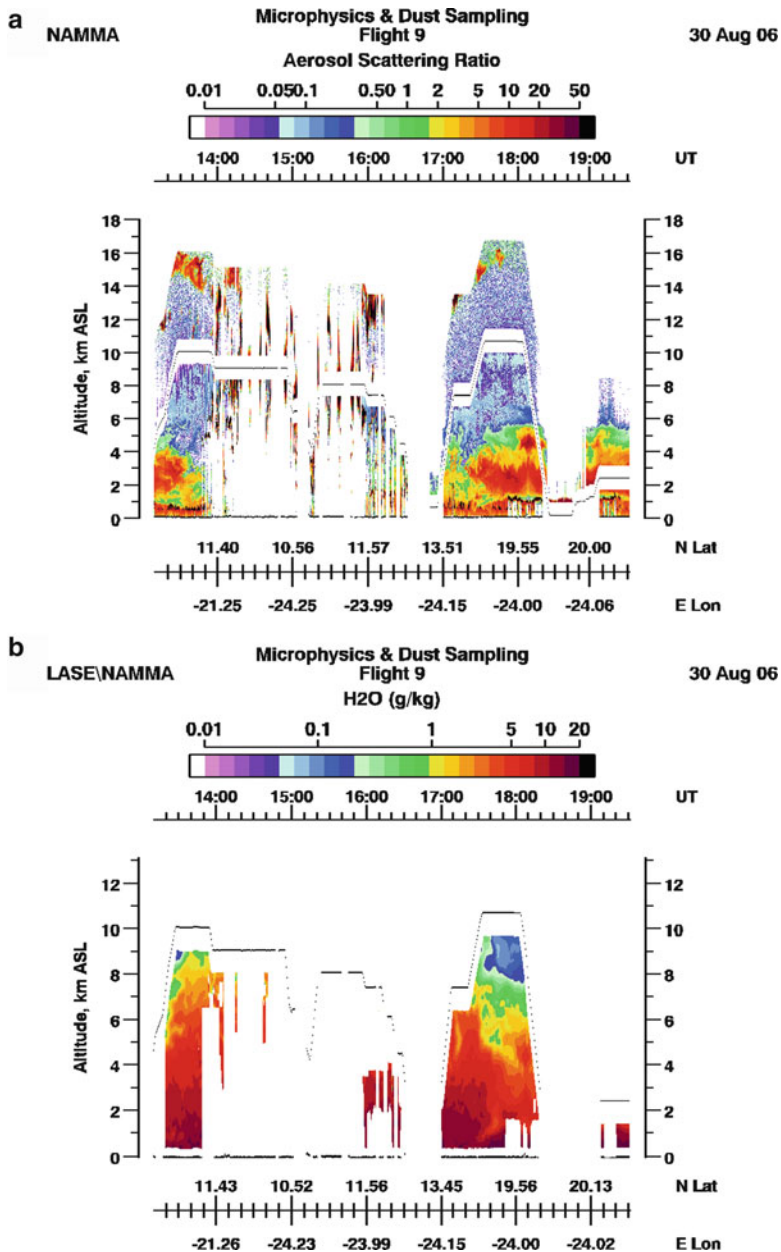


**Fig. 15.9** (a) The vertical cross-section made from one leg of the DC8 flight. This shows the LASE instrument seeing the aerosol dust sampling as indicated by the vertical profiling of the aerosol scattering ratio. The vertical shown on right is height in kms. The zero line on left is the height in kms with respect to flight altitude of aircraft which was flying at near 10.5 kms. (b) Same as (a) but it shows the vertical profiling of specific humidity in units of gm/kg (From Browell et al. 1997)

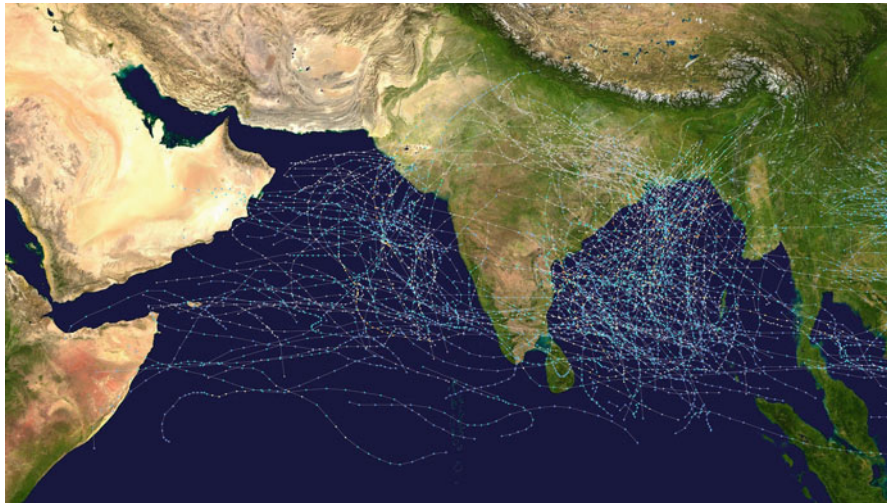
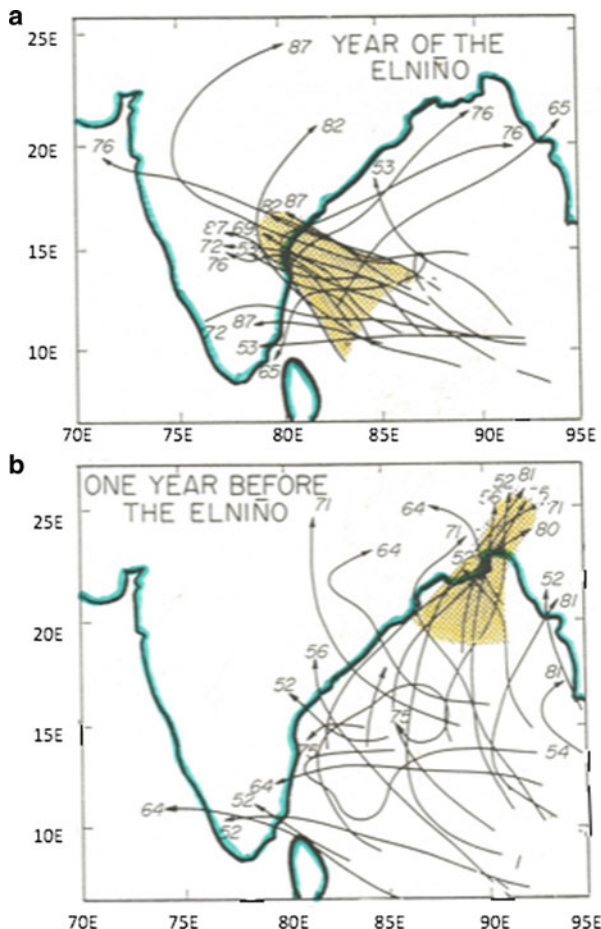


**Fig. 15.10** Climatological tracks of tropical cyclones over the Bay of Bengal and the Arabian Sea covering all seasons (Image courtesy of the Indian Meteorological Department)

shear and warm SSTs in excess of  $27^{\circ}\text{C}$ , tropical cyclones form. These waves are located over the cyclonic shear side of the strong trade winds of the Pacific Ocean. Conversion of shear to curvature vorticity assists in the strengthening of these easterly waves. These trade winds extend into the Bay of Bengal across Southern Malaysia. The extension of the subtropical high and the trade winds from the Pacific to the Bay of Bengal seems to be strongly influenced by the phase of El Niño. Figure 15.11 illustrates composites of tracks of tropical cyclones over the Bay of Bengal for the year during El Niño and for the year before El Niño. What is clear from this illustration is the channeling of a preponderance of cyclone tracks towards Bangladesh during the year before the El Niño. This channeling focuses most cyclone tracks over the central eastern Indian coast during El Niño years. This shift of cyclone tracks is related to the more westward penetration of the subtropical high in the year before the El Niño. During El Niño years, on the other hand, the subtropical high shows less of a westward penetration over the Bay of Bengal. These changes result in somewhat different steering of tropospheric winds for the tropical cyclones of the Bay of Bengal in these different periods.

**Fig. 15.11** Composite cyclone tracks of the Indian summer monsoon during (a) El Niño years and (b) one year prior to El Niño years (Image courtesy of the Indian Institute of Tropical Meteorology, Pune)



## References

- Browell, E.V., Ismail, S., Hall, W.M., Moore, A.S., Kooi, S.: LASE validation experiment. In: Ansmann, A., Neuber, R., Rairoux, P., Wandinger, U. (eds.) *Advances in Atmospheric Remote Sensing with Lidar*, pp. 289–295. Springer, Berlin (1997)
- Hawkins, H.F., Imbembo, S.M.: The structure of a small, intense hurricane – Inez 1966. *Mon. Weather Rev.* **10**, 418–442 (1976)
- Kamini, R., Krishnamurti, T.N., Pattnaik, S., Browell, E.V., Ismail, S., et al.: Impact of CAMEX-4 datasets for hurricane forecasts using a global model. *J. Atmos. Sci.* **63**(1), 151–174 (2006)
- Wiloughby, H.E.: The dynamics of the tropical hurricane core. *Aust. Meteor. Mag.* **36**, 183–191 (1988)

# Chapter 16

## Genesis, Tracks, and Intensification of Hurricanes

### 16.1 Introduction

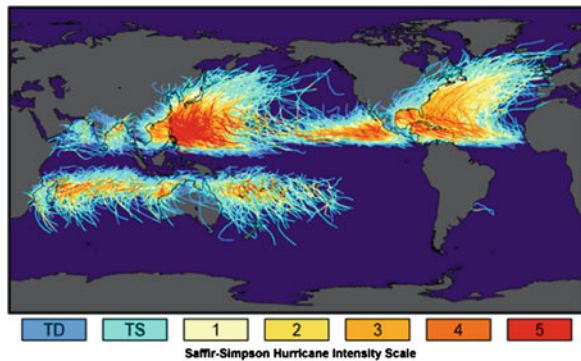
A global map showing over 150 years of hurricane/typhoon/tropical cyclone tracks is presented in Fig. 16.1. The starting points of these tracks are the genesis locations in the different ocean basins. These genesis locations pertain to different months and seasons. The Northern Atlantic and Pacific Oceans' genesis locations pertain mostly to the months of June through October. The Northern Indian Ocean locations refer mostly to the pre- and post summer and winter monsoon months, i.e., April, May, November and December. In the Southern Indian Ocean and the South Pacific (close to Australia) the months of genesis are December and January. The South Pacific east of Australia encounters a few typhoons each year during the southern summer months of November, December, and January.

It is interesting to note that tropical cyclones in the North Pacific have the most frequent occurrence of the most intense storms compared to all other basins. Another interesting feature is the fact that the tropical cyclone tracks are longer in the North Pacific and Atlantic Oceans, while in the Bay of Bengal and Arabian Sea the storms are more short-lived. The land to the north of the North Indian Ocean restricts the lifespan of the tropical cyclones over the Arabian Sea and Bay of Bengal. Similarly, the tracks in the southern hemisphere are also relatively short as a result of the extension of the subtropical jet into the tropical latitudes that acts to constrain the tracks of the tropical cyclones.

The terms “hurricane”, “typhoon”, and “tropical cyclone” reflect only a difference in geographical location, but not of underlying physical principles. For this reason, when geographical considerations are not relevant, the above terms will be used more or less interchangeably throughout this chapter.

At the locations of tropical cyclone genesis, warm surface temperatures ( $>27^{\circ}\text{C}$ ), weak vertical shear of horizontal winds and somewhat moist middle troposphere appear to be some of the necessary ingredients for genesis.

**Fig. 16.1** Global distribution of observed tropical cyclone tracks and intensity from 1851 to 2006 (Adapted from the COMET program)



## 16.2 Genesis

There is some observational and theoretical evidence that horizontal shear flow instability and organization of convection play a key role in the genesis of tropical storms.

### 16.2.1 Horizontal Shear Flow Instability

Over West Africa a low-level easterly jet resides near 13N, at the 600 mb and between the longitudes of roughly 20E and 20W. This is the African Easterly jet. The cyclonic shear side of this jet gives rise to a number of African waves.

In the barotropic (horizontal shear flow) context, the conservation of absolute vorticity for parcels moving within an easterly wave is expressed by

$$\frac{d\zeta_a}{dt} = 0 \quad (16.1)$$

or

$$\frac{d\zeta_a}{dt} = \frac{d}{dt} \left( \frac{\partial v}{\partial x} - \frac{\partial u}{\partial y} + f \right) = 0. \quad (16.2)$$

In natural coordinates,

$$\frac{d\zeta_a}{dt} = \frac{d}{dt} \left( \frac{V}{R_s} - \frac{\partial V}{\partial n} + f \right) = 0 \quad (16.3)$$

Where  $V$  is the total wind,  $R_s$  is the radius of curvature of the flow,  $-\frac{\partial V}{\partial n}$  is the wind shear, and  $f$  is the Coriolis parameter. Using  $C$  to denote curvature vorticity  $\frac{V}{R_s}$ ,

$S$  to denote shear vorticity and  $E$  to denote the Earth's vorticity ( $f$ ), (16.3) can be written compactly as  $\frac{d}{dt}(S + C + E) = 0$ . This means that parcels moving with respect to the waves undergo changes in shear, curvature and vorticity with the constraint that the sum of the three is conserved. The implied exchange of vorticity between shear and curvature is an important consideration in the tropics since it illustrates how a simple barotropic shear flow dynamics can call for tropical cyclone formation from a conversion of shear to curvature vorticity. The resulting disturbance would not be very strong, initially, but could subsequently develop further by means of other processes. The method of calculation of shear to curvature vorticity transformation is provided in [Appendix 1](#).

### 16.2.2 Conservation of Potential Vorticity (PV)

This is the second of a hierarchy of theoretical frameworks that address the formation of weak tropical disturbances. The conservation of PV includes effects of both horizontal and vertical wind shears. This describes the possibility for combined barotropic instability. PV is defined as  $\zeta_p = \zeta_a \Gamma_d$  where  $\Gamma_d = -g \frac{\partial \theta}{\partial p}$  is the dry static stability. The equation for conservation of PV is then given by

$$\frac{d\zeta_p}{dt} = \frac{d}{dt}(\zeta_a \Gamma_d) = 0. \quad (16.4)$$

According to this equation, parcels moving within an easterly wave conserve PV. Consider the implications of this conservation principle for a cloudy region within the easterly wave.. The stability equation states that

$$\frac{d\Gamma_d}{dt} = \Gamma_d \nabla \cdot \mathbf{V}. \quad (16.5)$$

A cloudy region implies an underlying area of convergence ( $\nabla \cdot \mathbf{V} < 0$ ). Since in the region of African easterly waves the static stability is always positive, it can be concluded that this convergence leads to a decrease of dry static stability, i.e., that  $\frac{d\Gamma_d}{dt} < 0$ . According to the conservation of PV principle, this decrease of dry static stability must lead to an increase of the parcels' absolute vorticity, i.e.,  $\frac{d\zeta_a}{dt} > 0$ . Since the changes in Coriolis parameter are very small in motions that are mostly zonal, the proportionate conversion from shear to curvature ( $S$  to  $C$ ) becomes larger under the PV conservation constraints compared to the barotropic problem (where absolute vorticity is conserved). Thus a slightly stronger storm forms when PV is conserved compared to when absolute vorticity is conserved. The hypothetical storm resulting from such considerations would still be weak since stability changes over the tropics are generally rather small.

### 16.2.3 Diabatic Effects

This could be examined in the context of a PV equation that includes the diabatic effects. The most fitting framework for discussing diabatic effects is the isentropic coordinate system. Neglecting friction, the complete PV equation in isentropic coordinates includes three diabatic terms, i.e.,

$$\frac{\partial}{\partial t} \zeta_{p\theta} = -\frac{d\theta}{dt} \frac{\partial \zeta_{p\theta}}{\partial \theta} + \zeta_{p\theta} \frac{\partial}{\partial \theta} \frac{d\theta}{dt} + \left\{ \nabla \frac{d\theta}{dt} \cdot \frac{\partial(\mathbf{V} \times \mathbf{k})}{\partial \theta} \right\} g \frac{\partial \theta}{\partial p} \quad (16.6)$$

We have not included here the (adiabatic) horizontal advection term and the friction terms. Horizontal advection is a very weak contributor to the potential vorticity change of a hurricane, since it can only redistribute PV from one geographic location to another. We will next discuss each of the right hand terms in sequence.

The first term on the right hand side of (16.6) is the vertical advection of potential vorticity in the isentropic coordinate system. The vertical advection is a diabatic term in this reference frame because the heating,  $\frac{d\theta}{dt}$ , is also the vertical velocity in the isentropic coordinate system. Near the surface level is where the strongest winds in a hurricane are found. The winds do not change much in the vertical, although a very slow decrease with height is always present. In a tropical cyclone, the strongest absolute vorticity is associated with the strongest winds. The dry static stability in the inner core of the hurricane is small but positive. The PV is generally large around the vertical levels at which the winds are the strongest.

Thus  $\frac{\partial \zeta_{p\theta}}{\partial \theta} < 0$  above the level of strongest winds; in conjunction with  $\frac{d\theta}{dt} > 0$ , this results in the vertical advection of PV contributing positively to the generation of PV in the lower troposphere. However, this effect is not a very strong contributor to the generation of PV of a hurricane.

The most important among the diabatic terms of the PV equation is the term  $\zeta_{p\theta} \frac{\partial}{\partial \theta} \frac{d\theta}{dt}$ .  $\zeta_{p\theta}$  is generally positive in the northern hemisphere and  $\frac{\partial}{\partial \theta} \frac{d\theta}{dt}$  is positive in the lower troposphere because the strong heating (large  $\frac{d\theta}{dt}$ ) is in the inner core of the hurricane, somewhere in the middle troposphere. As a result, the sign of the term  $\zeta_{p\theta} \frac{\partial}{\partial \theta} \frac{d\theta}{dt}$  is positive, thus contributing to a net generation of PV in the lower troposphere. This is the largest term in the PV equation, with largest contribution to the several-fold increase in PV during the formation of a hurricane. A much enhanced PV in the inner core contributed by  $\zeta_{p\theta} \frac{\partial}{\partial \theta} \frac{d\theta}{dt}$  results in much enhanced values of absolute vorticity over the region of deep convective activity (when  $\frac{d\theta}{dt}$  and  $\frac{\partial}{\partial \theta} \frac{d\theta}{dt}$  are large and the stability  $\Gamma_d = -g \frac{\partial \theta}{\partial p}$  is small). The enhanced values of  $\zeta_a$  generally go with enhanced conversions of shear to curvature vorticity. It is this mix of thermodynamics (larger heating) and dynamics (enhanced curvature vorticity) that is important for the genesis of hurricane. There are many factors that contribute to enhanced heating that are a part of this scenario. Factors such as the organization of convection and even components of cloud microphysics are

important for the existence of enhanced heating in hurricanes. These topics are addressed in separate sections of this text.

The third diabatic term in the complete PV equation represents the effects of the horizontal differential of heating. In local cylindrical coordinates ( $r, \lambda, \theta, t$ ) – the natural reference frame to address a hurricane from – it can be expressed as

$$\left\{ \nabla \frac{d\theta}{dt} \cdot \frac{\partial(\mathbf{V} \times \mathbf{k})}{\partial\theta} \right\} g \frac{\partial\theta}{\partial p} = \left\{ \frac{\partial v_\lambda}{\partial\theta} \frac{\partial}{\partial r} \left( \frac{d\theta}{dt} \right) - \frac{\partial v_r}{\partial\theta} \frac{\partial}{\partial\lambda} \left( \frac{d\theta}{dt} \right) \right\} g \frac{\partial\theta}{\partial p} \quad (16.7)$$

If we replace  $\theta$  by  $p$  and  $\frac{d\theta}{dt}$  by  $\omega$ , the term within the parentheses is exactly the same as the twisting term of the vorticity equation. It is a dot product of the horizontal differential heating and the vertical shear of wind. Let us consider this term in the eye wall region of a hurricane. In the lower troposphere, inwards of the radius of maximum heating,  $\frac{\partial}{\partial r} \left( \frac{d\theta}{dt} \right) > 0$ .  $\frac{\partial v_\lambda}{\partial\theta}$  is the vertical change of the tangential wind. The tangential wind tends to decrease very slowly with height in the lower troposphere, therefore  $\frac{\partial v_\lambda}{\partial\theta}$  is negative and small. The dry static stability,  $-g \frac{\partial\theta}{\partial p}$ , is positive. Assuming that the azimuthal gradient of heating is relatively small, we can conclude that inside the radius of maximum heating the horizontal differential of heating term would be positive and contribute to a net generation of potential vorticity in the lower troposphere. Outside the radius of maximum heating the converse may be expected.

### 16.2.4 Order of Magnitudes for the Terms of the PV Equation in a Hurricane

To obtain a better feeling for the above components of the PV equation, it is of interest to explore the magnitudes of these three diabatic terms.

A typical value for the dry static stability can be obtained by estimating

$$\Gamma_d = -g \frac{\partial\theta}{\partial p} \sim -9.8 \text{ m s}^{-1} \times \frac{-10 \text{ K}}{500 \text{ hPa}} \sim 2 \times 10^{-3} \text{ K m}^2 \text{ kg}^{-1}.$$

Using this result, the potential vorticity can be estimated as

$$\zeta_{p\theta} = \zeta_a \Gamma_d \sim 10^{-3} \text{ s}^{-1} \times 2 \times 10^{-3} \text{ K m}^2 \text{ kg}^{-1} = 2 \times 10^{-6} \text{ K m}^2 \text{ kg}^{-1} \text{ s}^{-1}.$$

Now, to estimate the three terms on the right side of the potential vorticity equation. We can assume that

(a)

$$\frac{d\theta}{dt} \approx \frac{L}{C_p} \frac{dq}{dt} \sim \frac{2.5 \times 10^6 \text{ J kg}^{-1}}{10^3 \text{ J kg}^{-1} \text{ K}^{-1}} \times \frac{20 \text{ g kg}^{-1}}{\text{day}} \sim 6 \times 10^{-4} \text{ K s}^{-1}$$

$$\frac{\partial \zeta_{p\theta}}{\partial \theta} \sim -\frac{\frac{1}{10}\zeta_{p\theta}}{10K} \sim -2 \times 10^{-8} m^2 kg^{-1} s^{-1}$$

$$-\frac{d\theta}{dt} \frac{\partial \zeta_{p\theta}}{\partial \theta} \sim 1.2 \times 10^{-11} K m^2 kg^{-1} s^{-2}$$

(b)

$$\frac{\partial}{\partial \theta} \frac{d\theta}{dt} \sim \frac{\frac{d\theta}{dt}}{10K} \sim 6 \times 10^{-5} s^{-1}$$

$$\zeta_{p\theta} \frac{\partial}{\partial \theta} \frac{d\theta}{dt} \sim 1.2 \times 10^{-10} K m^2 kg^{-1} s^{-2}$$

(c)

$$\frac{\partial v_\lambda}{\partial \theta} \sim \frac{-4 m s^{-1}}{10K} \sim -0.25 m s^{-1} K^{-1}$$

$$\frac{\partial}{\partial r} \left( \frac{d\theta}{dt} \right) \sim \frac{\frac{d\theta}{dt}}{30 km} \sim \frac{6 \times 10^{-4} K s^{-1}}{3 \times 10^4 m} \sim 2 \times 10^{-8} K s^{-1} m^{-1}$$

$$\frac{\partial v_\lambda}{\partial \theta} \frac{\partial}{\partial r} \left( \frac{d\theta}{dt} \right) g \frac{\partial \theta}{\partial p} \sim 10^{-11} K m^2 kg^{-1} s^{-2}$$

## 16.3 Tracks

The motion of the tropical cyclone has historically been related to the deep layer mean wind (average wind calculated over a deep layer of atmosphere between 850 and 200 mb; Kasahara 1957, 1960). Fiorino and Elsberry (1989) however show that 500 mb wind averaged over a circle centered over the tropical cyclone serves as a good alternative to the deep layer wind. Although, the deep layer wind is an easy concept to grasp, the limited success of this methodology in forecasts necessitated more extensive explorations of tropical cyclone motion.

### 16.3.1 The $\beta$ Effect

To the extent that the tropical cyclone motion is associated with the deep layer wind, a natural approach is to start with the barotropic potential vorticity equation, which assumes that the horizontal structure is similar between levels in the vertical. Then the barotropic PV comprises of the vertical component of the absolute

vorticity, and the barotropic, non-divergent potential vorticity equation can be written as:

$$\frac{d(\zeta + f)}{dt} = \frac{\partial(\zeta + f)}{\partial t} + \vec{v} \cdot \nabla(\zeta + f) = 0 \quad (16.8)$$

Since  $\frac{\partial f}{\partial t} = 0$ , (16.8) can be re-written as

$$\begin{aligned} \frac{\partial \zeta}{\partial t} &= -\vec{v} \cdot \nabla(\zeta + f) \\ &= -\vec{v} \cdot \nabla \zeta - \vec{v} \frac{\partial f}{\partial y} \\ &= -\vec{v} \cdot \nabla \zeta - \vec{v} \beta \end{aligned} \quad (16.9)$$

The above equation suggests that, in order to conserve the barotropic potential vorticity, the tropical cyclone motion is not only governed by the large-scale steering flow but also by the vortex interaction with the Earth's background vorticity gradient. This is known as the  $\beta$  effect or as propagation due to  $\beta$  gyres. Although the  $\beta$  effect is quantitatively small compared to that of the steering flow, it has a subtle impact on the tropical cyclone motion. The  $\beta$  effect can make small changes to the track of a tropical cyclone that can then result in the storm interacting with a different phenomenon (e.g. a moving frontal system, SST anomalies) which can steer the tropical cyclone distant from its original track.

### 16.3.2 The Fujiwhara Effect

The term Fujiwhara effect relates to two typhoons rotating around each other. A Japanese Meteorologist Dr. Sakuhei Fujiwhara first noted this in 1921. Often these typhoons merge to form one larger typhoon. Basically the outer cyclonic winds of one steers the motion of the adjacent one. Figure 16.2 is a schematic of the Fujiwhara effect. The two storms rotate around a common center of mass. The relative intensity and the distance between the two storms determine the location of this center. Figure 16.3 shows a satellite image of two storms that exhibited such an effect. The fuller understanding of this problem may require investigations on what one storm does to an adjacent one in terms of dynamics and physics. However the first order effect comes from the broad outer steering flow of the two storms as illustrated in Fig. 16.2.

### 16.3.3 The Extratropical Transition of Tropical Cyclones

As shown in Fig. 16.1, the tracks of the northern hemisphere tropical cyclones in the Pacific and in the Atlantic indicate cyclones moving to high latitudes. In many of these northward tracks, the storms invariably undergo extratropical transition.

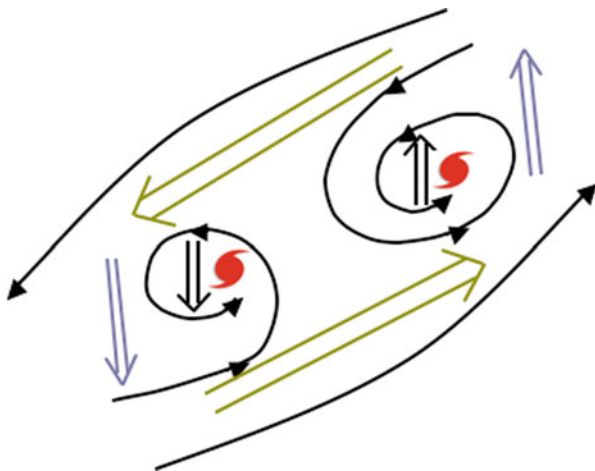


**Fig. 16.2** Schematic illustration of the interaction of binary tropical cyclones (Fujiwhara effect)



**Fig. 16.3** Satellite imagery (NOAA-3 visible range VHRR of August 24 1974, 1749 GMT) of the Fujiwhara effect, showing hurricanes Ione (*left*) and Kirsten (*right*) (From NOAA photo library, NOAA in space collection)

Figure 16.4 illustrates the thermal structure of a hurricane as contrasted with that of an extratropical cyclone. Here the geopotential surfaces with a bulge showing the warm core tropospheric structure of a hurricane are contrasted with the closely packed cold core trough of an extratropical cyclone. How does this tropical structure transition into the extratropical structure is the important question here.

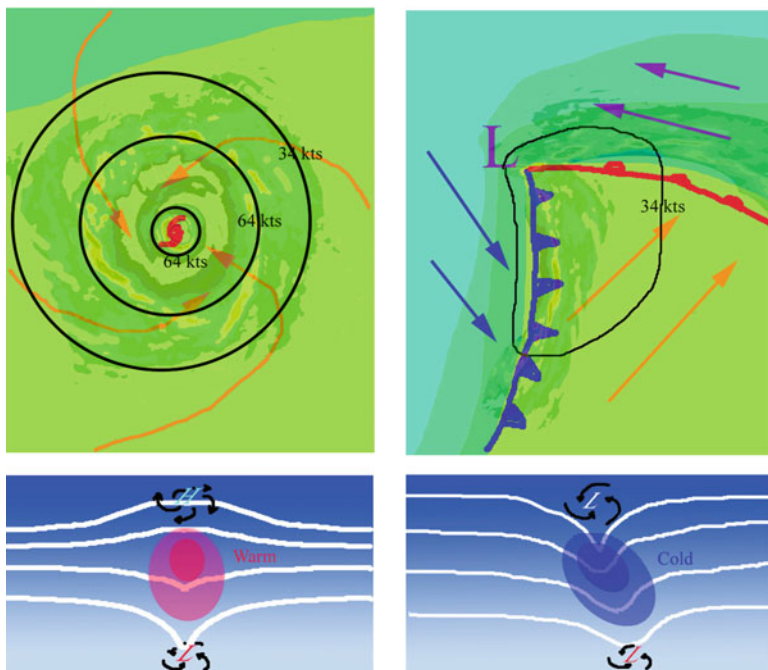


**Fig. 16.4** Maps of temperature (shaded) and wind field (contoured) associated with a tropical cyclone (top left) and extratropical cyclone (top right). Colors indicate temperature (blue 15C = 59F; blue green 20C = 68F; green 25C = 77F). The corresponding schematic of the vertical structure for tropical cyclone and extratropical cyclone are shown in bottom left and bottom right respectively. The contours are geopotential surfaces and temperature is shaded with schematic of the circulation overlaid (From Merrill 1993)

An obvious factor in this transition is that as the tropical storm moves to higher latitudes, it encounters colder sea surface temperatures that cannot sustain the high rates of evaporation and moisture supply necessary to maintain a hurricane. However, strong evaporation from strong winds at the surface level of the hurricanes, once formed, can sustain the cyclone at sea surface temperatures below 27C. The thermal transitions can easily occur from the sweep of a strong cold front (which has a scale of many thousands of kilometers) that can easily absorb the small tropical cyclone (which has a scale of few hundred kilometers).

In an exhaustive review on this transition climatology, Evans and Hart (2003) noted that in the last 50 years nearly 46 % of all tropical cyclones of the North Atlantic Ocean underwent a transition. Many of these transitions over the Atlantic Ocean seem to occur in the month of October. Most East Coast cities of the US and even the maritime provinces of Canada experience the landfall of these extratropical systems with occasional heavy rains and floods at a frequency of roughly one landfall per 2–4 years. Such extratropical transitions are noted generally in the latitude belt of 30–35N during the early and late parts of the hurricane season. At the peak of the Atlantic hurricane season (i.e., October) the transitions

occur between latitudes of 40N–50N. It is not a straight forward issue that all tropical cyclones diminish in intensity after the transition, to the contrary, as many as 52 % have shown rapid intensification at the time of start of recurvature. There are several climatological remote connections, such as the Pacific North American PNA, the North Atlantic Oscillation and the Southern Oscillation that have been found to be relevant to some aspects of interannual variability of tropical cyclones. The phases of these climate oscillations do not, however, seem to have a strong influence on the year to year variability of the frequency of extratropical transitions of the tropical cyclones.

Prior to the transition, the hurricane is generally contained within the easterly trade winds. Thus the steering of the hurricane is dominated by the deep easterly wind systems of the trades. Subsequent to the recurvature, the hurricane is embedded within middle latitude westerlies and a steering from west to east is a consistent consequence of that steering. This leads one to state that steering is a possible factor for these transitions. Recurvature is also facilitated by strong convergence and generation of cyclonic vorticity in the forward and left sectors of a hurricane. That increase of large scale convergence is facilitated by the entire hurricane being influenced by the warm air advection of an extratropical storm as it arrives closer to the longitudes of a tropical cyclone. The large scale rising motion is more conducive to the formation of large non-convective rain, which is an important thermodynamical mechanism for the formation of the cold core from the combined processes of adiabatic cooling of the large scale ascent and the evaporation over large areas of the falling non convective rains. Unlike the core of the hurricane, where the ascent is in a near saturated environment that inhibits the evaporation of falling rain, this larger scale extratropical environment is not saturated and here the ascending air does not follow a moist adiabat but follows more a dry adiabatic ascent and the adiabatic cooling rates are higher. Thus the combined effects of adiabatic ascent and the evaporation of falling rain facilitates the conversion of the warm core into a cold lower troposphere. This environment does not favor close knit organized deep convection and slowly the organized convection of a hurricane takes on the familiar comma shaped ascent of an extratropical storm.

Hart (2003) proposed a phase space diagram for providing some insights on the possibility that a tropical cyclone might undergo an extratropical transition. It makes use of three parameters for the construction of this diagram, namely: (1) the azimuthally averaged symmetric thermal structure based on information from 900 to 600 hPa levels, (2) the thermal wind over the layer 900–600 hPa levels, and (3) the thermal wind of the upper layer i.e., 600–300 hPa levels. He makes use of data sets from large scale model assimilation (or analysis) at resolutions of the order of around 100 km to prepare the phase space diagram. The abscissa of this diagram carries the thermal wind for the lower layer between 900 and 600 hPa levels. A single number for a single storm at a single time arises from an azimuthal average over several 100 km radii. The ordinate of the phase space diagram carries the thickness (i.e., layer temperature) between 900 and the 600 hPa levels, again azimuthally averaged for each storm in a storm relative coordinate. During the life cycle of the storm, the hourly (or 12 hourly) plotted points move in this diagram according to the changes in their thermal structure. Figure 16.5a–c respectively

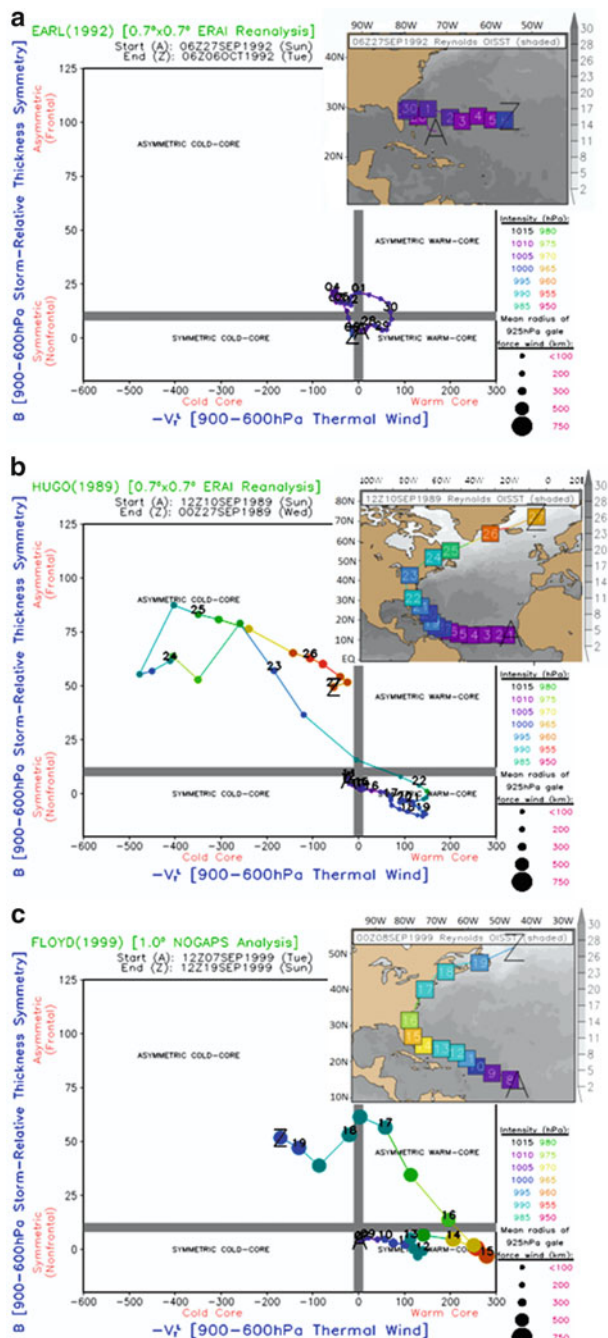


**Fig. 16.5** Illustrations of various trajectories of extratropical transition of TCs. **(a)** Slow transition of a weak tropical storm Earl (1992), **(b)** Rapid transition of a landfalling hurricane Hugo (1989), and **(c)** slow transition of a major hurricane Floyd (1999). The start and end of transition are labeled on each. ‘A’ indicates the beginning of the plotted lifecycle and ‘Z’ indicates the end. A marker is placed every 6 h to indicate analysis times. Positions at 0000UTC are labeled with the day (except on **(a)**, for clarity). Marker shading indicates intensity (white >1,010 hPa, black <970 hPa). ERA Interim analysis is used in the *top* two analysis and in the *bottom* panel US Navy Operational Global Atmospheric Prediction System (NOGAPS) analysis is used (Courtesy R. Hart (Florida State University, 2011, personal communication))

show the phase space transitions for hurricanes Earl of 1992, Hugo of 1989 and Floyd of 1999. These illustrations simply place the life cycle of an evolving storm on this phase space diagram. To understand what this means one needs to refer to the key diagram in Fig. 16.5. This illustration carries four possibilities, i.e., an asymmetric cold core, a symmetric cold core, asymmetric warm core and a symmetric warm core. This utilizes as its ordinate the 900–600 mb storm relative thermal wind field. For deeper storms one can make use of the upper layer thickness i.e., the thermal wind for the layer 600–300 hPa levels, all in storm relative coordinates. This differentiates between a deep cold core, a shallow warm core, a moderate warm core, a deep warm core and a shallow cold core. As a storm moves, its reference point in these diagram meanders and one can learn about the thermal structure transitions during the cyclones life cycle. Instead of analysis one can also make use of forecast fields to prepare these diagrams and obtain some insights on the thermal structures during extratropical transitions.

Each panel is divided into four quadrants, according to the values of the 900–600 hPa storm relative thermal wind field on the ordinate (this determines whether the storm core is cold or warm), and the values of values of the storm-relative thermal symmetry in the same layer (this determines whether the storm is symmetric or asymmetric). At any given point in its life cycle, a storm can be categorized according the quadrant in which its characteristics place it, as one of the following: an asymmetric cold core system, a symmetric cold core system, an asymmetric warm core system, or a symmetric warm core system.

## 16.4 Intensity

### 16.4.1 *The Angular Momentum Principle*

In spherical coordinates over the Earth, the angular momentum  $M$  per unit mass of air is written as

$$M = ua \cos \varphi + \Omega a^2 \cos^2 \varphi$$

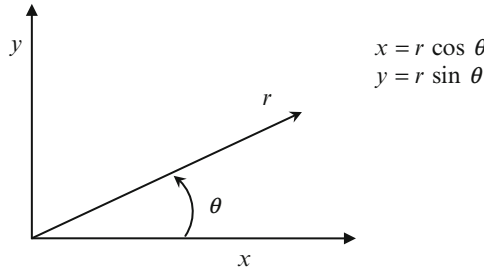
where  $u$  is the zonal wind component,  $a$  is the radius of the Earth,  $\varphi$  is the latitude, and  $\Omega$  is the Earth's speed of rotation. In the absence of friction and pressure gradients, parcels conserve their angular momentum, i.e.,  $\frac{dM}{dt} = 0$ . An assumption of constant angular momentum would imply dropping the pressure gradient and frictional forces in the momentum equations. In the actual atmosphere angular momentum is not conserved, since pressure gradients and friction are generally not negligible. In order to analyze the angular momentum of a hurricane, a local cylindrical coordinate system can be derived about a hurricane's center as an origin. In such a system the angular momentum can be written as

$$M = u_\theta r + \frac{f_0 r^2}{2},$$

where  $u_\theta$  is the tangential velocity and  $f_0$  is the Coriolis parameter (assumed constant on the scale of a hurricane). The angular momentum principle directly applies to the maximum wind in a hurricane. For this reason it should be considered a centerpiece in addressing the hurricane intensity issue. We will illustrate that in the following sections.

### 16.4.2 Local Cylindrical Coordinates

The equations of motion can be transformed from the Cartesian  $(x,y)$  tangent plane to cylindrical  $(r, \theta)$  coordinates in the following way.



The radial velocity  $u_r$  and the tangential velocity  $u_\theta$  can be expressed as follows:

$$u_r = \frac{dr}{dt}, \quad u_\theta = r \frac{d\theta}{dt} \quad (16.10)$$

These can be related to  $u$  and  $v$  by in the following way:

$$u = \frac{dx}{dt} = \frac{d}{dt}(r \cos \theta) = \frac{dr}{dt} \cos \theta - r \sin \theta \frac{d\theta}{dt} = u_r \cos \theta - u_\theta \sin \theta \quad (16.11)$$

$$v = \frac{dy}{dt} = \frac{d}{dt}(r \sin \theta) = \frac{dr}{dt} \sin \theta + r \cos \theta \frac{d\theta}{dt} = u_r \sin \theta + u_\theta \cos \theta \quad (16.12)$$

Using these, we can also derive the following

$$\frac{du}{dt} = \frac{du_r}{dt} \cos \theta - u_r \sin \theta \frac{d\theta}{dt} - \frac{du_\theta}{dt} \sin \theta - u_\theta \cos \theta \frac{d\theta}{dt} \quad (16.13)$$

$$\frac{dv}{dt} = \frac{du_r}{dt} \sin \theta + u_r \cos \theta \frac{d\theta}{dt} + \frac{du_\theta}{dt} \cos \theta - u_\theta \sin \theta \frac{d\theta}{dt}. \quad (16.14)$$

If we let the  $x$ -axis coincide with  $r$ , so that  $\theta = 0$  as a reference azimuth, then  $\cos \theta = 1$ ,  $\sin \theta = 0$ , (16.13) and (16.14) reduce to:

$$\frac{du}{dt} = \frac{du_r}{dt} - u_\theta \frac{d\theta}{dt} = \frac{du_r}{dt} - \frac{u_\theta^2}{r} \quad (16.15)$$

$$\frac{dv}{dt} = \frac{du_\theta}{dt} + u_r \frac{d\theta}{dt} = \frac{du_\theta}{dt} + \frac{u_r u_\theta}{r} \quad (16.16)$$

From the tangent plane equations,

$$\frac{du}{dt} = fv - \frac{1}{\rho} \frac{\partial p}{\partial x} + F_x \quad (16.17)$$

$$\frac{dv}{dt} = fu - \frac{1}{\rho} \frac{\partial p}{\partial y} + F_y \quad (16.18)$$

Substituting the transformations, we obtain, in  $(r, \theta, z, t)$  coordinates:

$$\frac{du_r}{dt} - \frac{u_\theta^2}{r} = fu_\theta - \frac{1}{\rho} \frac{\partial p}{\partial r} + F_r \quad (16.19)$$

$$\frac{du_\theta}{dt} + \frac{u_r u_\theta}{r} = -fu_r - \frac{1}{\rho} \frac{\partial p}{r \partial \theta} + F_\theta \quad (16.20)$$

Or, in  $(r, \theta, p, t)$  coordinates,

$$\frac{du_r}{dt} - \frac{u_\theta^2}{r} - fu_\theta = -g \frac{\partial z}{\partial r} + F_r \quad (16.21)$$

$$\frac{du_\theta}{dt} + \frac{u_r u_\theta}{r} + fu_r = -g \frac{\partial z}{r \partial \theta} + F_\theta \quad (16.22)$$

The total derivative in  $(r, \theta, p, t)$  coordinates is given by:

$$\frac{d}{dt} = \frac{\partial}{\partial t} + u_\theta \frac{\partial}{r \partial \theta} + u_r \frac{\partial}{\partial r} + \omega \frac{\partial}{\partial p}, \quad (16.23)$$

or, in  $(r, \theta, z, t)$  coordinates

$$\frac{d}{dt} = \frac{\partial}{\partial t} + u_\theta \frac{\partial}{r \partial \theta} + u_r \frac{\partial}{\partial r} + w \frac{\partial}{\partial z}$$

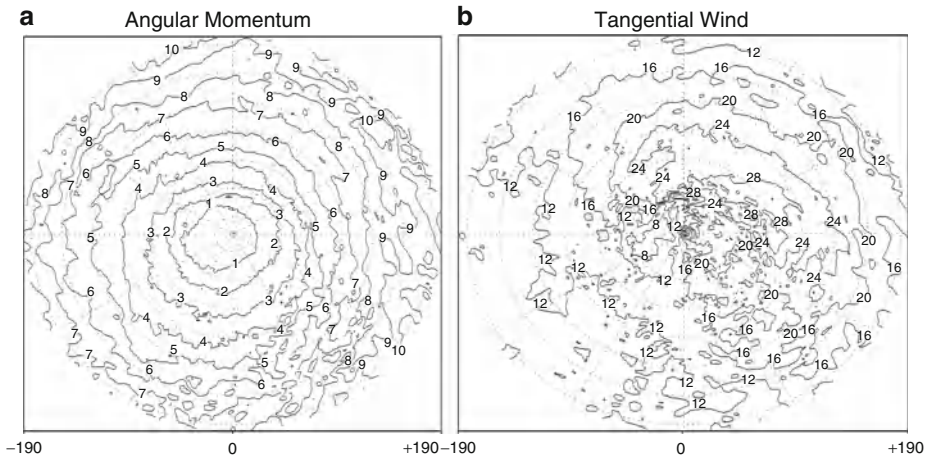


**Fig. 16.6** 850 mb (a) tangential wind (m/s) and (b) angular momentum ( $10^6 \text{ m}^2 \text{s}^{-1}$ ) in Hurricane Bonnie, 00Z 24 August 1998

### 16.4.3 The Torques

It is preferable to look at the angular momentum problem in the context of  $(r, \theta, z, t)$  coordinates because of the future applications of hurricane modeling at high resolutions that will largely deploy non-hydrostatic microphysical models at very high resolutions. From the tangential equation of motion (16.11), upon multiplication by  $r$  and noting that  $u_r = \frac{dr}{dt}$ , we obtain

$$\frac{d}{dt} \left( u_\theta r + \frac{fr^2}{2} \right) = -\frac{1}{\rho} \frac{\partial p}{\partial \theta} + F_\theta r.$$

This is the angular momentum equation in local cylindrical coordinates. The angular momentum per unit mass of air  $\left( M = u_\theta r + \frac{f_0 r^2}{2} \right)$  is modified by pressure torques  $\left( -\frac{1}{\rho} \frac{\partial p}{\partial \theta} \right)$  and by frictional torques  $(F_\theta r)$ . The frictional torques constitute a central component for the angular momentum changes and hence also for the hurricane intensity issue.

### 16.4.4 What Does the Angular Momentum Field in a Hurricane Look Like?

Figure 16.6a shows the tangential velocity  $u_\theta$  at 850 mb in hurricane Bonnie of 2001. Figure 16.6b shows the field of angular momentum  $M = u_\theta r + \frac{f_0 r^2}{2}$  at the same level. Large values of angular momentum reside outside the hurricane center. As we go towards the center the angular momentum decreases.

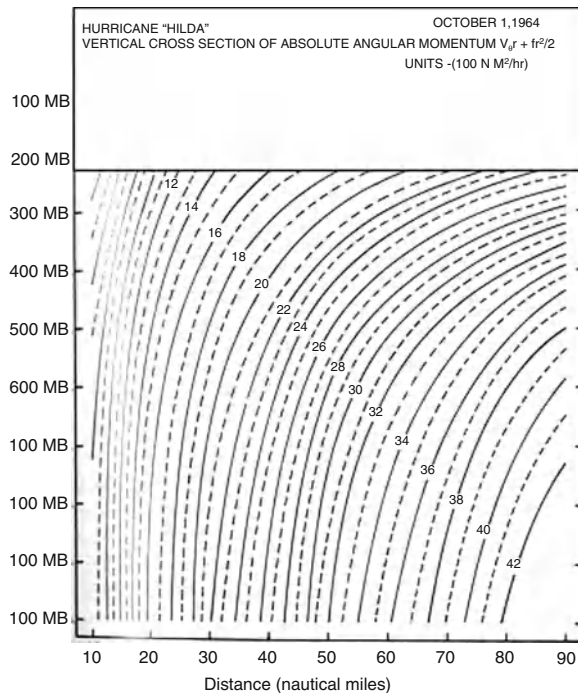


**Fig. 16.7** Vertical cross-section of angular momentum that is azimuthally averaged about the moving storm (hurricane Hilda, 1 October 1964) (From Hawkins and Rubsam 1968)

In the lower troposphere there are inflowing streamlines and trajectories. Parcels of air are coming in from outside. In a plane view we can look at the  $r-p$  cross section of a hurricane. Figure 16.7 shows the angular momentum of hurricane Hilda of 1964. Clearly, the angular momentum decreases as we go towards the center of the hurricane, i.e.,  $\frac{dM}{dr} \neq 0$ . In the lower troposphere, the value of outer angular momentum at a radius  $r = 80$  nmi (1 nmi = 1.852 km) is as high as  $4,200 \text{ nmi}^2 \text{h}^{-1}$ , whereas at a radius  $r = 20$  nmi the angular momentum is around  $16 \text{ nmi}^2 \text{h}^{-1}$ . This illustrates that along the inflowing channels in the lower troposphere there is a very large loss of angular momentum. However in the outflow near 200 mb there appears to be more of a conservation of angular momentum. Note that inflowing parcels lose as much as 60 % of their angular momentum as they reach the region of maximum winds. What is decreasing the value of  $M$ ? Clearly, it is the pressure torques and the frictional torques. Of these, the frictional torques contribute the most towards the depletion of the outer angular momentum of the inflowing parcel. The frictional torque  $F_\theta r$  has two important components one related to surface friction and one related to internal friction. These are described in the following two sections.

### 16.4.5 Cloud Torques

The cloud torques constitute a major component of the internal frictional torques in a hurricane. As a lower-tropospheric parcel is entering the interior of a hurricane from outside, it encounters a plethora of clouds – stratocumulus, fair weather cumulus, towering cumulus, and cumulonimbus. These are smaller scale cloud elements whose sizes are a few km or less. Within each of these clouds there are vertical motions  $w'$  that can be upward in parts of the cloud and downward around it. The prime here refers to a departure from a larger scale mean, which is denoted by an overbar. These up and down motions (regarded as sub-grid scale, compared to the few km grid scale in mesoscale hurricane models) carry upward or downward fluxes of angular momentum. A net vertical divergence of angular momentum flux is generally experienced by the larger scale inward moving parcels. That divergence of flux is expressed by the relation  $r \frac{\partial}{\partial z} \overline{w' u' \theta} > 0$ . In the equation for the angular momentum this friction term is a Reynolds stress term for the larger grid scale motion, i.e.,  $(\frac{dM}{dt})_{\text{clouds}} = -r \frac{\partial}{\partial z} \overline{w' u' \theta}$ . With the minus sign, a vertical divergence of flux of sub-grid scale angular momentum leads to a diminution of the momentum of inflowing parcels, i.e.,  $\frac{dM}{dt} < 0$ .

Cloud-resolving non-hydrostatic mesoscale models with cloud microphysics can resolve these scales explicitly. It is difficult to measure these angular momentum fluxes from aircraft observations since it would take two levels of flight data simultaneously sampling the same cloud. Numerical models seem to be the only way at present to obtain such estimates.

The four panels in Fig. 16.8 show the vertical velocity, the angular momentum flux ( $\overline{w' u' \theta}$ ) at two adjacent vertical levels, and the cloud torque  $-r \frac{\partial}{\partial z} \overline{w' u' \theta}$  along a segment of a large-scale parcel trajectory that encounters a mesoscale convective cloud. Presence of clouds can be inferred easily in such microphysical models that carry cloud water mixing ratio as a dependent variable of the model, by identifying regions where the cloud water mixing ratio exceeds  $0.2 \text{ g kg}^{-1}$ . It is of considerable interest to ask what happens to the angular momentum as a parcel following the large scale flow traverses across a mesoconvective cloud system. As seen in Fig. 16.8, such parcels encounter large negative values of  $-r \frac{\partial}{\partial z} \overline{w' u' \theta}$  in going across a cloud element. These large negative torque contributions lead to a diminution of the parcel's angular momentum. If the value of the angular momentum the parcel eventually acquires is known, the corresponding value of the tangential wind speed is easily calculated from the angular momentum definition as  $u_\theta = \frac{1}{r} \left( M - \frac{f_0 r^2}{2} \right)$ . The table below shows the changes of angular momentum and tangential velocity observed along a streamline traversing a cloud element.

Table 16.1 shows that  $M$  decreases by  $4 \text{ nmi}^2 \text{h}^{-1}$  across this element. Since the radial distance  $r$  decreases from 40 to 35 nmi,  $u_\theta$  increases from 110 to 114 kt. In the total absence of frictional torques,  $M$  would be conserved across this cloud element and  $u_\theta$  would have increased from 110 to 121 kt. This shows the large sensitivity of hurricane intensity to cloud torques. If there are no clouds

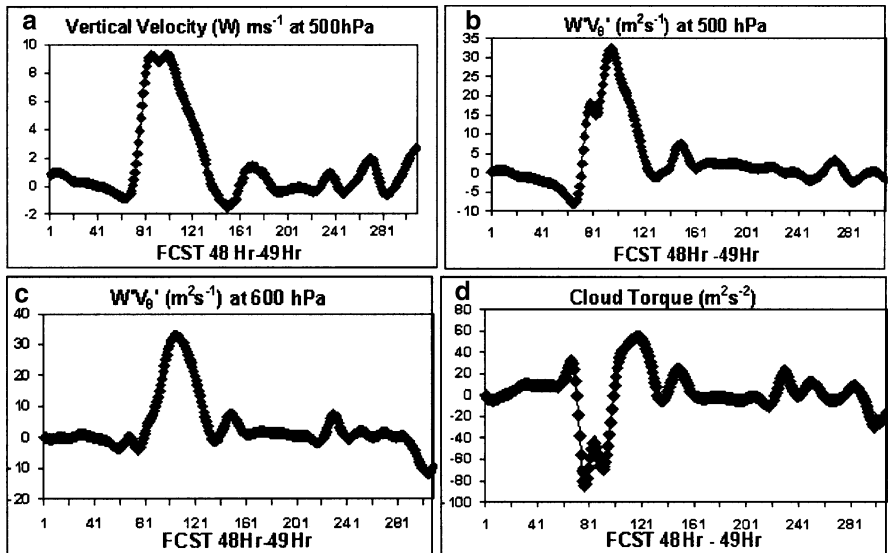


**Fig. 16.8** (a) Vertical velocity ( $\text{ms}^{-1}$ ) at 500 mb, (b) vertical eddy flux of momentum ( $\text{m}^2\text{s}^{-2}$ ) at 500 mb, (c) vertical eddy flux of momentum ( $\text{m}^2\text{s}^{-2}$ ) at 600 mb, (d) cloud torque ( $\text{m}^2\text{s}^{-2}$ ) during every time step of a 1-h forecast between the 48th and 49th hour of model integration of Hurricane Bonnie of 1998 (From Krishnamurti et al. 2005)

**Table 16.1** Angular momentum and tangential wind observed along a streamline traversing a cloud element in a hurricane

Radius (nmi)	Across clouds		Assuming conservation of angular momentum	
	M ( $\text{nmi}^2\text{h}^{-1}$ )	$u_\theta$ (kt)	M ( $\text{nmi}^2\text{h}^{-1}$ )	$u_\theta$ (kt)
R1 = 40	32	110	32	110
R2 = 35	28	114	32	121

along inflow channels, the tangential velocity would increase rapidly. Conversely, if along the inflow channels there are too many cloud elements, the hurricane intensity may be weaker.

### 16.4.6 Surface Frictional Torques

The surface frictional torque can be estimated from the surface tangential wind using a modified bulk aerodynamic formula that is described by the equation

$$(F_\theta)_{SFC} = -\frac{1}{\rho} \frac{\partial u_\theta}{\partial z}, \text{ where}$$

$$\tau_\theta = \rho C_D u_\theta \sqrt{u_\theta^2 + u_r^2} = \rho C_D u_\theta |U|.$$

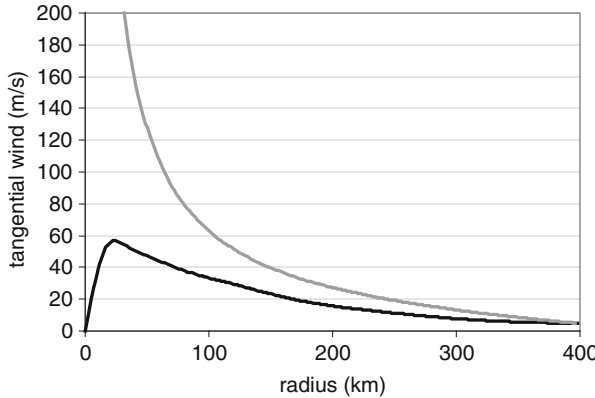


**Fig. 16.9** Observed surface tangential wind in  $\text{ms}^{-1}$  as a function of radius for Hurricane Isabel (19:30GMT 14 September 2003) (black line), and a theoretical profile obtained through the principle of conservation of angular momentum for a parcel starting at a radius of 400 km with tangential wind speed of  $5 \text{ ms}^{-1}$  (grey line)

The value of  $C_D$  is a function of the surface wind speed, and is often parameterized as

$$C_D = \begin{cases} C_{D0} = 1.1 \times 10^{-3} & \text{for } |U| < 5.8 \text{ ms}^{-1} \\ C_{D0} \times (0.74 + 0.046|U|) & \text{for } 5.8 \text{ ms}^{-1} \leq |U| \leq 16.8 \text{ ms}^{-1} \\ C_{D0} \times (0.94 + 0.034|U|) & \text{for } |U| > 16.8 \text{ ms}^{-1} \end{cases}$$

Given the surface stress  $\tau_\theta$ , we can calculate the change in angular momentum stemming from the frictional torques as  $(\frac{dM}{dt})_{SFC} = -\frac{r}{\rho} \frac{\partial \tau_\theta}{\partial z}$ . In regions of cyclonic winds  $\tau_\theta$  is positive. As the winds increase with height just above the surface, the vertical gradient of  $\tau_\theta$  is also positive. Thus  $-\frac{r}{\rho} \frac{\partial \tau_\theta}{\partial z}$  is negative, i.e., the surface frictional torques lead to a reduction in the angular momentum as parcels pass through regions of strong tangential surface wind stress, i.e., regions of strong surface winds. This reduction is generally small – its magnitude is about 20–25 % of the angular momentum reduction brought about by cloud torques.

### 16.4.7 What Is a Constant Angular Momentum Profile

Figure 16.9 shows an azimuthally averaged profile of the surface tangential winds as a function of radius for Hurricane Isabel on 14 September 2003 (black line). If an outer parcel at  $r = r_0$  had moved inward conserving its angular momentum  $M_0$ , its tangential velocity at small  $r$  would become much higher than the one observed in practice. Let us consider a starting radius  $r_0$  and an

arbitrary smaller radius  $r$ . Let the tangential wind at the starting point be known and equal to  $u_{\theta 0}$ . What would the tangential wind  $u_\theta$  at radius  $r$  be? If we assume that angular momentum is conserved, we can write

$$M_0 = u_{\theta 0} r_0 + \frac{f r_0^2}{2} = u_\theta r + \frac{f r^2}{2}.$$

Solving for the tangential wind  $u_\theta$  yields

$$u_\theta = \frac{u_{\theta 0} r_0 + \frac{f(r_0^2 - r^2)}{2}}{r}.$$

We can now plot  $u_\theta$  as a function of  $r$ . This is the hypothetical tangential velocity a parcel starting at  $r_0$  with a tangential velocity  $u_{\theta 0}$  would acquire upon arrival at  $r$  following the conservation of angular momentum principle in a frictionless and torqueless environment. The grey line on Fig. 16.5 illustrates the hypothetical profile that would be attained from such calculations using the observed tangential wind  $u_{\theta 0} = 5 \text{ ms}^{-1}$  at  $r_0 = 400 \text{ km}$  as a starting point for the parcel.

The differences between the actual and the hypothetical profiles are quite large, implying that the role of torques in determining the angular momentum of a hurricane is quite significant. At large radii, outside of the radius of maximum winds, the differences between the two profiles are arising from both outer cloud torques and surface frictional effects. At smaller radii, near the radius of maximum winds, the difference is particularly large due to the eye wall-related cloud torques.

### 16.4.8 Pressure Torques

In the equation for the rate of change of angular momentum the pressure torques are expressed by  $-\frac{1}{\rho} \frac{\partial p}{\partial \theta}$ , which implies that the pressure torques are dictated by the azimuthal variations of pressure. Such variations are generally small, since for the most part the isobars in the analysis of a hurricane appear as concentric circles. This axisymmetry however is not perfect. The departure of the pressure field from its azimuthal average, i.e., the departure from axisymmetry, displays a characteristic structure called a beta gyre. This consists of a high pressure anomaly over the right section of the storm (with respect to the storm's motion) and a low pressure anomaly to the left. The amplitude of this gyre is on the order of a few mb. It is called a beta gyre because an azimuthally averaged equation of motion largely carries a balance among the parcel acceleration and the beta term. The beta gyres carry largely a wave number 1 asymmetry in the azimuthal direction and do not contribute much to the magnitude of the overall torques affecting a hurricane.

There is one other possibility for large pressure torques, which can come from non-hydrostatic pressure anomalies. There can be nonhydrostatic pressures as large as 3–4 mb on scales of individual clouds within large cumulonimbus clouds.

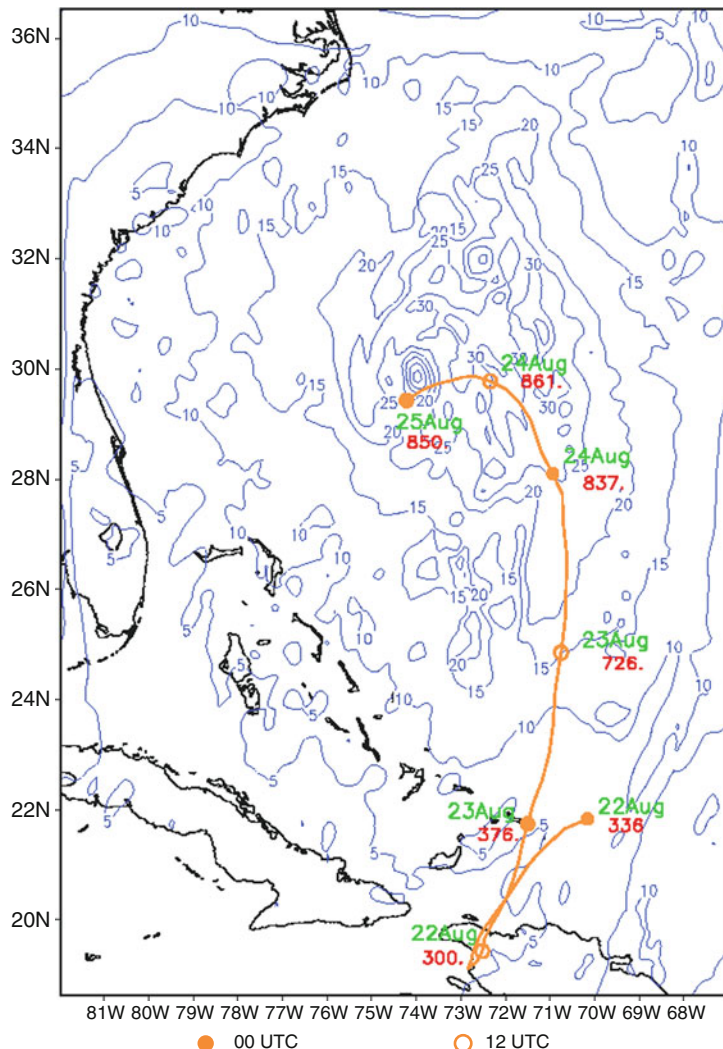


**Fig. 16.10** 72 h 3-D backward trajectory of maximum wind at 850 hPa ( $\text{ms}^{-1}$ ) for Hurricane Bonnie of 1998. Shown here is a trajectory terminating at the wind maxima in the vicinity of the center of the hurricane at the end of the 72 h forecast. Isopleths in blue indicate the maximum wind distribution at 72 h forecast time (From Krishnamurti et al. 2005)

They always occur as a dipole in the pressure gradient, i.e. large positive value is followed by a negative value. Thus following a parcel motion these positive and negative torques tend to cancel each other out on scales larger than the cloud. Hence the nonhydrostatic pressure anomalies are not considered important for major changes of angular momentum in a hurricane.

In Fig. 16.10 we show the three dimensional backward trajectory of an air parcel in a hurricane Bonnie (1998) constructed using the motion field in storm relative

coordinates (Krishnamurti et al. 2005). The figure shows that the parcel at 850 mb has its origins from 336 mb from 3 days prior to its termination at 850 mb. The air parcels generally descend from the upper troposphere to the 850 mb level. In Table 16.2, among other things the contribution of the cloud and friction torque to the total angular momentum budget following air parcel is computed. The table shows that the angular momentum change due to pressure, friction, and cloud torques was about  $10^6 \text{ m}^2\text{s}^{-1}$ . The negative sign for net angular momentum change due to pressure torque indicates that the parcel was moving closer to  $r = 0$  for most of the time. The angular momentum change due to frictional torque (exclusive of cloud torque) arises from horizontal and vertical diffusion, which is relatively small above 850 mb.

### 16.4.9 Inner Versus Outer Forcing

There often is mention of large-scale flare-ups of convection as possible precursors to TC genesis. One does wonder then how necessary and important is the outer angular momentum. If there were no outer circulation outside of some radius  $r_c$ , can inner convection still flare up to form a TS or a CAT1, CAT2 or CAT3 storm? Our limited experience in the drainage of outer angular momentum by surface frictional torques, pressure torques and cloud torques (and even the differences in the circulation based on constant angular momentum) suggests that roughly 20–50 % of the outer angular momentum is generally drained out by these torques. If such a drain occurs, how far out from, say, the 30 km radius would one have to go to see a closed circulation of a given strength? The answer to this would provide rough measure of the reach of the outer influences.

For this purpose we use the system of equations

$$M_F = U_F R_F + f R_F^2 / 2$$

$$M_S = f R_S^2 / 2$$

where MF, UF, and RF are the final (30 km) angular momentum, tangential wind, and radius, respectively, and MS and RS are the starting angular momentum and radius. We have assumed that the starting tangential velocity is negligible. The relationship between the starting and final angular momentum values is given by

$$M_F = M_S \exp[\alpha(R_F - R_S)]$$

where  $\alpha$  is exponential decay coefficient. If there is no loss of angular momentum,  $\alpha = 0$ .

If p is the rate of angular momentum loss per 100 km,  $\alpha = -\frac{\ln(1-p)}{100\text{km}}$ . The solution to the problem is presented graphically as the radius R at which the two curves,

**Table 16.2** Values of different torques ( $\text{m}^2\text{s}^{-1}$ ) along the path of the 3-D trajectory of wind maximum at 850 hPa for Hurricane Bonnie of 1998 (From Krishnamurti et al. 2005)

Forecast hours	00	12	24	36	48	60	72
<b>Position of <math>V_{\max}</math> at 850 hPa</b>	20.74N 68.32W	22.58N 69.95W	25.56N 70.81W	25.17N 71.37W	26.60N 72.36W	27.65N 72.12W	29.48N 850
<b>Pressure of the parcel (hPa)</b>	336 74.54	300 65.31	376 53.84	726 45.10	837 34.86	861 21.05	12.41
<b>Angular Momentum <math>\mathbf{M}</math> (<math>\times 10^6</math>)</b>							
Total angular momentum change $\Delta \mathbf{M}$ ( $\times 10^6$ )	–	–9.23	–11.47	–8.14	–10.24	–13.81	–8.64
Pressure	–	–2.47	–3.17	–3.46	–2.69	–3.20	–3.66
Torque angular momentum change $\Delta \mathbf{M}_{PT}$ ( $\times 10^6$ )	–						
Frictional torque angular momentum change $\Delta \mathbf{M}_{FT}$ ( $\times 10^6$ )	–	–0.8	–1.35	–1.59	–3.39	–4.9	–3.2
Cloud torque angular momentum change $\Delta \mathbf{M}_{CT}$ ( $\times 10^6$ )	–	–5.96	–6.95	–3.09	–4.16	–5.71	–1.78

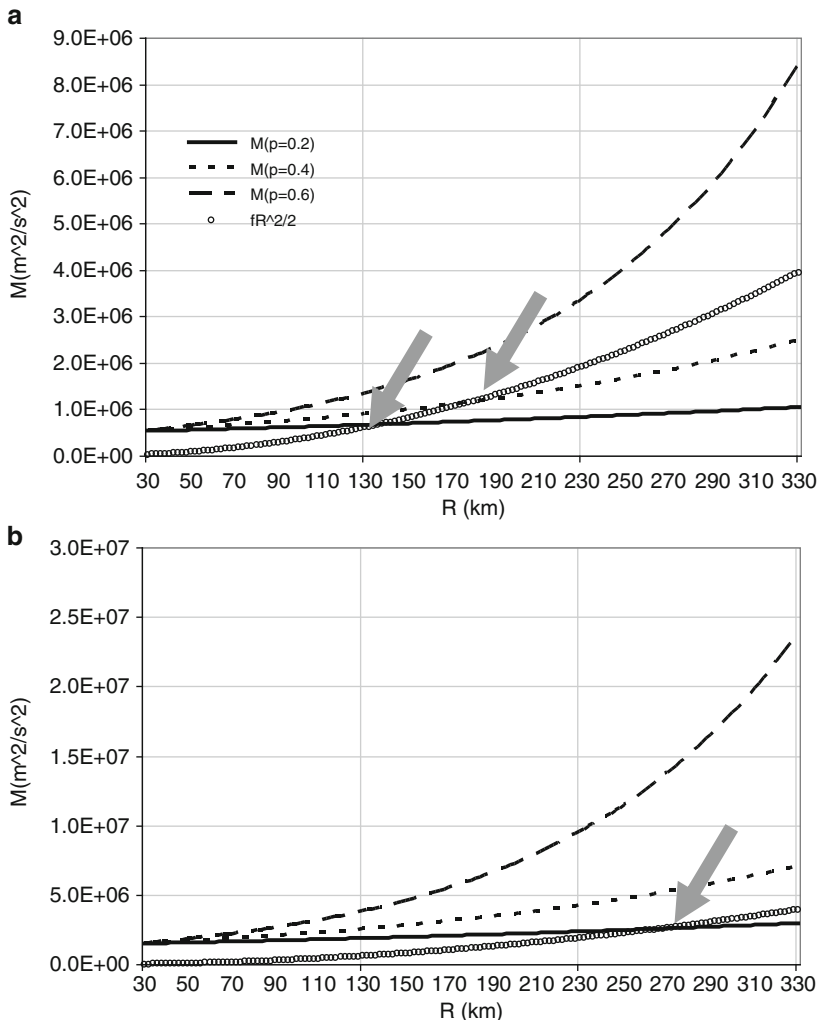


**Fig. 16.11** Illustration of the problem of how far from the 30 km radius would one have to go to see a closed circulation of (a) tropical storm-force winds, or (b) CAT-3 winds. The solution is given by the intersect of the  $M = f R^2 / 2$  line and the  $M = M_S \exp[\alpha(R - R_S)]$  line for different values of angular momentum loss rate. The solutions, when existent, are marked with thick gray arrows

$M = M_S \exp[\alpha(R - R_S)]$  and  $M = f R^2 / 2$ , intersect. Taking  $p = 0.2, 0.4$  and  $0.6$  we illustrate the solution for TS and CAT3 storms forming at  $r = 30$  km (Fig. 16.11a, b).

Figure 16.11 a shows the solution for the case of tropical storm winds (17 m/s) at a radial distance of 30 km. The lines on the graph represent the angular momentum  $M$  as a function of radius, given different values of  $p$ , and subject to the constraint

that  $M(30 \text{ km}) = M_S$ . From the graphic, we can tell that a parcel has to start 140 km away if it loses 20 % of its angular momentum per 100 km radial distance, or from approximately 170 km away if it loses 40 %. If it loses 60 %, the problem has no solution, because no matter how far away the parcel starts, it cannot retain sufficient angular momentum to produce tropical storm force winds at 30 km. Figure 16.11b shows a similar diagram, but for CAT 3 winds (50 m/s) at 30 km. Now, a parcel has to start from a radial distance of 260 km in order to retain enough angular momentum to realize category-3 winds at 30 km, given 20 % loss of angular momentum per 100 km. For 40 % or above, the problem has no solution.

This exercise illustrates not only that the reach of cyclonic circulation goes farther and farther out as more and more of the torque effect modifies the hurricane intensity, but also that if the torques are too strong, the influx of outer angular momentum cannot be the mechanism behind storm intensification. This is an indirect evidence for stating that outer effects are necessary but not sufficient for the hurricane intensity.

#### 16.4.10 Vortical Hot Towers

Along the inner radii of the eye wall of a hurricane there is observational evidence for the presence of vortical hot towers in some of the intense hurricanes. These are undilute tall cumulonimbus clouds that show cloud scale maxima of cyclonic vorticity, with a suggestion for rotation on the cloud scale. These undilute tall cumulonimbus clouds do not entrain much of the environmental drier air and are essentially moist adiabatic in their vertical structure, hence the name undilute. Clouds often tend to flare up on the inner cyclonic shear side of the eye wall with strong rising motions, strong horizontal convergence and generation of localized strong vorticity on these cloud scales. Azimuthally along these radii (around 10–30 km from the hurricane center) three to five such vortical events have been noted in satellite and radar imagery in some of the more intense storms of the Atlantic Ocean basin. Figure 16.12 illustrates a polygonal arrangement of the inner eye region for Hurricane Isabel that was a category 5 hurricane when these features were noted. Clearly this is a non barotropic event, because of the very large localized increase of vorticity. Intense convective heating and large lower tropospheric convergence are important elements for our understanding of these vortical hot towers. The polygonal features are ascribed to barotropic instability of the fast azimuthal cyclonic flows. It is not adequate to demonstrate the formation of such features from pure barotropic models, since the barotropic dynamic coexists with the strong heating and divergence,. Thus any conclusion on barotropic formations must allow the barotropic dynamics to co-evolve in a fully baroclinic system with heating. A subsequent proper partitioning of all possible effects should place the proper weight to the role of barotropic forcing as an entire system is allowed to fully evolve. The major question on these polygonal patterns needs further work. Why

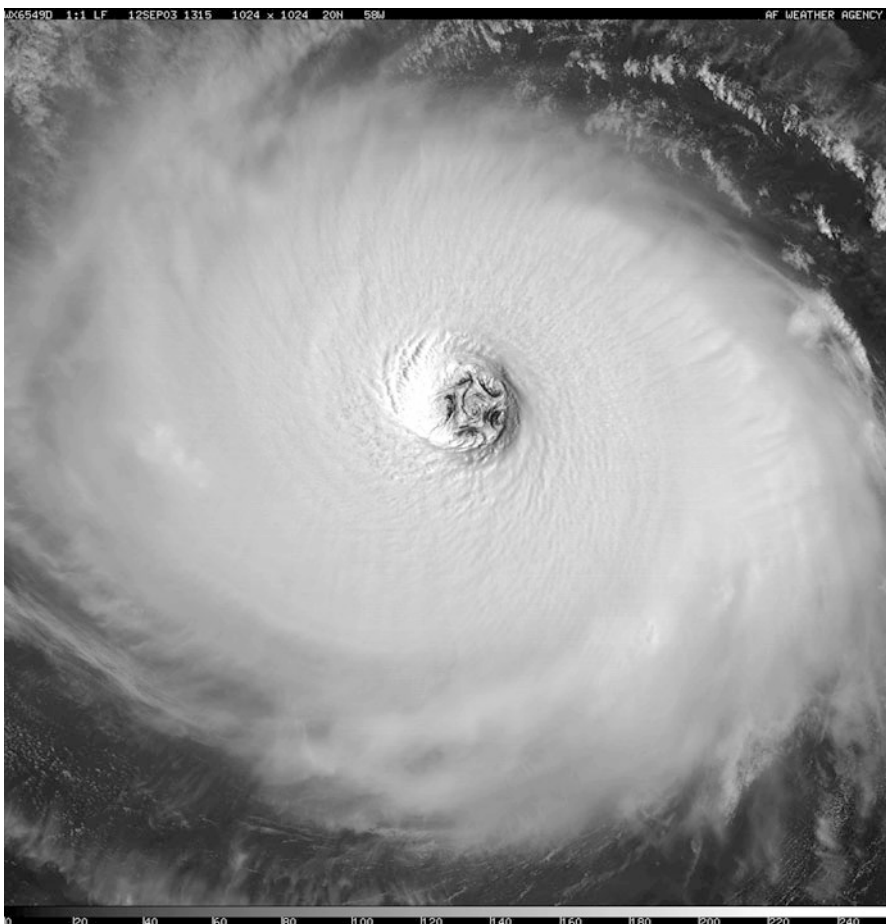


**Fig. 16.12** Defense Meteorological Satellite Program (DMSP) image of Isabel on 12 September 2003 at 1315 UTC. This shows the star fish pattern with six meso-vortices in the eye. The picture shown Isabel in a transient phase where Wavenumber 5 is present. Isabel eventually stabilized at a Wavenumber 4 pattern (From Kossin and Schubert 2004)

they seem to form only in very strong storms and why more so over the Atlantic basin. Numerous satellite images of super typhoons over the Pacific and Indian Ocean basins fail to show such polygonal features.

#### 16.4.11 Vortex Rossby Waves

Within the inner rain area of the hurricane, radii roughly less than 100 km, propagation of Rossby like waves have been noted. These waves can be seen by taking the wind data sets in that region and performing Fourier analysis of

the wind, along selected radii, for each azimuthal wave number. Montgomery and Kallenbach (1997) pioneered these findings. Basically they noted from modeling that axisymmetrization occurs as these Rossby waves emanating from, one or more, of convective towers within the hurricane core contribute to the strengthening of a hurricane. Since these waves, once formed, have to propagate in a cloudy divergent atmosphere, these Rossby waves are continually modified by non barotropic effects. Azimuthal wave numbers 1 and 2 show the largest amplitudes in this region. Wave number 1 may be related to vertical shear of the horizontal wind within the hurricane, whereas wave number 2 may be related to the emanation of Rossby Waves from the source regions of heavy convective elements.

Shapiro and Montgomery (1993) showed that vortex Rossby waves propagate both azimuthally and radially. It propagates vertically as well and the propagation is inversely proportional to the wavenumber. Wang (2002) show that the eyewall shape is influenced by the propagation of the vortex rossby waves and polygonal eyewalls with cyclonic rotation. It can initiate outward-propagating inner spiral rainbands, and cause a breakdown of the eyewall. This is accompanied by an intensity change of the tropical cyclone when the eyewall is perturbed by an outer spiral rainband.

## Appendix 1: Transformation of Shear to Curvature Vorticity

The transformation of shear vorticity to curvature vorticity is one of the parameters that is important for the formation of closed circulations. The rates of changes of curvature vorticity and the shear vorticity in natural co-ordinates can be written (respectively) following Bell and Keyser (1993) and Viudez and Haney (1996) as:

$$\frac{d}{dt} \left( f + V \frac{\partial \alpha}{\partial s} \right) = - \frac{\partial V}{\partial s} \frac{d\alpha}{dt} - \frac{\partial}{\partial n} \left( \frac{\partial \phi}{\partial s} \right) - \left( f + V \frac{\partial \alpha}{\partial s} \right) \nabla_p \cdot V - V \frac{\partial \omega}{\partial s} \frac{\partial \alpha}{\partial p} \quad (16.24)$$

$$\frac{d}{dt} \left( - \frac{\partial V}{\partial n} \right) = \frac{\partial V}{\partial s} \frac{d\alpha}{dt} + \frac{\partial}{\partial n} \left( \frac{\partial \phi}{\partial s} \right) - \left( - \frac{\partial V}{\partial n} \right) \nabla_p \cdot V + \frac{\partial \omega}{\partial n} \frac{\partial V}{\partial p} \quad (16.25)$$

and the tendency equation for absolute vorticity can be written as:

$$\frac{d}{dt} \left( f + V \frac{\partial \alpha}{\partial s} - \frac{\partial V}{\partial n} \right) = - \left( f + V \frac{\partial \alpha}{\partial s} - \frac{\partial V}{\partial n} \right) \nabla_p \cdot V - V \frac{\partial \omega}{\partial s} \frac{\partial \alpha}{\partial p} + \frac{\partial \omega}{\partial n} \frac{\partial V}{\partial p} \quad (16.26)$$

Here  $V$  and  $\phi$  denote the scalar wind and geopotential respectively and  $\alpha$  is the angle subtended by the velocity vector with respect to the x-axis (positive in the anticlockwise orientation). The first and second terms of equation on the right-hand side (16.10) and (16.11) describes the conversion between shear and curvature vorticity. A computational form for the shear to curvature conversion term in the Cartesian co-ordinates is also given by Bell and Keyser (1993) as:

$$\frac{\partial V}{\partial s} = \frac{1}{V^2} [(u^2 u_x + v^2 v_y) + uv(v_x + u_y)] \quad (16.27)$$

$$\frac{d\alpha}{dt} = \frac{1}{V^2} (v\phi_x - u\phi_y) \quad (16.28)$$

$$\begin{aligned} \frac{\partial}{\partial n} \left( \frac{\partial \phi}{\partial s} \right) &= \frac{1}{V^2} [(u^2 - v^2)\phi_{xy} - uv(\phi_{xx} - \phi_{yy})] \\ &\quad + \frac{uv}{V^4} [(v_x + u_y)(v\phi_x - u\phi_y) + vu_x\phi_y - uv_y\phi_x] \\ &\quad - \frac{1}{V^4} (u^3 v_y \phi_y - v^3 u_x \phi_x) \end{aligned} \quad (16.29)$$

These are important equations for anyone trying to code these terms using data sets that are provided in Latitude/Longitude coordinates.

These are not simply the barotropic equations for the conversion of shear vorticity into curvature vorticity. They come from complete equations, thus they include the effects of baroclinicity as well as diabatic effects. It is important to recognize that the kinematics of shear to curvature vorticity is influenced by non barotropic effects as well in this mathematical formulation.

## References

- Bell, G.D., Keyser, D.: Shear and curvature vorticity and potential-vorticity interchanges: interpretation and application to a cutoff cyclone event. *Mon. Wea. Rev.* **121**, 76–102 (1993)
- Evans, J.L., Hart, R.E.: Objective indicators of the life cycle evolution of extratropical transition for Atlantic tropical cyclones. *Mon. Weather Rev.* **131**, 909–925 (2003)
- Fiorino, M., Elsberry, R.L.: Some aspects of vortex structure related to tropical cyclone motion. *J. Atmos. Sci.* **46**, 975–990 (1989)
- Hart, R.E.: A cyclone phase space derived from thermal wind and thermal asymmetry. *Mon. Weather Rev.* **131**, 585–616 (2003)
- Hawkins, H.F., Rubsam, D.T.: Hurricane hilda, 1964. *Mon. Wea. Rev.* **96**, 617–636 (1968)
- Kasahara, A.: The numerical prediction of hurricane movement with the barotropic model. *J. Meteor.* **14**, 386–402 (1957)
- Kasahara, A.: The numerical prediction of hurricane movement with a two-level baroclinic model. *J. Meteor.* **17**, 357–370 (1960)

- Kossin, J.P., Schubert, W.H.: Mesovortices in Hurricane Isabel. *Bull. Am. Meteor. Soc.* **85**, 151–153 (2004)
- Krishnamurti, T.N., et al.: The hurricane intensity issue. *Mon. Weather Rev.* **133**, 1886–1912 (2005)
- Merrill, R.T.: Tropical cyclone structure – chapter 2. In: Global Guide to Tropical Cyclone Forecasting, WMO/TC-No. 560, report no. TCP-31. World Meteorological Organization, Geneva (1993)
- Montgomery, M.T., Kallenbach, R.J.: A theory for vortex Rossby-waves and its application to spiral bands and intensity changes in hurricanes. *Q. J. Roy. Meteor. Soc.* **123**, 435–465 (1997)
- Shapiro, L.J., Montgomery, M.T.: A three-dimensional balance theory for rapidly rotating vortices. *J. Atmos. Sci.* **50**, 3322–3335 (1993)
- Viúdez, Á., Haney, R.L.: On the shear and curvature vorticity equations. *J. Atmos. Sci.* **53**, 3384–3394 (1996)
- Wang, Y.: Vortex Rossby waves in a numerically simulated tropical cyclone. Part II: The role in tropical cyclone structure and intensity changes. *J. Atmos. Sci.* **59**, 1239–1262 (2002)

# Chapter 17

## Modeling and Forecasting of Hurricanes

### 17.1 Introduction

Both global and mesoscale models have provided useful information about the structure, motion and life cycle of hurricanes. The global models have horizontal resolution of roughly 80 km in the tropics, with some 25 vertical levels. The mesoscale models currently have horizontal resolution of much less than 10 km, with upwards of 50 vertical levels. These models have built in a full array of physical parameterizations, such as surface and planetary boundary layer physics (for transfer processes), cumulus parameterization, large scale condensation, radiative transfer with effect of clouds, water vapor, carbon dioxide and ozone, surface energy balance, air-sea interactions, inclusion of topography and sub-grid scale diffusive processes.

The mesoscale models are almost always nested within models with coarser resolution, such as global, providing locally higher resolution for mesoscale phenomena such as squall lines, hurricanes, and fronts. Most mesoscale models carry an option of explicit clouds (instead of cumulus parameterization) for the innermost, highest resolution nested grid. These explicit clouds use a non-hydrostatic version of the model with explicit cloud microphysics. For details of such large- and mesoscale models, the reader may find useful information in texts in numerical and mesoscale modeling, such as Haltiner and Williams (1980), Pielke (2001), Kalnay (2002) among others.

These numerical models have become powerful tools for providing insight on the processes, sensitivity and mechanisms that are important for mesoscale phenomena such as hurricanes. There are several operational global models of the major weather services, such as the US National Weather Service (GFS), the US Navy (NOGAPS), the Australian Bureau of Meteorology and Research Centre (BMRC), the U.K. Met Office (UKMet), the Japanese Weather Service (JMA), the Canadian Weather Service (RPN), and the European Centre for Medium-Range Weather Forecasts (ECMWF). These models routinely provide track and intensity forecasts for hurricanes, typhoons, and tropical cyclones.

The model tracks are based on the tracking of the location of the minimum surface pressure and the intensity is estimated using the maximum winds at or near the surface level and the amplitude of the minimum surface pressure.

## 17.2 The Axisymmetric Hurricane Model

This is one of the simplest hurricane models. It is not a forecast model, since the model hurricane is not moving, but it provides a great insight for the modeling of the structure of a hurricane. Such a model was first developed by Ooyama (1963) and was followed by numerous studies by Rosenthal (1969), Yamasaki (1968) and Lord et al. (1984). This model is ideally suited for examining the growth of an incipient weak vortex the sensitivity to physical parameterization, sensitivity to the initial base state, and microphysical processes. The model based on a recent study of Rao and Ashok (1999) is given by the following system of equations, written in a storm-centered cylindrical coordinate system  $(r, \theta, z)$ :

- The equation of motion for the radial wind component

$$\frac{\partial V_r}{\partial t} = -V_r \frac{\partial V_r}{\partial r} - w \frac{\partial V_r}{\partial z} + \left( f + \frac{V_\theta}{r} \right) V_\theta - \theta \frac{\partial \phi}{\partial r} + K \left( \nabla_1^2 - \frac{1}{r^2} \right) V_r + \frac{1}{\bar{\rho}} \frac{\partial \tau_r}{\partial z} \quad (17.1)$$

- The equation of motion for the tangential wind component:

$$\frac{\partial V_\theta}{\partial t} = -V_r \frac{\partial V_\theta}{\partial r} - w \frac{\partial V_\theta}{\partial z} - \left( f + \frac{V_\theta}{r} \right) V_r + K \left( \nabla_1^2 - \frac{1}{r^2} \right) V_\theta + \frac{1}{\bar{\rho}} \frac{\partial \tau_\theta}{\partial z} \quad (17.2)$$

- The equation for the potential temperature

$$\frac{\partial \theta}{\partial t} = -V_r \frac{\partial \theta}{\partial r} - w \frac{\partial \theta}{\partial z} + \frac{1}{\bar{\rho} \phi} \left( M_c \frac{\partial s}{\partial z} + D(s_c - s - Ll_c) \right) + \frac{L}{\phi} C + K_\theta \nabla_1^2 \theta \quad (17.3)$$

- The moisture conservation equation

$$\frac{\partial q}{\partial t} = -V_r \frac{\partial q}{\partial r} - w \frac{\partial q}{\partial z} + \frac{1}{\bar{\rho}} \left( M_c \frac{\partial q}{\partial z} + D(q_c - q + l_c) \right) - C + K_q \nabla_1^2 q \quad (17.4)$$

- The mass continuity equation

$$\frac{\partial}{\partial z} \bar{\rho} w = -\frac{1}{r} \frac{\partial}{\partial r} \bar{\rho} r V_r \quad (17.5)$$

– The hydrostatic equation

$$\frac{\partial \phi}{\partial z} = -\frac{g}{\theta}, \text{ with } \phi = C_p \left( \frac{p}{p_0} \right)^{R/C_p} \quad (17.6)$$

In this system,  $V_r$  and  $V_\theta$  are the radial and tangential wind components,  $w$  is the vertical velocity,  $\theta$  is the potential temperature,  $q$  is the mixing ratio, and  $\phi$  is given by  $\phi = C_p \left( \frac{p}{p_0} \right)^{R/C_p}$ ;  $f$  is the Coriolis parameter;  $K$  is the horizontal eddy viscosity coefficient,  $K_\theta$  and  $K_q$  are the horizontal diffusivities for temperature and moisture respectively;  $s$  is the dry static energy,  $h$  is the moist static energy,  $l$  is the mixing ratio of liquid water;  $L$  is the latent heat of condensation,  $C$  is the large-scale condensation per unit volume;  $D$  is the total detrainment of cloud mass at a given level, and  $M$  is the total vertical cloud mass flux at a given level; subscript  $c$  indicates cloud values; the overbar indicates a horizontal average. The boundary conditions for the model are that the radial and tangential winds are zero at the center and at the outer edge of the domain, the vertical velocity  $w$  is considered to vanish at the top and bottom of the domain, and the radial derivatives of  $\phi$ ,  $\theta$  and  $q$  are set to zero at the center and at the domain edges.

To illustrate the workings of this model we show some results from Rao and Ashok (2001). Using sea surface temperatures of 302°K and a Coriolis parameter  $f = 5 \times 10^{-5} \text{ s}^{-1}$  they obtained the time evolution of the minimum pressure and maximum tangential wind and time-radial cross section of the tangential wind at the 1 km level as shown in Fig. 17.1a–c.

The initial sea level pressure is close to 1,005 mb. Figure 17.1a shows that it experiences a rapid decline after hour 96 of the forecast, reaching a minimum of near 800 mb by hour 160. The initial tangential wind is on the order of  $10 \text{ ms}^{-1}$ . Figure 17.1b shows its increase to nearly  $90 \text{ ms}^{-1}$  by hour 144. The evolution of the tangential wind shows the radial spread of strong winds. Tropical storm force winds spread to nearly 100 km out from the storm center; the strongest winds are seen at a radial distance of roughly 25 km at about 120 h after the initial time (Fig. 17.1c). The above illustrates that a simple model can simulate a relatively realistic symmetric hurricane.

We shall next illustrate the radial-vertical structure of the mature hurricane simulated by this model. Figure 17.2a–e shows the structure of:

- (a) Tangential wind in  $\text{ms}^{-1}$ ;
- (b) Radial wind in  $\text{ms}^{-1}$ ;
- (c) Vertical velocity in  $\text{cm s}^{-1}$ ;
- (d) Potential temperature anomaly in  $^{\circ}\text{K}$ ;
- (e) Relative humidity in percent.

The model uses SST temperature of 302°K and a Coriolis parameter  $f = 5 \times 10^{-5} \text{ s}^{-1}$ . At hour 120 (the mature stage) the hurricane acquires a tangential wind of  $80 \text{ ms}^{-1}$ . The isopleths of strong tangential wind are nearly vertical to almost 10 km.

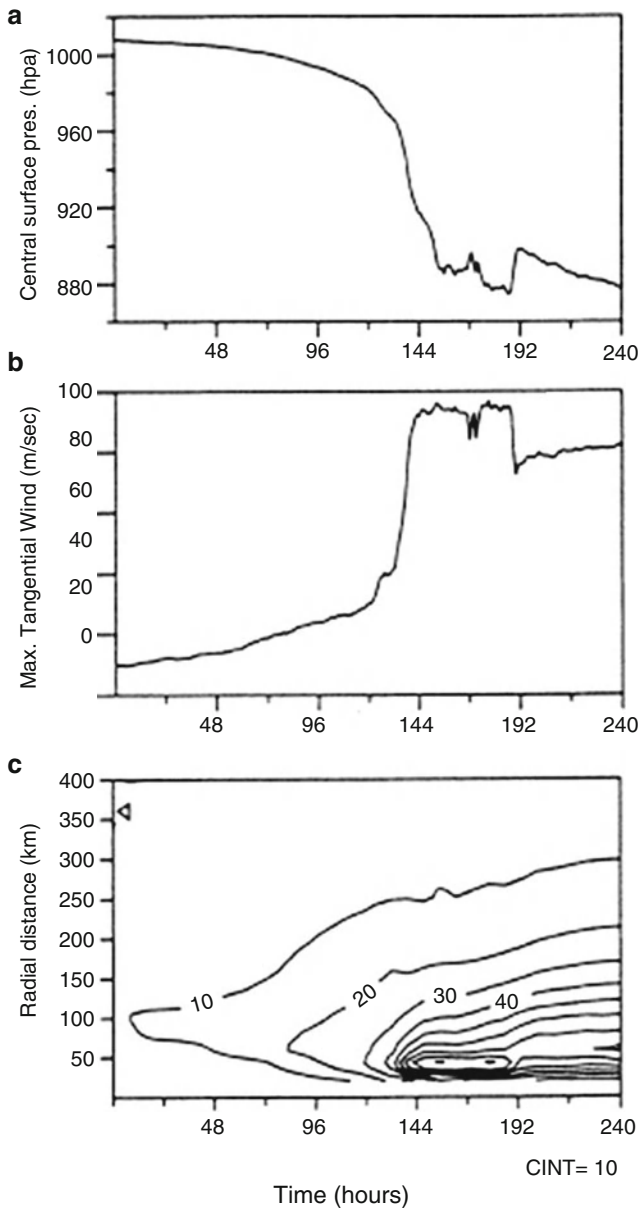


**Fig. 17.1** The 240 h evolution of (a) central pressure and (b) maximum tangential wind and (c) radius-time cross section of 1 km tangential winds (From Rao and Ashok 2001)

The radial winds are as strong as  $40 \text{ ms}^{-1}$  in the outflow layer located at a height of about 16 km (unrealistically high up in the atmosphere). A thin inflow layer resides below the 0.5 km level. This inflow appears to be largely frictionally controlled. A deeper inflow layer is often seen in real data structures of hurricanes

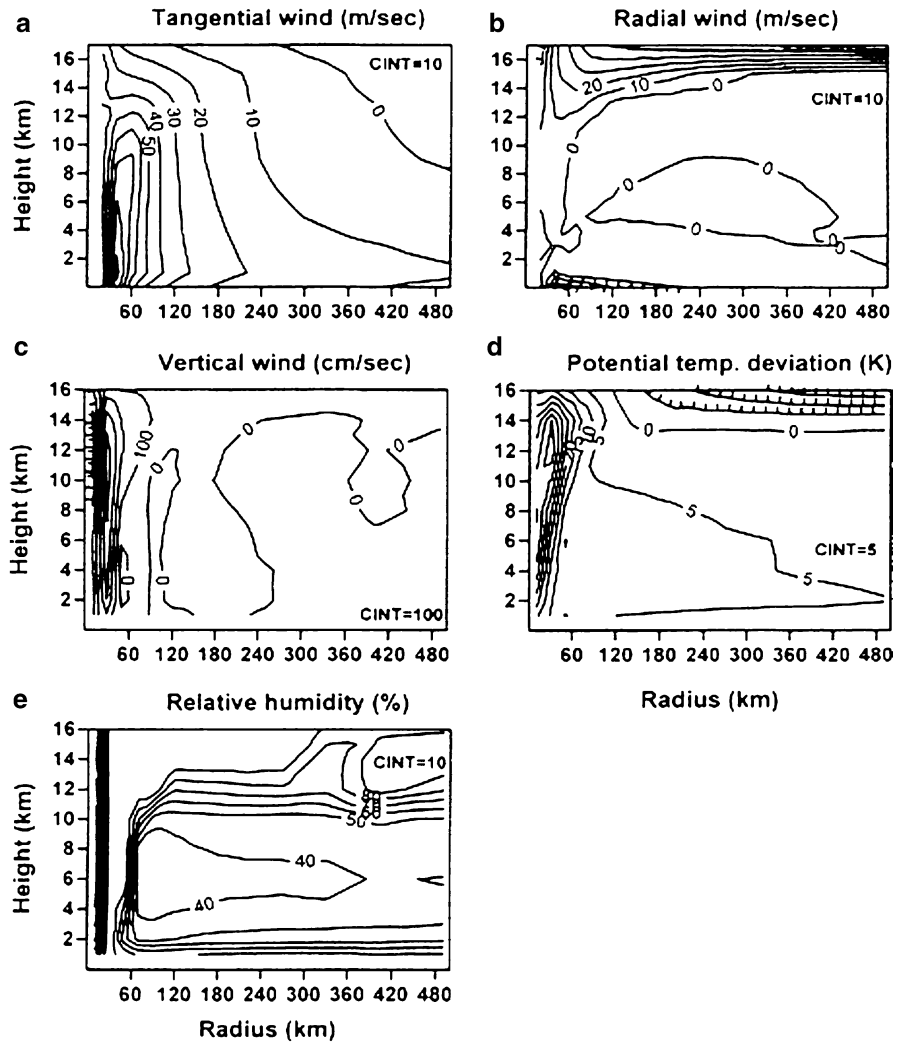


**Fig. 17.2** Height-radius cross section of (a) tangential wind, (b) radial wind, (c) vertical velocity, (d) potential temperature anomaly, and (e) relative humidity for the mature stage of a simulated storm (From Rao and Ashok 2001)

(Hawkins and Rubsam 1968). The vertical velocity shows the most intense upward motion near approximately 15 km from the axis of the hurricane. Much weaker vertical motions are noted near the axis  $r = 0$ . The largest upward motions are of the order of  $1 \text{ ms}^{-1}$ . The potential temperature deviation shows a well-marked warm core near the 12 km level. In most real hurricanes the warm core (temperature anomaly) is generally near the 10 km level. The potential temperature anomaly can be somewhat higher than the 10 km level because of the pressure dependence of potential temperature.

The field of relative humidity shows a vertical wall near the 15 km radius where the values are near 100 %. In the radial belt  $60 \text{ km} < r < 360 \text{ km}$  a dry middle troposphere with  $r < 40 \text{ %}$  is seen. Moist air resides in the boundary layer  $r < 2 \text{ km}$  where the relative humidity is close to 80 %. This air gets saturated as it is carried up in the fast-ascending air. This moist air is carried to outer radii in the deep outflow layer by the strong radial winds where unrealistically high relative humidity in excess of 80 % is seen over a very deep layer above the 12 km level. This simulation is relatively easy to perform; its deficiencies can be corrected by a judicious choice of model parameters. This model is ideal for performing sensitivity studies on model physics.

Rao and Ashok (2001) noted that hurricanes did not form if the SST was kept below  $299^{\circ}\text{K}$ . They experimented with different values of the Coriolis parameter and noted a strong development when the storm was located at  $10^{\circ}\text{N}$  compared to  $25^{\circ}\text{N}$ .

Other sensitivity studies have shown that a mean hurricane season sounding (Jordan 1958), if used for the initial base state, does not produce a hurricane in the first 96 h of forecast. If that sounding were rendered moister by raising the Jordan sounding's moisture by 20 % the hurricane forms more readily. The mean hurricane season sounding of Jordan includes a number of rather dry soundings from dust episodes that tend to provide a somewhat drier environment for hurricane simulations, thus the artificial moistening seems logical for the simulations.

Lord et al. (1984) examined the microphysical sensitivities for hurricane simulations in an axisymmetric model. They noted the following areas of sensitivity:

- Inclusion of ice processes produced dramatic differences in the structure and evolution of simulated hurricane vortex.
- Cooling due to melting of ice particles can initiate and maintain mesoscale downdrafts on a horizontal scale of tens of kilometers.
- This scale depends upon the both the horizontal advection of parameterized snow particles detrained from the tops of convective down drafts and mean fall speed of particles toward the melting level.
- The production rate of snow particles depends upon several parameterized microphysical processes and is significant in maintaining the upper level snow concentration.
- Interaction of cloud microphysical processes and basic dynamical processes on the mesoscale occurs through melting and cooling.

### 17.3 Current Suite of Operational Models

Current suite of operational models for hurricane forecasts in the USA includes the GFS model which is the operational weather prediction model of USA. This is currently run at a triangular truncation of 382 waves that corresponds to a tropical

horizontal grid size of the order of 40 km. This is a comprehensive model that includes data assimilation where conventional data sets and satellite based data sets, such as those described in Chapter x are included. In addition for the hurricane season the assimilation also incorporates all available reconnaissance aircraft data sets such as the flight level and the dropwindsondes (Kalnay et al. 1990). The GFS is run four times a day 00, 06, 12, 18 UTC. For hurricane forecasts it also includes a synthetic vortex based on the method developed by GFDL described below. A hurricane tracker code is also run in a post processing mode to determine the location of the center of a hurricane as implied by the GFS data sets. Such a code is necessary for operations since it is hard to follow the center of a hurricane by simply looking at charts. Details of the model and its changes can be found out at <http://www.meted.ucar.edu/nwp/pcu2/avintro.htm>.

The Navy NOGAPS model is used by the US Navy for its global forecast operations. This is also a member model for the hurricane forecast suite of the National Hurricane Center in Miami. This model is being used for typhoon forecasts over the Pacific Ocean and also covers the forecasts of tropical cyclones over the Indian Ocean basins. This model utilizes a triangular truncation of 239 waves currently that corresponds to a horizontal resolution of roughly 60 km over the tropics (<http://www.meted.ucar.edu/nwp/pcu2/nogaps/index.htm>). It carries a comprehensive array of physical and land surface processes in its design. This model provides 180 h forecasts four times a day. This model also carries a detailed data assimilation component and includes much of the same global data sets as the other global centers.

The GFDL hurricane model is a useful member model of the NHC suite of models. This model is triply nested, covering three domains. The outer grid covers an area roughly  $75^{\circ}$  by  $75^{\circ}$  (latitude/longitude) at a resolution of roughly 30 km. Outside of this outermost domain the model is driven by the GFS based boundary conditions. The next two inner domains respectively carry  $11^{\circ}$  by  $11^{\circ}$  domains at a horizontal resolution of one sixth of a degree and the inner most domain spans a  $5^{\circ}$  by  $5^{\circ}$  box at a horizontal resolution of approximately 7.5 km. In effect this is like a mesoscale model in the inner most domain. A unique aspect of this model is the synthetic (bogus) vortex insertion at the location of the hurricane. Since the data assimilation for this model is entirely based on the GFS, this in fact requires the removal of a hurricane from the GFS assimilation. The synthetic vortex is based on aircraft reconnaissance data sets to first define a symmetric vortex (based on observations) and its insertion into the GFS initial state. The details are provided in a paper by Kurihara et al. (1993, 1995). This inserted vortex also makes use of official initial estimates on the storm position and its intensity.

The United Kingdom's operational forecast model called UK Met Model, is another major forecast provider for hurricanes, tropical cyclones and typhoons world wide. This is regarded among the better models. This is a grid point model that carries a horizontal resolution of roughly  $0.5^{\circ}$  latitude by longitude (<http://www.metoffice.gov.uk/research/nwp/>). This model is run twice daily at 00 and 12 UTC. This is a comprehensive weather forecast model that carries the state of the art physical processes and surface boundary conditions. More detailed description can be found in their web site and in the references therein.

In addition to the above models, the last but not the least, is the ECMWF model, which is also currently monitoring global tropical systems such as the hurricanes. Their model is described within the ECMWF web site ([http://www.ecmwf.int/products/forecasts/guide/The\\_ECMWF\\_global\\_atmospheric\\_model.html](http://www.ecmwf.int/products/forecasts/guide/The_ECMWF_global_atmospheric_model.html)). This model is considered the best model currently for predicting the global weather on the medium range time scales. Because of its holding the least errors in predicting the hurricane environment, this model has been noted to be one of the better models on the time frame of 3–6 days for predicting hurricane tracks. The dynamical steering of hurricanes requires a better forecast of the hurricane environment, where many models show a large growth of errors on the medium range time frame.

GUNA is another forecast product that is being used by the National Hurricane Center. This is simply the ensemble mean of forecasts provided by GFDL, UK Met, NOGAPS and the GFS models. This is supposedly a ensemble averaged forecast provided including some of the best current operational models. This product has been noted to be quite useful in the operational forecasts in the US.

The results from the above models are used for real time hurricane track forecasts by the National Hurricane Center in Miami, they are also being used by the US Navy's Joint Typhoon Warning Center at Honolulu for the Pacific ocean storms. Two additional statistical models are being used for hurricane intensity forecasts. SHIPS is utilizes model forecasts of intensity and statistical post processing. SHIPS are based on a multiple regression technique (De Maria et al. 2005). The methodology is derived from past open ocean storms. The predictands for the intensity forecasts include member model forecasts of intensity, environmental vertical wind shear, sea surface temperatures, the upper ocean heat content. Persistence and climatology are additional parameters of this computation. The predictands utilize recent past years data sets thus the statistical regression coefficients change each year. This method has demonstrated considerable skill. A variant of this called Decay-SHIPS (DSHP) is designed to better predict the weakening of hurricane intensity after land fall. This is essentially an empirical add on to the SHIPS method and is based on the behavior of past land falling storms. Students wishing to work on such problems need to thoroughly understand the linear multiple regression methods, which are described in standard statistical methods texts. Then they do need some synoptic and physical knowledge on the behavior of past storms, thus to know what predictands to include and which ones to exclude. This does require some experience.

## 17.4 Multimodel Superensemble for Atlantic Hurricanes

We shall present typical seasonal performances of the above models in the context of ensemble forecasts.

Ensemble and Superensemble forecasts of hurricanes/typhoons Appendix 1 provides the principle of the superensemble methodology. This carries a training and a forecast phase, Fig. 17.3. Thus each forecast of the multimodels is regressed,

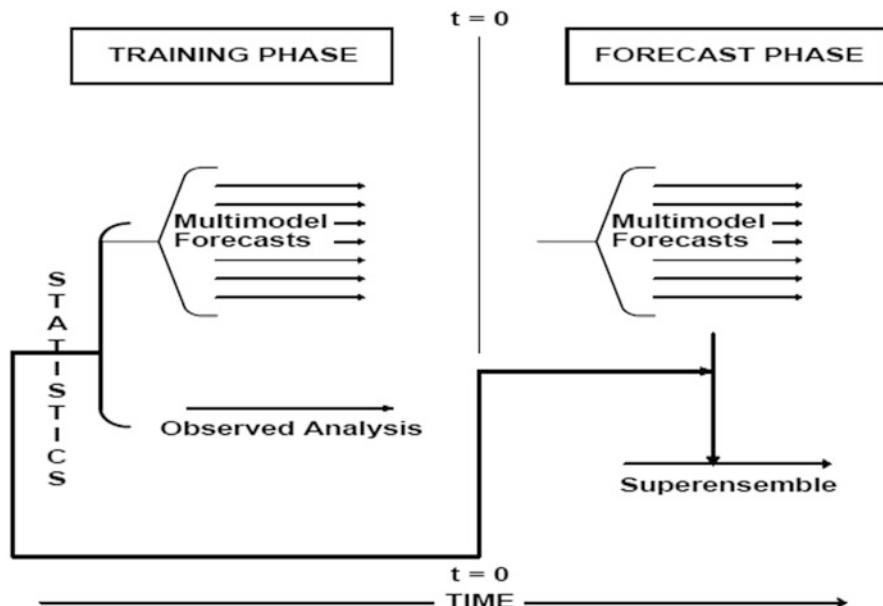


**Fig. 17.3** A schematic illustration of the methodology of superensemble forecasts

using multiple regression, against the observed best estimates of that variable for which a superensemble is being constructed. It was noted that some 60 past forecasts from each member model was needed to obtain somewhat stable statistics during the training phase. Such statistical weights are obtained for every 6 h as the models make new forecasts for each storm. Different weights for different forecast hours is brought about because some models perform better in the initial forecast hours and some models do better late in their forecasts. The variables that one uses, in the context of hurricane forecasts are the latitudinal position of the storm's center at each forecast hour, the corresponding longitudinal position, the intensity of the predicted storm (as inferred from the minimum pressure in the hurricane, or the maximum intensity as seen from near surface winds in the vicinity of the hurricane). In Fig. 17.4 we show typical model performances during one hurricane season, here the year 2004 is being shown (Krishnamurti et al. 2011). All of the hurricanes of the year 2004 are included in this summary. In this illustration we show the seasonal forecast errors for track in km and for intensity (maximum wind) in m/s. This inter-model comparison of errors includes results from the Official forecasts of the National Hurricane Center, GFDL, UK Met, GFS, NOGAPS, GUNA (the selected model ensemble), the overall ensemble mean forecasts and those from the superensemble. In the intensity forecasts the Ships and the DSHIPS are included. This illustration shows that errors of the order of 50 km at hour 12 increase to around 500 km by hour 120 of forecasts typically for these member models. The superensemble is able to reduce these errors by almost 100 km at hour 120 in a systematic manner. The intensity forecast range from 4 to 16 m/s between hours

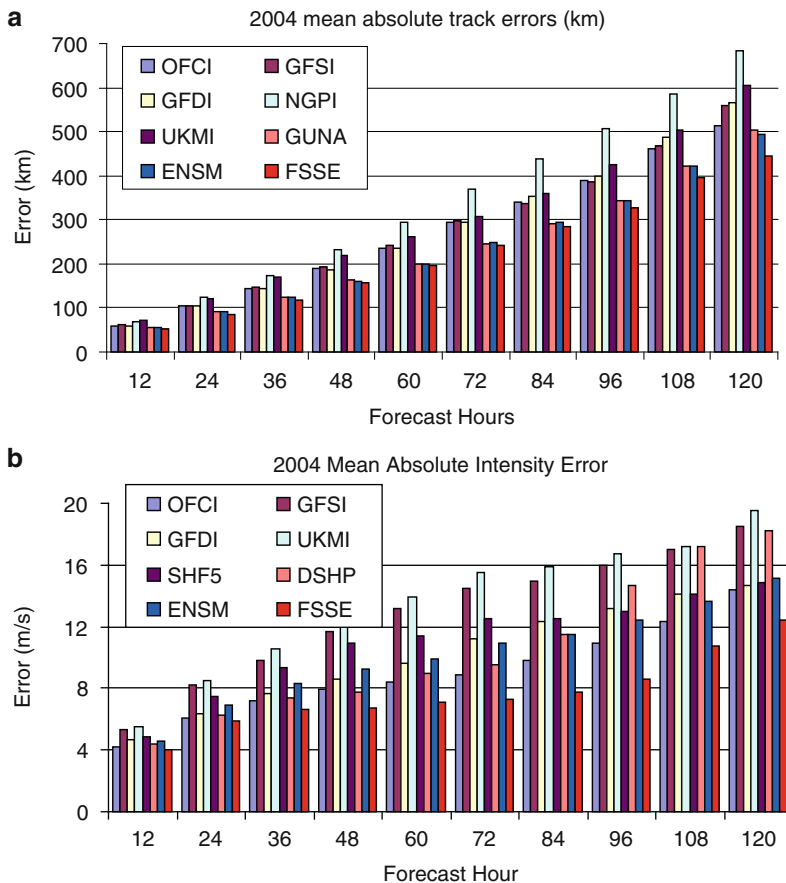


**Fig. 17.4** Forecast skills of several operational models and FSU superensemble (FSSE) for the Atlantic hurricanes season of 2004 showing (a) track errors and (b) intensity errors

12 and 120 h of forecast, with a reduction by almost 4 m/s from the deployment of the superensemble. The ensemble mean based on member model forecasts is better than most models in terms of track and intensity errors but is inferior to the superensemble because it assigns the same weight to good and bad models in its ensemble averaging. The superensemble is more selective in assigning proper weights to each model based on their past performances.

The same promises of the multimodel superensemble based forecasts have consistently held over many years. The most recent year was 2011, when a mix of large scale and mesoscale models provided the best intensity forecast skills for the Atlantic Ocean hurricanes. Those are shown in Fig. 17.5 and the models that went into making these forecasts are shown in Table 17.1. It appears that the multimodel method, illustrated here, has the most promise for providing the highest skills for 5 day forecasts for hurricane tracks and intensity.

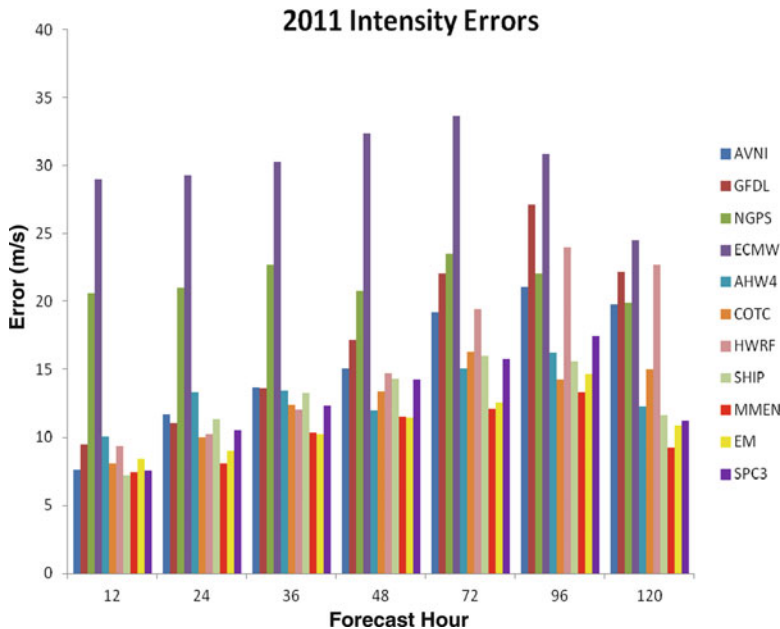


**Fig. 17.5** This histogram shows the intensity errors, covering all the hurricanes of the 2011 season for the Atlantic Ocean, Caribbean and the Gulf of Mexico. Units are in m/s

**Table 17.1** Details of the models included in this study

ATCF IID	
AVNI	GFS
GFDL	Geophysical fluid dynamics laboratory (NOAA/GFDL)
NGPS	NOGAPS
BAMS	Beta and advection model (shallow layer)
EMX	ECMWF
H3GP	3 Nest HWRF 27/9/3
HWRF	Hurricane WRF 27/9
AHW4	NCAR AHW
COTC	Coupled ocean/atm mesoscale prediction system – tropical cyclone (COAMPS-TC)
FIMY	Flow-following finite-volume icosahedral model
SPC3	Statistical prediction of intensity from a consensus ensemble
SHIP	Statistical hurricane intensity prediction scheme
ARFS	FSU ARW

## 17.5 Multimodel Superensemble for Pacific Typhoons

Similar forecasts were carried out for the Pacific Ocean, all of the typhoons for the 3 years 1998 through 2000 were evaluated by Vijay Kumar et al. (2003). Figure 17.6 shows similar results as for the tropical Pacific typhoons. Here the position errors

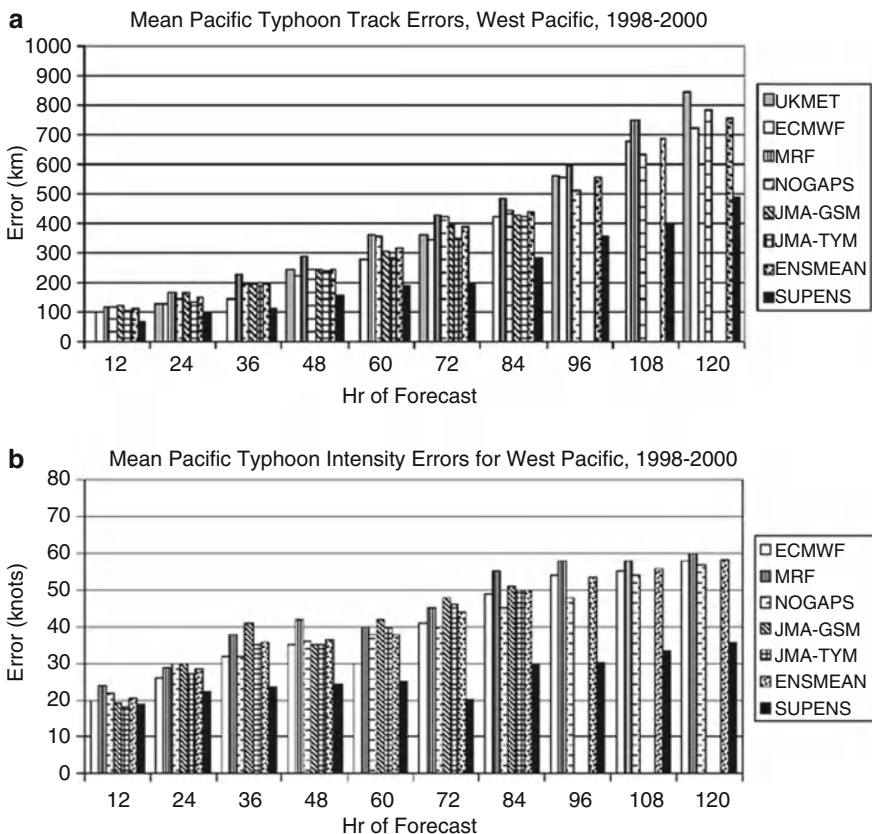


**Fig. 17.6** Same as Fig. 17.4 but for Pacific typhoons and covering a period of 3 years from 1998 to 2000

are listed in kms and the intensity errors use knots for the average errors. The suite of models here are somewhat different. These include the ECMWF model based typhoon forecasts for the 3 years. Remarkably large reductions in forecasts errors were provided by the multimodel superensemble. The superensemble based forecast errors for the Pacific Ocean typhoons at hour 120 of forecasts, for both the track and intensity, were almost comparable to those of the member models at hour 36 of forecasts. This large reduction of errors from the superensemble suggests that such formulations, as the superensemble, are clearly needed for typhoon forecasts. Given that models carry large errors arising from the formulations of physics, dynamics, lack of microphysics, treatment of the boundary layer and surface processes, adequate data sets at hurricane resolutions, data assimilation procedures and the overall lack of adequate resolution for the models it may be desirable to devise post processing statistical algorithms such as the superensemble, towards the goal of overall error reductions.

## 17.6 Ensemble Forecasts from a Suite of Mesoscale Models and Combination of Mesoscale and Large Scale Models for Atlantic Hurricanes

It is also possible to put together a suite of mesoscale models, each of which, provide hurricane forecasts. From the efforts at the US National Weather Service and efforts at NCAR three mesoscale models have become available to the research community. These are called the HWRF, MM5 and WRF. Several variants of these

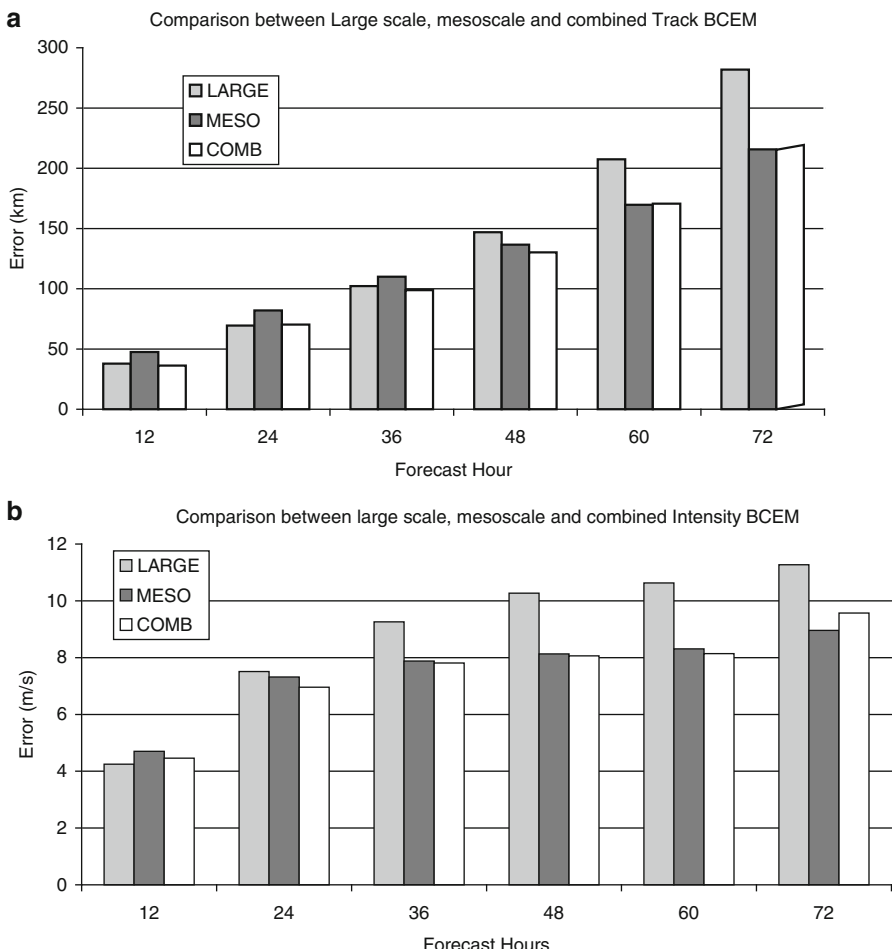


**Fig. 17.7** FSU superensemble forecast errors of (a) track and (b) intensity of all Atlantic hurricanes for years 2004, 2005, and 2006 using a suite of mesoscale models listed in Table 17.2, large-scale models used in Figs. 17.4 and 17.6 and using both the meso and large scale models

**Table 17.2** Descriptions of the mesoscale models used in FSU superensemble

Parameters	MM5A	WRF-A	WRFB	HWRF	GFDL
Horizontal resolution	9 km	9 km	9 km	27/9 km	30/15/7.5
Vertical sigma layers	23	31	28	43	42
Initial and boundary conditions	NCEP's final analysis ( $1^{\circ} \times 1^{\circ}$ )	NCEP's final analysis ( $1^{\circ} \times 1^{\circ}$ )	NCEP's final analysis ( $1^{\circ} \times 1^{\circ}$ )	GFS model	GFS model
Radiation parameterization	Dudhia	RRTM and Dudhia	RRTM and Dudhia	GFDL scheme	
Cumulus parameterization	Bettis and Miller	Kain-Fritsch (new Eta)	Bettis-Miller-Janjic	Simplified Arakawa Schubert	Arakawa Schubert
Microphysics	Goddard	WRF 6-class	Ferrier	Ferrier	Ferrier
parameterization	Blackadar	Mellor-Yamada-Janjic TKE	Yonsei University (YSU)	GFS non-local PBL	GFS non-local PBL
Planetary boundary parameterization	Multilayer soil model	5 layer thermal diffusion	5 layer thermal diffusion	GFDL slab model	Slab model
Land surface model	NCEP's final analysis ( $1^{\circ} \times 1^{\circ}$ )	NCEP's final analysis ( $1^{\circ} \times 1^{\circ}$ )	NCEP's final analysis ( $1^{\circ} \times 1^{\circ}$ )	Princeton ocean model	Princeton ocean model
SST	72 h	72 h	72 h	96 h	120 h
Duration of forecast	Single	Single	Single	Two	Triply
Nest	No	No	No	Yes	Yes
Bogus vortex/vortex relocation					

models are possible by changing the available physics options provided by these modeling groups. Those plus the GFDL model (which is at a mesoscale resolution in its inner most nested grid) provide a possible mesoscale suite of models for advancing the hurricane forecast accuracies. The need for a mesoscale suite is recognized because of the importance of the inner rainfall and strong wind areas of hurricanes at radii less than 100 km. The hurricane intensity is impacted by the convective and dynamic processes of this inner core. These are not resolved by large scale models. A comparison of forecast errors using (a) a suite of mesoscale models; (b) a suite of large scale models and (c) using all of the above models for all the hurricanes of the years 2004, 2005, 2006 is presented in Fig. 17.7 (Krishnamurti et al. 2010). This illustration suggests that during the initial 48 h the bias corrected ensemble mean from the suite of large plus a suite of the mesoscale models provides the least track errors. At hours 60 and 72 the mesoscale suite performs the best. The intensity errors show a similar error structure when the mesoscale and the combined suite of models are used. Further research is clearly needed in areas such as improvement of each of the member models, that is a difficult research area where one chips away at errors from improvements of model physics, microphysics, dynamics, data assimilation and improved data coverage. Post processing algorithms also have an important place parallel with the model improvements.

## References

- DeMaria, M., Mainelli, M., Shay, L.K., Knaff, J.A., Kaplan, J.: Further improvement to the statistical hurricane intensity prediction scheme (SHIPS). *Weather Forecast.* **20**(4), 531–543 (2005)
- Haltiner, G.J., Williams, R.T.: *Numerical Prediction and Dynamic Meteorology*. Wiley, New York (1980). 477pp
- Hawkins, H.F., Rubsam, D.T.: Hurricane Hilda, 1964, II. Structure and budgets of the hurricane on October 1, 1964. *Mon. Weather Rev.* **97**, 617–636 (1968)
- Jordan, C.L.: Mean soundings for the West Indies area. *J. Meteor.* **15**, 91–97 (1958)
- Kalnay, E.: *Atmospheric Modeling, Data Assimilation, and Predictability*. Cambridge University Press, Cambridge (2002). 341pp
- Kalnay, E., Kanamitsu, M., Baker, W.: Global numerical weather prediction at the national meteorological center. *Bull. Am. Meteor. Soc.* **71**, 1410–1428 (1990)
- Krishnamurti, T.N., Pattnaik, S., Biswas, M.K., Kramer, M., Bensman, E., Surgi, N., Vijay Kumar, T.S.V., Pasch, R., Franklin, J.: Hurricane forecasts with a mesoscale suite of models. *Tellus* **62**, 633–646 (2010)
- Krishnamurti, T.N., Biswas, M.K., Mackey, B.P., Ellingson, R.G., Ruscher, P.H.: Hurricane forecasts using a suite of large-scale models. *Tellus* (2011). doi:[10.1111/j.1600-0870.2011.00519.x](https://doi.org/10.1111/j.1600-0870.2011.00519.x)
- Kurihara, Y., Bender, M.A., Ross, R.J.: An initialization scheme of hurricane models by vortex specification. *Mon. Weather Rev.* **121**, 2030–2045 (1993)
- Kurihara, Y., Bender, M.A., Tuleya, R.E., Ross, R.J.: Improvements in the GFDL hurricane prediction system. *Mon. Weather Rev.* **123**, 2791–2801 (1995)
- Lord, J.S., Willoughby, H.E., Piotrowicz, J.M.: Role of a parameterized ice phase microphysics in an axisymmetric, non-hydrostatic tropical cyclone model. *J. Atmos. Sci.* **41**, 2836–2848 (1984)
- Ooyama, K.: A dynamic model for the study of tropical cyclone development. *Geophys. Int.* **4**, 187–198 (1963)

- Pielke, R.A. (ed.): Mesoscale Meteorological Modeling. International Geophysics Series, vol. 78. Academic, London (2001). 676pp
- Rao, D.V.B., Ashok, K.: Simulation of tropical cyclone circulation over the Bay of Bengal using the Arakawa-Schubert cumulus parameterization. Part I—description of the model, initial data and results of the control experiment. *Pure Appl. Geophys.* **156**, 525–542 (1999)
- Rao, D.V.B., Ashok, K.: Simulation of tropical cyclone circulation over the Bay of Bengal using the Arakawa-Schubert cumulus parameterization. Part II: some sensitivity experiments. *Pure Appl. Geophys.* **158**, 1017–1046 (2001)
- Rosenthal, S.L.: Numerical experiments with a multi-level primitive equation model designed to simulate the development of tropical cyclones. Experiment I. U.S. Department. of Commerce, ESSA Technical Memorandum No. NHRL-82, 32pp. (1969)
- Vijaya Kumar, T.S.V., Krishnamurti, T.N., Fiorino, M., Nagata, M.: Multimodel superensemble forecasting of tropical cyclones in the Pacific. *Mon. Weather Rev.* **131**, 574–583 (2003)
- Yamasaki, M.: Detailed analysis of a tropical cyclone simulated with a 13 layer model. *Pap. Meteorol. Geophys.* **19**, 559–585 (1968)

# Chapter 18

## Sea Breeze and Diurnal Change Over the Tropics

### 18.1 Introduction

The sea breeze phenomenon is very striking over many parts of the tropics since it is known to produce cooling associated with afternoon showers that occur with regularity on most undisturbed days. Figure 18.1 from a classical diagram of van Bemmelen (1922) illustrates the time evolution of the sea breeze (on shore winds) in Batavia (now Jakarta). The Batavia sea breeze time section shows that it is a shallow circulation essentially confined to the lowest 3 km. The intensity of the upper land breeze is roughly half that of the sea breeze. The land breeze (off shore winds) during the early morning is much less intense by comparison. Extensive observational studies of sea breezes have been conducted by Hsu (1970), Flohn (1965) and many others. Hsu (1970) portrayed a schematic evolution of the land/sea breeze phenomenon based on observations in the Gulf Coast of Texas. Figure 18.2 illustrates this evolution, the diagram being self explanatory. Here the horizontal and vertical extent of the wind system is enclosed within a heavy solid elliptical curve.

Sea breeze is a manifestation of diurnal variability. Although the main intensity of the sea breeze is confined to the lower troposphere, the phenomenon of diurnal change is known to occur at all latitudes and even in the stratosphere. We recognize that the sea breeze is primarily driven by the differential heating of land and sea. Simple numerical models have gone a long way towards exploring the role of externally imposed diurnal heating cycles on the evolution of sea breeze circulations. The problem of simulating sea breeze is an important because of its large spatial extents. At times one can see a late evening line of coastal clouds for thousands of miles; occasionally such examples of cloud lines have been observed on the Atlantic coast from Florida to Newfoundland during the summer months. Because of associated cumulonimbus convection such a long line of convergence can have important implications in the atmospheric general circulation. We shall next address some of the well-known dynamical studies of the sea breeze phenomenon.

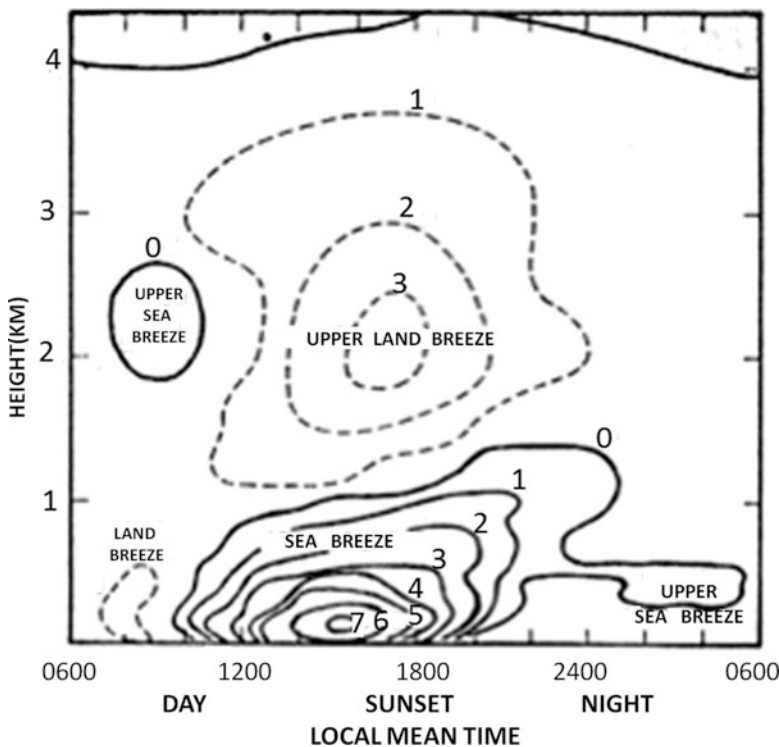


**Fig. 18.1** Velocity isopleths ( $\text{ms}^{-1}$ ) for the land/sea breeze in Batavia; shaded area indicates onshore flow and unshaded area offshore flow (After van Bemmelen 1922)

## 18.2 Sea Breeze Models

A large number of sea breeze models are described in the literature. Some of the well-known studies are by Estoque (1961) and by Pielke (1974). Estoque (1961) considers the sea breeze problem in an x-z plane where x is normal to the coastline and z is the vertical coordinate. The closed system of equations of the linear sea breeze problem is formed by the following:

- The equations of motion,

$$\frac{\partial u}{\partial t} = f v - \sigma u - \frac{1}{\rho} \frac{\partial p}{\partial x} \quad (18.1)$$

$$\frac{\partial v}{\partial t} = -f u - \sigma v - \frac{1}{\rho} \frac{\partial p}{\partial y} \quad (18.2)$$

$$\frac{\partial w}{\partial t} = -\sigma w - \frac{1}{\rho} \frac{\partial p}{\partial z} - g \quad (18.3)$$

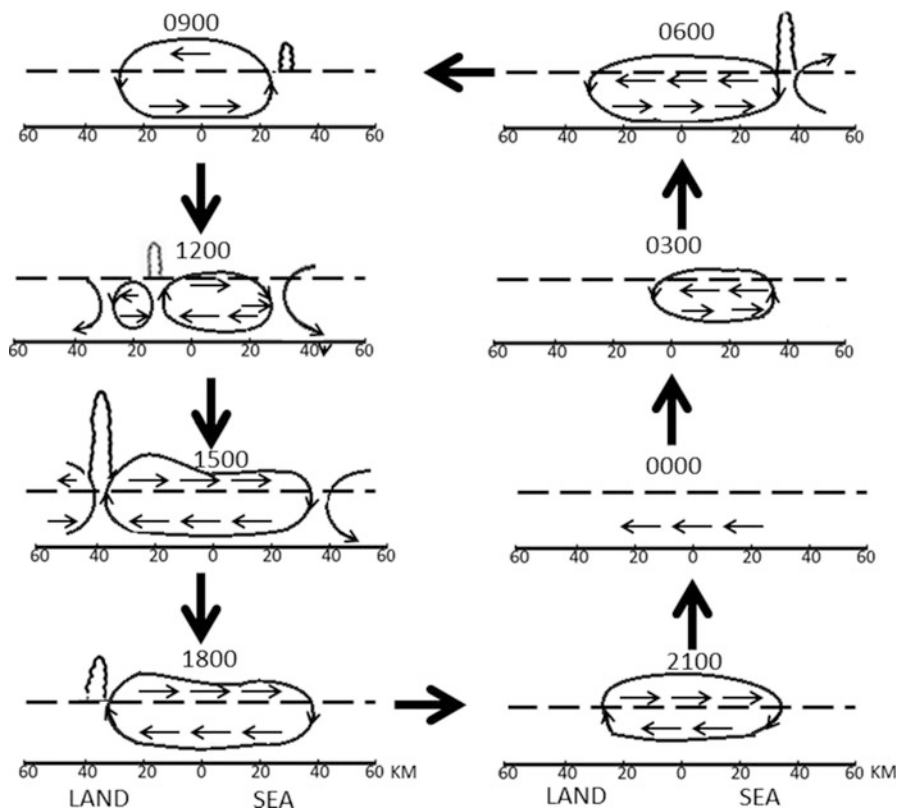


**Fig. 18.2** Synthesized empirical model of the land/sea-breeze system along the Texas Gulf Coast. Arrow lengths proportional to wind speed (Adapted from Hsu 1970)

- The mass continuity equation,

$$\frac{\partial u}{\partial x} + \frac{\partial w}{\partial z} = 0 \quad (18.4)$$

- The first law of thermodynamics,

$$\frac{\partial T}{\partial t} + \beta w = \kappa \left( \frac{\partial^2 T}{\partial x^2} + \frac{\partial^2 T}{\partial z^2} \right) \quad (18.5)$$

The diurnal heating is introduced via a prescribed variation of the surface temperature  $T$  by a relation of the form

$$T = M e^{int} \sin \frac{2\pi x}{L} \quad (18.6)$$

Here  $u$ ,  $v$  and  $w$  are the three velocity components,  $\rho$  is the density of air,  $f$  is the Coriolis parameter and  $\sigma$  is a coefficient of friction.  $\kappa$  stands for a thermal diffusivity coefficient and  $\beta$  denotes the lapse rate of the undisturbed thermal stratification.  $M$  is an arbitrary amplitude function and  $L$  is the horizontal scale of the sea breeze. The standard procedure of solving linear systems of equations as those given above consists in assuming solutions of the form

$$q = Q(z)e^{int} \cos mx \text{ or } q = Q(z)e^{int} \sin mx \quad (18.7)$$

where  $q$  stands for one of the dependent variables  $u$ ,  $v$ ,  $w$ ,  $T$  or  $p$ . The substitution of such forms of solutions with appropriately prescribed boundary conditions leads to a separation of variables in the  $x$ ,  $z$  and  $t$  coordinates. The usual boundary conditions for this problem are

$$w(z = 0) = 0, \quad T(z = 0) = Me^{int} \sin mx, \quad m = \frac{2\pi}{L} \quad (18.8)$$

$$w(z = \infty) = 0, \quad T(z = \infty) = 0 \quad (18.9)$$

All the solutions are periodic in  $x$ . The solutions for Estoque's problem are

$$u = \frac{rM}{m(a^2 - b^2)} (ae^{az} + be^{-bz}) e^{int} \cos mx$$

$$v = \frac{frM}{m(\sigma + in)(a^2 - b^2)} (ae^{az} + be^{-bz}) e^{int} \cos mx$$

$$w = \frac{rM}{a^2 - b^2} (e^{az} - e^{-bz}) e^{int} \sin mx$$

$$T = Me^{-bz} + \frac{b^2 - s}{b^2 - a^2} (e^{az} - e^{-bz}) e^{int} \sin mx.$$

Here  $r = \frac{g\alpha m^2 (\sigma + in)^2}{f^2 + (\sigma + in)^2}$ ,  $s = \frac{in}{\kappa} + m^2$ , where  $\alpha$  is a coefficient of thermal expansion, and  $a$  and  $b$  are constants determined by the initial conditions.

Estoque used the following values of the constants to portray his solutions of the linear sea breeze problem:  $n = 7.273 \times 10^{-5} s^{-1}$ ,  $f =$  the Coriolis parameter at  $45^\circ N$ ,  $\beta = 2.5 \times 10^{-5} K cm^{-1}$ ,  $\sigma = 2.5 \times 10^{-4} s^{-1}$ ,  $L = 120 km$ , and  $\kappa = 2.25 \times 10^5 cm^2 s^{-1}$ .

It should be emphasized again here that the sea breeze is driven by the imposed temperature perturbation in space and time along the lower boundary. How this temperature perturbation is realized is not being addressed here. Estoque noted a number of interesting properties of this solution:

- (i) Even though the imposed temperature perturbation at the surface has a maximum at noon, the maximum of temperature occurs later at higher levels. The vertical transport of heat is achieved by mixing and vertical advection.
- (ii) The motion field clearly shows a sea breeze component. The lower branch of the sea breeze (ocean to land) is only 0.5 km deep, while the return flow is much deeper. The maximum intensity of the sea breeze is reached about 1 h after the maximum heating at the surface (i.e., at 1 p.m.). Maximum vertical motion occurs at a height of 0.4 km.
- (iii) A hodograph of the surface wind ( $u, v$ ) shows that the sea breeze during the day and the land breeze at night are of equal intensity. This is unrealistic — a consequence of the imposed periodic temperature cycle at the surface. The actual observed sea breeze ellipse is usually pear-shaped.
- (iv) The solution depends strongly on the magnitude of the friction coefficient. The larger its value, the closer to the time of maximum heating do the strongest winds from the ocean tend to occur. The solutions from this linear theory appear quite realistic in many ways, in spite of its limitations, such as the artificially imposed cyclic conditions and the lack of interaction with a basic large-scale prevailing synoptic conditions.

Some additional advances in the understanding of the sea breeze dynamics were provided by the studies of Pielke (1974). Pielke (1974) integrated a three-dimensional hydrostatic system of primitive equations to study the sea breeze over south Florida. The forcing included the surface heat and momentum fluxes, as well as the prevailing synoptic conditions. We shall not go into the details of the closed system of the primitive equations although it should be emphasized that a qualitative discussion of the results of a complex numerical model is no substitute for a detailed step by step understanding of the model, especially to those who wish to follow the modelling approach towards understanding a phenomenon.

Pielke (1974) integrated the motion and thermal variables using a semi-implicit form of the upstream differencing scheme. Similarly to Estoque's formulation, at the Earth's surface, the potential temperature variation is described by an equation of the form  $\theta = A(x, y) \sin \frac{2\pi t}{T}$ , where  $A$  was chosen to be 10K over land and 0K over water. The period  $T$  was taken as 13 h, the duration of sunlight over Florida. Effectively, this fixes the potential temperature over water at a constant value (no diurnal variation, consistent with the large heat capacity of water), while the land temperatures fluctuate by up to  $\pm 10$ K over 24 h. The 10K differential between land and ocean is the critical factor in this problem. The absolute values of temperature do not explicitly enter the analysis.

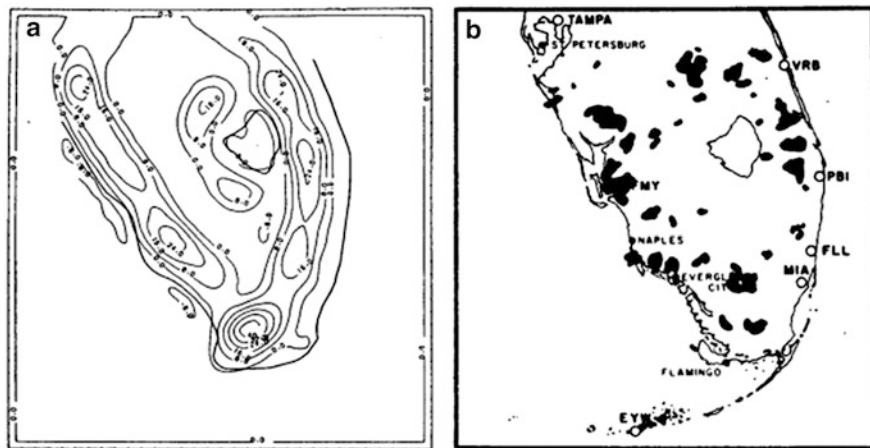


**Fig. 18.3** (a) The numerically predicted vertical velocity field (contour interval is  $8 \text{ cm s}^{-1}$ ) and (b) corresponding radar depiction from the Miami WSR-57 radar, 7 h 30 min after sunrise for 29 June 1971 (Adapted from Pielke 1974)

The vertical velocity was determined from the vertical integration of the mass continuity equation and the pressure from an integration of the tendency equation. Pielke (1974) notes the following interesting results in his studies:

- (i) The curvature of the coastline of south Florida has a significant influence on the location of the sea breeze convergence zone.
- (ii) Under both southwesterly and southeasterly basic flows the convergence zone forms parallel and near the coast and moves inland during the day.
- (iii) Lake Okeechobee, located in central Florida, is a region of descent, this being a consequence of the cold water temperatures that are prescribed.
- (iv) The predicted evolution of the sea breeze convergence zone is in close agreement with the organization of line convection over south Florida during undisturbed days.
- (v) Figure 18.3 shows the locations of cumulonimbus convection based on composite radar returns over Florida for a selected day and the numerically predicted field of vertical velocity between 3 and 4 p.m. This comparison was a highlight of Pielke (1974) simulation of the three-dimensional sea-breeze circulation.

Similar studies can be formulated to investigate the effect of differential diurnal cycle of heating on the coastal circulation over many tropical land masses, large and small islands, and peninsulas. Models need to be further refined; in particular, the diurnal radiative heating, its feedback, convection (shallow, deep, dry and moist) require better formulation.

### 18.3 Some Observational Aspects of Diurnal Changes

Lavoie (1963) presented a detailed investigation of the rainfall over oceanic atolls and showed the existence of a pronounced nocturnal rainfall maximum. The nocturnal or early morning maximum has been noted over different parts of the tropical oceans. Many hypotheses have been advanced for the nocturnal rainfall maximum such as: radiative effects due to differential cooling over cloudy and cloud-free regions, radiative effects on the dry and moist static stability, radiative destabilization of the cloudy region at night, and tidal effects (diurnal, as well as semi-diurnal).

The semi-diurnal variation of sea level pressure in the tropics is quite apparent in the observations (Haurwitz and Cowley 1973; Hamilton 1980). The basis for this semidiurnal pressure cycle follows from the atmospheric thermal tide theory (Chapman and Lindzen 1970). In short, atmospheric thermal tides is primarily generated from the heating in the atmosphere due to the absorption of solar radiation by ozone in the stratosphere. It may be mentioned that the contributions to this atmospheric heating from absorption of solar radiation by water vapor and clouds in the troposphere is comparatively far less. This heating in the atmosphere excites vertically propagating modes that carry the signal from the stratosphere and upper troposphere to the ground. Nearly 80 % of the diurnal pressure variability is in modes whose energy is trapped at the level of forcing in the stratosphere (Lindzen 1967). Therefore the atmospheric surface tidal pressure signal is predominantly semidiurnal.

Gray and Jacobson (1977) have examined in some detail the diurnal variation of disturbance cloudiness over oceans. They found that oceanic intense rainfall from disturbances shows a maximum in the early morning hours. They found that this was true for most of the small islands, presumably due to the effect of the diurnal heating of the island, and a bimodal distribution of rainfall was documented in the large islands. Figure 18.4a, b illustrate these features for small and large islands.

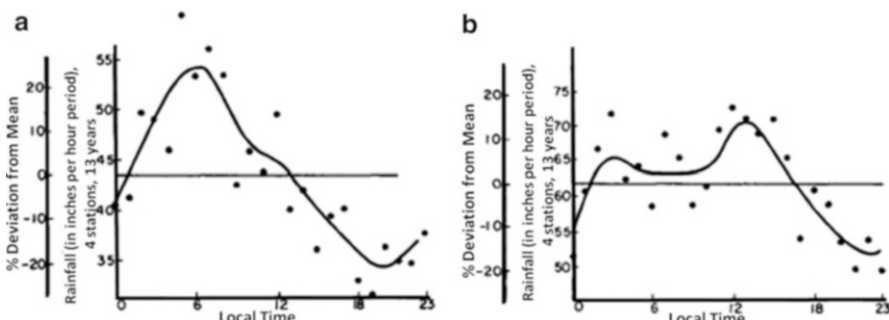


**Fig. 18.4** Precipitation curve over (a) small island and (b) large island over western Pacific Ocean (Adapted from Gray and Jacobson 1977)

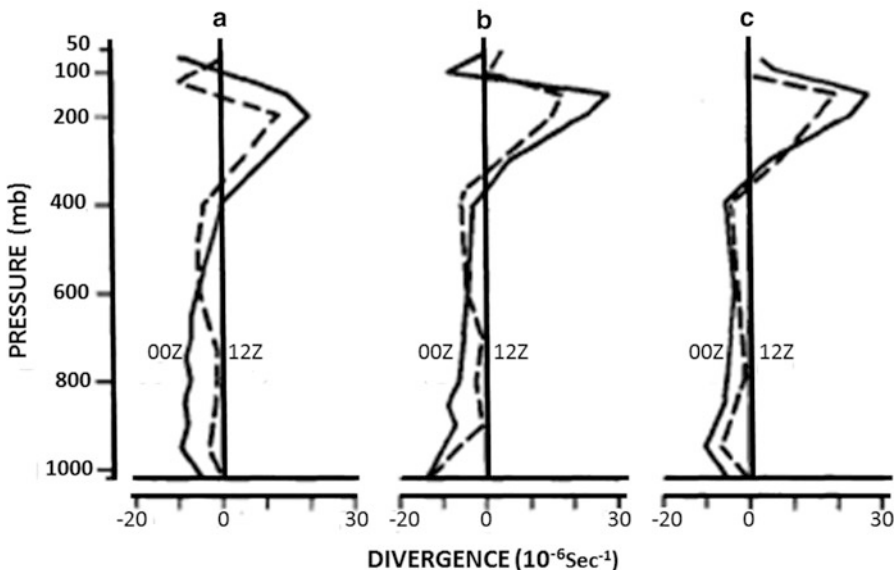


**Fig. 18.5** Average divergence profiles at 0000 and 1200 UTC for three groups of West Pacific cloud clusters: (a) non-intensifying cloud clusters; (b) under  $12\text{--}15 \text{ ms}^{-1}$  sustained which later developed into tropical cyclone, and (c) like B but under  $\sim 20 \text{ ms}^{-1}$  sustained winds (Adapted from Gray and Jacobson 1977)

The results here are based on observations over the western Pacific Ocean. The small islands reflect oceanic conditions and show a maximum at around 6 a.m. The large islands show an additional peak around 3 p.m. Gray and Jacobson (1977) have analyzed this diurnal feature in some detail. They have, quite correctly, emphasized the importance of this problem for tropical meteorology. They found a marked difference in the vertical distributions of divergence between 00 and 12Z and an enhanced lower tropospheric convergence at 00Z (10:00 a.m. local time) compared with 12Z (10:00 p.m. local time). This is true for most of their categories shown in Fig. 18.5, which illustrates these distributions.

The explanation proposed for the enhanced convergence in the early morning hours over the oceans is as follows. The disturbed region with low-level convergence has an excessive rainfall, this being a region with cloud cover. There exists a differential radiation field between the cloudy and surrounding clear regions. Figure 18.6 shows typical vertical profiles of net radiative warming (or cooling) rates within a tropical disturbance during the day and night. The intensity of differential radiative heating (or cooling) between the cloudy and cloud-free regions is quite different for daytime and night-time conditions. Figure 18.7, also from the same study, describes in a schematic manner the influence of such a radiative effect on the enhancement of convergence during the early morning hours. Here the heating rates are implied to produce bulges in the thickness patterns

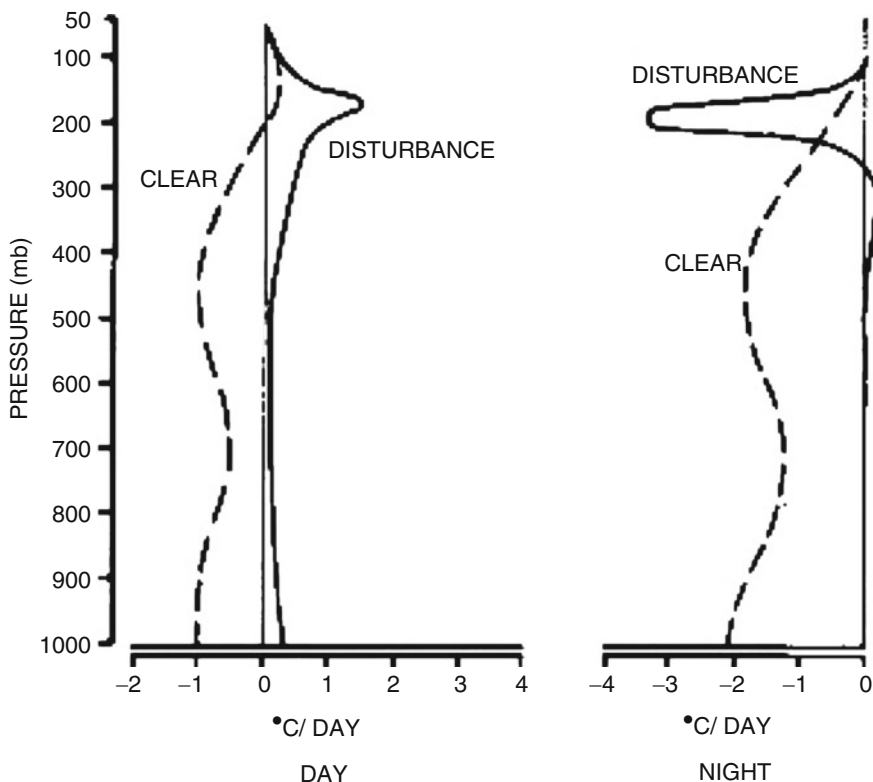
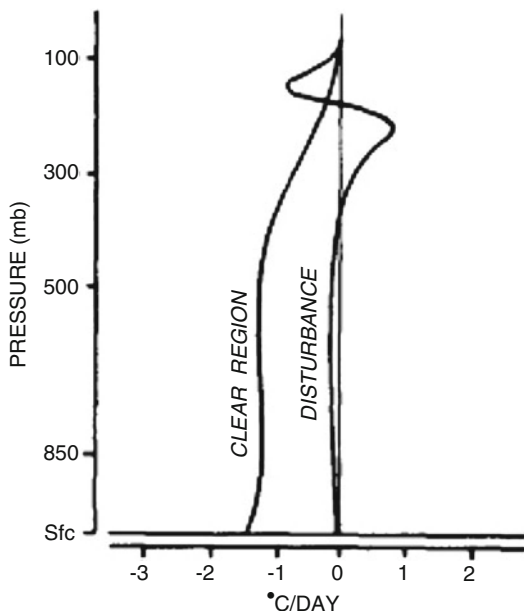


**Fig. 18.6** Estimated net radiative heating rates for day and night for tropical disturbance and clear regions (Adapted from Gray and Jacobson 1977)

between pressure surfaces, leading to stronger horizontal pressure gradients, and consequent stronger cross-isobaric flows that result in an enhancement of the low-level convergence and upper level divergence. This conceptual model is worthy of detailed investigation.

The diurnal changes over Africa and over the GATE experimental region in the eastern Atlantic have been examined in considerable detail by McGarry and Reed (1978). They show that over northern Africa between  $15^{\circ}$  and  $20^{\circ}\text{N}$  thunderstorms are most prevalent in the late afternoon/early evening period, even though the convective cloud cover and the rainfall are maximum just after midnight. They attributed this feature to the long-lived squall systems that form in the afternoon but take several hours to reach their maximum rain production. McGarry and Reed (1978), as well as Gray and Jacobson (1977), examined the rainfall over the eastern Atlantic and noted a distinct early afternoon maximum. This was also confirmed by Murakami (1979) from his analysis of satellite cloud cover distributions. The GATE region of the eastern Atlantic is thus different from western Pacific Ocean. No explanation was offered by McGarry and Reed (1978) for this dissimilarity.

**Fig. 18.7** Radiative cooling rates in a tropical disturbance with an opaque high cloud cover and in a tropical clear region (Adapted from Gray and Jacobson 1977)



## 18.4 Diurnal Variation in the Monsoon Belt

Ananthakrishnan (1977) has examined the diurnal changes of wind, pressure and temperature distribution over India. Figure 18.8 from his work illustrates the diurnal variation of winds (12Z minus 00Z winds) for four selected stations. The four stations are:

- (i) Madras, located on the south-east Indian coast, which experiences much of its rainfall in October and November;
- (ii) Bombay, located on the west Indian coast, which experiences most of its rainfall in June, July and August;
- (iii) Calcutta, located over coastal northeastern India, which also experiences most of its rainfall in June, July and August; and
- (iv) Delhi, located over northern central India near a desert, experiencing most of its rainfall in July and August.

These diagrams are good illustrations of the vertical distribution of the diurnal change.

Over Madras the 12Z (5:30 p.m. local time) winds are easterlies, stronger than those at 00Z (5:30 a.m. local time) in the lowest kilometer. This is indicative of the sea breeze over Madras, where it is strongest during the summer months, at around 0.3 km above sea level. The depth of the sea breeze circulation is roughly 4 km.

Over Bombay the sea breeze is pronounced from September to May (i.e., the non-monsoon months). The depth of the sea breeze over Bombay can be as much as 5–6 km. This is noted between February and April.

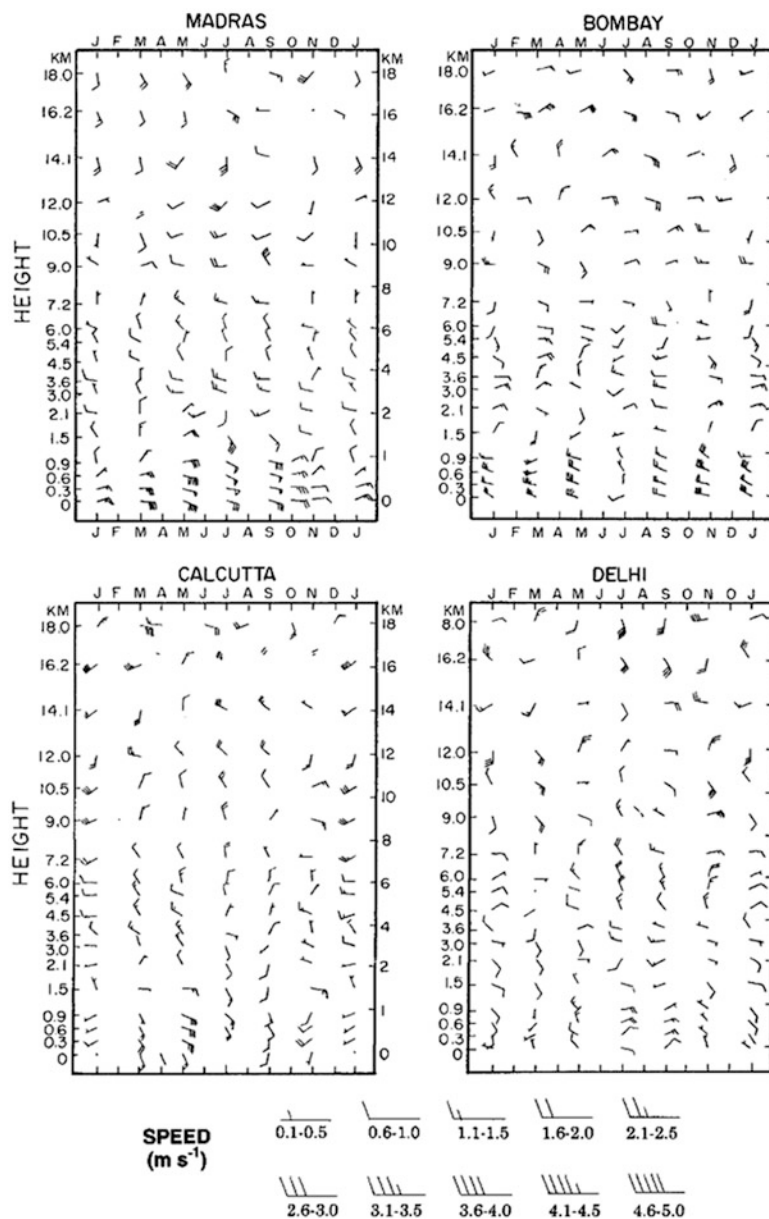


**Fig. 18.8** Diurnal variation of upper winds (difference between 12Z and 00Z values) at Madras, Bombay, Calcutta and New Delhi (From Ananthakrishnan 1977)

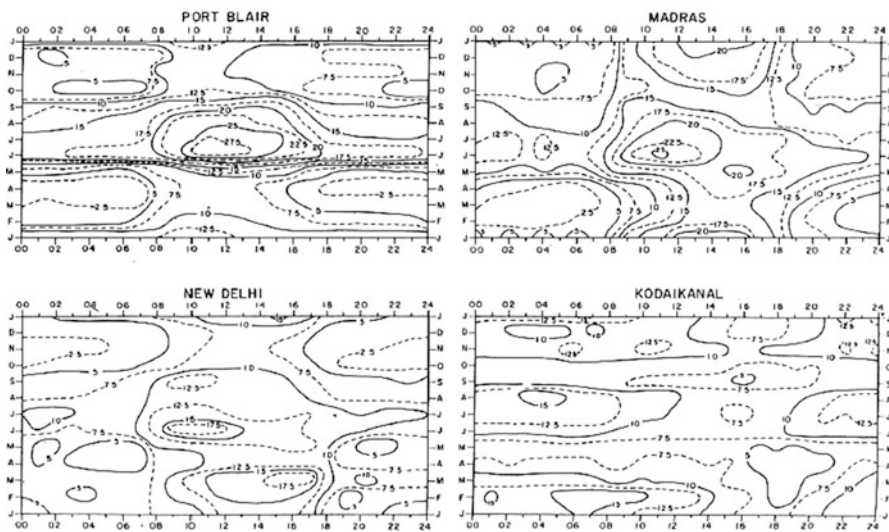


**Fig. 18.9** Hourly variation of surface wind speeds ( $\text{ms}^{-1}$ ) at Port Blair, Madras, New Delhi, and Kodaikanal (From Ananthakrishnan 1977)

Over Madras, as well as over Bombay, there exists a diurnal component between 9 and 12 km during the summer months. Figure 18.9 shows the diurnally stronger easterlies over Bombay and stronger westerlies over Madras. Although the amplitude of this phenomenon is only around  $2 \text{ ms}^{-1}$ , it is significant, since the averages are based on roughly 10 years of observations. An important question remaining unsolved is how this diurnal feature is maintained. Since the axis of the tropical easterly jet of northern summer is located closer to Madras, the above data implies that the jet is stronger at 00Z (i.e. 5:30 a.m.) than at 12Z (i.e. 5:30 p.m.). This may be a result of radiative effects associated with diurnal variations of convection and cloud cover.

Over Madras the rainfall maximum (see Table 18.1) occurs between 6:00 p.m. and midnight local time, while at Bombay the period of most intense rainfall is between 6:00 a.m. and 9:00 a.m. local time. This diurnal change over Bombay is more maritime (during June, July and August) while that of Madras seems more continental. Cloud cover and associated radiative cooling can affect the meridional thermal gradients and the winds may intensify or decrease accordingly at upper levels.

Over Delhi, located in north-central India, there exists an interesting diurnal fluctuation during the summer monsoon months. Winds in the lowest 1 km are more from the east at 12Z (5:30 p.m. local time) than at 00Z (5:30 a.m. local time). Delhi is located on the eastern edge of the Rajputana desert. The diurnal change in winds at low levels is most likely in response to the diurnal heating of the desert and a flow towards it in the day time. The reverse evidently occurs as a response to the cooling of the desert at night.

**Table 18.1** Diurnal variation of rainfall (From Ananthakrishnan 1977)

Diurnal Variation of Rainfall			Percentage of seasonal rainfall								Seasonal rainfall (mm)
Station	Elevation (m)	Season	00-03	03-06	06-09	09-12	12-15	15-18	18-21	21-24	
1. Cherrapunji	1,313	I	18.2	17.5	12.4	7.8	5.1	6.4	11.8	20.9	2,360
		II	17.4	18.4	14.5	12.8	7.4	5.7	8.6	15.3	8,481
		III	18.2	15.3	11.7	9.7	12.1	9.8	9.2	14.1	413
2. Mahabaleshwar	1,382	I	7.7	6.4	2.5	1.2	12.1	40.0	18.0	12.1	104
		II	11.9	11.9	11.0	11.0	14.4	16.0	12.6	11.3	5,521
		III	8.6	8.7	7.5	7.4	15.4	23.5	17.5	11.1	2.5
3. Bombay	11	I	58.4	16.8	9.3	3.4	0.0	2.1	3.1	6.9	29
		II	13.6	14.7	15.3	13.4	11.3	9.3	9.8	12.5	2,116
		III	13.7	34.1	12.6	7.4	5.2	8.6	11.6	6.7	85
4. Madras	16	I	10.4	16.6	13.3	17.2	12.7	8.8	9.5	11.6	75
		II	19.0	12.8	3.3	2.4	3.9	14.2	22.1	22.5	421
		III	17.8	16.8	11.6	11.6	10.0	9.8	8.5	13.8	605
5. Sagar Island	3	I	11.0	6.6	10.6	8.6	5.4	11.3	24.4	22.1	127
		II	15.2	19.0	14.2	14.8	11.2	7.6	8.0	10.0	1,208
		III	13.0	15.5	13.6	16.9	15.1	11.4	5.2	9.3	221
6. New Delhi	216	I	11.3	6.1	7.8	4.3	7.8	37.4	11.3	13.9	12
		II	8.5	15.2	14.7	15.1	16.1	16.9	7.4	6.1	539
		III	23.8	8.9	12.3	15.4	14.2	6.7	7.9	10.8	42
7. Jamshedpur	129	I	2.3	0.4	3.8	0.6	8.2	51.1	24.5	9.0	78
		II	8.9	9.2	7.9	9.6	17.8	23.3	14.1	9.2	1,085
		III	12.4	14.1	9.4	7.6	16.0	18.4	11.6	10.4	89
8. Hyderabad	545	I	21.2	8.7	3.5	0.0	5.9	20.3	26.8	13.5	54
		II	14.5	10.6	5.0	4.9	9.7	18.4	18.1	18.7	605
		III	17.3	8.9	4.4	6.5	13.6	15.6	12.8	12.8	106

Calcutta, located in north-eastern India, experiences a strong diurnal fluctuation of winds during April, May and June in the lowest km. This diurnal component is not well understood.

The diurnal fluctuation is important for several reasons. A proper understanding of the diurnally varying component of the motion field could provide a better understanding of the diurnal variability of rainfall. Furthermore, there exists evidence that synoptic disturbances enhance and decay diurnally thus suggesting possible interactions of the synoptic and diurnal modes.

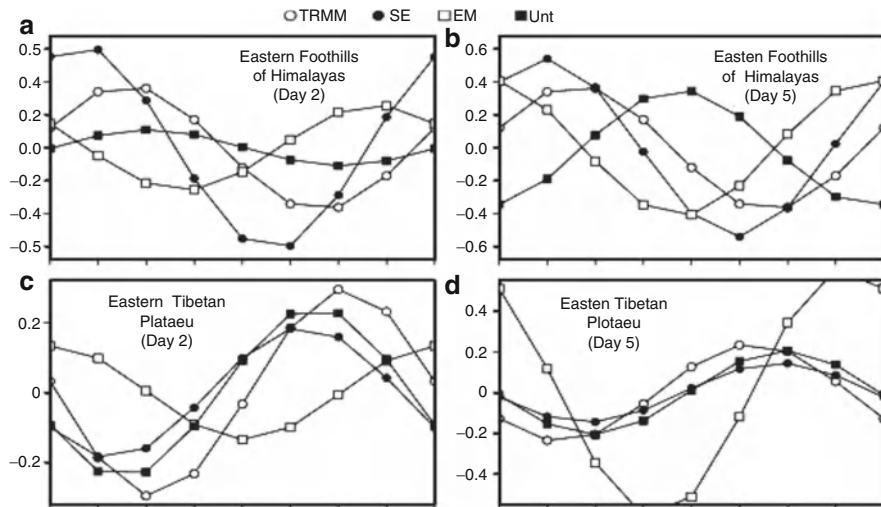
### 18.4.1 *Diurnal Variation in Rainfall Over India*

Table 18.1 from Ananthakrishnan (1977) lists three-hourly rainfalls for a number of weather stations over India. Cherrapunji is one of the stations that experiences record rainfall amounts. Here the maximum rainfall occurs during the early morning, between 3:00 and 6:00 a.m. local time. Some of the stations show a single rainfall maximum around the early morning or late afternoon, while others display a bimodal character. During the summer monsoon, stations over north central India exhibit two maxima. A detailed explanation of the diurnal modes is presently lacking.

A wind maximum around noon is seen in the surface wind speed field. Figure 18.9, from Ananthakrishnan (1977) shows the hourly surface winds for selected stations. The maximum wind for Port Blair, Madras and New Delhi is found during the northern summer months. A secondary maximum around 3:00 p.m. local time is also noted at New Delhi in the late winter months. The strong surface winds at noon over Port Blair and Madras are most probably related to the sea breeze. The strong diurnal winds at New Delhi are in response to the heating of the desert to the west and the diurnal strengthening of the heat low. Kodaikanal is located at 1,200 m above sea level and is several 100 km from the Arabian Sea and Bay of Bengal coast. Here the surface wind speeds are out of phase with the coastal winds. A suggested explanation for this phase difference is based on momentum mixing in the vertical. Mixing is stronger in the summer months and tends to increase the surface winds while it reduces the winds at a higher elevation (such as at the level of Kodaikanal). The vertical distribution shows an increase of mean wind speed with height (with diurnal effects removed) above the surface at these locations. The amplitude of the diurnal change is found to be consistent with the mixing concept applied to the daytime hours. This implies a momentum mixing over a layer some 1,500 m deep. This is most probably brought about by the upward and downward fluxes of mass in and around the shallow convective clouds that are predominant during the summer months.

### 18.4.2 *Diurnal Change Transitions Between the Himalayan Foothills and the Eastern Tibetan Plateau*

Cherrapunji is located in the eastern foothills of the Himalayas. This region encounters as much as 1,250 mm of rain in a summer monsoon season. Much of this rain occurs in the early morning hours. If we proceed some 400 km to the northwest we are over the eastern Tibetan Plateau. This region shows an early afternoon rainfall maximum, with total seasonal amounts on the order of 760 mm over the summer monsoon season. This large change of phase of the diurnal cycle of precipitation is an interesting scientific problem. Since this problem could involve the surface heating of the Tibetan Plateau and possibly long wave radiative destabilization of layer clouds at night time hours and stabilization arising from short wave warming (cloud albedo issue) in the afternoon hours over the eastern foothills, this becomes a complex modeling problem. The treatment of sensible heating over a strongly sloping terrain of the Himalayas could also be an issue. There is also a possible added issue, i.e., the ascending air during the day time heated region of the eastern Tibetan Plateau carries a compensating descending lobe over the eastern foothills of the Himalayas and suppresses the rains of the afternoon over the latter region, and the converse is also possible during the early morning hours. That question of push versus pull has not been answered. One does wonder if vertical circulations of a heated plateau, where the rainfall amounts are small, can push the diurnally intense rainfall region of the foothills of Himalayas from its descending lobe. A satisfactory modeling of this diurnal change remains to be done. When this is done we would have a better insight on the physical processes these phase changes of the diurnal precipitation. Most single weather and climate models carry consistently large systematic errors. Krishnamurti et al. (2007) have designed a ensembling of multimodel's, here each member model carries persistent phase errors. The proposed method removes such biases within its ensembling, called the multi model superensemble, to reduce such collective phase errors. This study is able to distinguish in its superensemble forecasts the correct phase of the diurnal rainfall maximum over the plateau and the foothills. It would however be desirable to find the correct physics within a single model that can provide these correct diurnal rainfall phases. Figure 18.10 illustrates the phases of four member models and those of an ensemble mean and of this superensemble over the eastern Tibetan Plateau and the foothills of the Himalayas. Here four curves based on model based forecasts of the diurnal change of precipitation are shown. These include the observed estimates from the TRMM satellite, ensemble mean of the four forecast models, the multimodel superensemble and from an advanced model called the Unified model. The panels presented here, show the forecasts for days 2 and 5 of forecasts. This shows the improvements that are currently possible towards the prediction of precipitation.



**Fig. 18.10** Diurnal cycle of precipitation from the TRMM rainfall estimates, from the superensemble, from the ensemble mean and from the unified model over selected domains. Left panels show diurnal cycle of day 2 forecasts and right panels are representing the same for day 5 forecasts over (a) and (b) Eastern foothills of Himalayas; (c) and (d) Eastern Tibetan Plateau

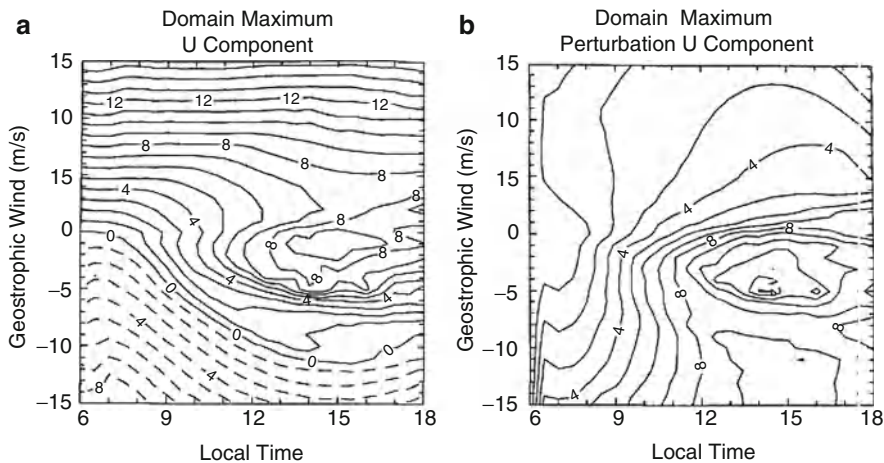
#### 18.4.3 The Arritt Nomogram

By conducting a large number of sea breeze prediction experiments under a variety of synoptic flow regimes, Arritt (1993) provides a useful nomogram (a diagram allowing the finding of a graphical solution to a numerical problem) for sea breeze forecasts. Arritt's collection of numerical experiments includes 31 different prevailing synoptic winds. They comprise of opposing (offshore) winds of  $15 \text{ ms}^{-1}$  all the way through supporting (onshore) winds of  $15 \text{ ms}^{-1}$ . The experiments are conducted with a two dimensional non-hydrostatic model in the vertical plane normal to a sea breeze, with the ocean to the south and the land to the north. Here the solar radiation and the fixed imposed sea surface temperature provide the differential heating for the driving of the sea breeze. The physics of this model include parameterizations of short and long wave radiative fluxes, and a detailed surface energy balance including a multilayer soil formulation. The increase of solar insolation after 6:00 a.m. local time leads to a warming of the soil layer and the initiation of convection. The sea breeze builds on a daily basis upon the effects of differential heating between the ocean and land over distances on the order of a few 100 km.

The planetary boundary layer model includes turbulent closure scheme following Mellor and Yamada (1982). The initial conditions use homogeneous constant values as a function of height for the temperature, specific humidity and the prevailing geostrophic wind. All forecasts are started at 6:00 a.m. local time and all outputs are stored at intervals of 30 min. Table 18.2 provides some of the constants used by Arritt in the modeling.

**Table 18.2** Parameter values in the numerical simulation following Arrit (1993)

<b>Surface properties</b>	
Roughness length	0.05 m (land):0.032 $u_e^2/g$ (sea)
Albedo	0.2
Solid density	1,500 kg m <sup>-3</sup>
Soil specific heat capacity	1,300 J kg <sup>-1</sup> K <sup>-1</sup>
Soil thermal diffusivity	$5 \times 10^{-7}$ m <sup>2</sup> s <sup>-1</sup>
Surface moisture availability	0.2 (potential evaporation)
Sea surface temperature	15°C
<b>Temporal discretization</b>	
Start time	0600 LST
Duration of simulation	12 h
Time step	4 s
<b>Spatial discretization</b>	
Horizontal grid increment	5 km
Number of horizontal grid points	82
Vertical levels	42 levels: 25, 50, 75, 100, 125, 150, 175, 200, 225, 250, 300, 350, 425, 500, 575, 650, 750, 1,000, 1,250, 1,500, 1,750, 2,000, 1,250, 2,500, 3,000, 3,750, (...constant $\Delta z = 750$ m), 15,750 m

**Fig. 18.11** Predicted maximum  $u$  component in the model domain as a function of the geostrophic wind and time. (a) Total  $u$  component, (b) perturbation from the model initial  $u$  component (From Arritt 1993)

The component of wind that is normal to the coastline is identified as the geostrophic wind of the large scale flow. That is shown along the ordinate of Fig. 18.11a. Negative/positive values along the ordinate denote the large scale offshore/onshore winds. If the prevailing synoptic situation is one of strong

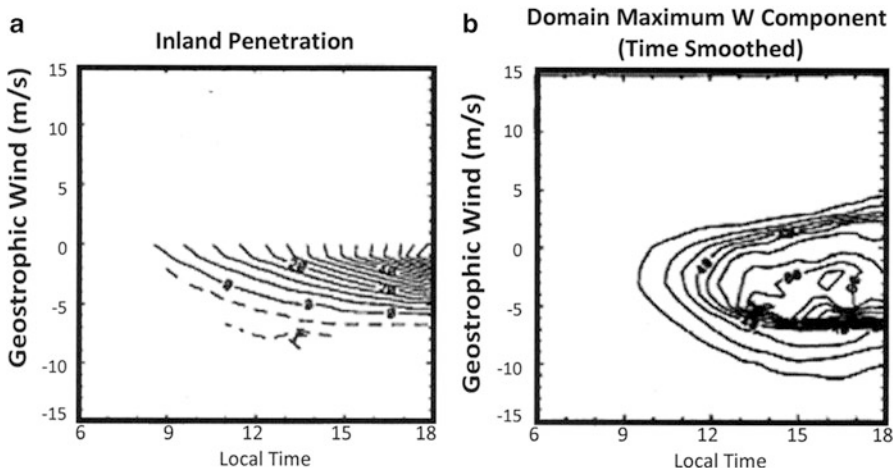


**Fig. 18.12** (a) The farthest inland location of the  $u$  component with a value of zero assigned to the coastline. (b) Domain maximum vertical velocity, smoothed in time using 1-2-1 filter (From Arritt 1993)

offshore winds, e.g.  $-10 \text{ ms}^{-1}$ , the sea breeze is completely suppressed. The illustration shows the domain-averaged large scale maximum onshore winds ( $>0$ ) as a function of the time of the day. When the prevailing synoptic situation is calm (zero along the ordinate), a strong sea breeze is established, approaching  $9 \text{ ms}^{-1}$  at around 3 p.m. local time. This state calls for a strong diurnal modulation of domain averaged strong winds being zero near 6:00 a.m. and a maximum around 3:00 p.m. This illustration can be used as a nomogram for indentifying conditions favoring strong or weak sea breeze winds as a function of the prevailing synoptic on- or offshore winds and the time of day.

A similar nomogram for the domain maximum of the perturbation onshore flow, also from Arritt (1993), is shown in Fig. 18.11b. These are the maxima of the point-by-point perturbations over the entire domain. This is again plotted as a function of the prevailing synoptic onshore geostrophic winds and the time of day. Here we note that the strongest perturbations develop at around 3 p.m. with offshore synoptic winds of about  $-4 \text{ ms}^{-1}$ . These perturbation winds are positive for all times of day and for all synoptic base winds.

The inland penetration is also illustrated using the same axes in Fig. 18.12a. The inland penetration is as large as 40–60 m by the late afternoon hours for calm prevailing wind conditions. The inland penetration starts to happen even with weak offshore winds on the order of a few  $\text{ms}^{-1}$ . The computations for onshore winds ( $u>0$ ) are not shown in this illustration because of computational uncertainties.

Figure 18.12b from Arritt's study provides information about the domain maximum vertical motion ( $\text{cm s}^{-1}$ ) as a function of the prevailing wind and local time of day. This shows that upward motions as large as  $100 \text{ cm s}^{-1}$  are realized by 3 p.m. local time even for offshore base winds on the order of  $5 \text{ ms}^{-1}$ .

The Arritt nomograms are useful tools for sea breeze forecasting. Such nomograms need to be prepared along all major coastlines, since one set of solutions would not meet the desired solutions for all sites. In principle such experiments can be run on personal computers and nomograms prepared for any site.

#### **18.4.4 Monsoonal Scale Diurnal Oscillation of the Monsoon**

While the small-scale aspect of the diurnal variations in associating with the sea breeze has been emphasized so far, we now look at the diurnal variations in association with the planetary scale phenomenon of the Asian monsoon. The land/ocean contrast of heating and cooling induces a diurnal land-sea breeze-type oscillation on the continental scale of south Asia. That can be seen from geostationary satellite-based 3 hourly infrared radiation fields.

A more interesting depiction of that comes from the analysis of three dimensional divergent circulations at around 6 hourly intervals. The choice of 6 h is dictated by the reanalysis interval of global data sets. Given the horizontal motion field, i.e., the  $u$  and  $v$  wind components at many pressure levels in the vertical, one can compute the horizontal divergence and set that equal to  $-\nabla^2\chi$ , where  $\chi$  is the velocity potential. One next solves a Poisson equation to obtain the  $\chi$  field at all desired pressure levels.  $-\nabla\chi$  corresponds to the divergent wind at any location at any pressure level.

One can composite this field at 6 hourly intervals to see the day-versus-night differences in the monsoonal divergent diurnal circulations. The composites of this diurnal component of the velocity potential at 6:00 a.m. and 6:00 p.m. local time, averaged over a 15 day period, over India, are shown in Fig. 18.13. The dark arrows follow the negative of the gradient of the velocity potential (i.e., the divergent wind) and show this grand diurnal continental scale divergent wind gyre at the 200 mb level.

At this level we can see the upper level outflows from the heated land mass and the converse circulation during the early morning hours. This illustrations clearly show the continental scale nature of this diurnal mode. This is a very large scale diurnal reversal of winds whose magnitude in the horizontal reaches amplitude of a few  $\text{ms}^{-1}$ . This feature was first noted by Krishnamurti and Kishtawal (2000). It is prominent during the Asian summer monsoon months of June, July, August and September. Since warm air is ascending over the land areas and relatively colder air is descending over the neighboring oceans (Arabian sea, Bay of Bengal and the Indian Ocean) during the afternoon hours, and the converse happens during the early morning hours. This is a thermally direct circulation, such that there is a net positive contribution over the troposphere for the covariance of vertical velocity and the temperature, i.e., where the mass integral extends over the domain of Fig. 18.13 and covers the entire troposphere between the surface level and the 150 mb level.

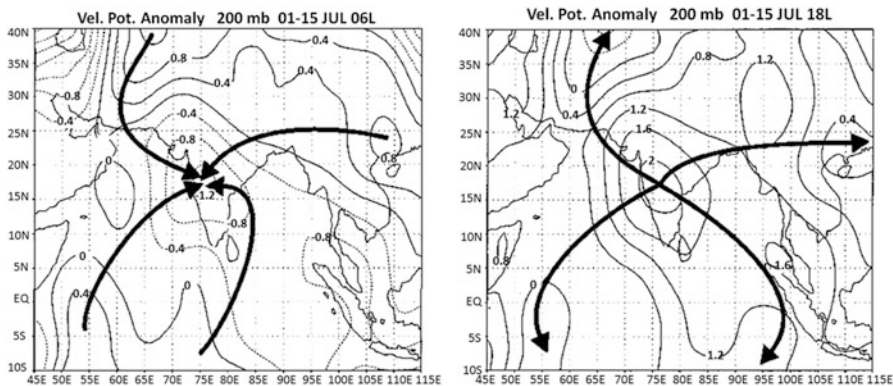


**Fig. 18.13** Composite diurnal averages (15–28 July 1998) of the 200 hPa velocity potential anomaly fields in units of  $10^6 \text{ m}^2 \text{s}^{-1}$  at 0600 and 1800LT (From Krishnamurti and Kishtawal 2000)

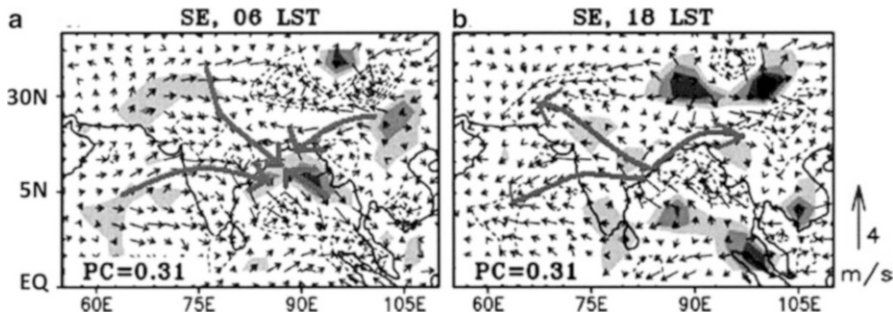


**Fig. 18.14** Superensemble forecast based divergent circulation (a) early morning (b) afternoon

One can then ask the question: given a total conversion of the available potential energy to kinetic energy from such vertical circulations on several time scales, what proportion of that conversion comes from this diurnal divergent circulation. Such computation would assess the importance of this monsoonal diurnal divergent circulation for the overall monsoons energetics. This question was addressed by Krishnamurthy et al. (2008) using a modeling approach wherein a suite of global models were deployed in the context of a multimodel superensemble, Krishnamurti et al. (2007). The prediction of the diurnal mode of the monsoon was examined for each member model of the ensemble suit. It was noted that each model made many errors in the description of this diurnal mode. Collectively, the superensemble was able to correct the phase (in space and time) errors of this mode and provide a geometry of this circulation that was very close to the one seen in Fig. 18.13.

The modeling results for the day and night reversal of the continental scale circulation, at the 200 mb level are shown in Fig. 18.14. These clearly show that with the removal of the model bias it is possible to predict this feature. The

percentage of the energy exchange from the available potential to the kinetic energy of the monsoon accounted for, by this (modeled) diurnal mode is significantly high. Thus it can be said that this continental diurnal divergent circulation between the land mass of the monsoon and the surrounding oceans is an important component of the Asian summer monsoon.

## References

- Ananthakrishnan, R.: Some aspects of the monsoon circulation and monsoon rainfall. *Pure Appl. Geophys.* **115**, 1209–49 (1977)
- Arrit, R.W.: Effects of the large-scale flow on characteristic features of the sea breeze. *J. Appl. Meteor.* **32**, 116–25 (1993)
- Van Bemmelen, W.: Land-und Seebrise in Batavia. *Beitr. Phys. Frei. Atmos.* **10**, 169–77 (1922)
- Chapman, S., Lindzen, R.S.: Atmospheric Tides. D. Reidel, Dordrecht (1970). 200pp
- Estoque, M.A.: A theoretical investigation of the sea-breeze. *Q. J. Roy. Meteor. Soc.* **87**, 136–46 (1961)
- Flohn, H.: Klimaprobleme am Roten Meet. *Erdkunde* **19**, 179–91 (1965)
- Gray, W.M., Jacobson Jr., R.W.: Diurnal variation of deep cumulus convection. *Mon. Weather Rev.* **105**, 1171–88 (1977)
- Hamilton, K.: The geographical distribution of the solar semidiurnal surface pressure oscillation. *J. Geophys. Res.* **85**, 1945–9 (1980)
- Haurwitz, B., Cowley, A.D.: The diurnal and semidiurnal barometric pressure oscillations: global distribution and annual variation. *Pure Appl. Geophys.* **102**, 193–222 (1973)
- Hsu, S.-A.: Coastal air-circulation system: observations and empirical model. *Mon. Weather Rev.* **98**, 487–509 (1970)
- Krishnamurti, T.N., Kishtawal, C.M.: A pronounced continental-scale diurnal mode of the Asian summer monsoon. *Mon. Weather Rev.* **128**, 462–73 (2000)
- Krishnamurti, T.N., Gnanaseelan, C., Chakraborty, A.: Prediction of the diurnal change using a multimodel superensemble. Part I: precipitation. *Mon. Weather Rev.* **135**, 3613–32 (2007)
- Krishnamurti, T.N., Gnanaseelan, C., Mishra, A.K., Chakraborty, A.: Improved forecasts of the diurnal cycle in the tropics using multiple global models part I: precipitation. *J. Climate* **21**, 4029–43 (2008)
- Lavoie, R.L.: Some aspects of the meteorology of the tropical Pacific viewed from an atoll. *Atoll. Res. Bull.* No. 96, Honolulu (1963)
- Lindzen, R.S.: Thermally driven diurnal tide in the atmosphere. *Q. J. Roy. Meteor. Soc.* **93**, 18–42 (1967)
- McGarry, M.M., Reed, R.J.: Diurnal variation in convective activity and precipitation during phases II and III of GATE. *Mon. Weather Rev.* **106**, 101–13 (1978)
- Mellor, G.L., Yamada, T.: Development of a turbulence closure model for geophysical fluid processes. *Rev. Geophys. Space Phys.* **20**, 851–75 (1982)
- Murakami, M.: Large-scale aspects of deep convective activity over the GATE area. *Mon. Weather Rev.* **107**, 994–1013 (1979)
- Pielke, R.A.: A three-dimensional numerical model of the sea breeze over South Florida. *Mon. Weather Rev.* **102**, 115–39 (1974)

# Chapter 19

## Tropical Squall Lines and Mesoscale Convective Systems

### 19.1 Introduction

Passage of tropical squall lines is a common phenomenon in the rain areas of the tropics. These systems form over the land areas and even continue over the ocean for several days. The meso/beta scale (20–200 km) is a common scale of organization of convection within what are called the Meso Convective Systems (MCS). These normally carry long anvil clouds that can extend for several 100 km. MCS carry both stratiform and convective rains.

Zipser (1977) and LeMone (1983) showed major differences in the vertical transports of momentum, heat and moisture in the convective and stratiform components. The convective component in a squall line contributes to large fluxes from the planetary boundary layer into the clouds above that layer. The organization of convection into a linear geometry is typical of the squall lines. The vertical momentum transport by clouds and the ascent/descent with respect to the moving convective systems appears to be an integral part of the linear organization of clouds within a squall line. If a tropical squall line is moving from west to east it generally carries an ascending lobe from front to rear and a descending lobe from rear to front. This is in the squall line relative frame of reference. These carry broad regions of trailing stratiform rain and a leading convective line. We will illustrate several cross sections of these features in this chapter. We will also make a distinction between squall clusters and non squall clusters, those distinctions arise from factors such as propagation speed, downdraft intensity, CAPE and the prevailing wind shear.

The issue of why do a number of cumulonimbus clouds align themselves along a straight line is not a simple one. The moving squall line holds such an integrity as determined by the thermodynamical constraints imposed by the recognition that the area of rising motion of a cloud is generally much smaller than that of the sinking motions. A circular or a linear organization can be accommodated easily by such a constraint. Close packed line of convection can permit a broad area of descent on one side of such a linear convection. That broad area of descent would inhibit

cloud growth and deep convection, limiting the convection to continue along the propagating squall line. The coupling among wind shear, deep convection, descending lobe and the vertical momentum flux is among finite amplitude entities, thus one cannot simply argue that the answer to the squall line orientation can be linearly explained as A causing B and B causing C etc. This is essentially a non linear problem where the above entities coexist with the manifestation of the linear alignment of deep convection.

## 19.2 West African Disturbance Lines

Squall lines are known to propagate westwards from the Sudan area towards the west coast of West Africa during the northern summer months (Hamilton and Archbold 1945; Eldridge 1957; Obasi 1974). Roughly seven disturbances are known to propagate westward during each summer month. From time-sections of surface and upper air data, Obasi (1974) has constructed some interesting west-to-east cross-sections relevant to their passage across Lagos (Nigeria). Figure 19.1 from Obasi (1974) illustrates the variations, from west to east, of surface temperature, surface relative humidity, surface pressure, and the 900 mb relative humidity. Prior to a squall line passage, the surface temperatures and the 900 mb relative humidity show larger than normal values, reflecting larger values of moist static stability near the ground and conditional instability. A pressure rise somewhat analogous to a pressure jump is found just after the temperature drops. The latter is used here as a reference to define the local passage of the disturbance line.

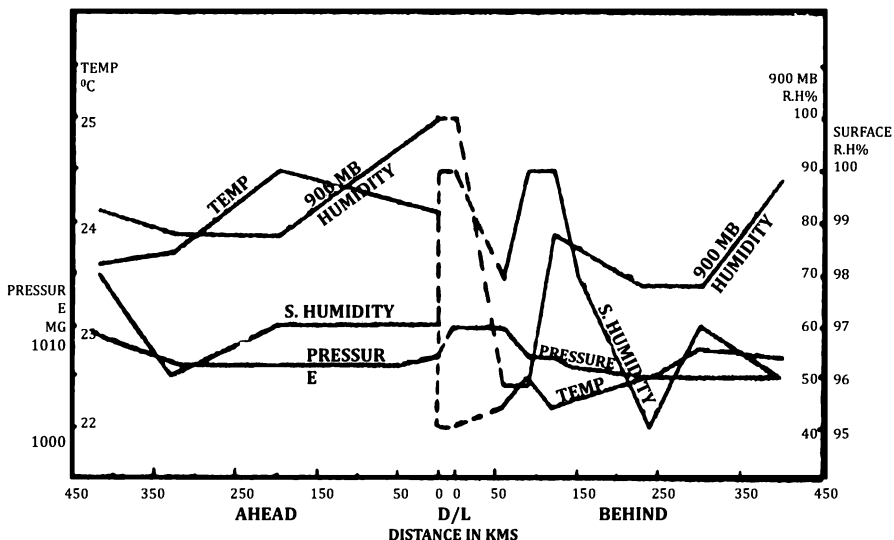


**Fig. 19.1** West to east cross-section across a model disturbance line showing the surface temperature, relative humidity and pressure. Also shown is the 900 mb relative humidity (After Obasi 1974)

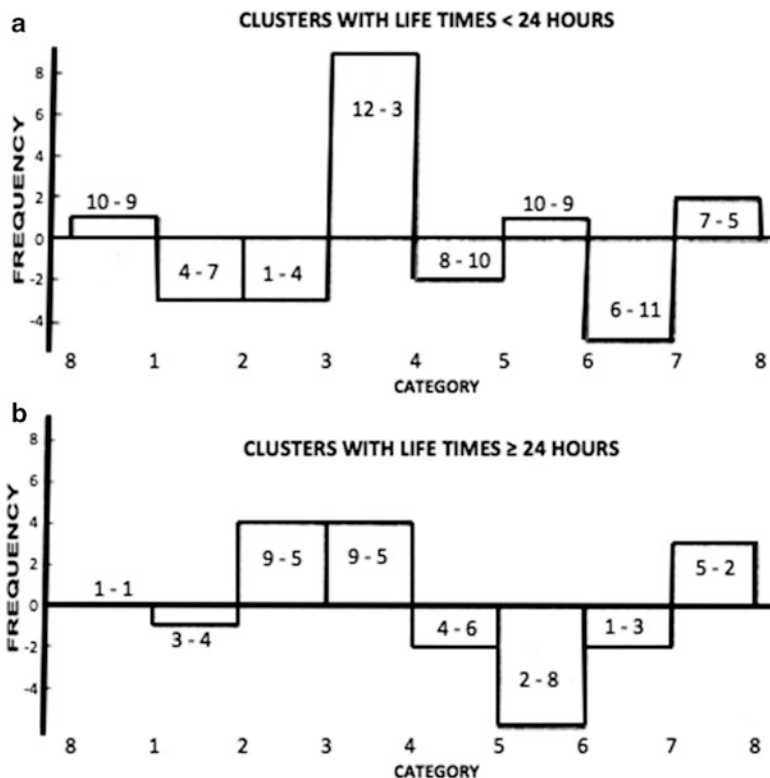


**Fig. 19.2** Frequency distribution of the excess (positive ordinate values) or deficit (negative ordinate values) of cluster genesis over cluster decay by African wave phase category for clusters (a) with lifetimes < 24 h, and (b) with lifetimes  $\geq$  24 h (After Payne and McGarry 1977)

### 19.2.1 Squall Lines “An Integral Part of the African Wave”

A study by Reed et al. (1977), and by their associates, Payne and McGarry (1977), provides a picture of the West African squall line. The idea is roughly as follows. Often West African squall lines move faster than the African waves. The speed of the West African squall line can be as large as  $10^\circ$  of longitude per day whereas the westward speed of the African wave is between  $5$  and  $7^\circ$  of longitude per day. It has also been noted that these squall lines acquire their largest amplitude after they pass the trough line of the African wave. Reed et al. (1977) divided an African wave into sectors numbered from 1 to 8 from east to west. A line between sectors 4 and 5 defines the trough line. The numbered sectors are used as a coordinate system for the purpose of obtaining a composite structure of the African waves. Many such waves are composited and properties such as winds, temperature, humidity and weather are obtained for each composite sector. Such a compositing was necessary at the time because the sparseness of observations made it difficult to define one wave completely. Figure 19.2 taken from their study shows that the frequency of

occurrence of cloud clusters as well as squall lines is largest in sectors 2–4 which are located roughly 300 km to the west of the trough line. These results are obtained by compositing a large number of episodes with reference to a trough line identified by category 4.

This study does raise the question as to whether squall lines ever go past African waves without any significant interactions, and the answer is that some of them probably do. An important question that needs to be addressed here is “why is the region ahead of the trough line preferred for the development of squall lines?” The answer to that must lie in the configuration of moist static stability and the vertical distribution of the horizontal wind. The moist southwesterly monsoonal low-level flows are capped by dry east-northeasterlies ahead of the trough line. The mid-tropospheric easterly jet at 600 mb and the moist southwesterly monsoonal current provide conditions quite similar to those encountered in the continental United States (see Petterssen 1956). Thus there may be some measure of similarity between the tropical and extratropical squall systems.

### ***19.2.2 Squall Lines Are Located Between Two Easterly Jet Streams***

In a pioneering study, Leroux (1976) noted that nearly all the West African squall lines are located between two easterly jet streams. The tropical easterly jet (TEJ), located near 7°N at about 175 mb level, and the African Easterly Jet (AEJ), located near 13°N at about 600 mb, enclose nearly all of the West African squall line activity. The anticyclonic shear side of the TEJ and the cyclonic shear side of the AEJ characterize this region. This is a favorable environment for the maintenance of squall systems in the tropics. This is somewhat different from the environment of the extratropical squall lines that are seen closer to an upper trough line. Similar squall lines as the West African squall line are also seen over northeastern India and Bangladesh during the northern winter months. There the western disturbances carry wind shifts and humidity contrast lines that favor the formation of squall lines. In these systems lower tropospheric cyclonic winds (which are a part of the western disturbances) are capped by a region of strong anticyclonic shear as well as by curvature to the south of the subtropical jet stream of winter.

### ***19.2.3 Other Squall Line Models***

A well-known field experiment called Global Atmosphere Research Program (GARP) Atlantic Tropical Experiment (GATE) was conducted in 1974. From an analysis of GATE data, Mower (1977) suggested a schematic structure of a squall line over the eastern Atlantic Ocean (Fig. 19.3). This may be thought of as the

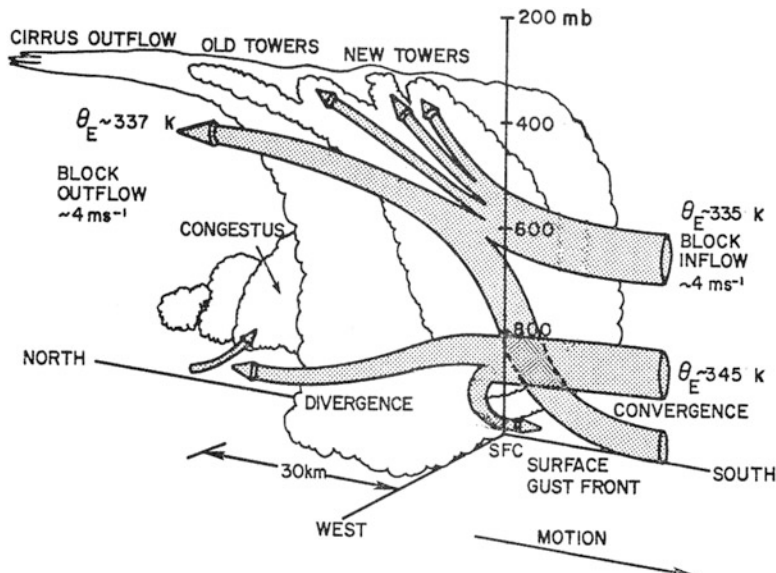


**Fig. 19.3** Schematic of stream tubes and characteristics of this line of convection (From Mower 1977)

structure of a West African squall line after it crosses over to the oceanic region. Mower (1977) notes the following features:

- Sharp convergence of high  $\theta_e$  air at the leading edge of the lines ( $10^{-3} \text{ s}^{-1}$ )
- Strong divergence of slightly smaller magnitude to the rear;
- Large drop in  $\theta_e$  indicating the presence of a downdraft at the surface with its origins in the 900–800 mb layer;
- Small ( $1.5^\circ\text{K}$ ) cooling at the surface after the line passage;
- Small but sharp pressure drop with a large decrease of incoming solar radiation, together with a lowering of the cloud base.

The wind profile showed:

- Surface westerlies ahead of the line;
- Very little vertical shear in both wind components;
- No observable steering level;
- Lines are embedded in a larger-scale motion field which is convergent and cyclonic from the surface to 700 mb.

The thermodynamic profile showed:

- Drying in the lowest 50 mb resulting from the downdraft;
- Drying at the surface and moistening above;
- Cooling at the surface of  $1.5^\circ\text{K}$  with warming aloft, and;
- A large  $\theta_e$  drop in the mixed layer.

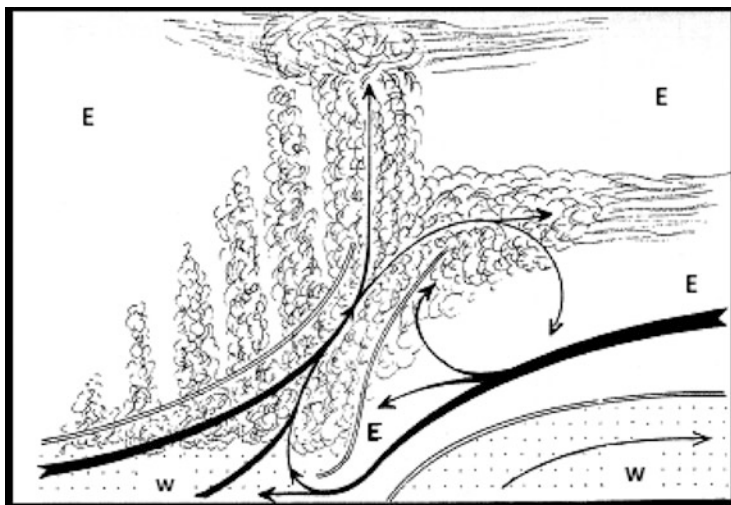


**Fig. 19.4** Schematic vertical cross-sections across an African squall line (From Leroux 1976)

The schematic diagram is drawn relative to the moving squall line. The driving mechanism for the squall line is thought to be an abundant supply of warm moist air in the sub-cloud layer with high enough value of  $\theta_c$ . The convergence and ascending motion are maintained by the downdraft reaching the ground. This seems to originate from a rather low level, i.e. 900–800 mb. This picture by Mower does not require a large-scale shearing environment (i.e. vertical shear of the horizontal wind) for the maintenance of the squall system. In this regard it is different from that of squall lines in the middle latitudes. Mower's picture of the squall system is somewhat similar to that presented by Moncrieff and Miller (1976), a three-dimensional numerical model which describes the passage of the squall line. In this study, the downdraft air is shown to originate from a rather low level just above the sub-cloud layer. The downdraft air is warmed adiabatically during the descent and is cooled by evaporation of the liquid water and rain. The final configuration of the surface air was noted to depend on the intensities of these opposing effects.

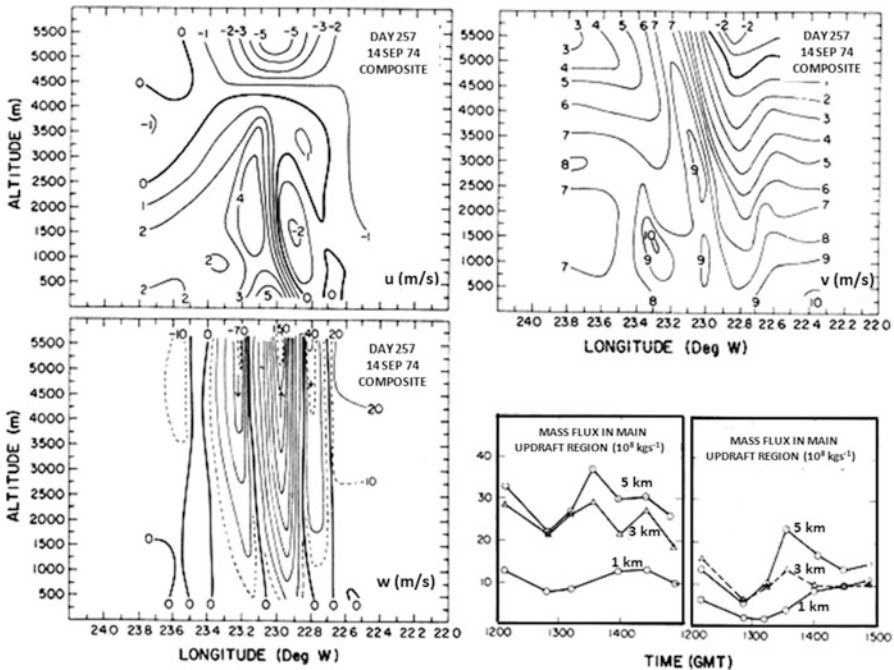
In another study, Leroux (1976) presents a different view of the squall system where the effect of the shearing environment is emphasized. Figure 19.4 from that study shows a schematic outline of the West African squall line. The emphasis here is on the downward flux of easterly momentum from the middle tropospheric easterlies over West Africa. The hypothesis of Leroux needs to be tested more closely with observations. According to this hypothesis the convergence at the surface occurs at the leading edge of the strong surface easterly surges. The southwesterly monsoon current is split into two parts by this easterly current. The precise reasons for the downward flux of easterly momentum are not explained by this study. The proposal of Leroux (1976) is not too different from that of Obasi (1974). Obasi noted strong easterlies with speeds of about 30–35 knots in the lower

troposphere (700–900 mb) and at roughly 100 km to the rear of the squall line. In the region ahead of the line he found weak westerlies. This asymmetry of the zonal flow provides a sustained field of low-level convergence ( $\frac{\partial u}{\partial x} < 0$ ) across the disturbance line. Squall line passages over the Atlantic Ocean are known to exhibit similar strong zonal flow asymmetries. The dynamics of the initiation of a strong surge in the easterlies is an unsolved problem in tropical meteorology. It is observed to occur over many parts of the global tropical belt (Krishnamurti et al. 1979a). Over West Africa this sudden surge of easterlies may be due to downward motion and a downward flux of easterly momentum from higher levels. This descent may be the mass compensation for the active ascent over an ITCZ disturbance in the near-equatorial rain belt. Once such a surge of easterlies is established, local convergence lines and the squall system could perhaps maintain themselves via mechanisms such as those proposed by Moncrieff and Miller (1976).

### **19.2.4 *Squall and Non-squall Systems***

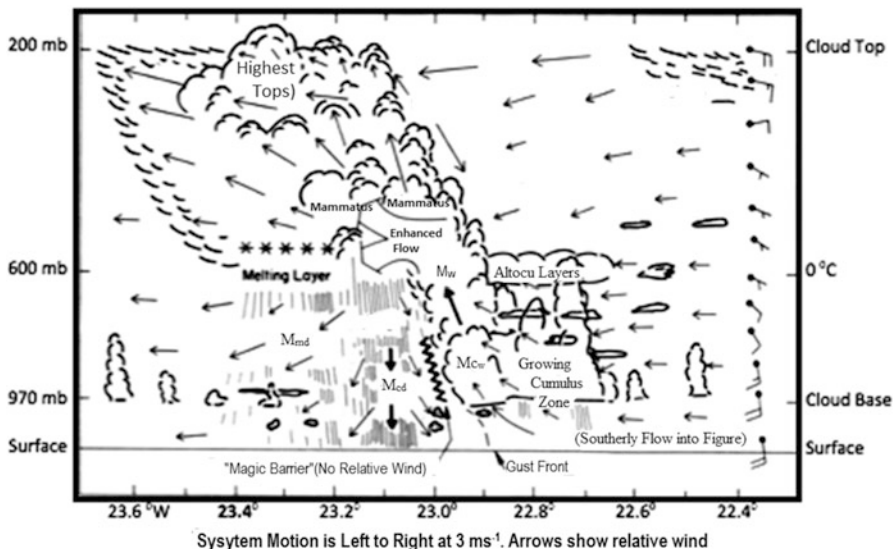
Zipser (1979) makes a sharp distinction between squall and non-squall systems over West Africa. The squall systems are faster moving (from east to west) systems that traverse faster than an African Wave and carry significant weather over a 30 km wide region (across the squall line). They are characterized by a substantial drop in temperature and equivalent potential temperature in the downdraft region. Although such downdraft regions are also present in the non-squall systems, the associated contrasts in temperature and equivalent potential temperature are absent. The non-squall systems are slower moving and can often traverse from west to east as well as from east to west. The GATE field experiment provided some of the best data sets for studying non-squall systems over the eastern tropical Atlantic Ocean. Much of this observational capability came from the deployment of aircraft reconnaissance. Multiple aircraft traverses and data gathering at several vertical levels across a non-squall system provided a lot of information.

Figure 19.5 shows an analysis based on aircraft dropwind side and flight level data sets. These include measurements of winds, temperature and humidity. In this illustration Zipser shows the fields of the three wind components and a time series plot of the mass flux, i.e. the up- and downdrafts at three different (1, 3, and 5 km) levels during the passing of a non-squall system. These mass fluxes are computed from the vertical velocity  $w$  which was obtained by the use of the kinematic method requiring a vertical integration of the horizontal divergence. The horizontal divergence was in turn obtained from a direct use of the measured and analyzed  $u$  and  $v$  components of the wind. Figure 19.5 illustrates rapid changes in the wind field as the non-squall system moves through the area. Wind changes on the order of  $6 \text{ ms}^{-1}$  are noted from the surface to the 3 km level. Unlike the typical squall systems that carry large relative winds across the squall line, these non-squall systems carry a



**Fig. 19.5** Analysis of (a) zonal, (b) meridional and (c) vertical wind from aircraft dropwindsonde and flight level data sets. From the same dataset, the time series of mass flux in (d) updraft and (e) downdraft region of the convective system are shown (After Zipser 1979)

stagnant region relative to the principal axis. The heavy precipitation moves with the non-squall system exhibiting almost no relative motion. In Fig. 19.5 vertically elongated adjacent regions of positive and negative zonal winds identify regions of principal lower tropospheric convergence, where the strongest ascent is located. In the kinematic depiction of vertical motion, magnitudes of  $w$  as large as  $1.5 \text{ ms}^{-1}$  can be seen. On adjoining vertically oriented flanks, strong descents on the order of  $0.4\text{--}0.7 \text{ ms}^{-1}$  are found. Using similar information from additional aircraft-based flight level data sets, Zipser (1979) arrived at a schematic structure of the non-squall system which is illustrated in Fig. 19.6. This illustration is self explanatory. There are no relative winds to the immediate west of the surface front, which makes this system quite unlike that of midlatitude squall systems. The life cycle of non-squall systems is of much interest. Observations were inadequate to portray these short life cycle systems (approx. 12 h). Further observational and modelling studies are needed to portray the formative, intensifying, mature, and dissipating systems. Noting that the scale of these systems is on the order of 200 km, a dense observational capability within that size is a great challenge. The next major field experiment that followed GATE over West Africa was the African Monsoon Multidisciplinary Analysis (AMMA) in the year 2006.



**Fig. 19.6** A schematic of a west-African non-squall system (After Zipser 1979)

### 19.3 Mesoscale Convective Systems

The TRMM satellite's precipitation radar has made it possible to obtain measures of convective and stratiform rains and to tag the rains from mesoconvective, convective and large scale systems. The rainfall over the tropical belt has been carefully examined by seasons and years since 1997, with the availability of TRMM data sets (Zipser et al. 2006). It has become apparent that a substantial proportion of the annual rains are from mesoconvective system passages over the tropics. An example of the fractional contribution to the total annual rainfall from mesoconvective systems is illustrated in Fig. 19.7.

Light to dark red regions here denote places where the fractional rain from mesoconvective systems exceeds 48 %. This illustration shows that mesoconvective systems abound over Central and West Africa, South America (where the largest fractions are found), the Coastal region north of the Gulf of Mexico, Gulf of Carpenteria and Northern Australia, southern Malaysian regions and the Bay of Bengal. The oceanic regions of the ITCZ show nearly 40 % of the rains resulting from the passage of mesoconvective systems. Similar annual features are also seen over the region of the ITCZ of the Southern Indian Ocean and the Western Pacific Ocean.

The important message of this illustration is that we need to study the mesoconvective rain producing systems of the tropics since nearly half of the tropical rainfall comes from these systems. The forecasting of these mesoconvective systems calls for high resolution models that can properly resolve such scales. Those mesoconvective scales are of the order of a few 100 km.

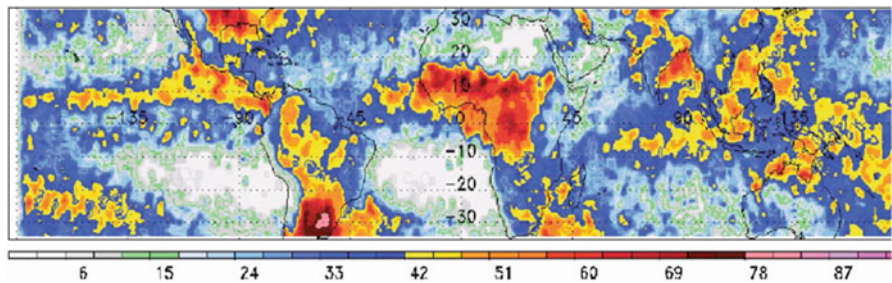


**Fig. 19.7** The fraction contribution to the total annual rainfall from mesoscale convective systems (After Zipser et al. 2006)

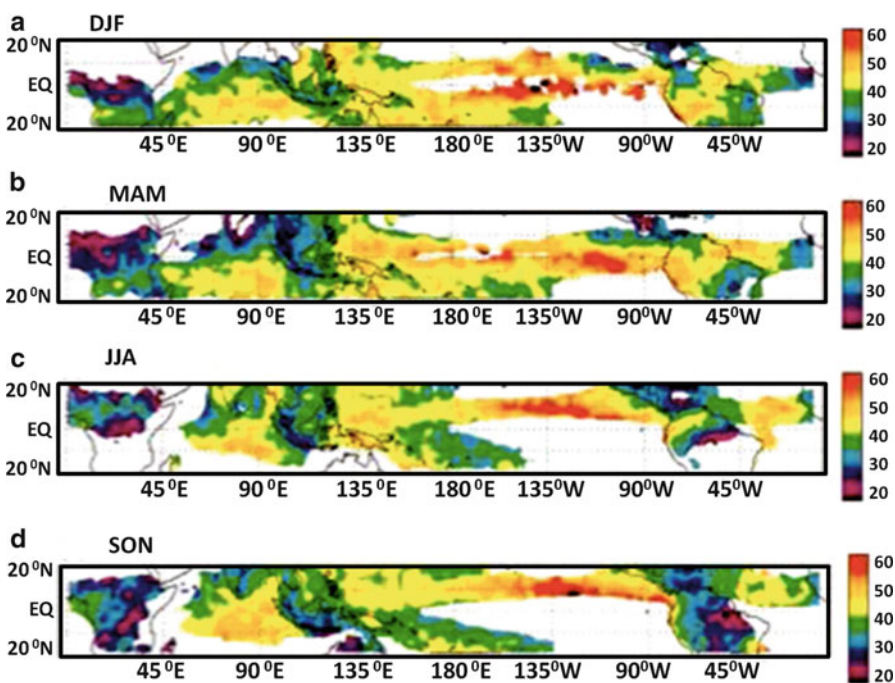


**Fig. 19.8** The seasonal precipitation radar stratiform rain fraction based on 2.5° grid averages for 1998–2000. Areas with annually averaged rain of less than  $0.6 \text{ m year}^{-1}$  were not included (After Schumacher 2003)

Zipser et al. (2006) has also partitioned stratiform versus convective rains of the tropical belt using several years of TRMM data sets. Using 4 years of data sets he portrays the seasonal fractions of the stratiform rains in Fig. 19.8.

Note that these are percentages, hence 100 minus these percentages provides the convective rain fractions, since most tropical precipitation can be traced to either convective or stratiform systems (Houze 1993).

Equatorial and West Africa stand out with low stratiform rain fractions during all seasons. The ITCZ over the Pacific Ocean carries slightly more than 50 % of rains of the stratiform type over all seasons. The Asian summer monsoon carries between 30 % and 50 % of the seasonal rains as stratiform during both the summer and the winter monsoon. During their austral winter and spring months, around 30–40% of the South Pacific Convergence Zone precipitation is attributable to stratiform sources. The stratiform rain fraction over this region is about 10 percentage points larger during the remaining parts of the year. A minimum of stratiform rain fraction is noted in the months of September, October and November over South and Central America. These regions see a maximum of nearly 40–50% of stratiform rain fraction during the months of March, April and May. Overall the message of this illustration is that nearly 40 % of the tropical rains are from a stratiform source. Hence in the modeling of tropical rains the large scale character of the tropical rains cannot be neglected in spite of the fact that mesoconvective rain systems abound.

Convective systems are usually characterized by strong vertical velocities, high rainfall rates and small area coverage cells. Stratiform systems, on the other hand, are distinguished by widespread rising motion and relatively smaller rain rates. This difference in the two forms of the rainfall has a bearing on the impact on ocean mixed layer characteristics and SST (Webster and Lukas 1992). More importantly, the latent heat release from the large amount of condensation of water vapor in convective systems heats the atmosphere, while evaporation of rain drops in the stratiform systems cools the atmosphere, resulting in a very contrasting heating profile for the two types of precipitating systems (Tao et al. 1993; Simpson et al. 1988). From the perspective of remote sensing of rainfall it is vital to distinguish between the two rainfall systems to account for inhomogeneity of rainfall within satellite fields of view. Due to the non-linear relationship between brightness temperature and rainfall, retrieval algorithms that do not consider inhomogeneity would cause an underestimation of the highly variable convective rainfall and an overestimation of the relatively homogenous stratiform precipitation (Short and North 1990).

## 19.4 Organization of Convection

This is a central feature of many tropical disturbances. A linearly elongated and nearly zonal organization of convection is typical of the ITCZ, where convection is important for driving the convergence from the two hemispheres. Nearly circular geometry characterizes the organized convection of hurricanes. Monsoon depressions are characterized by organization of convection following the vertically integrated flows of the lower troposphere around their more elliptical geometry. Figure 19.9 schematically illustrates these features.

There are certain preferred geometries of lower tropospheric vertically integrated flow fields in tropical disturbances. If the convection is organized along those geometries, then the heat released by convection can play an important role in the

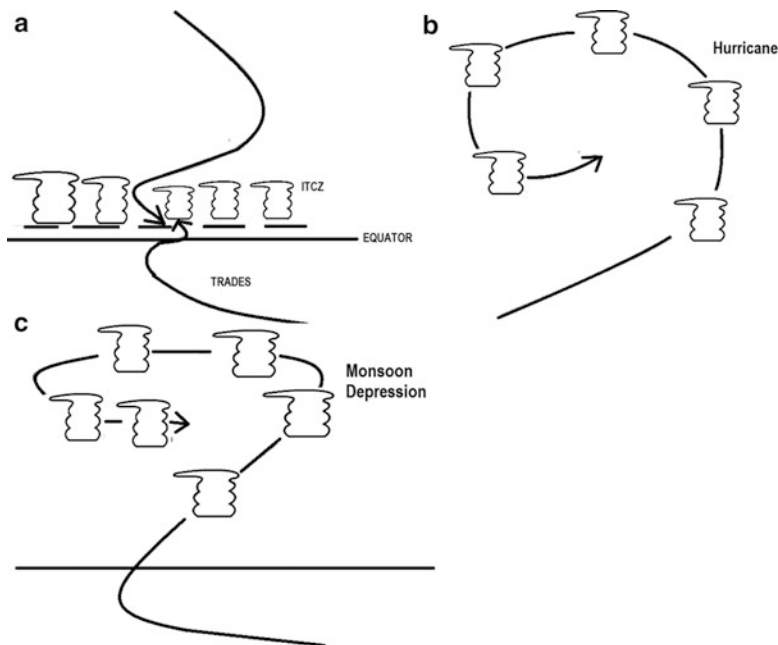


**Fig. 19.9** Schematic illustration of organization of convection in (a) ITCZ (linear organization of convection), (b) Hurricane (circular organization of deep convection), and (c) Monsoon depression (organization along lower tropospheric winds)

maintenance of those geometries. This type of organization of convection can maintain linear, circular or curvilinear geometries of the flow fields that are typically seen in tropical disturbances and tropical weather maps as illustrated in Fig. 19.9.

The evolution of the organization of convection as a typhoon (the Pacific typhoon Omar of 1992) forms in a model forecast is illustrated in Fig. 19.10. Initially there are a few disorganized mesoconvective elements (one can follow the major elements as the forecast proceeds) embedded in an easterly wave. As the development of this wave progresses, we note a gradual increase of the organization of convection around a circular geometry. This azimuthal organization of convection can be seen often in radar or high resolution satellite imagery. In the context of energetics the following is important. The typical scale of a hurricane is mostly described by azimuthal wave numbers 0, 1 and 2. On these scales the organization of convection brings about a heating field (related to the convective heating) distributed at azimuthal wave numbers 0, 1 and 2. That heating in turn plays a role in producing warm thermal anomalies on the same scales. This leads to a strong contribution to the generation of available potential energy on the same scales. The generation of available potential energy is simply the domain averaged covariance of heating and temperature. The heating results in ascending air over the regions of heating and a compensating descent occurs in neighboring relatively cooler areas. This vertical

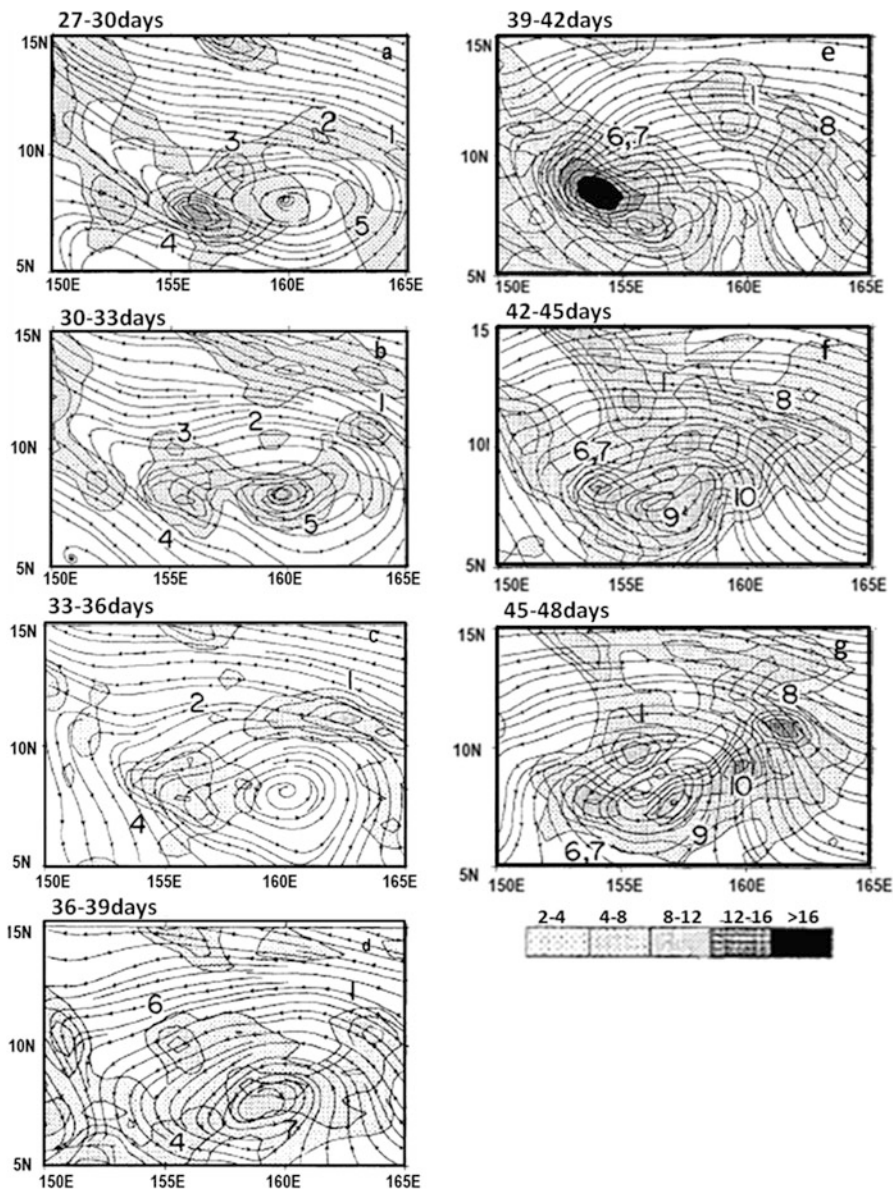


**Fig. 19.10** 850 mb flow field at three hourly intervals with superimposed three hourly rainfall for hour 30 to hour 48 of Typhoon Omar forecast starting 12 UTC of August 20, 1992 using T213 global spectral model. (Rainfall units: mm/3 h) (From Krishnamurti et al. 1998)

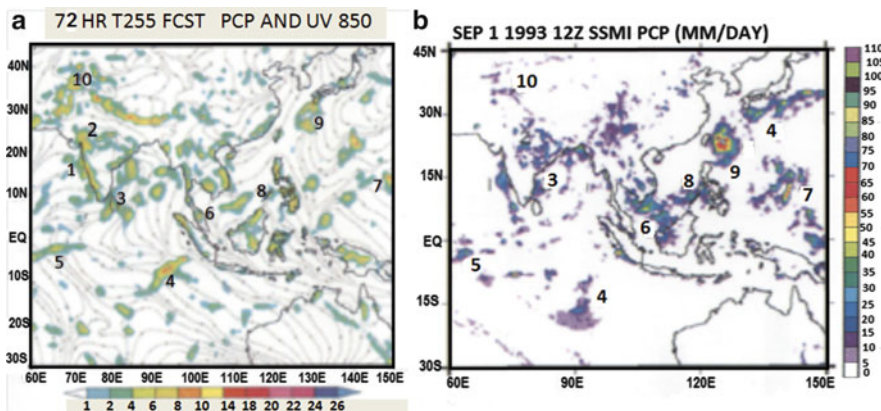


**Fig. 19.11** (a) 850 mb flow field with superimposed two-hourly accumulated rainfall from T255 forecast at 72 h (Rainfall units: mm/2 h), (b) Observed 24 h rainfall valid 12UTC of September 1, 1993 (Rainfall units: mm/day)

circulation plays an important role in transforming the available potential energy into kinetic energy, which leads to the strengthening of the storm in the circular geometry. The energetic argument provides a perspective for the link between the organization of convection and the eventual formation of a tropical storm.

The formation of a monsoon depression also sees the evolution of organized convection around its geometry. One can follow mesoconvective precipitating elements in forecasts and tag the gradual organization of individual elements as a forecast proceeds. Those can also be tagged from high resolution satellite imagery especially using rapid scan imagery at time intervals of roughly every 15 min and at a resolution of a few kms. Those are ideal for animations where one can see the evolution of the organization of deep convection around a developing wave.

Figure 19.11 shows an example of a forecast for the Indian monsoon where the evolution of mesoconvective rain elements is followed throughout a 72 h forecast. That initial state had been obtained after performing physical initialization. Physical initialization of rain rates that increases the nowcast skill at initial time and forecast skill of rain rates. Also shown in Fig. 19.11 is the observed, satellite based, IR imagery that identifies the mesoconvective rain elements. As the monsoon strengthens one can see the organization of convection around the monsoonal flows. In this forecast the major mesoscale precipitating elements were tagged at time zero of forecast and were then followed with time throughout the forecast. Although a few elements died, new ones often formed within those mesoscale rain areas during the forecasts and we were able to follow a number of those and verify mesoscale rainfall activity through 72 h of forecasts. This is possible with high resolution models that include a rain rate initialization.

## References

- Eldridge, R.H.: A synoptic study of West African disturbance lines. *Q. J. Roy. Meteor. Soc.* **83**, 357–367 (1957)
- Hamilton, R.A., Archbold, J.W.: Meteorology of Nigeria and adjacent territories. *Q. J. Roy. Meteor. Soc.* **71**, 231–250 (1945)
- Houze Jr., R.A.: Cloud dynamics, 573 pp. Academic, San Diego (1993)
- Krishnamurti, T.N., Bedi, H.S., Han, W.: Organization of convection and monsoon forecasts. *Meteorol. Atmos. Phys.* **67**, 117–134 (1998)
- Krishnamurti, T.N., Pan, H.L., Chang, C.B., Ploshay, J., Walker, D., Oodally, A.W.: Numerical weather prediction for GATE. *J. Roy. Mete. Soc.* (1979a) (To appear in the October issue of the Quart)
- LeMone, M.A.: Momentum transport by a line of cumulonimbus. *J. Atmos. Sci.* **40**, 1815–1834 (1983)
- Leroux, M.: Processus de formation et d'évolution des lignes de grains d'Afrique tropicale septentrionale. Université de Dakar, Dakar (1976). 159pp
- Moncrieff, M.W., Miller, M.J.: The dynamics and simulation of tropical cumulonimbus and squall lines. *Q. J. Roy. Meteor. Soc.* **102**, 373–394 (1976)
- Mower, R.N. (ed.): Case Study of Convection Lines During GATE. Atmospheric Science Paper, vol. 271. Colorado State University, Fort Collins (1977). 93pp
- Obasi, G.O.P.: The environmental structure of the atmosphere near West African disturbance lines. In: Proceedings of an International Conference on Tropical Meteorology, vol. II, pp. 62–66. American Meteorological Society, (1974)
- Payne, S.W., McGarry, M.M.: The relationships of satellite infrared convective activity to easterly waves over West Africa and the adjacent ocean during phase III of GATE. *Mon. Weather Rev.* **105**, 413–420 (1977)
- Petterssen, S.: Weather Analysis and Forecasting, I, Chapter 9. McGraw-Hill Book, New York (1956)
- Reed, R.J., Norquist, D.C., Recker, E.E.: The structure and properties of African wave disturbances as observed during phase III of GATE. *Mon. Weather Rev.* **105**, 317–333 (1977)
- Schumacher, C.: Tropical precipitation in relation to the large-scale circulation. A dissertation submitted in partial fulfillment of the requirements for the degree of Doctor of Philosophy, University of Washington (2003)
- Short, D.R., North, G.R.: The beam filling error in the Nimbus 5 electronically scanning microwave radiometer observations of global Atlantic tropical experiment rainfall. *J. Geophys. Res.* **95**, 2187–2193 (1990)
- Simpson, J., Adler, R.F., North, G.R.: A proposed tropical rainfall measuring mission (TRMM) satellite. *Bull. Am. Soc.* **69**, 278–295 (1988)
- Tao, W.K., Simpson, J., Sui, C.H., Lang, S., Scala, J., Ferrier, B., Chou, M.-D., Pickering, K.: Heating, moisture, and water budgets of tropical and mid-latitude squall lines: comparisons and sensitivity to longwave radiation. *J. Atmos. Sci.* **50**, 673–690 (1993)
- Webster, P.J., Lukas, R.: TOGA COARE: The coupled ocean–atmosphere response experiment. *Bull. Am. Soc.* **73**, 1377–1416 (1992)
- Zipser, E.J.: Mesoscale and convective-scale downdrafts as distinct components of squall-line structure. *Mon. Wea. Rev.* **105**, 1568–1589 (1977)
- Zipser, E.J.: Kinematic and thermodynamic structure of mesoscale systems in GATE. In: Proceedings of the Seminar on the Impact of GATE on Large-Scale Numerical Modeling of the Atmosphere and Ocean, pp. 91–99. Woods Hole, August 20–29 (1979).
- Zipser, E.J., Cecil, D.J., Liu, C., Nesbitt, S.W., Yorty, D.P.: Where are the most intense thunderstorms on earth? *Bull. Am. Soc.* **87**, 1057–1071 (2006)

# Index

## A

Adrian Gill's atmospheric model  
antisymmetric forcing, 55–59  
non-dimensional pressure, 49–50  
parabolic cylinder functions, 51–53  
shallow water equations, 48  
symmetric forcing, 53–56  
African Easterly Jet (AEJ), 402  
African easterly waves (AEFs), 123  
African Monsoon Multidisciplinary Analysis (AMMA), 406  
African waves  
    Atlantic hurricane season, 138  
    meridional winds, 137, 138  
    northern and southern wave, 139–141  
Asian monsoon  
    differential heating  
        convective heating, 76, 78  
        dry static energy, 77–78  
        eddy flux convergence, 77–78  
        elevated heat source, 76  
        heat sink, 77, 78  
        Tibetan Plateau, 76–77  
        vertically integrated apparent heat source, 77, 78  
    principal axis, 78, 79  
    summer  
        features, 78–80  
        Somali jet (*see* Somali jet)  
        withdrawal dates, 82  
    winter features, 79–81  
Atlantic hurricanes  
    mesoscale models, 373–375  
    multimodel superensemble  
        forecast phase, 368, 369  
        hurricane season, 369, 370  
        intensity errors, 370, 371

intensity forecast, 369  
member model forecasts, 370  
official forecasts, 369

Atmosphere net radiation fluxes

    solar radiation, 291–293  
    thermal radiation, 293, 294

Axisymmetric hurricane model

    Coriolis parameter, 363  
    field of relative humidity, 366  
    hydrostatic equation, 363  
    microphysical sensitivities, 366  
    potential temperature, 362, 365  
    radial-vertical structure, 363, 365  
    radial wind component, 362  
    sea level pressure, 363, 364  
    vertical velocity, 365

## B

Barotropic instability  
    finite difference methods, 127–128  
    perturbation stream function, 124–125  
    phase speed, 125–126  
Batavia sea breeze time section, 377, 378  
Buoyancy-driven shallow moist convection  
    closed system of equations, 239–240  
    cloud model, 237  
    independent and dependent variables, 239  
    initial and boundary conditions and domain definition, 241–242  
numerical model results  
    initial state distribution, 242, 243  
    streamlines and liquid water mixing ratio, 242, 246  
    vertical velocity and temperature departure, 242, 246

**C**

- Cloud microphysics
  - hydrometeor species, 249
  - prognostic equations, 248
- Cloud torques, 347–348
- Combined barotropic-baroclinic instability
  - African easterly waves, 135–136
  - diabatic heating, 131
  - EKE and EAPE, 134–135
  - Fourier transformation method, 132
  - hydrostatic law, 132
  - latitude function, 129
  - low-level jets, 129, 130
  - predictor-corrector scheme, 134
  - quasigeostrophic potential vorticity, 128
  - spectral equations, 133
  - wave disturbances, 130
  - zonal flow, 129–130
  - zonal kinetic energy, 135
- Conservation of potential vorticity (PV), 333

**D**

- Decay-SHIPS (DShP), 368
- Defense Meteorology Satellite Program (DMSP), 29
- Desert heat lows
  - diurnal change, 61–64
  - heat low and lateral teleconnections, 71
  - July and January sea level pressure, 59–60
  - radiative transfer, 68–71
  - Stefan-Boltzman law, 60
  - surface air temperature and sea level pressure, 61, 62
- vertical motion and divergence structure
  - average horizontal divergence and vertical velocity, 66, 67
  - dropwindsondes, 65
  - heat low circulation, 62, 65
- Diabatic effects, 334–335
- Diabatic potential vorticity equation, 223–225
  - absolute and potential vorticity, 221
  - frictional contribution, 228–229
  - horizontal advection, 224
  - horizontal differential heating, 227–228
  - hurricanes
    - differential heating and horizontal advection, 230
    - easterly wave, 230
    - tropical disturbances, 230–231
  - isentropic surface, 223
  - stability equation, 221
  - vertical advection, 224
- vertical differential heating
  - low cloud motions, 226
  - shallow convective, 227
- Diurnal changes
  - Africa and GATE experimental region, 385
  - atmospheric surface tidal pressure signal, 283
  - average divergence profiles, 284
  - convergence, 284
  - disturbance cloudiness, 283
  - monsoon belt
    - Arritt nomogram, 392–395
    - diurnal fluctuation, 390
    - Himalayan Foothills and the Eastern Tibetan Plateau, 391, 392
    - hourly variation, surface wind speeds, 387
    - monsoonal scale diurnal oscillation, 395–397
    - rainfall, 387, 388
    - rainfall over India, 390
    - vertical distribution, 386
    - winds, 386, 387
  - net radiative warming, 284, 285
  - nocturnal rainfall maximum, 283
  - oceanic atolls, 283
  - precipitation curve, 283
  - radiative effect, 284, 286
  - sea level pressure, 283
- Dry static energy
  - conservation of potential temperature, 301
  - definition, 300
  - dry static stability equation
    - diabatic heating, 303
    - eastern oceans, 304
    - eastern tropical oceans, 305
    - eddy heat flux, 303
    - first law of thermodynamics, 303
    - trade wind inversion, 303, 304
    - vertical diffusion model, 306
  - equations of motion, 301
  - first law of thermodynamics, 301
  - hydrostatic law, 301
  - scale analysis, 301
- E**
  - Eddy correlation method, 266
  - El Niño and southern oscillation
    - PNA, 208, 209
    - sea level pressure anomaly, 200–202
    - SST anomaly, 206–207
    - thermocline transitions, 204–206

- trade winds, 202–203
- westerlies, 208–209
- Western Pacific Ocean, 203–204
- Zebiak-Cane Ocean model
  - mass continuity equation, 210–211
  - Rayleigh friction, 211
- European Centre for Medium-Range Weather Forecasts (ECMWF) model, 368
- Explicit clouds, 361
- Extratropical transitions
  - Atlantic hurricane season, 339–340
  - climatological remote connections, 340
  - non-convective rain, 340
  - northern hemisphere tropical cyclones, 331, 337
  - phase space diagram, 340–342
  - storm relative thermal wind field, 342
  - thermal structure, 338, 339
  - transition climatology, 339
  - tropical storm, 339
- F**
- First GARP Global Experiment (FGGE), 87
- Fujiwhara effect, 337, 338
- G**
- GFDL hurricane model, 367
- GUNA forecast, 368
- H**
- Hadley cell
  - Kuo-Eliassen equation
    - boundary eddy momentum forcing *vs.* internal differential heating, 14–15
    - diabatic heating, 14
    - elliptic partial differential equation, 14
    - primitive equations, 10–11
    - stream function, 12–13
    - zonal mean circulation, 13
  - radiative forcing, 293, 294
- Heat induced circulation
  - Adrian Gill's atmospheric model
    - antisymmetric forcing, 55–59
    - non-dimensional pressure, 49–50
    - parabolic cylinder functions, 51–53
    - shallow water equations, 48
    - symmetric forcing, 53–56
  - desert heat lows
    - diurnal change, 61–64
    - heat low and lateral teleconnections, 71
- July and January sea level pressure, 59–60
- radiative transfer, 68–71
- Stefan-Boltzman law, 60
- surface air temperature and sea level pressure, 61, 62
- vertical motion and divergence structure, 62, 65–67
- heat budget, 72–73
- Horizontal shear flow instability, 332–333
- Hurricanes
  - axisymmetric hurricane model
    - Coriolis parameter, 363
    - field of relative humidity, 366
    - hydrostatic equation, 363
    - microphysical sensitivities, 366
    - potential temperature, 362, 365
    - radial-vertical structure, 363, 365
    - radial wind component, 362
    - sea level pressure, 363, 364
    - vertical velocity, 365
  - cold temperature anomalies, 319
  - curvature vorticity, 357–358
  - different typhoons, 322, 323
  - equivalent potential temperature, 321
  - forecast
    - Atlantic Hurricanes, 368–371
    - mesoscale models, 373–375
    - operational models, 366–368
    - Pacific typhoons, 371–372
  - genesis
    - conservation of potential vorticity (PV), 333
    - diabatic effects, 334–335
    - horizontal shear flow instability, 332–333
    - potential vorticity equation, 335–336
  - global map, 331
  - gradient thermal wind, 320, 321
  - inner core
    - dropwindsondes, 324–326
    - LASE, 325, 327, 328
    - scatterometer, 323–324
  - intensity
    - angular momentum, 342–343, 345–346
    - constant angular momentum profile, 349–350
    - inner *vs.* outer forcing, 352–355
    - local cylindrical coordinates, 343–344
    - tangential wind, 345
    - torques (*see* Torques)
    - vortex Rossby waves, 356–357
    - vortical hot towers, 355–356

### Hurricanes (*cont.*)

- Northern Atlantic genesis location, 331
- Pacific Oceans' genesis location, 331
- shear vorticity, 357–358
- storm-relative wind speeds, 317, 318
- temperature anomaly, 318, 319
- tracks
  - $\beta$  effect, 336–337
  - extratropical transitions
    - (*see* Extratropical transitions)
  - Fujiwhara effect, 337, 338
  - wind, 336
- tropical cyclone, 322
  - Bay of Bengal, 329, 330
  - climatological tracks, 327, 329
- wave-number domain
  - azimuthal hurricane scales, 181, 185
  - cloud-scale, 183
  - energy transfer, 185, 188
  - kinetic energy, 185, 187
  - potential energy, 185, 186
  - rainwater mixing ratio, 183–184
  - short and the long wave scales, 182

### I

#### Indian monsoon

- active, break and withdrawal phases
- climatological daily rainfall
  - values, 106, 107
- clockwise and counterclockwise gyres, 107
- CLOUDSAT imagery, 108
- daily all-India observed rainfall, 106, 107
- dry spells, 107–108
- MJO time scale, 109
- MODIS satellite, 108
- quasi-biweekly mode, 107, 109
- ten-year-averaged power spectrum, all-India summer monsoon, 109
- breaks
  - antecedents, 104
  - composed OLR anomalies, 104, 106
  - daily rainfall, 19, 72, 103, 104
  - equatorial latitudes, 104–105
  - OLR and OLR anomaly, 103–105
  - phenomenological scenario, 106
- Intertropical Convergence Zone (ITCZ)
  - aqua planet integrations, 42
  - Coriolis force, 39
  - Earth's rotation, 39, 41
  - global tropics, 38

### Indian Ocean, 43

- OLR, 35, 36
- precipitation, 35, 37
- SSTs, 39, 40
  - cloud thermostat theory, 45
  - homogenize and heterogenize, 44–45
  - warm pools, 43
- stratus clouds, 43
- thermocline, 42
- warmest sea surface temperatures, 39

### L

#### Lidar atmospheric sensing experiment (LASE), 325

### M

- Madden Julian Oscillation (MJO), 173
- baroclinic structure, 145
- CISK mechanism, 154
- cloud elements, 148
- Ekman pumping, 154
- ENSO, birth and demise of, 158, 159
- global spectral model, 153
- heating profile, vertical structure of, 154
- Hovmöller diagram, 147, 148
- intraseasonal oscillation, 149
- ISO, real data forecasts of
  - Australian monsoon, 162, 164
  - Chinese monsoon, 162, 163
  - Indian monsoon, 162
- ISO waves, 149
- latitude-time cross-section, 149, 150, 152
- off-equatorial component, 149
- oscillating dipole heat source, 154, 155
- power spectra, 145
- pressure-time analysis, 145, 146
- $\sigma$ -coordinate system, 151, 153
- time longitude section, 154, 155
- velocity potential charts, 146, 147
- wave CISK, 156
- wave energy flux, 158, 160–161
- westerly wind burst, 157–158
- zonal wind anomalies, 142, 143
- Meso Convective systems (MCS)
  - Asian summer monsoon, 409
  - convective rain fractions, 408
  - ITCZ, 407
  - meso/beta scale, 399
  - mesoconvective rain producing systems, 407

- South Pacific Convergence Zone**  
 precipitation, 409
- stratiform rains fractions**, 408–409
- total annual rainfall**, 407, 408
- TRMM satellite's precipitation radar**, 407
- vertical momentum transport**, 399
- Mesoscale model**  
 Atlantic Ocean hurricanes, 370, 373–375  
 coarser resolution, 361  
 explicit clouds, 361  
 structure, motion and life cycle, 361
- MJO.** *See* Madden Julian Oscillation (MJO)
- Moist static energy.** *See also* Trade wind inversion  
 definition, 300  
 moist static stability equation, 306–308  
 radiative heating, 302  
 rate of evaporation, 302  
 sensible heat flux, 302
- Monsoon onset**  
 Arabian Sea cooling  
 bulk aerodynamic formula, 87  
 FGGE, 87  
 mechanisms, 90–92  
 onset vortex, 89  
 sea level wind speed, 87, 88  
 sea surface temperatures, 90, 91  
 streamline and isotachs chart, 87, 88  
 surface wind speed, 89  
 surface wind stress, 89, 90  
 wind stress curl, 89, 90
- dynamical fields  
 kinetic energy spectra, 93, 94  
 meridional temperature gradient, 93, 95  
 planetary scale, 93  
 rotational and divergent kinetic energy, 92–93  
 zonal and meridional winds, 93  
 zonal wave number, 93, 94
- features  
 climatological precipitation, 84, 85  
 onset date over Kerala, 83, 84  
 onset date over Tamil Nadu, 84, 85
- wall of moisture, 84, 86
- and withdrawal isochrones  
 Asian summer monsoon dates, 82  
 CLOUDSAT imagery, 83  
 isopleths, 83  
 land-atmosphere coupling, 81  
 Maritime Continent region, 82–83  
 northward steering, 83  
 northwestward progression, 81  
 semi-arid land surface, 81
- Monsoons**  
 Asian (*see* Asian monsoon)  
 climatological 925 mb streamlines, 75, 76  
 definition, 75  
 differential heating  
 convective heating, 76, 78  
 dry static energy, 77–78  
 eddy flux convergence, 77–78  
 elevated heat source, 76  
 heat sink, 77, 78  
 Tibetan Plateau, 76–77  
 vertically integrated apparent heat source, 77, 78
- domain, 75, 76  
 heaviest rainfall of summer, 102–103
- Indian monsoon** (*see* Indian monsoon)
- $\psi\chi$  interactions  
 arbitrary vector and scalars, 97–98  
 area average, 97  
 boundary flux term, 100–101  
 continuity equation, 95  
 covariance, 102  
 divergence equation, 95–97  
 energy equation, 98–99  
 $\psi\chi$  equations, 101  
 first law of thermodynamics, 95, 99–100  
 horizontal wind vector, 95  
 hydrostatic law, 95  
 inequality arguments, 101–102  
 relative vorticity, 96  
 rotational wind, 96  
 total energy, 100  
 total kinetic energy, 96  
 vorticity equation, 94
- onset (*see* Monsoon onset)
- Somali jet (*see* Somali jet)
- N**
- National Hurricane Center (NHC), 121
- Navy NOGAPS model, 367
- Net solar radiation, 291–293
- Net thermal radiation, 293, 294
- O**
- Organization of convection  
 hurricanes, 409  
 Indian monsoon forecast, 412  
 ITCZ, 409  
 mesoconvective precipitating elements, 412  
 mesoconvective rain elements, 412

- Organization of convection (*cont.*)  
 monsoon depression, 409, 412  
 tropical disturbances, 409–410  
 typhoon, 410, 411
- Outgoing long wave radiation (OLR), 103–104
- P**
- Pacific North American Pattern (PNA), 208, 209  
 Parseval's Theorem, 189  
 Pressure torques, 350–353
- R**
- Radiative forcing  
 atmosphere net radiation fluxes  
   solar radiation, 291–293  
   thermal radiation, 293, 294  
 Hadley and east–west circulation, 293, 294  
 monsoon, 295–297  
 shallow stratocumulus clouds and radiative transfer, 282–283  
 surface energy balance  
   constant flux layer, 284  
   ground temperature Tg, 285  
   hydrological budgets and water cycle studies, 285  
   net solar (shortwave) radiation, 283–284, 286, 287  
   net thermal (longwave) radiation, 283–284, 286–288  
   surface latent heat flux, 290–291  
   surface sensible and latent heat fluxes, 286  
   surface sensible heat flux, 288–289
- Relaxed Arakawa Schubert (RAS), 42  
 Rossby waves, 356–357
- S**
- Scale interactions  
 definition, 169  
 Fourier coefficients, 194–196  
 frequency domain  
   latent-heat fluxes, 174, 175  
   MJO, 173, 176  
   synoptic and mesoscale disturbances, 177  
   West Pacific Ocean, 174, 176  
 Parseval's theorem, 194  
 wave-number domain  
   derivation of, 185, 187–193  
   energy exchanges, 170–173
- global tropics, 177–180  
 hurricanes, 180–185  
 kinetic energy, waves exchange of, 170–171  
 quadratic non-linearities, 172  
 trigonometric selection rules, 170  
 triple product non-linearities, 172
- Sea breeze phenomenon  
 Batavia sea breeze time section, 377, 378  
 cumulonimbus convection, 377  
 linear sea breeze problem  
   equations of motion, 378  
   Estoque's problem, 380–381  
   first law of thermodynamics, 379  
   mass continuity equation, 379  
   motion and thermal variables, 381  
   surface temperature, 340  
   temperature perturbation, 381  
   three-dimensional hydrostatic system, 381  
   vertical velocity field, 382  
 Texas Gulf Coast, 377, 379  
 time evolution, 377
- Sea surface temperatures (SST), 39, 40, 90  
 cloud thermostat theory, 45  
 homogenize and heterogenize, 44–45  
 warm pools, 43
- SHIPS method, 368
- Somali jet  
 boundary layer dynamics  
   balance of forces, 116, 117  
   eddy diffusion coefficient, 115  
   Ekman, advective and stokes regimes, 114  
   equation of motion, 113, 115  
   horizontal wind barbs, meridional-vertical plane, 115, 116  
   ITCZ, 116  
   mass continuity equation, 115  
   scaling, 113–114  
   ω-f space, 114  
   climatological flow splits, 110  
   climatological horizontal spread, 109, 110  
   French METEOSAT-East, 111  
   INSAT, 110  
   Kenya highlands and Ethiopian mountains, 111  
   850 mb analysis, 111  
   meridional component, 111, 112  
   northward passage, monsoon gyre, 112, 113  
   rotational wind component, 112  
   upwelling, 117, 118

- South Pacific Convergence Zone (SPCZ), 31, 409
- Squall lines. *See* Tropical squall lines
- Surface energy balance  
constant flux layer, 284  
ground temperature Tg, 285  
hydrological budgets and water cycle studies, 285  
net solar (shortwave) radiation, 283–284, 286, 287  
net thermal (longwave) radiation, 283–284, 286–288  
surface latent heat flux, 290–291  
surface sensible and latent heat fluxes, 286  
surface sensible heat flux, 288–289
- Surface frictional torques, 348–349
- T**
- TEJ. *See* Tropical easterly jet (TEJ)
- Torques  
cloud torques, 347–348  
pressure, 350–353  
surface frictional torques, 348–349
- Trade wind inversion  
climatology, 308, 309  
coastal region, 309  
dry and moist static stability, 314, 315  
height of, 310–312  
high-pressure system, 309  
Los Angeles, 309–310  
relative humidity, 310, 313  
subtropical high, 309  
temperature, 310–313  
undisturbed tropical environment, 314
- TRMM. *See* Tropical Rainfall Measurement Mission (TRMM)
- Tropical boundary layer  
bulk aerodynamic method, 264–265  
cross-equatorial flows and planetary boundary layer dynamics  
advection boundary layer, 278  
Ekman solution, 277  
friction layer, 278  
meridional-vertical plane, 277, 278  
Somali jet, 278–279  
dry and moist static energy, 267  
eddy correlation method, 266  
Ekman spiral, 270  
Meteor Profile Buoy, 266  
mixed layer, 268–269  
mixing-length, 261–262  
scale analysis, 275–276
- sea surface fluxes, 267, 268
- surface similarity theory  
Monin-Obukhov length, 272
- Stable Planetary Boundary layer, 274–275  
vs. dimensionless wind shear and dimensionless temperature gradient, 273, 274
- undisturbed and disturbed conditions, 269
- wind profile and surface drag, 262–263
- Tropical cloud ensembles  
buoyancy-driven dry convection  
continuity equation, 236  
diabatic heating, 237  
dry convection thermals, 235  
solid lines and dashed lines, 237, 238  
buoyancy-driven shallow moist convection  
initial and boundary conditions and domain definition, 241–242  
numerical model results, 242–246  
simple cloud model, 237–241
- cloud microphysics, 247–251
- cloud types, 233, 234
- conversion processes  
accretion, 252–253  
autoconversion, 251–252  
evaporation, 253–254
- kinematics and thermodynamics, 244–247
- modeling results  
heating/cooling profiles, 256, 258  
hydrometeors, 254–255, 257  
ice phase, 254, 255  
squall line, 254, 255
- Tropical easterly jet (TEJ), 402
- Tropical Rainfall Measurement Mission (TRMM), 28
- Tropical squall lines  
convective component, 399  
rain areas, 399  
thermodynamical constraints, 399
- West African disturbance lines  
AEJ, 402  
African squall line, 404  
African waves, 401–402  
Atlantic Ocean, 402, 403  
GARP, 402  
GATE, 402  
ITCZ disturbance, 405  
Mower's picture, 404  
oceanic region, 403

- Tropical squall lines (*cont.*)**
- relative humidity and pressure, 400
  - squall and non-squall systems, 405–407
  - surface temperatures, 400
  - TEJ, 402
  - thermodynamic profile, 403
  - wind profile, 403
- Tropical waves and tropical depressions**
- AEFs, 123
  - African waves
    - Atlantic hurricane season, 138
    - meridional winds, 137, 138
    - northern and southern wave, 139–141
  - Atlantic tropical cyclones, 124
  - barotropic instability
    - finite difference methods, 127–128
    - perturbation stream function, 124–125
    - phase speed, 125–126
  - combined barotropic-baroclinic instability
    - African easterly waves, 135–136
    - diabatic heating, 131
    - EKE and EAPE, 134–135
    - Fourier transformation method, 132
    - hydrostatic law, 132
    - latitude function, 129
    - low-level jets, 129, 130
    - predictor-corrector scheme, 134
    - quasigeostrophic potential vorticity, 128
    - spectral equations, 133
    - wave disturbances, 130
    - zonal flow, 129–130
    - zonal kinetic energy, 135
  - inverted-V, 121
- U**
- UK Met Model, 367
- W**
- Wave-number domain
- closed system, 190–191
  - energy exchanges, 170–173, 192–193
  - Fourier transform, 187–189
  - global tropics
    - east–west thermal asymmetry, 178–179
    - energy exchanges, 179, 180
    - kinetic energy spectra, 177, 178
    - planetary scale monsoon, 178
    - velocity potential and divergent wind, 179
  - hurricanes
    - azimuthal hurricane scales, 181, 185
    - cloud-scale, 183
- Z**
- Zonally asymmetric climatology
- dynamical parameters
    - charts of, 32
  - east/west circulations, 24–26
  - moisture field, 25–27
  - motion field, upper troposphere
    - northern summer 200 mb, 20, 21
    - northern winter 200 mb, 20
  - precipitation field
    - DMSP, 29
    - features, 31–32
    - TRMM, 29, 30
  - sea level pressure field, 27–28
  - temperature field
    - boreal summer season, 23, 24
    - northern hemisphere summer, 22, 23
    - northern hemisphere winter, 22
    - Tibetan plateau, 23
  - tropospheric winds, 850 and 200 mb levels, 17–20

- Zonally averaged tropical circulation
  - Kuo-Eliassen equation
    - derivation of, 10–13
    - interpretation of, 13–15
  - meridional transports
    - Hadley cell, 9
    - kinetic energy, 9
    - momentum, 7, 8
  - potential energy, 7, 8
  - sensible heat, 7, 8
- meridional-vertical plane, 1
- zonally averaged time mean fields
  - mean meridional circulation, 3–5
  - moisture field, 6, 7
  - temperature field, 5–6
  - zonal velocity, 2–3